KERNFORSCHUNGSANLAGE JÜLICH
GESELLSCHAFT MIT BESCHRÄNKTER HAFTUNG

International Conference on Vacancies and Interstitials in Metals

Sept. 23 – Sept. 28, 1968

Kernforschungsanlage Jülich, Germany

Preprints of conference papers

Jül - Conf - 2 (Vol. I)
September 1968

Als Manuskript gedruckt

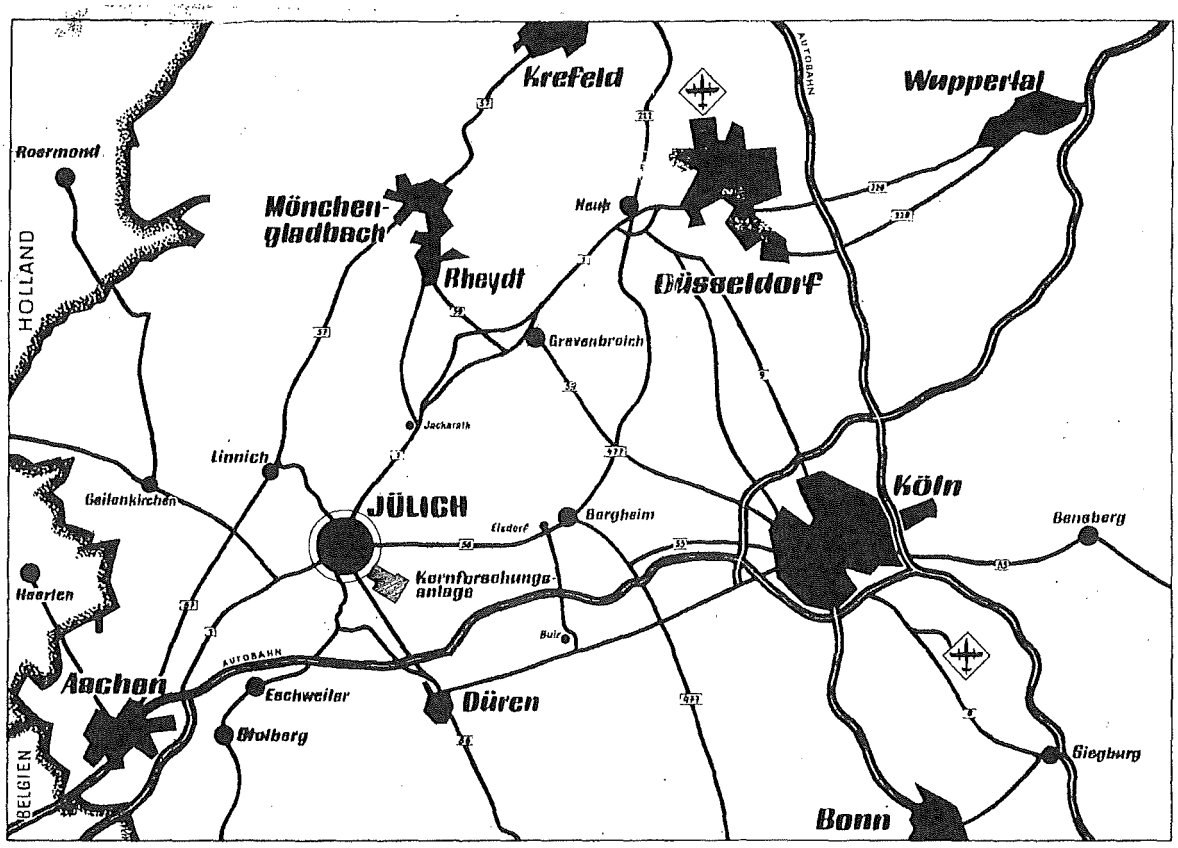

Berichte der Kernforschungsanlage Jülich – Jül – Conf – 2 (Vol. I)

Dok.: Solid State Physics - Conferences
Conferences - Federal Republic of Germany
Metals - Point Defects

DK: 539.2 : 061.3
061.3 (430.1)
669 : 539.2

Zu beziehen durch: ZENTRALBIBLIOTHEK der Kernforschungsanlage Jülich GmbH,
Jülich, Bundesrepublik Deutschland

Schutzgebühr DM 16,- für Vol. I und Vol. II

International Conference on

Vacancies and Interstitials in Metals

Kernforschungsanlage Jülich, Germany

September 23 – 28, 1968

PREPRINT OF CONFERENCE PAPERS Vol. I

The conference is organized by the Kernforschungsanlage Jülich, Germany, in collaboration with the Arbeitsgemeinschaft Metallphysik (Deutsche Physikalische Gesellschaft, Deutsche Gesellschaft für Metallkunde, Verein Deutscher Eisenhüttenleute). The conference is sponsored by the International Union of Pure and Applied Physics and the Bundesministerium für wissenschaftliche Forschung.

Scientific Committee:

R.S. BARNES (Harwell, U.K.)
L.M. CLAREBROUGH (Melbourne, Australia)
D. DAUTREPPE (Grenoble, France)
J.S. KOEHLER (Urbana, Ill., U.S.A.)
S. OKUDA (Tokai-mura, Ibaraki-ken, Japan)
A. SEEGER (Stuttgart, Germany)
F.W. YOUNG (Oak Ridge, Tenn., U.S.A.)

Organizing Committee:

J. DIEHL (Stuttgart, Germany)
W. SCHILLING (Jülich, Germany)
D. SCHUMACHER (Grenoble, France)

Preface

The International Conference on Vacancies and Interstitials in Metals, Jülich 1968, has been organized with the intent to give a general survey of our present knowledge on point defect phenomena in metals. Although the rapid development of this field in the early sixties seems to have slowed down, at present many of the fundamental problems are still unresolved. This holds especially for the problem of defect identification and the interpretation of annealing stages. Further progress is to be expected mainly from the application of experimental tools which give more detailed information about the structure of the single defect and from a better correlation of experiments in which the defects have been generated by different techniques e.g. quenching, particle irradiation, plastic deformation.

For this reason, particular attention is focused on reviewing the information accumulated from equilibrium, quenching, irradiation and plastic deformation experiments employing the more common techniques, as well as to the search for new, more powerful tools for the study of interstitials and vacancies.

The scientific program of the conference is based on about 25 invited lectures (with ample discussion time) which are thought to cover the essential topics of the field. Abstracts of these lectures, in so far as they have been received, are included in the present report. The full papers will be published in book form a few months after the conference.

In addition to the invited lectures the organizing committee has received an unexpectedly large number of contributed papers. Only about 30 of these papers can be presented orally. The other papers will be introduced by the invited speakers and will be open for discussion thereafter. Nevertheless, all contributed papers accepted have been reproduced in this pre-conference report and will be distributed to the conference participants before the beginning of the conference. This procedure is hoped to give a basis for fruitful discussions and individual scientific contacts at the meeting. Reproduction directly from the as-received manuscripts has been employed to assure early distribution of this report.

Jülich, September 1968

J. Diehl, W. Schilling
D. Schumacher, A. Seeger

Contents

I. DIFFUSION AND EQUILIBRIUM MEASUREMENTS

Analysis of Diffusion and Equilibrium Measurements

A.Seeger, Max-Planck-Institut für Metallforschung,
Institut für Physik, Stuttgart

A b s t r a c t

It has been customary to interpret high-temperature experiments on metals in which point defects are in thermal equilibrium (e.g., self-diffusion measurements, electro-transport, lattice parameter and thermal expansion measurements) in terms of monovacancies. The present paper reviews the following questions:

(i) How can we decide whether this assumption is justified?

(ii) If it is not justified, how can we nevertheless extract reliable information on monovacancies from such experiments?

(iii) How can we obtain from high-temperature measurements on metals information on point defects other than monovacancies, e.g. divacancies?

The review is divided into two parts. Part I gives a survey of the available approaches to the solution of these questions, and emphasizes the need for the further extension of experimental techniques. Part II illustrates the general concepts by a number of selected examples.

I. If the Arrhenius plot of the self-diffusion coefficient is straight within the experimental accuracy, two pieces of information can be deduced, the activation energy of self-diffusion and the pre-exponential factor. The magnitude of the preexponential factor allows us to judge whether the activation energy may be interpreted as the sum of the formation and migration energy of monovacancies or not. If the preexponential factor is too large for a monovacancy interpretation, we may expect that improved accuracy or extension of the self-diffusion

measurements will show up a curvature in the Arrhenius plot. Such a curvature may have three origins: (i) A significant contribution of more than two defects, e.g. monovacancies and divacancies. (ii) A temperature dependence of the activation energies and entropies. (iii) A contribution of short-circuits (e.g., dislocations or grainboundaries) at low temperatures.

Mechanism (iii) can be eliminated by confining the low temperature experiments to short penetration depths, by careful analysis of the penetration plots, and by use of nuclear magnetic resonance for the determination of self-diffusion coefficients. The various NMR techniques will be reviewed with particular emphasis on the relaxation in the rotating field. Mechanisms (i) and (ii) can be separated from the temperature dependence of the self-diffusion isotope effect or by comparison of self-diffusion and electro-transport experiments. If these informations are not available with sufficient precision, we have to resort to a least square analysis of the temperature dependence of the self-diffusion coefficient, which is affected differently by (i) and (ii).

Equilibrium concentrations of vacant lattice sites are usually known with less accuracy than the self-diffusion coefficients. It will be discussed how the information contained in them can be used in conjunction with self-diffusion data to determine the properties of vacancy-type point defects.

II. The general ideas outlined in I will be illustrated by examples which include Al, Ag, Au, Ni, and also some b.c.c. metals.

EQUILIBRIUM MEASUREMENTS

IN HIGH MELTING POINT MATERIALS

M. Hoch
Department of
Materials Science and Metallurgical Engineering
University of Cincinnati
Cincinnati, Ohio 45221, U.S.A.

ABSTRACT

The energy and entropy of formation of vacancies in metals can be determined from measurements at temperature of properties, which are influenced by the vacancies. Such properties are specific heat, heat content, thermal expansion, and electrical resistivity. These measurements are in contrast to property measurements on quenched samples.

In all equilibrium measurements, a base line is established at low temperatures, where the vacancy does not contribute to the property measured. This base line is then extrapolated to high temperatures, and, from the difference between the actual measurement and the base line, the influence and concentration of vacancies can be deduced. From the equilibrium measurements only the specific heat and heat content data yield directly the energy and entropy formation of vacancies, and thus their concentration at any temperature. In the other methods, only the energy is obtained directly; the entropy is obtained only within a factor, which relates the contribution of the vacancy to the property measured: e.g. the volume of a vacancy compared to that of an atom, or the resistance increment due to a vacancy.

To obtain heat content and specific heat at elevated temperature, three general methods are available: adiabatic calorimetry, drop calorimetry, and transient techniques. Adiabatic calorimetry is the most direct method to obtain specific heat. The method is limited to 1300 - 1400°K. Drop calorimetry has no temperature limitations; it yields heat content data. Because the contribution of the vacancies to the heat content even at the melting point is only five percent, very accurate data are required to obtain meaningful vacancy properties. Transient techniques, such as the modulation method, must rely on the accurate knowledge of the variations of the resistance of the sample with temperature.

The present paper will concentrate on the discussion of the specific heat and heat content measurement at elevated temperature T>1000°K.

To show the agreement between the various specific heat methods, and the apparent disagreement with other methods used, Table I shows the energy and entropy of formation of vacancies in copper and molybdenum and their concentration at the melting points (1356 and 2700°K). The methods using specific heat and heat content give identical concentration of vacancies at the melting point which are much larger than those obtained by other methods. The entropy of formation is large, indicating a very significant relaxation around a vacancy. This relaxation probably involves not only the atoms next to a vacancy, but those farther away. The disagreement between the various methods is due to this large relaxation and will be discussed in detail.

Experimental data for gold, platinum, aluminum, chromium, niobium, tungsten, and tantalum will also be discussed.

Table I

Energy and entropy of vacancy formation in Cu and Mo:

	E ev	$\frac{\Delta S}{k}$	$C_{mp\%}$	Method
Cu				
	1.05	3.7	0.5	modulation, Cp
	1.22	5.25	0.57	adiabatic calorimetry
	0.7		0.2	thermal expansion
	1.17	1.5	0.02	simultaneous bulk and lattice expansion
Mo				
	1.77	3.55	1.7	drop calorimetry
	1.86	3.95	1.7	drop calorimetry
	2.24	5.7	2.2	modulation, Cp

FORMATION ENERGY OF HEAT VACANCIES IN MOLYBDENUM AND THEIR CONCENTRATION

V.Ya.Chekhovskoy, V.A.Petrov

Institute for High Temperatures
Academy of Sciences of the USSR

Moscow,USSR

Formation energy of vacancies in molybdenum-I,86 formation entropy of vacancies -7,8 and dependence of heat vacancies concentration on temperature have been for the first time calculated on the basis of experimental data on enthalpy of molybdenum obtained by "drop method" for temperature range of I000-2850°K. The vacancies concentration at the molybdenum metting point has been found to amount to 2,9%. The results obtained are compared with the data calculated by other authors, on the basis of data on trueheat capacity of molybdenum at high temperatures.

More than 40 years ago Ya.I.Frenkel[I] predicted theoretically formation of point defects in crystal lattice. However, experimental study of heat vacancies has so far covered relatively few metals despite that different methods have been used for the purpose, connected with measurement of additional resistance, accumulated energy and change in the volume of annealed samples, heat expansion, electrical resistivity, heat capacity and etc. [2] Recently basing on data obtained on true heat capacity at high temperatures, formation energy of vacancies and their concentration have been determined for potassium and sodium [2,3], gra-

phite [4] , lead and aluminium [5] , tungsten [6,7] , molybdenum [8] , tantalum [9] , niobium, platinum, copper, gold [10] and cesium [11] .

A study of niobium [12] has shown that high temperature measurements of enthalpy can be successfully applied for calculating energy of vacancy formation and temperature dependence of vacancy concentration.

The work has been continued in [13] and thourough investigation of molybdenum entalphy and mean heat capacity has been carried out by the present authors in a wide temperature range from 1000 to 2850°K using "drop" method. The extreme temperature achieved in this investigation is only some tens degrees lower than the molybdenum melting point, 2890°K. The enthalpy of molybdenum has been measured with several samples machine-tooled of molybdenum rods prepared either by the method of powder metallurgy or by metal remelting in a vacuum arc furnace. Samples of different weight from 50 g to 100 g were used, dependent on the temperature of investigation. Geometrical dimensions of the samples were as follows: diameter of 18 to 20 mm, height of 25 to 40 mm. Impurities in molybdenum amounted to about 0,05%. The samples under study were heated in a tungsten-heater furnace in an atmosphere of pure argon.

The high temperature of the samples in the furnace was measured with disappearing - filament monochromatic optical pyrometers of OPI -48 or PyroluxII types, which were focused onto a cavity in the sample, imitating an ideal black body. The pyrometers were calibrated against reference temperature

lamps of class I. A copper block in an isothermal envelope was used as a calorimeter. The procedure of measurements and the description of the calorimetric set-up are dealt with in detail in [I4-I6].

Fig.I gives the results of molybdenum mean heat capacity measurements against temperature [I3].

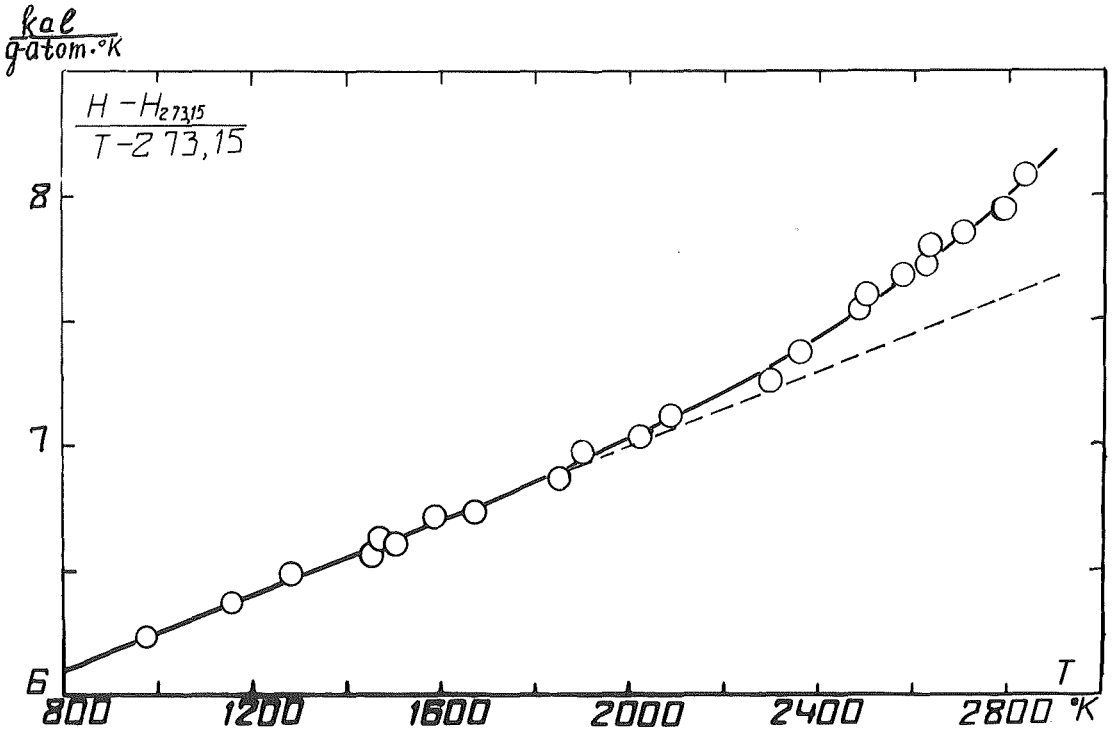

Fig. I

24 experimental points were obtained altogether. Approximately up to I700-I800°K, linear dependence of mean heat capacity on temperature was observed. Above this temperature, temperature coefficient of heat capacity was observed to constantly increase. Assuming, as in the case of vacancies' investigation using the

results of true heat capacity measurement [3-II], that the increase in mean heat capacity (and, consequently, in enthalpy ΔH) in relation to extrapolated linear dependence (dotted line in Fig.I) at temperatures above I700-I800°K is due to vacancy contribution, it is possible to calculate energy of vacancy formation E_{1V}^F

$$\Delta H = E_v^F \cdot A \cdot exp\left(-\frac{E_v^F}{RT}\right) \qquad (I)$$

and the dependence of vacancy concentration on temperature.

$$C_v = A\, exp\left(-\frac{E_v^F}{RT}\right) = exp\left(\frac{S_v^F}{R}\right) exp\left(-\frac{E_v^F}{RT}\right) \qquad (2)$$

where A - entropy factor ; S_{1V}^F - entropy of vacancy formation; R - gas constant; T - temperature in Kelvin degree.

In order to obtain a more accurate value of ΔH, linear dependence of molybdenum mean heat capacity on temperature has been calculated with the method of least squares from experimental points below I700-I800°K where vacancy contribution can be neglected

$$C_p^{расч.} = \frac{H_T - H_{273,15}}{T - 273,15} = 5,7188 + 1,5153 \cdot 10^{-4}(T - 273,15) \frac{кал}{г\text{-}ат \cdot град} \qquad (3)$$

where $H_t - H_{273,15}$ - change in molybdenum enthalpy for the temperature interval from 273,I5°K up to T.

Increase in mean heat capacity for each experimental point relative to extrapolated line(3) can be expressed through logarithm of the respective increase in enthalpy in terms of reciprocal temperature value according to eq. (I) (ref.to Fig.2)

$$\ln \Delta H = \ln(AE_v^F) - \frac{E_v^F}{RT} \qquad (4)$$

where

$$\Delta H = (H_T - H_{273,15})_{оп.} - (H_T - H_{273,15})_{расч.} = (\bar{C}_p^{оп} - \bar{C}_p^{расч})(T - 273,15)$$

Since logarithm values of enthalpy gain for experimental points in Fig.2 fall onto a straight line, it is not difficult to calculate coefficients of equation (4), with least squares method, which allow to determine energy of vacancy formation in molybdenum E_{1V}^{F} = I.86 ev or 42.9 kcal/gr.at, vacancy concentration in molybdenum $C_v = 50.9 \exp \frac{429 \cdot 10^2}{RT}$ and entropy of vacancy formation S_v^f = 7.8 cal/gr.-at degree.

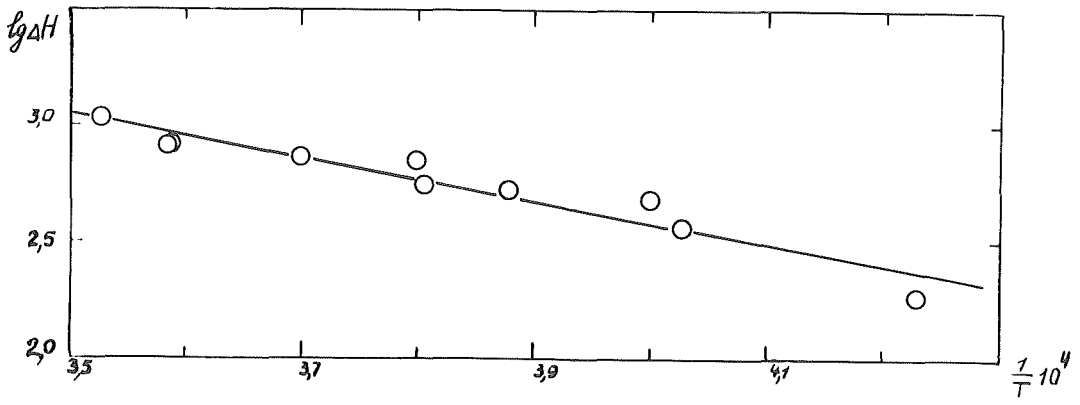

Fig.2

Final equation for molybdenum mean heat capacity for the temperature range of I000 to 2890°K will assume the form.

$$\bar{C}_p = 5{,}7188 + 7{,}5153 \cdot 10^{-4}(T-273{,}15) + \frac{2184 \cdot 10^3}{T-273{,}15} \exp\left(-\frac{429 \cdot 10^2}{RT}\right) \frac{кал}{2\text{-ат. }°K} \quad (5)$$

Values of mean heat capacity calculated from (5) are indicated by solid line in Fig.I. Arithmetic mean deviation of experimental points from the averaging curve is equal to $\frac{\Sigma|\varepsilon|}{n}$ = 0.32%, standard error is $\sqrt{\frac{\Sigma \varepsilon^2}{n-1}}$ = ± 0.40%, and doubled mean square error of mean heat capacity calculated from equation (5) amounts to $2\sqrt{\frac{\Sigma \varepsilon^2}{n(n-1)}}$ = ± 0.I7%. With regard to

enthalpy increase due to vacancy formation at molybdenum melting point being 5.8%, it is possible to estimate calculation error in energy of vacancy formation, as equal to I5-20%.

The early high temperature investigation of molybdenum [I7-2I] fail to be of use for studying vacancies, though the extreme temperatures of the measurement were as high as 2400 to 2600°K. This failure is due to the fact that vacancy contribution into the mean heat capacity, even at so elevated temperatures, is comparable to experimental error, while relative increase in true heat capacity for molybdenum, due to vacancies, is several times the mean heat capacity. This is well demonstrated in Fig.3 which shows the results of direct measurement of true heat capacity for molybdenum [4,8,22] up to melting point.

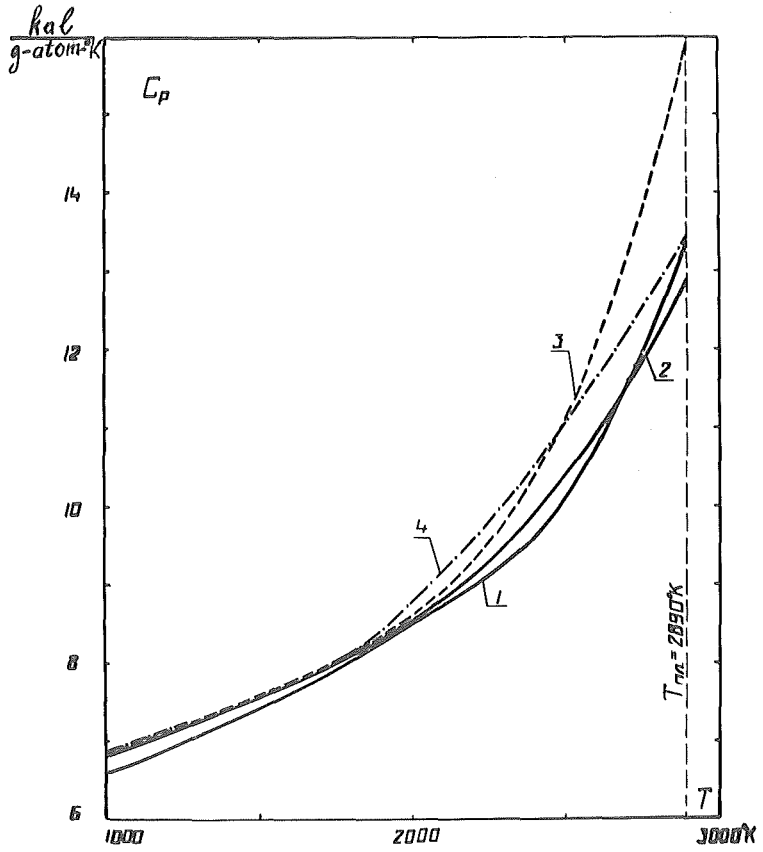

Fig.3. Temperature dependence of true heat capacity of molybdenum I - [22]; 2 - true heat capacity as obtained by differentiating enthalpy equation [I3]; 3 - [8]; 4 - [4].

Equation expressing dependence of increase in true heat capacity due to vacancies, is obtained, following differentiation of eq. (I)

$$\Delta C_p = \frac{(E_v^F)^2}{RT^2} A \exp\left(-\frac{E_v^F}{RT}\right) \qquad (6)$$

Taking logarithm of eq. (6) we obtain

$$\ln\left(T^2 \Delta C_p\right) = f\left(\frac{1}{T}\right) \qquad (7)$$

From this, following the above procedure, it is possible to calculate energy of vacancy formation and vacancy concentration This has been done in [8] and the calculation results are included into Table I. True heat capacity of molybdenum was measured in [8] by means of modulation technique for temperature range of I300° to 2500°K, experimental points scatter being equal to ± I%. Specimens under study were molybdenum wire of 0.03 to 0.05 mm in dia. The specimen temperature was measured from electrical resistivity as determined in [23] . Molybdenum content in the specimens was not determined.

As no detailed calculation was carried out in [4,22] , it seemed worth while to perform this in the present work, so as to be able to compare the results of different studies.True heat capacity in [4] was measured with pulse technique for molybdenum rods or wire in the temperature range of II20 to 2870°K. The temperature was measured with an optical pyrometer against a black body model, with experimental points scatter

being equal to ± 5%. Impurities in molybdenum under study were determined in weight per cent as follows: Fe = 0.25; Si =0.063; Cu = 0.013; Cr = 0.0003; Ti = 0.021; C = 0.008. The result obtained in [4] have been plotted and the plot is reproduced in Fig. 4. The linear portion of the heat capacity curve and its extrapolation (dotted line) can be clearly distinguished, which makes it possible to find an increase in heat capacity due to vacancies. Calculation results are included into Table I.

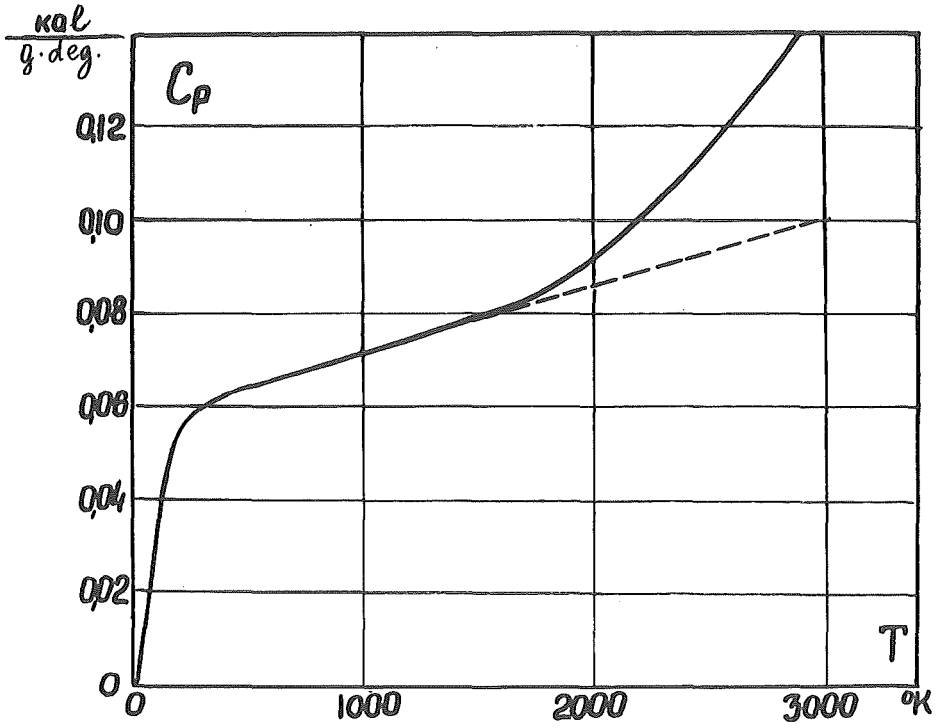

Fig.4. True heat capacity of molybdenum in terms of temperature [4] and extrapolation of linear portion.

True heat capacity of molybdenum in [22] was studied with pulse technique in the temperature range of 200 to 2880°K, temperature being measured from electrical resistivity of the sample wire. The work contains no data on impurities included in

the samples. Maximum scatter in experimental points amounted to ± 6% for temperatures below 2400°K, and to ±10% for the temperature interval above the figure.

The measurement results are presented by a smoothing curve, a portion of which (for temperature range of 400 to 2400°K) was calculated from second power equation. It is natural that, with this wide scatter in experimental points, this equation can satisfactorily average measurement results but hardly describes the actual temperature dependence of heat capacity. Consequently, in this case, unlike that in [4,8], it is rather difficult to distinguish a linear portion of true heat capacity curve (Fig.5) and a linear portion in coordinates of Fig.6, according to eq.(7).

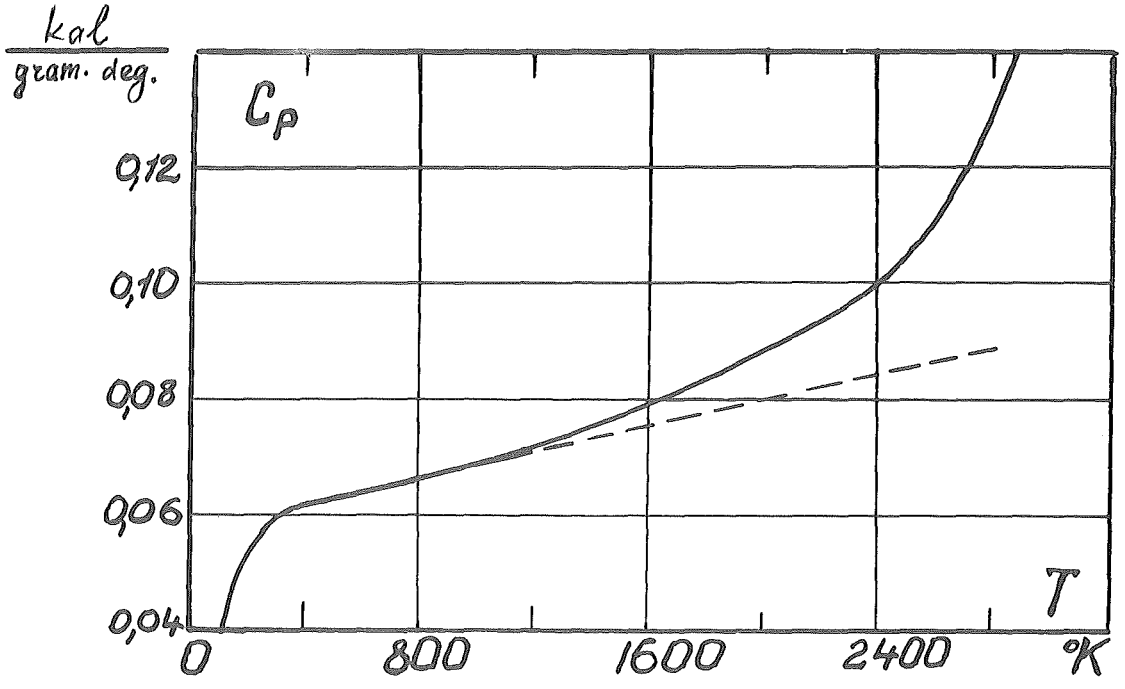

Fig. 5. Temperature dependence of true heat capacity of molybdenum, as in [22].

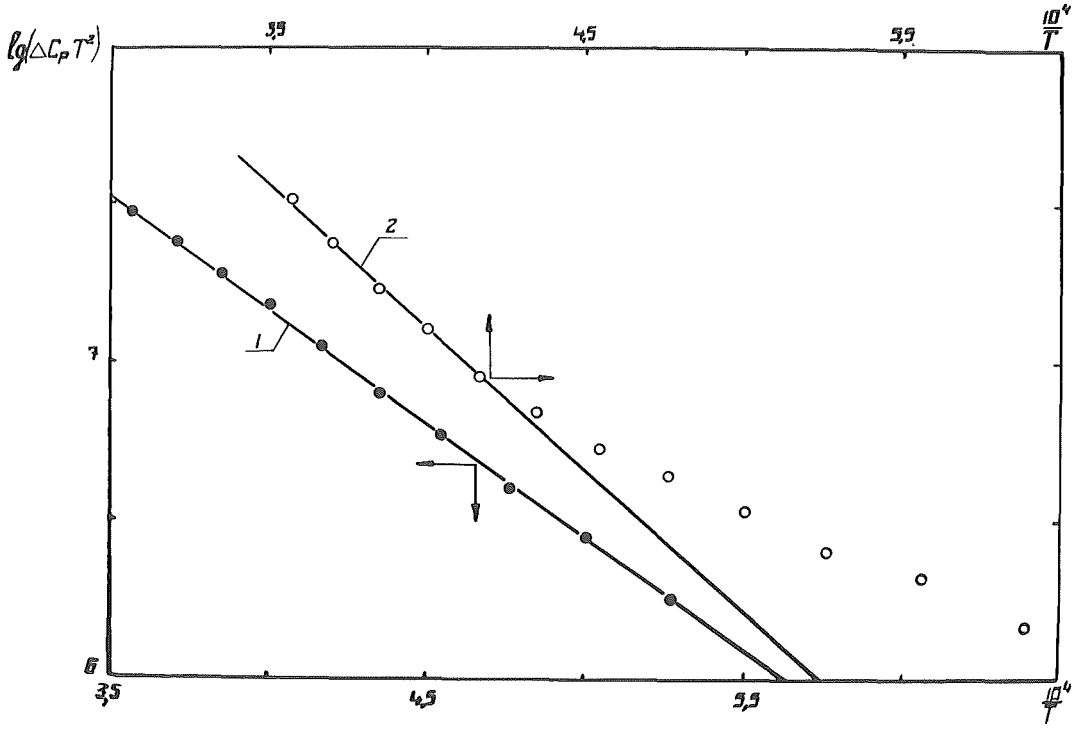

Fig.6. Illustration to calculation of energy of molybdenum vacancy formation
I - data from [4]
2 - data from [22]

Table I summarizes calculation results for all the above papers for the following quantities: energy of vacancy formation, enthalpy factor, entropy of vacancy formation, and vacancy concentration.

TABLE I

Authors	E_v^F ev	E_v^F kcal/gr.at	$\frac{E^F - E^F}{E^F}$ %	A	S_v^F кал/г-ат·град	$\frac{S_v^F}{R}$	C_v %
present work	I,86	42,9	-	50,9	7,8	3,9	2,9
[8]	2,24	5I,5	± 20	300	II,3	5,7	3,8
[4]	I,43	32,8	- 23	I9,2	5,9	3,0	6,3
[22]	I,79	4I,2	- 4	57,6	8,I	4,I	4,4
[24]	2,0I	46,2	+ 8	-	-	-	-

The results of the above studies are, on the whole, in fair agreement, despite considerable errors in initial measurements. In particular, energy of vacancy formation in molybdenum in the above papers is in agreement with the present results within ± 20%. Moreover, there is a fairly good coincidence of this value with that calculated in [24] . The low value for formation energy and comparatively high vacancy concentration in [4] seems to be due to substantial impurities in molybdenum under test [2] .

Temperature dependence of vacancy concentration in molybdenum, as evidenced by all the above studies, is presented in Fig.7.

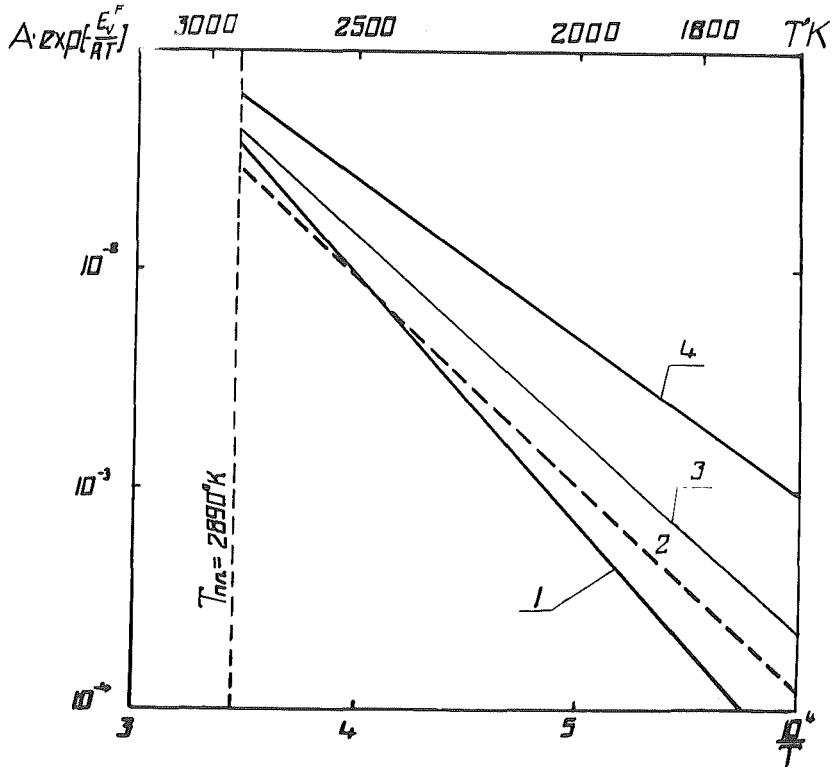

Fig.7. Vacancy concentration in molybdenum.
1.-data from [8]
2 -present data
3 -data from [22]
4 -data from [4]

REFERENCES

I. Ya.I.Frenkel. Zt.Phys.,I926, 35 , 652.

2. Vacancies and other point defects in metals and alloys. Proc.of Symposium held at the Atomic Energy Research Establishment, Harwell Berks on I00 ec.I957,London I958

3. L.Y.Carpenter. J.chem.Phys., I953, 2I , 2244.

4. N.S.Rasor, J.D.McClelland. J.Phys.Chem.Solids,I960, I5, (N°I/2), I7.

5. T.E.Pochapsky. Acta met.,I953, I, 747.

6. Ya.A.Kraftmakher, PMTF, I962,N°5, I76;I963 , N°2.

7. Ya.A.Kraftmakher,P.G.Strelkov,FTT, I962,4, 227I.

8. Ya.A.Kraftmakher,FTT,I964,6, 503.

9. Ya.A.Kraftmakher, PMTF, I963,N°2,I58.

I0. Ya.A.Kraftmakher,FTT, I963,5? 950; I967, 9, I850.
Ya.A.Kraftmakher,E.B.Lanina,FTT, I965,7,I23.
Ya.A.Kraftmakher,P.G.Strelkov,FTT, I966,8,580.

II. J.D.Feder,D.I.Martin.Proc.Roy.Soc.,I965,A284,83.

I2. V.Ya.Chekhovskoy,I.A.Zhukova,FTT, I966,8,9.

I3. V.A.Kirillin, A.E.Sheindlin,V.Ya.Chekhovskoy,V.A.Petrov. Proc.4th Symposium on Thermophysical Properties,april I-4, I968,Univ.of Maryland, USA,p.

I4. V.A.Kirillin, A.E.Cheindlin,V.Ya.Chekhovskoy,DAN SSSR,I960, I35,I25.

I5. V.Ya.Chekhovskoy,A.E.Sheindlin. Zavodskaja laboratoria(Industrial laboratory), I963,29,I258.

I6. V.A.Kirillin,A.E.Cheindlin,V.Ya.Chekhovskoy,Inzhenerno-fizicheskiy zhurnal,I96I,4,3.

I7. C.W.Kothen.Dissert.Abstr.,I957,I7, 2842.

I8. L.S.Lazareva,P.B.Kantor,V.V.Kandyba,Fizika metallov i metallovedenie, I96I,II,628.

I9. V.A.Kirillin, A.E.Sheindlin,V.Ya.Chekhovskoy, DANSSSR,I96I, I39,645.

20. V.Ya.Chekhovskoy.Inzhenerno-fizicheskiy zhurnal AN BSSR, I962,5, 43.

2I. V.A.Kirillin,A.E.Sheindlin,V.Ya.Chekhovskoy.Int.J.Heat Mass Transfer,I962,5, I.

22. R.E.Taylor,R.A.Finsh.J.Less-commen Met.,I964,6, 283.

23. A.G.Worthing.Phys.Rev.,I926,28, I90.

24. K.A.Osipov. "Some activated processes in solid metals and alloys". Moscow,AN SSSR,I962.

THE DYNAMIC EQUILIBRIUM OF POINT DEFECTS IN METALS

K. Míšek, P. Vašek

Institute of Solid State Physics,
Czechoslovak Academy of Sciences,
Prague, Czechoslovakia

The system of simultaneous differential equations, which describe the reactions between vacancies and impurities in f.c.c. metals, is used to the determination of equilibrium concentrations of divacancies and impurity-vacancy complexes. The relations between the local atomic frequencies and the entropy of association are also determined.

INTRODUCTION

Much attention has been paid recently to the study of point defects [1] . Some authors were able to determine consistent sets of vacancy properties for gold, silver, copper [2] and platinum [3] by combining experimental results of annealing and self-diffusion studies with theoretical calculations. Also the application of chemical kinetics to point defect reactions in metals has advanced appreciably and some problems are solved in detail [4,5] .

We are going to show how the kinetic equations may be used to derive formulae relating equilibrium concentrations of divacancies and impurity-vacancy complexes with the kinetic coefficients, and local effective frequencies with association entropies.

DEFECT REACTIONS IN THERMAL EQUILIBRIUM

We shall confine ourselves to the processes which may be

symbolized by the following chemical equations:

$$
\begin{aligned}
&V_1 + V_1 \underset{K_2}{\overset{K_1}{\rightleftharpoons}} V_2 \quad , \quad V_1 \overset{K_9}{\rightleftharpoons} \text{Sink}, \\
&V_1 + J \underset{K_4}{\overset{K_3}{\rightleftharpoons}} C_{11}, \quad V_2 \overset{K_{10}}{\rightleftharpoons} \text{Sink}, \\
&V_2 + J \underset{K_6}{\overset{K_5}{\rightleftharpoons}} C_{21} \ , \\
&V_1 + C_{11} \underset{K_8}{\overset{K_7}{\rightleftharpoons}} C_{21} \ ,
\end{aligned}
\tag{1}
$$

where V_1 denotes single vacancies, V_2 divacancies, J unbound substitutional impurities, C_{11} single vacancy - impurity complexes, and C_{21} divacancy - impurity complexes. K_i are the rate constants. For these reactions in f.c.c. metals the differential equations may be written in the following way:

$$
\begin{aligned}
dv_1/dt &= 2K_2v_2 + K_4c_{11} + K_8c_{21} - 2K_1v_1^2 - K_3v_1i - \\
&\quad - K_7v_1c_{11} - K_9\left[v_1 - v_1\,(T_a)\right] \ , \\
dv_2/dt &= - K_2v_2 + K_1v_1^2 - K_5v_2i + K_6c_{21} - K_{10}\left[v_2 - v_2(T_a)\right] \ , \\
di/dt &= K_4c_{11} + K_6c_{21} - K_3v_1i - K_5v_2i, \\
dc_{11}/dt &= K_3v_1i - K_4c_{11} - K_7v_1c_{11} - K_8c_{21} \ , \\
dc_{21}/dt &= K_5v_2i - K_7c_{11}v_1 - (K_6 + K_8)\ c_{21} \ .
\end{aligned}
\tag{2}
$$

In these equations v_1, v_2, i, c_{11} and c_{21} are the concentrations of defects. The terms describing migration to sinks (with rate constants K_9 and K_{10}) take account of the fact, that after infinite time the equilibrium concentration will be reached, which corresponds to the annealing temperature T_a .

When this system is in thermodynamic equilibrium at temperature T , the left-hand sides of the equations will be zero. Because $T = T(a)$, i.e. $v_1 = v_1(T_a)$, there will be zeros in the paranthesesis near K_9 and K_{10}. There are four unknowns in the resulting set of simultaneous nonlinear algebraical equations, i.e. v_2, c_{11}, c_{21} and i ; the concentration of single vacancies v_1 is supposed to be known.

When combining the equations we can express the concentration of divacancies by means of the other concentrations, e.g.

$$v_2 = (K_1/K_2)v_1^2 - 2(K_8/K_2)c_{21} - 2(K_7/K_2)v_1\, c_{11} ,$$

which contains always some of the other unknowns. In order to get a better insight, we have to simplify the system (2). This can be done by excluding the reaction between C_{11} and C_{21} (we put $K_7 = 0$ and $K_8 = 0$). This in fact corresponds to the assumption that $E^B_{2V} > E^B_{C_{11}}$, which is a special choice, having profound influence on the reactions studied. Then it is easy to show, that the following formulae hold:

$$v_2 = (K_1/K_2)\, v_1^2 ,$$

(3)
$$c_{11} = (K_3/K_4)\, v_1\, i ,$$

$$c_{21} = (K_5/K_6)v_2\, i = (K_1K_5/K_2K_6)\, v_1^2\, i .$$

The formulae (3) are in fact identical with those derived directly from the mass-action law, applied separately to each of the chemical equations (1).

Now we have to look how the formulae (3) will change when the total concentration i_o of impurities will be used instead of i.

In dilute alloys, where $i_o \gg v_1$, there is almost no difference between i and i_o. We can therefore use i_o instead of i in the formulae (3).

When the total concentration of impurities is very low as in zone melted materials and the total concentration of vacancies high, i.e. $v_1 > i_o$, and eventually $v_2 > i_o$, we have to look for the solution of the system (2) with the substitution

$$i = i_o - c_{11} - c_{21} .$$

It may be shown, that the following formulae hold:

$$v_2 = (K_1/K_2)\, v_1^2 ,$$

$$(4) \qquad c_{11} = K_3K_6\, v_1\, i_o \,/\, (K_4K_6 + K_3\, K_6\, v_1 + K_4K_5\, v_2),$$

$$c_{21} = K_4K_5\, v_2 i_o \,/\, (K_4K_6 + K_3K_6\, v_1 + K_4K_5\, v_2) .$$

COMBINATION NUMBERS

Alhough the kinetic coefficients are frequently used [4 - 6], a general agreement in combination numbers has not yet been reached. We will recalculate them with the help of Fig.1, where three layers of atoms in the (111) plane are

shown. The diameters of the circles representing atoms change with the distance from the observer. Two lattice sites in the middle layer are vacant. There are 18 nearest neighbors of the divacancy, 4 of them common to both vacancies; each of them has 7 neighbors of its own. There are totally 14 ways how to dissociate the divacancy. It will be formed when the second vacancy reaches one of the 12 nearest sites, each of which is accessible from 7 second nearest positions; so we get combination number 84 .

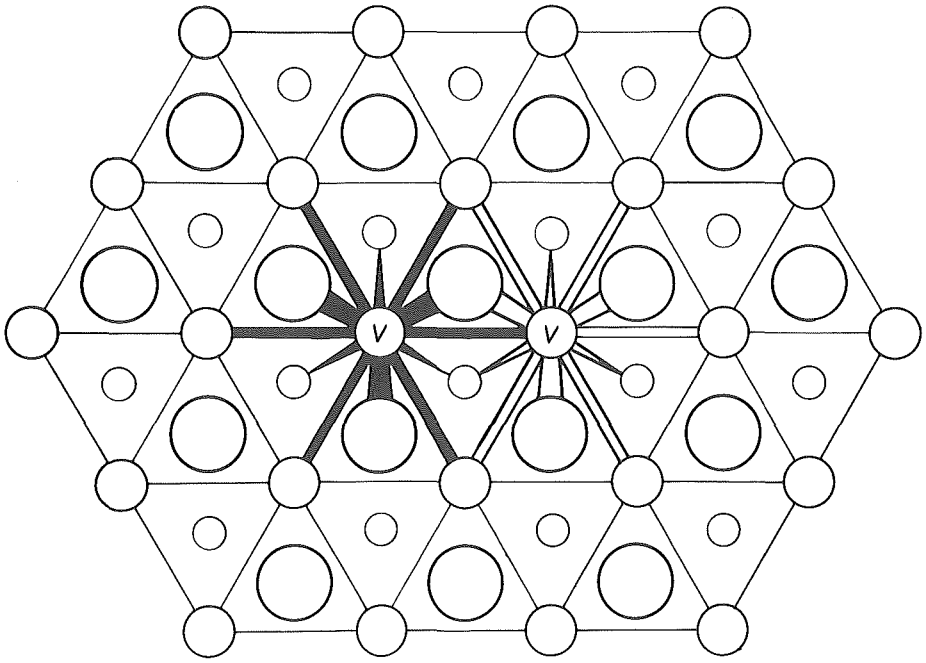

Fig.1. A divacancy in f.c.c. lattice - (111) plane.

The simple complex C_{11} may be formed also in 84 ways, and dissociated in 7 ways, as only the vacancy is mobile.

Having in mind that the binding between two vacancies is stronger than between a vacancy and an impurity atom, we have to suppose that the impurity atom must occupy one of the 4 sites common to both vacancies in the complex C_{21}. It may be for-

med in the following way (see Fig. 2a); The first vacancy has to reach one of the 12 nearest neighbour positions of an immobile impurity. Then the divacancy may have 6 different

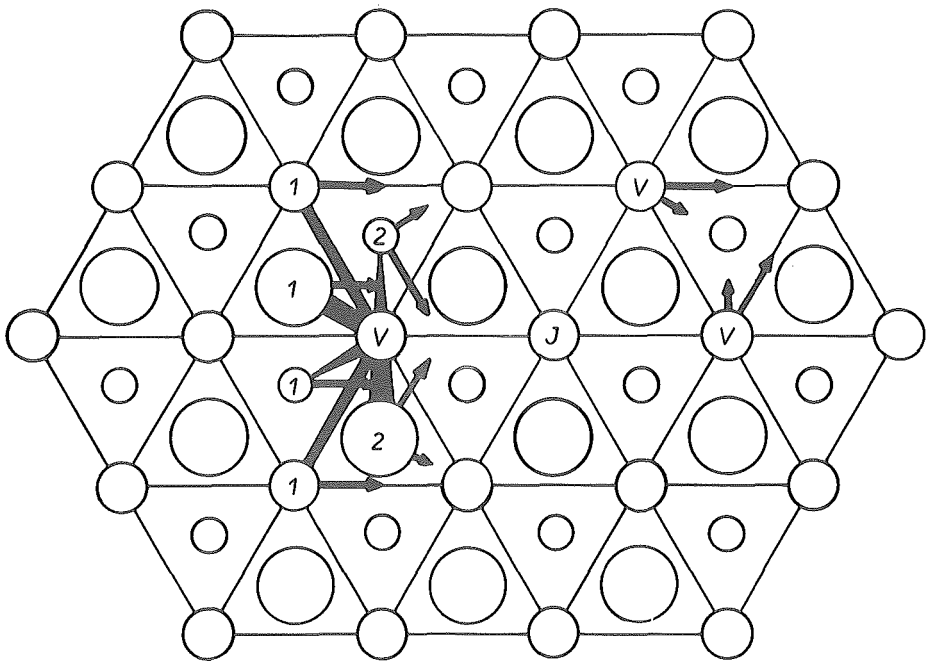

Fig.2. Association and dissociation of a C_{21} complex.

orientations; the second vacancy can reach its final position in one of the sites which is nearest to the first vacancy and the impurity atom by 8 different ways. There are altogether 96 possibilities how to form the C_{21} complex, and 4 how to dissociate it without dissociating the divacancy. This situation is shown in Fig. 2b. These results are in agreement with [6].

When the reaction $C_{11} + V_1 \rightleftharpoons C_{21}$ takes place, the inequality $E^B_{V-J} \geq E^B_{V-V}$ holds; the very complicated situation has been treated in detail by Doyama [5].

MODEL WITH EINSTEIN FREQUENCY

Let us suppose, that there is a single atomic vibration frequency in the crystal, whose temperature is well above the Debye temperature. Then the rate constants will be:

$$
\begin{aligned}
K_1 &= 84\,\nu \exp\left(-E^M_{1V}/kT\right), \\
K_2 &= 14\,\nu \exp\left(-\left(E^M_{1V} + E^B_{2V}\right)/kT\right), \\
K_3 &= 84\,\nu \exp\left(-E^M_{1V}/kT\right), \\
K_4 &= 7\,\nu \exp\left(-\left(E^M_{1V} + E^B_{1V-J}\right)\right)/kT, \\
K_5 &= 96\,\nu \exp\left(-E^M_{2V}/kT\right), \\
K_6 &= 4\,\nu \exp\left(-\left(E^M_{2V} + E^B_{2V-J}\right)\right)/kT .
\end{aligned}
\tag{5}
$$

When we introduce these rate constants into the system of equations (3), we shall get the following formulae:

$$
\begin{aligned}
v_2 &= 6\,v_1^2 \exp\left(E^B_{2V}/kT\right), \\
c_{11} &= 12\,v_1\, i \exp\left(E^B_{1V-J}/kT\right), \\
c_{21} &= 24\,v_2\, i \exp\left(E^B_{2V-J}/kT\right) = \\
&= 144\,v_1^2\, i \exp\left(E^B_{2V} + E^B_{2V-J}\right)/kT .
\end{aligned}
\tag{6}
$$

We can see that these results are in good agreement with those of Damask and Dienes [1]. The assumption concerning the single Einstein frequency is essential.

MODEL WITH LOCAL FREQUENCIES

The authors of several recent papers [4,5] use the local effective frequencies in the vicinity of point defects when calculating the rate constants. We shall confine ourselves to a simple model, where an effective frequency is used for each type of defect, i.e.

ν_{1V} for the nearest neighbors of a single vacancy,

$^{*}\nu_{2V}$ for atoms the jump of which dissociates the divacancy,

$^{*}\nu_{C_{11}}$ for atoms the jump of which dissociates the C_{11} complex,

$^{*}\nu_{C_{21}}$ for atoms the jump of which dissociates the C_{21} complex.

Then the formulae (6) will change to

$$
\begin{aligned}
v_2 &= 6 \left(\nu_{1V} / {}^{*}\nu_{2V} \right) v_1^2 \exp \left(E^B_{2V} / kT \right) , \\
(7) \quad c_{11} &= 12 \left(\nu_{1V} / {}^{*}\nu_{C_{11}} \right) v_1 \, i \exp \left(E^B_{IV-J} / kT \right) , \\
c_{21} &= 24 \left(\nu_{2V} / {}^{*}\nu_{C_{21}} \right) v_2 \, i \exp \left(E^B_{2V-I} / kT \right) .
\end{aligned}
$$

Let us concentrate to the case of divacancy concentration. The formula for v_2 can be directly compared with that used recently for the calculation by Seeger [2]. He uses the formula

$$
(8) \quad v_2 = 6 \exp \left(\Delta S_2 / k \right) \exp \left(E^B_{2V} / kT \right) v_1^2 ,
$$

where $\Delta S_2 = S^F_{2V} - 2\, S^F_{1V}$ is the association entropy. The comparison of formulae (7) and (8) gives

$$\nu_{1V} / {}^{*}\nu_{2V} = \exp (\Delta S_2 / k) ,$$

and therefore

(9) $$\Delta S_2 = k \cdot \ln (\nu_{1V} / {}^{*}\nu_{2V}) .$$

Similar formulae can be deduced for other association entropies and local frequencies near other point defects, which all are analogous to that derived by Mott and Gurney [7] . In order to see the significance of the frequencies, we have labeled the 18 nearest atoms of the divacancy in Fig. 3 with the effective frequencies, which are different when the atoms have

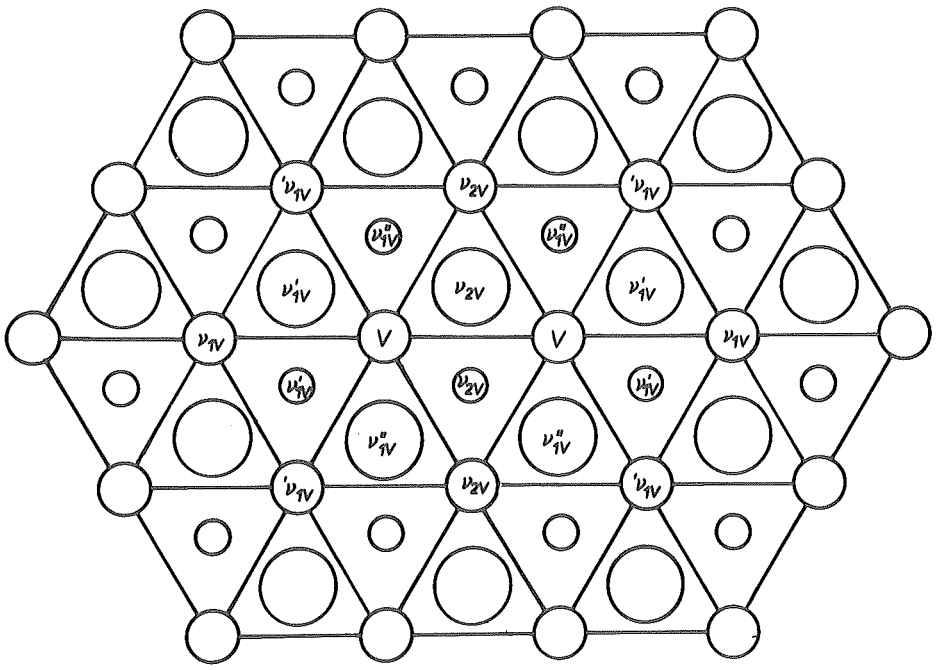

Fig.3. Effective frequencies in the vicinity of a divacancy.

different neighbours. For example the 4 common neighbors have

the frequency ν_{2V} ; when these atoms jump into the divacancy, it moves. The other atoms jumping into the divacancy dissociate it. Their frequencies are summarized in Table I.

Table I. Nearest neighbours of a divacancy in f.c.c. lattice

Freq.	Number of identical	Neighbour. vacancies	Number of atoms having frequency					
			ν_{2V}	ν''_{1V}	ν'_{1V}	$'\nu_{1V}$	ν_{1V}	ν
ν_{2V}	4	2	1	2		2		5
ν''_{1V}	4	1	1	2		2		6
ν'_{1V}	4	1	1	1		1	1	7
$'\nu_{1V}$	4	1	1	1	1		1	7
ν_{1V}	2	1			2	2		7

It is obvious, that the neighbours of the different species are not the same, and this leads us to the conclusion, that the frequencies are really different. Which of these frequencies is identical with $^{*}\nu_{2V}$ is difficult to say; it is most probably ν'_{1V}, if it is nearly equal to $'\nu_{1V}$; ν_{2V} and ν_{1V} are excluded. With the help of (9) we can calculate $^{*}\nu_{2V}$ from the data given in [2] and [3] (see Table II).

Table II. Effective dissociation frequency of a divacancy

Material	Au	Cu	Pt
$\nu_{1V}\exp(S^{M}_{1V} / k)$	1×10^{14}	2×10^{13}	3.5×10^{13}
$\Delta S_{2V} / k$	1.8	2.2	2.5
$\exp(\Delta S_{2V} / k)$	6.05	9.03	12.2
$^{*}\nu_{2V}$	1.6×10^{13}	2.2×10^{12}	2.8×10^{11}

Some authors suppose, e.g. Doyama [5], that ${}^{*}\nu_{2V} = \nu_{1V}$. In such case ΔS_{2V} would be zero, but we have good reasons to suppose, that $\Delta S_{2V} > 0$. Therefore ${}^{*}\nu_{2V}$ is different from ν_{1V}.

CONCLUSIONS

We have used chemical rate equations to determine the equilibrium concentrations of different point defects. It turned out that the effective dissociation frequencies are related simply to the association entropies of the complexes. The dissociation frequencies have been calculated for the divacancy in several metals, where values of association entropy are approximately known. The systemy of chemical equations usually used [6] hides the assumption on binding energies which is not always very realistic.

REFERENCES

[1] A.C. Damask, G.J. Dienes: Point Defects in Metals, Gordon & Breach, New York - London, 1963.

[2] D. Schumacher, A. Seeger: Quenching of noble metals and nickel in "Lattice Defects in Quenched Metals", Academic Press, New York - London 1965, p. 15.

[3] D. Schumacher, A. Seeger, O. Härlin: Vacancies and Self-Diffusion in Platinum, phys. stat. sol. 25, 359 (1968).

[4] M. Doyama: Divacancies in Pure Metals, in "Lattice Defects in Quenched Metals", Academic Press, New York - London 1965, p. 168.

[5] M. Doyama: Effects of Impurity Atoms on Quenching and Annealing Experiments, in "Lattice Defects in Quenched Metals", Academic Press, New York - London 1965, p. 185.

[6] J.W. Kauffman, G.J. Dienes: Effective Migration Energies Associated with Vacancies, Di-vacancies and Impurities, Acta Metallurgica 13, 1049 (1965).

[7] N.F. Mott, R.W. Gurnay: Electronic Processes in ionic crystals, Clarendon Press, Oxford 1958.

Thermal and Radiation Enhanced Self-Diffusion in Gold Single Crystals at Low Temperatures

U. Ermert, W. Rupp and R. Sizmann

Sektion Physik der Universität München

Abstract

With an improved electrochemical sectioning technique we succeeded in removing about 20 Å thick layers in a controlled manner from gold single crystals. With this technique diffusion profiles of radioactive gold of only about 1000 Å depth can be accurately determined.

Thermal self-diffusion measurements in gold in the temperature range of 286 to 412°C yield

$D = (4 \cdot 10^{-2} \, {}^{+0.02}_{-0.01}) \exp(-1{,}75 \pm 0{,}02 \text{ eV}/kT) \text{ cm}^2/\text{sec}$.

There is no interference with short circuiting paths.

Radiation enhanced self-diffusion by irradiation with 3,0 MeV α-particles at a flux density of $5 \cdot 10^{10}/\text{cm}^2\text{sec}$ up to a total dose of $5 \cdot 10^{15}$ α/cm² yields a practically temperature independent enhanced diffusion coefficient of $D = 1{,}3 \cdot 10^{-16} \text{cm}^2/\text{sec}$ in the region 60 to 150°C. At lower temperatures (between 10 and -18°C) the estimated enhanced diffusion coefficient is $D = 6 \cdot 10^{-17} \text{cm}^2/\text{sec}$. Below -60°C no diffusion is observable.

In the higher temperature region excess vacancies and interstitials contribute to the enhanced diffusion; in the lower temperature range it is likely that only interstitials promote the diffusion.

1. Introduction

Direct measurements of small self-diffusion coefficients in single crystals allow the extension of thermal diffusion studies to lower temperatures and the investigation of radiation enhanced diffusion in one-component systems.

A sectioning technique which allows the removal of about 20 Å thick layers in a controlled manner from gold single crystals can be used on the basis of anodic oxidation of the metal and the subsequent dissolution of the oxide. (1) With such a method it was possible to determine diffusion profiles of Au -198 atoms

of only 200 Å depth. The lower limit of the diffusion coefficient accessible in that way was $D = 5 \cdot 10^{-19} cm^2/sec$. The low penetration depth of the diffusing atoms requires particular care in the surface preparation of the single crystal to avoid short circuit effects.

In the temperature range of 286 to 412°C the thermal self-diffusion coefficient in gold single crystals was measured. In a second series of experiments the enhanced self-diffusion by radiation with 3.0 MeV α-particles at a flux density of $5 \cdot 10^{10}$ $\alpha/cm^2 sec$ up to total doses of $5 \cdot 10^{15}$ α/cm^2 was investigated in the temperature range of -18°C to + 150°C.

2. Experimental

The experiments were made on <111> single crystal cylinders (Ø 8 mm, length 4 mm) of 99.99 % gold. For each diffusion experiment the {111} face was prepared in the following way: A layer of ≈ 200 µm was removed from that face by anodic oxidation in 35.8 n - H_2SO_4 with a high current density (1 A/cm^2). After that treatment which also resulted in a flattening of the surface, the crystal was electropolished at room temperature in a solution which consisted of : 34 g KCN, 15 g K-Na-Tartrat, 15 g K_3 Fe $(CN)_6$, 7 cm^3 ammonia, 2 cm^3 H_3PO_4 and 1000 $cm^3 H_2O$. The best current density for polishing was found to ~1 A/cm^2. After removal of a layer of 200 µm the desired surface finish was obtained. Tolansky interferometry allowed to estimate a resulting surface roughness to be <30 Å.

Very thin (~10 Å) layers of Au -198 were electroplated from a solution of: 6 mg KCN, 4 mg Au, 4 mg K_3PO_4 and 2 ml H_2O on such prepared surfaces. For reasons associated with the determination of the depth of the diffusion profiles which will be described later, these layers were ring-shaped. This is achieved by covering the rest of the surface before plating with Lacomit lacquer. The inner diameter of that Au -198 ring layer was 1.5 mm. The specific activity of the Au -198 used in the solution was 50 Ci/g.

Thermal diffusion between 286 and 412°C was accomplished in a temperature controlled vacuum furnace. The diffusion temperature was measured ± 0.7°C absolute with a calibrated Chromel-Alumel thermocouple and recorded continuously during the diffusion annealing.

The experimental arrangement for runs of radiation enhanced diffusion is shown in Fig. 1

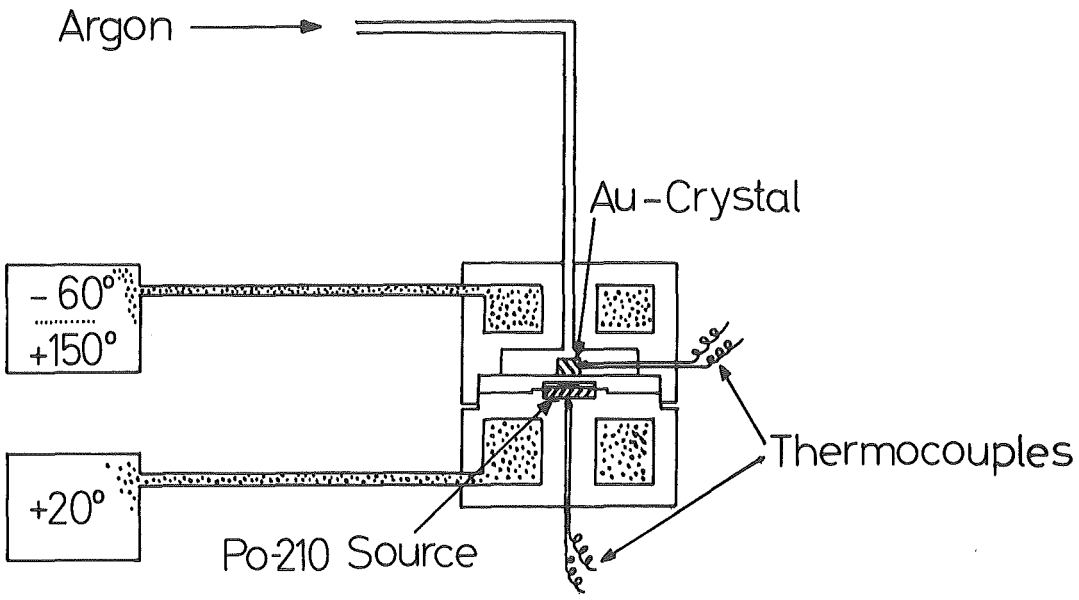

Fig. 1

The single crystal probe and an 1 Ci Po-210 α-source (Radiochemical Centre, Amersham, England) are oppositely mounted in a distance of 1 mm in the centre of an argon flooded chamber. The upper part of that chamber with the diffusion specimen is held by a thermostate at various irradiation temperatures from -20°C to + 150°C, while the lower part with the polonium source is maintained at + 20°C. Two thermocouples control the temperatures at the surfaces of the gold probe and the polonium source. The active area (Ø 7 mm) of the Po -210 source is covered with a 5 µm thick stainless steel foil which reduced the energy of the emitted α-particles to 3.0 MeV. The energy and the strength of

the Po-source was measured in a low geometry counting equipment. The flux density of the source was determined to be $5 \cdot 10^{10} \alpha/cm^2 sec$.

The determination of the actual diffusion profiles was done by sectioning thin layers (minimal 20 Å) from the specimen in the two stage process of anodic oxidation and the following dissolution of the formed oxide. The gold crystal is the anode in an electolytic cell with 1m H_2SO_4 acting as electrolyt. During the determination of a diffusion profile for every oxidation step the current density and the oxidation time were held constant ($j = 0.5 - 1.0$ mA/cm^2, $t = 6$ min). The crystal which is mounted in a teflon-holder is brought after each oxidation step in 2 ml 5 n HCl for dissolving the produced gold-oxide. In a series of experiments this sectioning technique was tested and found to be reproduceable within $\pm$ 5% for the thickness of the removed crystal layer. For more details see (2).

To measure directly the thickness of the removed layers from a diffusion specimen a spot of Lacomit lacquer (Ø 1 mm) was brought on the surface inside the electroplated Au -198 ring. The lacquer spot prevents anodic oxidation and the repeated peeling process results in a step with the height of the removed layer. The step is then measured in a Tolansky multiple beam interferometry microscope. By this technique the total removed layer of gold is measured; the thickness of the individual steps is obtained as the proper fraction of this total value. This gives better values than the calibration of the thickness of the removed layers with the current density which is only an integral measurement over the total crystal surface.

The concentration of Au -198 in the dissolved layers was determined from the difference in the residual activity of the crystal before and after each sectioning step. The residual Au -198 activity of the diffusion specimens after each peeling step was counted by means of standard NaJ (Tl) well scintillation crystal. A discriminator selected the 0.4117 MeV γ-line of Au-198. Prior to the evaluation of the results all measured radioactivity data

were corrected for background and decay and were normalized for comparison.

3. Results

a. Thermal self-diffusion

The appropriate diffusion equation for the thin instantaneous plane source of the diffusing radioactive gold is

$$c(x) = M_o/(4\pi\ Dt)^{-1/2} \cdot \exp\ (-x^2/4Dt) \qquad (a)$$

with M_o: surface density of the source (3).

The measured radioactivity A(x) is the residual activity of the gold crystal after removal of a layer thickness x.

$$A(x) = (A_o/M_o)\int_x^\infty C(x)\ dx \qquad (b)$$

($A_o = A(x=o)$ is the activity of the total diffusing material)

From a plot A(x) vs. x we found by numerical differentiation with a least squares method (4) the slopes dA/dx, corresponding to the concentration c(x)

$$\bar{A} = dA/dx = (A_o/M_o) \cdot c(x) \qquad (c)$$

Thus, by plotting log $\bar{A}(x)$ vs. x^2 equation (a) predicts a straight line with the slope $-1/4\ Dt$. Since the diffusion time is known we finally obtain the desired D(T). (The diffusion time is the actual heating time corrected for the transient T(t) during the heating and cooling period.)

In Fig. 2 and 3 two $\bar{A}(x)$vs. x^2 plots are shown with the diffusion times $2.29 \cdot 10^5$sec and $1.08-10^4$ sec at the diffusion temperatures 285.4°C and 349.7°C, respectively. The resulting diffusion coefficients are $D(T = 285,9^oC) = 6.5 \cdot 10^{-18} cm^2/sec$ and $D(T = 349.7^oC) = 2.6 \cdot 10^{-16} cm^2/sec$.

Diffusion coefficients between T = 286°C and 412°C are plotted as an Arrhenius diagram log D vs. 1/T in Fig. 4. From a straight line fit the resulting self-diffusion coefficient in this temperature range is

$$D = D_o \exp\ (-Q/RT) = (4 \cdot 10^{-2}\ {}^{+0.02}_{-0.01}) \exp(-1,75\ \pm 0.02\ eV/kT)\ cm^2/sec.$$

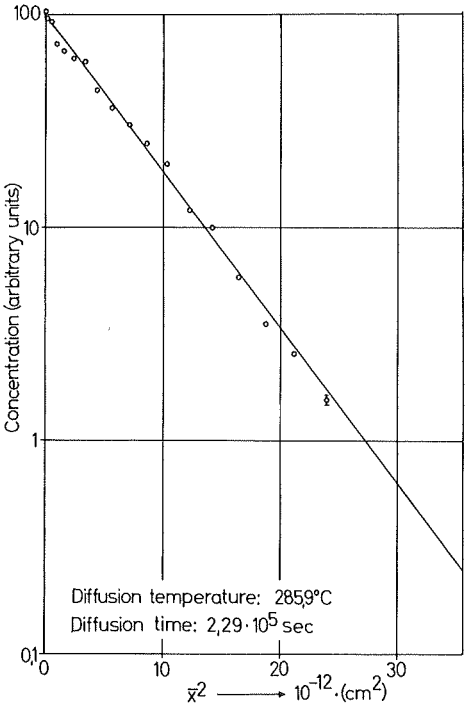

Fig. 2

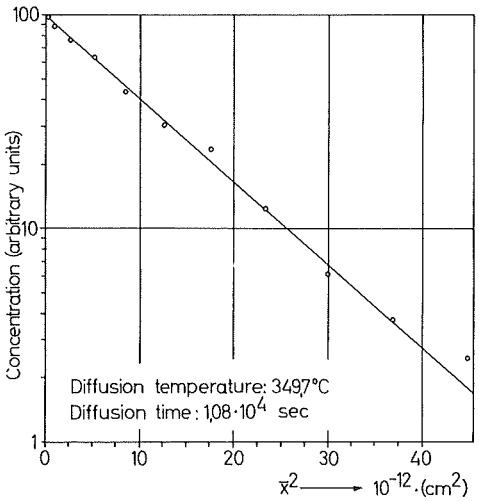

Fig. 3

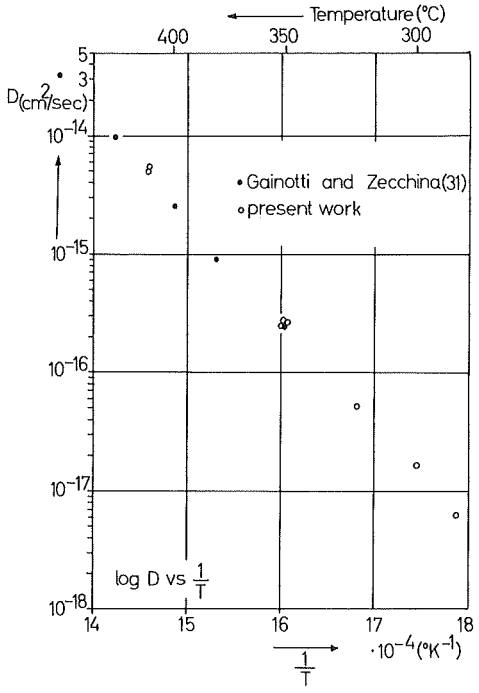

Fig. 4

Even without thermal treatment the peeling revealed some background profile of the radioactivity distribution in the crystal. Although the radioactive gold was plated in a homogeneous layer thinner than 10 Å we found in two independent test runs a steeply decreasing profile extending as far as 100 Å (10% residual value) into the crystal. The main reason for this are spurious contaminations of the crystal and the crystal mounting with radioactive gold. The background profile corresponds roughly to an apparent (thermal) diffusion coefficient of $\leq 5 \cdot 10^{-19} cm^2/sec$ in the typical diffusion time of 10^5 sec applied in the experiments.

b. Radiation enhanced self-diffusion

In this case we have to take into account the (linear) local variation of the diffusion coefficient as $D = D_x x$ (the reasons for this are explained in the discussion). Then the expected concentration profile is given by (5)

$$c(x) = (M_o/D_x t) \exp(-x/D_x t) \qquad (d)$$

Hence, with c(x) prop. $d\bar{A}/dx = \bar{A}(x)$ as discussed in the thermal case, 3.a, a plot log $\bar{A}(x)$ vs. x/t should show a straight line with the slope $-1/D_x$. That this happens is shown in the Fig. 5. From the slopes the values of the corresponding values D_x are calculated and presented in Fig.6 as a function of the irradiation temperature T. There is an additional experiment at -60^oC that is not in the Fig.5. In this case we observed no diffusion in an irradiation time $t = 9.4 \cdot 10^4$ sec; the resulting "profile" is essentially the background $\bar{A}(x)$ observed without any irradiation or thermal treatment.

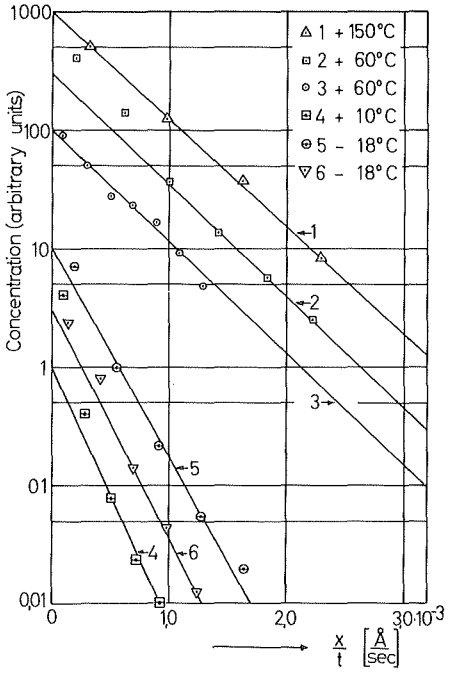

Fig. 5

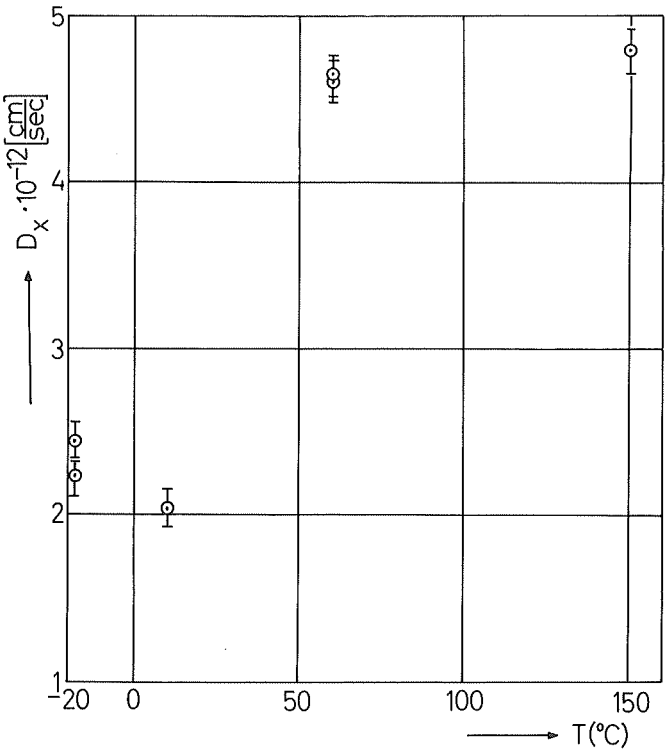

Fig. 6

4. Discussion

á. Thermal self-diffusion

The Arrhenius plot, Fig. 4 also shows the self-diffusion data of Gainotti and Zecchina (6). They agree very well with our results in the overlap region between 400 and 350°C. Since we were able to extend the diffusion measurements to lower temperatures the total experimental accessible range of the self-diffusion in gold spans now from $D = 1.15 \cdot 10^{-8}$ cm^2/sec (1048°C) to $D = 6.5 \cdot 10^{-18}$ cm^2/sec (286°C). The deductions that can be drawn from the non linearity of the T-dependence of D in this very wide region are recently fully discussed by A. Seeger and H. Mehrer (7).

It is often pretended that diffusion measurements at low temperatures are unreliable due to prevailing short circuiting effects, for instance pipe diffusion along dislocations. (8) However, in our experiments there are no indications of severe enhanced diffusion paths from the log $c(x)$ vs. x^2 plots or the positions

of the points in the Arrhenius diagram. Although we used two differently oriented gold single crystals the resulting diffusion coefficients were practically identical (see the practically coinciding points at T = 350°C in Fig. 4).
In fact in the well annealed crystals we have to take into account a dislocation density of about $10^8/cm^2$. That corresponds to a mean distance between dislocation lines or a size of sub-graines of greater than 10^3 Å. It can be shown that then diffusion profiles extending only 10^3 Å into the crystals are insensibly effected by dislocation short circuiting paths. (For a detailed calculation see (2)). Thus, the very fact of our little penetrating profiles ensures the measurements being reliable volume self-diffusion data.

b. Radiation enhanced self-diffusion
The α-irradiation produces vacancy-interstitial pairs; both defect species are capable of promoting the self-diffusion. The radiation enhanced diffusion coefficient is

$$D_{rad} = D_i \cdot i + D_v \cdot v \qquad (e)$$

Here the products $D_i \cdot i$ and $D_v \cdot v$ are the diffusion coefficients of the gold atoms by interstitial and vacancy motion, respectively; i,v are the concentrations of interstitials, vacancies.
The first problem is to calculate the produced i and v as a function of the α-flux density, of the temperature and, last not least of the position x below the irradiated crystal surface. The mobile excess point defects are known to annihilate at sinks like dislocations, grainboundaries and of course the free surface of a crystal. Hence, the very surface, where the instantaneous source of the radioactive Au-198 is located is the place of zero excess vacancy- and interstitial concentration.

If i and/or v is linearly dependent on x, e.g. $i = i_1 \cdot x$, $v = v_1 \cdot x$, then the proper solution of the diffusion problem is (5)

$$c(x) = (M_o/D_x t) \exp(-x/D_x t) \qquad (d)$$

with

$$D_x = D_i i_1 + D_v v_1 \qquad (f)$$

The general solution of $i(x)$ can be expanded into a power series $i = i_1 x + i_2 x^2 + \ldots$; then the range of x can be estimated where only the linear term $i_1 x$ is the dominant one. Inside this range eq.(d) is applicable.

To obtain the solutions for $i(x)$ and $v(x)$ we have to deal with the following balance equations

$$\begin{aligned} \partial i/\partial t &= J_o - k_i iv - k_i i s_i + D_i \, \partial^2 i/\partial x^2 \\ \partial v/\partial t &= J_o - k_i iv - k_v v s_v + D_v \, \partial^2 v/\partial x^2 \end{aligned} \qquad (g)$$

J_o is the Frenkel defect production term, $k_i iv$ is the binary recombination determined by the faster moving interstitials (k_i is the reaction rate coefficient), $k_i i s_i$ and $k_v v s_v$ are the annihilation reaction rates of interstitials and vacancies, respectively, at inexhaustible and homogeneously distributed sinks with the sink densities s_i and s_v. The (calculated) J_o due to the flux density of $5 \cdot 10^{10}$ $\alpha/cm^2 sec$ in gold is $6 \cdot 10^{-8}$ sec^{-1}. The temperature independant ratio D_i/k_i is $\sim 2 \cdot 10^{-17}$ cm^2. $D_v = 10^{-2} \exp(-0.83 \text{ eV}/kT)\, cm^2 sec^{-1}$.

At not too low temperatures and short irradiation times (mean transport length of both the vacancies and interstitials not small compared with the (stationary) depth of the resulting i or v diffusion profiles) the i and v distributions are stationary: $\partial i/\partial t = 0$, $\partial v/\partial t = 0$.

With the further simplification $k_i s_i / k_v s_v \doteq D_i/D_v$ (that means essentially $s_i \doteq s_v$) the solutions of the equations (g) are

$$\begin{aligned} i(x) &= i_o + i' /(\beta e^{\alpha x} + e^{-\alpha x})^2 \quad \text{and} \\ v(x) &= v_o + v' /(\beta e^{\alpha x} + e^{-\alpha x})^2 \end{aligned} \qquad (r)$$

The coefficients are

$$v_o = -s/2 + \sqrt{(s^2/4 + J_o D_i / k_i D_v)}$$

$$v' = -12(v_o + s/2)\beta$$

$$\beta = (1/v_o)(5v_o + 3s + \sqrt{((5v_o + 3s)^2 - v_o^2)})$$

$$\alpha^2 = (k_i/2D_i)(v_o + s/2)$$

and $i_o = D_v v_o / D_i$, $i' = D_v v'/D_i$

The series expansion of equations (h) yields in the case

A) $s^2 > 4J_o D_i/k_i D_v$

$$v_1 = 12\ ß(ß-1)(ß+1)^{-3}.(J_o/D_v).\sqrt{(D_i/k_i s)} \qquad (i)$$

and in the case

B) $s = 0$

$$v_1 = 1.15\cdot(J_o/D_v)^{3/4}.(D_i/k_i)^{1/4} \qquad (j)$$

with $i_1 = D_v v_1/D_i$ in both cases.

The validity range of the linear approximation $i(x) = i_1 x$ of eq.(h) depends on $D_i D_v/J_o k_i$ and is in our case several hundred angstroms above 40^oC.

The two cases A and B need further explanation. At high temperatures are the transport lengths $L_i = \sqrt{(D_i t)}$ and $L_v = \sqrt{(D_v t)}$ in the order of several / µm. Then the interstitials and vacancies react with the dislocations like homogeneously distributed sinks; the sink density s can be calculated from the dislocation density (case A). At lower temperatures the transport lengths L_i and L_v are within the mean distance of the dislocations. In this case there is no effective sink density (case B); the sink property of the surface is taken into account by the diffusion terms $D_{i,v}\ \partial^2(i,v)/\partial x^2$ and the boundary conditions $i(x=0) = v(x=0) = 0$.

At still lower temperatures first the vacancies and then the interstitials become immobile. The consequence is that $D_{rad} = 2D_v v_1$ at the higher temperatures changes to $D_{rad} = D_i i_1$ and finally becomes 0.

In the case of mobile interstitials only, the solutions of the equations (g) are no longer stationary. The vacancy concentration continuously increases with time, because the mobile interstitials flow and annihilate in the surface and are lost for the recombination with the vacancies. After a while the interstitial concentration is suppressed so much by the increased vacancy concentration that the product $D_i i \approx 0$: the enhanced diffusion ceases.

The experimental results can be divided into two main classes:

(i) Above 50°C case A is operative: the transport lengths of interstitials and vacancies are in the typical irradiation time of 10^5 sec $L_i \gtrsim 13 \cdot 10^3$ Å, $L_v > 1.4 \cdot 10^3$ Å

Then it follows from equation (h) that the bulk values (that means far away from the surface) of the radiation enhanced diffusion coefficients are $D_v v_o = D_i i_o = J_o D_i / k_i s$, hence $D_{rad} = 2 J_o D_i / k_i s$. This is a temperature independent quantity.

The coefficients $D_i i_1$ and $D_v v_1$ are equal to $\approx J_o \sqrt{(D_i / k_i s)}$, because $\beta(\beta-1)(\beta+1)^{-3}$ is close to 1/12. Hence the experimental accessible D_x should equal $2 J_o \sqrt{(D_i / k_i s)}$ and is also temperature independent. That agrees well with the observed practically identical D_x values at 60 and 150°C.

From the measured D_x the radiation enhanced self diffusion coefficient in the bulk material can be calculated

$$D_{rad} = D_x^2 / 2 J_o \qquad (k)$$

The numerical result is with $6 \cdot 10^{-8}$ sec^{-1} and the experimental value $D_x \approx 5 \cdot 10^{-12}$ $cm sec^{-1}$ (see Fig.6)

$$D_{rad} = 2 \cdot 10^{-16} \ cm^2 sec^{-1}$$

(ii) Below 10°C the transport lengths are $L_i \lesssim 2\,000$ Å and $L_v \ll 100$ Å . From this it follows that only interstitials contribute to the enhanced diffusion. The experimental mean D_x value is about $2 \cdot 10^{-12}$ cm sec^{-1} (see Fig. 6). An analytical solution of the quasi stationary interstitial concentration i(x) is not available. The diffusion coefficient is time dependent; we have to use $D_x t = \int_0^t D_x'(t) dt$ in equation (d), where $D_x'(t)$ is the instantaneous coefficient. An estimated mean value of the quasi stationary bulk diffusion coefficient is in this case

$$D_{rad} \approx D_x^2 / J_o = 6 \cdot 10^{-17} \ cm^2 sec^{-1}$$

(iii) At -60°C the transport length $L_i = 10$ Å is too small to allow any detectable enhanced diffusion rate. That is in accord with the experimental result $D_{rad} = 0$.

The conclusion is that in the experiments on radiation enhanced self diffusion in gold there is evidence for an interstitial

promoted diffusion in the temperature region at and below 10°C, and above -60°C.

References

1. J.L. Whitton, J.A. Davies
   J. Electrochem. Soc. 111, 1347 (1964)

2. W. Rupp, U. Ermert, R. Sizmann to be published

3. J. Crank "The Mathematics of Diffusion" p. 27
   Oxford 1956

4. R. Sauer, H. Pösch
   Z. Verh. dtsch. Ing. 85, 195 (1941)

5. H.S. Carslaw, J.C. Jaeger "Conduction of Heat in Solids"
   p. 412 Second Edition, Oxford 1959

6. A. Gainotti, L. Zecchina
   Il Nuovo Cimento XL B, 295 (1965)

7. A. Seeger, H. Mehrer
   phys. stat. sol. to be published

8. P.G. Shewmon "Diffusion in Solids" chapter 6
   New York 1963

Self-Diffusion and Impurity Diffusion in Lithium.

A. Ott and A. Lodding

Physics Department, Chalmers University of Technology
Gothenburg, Sweden.

(Abstract)

The diffusion of ten different metallic tracers in lithium metal has been investigated. The diffusion coefficients, extrapolated to the m.p., range between about 10^{-8} and 10^{-5} cm^2/sec, with the self-diffusion value just above 10^{-7}. The activation energies (in kcal/mole) are: Q_{Li}=12.6; Q_{Na}=12.6; Q_{Ag}=12.9; Q_{Au}=10.5; Q_{Zn}=13.0; Q_{Cd}=16.1; Q_{Hg}=14.5; Q_{Ga}=12.7; Q_{In}=15.9; Q_{Sn}=13.6 . The activation energy found for the ^6Li tracer lies about half-way between the differing results of earlier self-diffusion measurements, and satisfies the same empirical rules as other alkali metals. No satisfactory explanation of the impurity diffusion results is provided by any existing theory. The importance of ion core differences between impurity and matrix atoms appears greatly to outweigh that of valency differences. Another insufficiently understood result has been obtained in inter-diffusion of Li tracer in isotopically separated lithium: the diffusivity in ^6Li matrix is by some 20% lower than in ^7Li.

For several reasons lithium is an attractive metal to investigators of atomic mobilities and binding energies, and of melting properties. The electronic structure is relatively simple, the melting point is low and the diffusivity high. Also, the easy availability of separated ^7Li and ^6Li allows valuable studies of isotope effects, and the extremely high Debye-temperature suggests the possible occurence of interesting quantum-effects.

Atom mobilities in solid and liquid lithium have been studied at this laboratory by thermotransport, electrotransport and diffusion techniques[1 - 5]. The present paper reports recent results obtained in a systematic investigation of tracer diffusivities in solid, quasi-monocrystalline lithium metal.

The technique has been described in detail elsewhere[6,7]. It has yielded very good penetration profiles for nearly all hitherto studied tracers. Results have hitherto been obtained (see Table 1) for ten metals in isotopically normal lithium (abt. 7.5% ^6Li) and for two metals in nearly pure (95%) ^6Li. Additional experiments with tracer (K, Be, Mg, Cu, Ge, Pb, Sb and Bi) diffusion in lithium

Table 1. Tracer diffusion in lithium metal. The parameters D_o abd Q refer to the Arrhenius equation $D=D_o \exp(-Q/RT)$. The results in brackets are preliminary.

Matrix % Li	Impurity isotope	Temp.-range °C	D_o cm^2/sec	Q kcal/mole
92.0	^{6}Li	60 - 170	$D_1=0.12\pm0.05$	12.62 ± 0.21
5.5	^{7}Li	60 - 170	$(D_2=0.82D_1)$	(12.62)
92.5	^{22}Na	52 - 176	0.41 ± 0.09	12.61 ± 0.15
92.5	^{110m}Ag	65 - 161	0.37 ± 0.13	12.83 ± 0.25
92.5	^{195}Au	45 - 155	$(D_1=0.21\pm0.09)$	(10.49 ± 0.35)
5.0	^{195}Au	85 - 130	$(D_2=1.08D_1)$	(10.49)
92.5	^{65}Zn	60 - 175	0.57 ± 0.26	12.98 ± 0.24
92.5	^{115}Cd	80 - 175	(2.35)	(16.05 ± 0.35)
92.5	^{203}Hg	55 - 175	(2.10)	(14.53 ± 0.35)
92.5	^{72}Ga	110 - 165	(0.16)	(12.71 ± 0.40)
92.5	^{114}In	80 - 175	0.39 ± 0.25	15.87 ± 0.36
92.5	^{113}Sn	90 - 160	(0.06)	(13.65 ± 0.45)

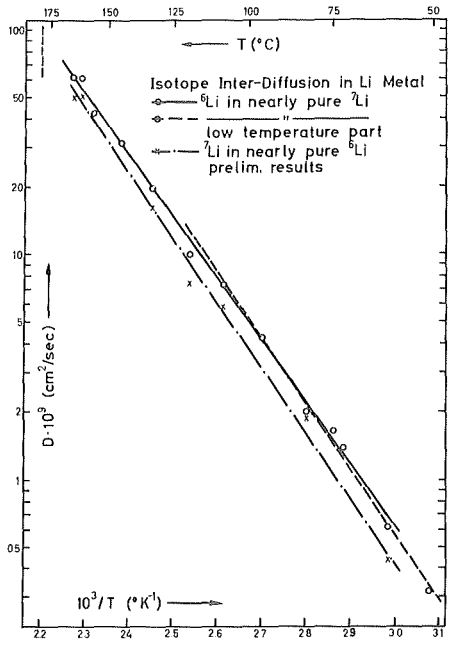

Fig.1
Isotope inter-diffusion in lithium metal

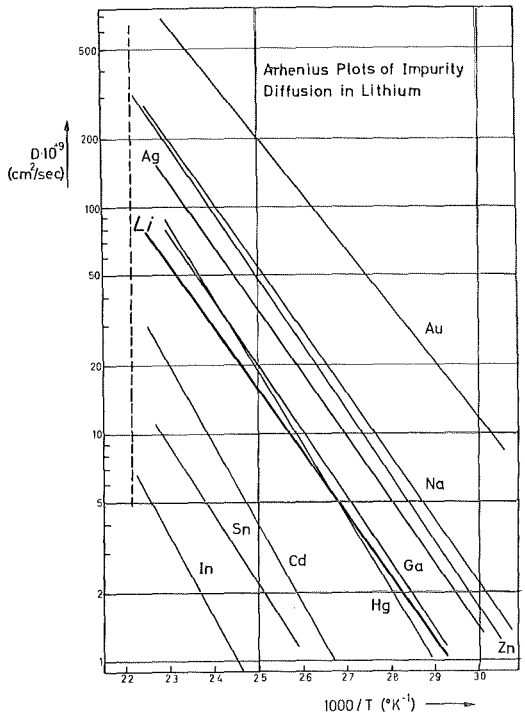

Fig.2
Arrhenius plots of impurity diffusion in lithium

are partly in progress, partly in the planning stage.

1) Self-diffusion.

Our measurements have been performed[8] with stable tracer isotopes and with mass-spectrometer analysis. Our results can be compared with those of four earlier measurements, three using NMR, one employing a diffusion couple technique. As seen in Table 2, our activation energy values fall roughly in the middle of the range of values covered by the various earlier investigators.

Table 2. Comparison of present results[8] with those of earlier investigations.

Method	Ref.	D_o	Q
Diffusion couple	9	0.39±0.04	13.49±0.07
NMR	10	0.24±0.17	13.20±0.40
NMR	11	---	12.0
NMR	12	---	11.79±0.28
Thin film, slicing	8	0.12±0.06	12.62±0.21

Table 3. Comparison with results in other alkali metals and with semi-empirical relations involving melting point and heat of fusion.

Metal	Ref.	D_o	Q	Q/RT_m	Q/L_m
Li	8	0.12	12.62	14.0	18.3
Na	6	0.145	10.09	13.7	16.0
K	13	0.31	9.75	14.5	17.4

Table 3 shows the agreement with two semi-empirical rules found valid for most classes of metals sharing the same diffusion mechanism as well as lattice types. It can be seen that a similar melting-point relation holds for all three investigated alkali metals. A certain tendency appears to be present in relation to the latent heat of melting, suggesting that the relative difference in mechanism between the solid and liquid state is smallest for lithium; however, the available data on the heat of fusion in Li show a considerable scatter. The values of L_m used in Table 3 are from Metals Reference Book[14].

Additional self-diffusion measurements are still in progress. Our aim is to extend the temperature range down to 35°C, in order to check the apparent tendency (see fig.1) of the Arrhenius line to become steeper at lower tempera-

tures. If the tendency (in qualitative agreement with the results obtained by Ailion and Slichter[12]) is real, then the presence of zero-point effects seems to be indicated.

Diffusivity has also been studied in nearly pure ^{6}Li, with ^{7}Li as tracer. Preliminary results[8] show that here the diffusion coefficients are lower by about 18% than at the corresponding temperatures in ^{7}Li. While a part of this ($\leq \sqrt{7/6} - 1 \simeq 8\%$) is no doubt due to the mass difference between the two tracers, nevertheless at least some 10% seems to be an intrinsic difference between the two isotopically separated matrices. Intuitive and semi-empirical reasoning (e.g. the Lindemann formula) would expect the Debye frequency of pure ^{6}Li to lie by some 8% higher than that of ^{7}Li, i.e. quite the opposite tendency to that found in the present experiments. So far no satisfactory explanation is available.

2) Impurity diffusion.

The aim of all hitherto propounded theories of impurity diffusion has been the computation, from fundamental physical parameters, of the difference $\Delta Q = Q_i - Q_o$ between the activation energy observed for impurity diffusion and that for the matrix self-diffusion. In Table 4, the ΔQ values are listed for all investigated impurities in lithium. Also listed are the Goldschmidt metallic radii, approximate bulk moduli, normal valences and periods of the element table. It can be at once seen, that the behaviour of ΔQ shows very little systematic dependence on any single one of these parameters. The progress Ag-Cd-In-Sn (group IB-IIB-IIIA-IVA in period) is from low or negative ΔQ for univalent impurities to high positive values for di- and trivalent, then apparently to somewhat lower values for tetravalent impurities. This behaviour, which is also confirmed by Zn-Ga in period 4 and Au-Hg in period 6, is very different from the systematics of impurity diffusion as known from close-packed systems[16]; in fcc and hcp matrices ΔQ becomes increasingly negative as the excess positive charge (impurity relative to

matrix atoms) increases. The vertical sequence Zn-Cd-Hg, group IIB, seems to reveal a striking maximum in the positive ΔQ in period 5, suggested also by Ag-Au on one hand, Ga-In on the other. As to the variation of ΔQ with size and elastic parameters, it seems to be either random or far from simple.

Table 4. Correlation between diffusion results, atom sizes, elastic moduli and positions in the periodic table.

	ΔQ kcal/mole	r Å-U	B kcal/cm^3	Group	Period
Li	0	1.51	2.5	IA	2
Na	0.0	1.85	1.0	IA	3
Ag	+0.3	1.40	21	IB	5
Au	-2.1	1.40	35	IB	6
Zn	+0.4	1.34	18	IIB	4
Cd	+3.5	1.50	11	IIB	5
Hg	+1.9	1.53	7	IIB	6
Ga	+0.1	1.37	12	IIIA	4
In	+3.3	1.61	8	IIIA	5
Sn	+1.0	1.58	11	IVA	5

All theories have been based on the assumption that the defects responsible for diffusion are simple vacancies. Two main lines of approach have been employed. Swalin[17] computed ΔQ from the impurity-solvent differences in atom sizes and elastic parameters, while Lazarus[18] and LeClaire[16,19] based their theories on electrostatic interactions between vacancies and impurities.

2a) Discussion in terms of "elastic" theory. Swalin's theory obtains ΔQ as the sum of the elastic binding energy between vacancy and impurity, E_b, and a motion energy difference, which we will denote by ΔE_m. The calculation, originally developed for fcc systems, has recently[20,7] been adapted for bcc metals. For lithium as matrix, a certain simplification is possible, owing to the fact that all impurities (except the alkali metals) possess considerably greater elastic moduli; it can easily be shown that for $B_i >$ approx. $3B_{Li}$ the energy terms, as presented in ref.[21], become

$$-E_b \simeq 0.7 \cdot B_{Li} r (r_i - r)^2 \simeq 3 (r_i - 1.51)^2 \quad , \qquad (1)$$

and

$$\Delta E_n \simeq 2 \cdot 10^{-3} C K_1 (r_i^3 + 2 r_i^2 r + r_i r^2 - 4 r^3) \simeq$$
$$\simeq 0.05 (r_i - 1.51)(r_i^2 + 4.53 r_i + 6.04) \quad , \qquad (2)$$

where B_{Li} is the bulk modulus of the solvent, C another elastic modulus of Li, of the order of 1 kcal/cm^3, K_1 a lattice constant obtainable from self-diffusion ($K_1 \simeq 25$), r_i the atomic radius (coord.number 8) of an impurity atom (in Å-U), and r the corresponding radius for Li. In the simplified treatment for an alkali matrix, the impurity radius in solution can be put equal to the listed Goldschmidt radius.

In Table 5, the energies in Swalin's theory have been calculated with the aid of formulae 1 and 2 (except for Na, where the more rigorous formula 1 of ref.[33] was used). A comparison of these theoretical predictions with the experimental results (ΔQ_{Sw} versus ΔQ_{exp}) shows that the "elastic" theory definitely fails to explain the diffusion behaviour of the investigated impurities, especially those of the 5th and 6th periods.

Table 5. Comparison of experimental results with theories. All energies in kcal/mole.

Impurity	$-E_b$	ΔE_n	ΔQ_{Sw}	z_{eff}	$\Delta E_{het.}$	U	$\Delta E_{hom.}$	ΔQ_{exp}
Na	0.14	+0.36	+0.22	1.85	-0.7	-40	-0.5	0.0
Ag	0.04	-0.11	-0.15	1.1	-0.1	+90	+1.1	+0.3
Au	0.04	-0.12	-0.16	1.2	-0.2	+150	+1.8	-2.1
Zn	0.09	-0.16	-0.25	1.8	-0.6	+250	+3.1	+0.4
Cd	0.00	-0.01	-0.01	2.2	-1.0	+200	+2.4	+3.5
Hg	0.01	+0.02	+0.01	2.4	-1.1	+210	+2.6	+1.9
Ga	0.06	-0.14	-0.20	3.0	-1.6	+380	+4.6	+0.1
In	0.04	+0.12	+0.08	3.4	-1.9	+320	+3.9	+3.3
Sn	0.02	+0.08	+0.06	4.4	-2.7	+410	+5.0	+1.0

2b) Discussion in terms of valency effects. Considerable success has been achieved for close-packed systems by theories based on primarily electrostatic interactions between impurities and vacancies[18,16]. The impurity was treated as an excess point charge, given simply by the valency difference between solute and solvent atoms; the vacancy was such a charge with zero valency. The potential due to a localized excess charge was first treated by a linearised Thomas-Fermi method[22], then more rigorously by a self-consistent Hartree method The latter treatment[23,24] introduces an oscillatory potential ("Friedel wiggle" which may in certain cases cause a negative charge to be repelled by a nearest neighbour positive charge. In univalent matrices, however, the Thomas-Fermi potential is probably justifiable as an approximation. This leads to an expression for the interaction energy impurity-vacancy in a univalent metal:

$$\Delta E = -(\Delta z \cdot \alpha)(e^2/a)\exp(-qa) \quad , \qquad (3)$$

where Δz is the excess charge on the impurity, α a constant of the order of unity (in our calculations we shall approximate $\alpha=1$), e the electron charge, a the nearest neighbour distance and q the screening constant (for Li approx. 1.6 $(Å\text{-}U)^{-1}$. According to LeClaire[16] for impurity diffusion

$$\Delta Q = \Delta E + \Delta H - C \quad , \qquad (1)$$

where ΔH is the motion energy difference and C a term involving the Bardeen-Herring correlation. It has, however, been pointed out by Barr & al.[25] that in alkali metals the motion and correlation terms are likely partially to cancel each other out:

$$\Delta H - C = \Delta H \Big/ \left(0.44\frac{w_2}{w_0} + 1\right) \quad , \qquad (5)$$

where w_2 is the frequency of impurity-vacancy jumps and w_0 that for solvent atom-vacancy jumps. For impurities which attract vacancies one would then expect the difference of the two terms to be only a fraction of ΔH. Moreover, in the alkali metals ΔH is likely to be small in comparison with ΔE[32]. The rigorous LeClaire treatment is rather arduous and, according to certain authors[28] likely to lead to an overestimate of both these quantities (a few results of the "rigorous" treatment are presented in ref.[33]). For these reasons we shall in this discussion content ourselves with comparing the experimental ΔQ with the quantity ΔE.

When assigning charges to the various impurities, we have made appropriate corrections (in analogy with the treatment by Lal[26]) for the electrostatic effects of different atom and ion core sizes. The resulting effective valences z_{eff} are listed in Table 5. Via formula 3, they lead to the $\Delta E_{het.}$ values in the adjacent column.

From Table 5 it is obvious that practically all the predictions of this "heterovalent" theory lead to the wrong sign and magnitude of ΔQ, and that the activation energies do not in a simple way depend on z_{eff}. It may be tempting to attribute the failure of the theory to the use of the Thomas-Fermi potential instead of the oscillatory self-consistent Hartree potential. However, a recent actual calculation of the "Friedel wiggle" for Li (by Bienenstock & al.[27]) appears to confirm that no serious error, and certainly none of sign, is introduced by the Thomas-Fermi approximation.

One is thus led to admit either that valency effects are not of primary importance in determining ΔQ for impurities in lithium, or that the vacancy model employed is unrealistic.

2c) Discussion in terms of core potential differences. To explain the occurence of considerable ΔQ values also for impurities with the same valency as the matrix, LeClaire[19] has extended his theory to cover the effects of differences in core potential. The new theory has been rather successful for certain homovalent impurities in close-packed metals. Hitherto it has not been applied to heterovalent impurities, and certain complications from coulomb, exchange and correlation effects may complicate such an issue. However, if the coulomb effects are relatively small, as indeed is suggested by the previous discussion, then the "homovalent" theory may prove illuminating, especially as regards vertical systematics within the various groups of the periodic table.

LeClaire treats the homovalent impurity as a square well potential U equal to the core potential difference $E_i^o - E_o^o$. Neglecting the abovementioned effects as well as elastic interactions, one may obtain U from a simple formula

$$E^o = F + H/n + (\sum_n I)/n \qquad , \qquad (6)$$

where n is the valency, F mean Fermi energy, H heat of sublimation and $\sum_n I$ the sum of n ionization potentials.

According to LeClaire the impurity can be assigned an effective charge

$$(\Delta z \cdot \alpha)_{eff} = -(U/2qe^2)(qR-1)\exp(qR) \qquad (7)$$

(where R is the radius of the Wigner-Seitz sphere or, in LeClaire's own usage, the Goldschmidt atomic radius), which can be substituted into eq. 3, yielding

$$\Delta E = (U/2aq)(qR-1)\exp\left[q(R-a)\right] \quad . \qquad (8)$$

In the last-but-one column of Table 5 ΔE has been calculated for the various impurities via eq.8. It can be seen that in spite of the abovementioned limitations, the "homovalent" theory is the only one to predict the correct signs (with the exception of Au). The predicted orders of magnitude are acceptable for certain of the investigated impurities. The agreement in other cases (Al, Zn, Cd, Sn) is poor, but even in its present imperfect version the last-mentioned theoretical approach suggests the relative importance of "homovalent" effects in ΔQ.

2d) Salient points. As LeClaire has pointed out, his "homovalent" theory does not explicitly take into account valency effects, nor those due to aton size differences and lattice distortions. It can hardly be permissible to perform a simple addition of $\Delta E_{hom} + \Delta E_{het} + \Delta Q_{Sw}$, but such a procedure can be seen on the whole to improve the qualitative agreement with experiments. Especially a possible amplification of the ΔE_n term (e.g. if the proper bulk moduli to employ are considerably greater than the listed, macroscopic, quantities) points in the correct direction; this may mean that the neglect of the ΔH in the homovalent theory was an oversimplification, and that the distortion of the lattice at the saddle point might have been important. Size effects seem also likely to be responsible for the conspicuous differences between the impurities of periods 4 and 5 in the same groups. The possibility of bound states in period 4, suggested by March[28], would decrease the valency differences and thus, unless motion energies are considerable, work in the "wrong" direction.

The most striking and unexpected result is probably the great difference found between the behaviour of the Ag tracer on one hand, Au on the other. Aton size differences are here ruled out. It has been suggested[29] that the tracer

gold might be dissolved mainly in trivalent form. While this would bring ΔE_{het} to the right order of magnitude (about -2 kcal/mole), it would also considerably increase ΔE_{hom}. A similarly great diffusivity has been found for Au in Na[30], and the question was raised, whether Au may not be an interstitial impurity; the atom radius ratio Au-Na seemed favourable. However, the ratio is considerably greater in Li, and it is also difficult to see why Ag should behave so differently. Recent thermotransport studies by Thernquist[31] of Au in Li gave a heat of transport possible to reconcile with interstitials. Hints of an unconventional mechanism have also been seen in other thermotransport studies of Li[1, 2]. One possibility suggested was that the region around a vacancy in Li is so relaxed, that it no longer constitutes a point defect. The relative importance of ΔE_{hom} would in such an extended defect probably be rather small, and the effects of motion energy, size and compressibility would gain weight. At this stage it is hardly profitable to indulge in too much qualitative speculation; however, if the defect mainly responsible for diffusion in Li is not a simple vacancy, or if the mechanisms of impurity-diffusion and self-diffusion are different, then the whole problem has to be examined in new light, and the complete or partial failure of hitherto developed theories is very understandable.

Special acknowledgement is due to Dr. J.N. Mundy (Argonne), who during his stay as a visiting scientist introduced the solid alkali diffusion technique in our laboratory. His collaboration has been most stimulating. We also acknowledge interesting discussions with profs. N.H. March (Sheffield) and A. Bienenstock (Stanford). This research has been supported by the Swedish Council for Applied Research and by Statens Naturvetenskapliga Forskningsråd.

References

1) A. Lodding and P. Thernquist, Z. Naturforschg. 21a, 857 (1966).

2) P. Thernquist and A. Lodding, Z. Naturforschg. 22a, 837 (1967); ibid. 23a, 473 (1968).

3) A. Lodding and A. Ott, Z. Naturforschg. 21a, 1344 (1966).

4) A. Ott and A. Lodding, Z. Naturforschg. 20a, 1578 (1965).

5) L. Löwenberg and A. Lodding, Z. Naturforschg. 22a, 2077 (1967).

6) J.N. Mundy, L.W. Barr and F.A. Smith, Phil. Mag. 14, 785 (1966).

7) J.N. Mundy, A. Ott, L. Löwenberg and A. Lodding, Phys. stat. sol., in print.

8) A. Ott, J.N. Mundy, L. Löwenberg and A. Lodding, Z. Naturforschg. 23a, 771 (1968).

9) A.N. Naumov and G. Ya. Ryskin, Zh. Techn. Fiz. 29, 189 (1959).

10) D.F. Holcomb and R.E. Norberg, Phys. Rev. 98, 1074 (1955).

11) R.A. Hultsch and R.G. Barnes, Phys. Rev. 125, 1832 (1962).

12) D.C. Ailion and C.P. Slichter, Phys. Rev. 137, A235 (1965).

13) J.N. Mundy, L.W. Barr and F.A. Smith, Phil. Mag. 15, 411 (1967).

14) "Metals Reference Book", C.J. Smithells, ed., 4th ed., Butterworths, London (1967).

15) D.D. Snyder and D.J. Montgomery, J. Chem. Phys. 27, 1033 (1957).

16) A.D. LeClaire, Phil. Mag. 7, 141 (1962).

17) R.A. Swalin, Acta Met. 5, 443 (1957).

18) D. Lazarus, Phys. Rev. 93, 973 (1954).

19) A.D. LeClaire, Phil. Mag. 10, 641 (1964).

20) N.L. Peterson and S.J. Rothman, Argonne Nat. Lab. Rep. 6568 (1965).

21) A. Lodding and A. Ott, to be published in Z. Naturforschg.

22) L.C.R. Alfred and N.H. March, Phys. Rev. 103, 877.

23) A. Blandin, J.L. Déplanté and J. Friedel, J. Phys. Soc. Japan, Suppl. 18 (1963).

24) C.K. Corless and N.H. March, Phil. Mag. 7, 1765 (1962).

25) L.W. Barr, J.N. Mundy and F.A. Smith, Phil. Mag. 16, 1139 (1967).

26) K. Lal, Thèses, Paris-Orsay (1966).

27) A. Bienenstock, private communication.

28) N.H. March, private communication.

29) A. Ott, Z. Naturforschg., in press.

30) L.W. Barr, Phil. Mag. 14, 1299, 301 (1966).

31) P. Thernquist and A. Lodding, to be published.

32) R. Feder and H.P. Charbnau, Phys.Rev. 149, 464 (1966).

33) J.N. Mundy, to be published in Phil. Mag.

Electro- and Thermotransport in Lithium.

P. Thernquist and A. Lodding
Physics Department, Chalmers University of Technology
Gothenburg, Sweden.

(Abstract)

The mobilities of defects and impurities in lithium have been studied by observing the motion of inert lattice markers, of stable isotopes or of radioactive tracers, induced by potential gradients (electrotransport) or by temperature gradients (thermotransport). The electrotransport experiments on pure Li indicate an effective defect resistivity of about 0.6 micro-ohms/% def., mass transport directed towards the anode. The thermotransport experiments give a heat of transport of about +8 kcal/mole, with mass transport towards the cold region, while the isotope effect of thermotransport is anomalously directed towards the hot region. From the temperature characterictics of both electro- and thermotransport one deduces an activation energy close to that of self-diffusion (12.6 kcal/mole). The thermotransport of ^{195}Au in Li enriches the tracer in the cold region. The transport mechanism in lithium appears to be governed by composite defects rather than "classical" vacancies.

Among the methods employed at this laboratory for the studies of atom mobilities in solid and liquid metals, those of electro- and thermotransport have proved particularly useful[1 - 8]. This report deals with investigations in lithium between 70°and 170°C. The results will be presented from four main lines of investigation: 1)electrotransport and 2)thermotransport in pure Li, both studied by an inert marker technique; 3)the Li-isotope de-mixing effect accompanying electro- and thermotransport in the pure metal; 4)the thermotransport of a radioactive tracer (^{195}Au) in Li, using a steady-state technique still in the stage of development.

1)Electrotransport of Lattice Markers.

The experimental arrangement was a further development of a method employed by Wever[9], Huntington[10,11], and Lodding[2]. Direct current was passed along cylindrical lithium samples, force-cooled at both ends.

The motion of inert lattice markers (surface scratches) in the hot portion of the samples was measured by means of a travelling microscope. Markers at the cold ends served as references. A more thorough description of the experimental details will be given in a forthcoming publication[12].

Electrotransport results are conveniently expressed in terms of the "effective valence", z^*, of the diffusing atom, defined by the relation

$$v_a \ (= -v_m/\alpha) = B_a j \rho e \, z^* \qquad , \qquad (1)$$

where v_a is the migration velocity of the species a, due to a current density j; ρ is the specimen resistivity, and e the electronic charge. α is an isotropy factor (between 0.3 and 1 for normal experimental conditions) which can be determined by comparing the marker motion with the observed radial dimension changes along the specimen. B_a is the "mobility" due to the self-diffusion mechanism, i.e. $B_a = D/fkT$, where D is the experimental self-diffusion coefficient, f the Bardeen-Herring correlation (0.73 for vacancies in bcc lattices), k the Boltzmann constant and T the abs. temperature. In comparison with B_a, which is an exponential Boltzmann function, $\alpha\rho$ vary only slowly with temperature and z^* can be expected to vary either slowly or exponentially; a logarithmic plot of v_m/j versus reciprocal temperature therefore should give a straight Arrhenius line, from which the activation energy of the true electrotransport mobility can be computed. The Arrhenius plot is shown in Fig.1. The computed activation energy is shown to be 12.9 ± 0.4 kcal/mole. This is very close to the activation energy of tracer self-diffusion, 12.62 ± 0.21, as recently determined by Ott & al.[13]. Therefore it seems reasonable to conclude that the mechanisms are in fact identical, and formula 1 represents not only a definition of z^*, but also a valid form of the Nernst-Einstein relation.

Several theories of electrotransport have been developed, all leading to rather similar predictions. A formula due to Huntington[11] comprehensively takes into account the influence of effective electron mass in imperfect electron conductors. Huntington's formula can be combined with one first given by

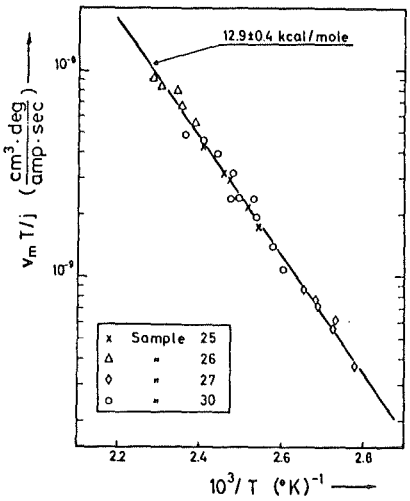

Fig. 1. Arrhenius Plot of Electrotransport in Pure Li.

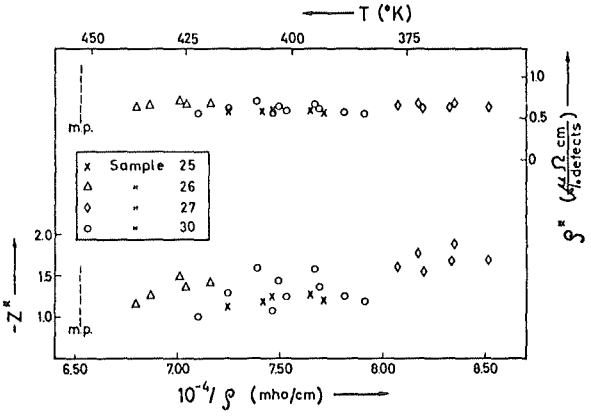

Fig. 2. Effective Valence and "Defect Resistivity" in Pure Li, as Functions of Temperature and Resistance.

Lodding[14] (see also Fiks[15]), to obtain

$$z^* = z\left[q^*/q - \tfrac{1}{2}(\rho^*/\rho)(m^*/|m^*|)\right] \quad . \quad (2)$$

Here z is the number of free electrons per atom, q^* and q are, respectively, the ionization degree of the diffusing atom and that of an atom at a lattice site, m^* the effective mass of the electron, ρ the defect-free metal resistivity and ρ^* the effective resistivity of an atom at the saddle point, which should be comparable to the effective defect resistivity. For self-transport in an alkali metal one may reasonably assume $q^* = q$, $m^* = |m^*|$ and $z = 1$. The effective valence z^*, obtained from experimental v_m via eq.1, thus conveniently yields ρ^* by means of

$$\rho^* = 2\rho\,(1 - z^*/z) \quad . \quad (3)$$

The results from all investigated samples give us the average values $z^* = 1.4 \pm 0.2$ and $\rho^* = 0.62 \pm 0.03\ \mu\Omega/\%$ defects. Fig.2 shows the dependence of z^* and ρ^* on temperature and inverse resistivity. The "effective resistivity" appears to be practically independent of temperature, while the slight decrease of $(-z^*)$ with rising temperature is to be attributed to the ρ term in the denominator in eq.2.

That ρ^* is independent of temperature has also been observed in other recent self-transport measurements[2,17,18], while most earlier marker-type experiments suggested a decrease of ρ^* with rising temperature. No existent theory does require ρ^* in a pure metal to be temperature dependent, and attempts have been made to account of the non-constancy in the early experiments in terms of dislocations[21] or impurities[3]. The constant value of ρ^* in the present investigation is gratifying and implies the possibility of evaluationg the true charge zq^*/q of an impurity in lithium from z^*, by linear extrapolation of eq.2 to $\rho^{-1} \to 0$.

The negative sign of z^* indicates that the "electron wind" (second term in parenthesis, eq.2) dominates over pure coulomb forces, which is hardly unexpected in a good electron conductor. A striking result is, however, the low

"effective resistivity". The value obtained, 0.62, is considerably lower than the theoretical estimate of vacancy resistivity in Li[16] (about 1.2 $\mu\Omega$/%def.). Recent electrotransport experiments on close-packed metals[17,18] have shown much better agreement between ζ^* and ζ_V. The present result is, however, comparable to that obtained by Sullivan[19] for sodium, $\zeta^*_{Na} = 0.44$ $\mu\Omega$/% def. The reason for these low values is still not quite clear. It has been proposed[19] that the saddle-point configuration in a bcc metal should be reassessed. A lowering of ζ^* would also be expected for a vacancy if a considerable relaxation is present in its vicinity. There are reasons to believe[20] that such is indeed the case in the alkali metals.

2) Thermotransport of Lattice Markers.

The experimental set-up resembled that used for electrotransport, with the main difference that alternating current was used instead of direct current A short description has been published[6], a more detailed one is under preparation[12].

Thermotransport ("thermal diffusion") results are usually described in a form derived from thermodynamic arguments:

$$v_a = -B_a Q^* \, \mathrm{grad}(\ln T) \quad , \qquad (4)$$

where Q^* is an energy characteristic of the material and of the transport mechanism (the nomenclature differs in different laboratories, but the term "heat of transport" will here be used for Q^*). As in Section 1, an activation energy for the dominant transport mechanism should be obtainable from the temperature behaviour of the marker displacement. Plotting $v_a T^2/\mathrm{grad}\ T$ vs. inverse temperature one indeed obtains an acceptable straight line (fig.3). A closer look reveals a tendency for increasing slope at lower temperatures. The points below some 90°C (underlined in fig.3) may, however, have been particularly influenced by grain boundary effects, as well as by errors in temperature determination, and it is probably correct to exclude them from the main phenomeno-

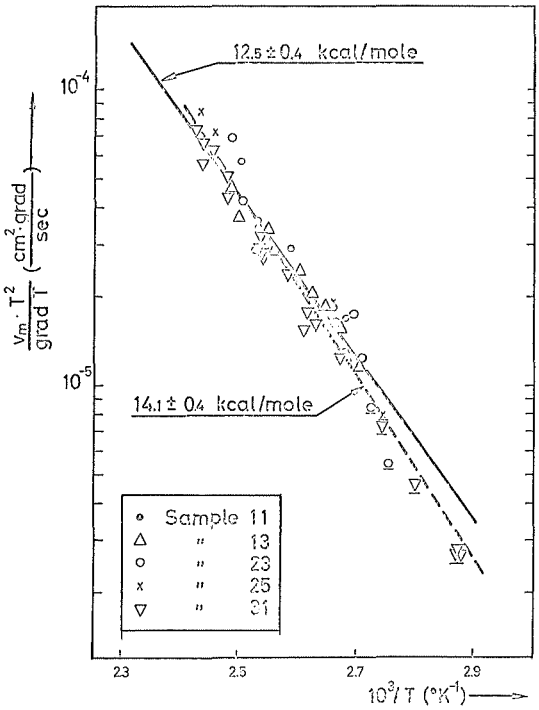

Fig.3
Arrhenius plot of thermotransport in pure lithium

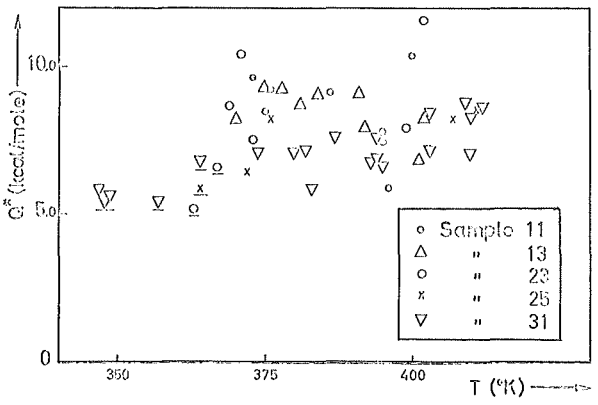

Fig.4
Heat of transport in pure lithium as a function of temperature

logical discussion. This results in an activation energy of 12.5 ± 0.4 kcal/mole, again very close to the value 12.62 ± 0.21 from experimental self-diffusion[7]. One may thus reasonably assume that thermotransport as well as electrotransport are governed by the same mechanism as self-diffusion, and Q^* can be considered as nearly constant. Combining eq.4 with $v_m = \alpha v_a$ and $B_a = D/fkT$, measuring α, and assuming f = 0.73, one can calculate Q^*. All calculated heats of transport are shown as function of temperature in fig.5. There is a considerable scatter, but at temperatures above 90°C certainly the temperature dependence is small, if any. The mean value obtained is $Q^* = 8.2 \pm 1.3$ kcal/mole.

From solid-state atomistic as well as from statistic arguments[22-25] (see also the review article on solid-state thermotransport by Allnatt and Chadwick[26]) one expects

$$Q_V^* = \beta E_M - E_F = (\beta + 1)E_M - Q_D \qquad (5a)$$

for the simple vacancy mechanism, and

$$Q_I^* = E_M + E_F = Q_D \qquad (5b)$$

for the simple interstitial mechanism. E_M and E_F are, respectively, the energies of motion and formation, Q_D is the self-diffusion activation energy and β is a constant near to unity. If the dominant transport mechanism is that of vacancies, as various evidence[27,28,20] from Na, i.e. the metal most similar to Li, seems to indicate, then one would from $Q^* = +8.2$ deduce E_M to be about 11 kcal/mole, i.e. the major part of Q_D. This is contradicted e.g. by the results obtained dilatometrically by Feder and Charbnau[28], implying that in the alkali metals E_M should be much smaller than E_F. Even for close-packed metals eq.5a would predict negative, or near-zero, heats of transport, and our high positive Q^* value for Li thus seems altogether incompatible with the "classical" vacancy mechanism. While the abovementioned evidence favours vacancies as the main mechanism in Na, the presence of interstitialcies is not excluded[28,20]. It seems possible that in the even more relaxed Li lattice interstitial defects are more common. The thermotransport treatment by Lodding[25] would indeed predict $Q^* \cong nQ_D$ for n-atom interstitialcies, which would permit

the contribution from such defects to outweigh that from vacancies even at superior concentrations of the latter. Another explanation, proposed in ref.[6], may be that the region around a vacancy is so extremely relaxed, that two different motion mechanisms may be combined with the same formation mechanism. One would be the discrete jumps of single atoms into the relaxed, perhaps "liquid-like"[29], region, the other would entail spontaneous co-operative motion of all the atoms in the region, moving the centre of the extended defect only by small displacements. The latter motion would (again as a consequence of the theory of ref.[25]) give a greater Q^{35} value than the former, causing the total heat of transport to be positive.

3) Isotope Effects in the Electro- and Thermotransport of Li.

A number of the samples on which marker-motion had been observed were sectioned, and each section was mass-analysed to yield the variation, along each sample, of the isotope separation factor Q_x, given by

$$Q_x = (c_7/c_6)/(c_7/c_6)_0 \quad , \qquad (6)$$

where c are the concentrations, the subscripts 6 and 7 refer to the two Li isotopes, and the subscript zero to the concentration ratio of normal lithium. In a publication a couple of years ago[7] the isotope effect of thermotransport was reported for the first time, and a method of quantitative evaluation was given. The arguments led to the formula (valid for small isotope enrichments)

$$Q_x - 1 = \frac{\partial (v_m t)}{\partial x} \alpha^{-1} (-a)(\Delta M/M) \quad , \qquad (7)$$

where t is the duration of experiment, x the coordinate along sample, ΔM the mass difference of two isotopes of mean mass M, and a the "isotope factor", defined for lithium by

$$a = \frac{v_6 - v_7}{v_m / \alpha} \cdot (M/\Delta M) \quad , \qquad (8)$$

v_6 and v_7 being the respective migration velocities of the isotopes.

It was related in ref.[7], and subsequent experiments have confirmed[12], that the light isotope was enriched at the hot portion of the specimen (i.e. the portion which the bulk motion was directed away from). The isotope factor was found to be $a_{th} = +0.35 \pm 0.10$ (the subscript referring to "thermotransport").

Quite recently we have also found an isotope effect (hitherto unreported) in electrotransport. This effect, although quite distinct, was more difficult to measure quantitatively than was the one in thermotransport. The reason for this was, that in the DC experiments the presence of a thermotransport effect was unavoidable, and had to be subtracted from the total migration effect to obtain the pure electrotransport behaviour. The procedure is illustrated by fig.5, showing the variation, along one of the samples, of total marker displacement and of isotope composition after a completed run of some three weeks. The upper half of the figure (marker motion) shows how the antisymmetric thermotransport contribution, known by calibration from separate AC runs, is subtracted from the experimental curve to yield the symmetrical electrotransport contribution. In the lower half of the figure (isotope separation factor) the thermotransport contribution to Q_x (the symmetrical curve) has been computed from the gradient of the above marker-motion curve, using $a_{th} = +0.35$ in formula 8. The electrotransport contribution (anti-symmetrical curve) was also calculated via eq.8, tentatively assuming $=+0.40$. The resulting theoretical curve (whole-drawn) is seen to agree in shape with the experimentally measured variation in isotope composition. The quantitative evaluation is obviously arduous, but the three hitherto investigated DC samples have yielded $a_{el} = -0.45 \pm 0.20$ (the index standing for "electrotransport"). The sign means that the light isotope is enriched at the anode, i.e. in the direction of bulk electrotransport, contrary to the results of the AC experiments.

The physical meaning of the isotope factor a has been discussed by one of the present authors[30], and it has been pointed out that if the bulk motion and the isotope effect are governed by the same mechanism, then the factor has to be negative. The kinetic energy factor ΔK, first discussed by

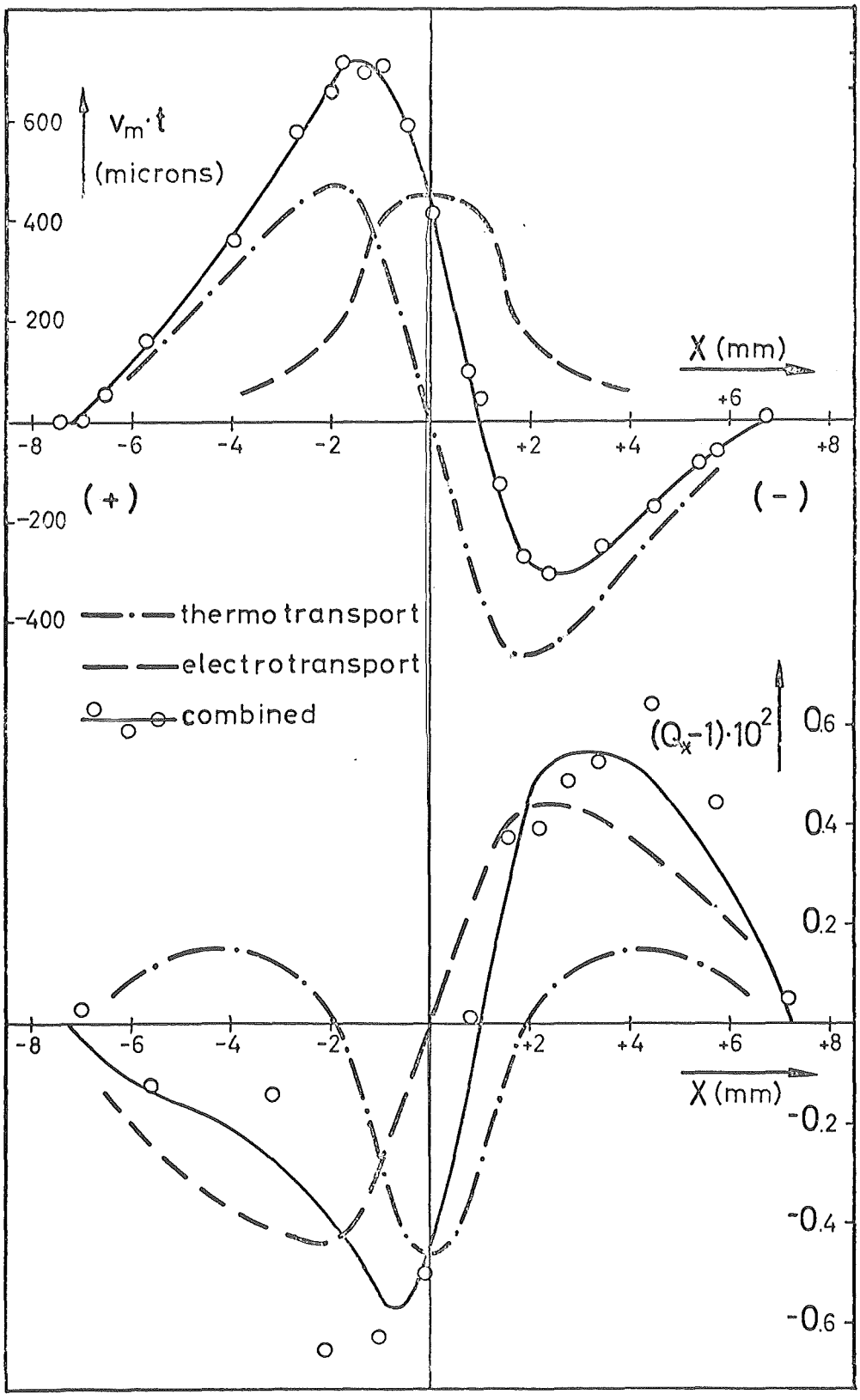

Fig.5 Evaluation of bulk electrotransport and of the associated isotope effect in pure lithium.

Mullen[30] (denoting the share of kinetic energy at the saddle-point which is possessed by the diffusing atom itself and not by its surroundings; see also ref.[31]) is by definition identical with (-2a).

Positive a-values are thus strongly indicative of composite mechanisms. From the sign of our experimental a_{th} one is led to infer, what has been suggested already in the previous section, namely that two modes of motion are present. The "diserete jumps" of single atoms give rise to an isotope effect, but contribute less to the bulk motion. On the other hand, the "cooperative motion" of extended defects favourises bulk motion in thermotransport on account of their size[25,5], but eludes isotope effects because of the large effective mass of the moving species.

The sign of a_{el} is the same as for "discrete jumps", which is to be expected,as a single atom at the saddle-point should scatter electrons more than one performing a small position adjustment together with its neighbours. The discrepancy between theoretical and experimental "defect resistivity" in the alkalis might also be qualitatively understood on this basis, as only one part of the atoms giving rise to the experimental self-diffusion coefficient D is also contributing to electrotransport. Accordingly, if formula 1 is to have a meaning in terms of the microscopic mechanism, B_a should not correspond to D, but to an effective share of the diffusion coefficient.

This isotope effect of electrotransport in Li appears to be the first observed instance of the Haeffner-effect[32,1] in any solid metal.

4) Thermotransport of Impurity Atoms in Lithium.

If a temperature gradient is imposed on an initially homogeneous alloy, a de-mixing occurs. Thermal diffusion phenomena have been studied rather extensively in gaseous systems and in liquid mixtures, but in spite of rapidly growing interest (see review article, ref.[26]) relatively little has hitherto been done in solids. In the alkalis, to our knowledge no thermotransport of impurities has hitherto been investigated.

From formula 4 the steady-state concentration c_i of dilute impurity

in a temperature gradient can be obtained under the assumption of identical mechanisms of inter-diffusion and thermotransport. In the steady state the flux due to the velocity v_a is completely balanced by back-diffusion, i.e.

$$-(D_i/fkT)Q_i^{**} \text{ grad}(\ln T)c_i = D_i \text{grad } c_i \qquad (9)$$

and so

$$k \frac{(\ln c_i)}{(1/T)} = Q_i^{**} \qquad (10)$$

The "heat of transport" Q_i^{**} by its sign and magnitude indicates the tendency of the alloy to segregate, and pertains to the relative velocity $V_i - V_a$ of the impurity with respect to the matrix lattice, which, of course, also moves under self-transport. To deduce a physical meaning via equations analogous to formulae 5, the entity to be substituted is therefore Q_i^*, from

$$D_i Q_i^* - DQ^* = D_i Q_i^{**} \qquad (11)$$

In lithium, measurements of D and Q^* have been made (see ref.[13] and section 2 of this report), and a systematic study of impurity diffusion is in progress at this laboratory. It is therefore a logical step to extend our investigations to impurities in a temperature gradient.

The experimental arrangement is a specialized vacuum development of a standard steady-state method[33], utilizing a slicing and counting technique. The high diffusivity of Li allows a rapid attainment of steady-state, permitting even relatively thick (approx.2 mm) samples. About 20 slices could be made (using the microtome procedure of ref.[13]), giving excellent profiles of $\ln c_i$ vs. $1/T$ (c_i varying over two orders of magnitude along the sample) in our test experiment with ^{195}Au in Li. These measurements showed a migration of Au towards the cold end of the specimen (Q_i^{**} positive). This is, via eqs.11 and 5b, compatible with an interstitial mechanism. Further work on the thermotransport of Au and Ag impurities in Li is in progress.

5) Conclusions.

While in thermotransport the sign of the isotope effect does suggest the presence of some type of a vacancy mechanism, the bulk effect in pure Li seems explicable only on the assumption that a cooperative mechanism ("extended defect") is competing with "discrete jumps" into vacancies.

The "discrete jump" mechanism is also implied by the results of electrotransport measurements, where no contradiction is found between the bulk effect and the isotope effect. The small effective defect resistivity obtained may, however, again be due to the "cooperative" contribution to self-diffusion.

The fact that the activation energies of electrotransport, thermotransport and self-diffusion are found to be practically the same suggests that the "cooperative" and "discrete" modes of motion are two manifestations of one kind of defect. This defect may be either an extremely relaxed vacancy, or a type of a Frenkel-pair in which the interstitial moves as a group of two or more atoms.

The positive heat of transport of Au impurity in Li is compatible with an interstitial mobility mechanism.

This work has been supported by the Swedish Council for Applied Research and by the Statens Naturvetenskapliga Forskningsråd. We thank Prof.H.B.Huntington (Troy, N.Y.), Prof. A. Klemm (Mainz) and Dr. A. Ott (Gothenburg) for stimulating discussions.

References.

1) A. Lodding, J.Phys.Chem.Solids 28, 557 (1967).
2) A. Lodding, ibid. 26, 143 (1965).
3) P. Thernquist and A. Lodding, Z.Naturf. 21a, 1310 (1966).
4) A. Lodding and A. Ott, ibid. 21a, 1344 (1966).
5) A. Lodding, Phys.stat.sol. 22, 157 (1967).
6) A. Lodding and P. Thernquist, Z.Naturf. 21a, 857 (1966).

7) P. Thernquist and A. Lodding, Z.Naturf. 22a, 837 (1967).
8) P. Thernquist and A. Lodding, ibid. 23a, 627 (1968).
9) H. Wever, Z.Elektrochem. 60, 1170 (1956).
10) H. B. Huntington and A. R. Grone, J.Phys.Chem.Solids 20, 76 (1961).
11) H. B. Huntington and S. C. Ho, J.Phys.Soc.Japan 18, Suppl.2, 202 (1963).
12) P. Thernquist and A. Lodding, J.Phys.Chem.Solids, to be published.
13) A. Ott, J.N.Mundy, L.Löwenberg and A.Lodding, Z.Naturf. 23a, 771 (1968).
14) A.Lodding, ibid. 14a, 939 (1959).
15) V.B.Fiks, Sov.Phys. Solid St. 1, 14 (1959).
16) D.K.C.MacDonald, Phys.Rev. 90, 177 (1953).
17) H.M.Gilder and D.Lazarus, ibid. 145, 507 (1966).
18) S.C.Ho and H.B.Huntington, J.Phys.Chem.Solids 27, 1319 (1966).
19) G.A.Sullivan, Phys.Rev. 154, 605 (1967).
20) J.N.Mundy, L.W.Barr and F.A.Smith, Phil.Mag.14, 785 (1966).
21) H. Wever, Acta Met. 15, 443 (1967).
22) J.A.Brinkmann, Phys.Rev. 93, 345 (1954).
23) A.D.LeClaire, ibid. 93, 344 (1954).
24) K. Wirtz, Z.Naturf. 3a, 672 (1948).
25) A.Lodding, ibid. 21a, 1348 (1966).
26) A.R.Allnatt and A.V.Chadwick, Chem.Reviews 67, 681 (1967).
27) G.A.Sullivan and J.W.Weymouth, Phys.Rev.136, A1141 (1964).
28) R.Feder and H.P.Charbnau, ibid. 149, 464 (1966).
29) N.H.Nachtrieb and G.S.Handler, Acta Met. 2, 797 (1954).
30) J.G.Mullen, Phys.Rev. 121, 1649 (1961).
31) A.D.LeClaire, Phil.Mag. 14, 1271 (1966).
32) E.Haeffner, Nature 172, 775 (1953).
33) D.Jaffe and P.G.Shewmon, Acta Met. 12, 515 (1964).

DETERMINATION OF THE CHARGE AND THE RESIDUAL RESISTIVITY OF ACTIVATED IMPURITY-VACANCY COMPLEXES IN METALS BY ELECTRO-TRANSPORT

Th. Hehenkamp, Ch. Herzig, Th. Heumann
Institut für Metallforschung der Universität Münster/Westf.

ABSTRACT

In order to check different theories for electrotransport, which have not been confirmed quantitatively, electrotransport, diffusion and residual resistivity of antimony in gold have been precisely measured. The results seem to best fit a model given by Huntington. A quantitative evalution is possible for the first time. The results yield a value of 3.3e for the screened charge of the activated antimony-vacancy complex. It is assumed that the residual resistivity of the antimony impurity which yielded 6.66 $\mu\Omega$cm/At.% is almost identical with that of the activated complexes. It has to be concluded that the charge of the impurity on normal lattice positions does not differ significantly from the charge of the activated complex. Further, the results show that the correlation coefficient for jumps between vacancies, the Sb-impurities and gold atoms does not vary in the limits of the experimental errors.

I. Introduction

By means of electrotransport measurements one is able to obtain information about the mutual energetic interactions between electrons or holes and point defects in activated states in solid metals. Such an activated state is the saddle-point configuration during a jump of an atom from one stable position in the lattice to another one. For a vacancy controlled diffusion process such an activated complex consists of the displaced atom at the saddle point and the neighboring vacancy. For interstitial diffusion only the displaced atom constitutes the activated complex. The current theories of electrotransport yield in particular information about the residual resistivity and the screened charge of such activated complexes.

In a metal two forces act upon a mobile atom resulting from passage of high direct currents. The first is the field force, the second a friction force resulting from a momentum transfer from the electrons or holes to the activated complex. These two forces are opposite in sign in electron conductors [1] and produce for mobile

atoms a flux of matter, the electrotransport. This problem has been treated theoretically by Huntington and Grone [2], Fiks [3] and Bosvieux and Friedel [4] and others. For a review see Verhoeven [5] and Adda and Philibert [6]. In all the theories the resulting force F is of the form

$$F = E\, e\, z_{eff} \qquad (1)$$

E being the electric field and $z_{eff}e$ an effective charge which is the sum of the screened charge z'e of the activated atoms and of the charge Z resulting from the momentum transfer. The drift velocity v is then given by the product of force F and mobility $B=\frac{D^*}{kTf}$

$$v = \frac{D^*}{kTf}\, j\, \varrho\, e\, z_{eff} \qquad (2)$$

D* is the self-diffusion coefficient of the transported species, j the current density, $\varrho(T)$ the specific resistivity at temperature T, and k Boltzmann's constant. The correlation factor f, introduced by Bardeen and Herring [7], takes into account the difference between the actual, statistical mobility and the mobility measured by means of the penetration of a radioactive tracer. The theories mentioned above give the following results for z_{eff}.

$$z_{eff} = z' - 1/2\, z\, \frac{\Delta\varrho_d\, N\, m^*}{\varrho_T\, N_d\, m^*|} \qquad (3)\ \text{Huntington and Grone [2]}$$

$$z_{eff} = z' - z\, \frac{\Delta\varrho_d\, N}{\varrho_T\, N_d} \qquad (4)\ \text{Fiks [3]}$$

$$z_{eff} = 1/2\, z - 1/2\, z\, \frac{1}{\varrho_T}\left(\Delta\varrho_d^{\Delta z}\, \frac{N}{N_d^{\Delta z}} + \Delta\varrho_d^{\Delta z+z}\, \frac{N}{N_d^{\Delta z+z}}\right) + C \qquad (5)$$

Bosvieux and Friedel [4]

These equations stand for the transport of substitutional impurities. Here C is a correction term which usually is small and negative, $\Delta\varrho_d$ the residual resistivity of the activated complexes, $\frac{N}{N_d}$ their concentration, m* the effective electron mass, and z the valence of the matrix. The first term in these equations corresponds to the screened charge, the following to the friction force. In contrast to eqns. (3) and (4) eqn. (5) has two terms for $\Delta\varrho_d$. $\Delta\varrho_d$ is assumed to be independent of temperature in analogy to Matthiessen's rule. Except the specific resistivity $\varrho(T)$ all factors determining z_{eff} are therefore constant. A plot of z_{eff} determined for different temperatures from eqn. (2) versus $1/\varrho$ should therefore be linear. An extrapolation of this plot to $1/\varrho = 0$ should give the screened charge of the activated comple-

xes according to eqns. (3) and (4). Logarithmic differentiation of the rewritten eqn. (2) with respect to 1/T yields

$$\frac{\partial}{\partial 1/T} \ln v/j = -\frac{Q}{k} + \frac{\partial}{\partial 1/T} \ln \frac{z_{eff} \varrho_T}{T f} = -\frac{Q'}{k} \quad (6)$$

with $D^* = D_o \exp(-\frac{Q}{kT})$, Q being the activation energy of diffusion. A plot of ln v/j versus 1/T yields almost the same activation energy because of the small contribution from $\ln \frac{z_{eff}\, \varrho(T)}{T\, f}$. The small difference $Q - Q' = \Delta Q'$ is essentially given by the dependence of z_{eff} on $1/\varrho$, since $\frac{\varrho(T)}{T}$ is approximately constant at higher temperatures. Comparing the results of electrotransport measurements published so far with theory, it is obvious that in many but not in all of them $\Delta Q'$ is much larger than expected. The values for z_{eff} therefore show a much stronger temperature dependence than $1/\varrho$. So far none of the experiments yielded the expected linear dependence between z_{eff} and $1/\varrho$.
Wever [8, 9] has proposed to attribute the large differences between Q and Q' to a dislocation pipe diffusion mechanism. On the other hand systematic errors might be involved in determining the electrotransport. For example, in gold Huntington and Grone [2], Gilder and Lazarus [10], Kuzmenko [11] und Herzig [12] using different experimental techniques obtained widely varying results. Large errors can be introduced by measuring temperature and calculating from it the diffusion constant D in eqn. (2), particularly using data from literature. It is therefore essential to measure diffusion and electrotransport simultaneously. Such measurements have been per-formed by Hehenkamp [13] and Gilder and Lazarus [10]. The simultaneously obtained D permits the determination of T from the well known Arrhenius plot. This indirect method has been used [10] [12] and seems to be the best at present.

II. Experimental procedure

1) Materials and method

The particular system and the method used for the present work was chosen for following reasons:

a) the transport effect should be large in this system
b) the method should be as free as possible of systematic errors as mentioned above and should have great spacial resolution in order to measure the shifts vt = x quite precisely.

The migration of antimony in gold was chosen. For given T and j

v is particulary large for high values of D and $\Delta\varrho_d$, cf. eqns. (2) and (3), if the friction force predominates. According to Linde [14] $\Delta\varrho_i$ for impurities in the noble metals Cu, Ag, and Au satisfies appoximately the equation

$$\Delta\varrho_i = a + b\Delta z^2 \qquad (7)$$

Δz is the difference in valence of the matrix and impurity atom. Supposing $\Delta\varrho_d$ and $\Delta\varrho_i$ are comparable to a first approximation impurities with a large valence difference are expected to give a large transport effect. The same holds for D as has been shown for impurity diffusion in silver by Tomizuka and Slifkin [15]. For antimony in gold $\Delta z = +4$. An experimental technique for simultaneous determination of diffusion and electrotransport has been described by Hehenkamp [16]. By this method systematic errors seem to be eliminated for suitable experimental conditions. The shift of the diffusion profile by electrotransport is measured with respect to a lattice-fixed reference system.

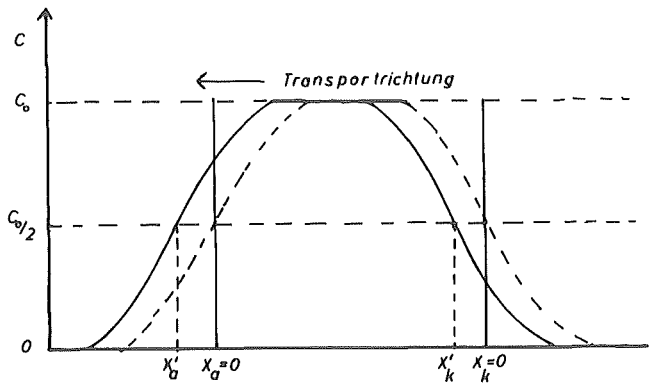

Fig. 1
Concentration penetration curves for pure diffusion (dotted line) and for diffusion and electrotransport

According to fig. 1 the sample consists of three parts. The antimony-gold alloy is placed between two 99,999 % pure gold specimens. These hollow cylinders are 5 mm in diameter and 4 mm in lenght. The bore in the center has a diameter of 2 mm. The planes $x_a = o$ and $x_k = o$ are the original welding interfaces. This arrangement corresponds to the well known boundary condition of the infinitely long sample. The flux of matter is given by a transport modified Fick's second law

$$\frac{\partial c}{\partial t} = \frac{\partial}{\partial x}\left(D\,\frac{\partial c}{\partial x}\right) \pm \frac{\partial}{\partial x}\,vc \qquad (8)$$

where c is the volume concentration of the antimony impurity. For D and v independent of x the solution of eqn. (8) is

$$c = c_o/2 \; (1 - \mathrm{erf} \frac{(x \mp vt)}{2\sqrt{Dt}} \qquad (9)$$

Since eqn. (8) is linear diffusion and electrotransport are additive. Therefore the profile for pure diffusion (dotted line) is shifted by vt where-as the shape remains the same. The shift by electrotransport is given then by $|x'_{a,k} - x_{a,k}| = |vt|$. Every experiment yields two independent results for vt, one for the anode side of the sample, another one for the cathode side. The experimental data are evaluated by plotting the concentration profiles on probability paper. For constant D and v, i.e. for D and v independent of c and isothermal conditions straight lines, the slope of which give a value of D, are to be expected. For electrotransport of impurity atoms it is quite necessary to check to what extent a variation of $\varrho(T)$ along the specimen gives rise to an electric field gradient. Hehenkamp [16] has shown that an evalution according to eqn. (9) is only possible for very small impurity concentrations. The straight lines representing the penetration curves on probability paper fix the points $x'_{a,k}$ at $c = c_o/2$. The problem is the determination of the reference system $x_{a,k} = o$. Transport of impurities offers the possibility to measure the concentration profiles by means of an electron microprobe. The applicability and the features of this instrument for such problems have been studied by Hehenkamp [16, 17] in detail, particulary for small impurity concentrations. The microprobe has also been used in the present work.

2) Experiments

The concentration of antimony was 0,255 At% for electrotransport specimens. The runs have been performed in a vacuum of about 10^{-5} torr. During the run the temperature was kept constant to $\pm$ 2,5°C with a Pt/Pt/Rh thermocouple as sensing element by means of a current control. This thermocouple was placed inside the hollow specimens and electrically isolated from them. The temperature measurement of the specimen itself was largely in error. The average current could be determined to about 1%. It was possible to establish isothermal conditions along the specimen by placing thin graphite plates between sample and the pure copper electrodes. In order to avoid deformations and evaporation of

antimony from the alloy the whole specimen was placed inside a quartz tube, which surrounded the specimen tightly at temperature. The results show, that the temperature variation along the penetration curve is less than $3^{o}C$. Therefore thermotransport is negligible.

For microprobe analysis the samples were prepared by embedding into an electrically conducting epoxy, by grinding, and by polishing perpendicular to the welding interfaces. The surface is then etched by aqua regia. A second polish removes the etched portion of the surface in order to avoid analytical errors. The welding interfaces, howewer, which are etched preferentially are still visible. Fig. 2 shows a few analytical points in the vicinity of the welding interfaces, visible due to burning spots of the electron beam. The distance between these points is 50 μm.

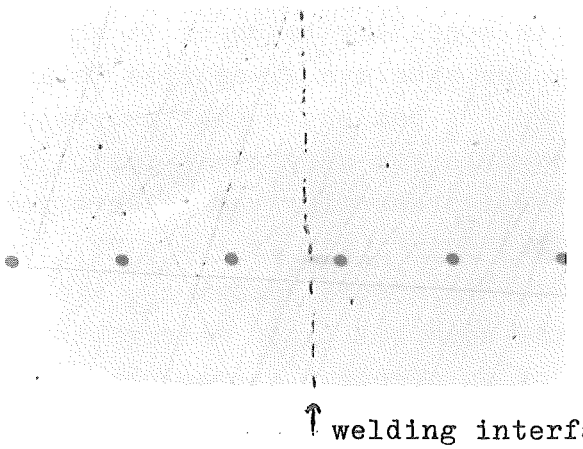

Fig. 2
Analytical points at distance 50 μm in the vicinity of the welding interface

By this preperation technique it is possible to fix the position of the analytical points with respect to the welding interface at $x_{a,k}=o$ precisely to $\pm$ 2 μm using the internal optical microscope in the microprobe analyzer. It is therefore possible to avoid all errors inherent in different techniques which use the shift of surface markers [2,18-20], since the transport is measured inside the specimen. Due to its nondestructive nature the analysis can be repeated for the same specimen.

Fig. 3 shows a penetration curve on probability paper as an example. For comparison both results the anodic as well as the cathodic part of the specimen are plotted with respect to their welding interfaces at SE = $x_{a,k}$ = 0 in the same fashion. Antimony has been transported to the anode in gold indicating a friction force much larger than the field force. The shift is then

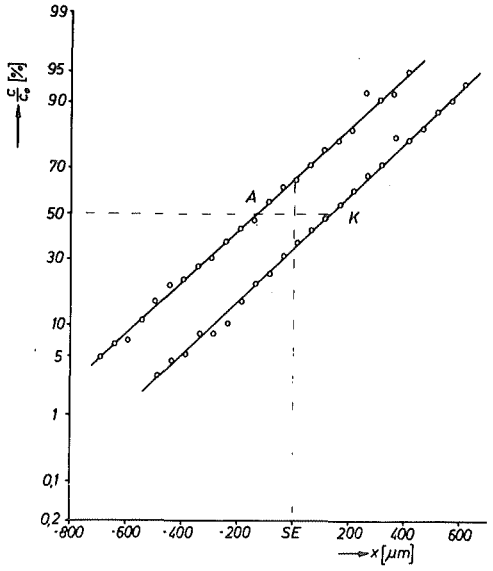

Fig. 3

Penetration curves for electrotransport on probability paper

SE = $x_{a,k} = 0$: Welding interfaces

$|x'_{a,k} - x_{a,k}|$ and can easily be obtained from the plot such as Fig.3. The penetration curves are straight lines for all 9 experimental runs and are almost parallel. This is a good check of the validity of the boundary conditions mentioned above for eqn.(9).

In order to confirm the independence of D of concentration and to provide a reliable temperature scale the pure diffusion of antimony in gold was measured as function of temperature. Previously these data were not available from the literature. The same metals as for the electrotransport measurements have been used in the same arrangement as in fig. 1. The diameter of these samples was 6 mm. Different initial concentrations between 0,15 At% and 0,4 At% antimony were chosen. The annealing temperature was measured with a platinum thermocouple placed inside the bore of the hollow specimen, to an accuracy of about 1,5°C. The anneal was carried out under an argon atmosphere at 14 different temperatures. The penetration plot on probability paper was linear for all runs indicating no detectable dependence of D on concentration up to about 0,4 At% antimony. Again the analysis was performed by means of the electron micropobe. Heating and welding time corrections have been made in the normal way.

III. Results and discussion

In fig. 4 the results of the diffusion runs are plotted versus 1/T. For a least squares fit of the straight line the three lowest temperature data have not been taken into account, since an influence of grain boundary diffusion could not be excluded. The data can be represented best by

$$D = (1{,}14 \pm 0{,}06) \cdot 10^{-2} \exp\left(-\frac{1{,}336 \pm 0{,}005\ \text{eV}}{kT}\right) \left(\frac{\text{cm}^2}{\text{sec}}\right) \qquad (10)$$

The average error of a single measurement with respect to the straight line is $\pm$ 4,7 %.

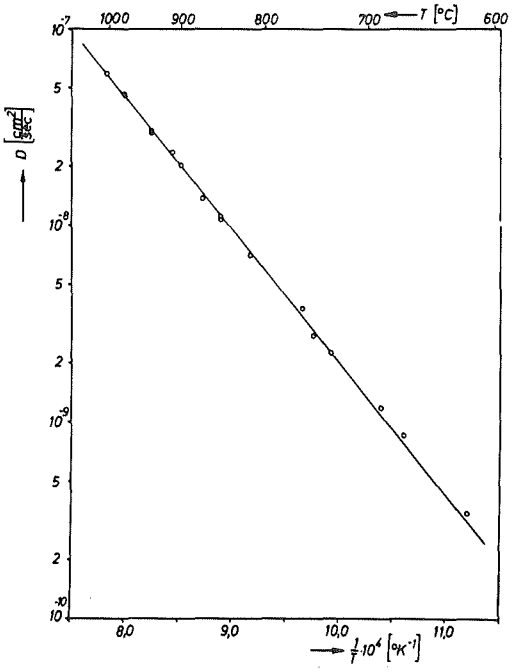

Fig. 4

lnD versus 1/T

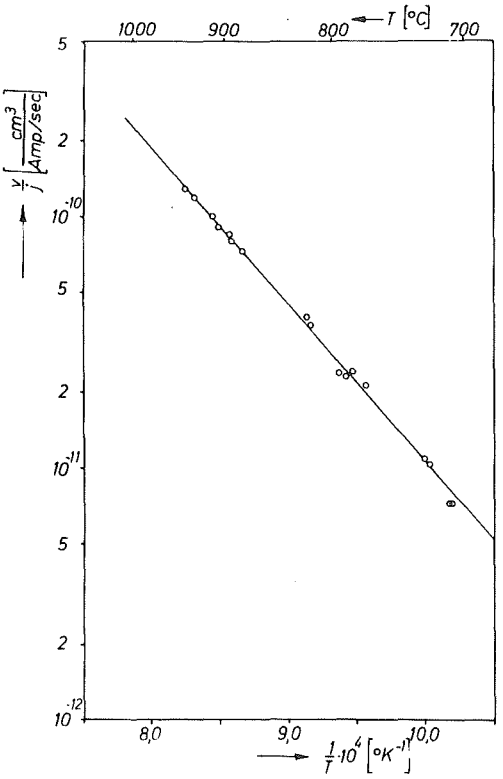

Fig. 5

ln v/j versus 1/T

Using eqn. (10) it is now possible to obtain the temperatures of the electrotransport measurements quite precisely via the simultaneously measured diffusion constants. Analysis of the penetration curves for electrotransport indicates almost the same margin of error as for pure diffusion. Hence the accuracy of T is about $\pm$ 4°K. Table 1 shows all experimental data for electrotrans-

ELECTROTRANSPORT OF ANTIMONY IN GOLD

Table 1

	D $\left[\frac{cm^2}{sec}\right]$	T [°K]	x [µm]	t [sec]	v/j $\left[_A \frac{cm^3}{sec}\right]$
A	$2,11 \cdot 10^{-8}$	1178	156	$4,69 \cdot 10^{4}$	$9,02 \cdot 10^{-11}$
K	$1,855\ 10^{-8}$	1168	147	$4,69\ 10^{4}$	$8,51\ 10^{-11}$
A	$4,59\ 10^{-9}$	1055	222	$1,91\ 10^{5}$	$2,44\ 10^{-11}$
K	$3,93\ 10^{-9}$	1045	193	$1,91\ 10^{5}$	$2,13\ 10^{-11}$
A	$7,79\ 10^{-9}$	1095	193	$9,25\ 10^{4}$	$4,02\ 10^{-11}$
K	$7,48\ 10^{-9}$	1092	178	$9,25\ 10^{4}$	$3,71\ 10^{-11}$
A	$1,50\ 10^{-9}$	982	90	$2,72\ 10^{5}$	$7,30\ 10^{-12}$
K	$1,43\ 10^{-9}$	978	90	$2,72\ 10^{5}$	$7,30\ 10^{-12}$
A	$1,83\ 10^{-8}$	1166	120	$2,92\ 10^{4}$	$7,98\ 10^{-11}$
K	$1,62\ 10^{-8}$	1155	110	$2,92\ 10^{4}$	$7,32\ 10^{-11}$
A	$2,32\ 10^{-8}$	1186	145	$2,58\ 10^{4}$	$1,01\ 10^{-10}$
K	$2,79\ 10^{-8}$	1203	171	$2,58\ 10^{4}$	$1,19\ 10^{-10}$
A	$5,36\ 10^{-9}$	1067	136	$1,05\ 10^{5}$	$2,39\ 10^{-11}$
K	$4,96\ 10^{-9}$	1061	132	$1,05\ 10^{5}$	$2,33\ 10^{-11}$
A	$1,89\ 10^{-9}$	996	86	$1,60\ 10^{5}$	$1,05\ 10^{-11}$
K	$2,01\ 10^{-9}$	1000	89	$1,60\ 10^{5}$	$1,09\ 10^{-11}$
K	$3,11\ 10^{-8}$	1213	125	$1,875\ 10^{5}$	$1,29\ 10^{-10}$
A	SE not visible				

z_{eff}/f calculated from the data according to eqn. (2)

Table 2

T [°K]	D $\left[\frac{cm^2}{sec}\right]$	v/j $\left[_A \frac{cm^3}{sec}\right]$	$\rho(T) = \rho_{Au} + 0,85$ ($\mu\Omega$ cm)	$-z_{eff}/f$
1280	$6,05 \cdot 10^{-8}$	$2,43 \cdot 10^{-10}$	13,42	33,04
1178	$2,11\ 10^{-8}$	$9,26\ 10^{-11}$	11,98	37,22
1155	$1,62\ 10^{-8}$	$7,27\ 10^{-11}$	11,67	38,31
1095	$7,77\ 10^{-9}$	$3,72\ 10^{-11}$	10,92	41,40
1045	$3,94\ 10^{-9}$	$1,98\ 10^{-11}$	10,30	43,97
978	$1,42\ 10^{-9}$	$7,74\ 10^{-12}$	9,52	48,3

port. The first column gives D for the anodic and cathodic part of the specimen, the second corresponding temperatures calculated from eqn. (10). In fig. 5 v/j is plotted logarithmically against 1/T. The error in v/j is mainly due to the uncertainties in the localization of the reference system, i.e. the points $x'_{a,k}$ and $x_{a,k}$. Due to the scattering of the data in fig. 3 the position $x'_{a,k}$ can only be fixed within $\pm$ 5 µm. The straight line, presented in fig. 5, was caculated from least squares and yields

$$\frac{v}{j} = (1{,}72 \pm 0{,}30) \cdot 10^{-5} \exp\left(-\frac{1{,}228 \pm 0{,}002\ eV}{kT}\right) \left(\frac{cm^3}{Asec}\right) \qquad (11)$$

The mean deviation of a single measurement is $\pm$ 6%. From eqns. (10) and (11) it can be seen that the pseudoactivation energy Q' of electrotransport is only 0,11eV less than for pure diffusion of antimony in gold.

In order to caculate z_{eff} from eqn.(2) $\varrho(T)$ has to be known. Therefore it was necessary to measure the residual resistivity of antimony in gold, which was not published previously. Starting with four different dilute antimony-gold alloys thin wires were drawn. The specific electrical resistivities of these alloys and of pure gold have been measured upto about 1000°C. These experiments, together with the measurements of D and v, are discussed in detail by Herzig [21]. The obtained value $\Delta\varrho_{Sb}$ = 6,66u cm/At% best correlates with observations of Linde [14] for cadmium, indium, and tin in gold. Friedel [22] and Blatt [23] have tried to calculate the scattering cross sections of impurities for electrons quantitatively on a theoretical basis. The theory of Blatt seems to give the best agreement with experimentel data of Linde, since it takes into account not only a valence effect but also an influence of a deformation of the lattice by the impurity. According to this theory antimony is expected to have an excess valence of z = + 3,71 in the gold matrix instead of + 4, as obtained without considering the increase in volume of the elementary cell. For this excess valence the residual resistivity of antimony in gold is caculated in analogy to that of antimony in silver to be 6,73 µΩcm/At% in best agreement with the experimental result.

Since $\varrho(T) = \varrho_{Au}(T) + \Delta\varrho_{Sb} c$ is a function of c and varies along the penetration curve, there can be a remarkable electric field gradient in the sample for large values of c. It has, however, been shown [21] that for initial concentrations c_o of less than 1 At%

antimony this dependence is almost negligible within experimental error. Therefore eqn. (10) is applicable. At $c \approx \frac{c_0}{2}$ $\Delta\rho_d c$ has a value of 0,85 $\mu\Omega$cm for c_o = 0,255At%. The correlation factor f is the only unknown quantity in eqn. (2). For this reason not z_{eff} bus only z_{eff}/f can be calculated. These values are listed for various temperatures in table 2, D and v/j are taken from eqns. (11) and (12) respectively. The transport is directed toward the anode. Therefore z_{eff} is negative in sign.

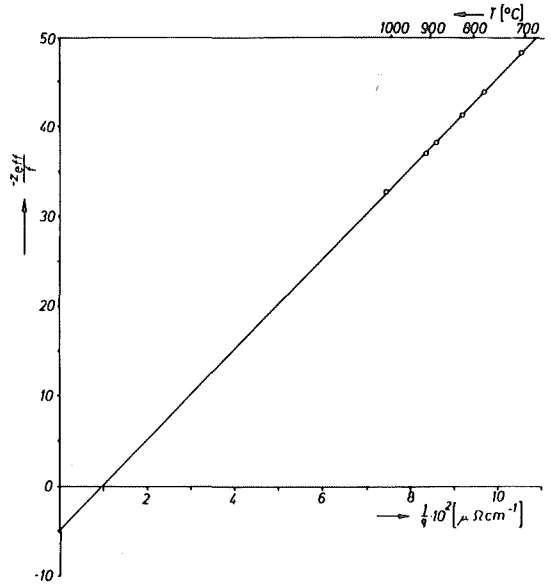

Fig. 6
z_{eff}/f versus $\frac{1}{\rho(T)}$

In fig. 6 the calculated z_{eff}/f has been plotted against $1/\rho(T)$. The data fit a linear dependence against $1/\rho$ in accordance with the theoretical expectation. The straight line is given by

$$\frac{z_{eff}}{f} = 5{,}0 - \frac{506}{\rho(T)} \qquad (12)$$

Since $\Delta\rho_d$ is assumed to be constant, the linear relation can only be understood in terms of the theoretical models, if f is also constant or only very weakly dependent on temperature. This result is corroborated by the measurements of Rottmann and Peterson [24]. For a quantitative comparison of eqn. (12) with eqns. (3) to (5) they must be divided by f. The residual resistivity $\Delta\rho_d$ due to activated complexes usually is given for 1 At% of such defects. The valence of the gold matrix is assumed here to be z = 1. The results are tabulated in table 3.

Comparison between experiment and theory

Table 3

	$\Delta\rho_d/f$ (uΩcm)	assumption: f = 0,65 $\Delta\rho_d$ (uΩcm)	charge number	assumption: $\Delta\rho_d = \Delta\rho_{Sb} = 6,66$ (uΩcm) f
eqn.(3)	10,12	6,58	z' = 3,25	0,66 → z' = 3,3
eqn.(4)	5,06	3,29	z' = 3,25	1,32 → z' = 6,6
eqn.(5)	10,12	6,58	z = 6,5	0,66 → z = 6,6

From the slope of eqn. (12) values of $\Delta\rho_d/f$ for the different models are calculated (second column). The correlation factor has been determined for the diffusion of antimony in silver. For this Lidiard [25] gives a value of f = 0,64. In a recent study of Howard and Manning [26] correlation factors of several impurities in silver are computed. For every impurity a range of values is given consistent with the experimental facts. The smallest possible value for antimony in silver is f = 0,51. For the diffusion of antimony in gold it seems quite reasonable to choose this factor in the vicinity of o,65. With this assumption it is possible to calculate $\Delta\rho_d$ itself (column 3) and from the intersept of the ordinate the screened charge (column 4). It has already been mentioned that $\Delta\rho_d$ ist comparable with $\Delta\rho_{Sb}$ at least to a first approximation. It is assumed that the neighboring vacancy, in the case of a vacancy controlled jump process, does not influence the scattering of the electrons too much for a complex in the activated state. Whereas the theories mentioned above take into account only the scattering of the impurities at the activated state, $\Delta\rho_i$ is determined for a substitutional or interstitial impurity in a non-activated state. Assuming both are approximately equal, i.e. $\Delta\rho_d \approx \Delta\rho_{Sb} = 6,66$ u cm/At%, it is possible to calculate f from the values in column 2 (column 5) and with these new data again z'. This assumption might be checked by the measurement of f. The measurements are planned. From table 3 the conclusion can be drawn that particularly the model given by Huntington is consistent with the experimental data. The screened charge of the activated complex is then 3,3 e. Therefore the charge in the activated state does not seem to be significantly different from that of the impurity on normal lattice positions.

A few data concerning the electrotransport of antimony in gold have been reported by Gilder and Lazarus [10]. Experiments carried out of two temperatures yielded $z_{eff} = -140$ e and $\Delta\varrho_d = 18 \mu\Omega cm/At\%$ calculated from eqn.(4). These data seem to be in error when compared with the results of the present work, since D has not been measured previously and the correlation factor has not been taken into account.

LITERATURE

1) W.Seith, H.Wever: Naturw. 19 447 (1954)
2) H.B.Huntington,A.R.Grone: J.Phys.Chem.Sol. 20 76 (1961)
3) V.B.Fiks: Sov.Phys.Sol.State 1 14 (1959)
4) C.Bosvieux,J.Friedel: J.Phys.Chem.Sol. 23 123 (1963)
5) J.Verhoeven: Met.Rev. 8 311 (1963)
6) Y.Adda,J.Philibert: La diffusion dans les solides,Paris (1966)
7) J.Bardeen,C.Herring: Am.Soc.Met.Cleveland 87 (1951)
8) H.Wever: Acta Met. 15 443 (1967)
9) H.J.Stepper,H.Wever: J.Phys.Chem.Sol. 28 1103 (1966)
10) H.M.Gilder,D.Lazarus: Phys.Rev. 145 507 (1966)
11) P.P.Kuzmenko: Ukr.Fiz.Zh. 7 117 (1962)
12) Chr.Herzig: Diplomarbeit, Münster (1965)
13) Th.Hehenkamp: Acta Met. 14 887 (1966)
14) J.O.Linde: Ann.d.Physik 15 219 (1932)
15) C.T.Tomizuka, L.Slifkin: Phys.Rev. 96 610 (1954)
16) Th.Hehenkamp: Habilitationsschrift, Münster (1966)
17) Th.Hehenkamp: Z.Metallk. 58 545 (1967)
18) R.V.Penney: J.Phys.Chem.Sol. 25 335 (1965)
19) A.Lodding: J.Phys.Chem.Sol. 26 143 (1965)
20) A.R.Grone: J.Phys.Chem.Sol. 20 88 (1961)
21) Chr.Herzig: Dissertation, Münster (1968)
22) J.Friedel: Advances in Phys. 3 446, London (1954)
23) F.J.Blatt: Phys.Rev. 103 285 (1957)
24) S.J.Rottmann,N.L.Peterson: Phys.Rev. 154 552 (1967)
25) A.B.Lidiard: Phil.Mag. 5 1171 (1960)
26) R.E.Howard,J.R.Manning: Phys.Rev. 154 561 (1967)

Sustained Vacancy Supersaturation in Metals and Alloys

D.A. Blackburn and J. Bleay

Department of Physics, University of York, England

Abstract:

The constituents of an alloy subject to a temperature gradient do not move randomly but drift parallel to the gradient. It is shown that this flow may cause perturbations of the vacancy concentration of magnitude comparable with those produced in the Kirkendall effect, and that this effect may greatly be increased when an electric current flows parallel to the temperature gradient. Equations of vacancy flow, based on the assumption of equilibrium, are shown to be in error at lower temperatures in the diffusion range.

Introduction:

When a current of heat or of electricity flows through a metal the carriers of heat or of electric charge are scattered by the point defects present in the material. When such a flow takes place in a hot material, the scattering interaction can be strong enough to influence the diffusion motion of the defects so that a small bias, parallel to the direction of flow, is superposed on their normal random motion. Under realisable laboratory conditions of temperature gradient or current density (10^3 °C/cm and 10^5 amps/cm^2) the rate of drift (1,2) is normally some tens of microns/day, and corresponds to a bias of several parts in 10^7 towards one atomic jump direction over another.

In such conditions of atomic flow, a material is clearly not in equilibrium and the vacancy concentration in particular, may be expected to vary from its equilibrium value. While major concentration changes from this cause seem unlikely, the importance of such effects

in the closely allied problem of Kirkendall diffusion (3) and the common use of equations of atomic flow based on the equilibrium assumption (4,5) suggest that the problem may be of some importance. We have therefore sought here to evaluate the effect of atomic flow upon vacancy concentration in some situations of experimental interest.

Vacancy concentration in a system subject to flow conditions:

Sustained variations from the equilibrium vacancy concentration are possible in any region of a metal where the atomic flow pattern introduces or removes vacancies; that is, in any region where the flow rate changes with position. If the magnitude of these concentrations changes is small, it will be determined primarily by the defect structure of the material, a vacancy excess raising the absorption rate for vacancies on dislocations, grain-boundaries etc., above the production rate, a deficit reducing it below this level. Thus highly faulted material should experience only minor changes of vacancy concentration, while effects in nearly defect free material will be relatively large.

For subsaturations, then, or for supersaturations too small to cause vacancy condensation into dislocation loops or porosities, the vacancy concentration will be calculable from a knowledge of the atomic flow rates and of the number and distribution of the vacancy generating sites.

As a model for calculation, we suppose that there exist, randomly distributed through the material, a number of fixed sites at which vacancies may be created or absorbed. A vacancy is thus created by thermal activation at one such site and then diffuses through the material making an average of p jumps before its arrival at another site where it is absorbed.

Over small variations of vacancy concentration, we may suppose that the rate of vacancy creation will remain constant and equal to the equilibrium absorption rate appropriate to the temperature. The net vacancy loss rate per unit volume, when the actual atomic fraction

of vacancies is C_v and the equilibrium fraction is C_{ve}, is then:

$$\frac{N\,(C_v - C_{ve})\,\Gamma_v}{p} = \frac{N\,q\,\Gamma_v}{p}$$

where Γ_v is the vacancy jump rate and N the number of atoms per unit volume. q denotes the supersaturation.

In a binary alloy with constituents A and B and diffusion by a vacancy mechanism, the rate of vacancy flow is:

$$F_v = -(F_A + F_B)$$

The rate of arrival of vacancies per unit volume within some closed region is thus:

$$-\operatorname{div} F_v = \operatorname{div}(F_A + F_B)$$

If we assumea nearly steady state, or equivalently that $\frac{C_{ve}\Gamma_v}{p} \gg |\operatorname{div} F_v|$, the conservation equation gives:

$$q = \frac{p}{N\Gamma_v} \operatorname{div}(F_A + F_B)$$

so the supersaturation may be computed for any situation for which the atomic flow rates are known.

Specific cases of vacancy supersaturation:

When an alloy is heated under conditions which cause atomic flow, some separation of its components will, in general, occur. Even under extreme experimental conditions however, this separation will be slow when compared with the lifetime of a vacancy so that, although atomic flow is taking place, the alloy will effectively retain its initial composition for some time and a nearly constant vacancy distribution will be maintained.

We shall obtain expressions for the vacancy concentration in a homogeneous alloy during this initial state of separation in the case of a) diffusion in a temperature gradient, and b) diffusion in a temperature gradient with an electric field superposed.

a) A homogeneous alloy subject to a temperature gradient:

Assuming that any deviations from equilibrium have only small effects on the flow rates, the rate of flow of component A is given by (56):

$$F_A = - N D_A \left[\text{grad}\, C_A + \frac{C_A E_A^T}{k T^2} \text{grad}\, T \right]$$

where D_A is the diffusion coefficient and E_A^T an energy of transport defining the bias experienced by the A atoms while diffusing in a temperature gradient. A similar expression holds for the flow of the other component.

Since the variation with temperature of D_A may be assumed known in terms of the diffusion energy E_A^D and grad T is given, the evaluation of div F_A hangs only upon the evaluation of C_A and grad C_A. For the purposes of this calculation however, the chemical composition of the alloy has been taken as constant: thus, $C_B/C_A = K$ = constant, and C_A is determined by the vacancy concentration:

$$C_A = \left(\frac{1 - C_V}{1 + K} \right)$$

The gradient of C_A follows immediately from that of C_V.

For a system subject to a temperature gradient parallel to the x-axis, we find, on performing the implied differentiations:

$$\frac{\partial F_A}{\partial x} = \frac{-N D_A (\text{grad}\, T)^2}{(1+K) k^2 T^4} \left[E_A^T (E_A^D - 2kT) - C_V (E_V^F + E_A^T)(E_V^F + E_A^D - 2kT) \right]$$

with comparable expression for $\frac{\partial F_B}{\partial x}$. Combination of these equations gives:

$$\text{div}\, F_V = \frac{N (\text{grad}\, T)^2}{k^2 T^4} [X]$$

and,

$$q = \frac{-P (\text{grad}\, T)^2}{\sqrt{\ } k^2 T^4} [X]$$

where:

$$[X] = \frac{D_A}{1+K}\left[E_A^T(E_A^D - 2kT) - C_V(E_V^F + E_A^T)(E_V^F + E_A^D - 2kT)\right.$$
$$\left. - \frac{D_B}{1+1/K}\left[E_B^T(E_B^D - 2kT) - C_V(E_V^F + E_B^T)(E_V^F + E_B^D - 2kT)\right]\right.$$
$$\approx \left[D_A C_A E_A^T E_A^D + D_B C_B E_B^T E_B^D\right]$$

since C_A, C_B >> C_V and E_A^E, E_B^D >> kT.

Figures (1) and (2) show the supersaturation and the divergence of the vacancy flow which

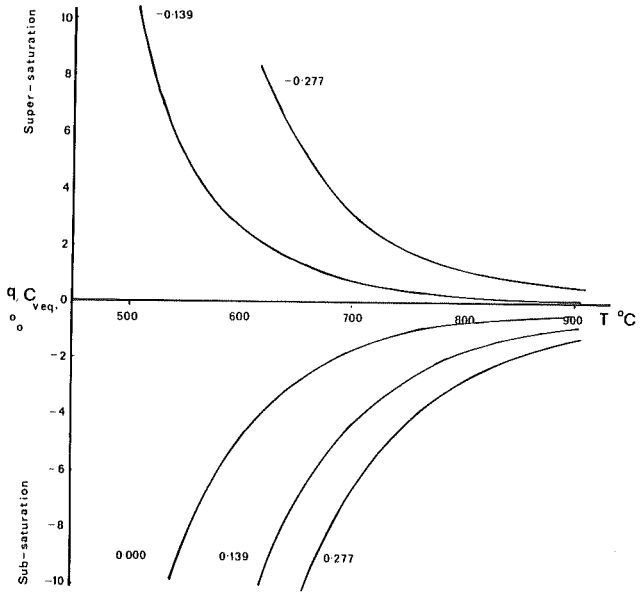

Figure (1). Vacancy supersaturations, computed for a temperature gradient of 1000°C/cm., in the case of a fixed transport energy E_B^T = 0.1 ev for the slower diffusing component with values for the faster component in the range $|E_A^T| < 0.28$ ev.

might occur in a hypothetical case approximating to that of diffusion in a 50% brass alloy subject to a temperature gradient of 1000°C/cm. The diffusion data used are those of Kuper et.al. (7), the values for the other parameters being taken arbitrarily as $E_V^M = 0.4\ E_{Zinc}^D$, $E_V^F = 0.6\ E_{Zinc}^D$, together with a vacancy diffusion frequency factor of 10^{12} sec^{-1} and a mean free path of 10^9 jumps. A fixed value of + 0.10 E_{Zinc}^D has been taken for the transport energy of the copper, while that for zinc covers the range $|E_{Zinc}^T| < 0.3\ E_{Zinc}^D$ which corresponds roughly to the range of known transport data (4).

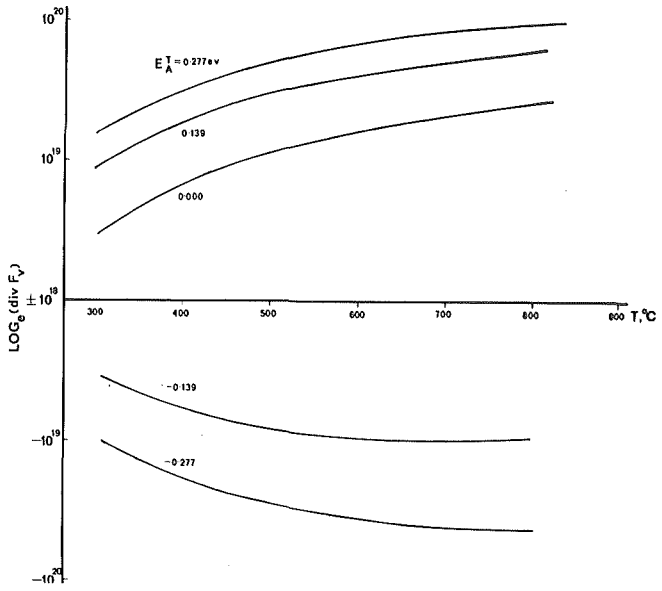

Figure (2). The data of Figure (1) expressed in terms of the divergence of the vacancy flow.

It will be seen that quite large supersaturations and subsaturations are possible even at high diffusion temperatures. So large are the effects that in materials subject to a large bias, or diffusing at low temperatures, the mathematical approximations of the present treatment will be inadequate and even the vacancy flow equation will require modification.

b) A homogeneous alloy supporting an electric current, while subject to a temperature gradient:

Biased atomic motion under the action of an electric field has been demonstrated in a number of materials, the flow rates accessible to experiment tending to be larger than those achieved in temperature gradients. While the high rate of flow allows the possibility of producing relatively large non-equilibrium effects, the difficulties of producing a flow divergence by variation of the electric field alone suggest that the situation may best be exploited by the superposition of a temperature gradient.

For this case, with the electric field, E, parallel to the temperature gradient, the flow equation is (8):

$$F_A = -N D_A \left[\text{grad}\, C_A + \frac{C_A E_A^T \text{grad}\, T}{kT^2} - \frac{Z_A e E\, C_A}{kT} \right]$$

where $Z_A e$ is the effective electronic charge of an atom of component A while diffusing. For flow parallel to the x-axis, the gradient is:

$$\frac{\partial F_A}{\partial x} = \frac{-N C_A D_A E_A^D \, grad\, T}{k^2 T^4} \left[E_A^T \, grad\, T - Z_A e E T \right]$$

where the first term is that derived previously for a temperature gradient alone and the second deals with the additional effect of the electric field. Completion of the differentation leads to:

$$\frac{\partial F_A}{\partial x} = \left[\frac{\partial F_A}{\partial x} \right]_{\nabla T} + Z_A e E N \, grad\, T \, \frac{C_A D_A}{k^2 T^3} \left[E_A^D - kT - \frac{C_V E_V^F}{C_A (1+K)} \right]$$

or, neglecting kT and the term in C_V/C_A;

$$\frac{\partial F_A}{\partial x} = - \frac{N C_A D_A E_A^D \, grad\, T}{k^2 T^4} \left[E_A^T \, grad\, T - Z_A e E T \right]$$

Thus:

$$div\, F_V = \frac{N \, grad\, T}{k^2 T^4} \left[\Upsilon \right]$$

and,

$$q = \frac{-p \, grad\, T}{\sqrt{v}\, k^2 T^4} \left[\Upsilon \right]$$

where,

$$\left[\Upsilon \right] = \left[C_A D_A E_A^D \left(E_A^T \, grad\, T - Z_A e E T \right) + C_B D_B E_B^D \left(E_B^T \, grad\, T - Z_B e E T \right) \right]$$

The known values of Z_A, Z_B tend to be in the range $|Z| < 20$ (4), and experiments are commonly performed with E ~ 0.2 volts/cm. Figure (3) shows the divergence of the vacancy flux calculated for the brass-like material of the previous section with E_A^T = -0.139 ev, Z_A = 1, Z_B = -5, and E = $\pm 10^{-2}$ volts/cm. The electrical terms have been chosen relatively small to show the inter-relation of the thermal and electrical components of the divergence.

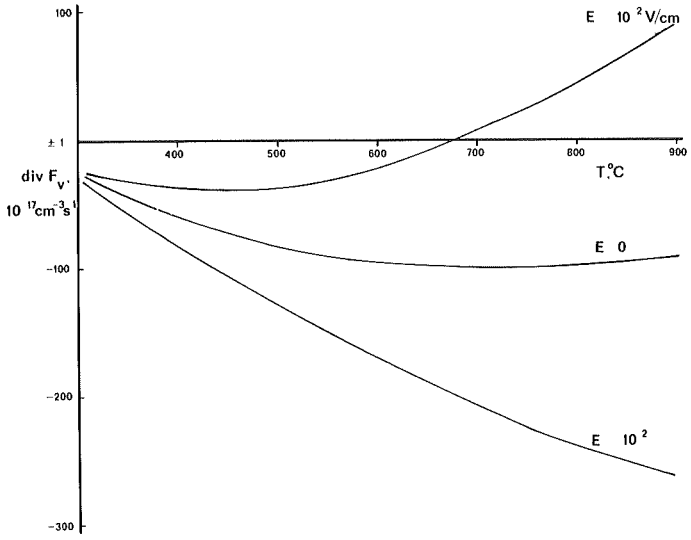

Figure (3). Modifications in the divergence of the vacancy flow produced by superposing an electric field of $\pm 10^{-2}$ volts/cm, upon a temperature gradient of 1000°C/cm. Computed for the case of $Z_A = 1$, $Z_B = -5$, $E_A^T = -0.139$ev, $E_B^T = 0.1$ ev.

Discussion

Atomic flow during diffusion in a temperature gradient or an electric field is a slow process, and is experimentally difficult to detect. The present calculations show, rather surprisingly, that it may yet cause appreciable disturbances of vacancy concentration in suitable materials.

The magnitudes of the supersaturations derived in the previous sections depend directly upon values assumed for vacancy mean free paths and lifetimes and must, for an alloy, be in some doubt. However, the predicted variations of vacancy concentration in the lower range of diffusion temperatures are so large that flow rates estimated on the assumption of equilibrium must be appreciably in error for any reasonable estimate for the mean free path. At high temperatures the equilibrium assumption should generally give a reasonable estimate of flow rates.

The importance of non-equilibrium effects lies less in their modification of the flow equations than in the possibility that conditions of supersaturation may lead to the formation of porosities in bulk material. This is a matter which could be of some industrial

importance, for example in hollow aircraft turbine blades which are subject both to high temperatures and to large temperature gradients.

To assess the probability of porosity formation, there is no need to introduce estimates of vacancy mean free path or lifetime since direct comparision, in terms of divergence, may be made with experiments on diffusion in concentration gradients. It has been shown in a number of experiments on the Kirkendall effect, where the divergence of the vacancy flow was measured directly from the movement of markers, that the centre of the porous zone is characterised by a divergence of the vacancy flow in the range $-(2\text{-}6)10^{-6}N \approx -2\ 10^{17}$ $cm^{-3}\ sec^{-1}$. In another analysis, the onset of porosity formation has been shown to occur at a divergence of about $-\ 10^{16}\ cm^{-3}\ sec^{-1}$ (3).

The present calculations which, give divergences of $\pm\ 10^{19}\ cm^{-3}\ sec^{-1}$, clearly suggest that many alloys are likely to show porosity formation in extreme temperature gradients and that almost all should show such effects when the gradient is combined with an electric field.

References:

(1) C.J. Meechan and G.W. Lehman, J.Appl. Phys., 33, 634 (1962).

(2) H.M. Gilder and D. Lazarus, Phys. Rev., 145, 507 (1966).

(3) R.W. Balluffi, Acta. Met., 2, 194 (1954).

(4) Y. Adda and J. Philibert, La Diffusion Dans les Solides, Presses Universitaires de France 1966 (pp 608, 835, 893).

(5) R.E. Howard and A.B. Lidiard, Rep. Progr. Phys., 27, 161 (1964)

(6) P.G. Shewman, Diffusion in Solids, McGraw-Hill, New York (1963).

(7) A.B. Kuper, D. Lazarus, J.R. Manning and C.T. Tomizuka, Phys. Rev., 104, 1536 (1956).

(8) H.B. Huntington and A.R. Grone, J.Phys. Chem. Solids, 20, 76 (1961).

DIFFUSION OF COBALT AND OF GOLD IN DHCP AND IN BCC PRASEODYMIUM

M.P. DARIEL, G. EREZ
Nuclear Research Centre - Negev, Israel

G.M.J. SCHMIDT
Weizmann Inst. of Science, Rehovoth

A B S T R A C T

The thin-layer sectioning technique has been used to measure the diffusion of cobalt and of gold in dhcp and bcc praseodymium. The diffusivities can be expressed as D_{Au}/dhcp Pr = 4.3×10^{-2} exp [-0.85 eV/kT] cm^2/sec;
D_{Au}/bcc Pr = 3.3×10^{-2} exp [-0.87 eV/kT] cm^2/sec;
D_{Co}/dhcp Pr = 4.7×10^{-2} exp [-0.79 eV/kT] cm^2/sec.

The results are several orders of magnitude higher than the self-diffusion coefficients of praseodymium. They are interpreted as being due to a diffusion mechanism in which solutes in interstitial positions play the predominant role.

INTRODUCTION

A large body of experimental data exists on solute diffusion in a variety of metallic solvents. A theoretical interpretation of some of these results (in noble metal matrices), has allowed insight into the interaction between point defects and solute atoms[1]. Experimental results are very scarce concerning diffusion in rare-earth metal based systems. With the increasing availability of relatively pure metals of this family, we chose to verify whether their diffusion behavior conformed to that of the more familiar and extensively investigated metals. Praseodymium was the first metal studied, mainly because of the relatively extended range of its high temperature bcc structure (795° - 940°C). The present paper reports results concerning the diffusion of cobalt and of gold in both the dhcp and the bcc phase of praseodymium.

EXPERIMENTAL

Praseodymium metal lumps, supplied by Messrs. Johnson-Matthey, were cast into high-purity magnesia crucibles in an induction furnace under purified argon atmosphere. The metallic impurity content was determined by spectros-

copical examination (Table I); 100 p.p.m. oxygen were detected by vacuum fusion analysis in a platinum bath. The density of the cast, 10 mm diameter rods, was measured by the liquid displacement method in monobromo - benzene; the values obtained were close to the theoretical X-ray density values. The rods were heat treated in evacuated silica capsules and then machined into 8 mm high samples. One of their surfaces was carefully polished and etched; the average diameter of the grains was above 1 mm.

Small amounts (20-30 mg) of 99.99% pure gold and cobalt were neutron irradiated in the reactor at the Nuclear Research Centre-Negev. Gold was evaporated in a standard vacuum evaporator from a tantalum resistance filament. Cobalt was evaporated from a tantalum cup heated by high-frequency induction. The sample holder which was placed above the tracer isotope source during the evaporation procedure, was designed to mask the rim of the coated surfaces of the samples and thereby to reduce surface diffusion effects.

Table I. Results of Spectrographic Analysis

Element	Concentration (ppm)	Element	Concentration (ppm)
Fe	200	Ta	<10
Mg	400	La	<10
Ni	<10	Gd	<25
Al	50	Ho	<50
Cu	50	Er	<25
Yb	<10	Dy	<50
Sm	<25	Eu	<25

After the samples had been coated, they were wrapped in tantalum foils and sealed in evacuated (2×10^{-5} mmg, Hg) quartz capsules. A horizontal furnace was used for the diffusion anneal; the temperature was controlled to within $\pm 1^{\circ}C$. During the diffusion anneal the sample containing quartz capsules were placed in a massive nickel block. The tip of a Pt/Pt-13 Rh thermocouple was inserted into a small hole drilled in this nickel block, at the same distance along the furnace axis as the sample. The temperature was continuously recorded and checked with a high precision manual potentiometer.

Since the diffusion anneals were very short (10-15 minutes in some instances) considerable error could be introduced by the heating-up time, even though the samples were inserted into a pre-heated nickel block. An additional

small heating element was therefore placed in the bore of the nickel block. Power in this heating element was turned on simultaneously with the insertion of the sample for about 60 seconds. The heating-up time was thus drastically reduced; it was also directly measured by carrying out an experiment similar to the one described by Peterson and Rothman[2].

No deformation whatsover of the samples was observed even after diffusion anneals in the high temperature bcc phase. A precision watch-maker lathe was used for sectioning the specimen. The alignment of the coated surface, normal to the axis of rotation was carefully checked, misalignment of this surface from the sectioned planes was estimated to be less than 0.1^{o}. After reducing the diameter of the samples by about 1 mm, 12 to 20 sections were taken from each sample. Although praseodymium is a soft metal burring was effectively eliminated by the use of suitably shaped cutting tools. The chips were collected in a vacuum suction device on a 325 mesh nylon sieve. This procedure allowed the recovery of 98 to 99.5% of the material removed. The weight of the chips was determined to within 0.1 mg with a Mettler balance. No weight increase of the chips due to oxidation was observed for about two hours following the sectioning. The thickness of each section was calculated from the weight of the chips, the final diameter of the sample,and its measured density.

The chips were transferred into glass vials and dissolved in equal parts of dilute nitric acid. The activity was measured in a well-type NaI (Tl) crystal, the bore of which closely fitted the glass vials. A standard Philips counting system with a single channel analyzer was used. Each section was counted twice and at least 10 000 counts were taken. The usual corrections for dead-time of the counting system, background and radioactive decay (in the case of Au^{198}) were applied.

RESULTS

A slightly modified version of a computer program described by Winslow[3] was used to treat the results. The concentration of cobalt, following diffusion in both phases of praseodymium, and the concentration of gold after diffusion in the bcc phase obeyed a Gaussian distribution (Figs. 1,2). The activity of gold was reduced in the first section of samples diffused in the bcc phase, owing to evaporation during the diffusion anneal in evacuated capsules. The diffusion coefficients were determined from the slopes of these plots.

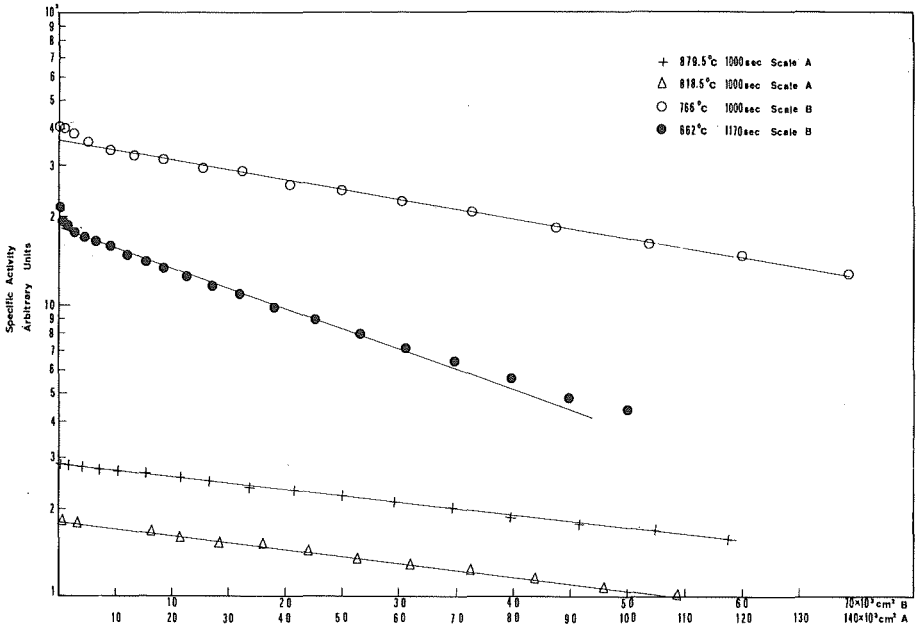

Figure 1: Penetration Curves for the Diffusivities of Cobalt in DHCP Praseodymium

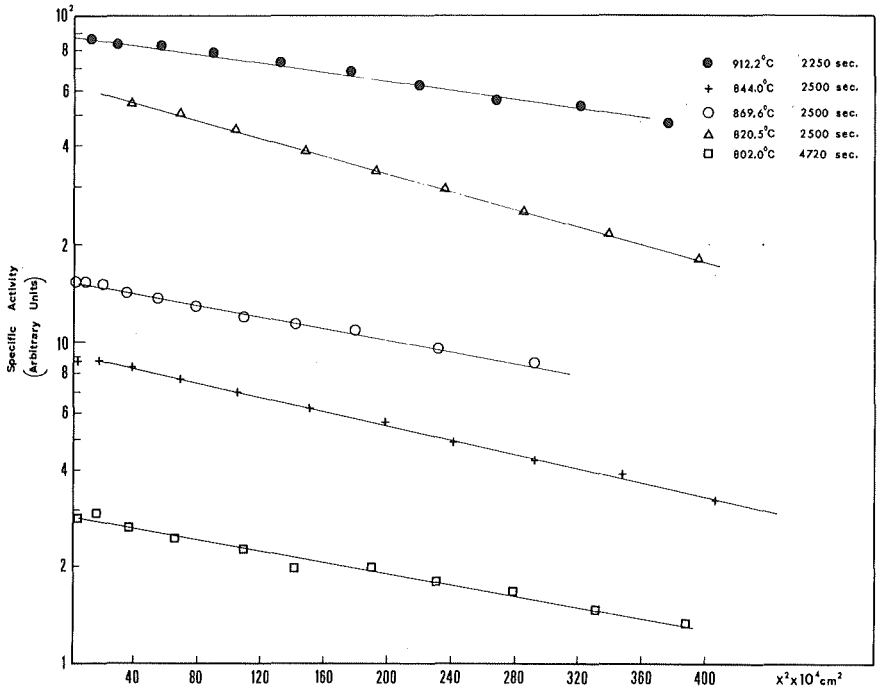

Figure 2: Penetration Curves for the Diffusion of Gold in BCC Praseodymium

An initial steep decrease of activity of gold in samples which were diffusion annealed in the dhcp phase, was followed by closely obeyed Gaussian behavior. These properties of the penetration plots were more pronounced the lower the diffusion anneal temperature. Similar observations have been made by Dyson[4] who attributed them to the transfer of the tracer isotope through the oxide barrier at the surface, and by Kidson[5] who assigned it to the low solubility limit of the solutes in the matrix. In the present case the diffusion coefficients were calculated from the straight portions of the log (activity) vs. squared (penetration) plots.

The Arrhenius plots of the diffusivities thus calculated are shown in Figure 3. The activation energies and the pre-exponential factors, including data for the self-diffusion of praseodymium are summarized in Table II. No values could be obtained for the diffusion of cobalt in the high-temperature bcc phase of praseodymium as a result of the very high values of the diffusivities and the limited length of the samples.

TABLE II. Diffusivities of Gold Cobalt and Praseodymium in Praseodymium

Solvent matrix	Diffusing solute	D_o (cm^2/sec)	Q eV/atom
DHCP α - praseodymium	Au	$\left(4.3\pm^{1.6}_{1.1}\right) \times 10^{-2}$	0.85±0.03
BCC β - praseodymium	Au	$\left(3.3\pm^{1.1}_{0.8}\right) \times 10^{-2}$	0.87±0.03
DHCP α - praseodymium	Co	$\left(4.7\pm^{2.3}_{1.6}\right) \times 10^{-2}$	0.79±0.03
BCC β - praseodymium	Pr	$1.23\pm0.9 \times 10^{-1}$	1.31±0.08

The values obtained for the diffusion of gold in dhcp praseodymium, are less accurate than tne over values, although they obey the Arrhenius law, because they were deduced from only partially Gaussian penetration plots. Dyson et Al.[4] report that diffusion coefficients, calculated from similar plots in the same way, were lower than those deduced from experiments in which the initial steep decrease was absent. It thus appears that the "true" diffusivities of gold in dhcp praseodymium are higher than those calculated here.

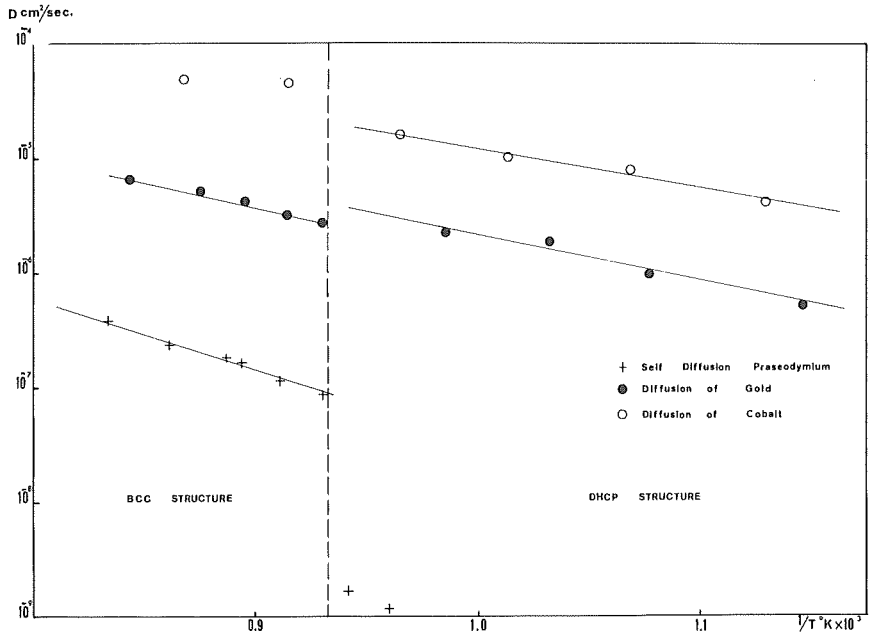

Fig. 3

Temperature Dependence of the Diffusivities of Cobalt, Gold and Praseodymium in Praseodymium

DISCUSSION

A meaningful discussion of the diffusion of gold and of cobalt in praseodymium must be based on a comparison of the results with the previously obtained values of the self-diffusion of praseodymium[6].

The diffusivities of gold and of cobalt are characterized by several features :

a. Appreciably lower activation energies than the corresponding value for self-diffusion in bcc praseodymium.

b. Pre-exponential factors, although of rather low value, remain well within the range associated with positive entropies of activation.

c. Diffusivities of gold and of cobalt are much higher than the corresponding self-diffusion coefficients. This effect is especially noticeable in the low-temperature dhcp phase where the diffusivity of cobalt is 4 orders of magnitude higher than the self-diffusion coefficient.

d. The diffusivity of gold is slightly decreased by the phase transformation from the dhcp to the bcc structure while the diffusivity of cobalt is increased.

In order to account for the present results we have examined several possibilities: 1- vacancy mechanism; 2- dislocation enhanced diffusion; 3- combined substitutional-interstitial mechanism.

VACANCY MECHANISM

Previous investigations of cerium-lanthanum diffusion couple[7] have shown the presence of a Kirkendall shift and pore formation on the cerium side of the couples. These observations as well as the results concerning self-diffusion[6] and rare-earth metal solutes diffusion in praseodymium, were interpreted as indicative of a vacancy controlled diffusion mechanism.

The much higher diffusivities of gold and of cobalt, as compared with the self-diffusion coefficients of praseodymium in the bcc phase, are not inconsistent with a vacancy mechanism. Similar high diffusivities of transition metal solutes in gamma-uranium have been observed by Peterson and Rothman[2].

The present case, however, shows an additional feature, namely the small effect of the phase transformation from the dhcp to the bcc structure on the diffusivities of gold and of cobalt, as compared to the two orders of magnitude increase of the self-diffusion coefficients. One can argue that if gold and cobalt diffused by a mechanism similar to that of self-diffusion, the diffusivities of these solutes would be similarly affected by the change in the crystalline structure of the matrix.

The electrostatic interaction theory developed by Lazarus[8] and by LeClaire[1] for the diffusion of impurities in noble metal solvents, predicts an increase of the activation energy for solutes with an effective negative charge. Monovalent gold solute atoms have a negative charge with respect to the three valent praseodymium solvent atoms thus qualitatively the present results are not in agreement with this theory. It is well understood that this theory cannot be applied in a straightforward way to the present system, since no information is available on a) the nature of the oscillatory potential of the solute atoms and b) the screening parameter which depends on the density

of states at the Fermi surface of praseodymium metal.

Although, no conclusive evidence is available as yet, the present results are difficult to reconcile with a vacancy mechanism. To check this point more thoroughly one should verify whether the self-diffusion of praseodymium is affected by the addition of the faster diffusing solutes, i.e. gold and cobalt. It is doubtful whether such an experiment can be carried out, since the solubility of gold and of cobalt in rare-earth metals is too low to permit the preparation of homogeneous solid solutions in which the solvent self-diffusion could be measured.

DISLOCATION ENHANCED DIFFUSION

Solute diffusion in aluminium[9] and in alpha-zirconium[10] has been treated in terms of dislocation-enhanced diffusion. The diffusivities of different solutes in these two metals are associated with activation energies which are considerably lower than those for self-diffusion and with unusually low pre-exponential factors of the order 10^{-6} - 10^{-9} cm^2/sec. Most of the solutes which have been examined have low solubilities in aluminium or zirconium. Similarly, the solubility of the transition metals, (gold and cobalt) in rare-earth metal solvents is limited.

Hart[11] has shown that, subject to certain conditions, dislocation enhanced diffusion can be expressed as

$$D_m = g\, D_d + (1 - g)\, D_\ell \qquad (1)$$

where D_m is the measured diffusivity, D_d and D_ℓ the diffusivities along dislocations and dislocation-free bulk metal, respectively. The factor g is the fraction of time spent by the diffusing atoms in the dislocation region.

For the diffusion of solutes which may segregate along dislocations

$$g = F\, K$$

where F is the site density in dislocations and K the segregation factor.

According to Kidson[5], eq.(1) can be written

$$D_m - D_\ell = g\, (D_d - D_\ell) \qquad (2)$$

and if one assumes

$$D_\ell << D_d \ , \ D_m \qquad (3)$$

$$D_m = g\, D_d = F\, K\, D_d$$

Taking the surface site density in praseodymium as 10^{15} cm^{-2}, ρ as the density of dislocations and A as the number of atoms in the cross section of the dislocation

$$D_m = \rho\, A\, K\, 10^{-15}\, D_d = \rho\, A\, K\, 10^{-15}\, D_d^o \exp\,(-Q_d/RT) \qquad (4)$$

where the diffusion along the dislocations is expressed in the usual form:

$$D_d = D_d^o \exp\,(-Q_d/RT)$$

Taking the ratio of eq.(4), written once for gold and once for cobalt, and assuming that the parameters D_d^o and Q_d for both solutes are equal in the first approximation one obtains :

$$\frac{D_m\text{-Co}}{D_{\blacksquare}\text{-Au}} = \frac{K_{Co}}{K_{Au}} \qquad (5)$$

The segregation factor can be expressed as : $K = \exp\,(-W/RT)$ where W is the interaction energy between dislocations and solute atoms.

This energy has been calculated theoretically by Friedel[12] on the basis of an elastic model: $W = W_1 + W_2 + W_3$, where W_1 and W_2 are due to the differences in size and elastic constants of solute and solvent atoms respectively W_3 is an electrostatic term, usually much smaller than the proceding ones.

Using the formula given by Friedel[12], and neglecting the last term W_3, we have calculated the interaction energy $W = W_1 + W_2$ for gold and cobalt solutes in praseodymium; the relevant parameters were taken from Gschneidner[13].

The results are :

$$W_{Co} = -\ 10.3 \text{ Kcal/mol}$$

$$W_{Au} = -\ 7.0 \text{ Kcal/mol}$$

The left and right sides of eq.(5) can be written :

$$\frac{D_{m\text{-}Co}}{D_{m\text{-}Au}} = \frac{D^o_{m\text{-}Co}}{D^o_{m\text{-}Au}} \exp\left((Q_{Au} - Q_{Co})/RT\right) \tag{6a}$$

$$\frac{K_{Co}}{K_{Au}} = \exp\left((W_{Au} - W_{Co})/RT\right) \tag{6b}$$

According to the experimental results the ratio of the measured pre-exponential terms is :

$$\frac{D^o_{m\text{-}Co}}{D^o_{m\text{-}Au}} \tilde{=} 1$$

It follows from eq.(5) that

$$Q_{Co} - Q_{Au} = W_{Co} - W_{Au} \tag{7}$$

Agreement is very good as one can see by comparing the measured activation energies Q,(Table II) to the calculated values of W. In fact, the agreement is surprising in view of the large number of assumptions which had been made.

According to eq.(4)

$$D^o_m \tilde{=} 4\times10^{-2} = \rho.A.10^{-15}\, D^o_d \tag{8}$$

The usual range of pre-exponential terms, consistent with positive entropies of activation is :

$$10^{-2} < D^o < D^o < 10$$

Substituting these values in eq.(8) one gets

$$4\times10^{12} < \rho.A < 4\times10^{15}$$

A reasonable value for the number of atoms in the cross-section of a dislocation is $A \tilde{=} 10$. Thus the dislocation density should be

$$10^{12} < \rho < 10^{15}$$

This is an exceedingly high density of dislocations in an annealed metal, even though precipitated oxides pin down dislocations.

It thus appears that although segregation effects along dislocations are able to explain the difference in activation energies of gold and of cobalt this model also leads to an unacceptably high dislocation density. Further

limitations of the dislocation enhanced diffusion model have been pointed out by Ballufi[14] for solute diffusion in aluminium; these limitations are probably also valid in the present case.

Results of recent indium solute diffusion experiments in praseodymium constitute another objection to the dislocation-enhanced diffusion model in our system. Briefly, the reasoning runs as follows: the solubility of indium in praseodymium being limited, segregation effects along dislocations should be appreciable. Nevertheless, in contrast to the effects observed for the diffusion of gold and of cobalt, the diffusion of indium is similar to the self-diffusion of praseodymium, both with respect to the magnitude of the diffusivities and their increase by two orders of magnitude upon transformation from the dhcp to the bcc structure of praseodymium.

It is therefore concluded that dislocation enhanced diffusion is unlikely to be the determining mechanism in the case of gold and cobalt diffusing in praseodymium.

INTERSTITIAL DIFFUSION

The noble metals have been observed to diffuse at extremely high rates in lead[4,5,15] tin[16,17] indium and thallium[19]. In order to account for the high mobilities of Cu, Ag and Au in these metals, a combined substitutional-interstitial mechanism was proposed, which involves partial interstitial solubility of the diffusing solutes.

Solute diffusion in these systems is expressed assuming an equilibrium concentration of vacancies:

$$D_m = \frac{C_i}{C_i+C_s} D_i + \frac{C_s}{C_i+C_s} D_s \qquad (9)$$

where C_i and C_s are the concentrations of interstitial and substitutional solutes, respectively, Di, interstitial diffusivity and Ds diffusivity by vacancy mechanism.

Since $D_i \gg D_s$ eq.(9) can be written for an appreciable fraction of the solute in interstitial position

$$D_m = \frac{C_i}{C_i+C_s} D_i = X_i D_i$$

thus, the measured diffusivity is entirely due to interstitials.

Turnbull[20] has summarized the conditions which favor the formation of this new kind of interstitial solutions: 1) a favorable size factor that is, interstitial sites delineated by the ion cores of the solvent matrix, which are large enough to accommodate solute atoms; 2) isoelectronic ion cores of solvent and solute atoms.

In the dhcp and bcc structures the atomic radius of praseodymium is 1.83Å, and 1.84Å respectively. The ionic radius of Pr^{+3} as calculated by Zachariasen is only 1.00Å. In the low temperature dhcp phase, delicated by the ion cores of the matrix, an octahedral site has a radius of 1.58Å, while the symmetrical tetrahedral interstitial hole in the bcc structure has a radius of 1.3Å. The atomic radii of cobalt and of gold are 1.25Å and 1.4Å, respectively. It follows that, for the two metals in the two structure types with the exception of gold atoms in the interstitial sites of the bcc structure, the solutes can be accommodated as interstitials with little or no overlap of ion cores.

Size factor considerations may qualitatively explain the decrease diffusivity of gold by the phase transformation from dhcp to bcc praseodymium, whereas that of cobalt is increased (Fig.3).

It was shown (eq.(10)) that the measured diffusivity is a product of two factors, D_i the interstitial diffusivity and X_i the relative concentration of interstitial solutes. The neglect of the contribution of substitutional solutes seems justified in the present case in view of the large difference between self and solute diffusion coefficients. Probably, the phase transformation to the more open bcc structure increased D_i for both, gold and cobalt solutes. Similarly the diffusivity of interstitial carbon is higher in bcc - α F_e than in fcc-γ F_e. The relative concentration of interstitials, X_i, is affected by the phase transformation, differently for gold than for cobalt. Since overlap of ionic cores occurs only for gold in bcc praseodymium, X_i for gold will be decreased by the phase transformation. The decrease in X_i outweighs the increase in D_i and the net result is a decreased diffusivity of gold in bcc praseodymium.

The other criterium proposed by Turnbull[21] for interstitial solubility, namely isoelectronic ion cores of solute and solvent, is not fulfilled in the

present case. Previously studied metal such as Pb, In, Sn, and Tl, in which interstitial diffusion has been found, have a "d" character ion core. In contrast to this, praseodymium and other rare-earth metals have a "p" character ion core. In this connection it should be noted that interstitial-like diffusivity of gold was observed in sodium[22] which fulfills the size criterium but which obviously has no "d" character ion core.

Thus, if one is to accept the idea of interstitial solubility of noble and possibly other transition metals, the ionic size factor condition seems to be the determining one. It also follows that interstitial diffusion of these solutes will occur in most, if not all, rare-earth metals. Preliminary results indicate that gold diffuses at very high rates both in fcc and bcc lanthanum[23].

Additional evidence for interstitial solubility, and thence diffusion of cobalt in indium, has been found by Mossbauer effect experiments[24], it will be interesting to verify to what extent the interstitial solubility is shared by other transition metal solutes.

CONCLUSIONS

Three possible mechanisms have been examined in order to explain the results found in the present study. Among these, the model according to which diffusion by interstitial solutes determines the high diffusivities of Co and Au in praseodymium, seems the most plausible. This conclusion is based to a large extent on the analogy of the present findings with the results of diffusion of noble metals in lead, tin indium and thallium. If this conclusion is borne out by additional studies in rare-earth metal systems it is hoped that the conditions favoring interstitial solubility in metals will be further clarified.

REFERENCES

1. LE CLAIRE, A.D., Phil Mag. 7: 141 (1962).
2. PETERSON, N.L. and ROTHMAN S.J., U.S.A.E.C. Rep. ANL-6568 (1964).
3. WINSLOW, F.R., U.S.A.E.C. Rep. ORNL-TM 726 (1963).
4. DYSON, B.F., ANTHONY, I. and TURNBULL, D., J. Appl. Phys. 37: 2370 (1966).
5. KIDSON, G.V., Phil. Mag. 13: 122 (1966).
6. DARIEL, M.P. and EREZ, G., Israel A.E.C. Rep. NRCN-199 (1967).
7. DARIEL, M.P. and EREZ, G., to be published
8. LAZARUS, D., Phys. Rev. 93: 973 (1954).
9. HIRANO, K.I., AGARWALA, R.P. and COHEN, M., Acta Met. 10: 857 (1962).
10. NAIK, M.C. and AGARWALA, R.P., Acta Met. 15: 1521 (1967).
11. HART, E.W., Acta Met. 5: 597 (1957).
12. FRIEDEL, J., "Dislocations" p.360 Pergamon Press N.Y. (1964).
13. GSCHNEIDNER, K.A., Jr, Solid State Physics,Vol 16 Eds. F. Seitz and D. Turnbull N.Y. Academic Press (1964).
14. BALLUFFI, R.W. Acta Met. 11: 1109 (1963).
15. ASCOLI, A., J. Inst. Metals 89: 218 (1961).
16. DYSON, B.F., J. Appl. Phys. 39: 2375 (1966).
17. DYSON, B.F., ANTHONY, T.R. and TURNBULL, D., J. Appl. Phys. 38: 3408 (1967).
18. ANTHONY, T.R. and TURNBULL, D., Phys. Rev. 151 495 (1966).
19. ANTHONY, T.R., DYSON, B.F. and TURNBULL, D., J. Appl. Phys. 39: 1391 (1968).
20. TURNBULL, D., Proceedings of the Memorial Lecture Meeting National Research Institute for Metals Tokyo Japan (1966).
21. ANTHONY, T.R. and TURNBULL, D., Appl. Phys. Let. 9: 120 (1966).
22. BARR, L.W., MUNDY, J.N. and SAITH, F.A., Phil. Mag. 14: 1299 (1966).
23. DARIEL, M., Unpublished Results.
24. FLINN, P.A., GONSER, U., GRANT, R.W. and HOUSELY, R.M., Phys. Rev. 157: 538 (1967).

Diffusion of Molybdenum and Cerium in Beta-Zirconium

A.R. Paul, M.S. Anand, M.C.Naik and R.P.Agarwala
Bhabha Atomic Research Centre
Chemistry Division
Trombay, Bombay -74

Abstract

Diffusion of molybdenum and cerium in beta zirconium has been studied by residual activity technique in the temperature range of 880° - 1600°C. The results thus obtained show a non-linearity in the plots showing temperature dependence of diffusivities as observed in the self and impurity diffusion of niobium and vanadium in beta-zirconium and low values of D_0 and Q in the low temperature range.

On the basis of dual mechanisms operating, the diffusivities (D cm^2/sec) in the above cases could be expressed as a sum of two exponentials:

$$D_{Mo/\beta\text{-}Zr} = 1.99 \times 10^{-4} \exp\left(-\frac{1.53\ ev}{kT}\right) + 2.63 \exp\left(-\frac{2.97\ ev}{kT}\right)$$

$$D_{Ce/\beta\text{-}Zr} = 3.16 \times 10^{-2} \exp\left(-\frac{1.80\ ev}{kT}\right) + 42.17 \exp\left(-\frac{3.22\ ev}{kT}\right)$$

The non-linearity in the Arrhenius plots has been explained on the basis of i) extrinsic defects being introduced by the presence of residual impurities, ii) enhancement due to the randomly oriented dislocations and iii) vacancy-divacancy model.

INTRODUCTION

Due to the importance of the refractory metals and the effect of impurities on their physical properties, considerable interest has arisen in the last few years to study diffusion behavior in these metals. It has been observed that the frequency factor (D_o) and the activation energy (Q) for diffusion of some of these metals[1-9] in α-phase, like α-zirconium, etc., are pretty low though diffusion obeys the Arrhenius relation $D=D_o \exp(-\frac{Q}{RT})$. With the beta phases of Zr,[8,10] Ti[11,12] and γ-U,[13] a deviation from linearity behavior in plots of log D vs. $\frac{1}{T}$ has been observed over a wide range of temperatures. In addition to this anomalous behavior, the diffusion parameters (D_o and Q) in the low temperature range are also low.

Though a large amount of data is available on impurity diffusion in β-Ti[11,12] yet only a few tracers in β-Zr have been studied[8,10] in a wide range of temperatures. The present study deals with impurity diffusion of molybdenum and cerium in the beta phase of zirconium over a temperature range of 880°-1600°C. Residual activity technique[14] has been used to study the penetration profiles. This investigation has been carried out to elucidate the non-linearity behavior in the Arrhenius plots and to explain it on the basis of various existing theories.[15-20]

Experimental Procedure

Specimens of 1cm. x 4mm. thick were machined from a high purity zirconium rod and the end faces were prepared flat and parallel. The zirconium used had the same analysis as that published earlier.[6]

Specimens were annealed for grain growth in vacuum at 1200°C for several days to give large grains (>3 to 4 mm). One face of each specimen was prepared for radioactive deposition as described earlier[6]. Cerium from a very dilute HCl solution (almost neutral) containing radioactive ^{141}Ce and molybdenum oxide from an aqueous solution containing a few drops of ammonia and having ^{99}Mo were deposited on the specimen surfaces. In order to convert cerium chloride into the oxide and homogenise the deposit, the specimens were annealed at 250°C for about two hours. The thickness of the total deposit on the specimen did not exceed in any case more than 0.1μ. The specimens were then diffusion annealed under vacuum in the temperature range of 880°-1600°C. For diffusion anneal upto 1100°C the temperature of the vacuum furnace was controlled within $\pm$2°C while for 1100°-1450°C the temperature variation was $\pm$5°C. Above 1450°C, specimens were diffusion annealed under a pressure of one atmosphere purified helium and the temperature was controlled within $\pm$10°C.

Residual activity technique[14] was used to study the concentration profile. Using NaI (Tl) scintillation counter and pulse height analyser, the activity of the 0.75 Mev and 0.145 Mev γ-radiation of ^{99}Mo and ^{141}Ce respectively were measured. Gruzin's residual activity technique[14] gives

$$C(X_n) = \mu I_n - \frac{dI_n}{dX_n} = \text{const.} \exp\left(-\frac{X_n^2}{4Dt}\right) \qquad (1)$$

where μ(cm^{-1}) is the linear absorption coefficient of radiation in zirconium, I_n is the total residual activity emitted after a thickness X_n(cm) is removed and t (sec) is the time of diffusion anneal.

The values of μ for 0.75 Mev γ-radiation of ^{99}Mo and 0.145 Mev γ-radiation of ^{141}Ce in zirconium have been calculated theoretically[21] taking into consideration the absorption due to photoelectric effect, Compton effect and pair production and was found to be 0.42 cm^{-1} and 1.60 cm^{-1} respectively. The graphical method[22] of determination of μ gives almost identical results. The values of μ are very small so that $\mu I_n \ll (-\frac{dI_n}{dX_n})$ and thus

$$C(X_n) = (-\frac{dI_n}{dX_n}) = \text{const.} \exp(-\frac{X_n^2}{4Dt}) \qquad (2)$$

The diffusion coefficient 'D' (cm^2/sec) can be determined from the slope of log $C(X_n)$ vs X_n^2.

Results and Discussion

The characteristic plots of log C vs X_n^2 for the diffusion of molybdenum and cerium in beta zirconium are shown in fig.1.

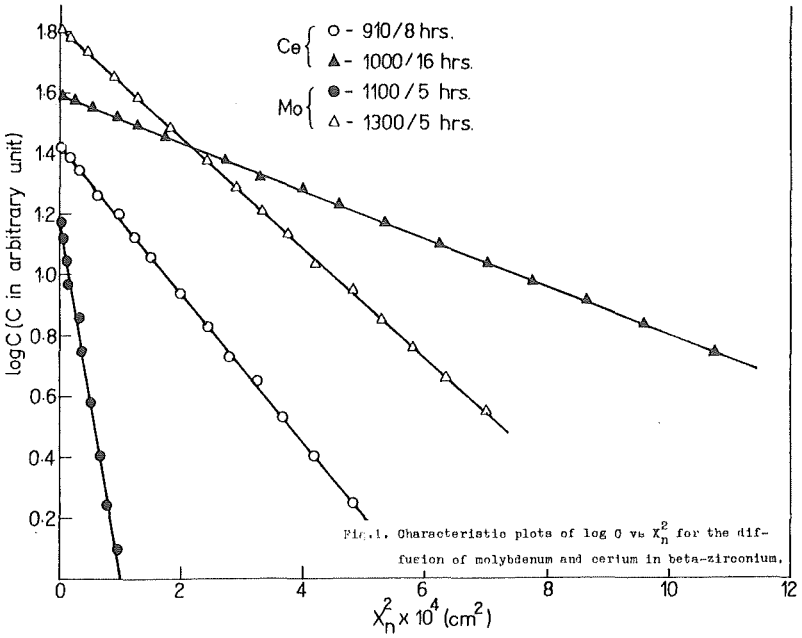

Fig.1. Characteristic plots of log C vs X_n^2 for the diffusion of molybdenum and cerium in beta-zirconium.

The diffusion coefficients at various temperatures and time of

annealing are given in table 1.

Table 1. Diffusivity of molybdenum and cerium in beta-zirconium.

Diffusing species	Temp. °C	Time (sec.)	Diffusion coefficient. (cm^2/sec.)
^{99}Mo	900	2.52×10^4	5.82×10^{-11}
	950	2.52×10^4	1.08×10^{-10}
	1000	2.52×10^4	1.91×10^{-10}
	1050	2.52×10^4	3.31×10^{-10}
	1100	1.80×10^4	5.13×10^{-10}
	1200	1.80×10^4	1.42×10^{-9}
	1300	1.80×10^4	3.33×10^{-9}
	1400	1.44×10^4	7.89×10^{-9}
	1500	1.44×10^4	1.86×10^{-8}
	1600	1.44×10^4	4.22×10^{-8}
^{141}Ce	880	6.48×10^4	4.44×10^{-10}
	910	6.48×10^4	6.86×10^{-10}
	950	5.76×10^4	1.22×10^{-9}
	1000	5.76×10^4	2.39×10^{-9}
	1050	5.76×10^4	4.46×10^{-9}
	1100	5.76×10^4	7.97×10^{-9}
	1200	0.72×10^4	2.26×10^{-8}
	1300	0.72×10^4	5.48×10^{-8}
	1400	0.72×10^4	1.27×10^{-7}
	1500	0.72×10^4	2.74×10^{-7}
	1600	0.72×10^4	5.47×10^{-7}

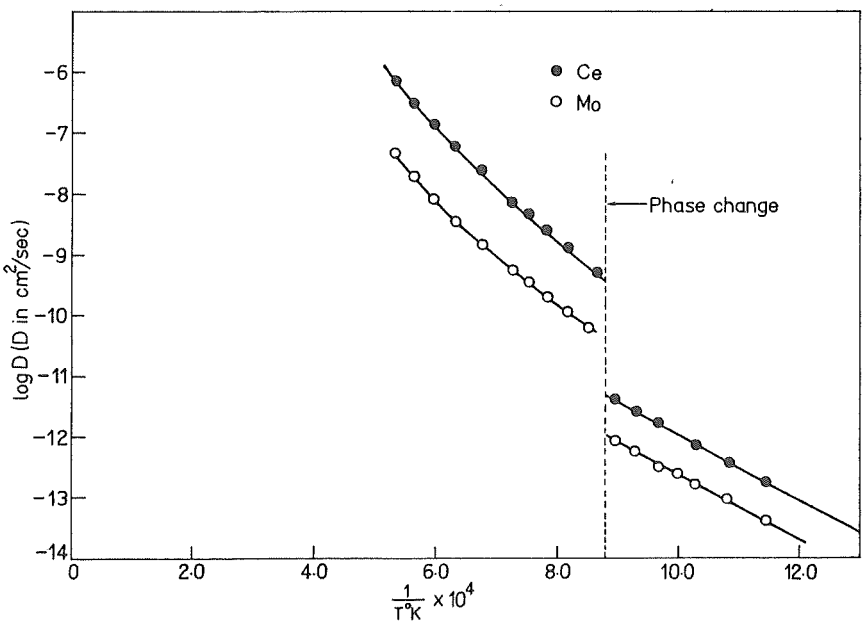

Fig.2. Temperature dependence of diffusivity of molybdenum and cerium in zirconium.

The error in D values is estimated to be nearly 8%. Fig.2. shows

the plots of log D vs $\frac{1}{T}$ for the diffusion of Mo and Ce in β-Zr. To compare the diffusion parameters of Mo and Ce in β-Zr with those in α-Zr, diffusion studies were also ~~been~~ carried out in the alpha phase and the corresponding temperature dependence of diffusivity plots in the α-Zr are also given in Fig. 2. It is seen that while diffusivity in α-phase could be represented by the Arrhenius type of relation following the expression:

$$D_{Mo/\alpha\text{-}Zr}(600^{\circ}\text{-}840^{\circ}C) = 6.22 \times 10^{-8} \exp(-\frac{1.07ev}{kT})$$

$$D_{Ce/\alpha\text{-}Zr}(650^{\circ}\text{-}850^{\circ}C) = 3.54 \times 10^{-7} \exp(-\frac{1.10ev}{kT})$$

the plots of log D vs $\frac{1}{T}$ for the diffusion in β-Zr show non-linearity and give rise to a spectrum of activation energies. Similar to this, non-linear plots have been obtained for the self and impurity diffusion of Zr,[10] Cb[10] and V[8] in β-Zr. The apparent activation energy obtained from the slopes of such non-linear plots at specified temperatures is found to be always higher in the higher temperature range than in the lower ones. The analysis of the present plots indicate a linear relationship in the Arrhenius plots upto a temperature of 1350°C or so for the diffusion of both the impurities. Deviation from the linearity starts at about 1350°C and becomes more pronounced at higher temperatures.

It is seen from Fig. 2 that the diffusivity (D_β) of Mo and Ce in β-Zr is always greater than the extrapolated values of diffusivity (D_α) in α-Zr. The ratio $\frac{D\beta}{D\alpha}$ at the phase transformation temperature (~863°C) are 32 and 80 for Mo and Ce respectively. In fact similar results have been reported for the diffusion of Zr and

Sn[1], Cr[6], Ag[7] and V[8] in zirconium (table 2).

Table 2. Diffusivities of various impurities in alpha and beta phases of zirconium at 863 °C.

Impurity	D cm²/sec. at 863 °C			Ref.
	α-phase	β-phase	Ratio D_β/D_α	
Zr	2.88×10^{-12}	6.24×10^{-10}	217	1
Sn	5.75×10^{-13}	1.52×10^{-10}	264	1
Cr	4.05×10^{-12}	4.81×10^{-10}	118	6
Ag	3.25×10^{-12}	2.68×10^{-10}	83	7
V	4.47×10^{-13}	1.00×10^{-11}	22	8
Ce	4.73×10^{-12}	3.76×10^{-10}	80	present work
Mo	1.12×10^{-12}	3.55×10^{-11}	32	present work

The high diffusivity in body centered cubic metals is explained[23] on the basis that the lattice is loosely packed compared to the hexagonal and face centered cubic closed packed lattices. No quantitative explanation has been reported herein.

The single mechanism[10,15] model of diffusion based on the temperature dependence of frequency factor (D_o) and activation energy (Q) has been applied by Lundy et al[10] to the impurity and self diffusion of Zr and Cb in β-Zr. A relation $D(T) = C\,T^{B/R} \exp(-\frac{A}{RT})$ was obtained to describe the temperature dependence of diffusivity, where D(T) is the diffusion coefficient at an absolute temperature 'T' and A, B and C are constants. Although the possibility of a temperature dependence of frequency factor and activation energy may not be ruled out on purely thermodynamic arguments yet its application to self and impurity diffusion in β-Zr does raise some difficulties in interpretation.

On the assumption that, simultaneously two modes of diffusion are operating in the present case, the diffusivity could be expressed as the sum of two exponential terms:

$$D_{Mo/\beta\text{-}Zr}\ (900^\circ\text{-}1600^\circ C) = 1.99 \times 10^{-4} \exp(-\frac{1.53ev}{kT}) + 2.63 \exp(-\frac{2.97ev}{kT})$$

$$D_{Ce/\beta\text{-}Zr}\ (880^{\circ}\text{-}1600^{\circ}C) = 3.16 \times 10^{-2} \exp\left(-\frac{1.80ev}{kT}\right) + 42.17 \exp\left(-\frac{3.22ev}{kT}\right)$$

In the high temperature range (>1350°C) for the diffusion of Mo and Ce in β-Zr, the values of frequency factors and activation energies (2.63 cm^2/sec, 2.97 ev and 42.17 cm^2/sec, 3.22 ev respectively) are normal in the sense that they satisfy reasonably well the empirical relationship[24-26] of Q with the melting point and give positive values of entropy of activation. Thus the normal values of D_o and Q obtained at high temperature suggest that the diffusion is proceeding through vacancies. On the other hand, the corresponding values of D_o and Q (1.99×10^{-4} cm^2/sec, 1.53 ev and 3.16×10^{-2} cm^2/sec, 1.80 ev respectively) in the temperature range of 863° to 1350°C are extremely small. Kidson[16] has attributed the low values of D_o and Q in self diffusion of beta zirconium to the diffusion through temperature independent extrinsic vacancies due to the interstitial impurity of oxygen. The extrinsic activation energy for the diffusion of Mo and Ce in β-Zr is more than half of the corresponding values from the intrinsic region. It thus cannot be said to represent simply the energy of migration of vacancies if a large excess of nonthermal vacancies were present. Furthermore, the above model predicted the dependence of diffusivity on oxygen content. Recently, Kidson[17] has quoted Graham's work in which a little effect on the rate of solute diffusion in β-Ti due to the presence of oxygen content has been reported. Moreover, this model, which has been treated more rigorously by Le Claire[27], assumes the binding energy of interstitial impurity-vacancy complex to be about 1.3 ev. This value is rather large and hence Kidson's model may perhaps not be applicable in the present case.

Another explanation for the low D_o and Q may be given on the basis of the enhancement of apparent volume diffusivity which arises due to the significant contribution from grain boundaries and randomly oriented dislocations. However, the contribution from the grain boundary is completely ruled out as the grains were pretty large (>3 mm) and plots of log C vs X_n^2 were all straight lines. The diffusion through dislocations seems probable as it does not affect the linearity of the plots of log C vs X_n^2. The low activation energies (1.53 ev and 1.80 ev) for the diffusion of Mo and Ce in beta zirconium are well accounted on the mechanism of dislocations.[17,18,28] Using Hart-Mortlock relation,[29,30]

$$D = D_v + gk_2D_d \text{ and } D_o = g\,D_{od}$$

(where D, D_v and D_d are apparent volume diffusivity, volume diffusivity through dislocation free single crystal and through dislocation respectively. D_o and D_{od} are frequency factors for apparent volume diffusion and dislocation diffusion respectively; g is the fractional site on dislocation and k_2 is the segregation coefficient for the impurity under consideration in β-Zr lattice) a dislocation density of the order of 10^9 - 10^{11} lines/cm^2 is required to account for the experimental D_o values (1.99×10^{-4} cm^2/sec and 3.16×10^{-2} cm^2/sec.) Though this value of dislocation density seems to be unusually high, yet it may be possible due to martensitic α-β phase transformation[31].

Recently, Peart and Askill[19] have proposed that the non-linearity in the Arrhenius plots for the self and impurity diffusion in β-Ti, β-Zr, γ-U and β-Hf may be due to two competitive mechanisms of diffusion, one involving a simple monovacancy accompanied by dislocation enhancement at lower temperatures and the other, involving a

divacancy at much higher temperatures. According to their analysis[19], there is an appreciable contribution of dislocation towards apparent volume diffusivity below a temperature of T_d ($T_d \simeq 0.7\ T_m$, where T_m is the absolute melting point of the solvent). For β-Zr, T_d comes out to be $\sim 1230^{o}C$. From T_d upto a temperature say T_c (the temperature at which the Arrhenius plot changes), the contribution of monovacancies is assumed to be predominant. Tentatively, it is also equal to the temperature where the contribution of divacancies diffusion D_2 to monovacancies D_1 (i.e. $\frac{D_2}{D_1}$) is about 10% . Above T_c upto the melting point of the solvent, divacancies play a significant role towards the apparent volume diffusivity. They[19] derived the following expressions for the impurity diffusion in β-Ti and β-Zr:

$$Q_2 = (1.9K_1 + K_3 - K_1K_3)Q_1$$

$$D_{20} = \frac{\beta}{2} a^2 \nu_1 f_1 \left(\frac{D_{10}}{a^2 \nu_1 f_1}\right)^{2K_2 + K_4(1-K_2) + K_2\frac{Z_2}{Z_1}}$$

$$\frac{D_2}{D_1} \simeq \frac{\beta}{2}\left(\frac{D_{10}}{a^2\nu_1 f_1}\right)^{(Z_2+Z_1)\frac{K_2}{Z_1} + (1-K_2)(K_4-1)} \exp\left(-\frac{0.9K_1 + (1-K_1)(K_3-1)}{RT} Q_1\right)$$

where Q_1 and Q_2 are the activation energies for the diffusion through monovacancies and divacancies respectively, D_{10} and D_{20} are the corresponding frequency factors, $K_1 = \frac{E^F_{1V}}{Q_1}$ is the ratio of formation energy for monovacancies E^F_{1V} to activation energy for diffusion Q_1. K_2 is the corresponding ratio of entropy terms, i.e., $\frac{S^F_{1V}}{S_{1V}}$; $K_3 = \frac{E^M_{2V}}{E^M_{1V}}$ the ratio of energy of migration of divacancies to the monovacancies and K_4 is the corresponding ratio of the entropy terms, i.e., $\frac{S^M_{2V}}{S^M_{1V}}$, β an orientation factor, 'a' the lattice parameter, ν_1 the atomic vibration frequency, f_1 the correlation factor and Z_1, Z_2 are the number of nearest neighbour to a monovacancy and a divacancy respectively.

The relations derived by Peart and Askill[19] have been applied for the diffusion of Mo, Ce, V and Nb in β-Zr. The results obtained are given in table 3. Fig. 3 and 4 show graphical representation of the divacancy-monovacancy model applied to the diffusion data of Mo and Ce in β-Zr.

Table 3. Diffusion of impurities in zirconium.

	Experimental					Predicted				
Solute	Q_1	D_{10}	Q_2	D_{20}	T_c(°C)	E^F_{1V}	E^F_{1V/Q_1}	E^M_{1V}	Q_2	D_{20}
Ce	1·84	$3{\cdot}84\times10^{-2}$	2·95	13·10	1330	1·10	0·60	0·74	2·78	96·80
Mo	1·76	$1{\cdot}57\times10^{-3}$	2·76	0·06	1350	1·06	0·60	0·70	2·71	0·02
V	2·15	$2{\cdot}90\times10^{-2}$	3·41	41·00	1320	1·29	0·60	0·86	3·30	61·55
Nb	1·74	$2{\cdot}51\times10^{-3}$	2·72	0·25	1370	1·04	0·60	0·70	2·68	0·09

All energies have been expressed in ev and frequency factors in cm^2/sec.

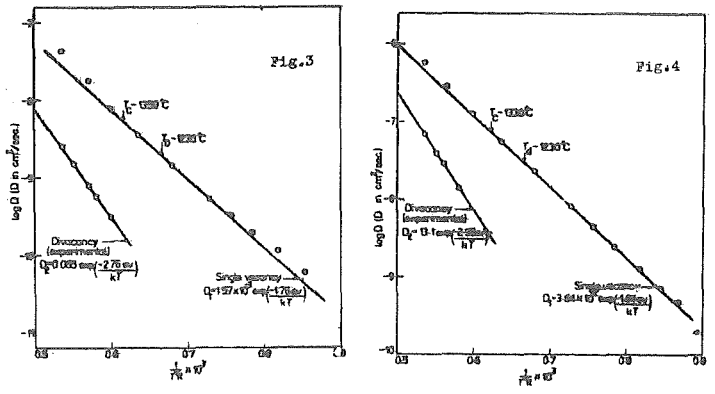

Fig.3 and 4. Divacancy/vacancy analysis applied to the diffusion of Molybdenum and cerium in beta zirconium.

It is seen from the table 3 and Fig. 3 and 4 that the experimental values of D_{20} and Q_2 are in fairly good agreement with corresponding theoretical values. Although the above explanation based on divacancies seems quite plausible yet it appears that vacancy complexes which are in dynamic equilibrium with monovacancies and divacancies, may also be taking part in the diffusion process.

Based on an electron-concentration concept for the diffusion process, Engel[20] has reported that the self and impurity diffusion in metals and dilute alloys depends on the lattice configuration and

the bond strength. In transition metals, electrons from unfilled 'd' and 'f' levels and the outermost 's' level participate in the bonding process and the bond strength depends on the total number of electrons involved. Though in most of the metals, the electronic bonding pattern is independent of temperature and gives rise to only one value of activation energy, in certain transition metals like β-Zr, a change in the distribution of bonding electrons may take place as a function of temperature resulting the non-linearity in the Arrhenius plots of log D vs $\frac{1}{T}$ for the self and impurity diffusion of Zr, Cb, Mo, Ce and V in β-Zr. Furtheremore, it is observed that the difference in activation energy Q for the diffusion of Cb and Zr in β-Zr[10] is 0.34 ev at 1600°K and increases with temperature. Engel has attributed qualitatively that 0.34 ev increase in activation energy may be due to the addition of one d-electron to the bonding strength of Zirconium lattice (the electron distribution of Zirconium along with other metals is given in Table 4).

Table 4. Electron distribution corresponding to the ground state, bcc and hcp lattices of the various elements.

Element	Electron distribution *		
	Ground state	bcc	hcp
Zr	$4d^2 5s^2$	$4d^3 5s^1$	$4d^2 5sp$
Cb	$4d^3 5s^2$	$4d^4 5s^1$	$4d^3 5sp$
V	$3d^3 4s^2$	$3d^4 4s^1$	$3d^3 4sp$
Ce	$4f^2 6s^2$	-	-
Mo	$4d^4 5s^2$	$4d^5 5s^1$	$4d^4 5sp$

* "Diffusion in body-centered cubic metals" page 94, A. S. M. (1965).

The higher temperature values of Q for the diffusion of Mo, Ce and Zr in β-Zr are 2.97 ev, 3.22 ev and 2.82 ev respectively. Thus Q for Mo and Ce in β-Zr is 0.15 ev and 0.40 ev higher as compared to the corresponding Q values for self diffusion of β-Zr.

According to qualitative analysis based on Engel[20] theory, it is seen that the total bond strength of the solvent lattice incre-

ases due to an increase in the number of bonding electrons when molybdenum and cerium go into solid solution of β-Zr. The increase in the activation energy for the diffusion of Mo and Ce in β-Zr by 0.15 ev and 0.40 ev respectively is thus due to an increase in the total number of bonding electrons compared to pure β-Zr lattice. Furthermore, the experimental results show that Q for diffusion of Ce in β-Zr is higher than that for Mo. The higher value of Q for Ce may be resulting from an additional increase in bond strength due to the interaction and participation of 'f' electrons in the solid solution of β-Zr lattice.

The various existing theories[15-20] have been applied to explain the experimental results of diffusivity of molybdenum and cerium in beta zirconium with considerable success. The observation that the material can be completely homogenised by diffusion process shows that there must be some bulk diffusion mechanism. The presence of Kirkendall effect[32] and the pore formation[32] in the chemical diffusion of zirconium and uranium system implies that the basic process of diffusion is either through vacancies or interstitialcies which can be created or annihilated locally in the lattice.

In view of the above discussion, it seems that the diffusion process observed in beta zirconium is not through simple vacancies.

Acknowledgement

Authors thank Dr. J. Shankar for his interest in the work and critically going through the manuscript.

References

(1) P.L. Gruzin, V.S. Emelyanov, G.G. Ryabova and G.B. Fedorov, 2nd Int.Conf. Peaceful uses of Atomic Energy, Geneva 19,187(1958).

(2) V.S. Lyashenko, V.N. Bykov and L.B. Pavlinov, Fiz. Metal. i Metalloved, 8, 362(1959).

(3) P. Flubacher, EIR - Bericht Nr. 49(1963).

(4) E.V. Borisov, Yu. G. Godin, P.L. Gruzin, A.J. Eustyukin and V.S.A. Emelyanov, Metall. and Metallog., All-Union Conf. Use of Isotopes and Radiation, Moscow, 1958 p. 291.

(5) G.B. Federov and F.I. Zhomov, Met. i Metalloved, Chistyh Metall., 1, 162(1959).

(6) R.P. Agarwala, S.P. Murarka and M.S. Anand, Trans. AIME; 233, 986(1965).

(7) M.C. Naik and R.P. Agarwala, Proc. Nucl.Rad.Chem.Symp., Waltair, Dept. Atomic Energy, India, 282(1966).

(8) R.P. Agarwala, S.P. Murarka and M.S. Anand; Acta Met., 16, 61(1967).

(9) C.M. Libanati and S.F. Dyment, Acta Met., 11, 1263(1963).

(10) J.I. Federer and T.S. Lundy, Trans. AIME, 227, 592(1963).

(11) D. Graham, Diffusion in Body Centred Cubic Metals, Proc.Int.Conf. Gatlinburg, Tenn., Am. Soc. Met., (1964) p.27.

(12) J.F. Murdock, T.S. Lundy and E.E. Stansburg, Acta Met., 12, 1033(1964).

(13) N.L. Peterson and S.J. Rothman, Phys. Rev., 136, 842(1964).

(14) P.L. Gruzin, Dokl.Akad.Nauk SSSR, 86, 289(1952).

(15) G.B. Gibbs, Acta Met., 12, 1302(1964).

(16) G.V. Kidson, Can. J. Phys., 41, 1563(1963).

(17) G.V. Kidson, Diffusion in Body Centred Cubic Metals, Proc.Int. Conf. Gatlinburg, Tenn., Am. Soc. Met., (1964) p.329.

(18) M.C. Naik and R.P. Agarwala - To be published.

(19) R.F. Peart and J. Askill, phys. stat. sol., 23, 263(1967).

(20) Niels Engel, Diffusion in Body Centred Cubic Metals, Proc. Int.Conf. Gatlinburg, Tenn., Am. Soc. Met., (1964) p.87.

(21) E. Segre, Experimental nuclear physics, Vol. 1, John Wiley and Sons, Inc. New York (1953) p. 311.

(22) E. Bleuler and G.J. Goldsmith, Experimental Nucleonics, Rinehart and Comp., New York (1957) p. 175.

(23) P.G. Shewmon, Diffusion in Solids, McGraw Hill Book Comp. Inc., New York (1963).

(24) M.H. Nachtrieb and G.S. Handler, Acta. Met., 2, 797(1954).

(25) O.D. Sherby and M.T. Simnad, Trans. ASM, 54, 227(1961).

(26) S.P. Murarka and R.P. Agarwala, A.E.E.T. - 233 (1965).

(27) A.D. Le Claire, Diffusion in Body Centred Cubic Metals, Proc. Int.Conf. Gatlinburg, Tenn., Am. Soc. Met., (1964) p.1.

(28) M.C. Naik and R.P. Agarwala, Acta Met., 15, 1521(1967).

(29) E. Hart, Acta Met., 5, 597(1957).

(30) A. Mortlock, Acta Met., 8, 132(1960).

(31) E.S. Fisher and C.J. Renken, Phys. Rev., 135(2A), A482(1964).

(32) Y. Adda and J. Philibert, 2nd Int. Conf. on Peaceful uses of Atomic Energy, Geneva, 6, 72(1958).

II. VACANCIES IN QUENCHED F.C.C. METALS

xxxxxxxxxxxxxxxxxxxxxxxxxxxxxxxxxxxxxxxxxxxxxxxxxxxxxxxxxxxxxxxxxxxxxxxxxxxxxxxxxxxxxxxxxxxxxxxxxxxxxxxx

On the Determination of Concentrations and Properties of Vacancy Defects from Quenching Experiments

R. W. Siegel, R. W. Balluffi, K. H. Lie, and D. N. Seidman
Cornell University, Ithaca, N. Y., USA

ABSTRACT

A survey of the experimental and analytical techniques available for the determination of concentrations and properties of vacancy defects in pure metals from quenching will be presented. Perturbations to the equilibrium population of vacancy defects caused by quenching will be considered in relation to their effect upon the quenched-in vacancy defects. The redistribution of vacancy defects as a result of vacancy interactions, the losses of vacancies to existing sinks or by precipitation, and the generation of new defects due to deformation during quenching will be examined. The results of recent computer calculations of vacancy losses in a multi-defect system will be presented. Next, experimental methods for the determination of the concentrations of quenched vacancy defects will be examined. Indirect techniques which utilize the measurement of a macroscopic property such as resistivity or length, for example, in which the change in the property per unit increment of vacancy defects must be known, as well as direct measurements such as electron or field-ion microscopy will be discussed. The problems involved in the interpretation of the experimental results from these techniques in terms of defect concentrations will be considered. Non-proportional variation of properties with order of vacancy cluster, non-uniformity of defect distributions and perturbations of the defect population by the observation technique will be discussed. Lastly, techniques available for the determination of the properties of single and multiple vacancies will be considered. Primary emphasis will be given to the problem of the determination of formation energies of vacancy defects. Possible curvature of Arrhenius plots will be considered in relation to both temperature dependence of defect activation energies and contributions from the various constituents of a multi-defect system. In addition, the determination of other characteristic properties of vacancy defects, such as resistivity and volume, by a combination of indirect and direct experimental quenching techniques will be considered. Throughout the discussion of the various topics mentioned, available experimental results will be considered where pertinent.

Electrical Resistivity Measurements During Vacancy Annealing

J. S. Koehler
University of Illinois
Urbana, Illinois

Abstract

The value of electrical resistivity measurements will be assessed and the major results achieved will be discussed. Annealing measurements after deformation, nuclear irradiation, and quenching will be considered. The results are most complete for gold so that it will be discussed first and the information resulting will be described. It will be shown that the annealing observed in 99.9999% pure gold near room temperature after a fast quench from 700°C, after a few percent deformation at 4.2°K and after 3 MEV electron irradiation at 100°K can all be ascribed to vacancy migration. It will be shown that divacancies dominate the annealing after a slow quench from 700°C. Differences in sink density account for the different behavior after fast and slow quenches. The influence of small amounts of impurity on the annealing behavior of gold will be described. Finally values for E_V^M, E_{2V}^M, E_V^F , B_{2V}, ρ_V etc will be given.

A similar discussion will be attempted for aluminum, silver, copper, platinum, nickel and tungsten. In each of these metals the information is not complete. The available data will be summarized. An attempt will be made to evaluate the present state of affairs and to describe what new data will be required. Values for E_V^F, E_V^M, etc will be given where data exists.

Annealing in Quenched Metals

K.P. Chik, Max-Planck-Institut für Metallforschung,
Institut für Physik, Stuttgart

A b s t r a c t

Of the three conventional ways of producing point defects in solids, namely, quenching, deformation and irradiation with energetic particles, quenching is supposed to produce the simplest type of damage. In f.c.c. metals, only vacancy type of defects can be quenched in and in ideal case these defects should distribute homogeneously after quenching over the crystals apart from small volume of denuded regions near grain boundaries and dislocations. This relative simple situation simplifies the mathematical treatment of the problem, enabling a more sound interpretation of experimental results. Thus quenching experiments may provide valuable informations on vacancy properties. In spite of these facts, the interpretations of experimental quenching results are by no means simple and unambiguous. The complications arise from our lack of knowledge about small vacancy clusters and about the interaction between vacancy and impurity atoms.

This review gives a survey of the present situation in annealing studies of quenched metals and is divided into three main sections.
(i) Annealing at high vacancy concentration. This involves inevitably clustering of vacancies. The central problem lies on the study of nucleation process of vacancy clusters and their subsequent growth which determine the whole annealing process. The appropriate nucleation models, the question of homogeneous and heterogeneous nucleation and the influence of impurities on nucleation will be discussed in some details.

(ii) Annealing at low and intermediate vacancy concentration. At low vacancy concentration, the main type of quenched-in defects should

be mono-vacancies. A simple first order kinetic should prevail if only one type of defects is present and anneals out at infinite sinks. Experimentally, deviations from first order kinetics are observed in many cases. The possible causes for such deviations are discussed, such as impurity effects and effect of strain fields.

(iii) Determination of vacancy parameters. The determination of important vacancy parameters such as migration energy, binding energy and binding entropy of vacancy defects is in fact the ultimate aim of studying annealing in quenched metals.

The difficulties involved in deducing vacancy parameters from annealing experiments are discussed. Specific examples are given for the case of quenched gold. It will be emphasized that unambiguous results cannot be obtained without a coordination among different kinds of experiments. Some new techniques are required to give a forward push to better understanding than that arrived at the present time.

KINETICS OF THE THERMAL VACANCY FORMATION IN PLATINUM

F. HEIGL and R. SIZMANN

Sektion Physik der Universität München, Munich, Germany

Abstract: (Manuscript not yet received)

It is well established that by rapid quenching platinum from a high temperature the thermodynamical vacancy concentration can be frozen in, and than easily determined at low temperatures by the change in residual electrical resistivity. Such experiments yield the energy of vacancy formation and by proper annealing procedures the energy of vacancy migration.
The goal of the present investigation is to provide information on the thermal sources of vacancies in platinum. We applied a pulse heating technique with electronically controlled rise time ($\leq$ 1msec), duration of heating at a preset temperature (time intervals from 1 msec to infinite), and quenching in a rapid He gas stream (initial quenching rate > 10^4 deg/sec). The experiments were done on well annealed 99,99 % pure platinum wire, o,1 mm in diameter. The residual electrical resistivity of the specimen was measured in liquid nitrogen by a modified potentiometric technique. The smallest detectible change in resistivity was $1 \times 10^{-11}\,\Omega$cm. The diagrams of the quenched-in resistance versus the pulse duration show a gradual increase of vacancy concentration up to the equilibrium value of the applied temperature. The half time of the equilibrium adjustment is about 1oo msec in most of the well recrystallized specimens, nearly independent of the temperature. The formation kinetics (time dependence and activation energy) unequivocally points to planar sources in the lattice (the surface of the specimen is not the prevailing source, however). The results are discussed in terms of the primary vacancy sources being dislocations (or their jogs), aligned in small angle grain boundaries.

VACANCIES IN GOLD*

H. I. Dawson and K. B. Das
Division of Metallurgical Engineering
University of Washington
Seattle, Washington
U.S.A.

ABSTRACT

Electrical resistivity recovery spectra of lattice defects in 99.9999 and 99.99% pure gold have been determined between -20° and +170°C. Defect structures were produced by quenching, quenching followed by deformation, and by deformation. An extensive recovery spectrum with a characteristic substructure is observed in all cases. Most of the defect resistivity of quenched gold recovers between 35° and 125°C. In this range three processes are observed which shift to lower temperatures with increasing quenching temperature, impurity concentration, and dislocation density. It is suggested that these could be due to tri-, di-, and single vacancies respectively. The recovery below 35°C and above 125°C is enhanced by impurities; some small vacancy cluster nucleated at impurities during the quench, could become mobile, below 35°C, while the recovery above 125°C could be due to the release of impurity trapped vacancies. A comparison of the recovery spectrum of deformed gold with these results indicates that most of the recovery in Stage III could be due to small vacancy clusters, divacancies, and single vacancies, while Stage IV could be caused by the release of trapped vacancies.

INTRODUCTION

The behavior of vacancies in gold is not well understood. Such basic quantities as the energies of motion and association of these defects are not precisely known. A supersaturation of vacancy type defects is readily obtained by quenching, but the precise quenched-in defect structure is not known. The most frequently used property in the study of the recovery of these defect structures is the electrical resistivity. The usual procedure is to measure the change in the quenched-in resistivity at a low temperature as a function of the annealing time at a constant annealing temperature.

Several attempts have been made to simplify the conditions for the recovery process by using high purity gold quenched with high speeds from relatively low temperatures,[1] but the isothermal recovery remains complex. One cannot identify the defect species from the observed isothermal behavior nor can one decide whether they are monovacancies or not by a simple comparison of the observed migration energy E^M for the recovery process, and the quantity $Q - E^F_{1V}$. (Here, Q is the high temperature self diffusion energy and E^F_{1V} the

*Work supported by the National Science Foundation under Grant GK 1307.

formation energy of a single vacancy.) This complication arises from the possibility of a strong temperature dependence of the motion energy E^M_{IV} of single vacancies, as recently discussed by Stoebe and Dawson.[2]

Several values for E^M have been determined,[1,3] but the value of about 0.70 eV, has been observed in several different investigations for a wide variety of experimental conditions, as has recently been reviewed by Wang, Seidman, and Balluffi.[4] This energy has been observed to be independent of the amount of resistivity due to the defects, if this lies between about 1.05×10^{-10} and 1.5×10^{-8} Ωcm. Nor does it depend on the purity of the gold indicated by the ratio R of the resistivities at room temperature and at 4.2°K. It remains about 0.70 eV for nominally 99.999% or 99.9999% pure gold with R values between 380 and 22500. Finally, this defect migration energy is independent of the properties of the sinks at which the defects disappear.[4]

The identity of these dominating defects remains unknown. Wang, Seidman, and Balluffi[4] assume that they are divacancies but suggest that they could also be trivacancies. Stoebe and Dawson[2] have argued that the observed 0.70 eV could conceivably be the value for the room temperature migration energy of monovacancies.

Complications in the analysis of isothermal recovery curves can arise if more than one distinct process is involved during the recovery at that particular temperature. Isochronal recovery experiments have been performed after quenching but with the main objective of establishing the general temperature range in which the recovery occurs,[5-7] or for the application of the Meechan-Brinkman[8] method for the determination of activation energies.[8] It has been observed[8] that the electrical resistivity of quenched gold decreases during annealing at all temperatures between -40° and +150°C. This temperature range of about 200 degrees is much wider than the restricted temperature interval in which a simple, singly activated point defect recovery process should take place during a typical isochronal anneal.

Precise isochronal measurements have proved to be very useful in the study of the substages of Stage I after electron irradiation,[9] but similar studies on quenched gold are not encountered in the present literature. One of the main objectives of this paper is to report on some of the results of such a study.

Vacancy-type defects are also known to be produced by plastic deformation, but there is no detailed agreement as to which portions of the resistivity recovery spectrum of deformed gold are caused by these defects. After a large deformation, one observes extensive recovery between about -190° and -60°C, Stage II; and between about -60° and +100°C, Stage III. No definite Stage IV has been observed in gold. Stage II, which occurs over a temperature range of about 150 degrees, is not caused by one process. Stored energy measurements by van den Beukel[10] have provided direct evidence for a substructure in this stage. Seeger[8,11] believes that this could be associated with certain multiple vacancies. Stage III is also about 150 degrees wide and cannot be interpreted as due to a simple, single process. Dawson[12] observed three substages of Stage III in resistivity recovery experiments and concluded that the recovery above about -20°C could be due to di- and single vacancies. Corbett[13] has argued that single vacancies could be responsible for part of Stage III, while Stage IV, i.e., the small amount of recovery after Stage III, could be caused by the release of vacancies from traps.

It is noted above that vacancy-type defects have been considered in the literature for all of the point defect Stages II, III, and IV. The other main objective of the present paper is, therefore, to discuss the recovery spectrum of deformed gold in comparison with that of quenched gold in an attempt to identify the recovery stages which are caused by the vacancy-type defects produced by deformation.

EXPERIMENTAL PROCEDURE

Specimens

All of the present experiments were performed on wire specimens of 0.25 mm diameter supplied by Cominco Products, Inc. Table 1 gives the purity analyses performed by the supplier.

TABLE 1
Impurities in the Specimens used in this Investigation

Nominal purity	Impurities in ppm by weight										
	Al	Ca	Cu	Ge	Fe	Mg	Si	Ag	Na	In	Total
99.9999% (6N)	1.0	0.7	0.5		1.0	0.2	5.0	0.3			8.7
99.99% (4N)	1.0	1.0	3.0	0.5	3.0	0.5	3.0	3.0	5.0	1.0	21.0

Before introducing the defects, the samples were always annealed for 1 hour at 450°C in air. No attempt was made to obtain extremely large resistivity ratios, R, in order to be able to compare the present results with the majority of the existing data. After this annealing treatment, the R values were typically between 600 and 800 for the 6N samples and around 200 for the 4N samples. Just before the quench the specimens were heated (in air) by an electric current for about four minutes at the quenching temperature which was controlled to within ±10 degrees. After the specimens were quenched in a brine solution below 0°C, they were transferred into a liquid nitrogen bath within 10 seconds. The quenching speed was detected by an oscilloscope and photographed with a polaroid camera. Potential leads of the same material as that of the specimen were spotwelded on the sample at about 5 cm apart.

Electrical Resistivity Measurements

The electrical resistivity measurements were always performed at 4.2°K with a standard potentiometric technique using a Leeds and Northrup six-dial microvolt potentiometer in combination with a Keithley 147 nanovolt null-detector. The current through the specimen connected in series with a standard resistor was controlled by manually keeping the voltage drop across the standard resistor constant, using a Leeds and Northrup K5 potentiometer. Resistivity changes of 1×10^{-12} Ωcm could be detected.

After introducing the defects, the samples were annealed by direct immersion in a liquid bath at the desired temperature controlled to within ±0.02°C using a Lauda NBSD constant temperature circulator. Pentane was used as thermostat liquid for temperatures between -20° and +20°C, distilled water between 20° and 90°C, and propylene glycol between 90° and 200°C.

Annealing was always performed at the same temperatures according to a schedule of 10 minutes at a series of increasing temperatures, T_1, T_2,...T_i, T_{i+1}...T_f, at 10 degree intervals. The resistivity at $4.2^{\circ}K$ was measured after each 10-minute anneal. The resistivity after annealing at the i^{th} temperature is called ρ_i. The resistivity at $4.2^{\circ}K$ before the first anneal is ρ_s and that after the last 10-minute anneal, at T_f, is ρ_f. By plotting 100 x $(\rho_i-\rho_f)/(\rho_s-\rho_f)$ versus T_i one obtains an isochronal recovery curve, indicating the recovery in percent as a function of the annealing temperatures. If a substructure is present in this curve, it will be more readily observed by plotting the recovery rate r, given by 100 x $\{[(\rho_i-\rho_f)/(\rho_s-\rho_f)] - [(\rho_{i+1}-\rho_f)/(\rho_s-\rho_f)]\} /(T_{i+1}-T_i)\frac{1}{2}(T_i+T_{i+1})$. The data points in the following figures are given by this expression and have an experimental error corresponding to the minimum detectable resistivity of 1 x 10^{-12} Ωcm. They are connected with straight line segments to indicate the recovery spectrum. In each figure the total amount of recovery, $\Delta\rho_o = \rho_s - \rho_f$, and other pertinent information is indicated. T_q is used for the quenching temperature, q_s for the quenching speed, and ϵ for the amount of plastic elongation.

EXPERIMENTAL RESULTS

Recovery spectra of gold were determined from -20° to $+170^{\circ}C$ after defect structures were introduced by quenching, quenching followed by deformation, and by deformation.

Recovery After Quenching

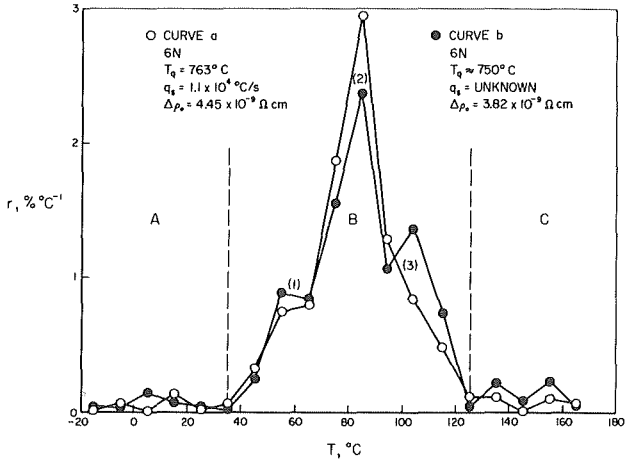

Figure 1
Recovery spectra of quenched 6N gold.

In Figure 1 two recovery spectra of the quenched-in electrical resistivity of 99.9999% (6N) pure gold are plotted. The experimental conditions were nearly the same for the two cases, and essentially the same recovery behavior is indicated by the two curves. Both exhibit the same general substructure in an extensive recovery spectrum between -20° and $+170^{\circ}C$. A small amount of the total recovery occurs below 35° and above $125^{\circ}C$; more than 90% of the defect resistivity recovers between 35° and $125^{\circ}C$. The regions below about 35° between 35° and $125^{\circ}C$ and above about $125^{\circ}C$, will be referred to as regions A, B, and C respectively, and are indicated in the figure by the dotted dividing lines.

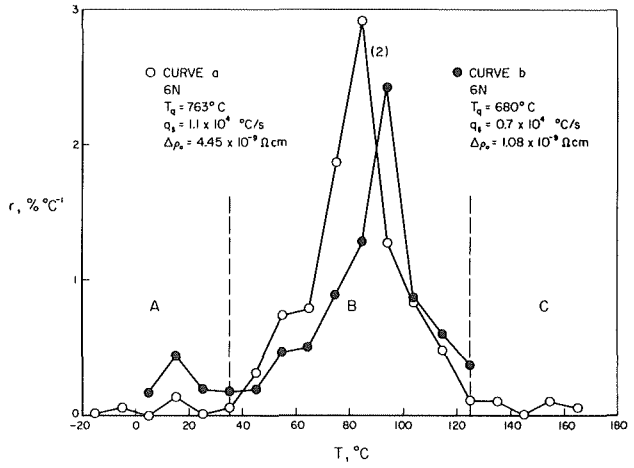

Figure 2
Recovery spectra of quenched 6N gold for different quenching temperatures.

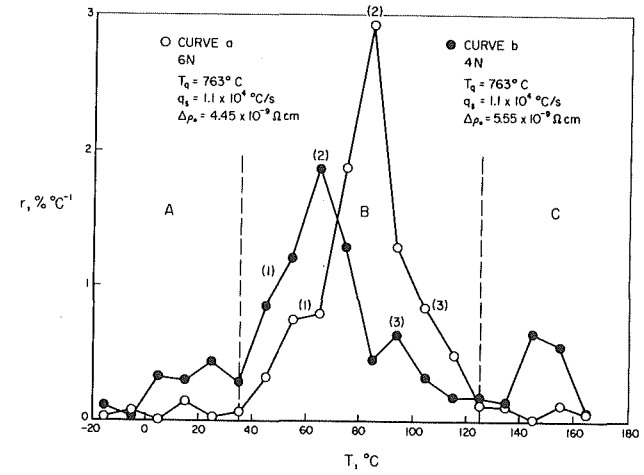

Figure 3
Curve a: Same as curve a from Figure 1.
Curve b: Recovery spectrum of 4N gold.
The specimens of the two curves were quenched and annealed under identical conditions.

Curve a from Figure 1 is reproduced in Figure 2 together with the recovery spectrum of a 6N sample quenched from a lower temperature. The same general structure is present in both curves, but the main peak occurs at a lower temperature in the specimen quenched from the higher temperature.

The recovery spectrum of 99.99% (4N) pure gold is shown in Figure 3, curve b. Substructure is also observed in this extensive spectrum. For a comparison, curve a from Figure 1 is also shown in Figure 3. The conditions for the quench as well as for the subsequent annealing were identical for the two specimens as they were mounted side by side on the same holder during this experiment. If one divides the recovery in the regions A, B, and C, the resistivity changes are as given in Table 2.

TABLE 2
Relative and Absolute Amounts of Recovery in the Various Temperature Regions for the Curves of Figure 3.

	Region A		Region B		Region C	
	%	10^{-9} Ωcm	%	10^{-9} Ωcm	%	10^{-9} Ωcm
Curve 3a (6N)	2.9	0.13	93.7	4.17	3.4	0.15
Curve 3b (4N)	14.0	0.78	70.9	3.93	15.1	0.84

The recovery in the regions A and C is enhanced, while that in region B is suppressed in the impure sample. One further observes that the recovery curve of this specimen in region B is shifted to lower temperatures compared to that of the purer sample.

Recovery After Quenching and Deformation

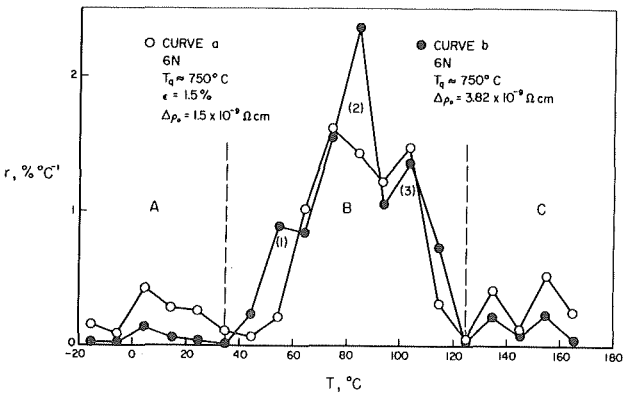

Figure 4
Curve a: Recovery spectrum of 6N gold after quenching and 1.5% deformation.
Curve b: Same as curve b from Figure 1.
The specimens of the two curves were quenched and annealed under identical conditions.

Figure 4 compares the recovery curve after quenching as previously illustrated in Figure 1 (curve b) with the recovery of a specimen in which a defect structure was produced by quenching plus subsequent deformation at 4.2°K (curve a). The two specimens were mounted side by side during the entire experiment. They were quenched simultaneously from the same temperature with the same quenching speed. After quenching, the specimen on which curve a was measured was deformed about 1.5% in tension. If an unquenched sample is deformed this amount, about 0.35 x 10^{-9} Ωcm recovers between -20° and +170°C. The amounts of recovery in the regions A, B, and C, are given in Table 3.

TABLE 3
Relative and Absolute Amounts of Recovery in the Various Temperature Regions of Figure 4.

	Region A		Region B		Region C	
	%	10^{-9} Ωcm	%	10^{-9} Ωcm	%	10^{-9} Ωcm
Curve 4a (quenched and deformed)	13.0	0.195	74.0	1.11	13.0	0.195
Curve 4b (quenched)	3.2	0.12	90.8	3.47	6.0	0.23

Due to the 1.5% plastic deformation, the total amount of recovery $\Delta\rho_o$, has been reduced by a factor of about 2.5. Only in region A is there a larger absolute amount of recovery in curve a (quenched and deformed) than in curve b (quenched). There is no evidence in these curves that new recovery peaks occur due to the deformation.

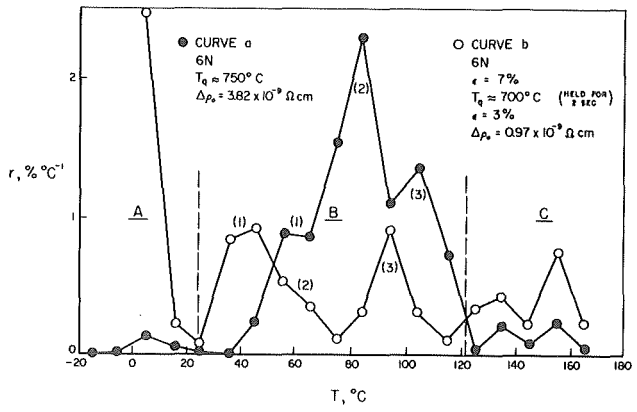

Figure 5
Curve a: Same as curve b from Figure 4.
Curve b: Recovery spectrum of 6N gold after 7% deformation at room temperature, heated to 700°C for 2 seconds, quenched, and then deformed 3%.

In Figure 5, curve b of Figure 4 (quenched) is compared with the recovery spectrum of a specimen which was treated as follows: First it was deformed about 7% in tension at room temperature. Then the sample was rapidly heated to about 700°C and held at that temperature for about 2 seconds after which it was quenched to 0°C. The specimen was then immediately cooled and deformed about 3% at 4.2°K. The total resistivity change during annealing from 0° to 170°C is only $0.97 \times 10^{-9}\ \Omega$ cm. About one-third of this recovers in region A. The recovery indicated by curve b has been shifted by about 20 degrees to lower temperatures in region B, but in region C the recovery is quite similar in both specimens. If an unquenched sample is deformed 3%, about $0.45 \times 10^{-9}\ \Omega$cm recovers between -20° and +170°C. As in Figure 4, there is no evidence for the occurrence of new peaks due to the deformation.

Recovery After Deformation

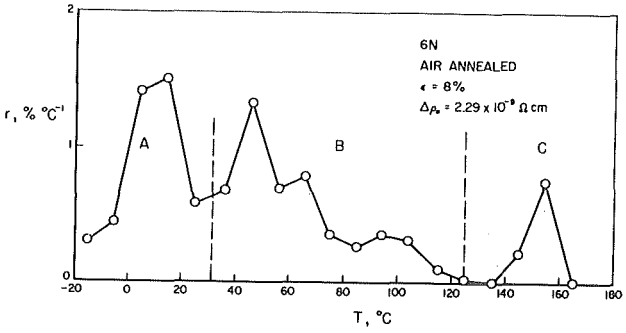

Figure 6
Recovery spectrum of 6N gold deformed 8% at 4.2°K.

The recovery spectrum of 6N gold deformed 8% in tension is plotted in Figure 6. The deformation was performed at 4.2°K after which the sample was slowly warmed up to -20°C before measuring the curve. An extensive recovery spectrum with 5 local maxima is observed between -20° and +170°C, and has been reproduced several times.

DISCUSSION

Substructure After Quenching

The present experiments on quenched gold are the first in which a substructure has been observed in the isochronal recovery of this system.

While this system has been studied more extensively than any other, only a few isochronal curves have been published, and none of them have been measured with the explicit objective of establishing whether or not a fine structure exists. Bauerle and Koehler[5] have measured the isochronal recovery of quenched gold, but in large temperature intervals of 20 degrees and with a long annealing time of 1 hour at each temperature. With such an annealing schedule, the fine structure could not have been observed in any case. Their recovery begins at about -40°C and is not finished at +90°C. Clarebrough, Segall, Loretto, and Haregreaves[7] have observed an isochronal behavior in agreement with the results of Bauerle and Koehler[5], but do not report further details. The isochronal curve shown by de Jong and Koehler[6] also shows one broad stage between 40 and about 150°C. The specimen was annealed for 3 hours at 40°C before this curve was measured in 10-minute periods at 20-degree intervals. These large temperature intervals and the long anneal at 40°C, would have precluded the observation of any substructure.

Schüle, Seeger, Schumacher, and King[8] measured several isochronal curves for 15 minute periods at irregularly spaced temperatures separated by 10 to 15 degrees. Recovery occurs between -40° and +150°C, but no substructure is observed. These measurements were carried out in liquid oxygen with a minimum detectable resistivity change of 3×10^{-11} Ω cm. This sensitivity which is more than an order of magnitude less than that of the present measurements at 4.2°K, would make the observation of substructure very difficult. It should also be pointed out that measurements designed to detect fine structure should use constant temperature intervals.

The present results are in agreement with previous conclusions[5-8] about the extent of the temperature range in which the recovery takes place. The observed substructure is not in conflict with these previous isochronal measurements. Rather, it supports the existing observations of a complex <u>isothermal</u> recovery behavior[1] in that it reveals explicitly the basis for this complexity to be due to the occurrence of several processes.

While this information seems promising for the ultimate objective of completely characterizing the nature and properties of vacancies in gold, more extensive experiments are needed before a detailed interpretation could be attempted. The present discussion will therefore be limited to a few qualitative remarks which seem justified by the presently available information. A detailed study of the problem is in progress in our laboratory.

Region B

More than 90% of the recovery of 6N gold quenched from about 700°C occurs between 35° and 125°C (region B). This is also the temperature range in which most of the isothermal studies have been performed.[1] Undoubtedly, the most often observed[14] migration energy of 0.70 eV is due to the defects which cause this recovery. Their migration energy is independent of the quenching temperature, the purity of the gold, and the properties of the sinks at which they disappear.[14]

Their identity, however, remains unknown, but from the recovery spectra it can be observed that multiple processes are involved.

If recovery processes are well separated, they will be observed as peaks in a recovery spectrum. If the temperature ranges in which they occur overlap considerably, the peaks will not be resolved. The precise shape of such a spectrum can depend very much on the exact annealing schedule. In region B, three maxima were observed in curve b of Figure 1 at 55°, 85°, and 105°C. The maximum at 85°C in curve a of the same figure is undoubtedly due to the same process as the peak at 85°C in curve b. Each of the two other maxima in curve b is determined by only one point. However, it is obvious from the shape of curve a around 60°C, that the process causing the local maximum at 55°C in curve b, is also present in curve a, although no peak is observed in this case. It is more difficult to decide whether the process which caused the maximum at 105°C in curve b, is also present in curve a, but it will be assumed for the moment that this is the case. Thus certainly two, and perhaps three processes are causing the recovery in region B. For the discussion these processes will be labeled (1), (2), and (3) starting at low temperatures.

In Figure 2 it is observed that the recovery in region B shifts to lower temperatures with increasing T_q. This observation is in agreement with the result of isothermal studies[5] where it was observed that the time $\tau_{\frac{1}{2}}$ required for 50% of the recovery to occur at a constant temperature, is reduced by a higher quenching temperature. This seems to be related to a larger probability for the formation of clusters if T_q is larger. These clusters are observed[15] as black spot defects when 5N gold is quenched from below 800°C and subsequently annealed at 100°C. The black spots are formed as a result of the precipitation of vacancy type defects and could act as sinks for (further) recovery which tends to shift this to lower temperatures. It was also observed that the formation of black spots is favored in impure gold as a result of heterogeneous nucleation at certain impurities.[16] In agreement with this, is the observation in Figure 3 that the recovery of the impure sample in region B occurs at lower temperatures than that of the pure sample, although both specimens were quenched from the same temperature. In this case one can identify the recovery maxima at 65° and 95°C of curve b with the processes (2) and (3). Process (1) is not observed as a peak, although there is an indication for its presence in the shape of the curve around 40° to 60°C. The temperature shift is also in agreement with the result of Ytterhus, Siegel, and Balluffi[17] that $\tau_{\frac{1}{2}}$ for isothermal recovery at 40°C after a 700°C quench, is smaller for samples having smaller resistivity ratios. The comparison of the two curves of Figure 3 is especially valid, since they were measured under identical conditions. The fact that $\Delta\rho_o$ is larger in curve b (4N) than it is in curve a (6N) could be the result of an increased equilibrium vacancy concentration at T_q due to a binding energy between vacancies and impurities.[18]

If three processes occur between 35° and 125°C, the question immediately arises why three different migration energies have not been observed in existing studies. This could be due to the fact that the actual values for the migration energies of these processes must be nearly the same. Since the three processes seem to respond in the same way to the addition of impurities, it is possible that they involve the migration of different defects to more or less the same sinks. Suppose that the main peak of curve b in Figure 1 due to process (2), has a migration energy of 0.70 eV, and that the relative locations of the three

maxima due to the three processes are only determined by the differences in migration energies. The energies corresponding to processes (1) and (3) can then be estimated to be about 0.64 and 0.75 eV respectively. These values are close to 0.70 eV, and it would be difficult to separate them experimentally. This should especially be true, since the relative contributions of processes (1) and (3) are less than that of process (2), at least for the cases studied here.

From the work of Kauffman and Meshii[19] one observes that the minimum and maximum values obtained for the migration energy E^M after a quench from 700°C are about 0.66 and 0.76 eV. E^M values determined by Ytterhus, Siegel, and Balluffi[17] lie between about 0.65 and 0.77 eV for defect resistivities less than 5×10^{-9} Ωcm, the range of the present investigation. In these cases, however, there is no systematic increase in E^M as recovery proceeds, but the variation is caused by random error. One observes in both experiments, however, that there is a trend of increasing energy with decreasing defect resistivity when one considers the entire range studied.[17,19] Extensive isochronal studies which cover this range are needed to investigate this aspect. It may very well be that the relative defect population in the three processes changes with quenching temperature.

The study of the influence of dislocation sinks on the recovery of quenched-in defects is difficult, since dislocations anneal out during the heating of the sample in order to quench it. If the dislocations are produced afterwards by plastic deformation, this is likely to alter the quenched-in defect structure. From Figure 4 one observes that the total amount of recovery has been reduced remarkably by 1.5% deformation, although plastic deformation by itself always increases the resistivity of pure gold. This observation can be explained by the sweeping up of quenched-in defects by moving dislocations.

Except for the plastic deformation in one of the samples (curve a) the two curves of Figure 4 were obtained under identical conditions. It appears that the recovery spectrum remains qualitatively the same after deformation. The peaks due to processes (2) and (3) are clearly resolved in both cases, but process (1) is not indicated in curve a.

The effect of a larger dislocation density on the recovery spectrum was presented in Figure 5, curve b. A larger dislocation density than that in the specimen of curve a (quenched only) must have resulted from the short annealing time (2 sec) at about 700°C prior to the quench of the deformed sample ($\epsilon = 7\%$) which was deformed again 3% after the quench. The recovery spectrum of this specimen (curve b) exhibits two peaks in region B with an indication for the occurrence of another process near 60°C. The recovery in this region occurs at lower temperatures than that of the undeformed sample quenched from approximately the same temperature (curve a). This recovery is likely to be produced by the same three processes (1), (2), and (3) in both curves. Their occurrence at lower temperatures in curve b (quenched and deformed) could then be explained by the larger density of dislocations acting as sinks for the defects. Ytterhus, Siegel, and Balluffi[17] quenched gold from 700°C and strained the samples between 0.75 and 1.0% at room temperature before measuring the isothermal recovery at 40°C. The observed $\tau_{\frac{1}{2}}$ is a factor of about 10 less for the strained samples. This was also interpreted as due to an increase in the dislocation sink density or possibly to additional precipitation at vacancy type debris produced by the deformation. The observed E^M values, however, remained the same[17] i.e., about 0.70 eV, which supports the conclusion that the same processes occur in region B of both curves of Figure 5.

From these discussions one can conclude that three processes (1), (2), and (3) occur between about 35° and 125°C in 6N as well as in 4N gold quenched from about 700°C and in 6N gold quenched from the same temperature and deformed a few percent. The present information does not allow a definite identification of the defects in these processes. However, the vacancy type defects in this range cannot be associated with impurities, since very similar recovery is observed in 4N and in 6N gold (Figure 3). The defects must therefore be single vacancies and/or some small vacancy clusters, including the divacancy. There are several possibilities, but the simplest one seems to be that tri-, di-, and single vacancies are involved. From the analysis of the self-diffusion data in gold by Stoebe and Dawson,[2] it appears possible that the migration energy of a single vacancy could be as low as 0.7 eV at low temperatures. Theoretical considerations lead to the conclusion that the migration energy of trivacancies could be close to that of the divacancy[20,21], and the divacancy should be more mobile than the single vacancy. The process at the highest temperature (process (3)) could therefore be due to single vacancies. Furthermore, since one expects that fewer trivacancies will be produced than divacancies during a quench from around 700°C, and the contribution of process (2) to the recovery in region B dominates that of process (1), these processes could be due to divacancies and trivacancies respectively.

Regions A and C

The recovery below about 35°C (region A) and above about 125°C (region C) amounts to less than 10% of the total recovery of 6N gold quenched from about 700°C. This recovery is therefore difficult to study. It appears to be more significant, however, in impure gold (see Figure 3 and Table 2), and is undoubtedly associated with impurities. Perhaps some highly mobile small vacancy cluster nucleated at impurities during the quench, anneals out in region A, while impurity trapped vacancies could be released in region C. This could explain the impurity dependence of the recovery in these regions. This dependence makes it unlikely that the defects annealing-out in region A are produced by uncontrolled plastic deformation during the quench. From Table 3 it follows, however, that the importance of the recovery in this region is somewhat greater in the quenched and deformed sample. Also, as has been observed in Figure 6, the largest peak after deformation occurs between -20° and about 35°C, the temperature range of region A. One cannot, therefore, exclude the possibility that part of the recovery in this region of the pure samples is due to plastic deformation.

Substructure After Deformation

The substructure observed in the recovery spectrum after deformation (Figure 6) is in general agreement with previous work by the author[12] in which the so-called stages c(-10° to +25°C) and d(25° to 90°C) were observed. Stage c is also present in Figure 6. Due to the fact that the previous experiments[12] were performed at 77° rather than at 4.2°K, the stages were less clearly resolved, and it now appears that stage d is actually a doublet as can be seen between 25° and 90°C in Figure 6. Upon close examination of the older data, one does observe an indication for this.[12]

Identification of the Defects

The temperature range of the present investigation covers the largest portion of Stage III (-60 to +100°C) and includes Stage IV (above about 100°C).

The recovery studied here occurs in the same temperature range as that after quenching. The most obvious difference between quenched and deformed samples is the difference in their dislocation sink density, but dislocations should not have a long range interaction with point defects.[22] Thus, if the same vacancy type defects are present in a deformed sample in a comparable concentration as that of the defects produced by quenching, one should be able to identify them. One expects these defects to occur between -20° and +170°C, the temperature range in which the quenched-in vacancy type defects disappear. The vacancy stages in a deformed sample could occur at slightly lower temperatures due to the larger dislocation sink density.

Perhaps the most direct indication so far that vacancy type defects are migrating in this temperature range after deformation is given by the experimental results of Korevaar[23] and Dawson.[12] These authors observed that the resistivity of quenched[23] as well as that of deformed[12,23] gold with a few atomic percent copper, increases strongly and then decreases during isochronal annealing in this temperature range using nearly the same schedule as in the present experiments. The large resistivity changes are due to changes in the degree of short range order of the alloys which are very likely caused by the migration of vacancy type defects.

The apparent activation energy values determined in Stage III by various authors do not preclude the vacancy type defects from occurring in this temperature range. Some of these results are given in Table 4.

TABLE 4
E^M Values Determined in the Temperature Range of Stage III

Investigator	Deformation	E^M(eV) for Stage III
Manintveld[24]	Straining, 6% in tension at -183°C	0.69 ± 0.06
Korevaar[23]	Straining, 15% in tension at -195°C	0.65 ± 0.04
Schüle, et al.[8]	Rolling, 50-85% reduction in thickness below -40°C	0.71 ± 0.02
Dawson[12]	Rolling, 83% elongation at -45°C	increasing from 0.6 to 0.8 as recovery proceeds

The value of Schüle, et al[8], with the narrow limits of error, was determined by the Meechan-Brinkman method and cannot be interpreted as the migration energy for the whole Stage III, as this is not due to a singly activated process.[12] One must also be careful with comparing results after rolling with those after straining. One can conclude, however, that the values in Table 4 are of the right magnitude for the migration of vacancy type defects to occur in Stage III when one compares these values with the 0.7 eV observed after quenching.[14] From previous work by the author it also follows that the E^M values increase as recovery proceeds at increasing temperatures in this stage.[12]

In Figure 7 the recovery curve b of Figure 5 is plotted together with the curve from Figure 6. Curve b in Figure 7 was measured on a sample which was first deformed 7%, heated at 700°C for 2 sec, quenched, and then deformed 3%. The dislocation density resulting from this treatment must have been larger than that in the other samples used for the quenching studies. It has been observed in Figure 5 that this results in a shift of the recovery in region B

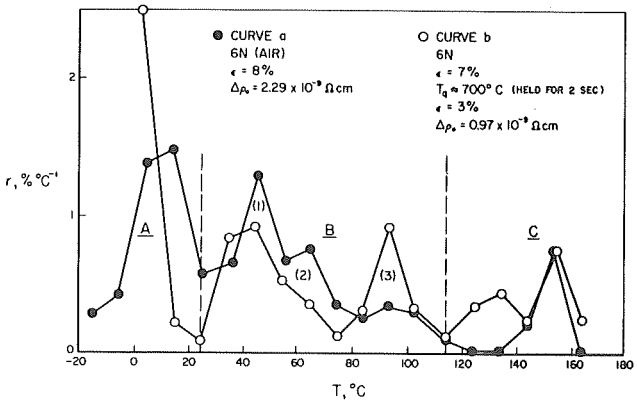

Figure 7
Curve a: Same as Figure 7.
Curve b: Same as curve b from Figure 5.

to lower temperatures, but the deformation did not produce new recovery peaks in this region. In view of the other observations discussed to show that vacancy type defects could anneal out in this temperature range in a deformed sample, it seems quite possible that the processes marked (1), (2), and (3) on the curves of Figure 7 are respectively the same in both cases. Their occurrence at approximately the same respective temperatures would, under this assumption, indicate that the total sink concentrations in both samples are about the same, which is not unreasonable. It is therefore suggested that in region B of the recovery spectrum of a deformed sample, tri-, di-, and single vacancies could become mobile just as was suggested for the recovery of a quenched sample. One observes in Figure 7 curve a, that the amount of recovery due to process (1) is larger than that of process (2), which is larger than that of process (3). The distribution is different in quenched samples (see for instance Figure 1). It is reasonable to expect that more small vacancy clusters will be produced by deformation than by quenching, since in all the models proposed for point defect production during deformation, the defects will occur in rows. With a positive binding energy between vacancies, one expects the formation of clusters from these rows.

The largest peak after deformation occurs in region A. It was suggested that in this region of the recovery spectrum of a quenched sample, small vacancy clusters, nucleated at impurities during the quench, could become mobile. It is possible that this recovery in a deformed sample is also due to small vacancy clusters which should be readily produced by deformation.

Little information is available about the recovery in region C of deformed gold. In Figure 7 it is observed that this recovery consists of one peak which occurs at the same temperature as one of the peaks observed after quenching. It is suggested therefore that this peak after deformation could also be due to the release of trapped vacancies.

CONCLUSIONS

The main results of the present study can be summarized as follows:

1. After quenching gold from about 700°C, an extensive recovery spectrum occurs upon annealing between -20° and +170°C. This recovery spectrum has a definite substructure.

2. In 6N gold more than 90% of this recovery occurs between about 35° and 125°C (region B).

3. Three processes (1), (2), and (3) occur in region B independent of the quenching temperature (between 680° and 763°C), the impurity concentration (in 4N and 6N gold), and the dislocation density (introduced by 3% deformation after the quench).

4. The processes (1), (2), and (3) shift to lower temperature with increasing quenching temperature, impurity concentration, and dislocation sink density.

5. It is possible that these processes are due to tri-, di-, and single vacancies respectively.

6. The amount of recovery below 35°C (region A) and above 125°C (region C) is increased by impurities. The low temperature region could be due to some highly mobile vacancy cluster nucleated at impurities during the quench, while the release of impurity trapped vacancies could cause the recovery in the high temperature region.

7. The recovery spectrum of 6N gold deformed 8% exhibits 5 peaks between -20° and +170°C. Three peaks occur between 35° and 125°C (region B) and could be due to the same processes (1), (2), and (3) which cause the recovery in this region after quenching.

8. The largest peak after deformation occurs below 35°C (region A) and could be due to some highly mobile small vacancy cluster, while the recovery above 125°C (region C) could involve the release of trapped vacancies.

ACKNOWLEDGMENTS

Thanks are due to Professor T. G. Stoebe for helpful discussions and for reading the manuscript.

REFERENCES

1. For a general review see the articles in "Lattice Defects in Quenched Metals," ed. R. M. J. Cotteril, M. Doyama, J. J. Jackson, and M. Meshii, Academic Press, N.Y. 1965.

2. T. G. Stoebe and H. I. Dawson, Phys. Rev. 166, 621 (1968).

3. T. Kino and J. S. Koehler, Phys. Rev. 162, 632 (1967).

4. C. G. Wang, D. N. Seidman, and R. W. Balluffi, Phys. Rev. 169, 553 (1968).

5. J. E. Bauerle and J. S. Koehler, Phys. Rev. 107, 1493 (1957).

6. M. de Jong and J. S. Koehler, Phys. Rev. 129, 49 (1963).

7. L. M. Clarebrough, R. L. Segall, M. H. Loretto, and M. E. Hargreaves, Phil. Mag. 9, 377 (1964).

8. W. Schüle, A. Seeger, D. Schumacher, and K. King, Phys. Stat. Sol. 2, 1199 (1962).

9. See for instance, G. W. Iseler, H. I. Dawson, and J. W. Kauffman, in "Lattice Defects and Their Interactions," ed. R. R. Hasiguti, Gordon and Breach, N.Y. 1967, pp. 653 and 681.

10. A van den Beukel, Acta Met. 11, 97 (1963).

11. A Seeger in "Radiation Damage in Solids," IAEA, Vienna, 1962, p. 101.

12. H. I. Dawson, Acta Met. 13, 453 (1965). See also Ph.D. Thesis, Delft, 1964.

13. J. W. Corbett, "Electron Radiation Damage in Semiconductors and Metals," Solid State Physics Suppl. 7, ed. F. Seitz and D. Turnbull, Academic Press, N.Y.1966.

14. See the review in reference 4.

15. R. M. J. Cotterill, Phil. Mag. 6, 1351 (1961).

16. R. M. J. Cotterill and R. L. Segall, Phil. Mag. 8, 1105 (1963).

17. J. A. Ytterhus, R. W. Siegel, and R. W. Balluffi, in "Lattice Defects in Quenched Metals," p. 679.

18. W. M. Lomer, in "Vacancies and Other Point Defects in Metals and Alloys," p. 79 (Inst. Metals Monograph and Report Series, London, Vol. 23, 1958).

19. J. W. Kauffman and M. Meshii, in "Lattice Defects in Quenched Metals," p. 83.

20. G. Schottky, Z. Physik 159, 584 (1960).

21. R. M. J. Cotterill and M. Doyama, in "Lattice Defects in Quenched Metals," p. 622.

22. J. Friedel, "Dislocations," Pergamon Press, New York, 1964.

23. B. M. Korevaar, Ph.D. Thesis, Delft (1960); Acta Met. 6, 572 (1958).

24. J. A. Manintveld, Thesis, Delft (1954); Nature 169, 623 (1952).

THE HETEROGENEOUS NUCLEATION OF TETRAHEDRA IN QUENCHED GOLD

I.A. Johnston, P.S. Dobson and R.E. Smallman

Department of Physical Metallurgy and Science of Materials,
University of Birmingham,
Birmingham, 15.

ABSTRACT

The influence of copper and magnesium impurities on the defect structure of quenched gold has been studied by electron microscopy. The magnesium additions resulted in an increase in the tetrahedra density but with higher impurity concentrations the nucleation of tetrahedra was suppressed in favour of dislocation loops. The efficiency of the impurities in promoting heterogeneous nucleation was much greater for magnesium where the observed effects were observed with concentrations of the order of parts per million whereas larger concentrations of copper of the order of a few percent are required.

From these results together with those of other workers it is concluded that divalent impurities are more efficient as nucleating agents than monovalent impurities. These conclusions are accounted for by a model in which divacancy-impurity atom interactions lead to enhanced tetravacancy formation because of attractive interactions between free and trapped divacancies, and the model also accounts for loop formation when a high impurity concentration is present. It is suggested that the high tetrahedra density observed in gold quenched from a reducing atmosphere is due to the presence of interstitial hydrogen and these predictions have been investigated by examining the structure of quenched gold which had previously been annealed in an atmosphere of air, carbon monoxide, or hydrogen.

INTRODUCTION

Recent experiments[1-5] have shown that the nucleation of tetrahedra in quenched gold is a heterogeneous process and that the size and density of the tetrahedra are determined by small impurity concentrations. Segall and Clarebrough[1] found that the distribution of tetrahedra depended on the quenching atmosphere and showed that a pre-quench oxidising treatment produced a low density of large tetrahedra whereas quenching from carbon monoxide resulted in an increase in density with an associated decrease in size. These observations were accounted for by postulating that the nucleating impurity centres were neutralised by internal oxidation. Following these observations a number of workers have studied the effects of added impurities on the nucleation of tetrahedra. Meshii[2] studied the nucleation of tetrahedra as a function of the immediate post-quench ageing treatment and found that nominally pure gold and gold containing up to 0.5 at.% of silver, copper or iron gave identical results. The effects of small impurity concentrations on vacancy clustering were studied by Siegel[3] using electron microscopy and electrical resistivity who showed that air annealing resulted in a decrease in the density of tetrahedra, but in contrast to the work of Meshii found that the addition of about 20 ppm. of copper generally caused a marked increase in tetrahedra density although similar doping concentrations of iron and nickel appeared to have no effect. More

recently Quader and Dodd[4] have reported that small additions (~0.1 at.%) of cadmium and zinc induce strong heterogeneous nucleation and a similar large effect has also been observed for magnesium[5]. In addition to promoting enhanced nucleation of tetrahedra, these impurities in greater concentration also result in the formation of dislocation loops.

In this paper the effect of copper and magnesium on the nucleation of tetrahedra in gold is re-examined together with further experiments on the effects of the pre-quench annealing atmosphere which lead to a nucleation model involving di-vacancy - impurity trapping.

EXPERIMENTAL

The starting material used in this work was Johnson Matthey 99.999% pure gold and dilute alloys containing copper or magnesium were made by sealing and melting measured amounts of gold and solute element in a silica tube under vacuum, followed by an homogenising anneal at 900°C. The composition of the alloys after quenching was determined by mass spectrographic analysis to be Au-1500 ppm. Cu, Au-200 ppm. Mg, and Au-500 ppm. Mg, and no pick-up of silicon during the preparation was detected. All the specimens were rolled into strip 0.12 mms. thick and resistance heated in vacuum until a molten zone appeared and then automatically quenched into iced brine. Since it is well established[6] that the final distribution of

tetrahedra is strongly influenced by the immediate post-quench ageing treatment, care was taken to ensure that the same pre-ageing and ageing treatments were used for each series of comparative experiments. Generally the specimens were pre-aged at 0°C for 5 minutes and aged in boiling water for 1 hour. To study the effect of the pre-quench annealing atmosphere the specimens were annealed at 950°C in either air, a mixture of 10% hydrogen and 90% nitrogen or carbon monoxide. The carbon monoxide was supplied by Air Products and contained 8 ppm. of hydrogen. Electron microscope foils were prepared in the usual cyanide electrolyte and examined in an A.E.I. EM6G.

RESULTS

The effect of magnesium additions on the defect structure of quenched gold is illustrated in Fig. 1.

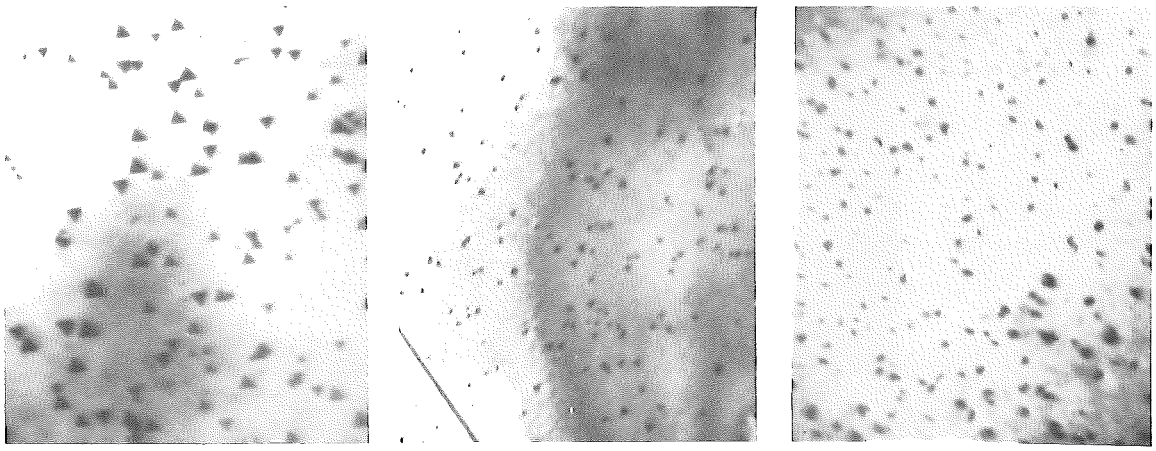

Fig. 1.

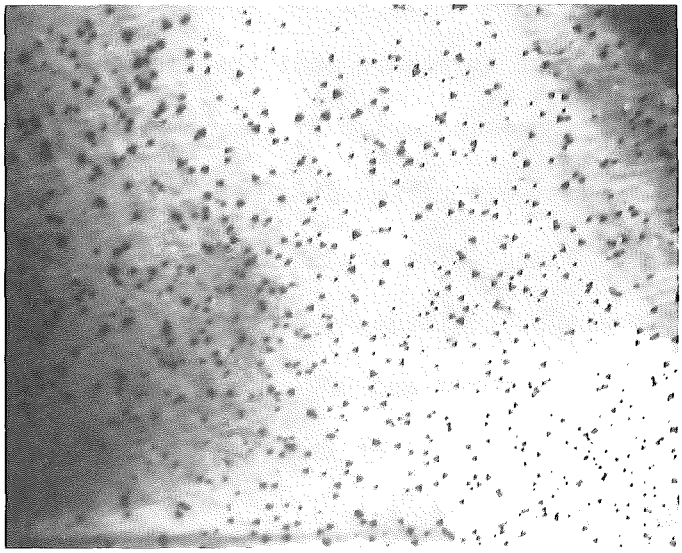

< 6 ppm Cu

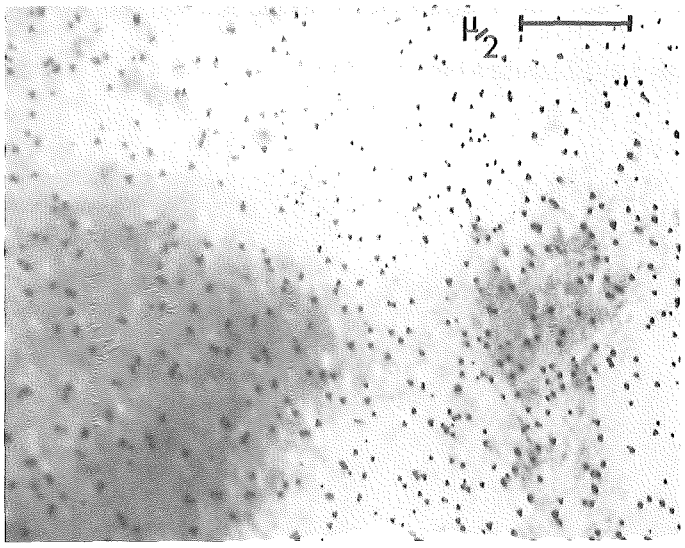

> 1000 ppm Cu

Quenched Gold

Fig. 2.

From measurements on up to 20 random areas remote from grain boundaries the arithmetic mean tetrahedron side length was found to be 380 ± 20Å in the as-received gold compared with 160 ± 20Å in the alloy containing 200 ppm. of magnesium with a corresponding increase in the tetrahedra density. However the addition of 500 ppm. of magnesium completely suppressed the nucleation of tetrahedra and the excess vacancies precipitated as dislocation loops about 200Å in diameter and of roughly the same density as that of the tetrahedra in the 200 ppm. alloy.

The effect of copper impurities on the nucleation of tetrahedra was examined by comparing a gold alloy containing 1500 ppm. of copper with the as-received gold which was shown by spectrographic analysis to contain approximately 4 ppm. of copper. However after quenching from vacuum and being held at the quenching temperature for less than 30 seconds to ensure that no oxidation of the impurity occurred, no detectable difference in the size and density of the tetrahedra was observed between the doped and pure gold (Fig. 2).

Annealing the pure gold in air for 48 hours at 950°C resulted in a large decrease in the density of tetrahedra from (1.2 ± 0.2) x 10^{14} cm.$^{-3}$ in the quenched as-received gold to (0.2 ± 0.2) x 10^{14} cm.$^{-3}$ in the specimens pre-annealed in air. After the air anneal some specimens were annealed in carbon monoxide for 30 minutes at 950°C and subsequently quenched from vacuum. As shown in Fig. 3, the carbon monoxide treated gold contained a higher density of tetrahedra by a

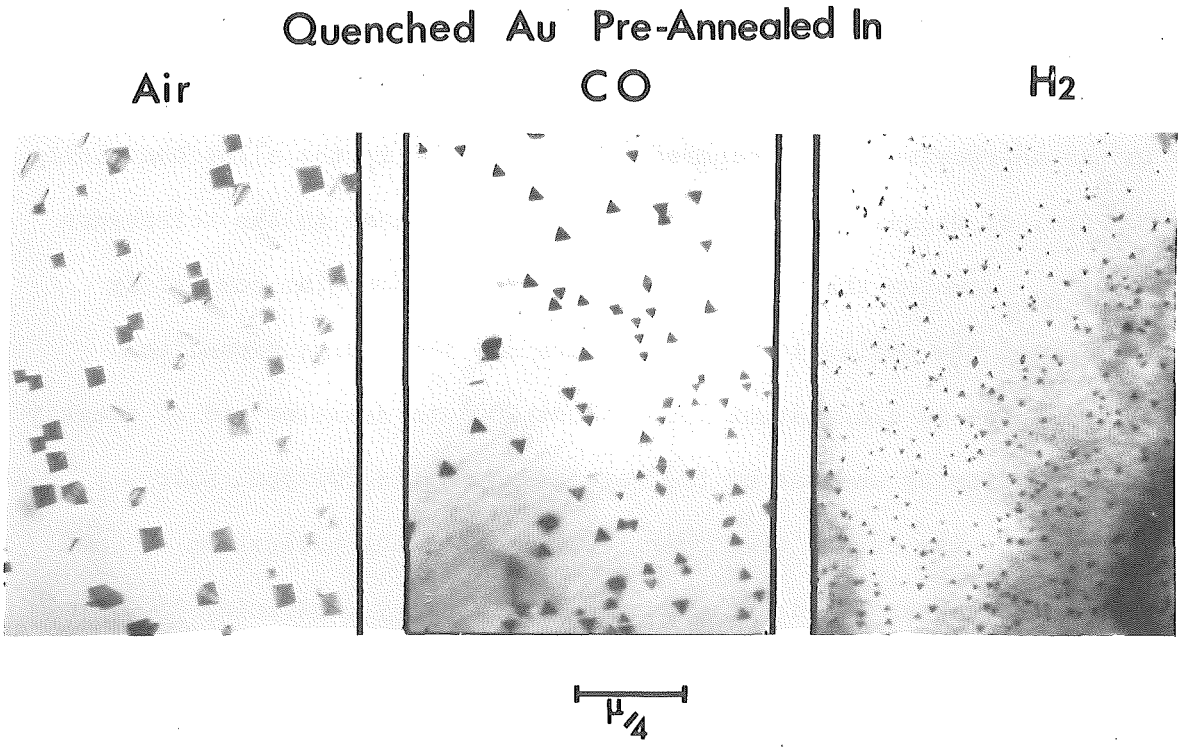

Fig. 3.

factor of approximately eight than the air annealed specimens. A further six to eightfold increase in the density of tetrahedra to $(1.9 \pm 0.2) \times 10^{14}$ cm.$^{-3}$ was observed on quenching the carbon monoxide treated gold from a 10% hydrogen atmosphere after being held at the quenching temperature for 3 minutes. The mean tetrahedra edge length for the specimens treated in air, carbon monoxide and hydrogen were 810 ± 20Å, 280 ± 20Å and 116 ± 20Å respectively. The density of tetrahedra in the quenched gold pre-annealed for 1 hour at 950°C in the hydrogen atmosphere was $(8.1 \pm 0.5) \times 10^{14}$ cm.$^{-3}$.

In addition to stacking fault tetrahedra three dimensional voids were also observed in the quenched gold specimens which although comprising only about 1% of the tetrahedra density followed the general tetrahedra distribution pattern with respect to the different annealing treatments. The hydrogen treated gold contained a relatively high density (10^{12} cm.$^{-3}$) of small octahedral voids whereas the air annealed specimens contained a lower density of much larger voids together with occasional large Frank loops (Fig. 4).

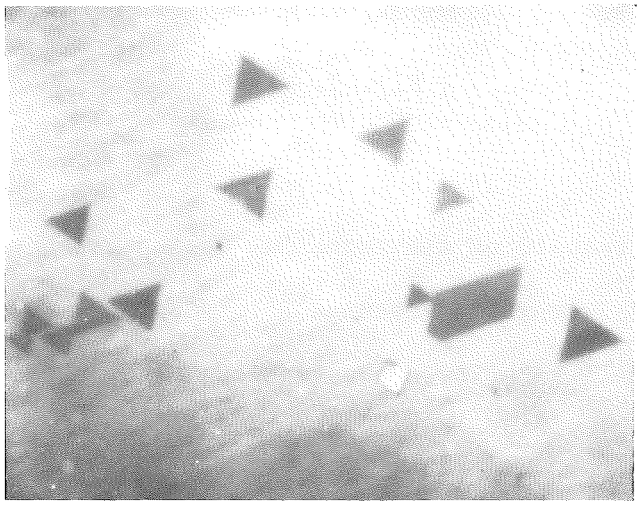

Fig. 4.

The air annealed specimens also contained large voids elongated along [110] directions (Fig. 5) in addition to the usual octohedral voids.

"Cigar" Voids In Quenched Gold

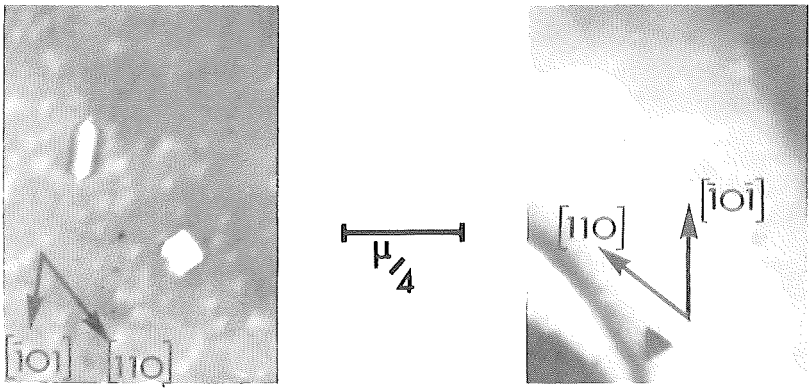

Fig. 5.

DISCUSSION

The results of the magnesium doping experiments together with the previously reported results[4] of doping with zinc and cadmium indicate that small impurity concentrations of divalent impurities are very effective in promoting the heterogeneous nucleation of tetrahedra. However the results also show that further increase in the impurity concentration causes the nucleation of tetrahedra to be suppressed and the excess vacancies to be precipitated as dislocation loops. No detectable difference in the distribution of tetrahedra was observed between the as-received gold and a gold alloy containing 1500 ppm. of copper and these results are thus in agreement with the observation of Meshii[2]. Concentrations of copper of an order of

magnitude greater than that used in the present work (4%) have however been shown to result in the enhanced nucleation of tetrahedra together with dislocation loops and helices[7].

The heterogeneous nucleation of tetrahedra is due to an interaction between vacancies and impurity atoms which may arise from either electrostatic fields or strain fields associated with the solute atoms. The electrostatic binding energy is proportional to the valency of the impurity atom[8] and provided that this is greater than the valency of gold it is to be expected that electrostatic effects will be the dominant contribution to vacancy-impurity binding. The strong effects of the divalent impurities is evidence for this general type of model whereas the relatively weak effects of copper are in accord with a much smaller interaction due to lattice strain.

Quader and Dodd[4] measured the activation energy for the nucleation of tetrahedra and obtained a value of 0.42 eV for zinc doped gold compared with 0.28 eV for pure gold whereas the activation energy for loop nucleation in the zinc doped gold was much higher at 0.7 eV. The values obtained in this work indicate that the migration of the divacancy controls the nucleation of tetrahedra and that the increase in the activation energy in the presence of zinc impurities is due to divacancy-impurity binding. The value of 0.7 eV observed for loop nucleation may also indicate that the migration of mono-vacancies is controlling this process. It is generally accepted that the nucleus

of a stacking fault tetrahedra contains six vacancies which is formed by the combination of a divacancy with a tetravacancy and that the final tetrahedra density is determined by the concentration of tetravacancies[9]. The tetravacancy itself is most probably formed by the combination of two divacancies since immediately after quenching the specimen contains relatively immobile impurities and mono-vacancies together with highly mobile divacancies. It is proposed therefore that the defect primarily responsible for the nucleation of tetrahedra is the divacancy and that the effects of small alloying additions are due to divacancy-solute atom interactions.

The divacancy is doubly negatively charged with respect to the matrix and will be attracted to a solute atom containing excess positive charge. Consequently there will be a strong attractive interaction between divacancies and divalent impurities which will lead to a proportion of the divacancies becoming immobilised. Because of their reduced net negative charge the combination of the immobilised divacancies with free divacancies is more likely to occur than the combination of two free divacancies in analogy with the impurity enhanced re-combination of electrons and holes in semi-conductors. By the same argument combination of the tetravacancy-solute atom complex with a further divacancy is enhanced and since the defects are not generally on the same crystallographic plane[10], three dimensional tetrahedra nuclei are formed. The density of nuclei will depend on the relative

concentrations of mobile and trapped divacancies which are determined by the solute concentration and further increases in solute content will eventually lead to the state where the majority of the divacancies are immobilised. In this situation the nucleation of defects will be determined by the combination of monovacancies with the immobilised divacancies which is more likely to lead to two dimensional nuclei than the divacancy-divacancy interactions.

This model accounts for the experimental results on the effects of magnesium where an initial increase in the density of tetrahedra was observed followed by the suppression of tetrahedra nucleation and the occurrence of dislocation loops in about the same density. The monovalent impurities have similar effects on nucleation to the divalent impurities but much higher solute concentrations are required due to their relatively small interaction with divacancies.

The concept of strong electrostatic interactions between divacancies and solute atoms leads to an alternative explanation to that of Segall and Clarebrough[1] of the effects of the pre-quench annealing atmosphere on the tetrahedra distribution. These workers showed that a reducing treatment following an oxidising treatment restored the tetrahedra density and concluded that previously oxidized impurities had thereby been reduced. However, spectrographic analysis of our as-received gold showed that small quantities (5 ppm.) of calcium, silicon and aluminium were present which would give rise to

enhanced nucleation but which would be internally oxidised during air annealing. The occurrence of the elongated voids in air annealed specimens suggests that oxide particles are present since similar elongated voids have been observed in quenched aluminium[11] and copper[12] where the presence of a small particle at one end of the void is clearly visible. However the oxides of these impurities will not be reduced by annealing at 1000°C in hydrogen or carbon monoxide[13] whereas the oxides of impurities such as iron, nickel and cobalt, which have little effect on nucleation, can be reduced in hydrogen at 1000°C, accounting for the observed resistivity changes. The increased density of tetrahedra observed after pre-quench reducing treatments is therefore more likely to arise as a consequence of the presence of hydrogen than the presence of reduced impurities. A divacancy associated with a proton has a greater probability of combining with a second divacancy, due to the reduced electrostatic repulsion, than has a free divacancy and thus the nucleation of tetrahedra is enhanced. The divacancy-hydrogen complex is also mobile which will allow tetrahedra to be nucleated irrespective of the hydrogen concentration and precludes the nucleation of loops. The results show that annealing in hydrogen results in an increase in the density of tetrahedra but the fact that a smaller increase was also observed following an anneal in carbon monoxide is notconclusive to either mechanism, since the carbon monoxide contained hydrogen as an impurity.

ACKNOWLEDGEMENTS

The authors wish to thank Professor G.V. Raynor F.R.S., for laboratory facilities, Mr. M.H. Loretto for useful discussion and the Science Research Council for a studentship for one of us (I.A.J.).

REFERENCES

1. Segall R.L. and Clarebrough L.M., (1964), Phil. Mag., 9, 865.

2. Meshii M., (1965), 'Lattice Defects in Quenched Metals', (Academic Press, New York,) p.387.

3. Siegel R.W., (1966), Phil. Mag., 13, 337.

4. Quader, M.A. and Dodd R.A., (1968), Phil. Mag., 17, 575.

5. Johnston I.A., Dobson P.S., and Smallman R.E., (1968), Phil. Mag., 17, 1289.

6. Mori T.H. and Meshii M., (1964), Acta Met., 12, 104.

7. Dobson P.S., reported by Smallman R.E., (1965), 'Lattice Defects in Quenched Metals' (Academic Press, New York), p.439.

8. Damask A.C. and Dienes G.J., (1963), 'Point Defects in Metals', (Gordon and Beach).

9. DeJong M., and Koehler J.S., (1963), Phys. Rev., 129, 40, 49.

10. Kiritani M., (1964), J. Phys. Soc. Jap., 19, 618, 1266.

11. Westmacott K.H., Smallman R.E., and Dobson P.S., (1968), Met. Sci. J. in press.

12. Johnston I.A., (1968), M.Sc. Thesis, Birmingham University.

13. Richardson F.D. and Jeffes J.H.E., (1948), J. Iron Steel Inst. 160, 261.

Vacancy-impurity atom interaction in Au-Pt dilute alloy*

A.Camanzi†, N.A.Mancini+, E.Rimini+, G.Schianchi†
†Istituto di Fisica dell'Università,Parma, Italy
+Istituto di Fisica dell'Università,Catania,Italy

Abstract

An experimental investigation has been carried out on vacancy-impurity atom interaction in Au+1 at% Pt alloy by quenching and aging experiments and by electron-microscope observations. A similar investigation has been carried out in 99.999% pure Au.

From the experimental results obtained it is possible to confirm that the interaction between the Pt atom and the vacancy is repulsive. The difference between the activation energy for formation of vacancies in Au+lat.%Pt and in 99.999 Au is +0.13±0.04 eV, while the difference between the activation energy for vacancy migration is -0.08±0.04 eV.

In the electron microscope observations a higher number of faulted loops are found in the Au+lat.% Pt specimens than in 99.999 Au specimens.

Introduction

The impurity-atom-vacancy binding energy has been determined by quenching and aging experiments in gold and in aluminium dilute alloys by several authors[1]). The binding energy gives some information about the diffusion of solute atoms in dilute alloys. In almost all cases the experiments show a positive binding energy; there are no similar experiments on dilute alloys,in which the existence of a negative binding energy has been established, for example, by diffusion experiments.

The gold-platinum system is well suited to such an investigation. The activation energy for diffusion of platinum in gold is

---

*Work supported by Gruppo Nazionale di Struttura della Materia del C.N.R.

about 1 eV larger than the self-diffusion energy in gold[2],and the charge on the platinum atom in gold(determined by magnetic measurements) is negative[3], i.e. of the same sign as the lattice vacancy. The change in the vacancy formation energy in the alloy is useful in comparing the Lomer[4] approximation for the total concentration of vacancies in a dilute alloy with the Shapink[5] approximation.

As a result of the above considerations it was decided to carry out some quenching and aging experiments and some electron microscope observations in Au-Pt alloys.

Experimental

Quenching and aging experiments were carried out on 0.12 mm diameter wires of Au+lat.%Pt and Au of 99.999% purity.The wires, resistance heated, were quenched by water from temperatures ranging between 500°C and 750°C.

After the determination of the resistance change on quenching from 700°C the wires were again resistance heated for annealing. The annealing temperatures ranged from 70°C to 150°C. Both annealing and quenching temperatures were determined during resistance heating by comparing the observed resistance of the specimen at that temperature with the annealed state at 20°C.

The complete measurements were carried out by comparing the resistance of the specimen after each of several temperature treatments, with the dummy specimen.

The wires were 16 cm long and the central portion (6-7 cm)was used for the measurements. The potentiometric contacts were made by spot welding two wires of the same materials but of less diameter.

All the measurements were carried out at room temperature.

For the electron microscope observations, thin foils 50μm thickness and 1 cm square, of Au+lat.%Pt and 99.999 Au were quenched from 940°C, after a suited pre-annealing, by sudden and forced immersion into a $CaCl_2$ bath at -5°C. The pre-aging time at -5°C was 1 min for all the specimens.

The quenched specimens were annealed respectively at 100°C

and 200°C for 1 hour. After this treatment the specimens were electropolished and then examined with a Siemens Elmiskope 1A at 100 kV. After any observation each specimen was heated by the beam and the thickness determined by measuring the slip trace wide. The thickness ranged between 800 Å and 2000 Å.

Results

Fig.1 shows the quenching results for Au+1 at.%Pt and Au 99.999 purity wires. $\Delta\rho$ is the quenched-in resistivity increment and $\rho_{20°C}$ is the resistivity of the wires. The straight-lines have been obtained as the best-fit of the experimental

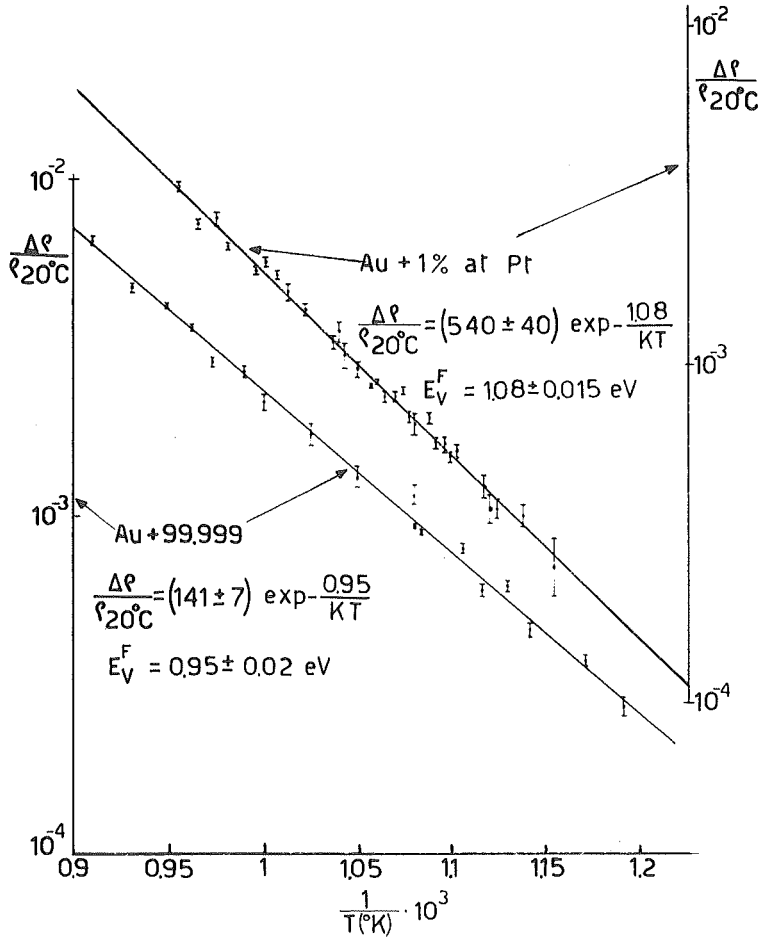

Fig.1 - Quenched resistivity in Au+1 at.% Pt and in Au 99.999 wires.

data and the results are tabulated below:

Au+1 at.%Pt $\quad \frac{\Delta\rho}{\rho_{20°C}} = (540\pm40)\exp(-\frac{1.08}{kT}) \quad E_V^F = 1.08\pm0.015$ eV

Au 99.999 $\quad \frac{\Delta\rho}{\rho_{20°C}} = (141\pm7)\exp(-\frac{0.95}{kT}) \quad E_V^F = 0.95\pm0.02$ eV

The activation energy for vacancy-formation is larger in the Au+1 at.%Pt alloy than in pure gold by 0.13±0.04 eV.

Fig.2 shows the isochronal annealing of the quenched-in resistivity respectively of Au+1 at.%Pt and 99.999 Au wires both quenched from 700°C and heated at different temperatues for 10 min. As it is seen in fig.2 the annealing out of the quenched-in resistivity occurs in one stage for both specimens,this stage being centred respectively at 90°C for the Au+1 at.%Pt specimen and at 110°C for the pure gold specimen. Thus the activation energy for vacancy-migration should be less in Au+1 at.%Pt than in Au 99.999.

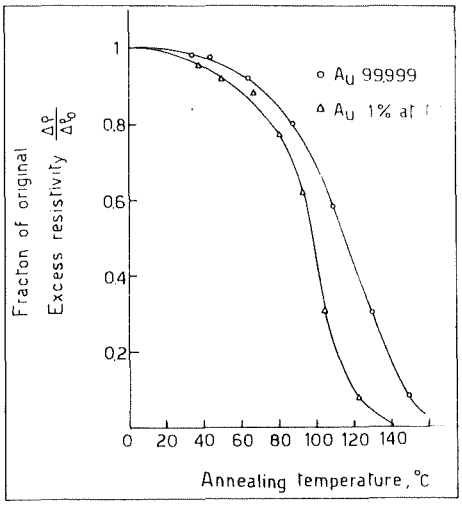

Fig.2 - Isochronal annealing of Au 99.999% and Au+1 at.%Pt,both quenched from 700°C and annealed at each temperature for 10 min.

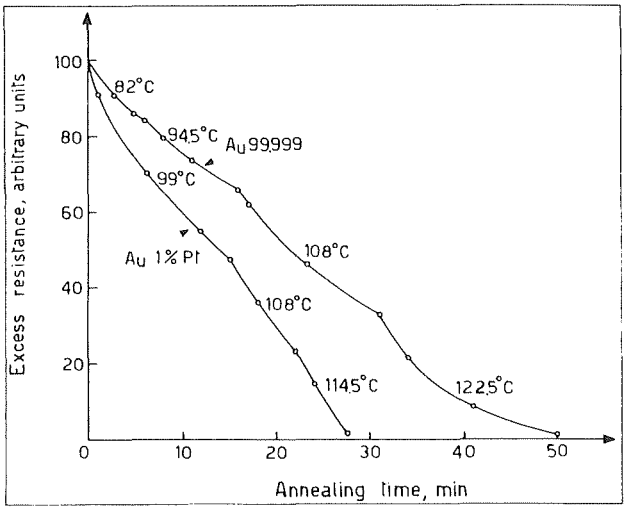

Fig.3 - Determination of the migration energy for Au 99.999 and Au+1 at.%Pt by the change-in-slope.

Two methods were used to determine the activation energy vacancy migration[6]):

i) isothermal annealing at different temperatures

ii) ratio of the slopes after the sudden alteration of the annealing temperature during the annealing of the specimen.

The activation energy is computed by the latter method using the formula:

$$E_V^M = \frac{k\, T_1 T_2}{T_2 - T_1} \log \frac{R_2}{R_1}$$

where R_1 and R_2 are the istantaneous annealing rates at temperature T_1 and T_2.

The values obtained by this method are,

for Au 99.999 $E_V^M = 0.78 \pm 0.02$ eV

for Au+1 at.%Pt $E_V^M = 0.71 \pm 0.02$ eV

The difference between these two values is 0.07±0.04 eV.

Fig.4a) shows with a semilogarithmic scale the time t_i as a function of 1/T, for several cross-cuts in the isothermal annealing curves (not reported here), for 99.999 Au and, in fig.4b for Au+1 at.%Pt specimens. The cuts have been made at 0.7, 0.5, 0.3 fractions of the quenched-in resistivity initial increment.

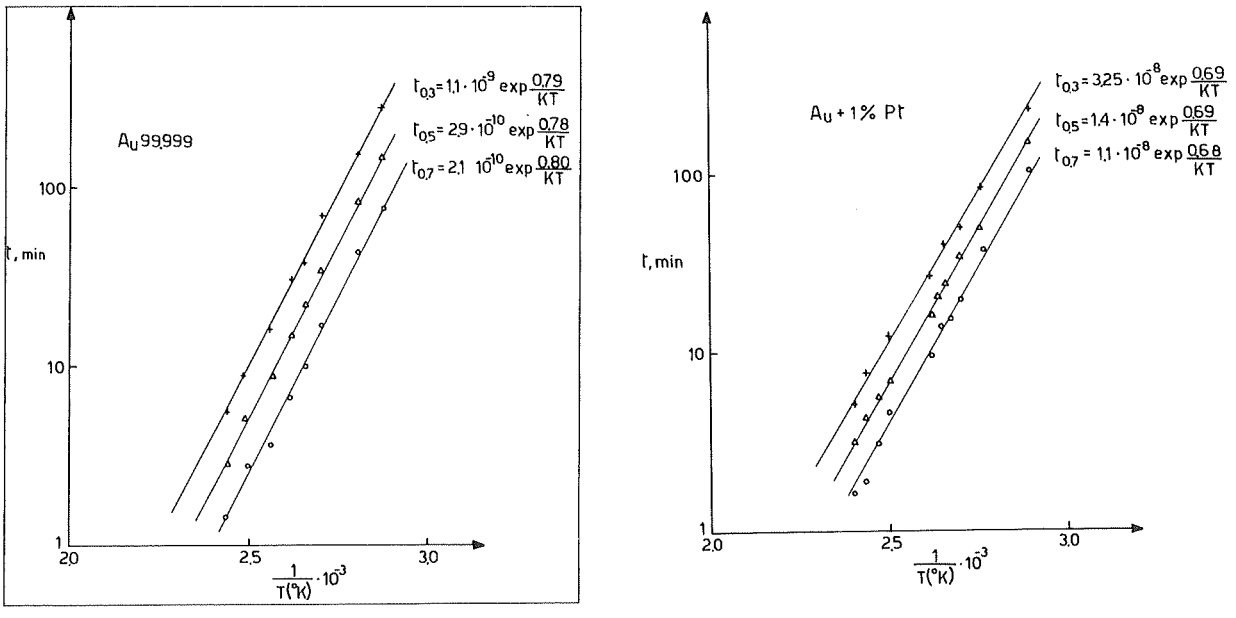

a) b)

Fig.4.- a) Determination of the migration energy for Au 99.999 by the cross-cut procedure for isothermal annealing.

b) Same as a) but for Au+1 at.% Pt.

The straight lines, obtained by best-fit of the experimental data,are parallel and this is check of the assumption taht a single process with a constant activation energy is operative.

The results are tabulated below:

Au 99.999	$t_{0.3} = 1.1 \cdot 10^{-9}$	exp (0.79/kT)	E_V^M = 0.79±0.02 eV
	$t_{0.5} = 2.9 \cdot 10^{-10}$	exp (0.78/kT)	0.78±0.02 eV
	$t_{0.7} = 2.1 \cdot 10^{-10}$	exp (0.80/kT)	0.80±0.02 eV
Au+1 at.%Pt	$t_{0.3} = 3.25 \cdot 10^{-8}$	exp (0.69/kT)	0.69±0.02 eV
	$t_{0.5} = 1.4 \cdot 10^{-8}$	exp (0.69/kT)	0.69±0.02 eV
	$t_{0.7} = 1.1 \cdot 10^{-8}$	exp (0.68/kT)	0.68±0.02 eV

The computed values for the activation energy are E_V^M = = 0.79±0.02 eV for 99.999 Au, E_V^M = 0.69±0.02 eV for Au+1 at.%Pt, the difference is 0.1±0.04 eV.

Figs. 5a) and 5b) show micrographs of typical zones in Au+1 at.%Pt and 99.999 Au respectiyely, quenched from 940°C to -5°C and aged 1 h at 100°C.

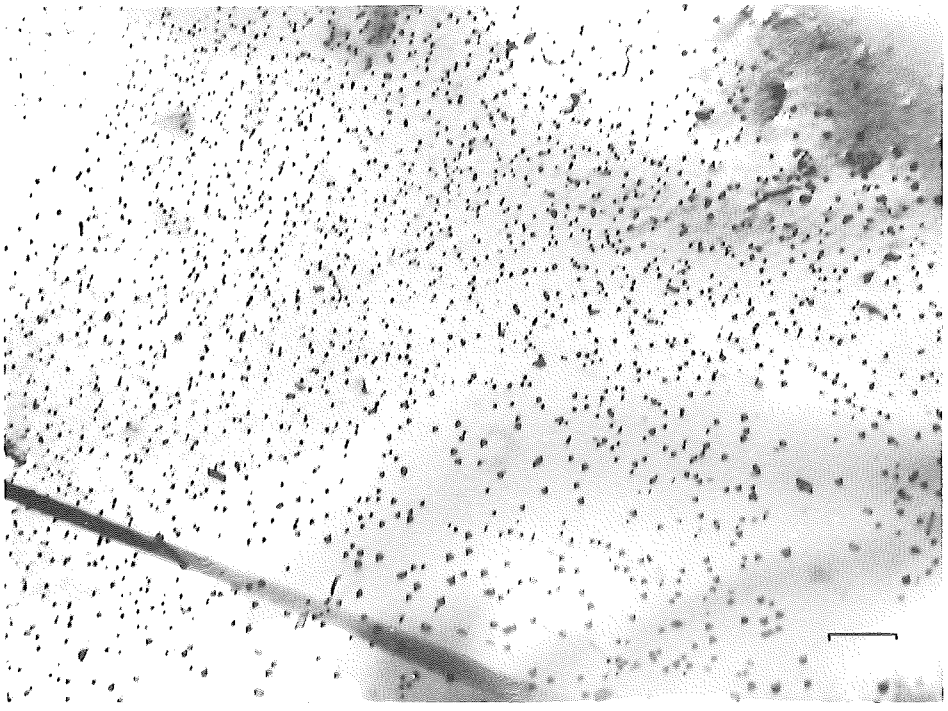

Fig.5.- a) Micrograph showing stacking-fault tetrahedra in Au+1 at.%Pt quenched from 940°C to -5°C and aged 1h at 100°C. $C_T \simeq 3 \cdot 10^{15}/cm^3$. The beam direction is near to [100] and the marking indicates 2500 Å.

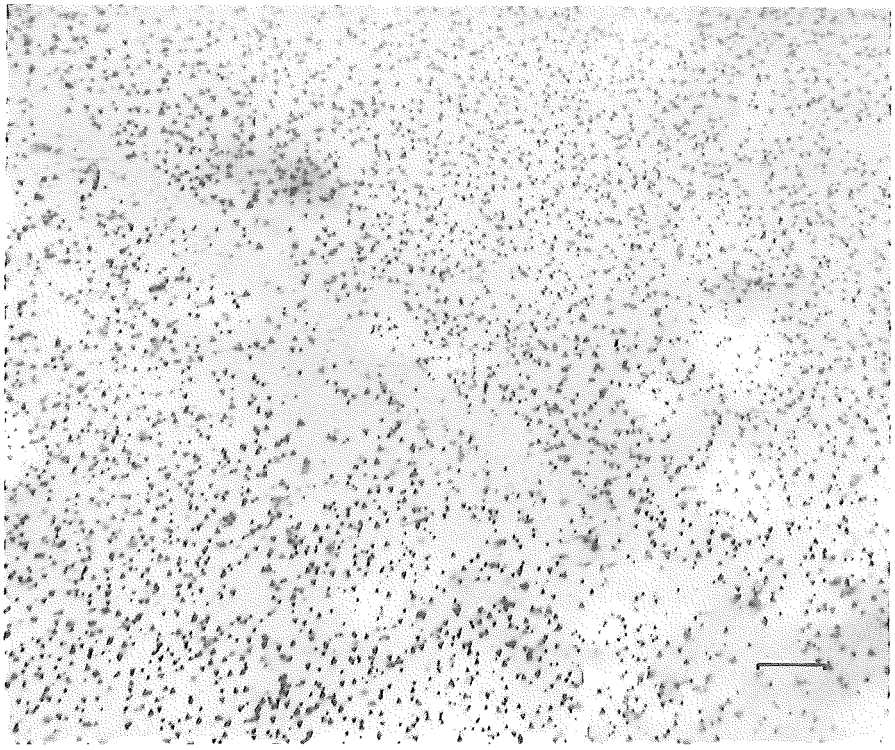

Fig. 5 b) same as a) but for 99.999 Au specimen. $C_T \simeq 4 \cdot 10^{15}/cm^3$. The beam direction is close to [110] .

The micrographs 6a) and 6b) show typical zones in Au+1 at.%Pt and 99.999 Au respectively, aged 1h at 200°C.

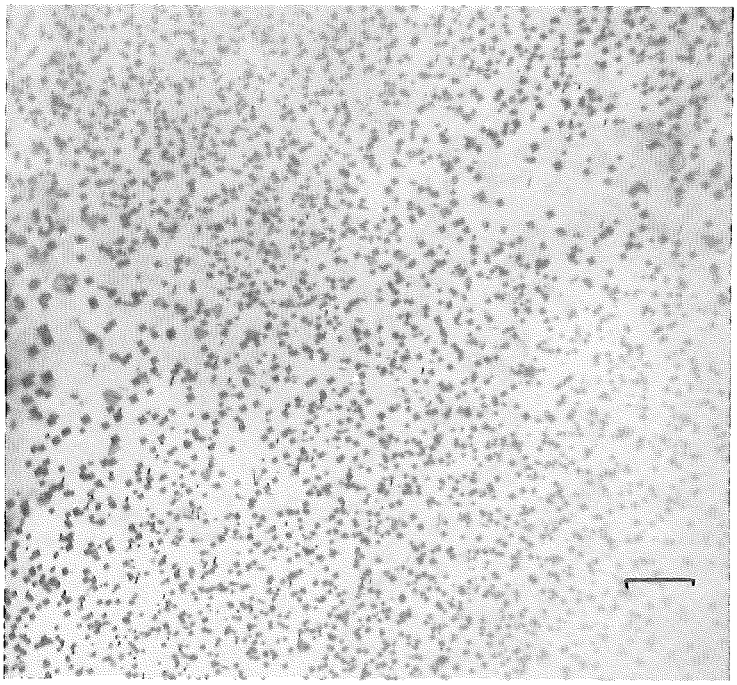

6a)

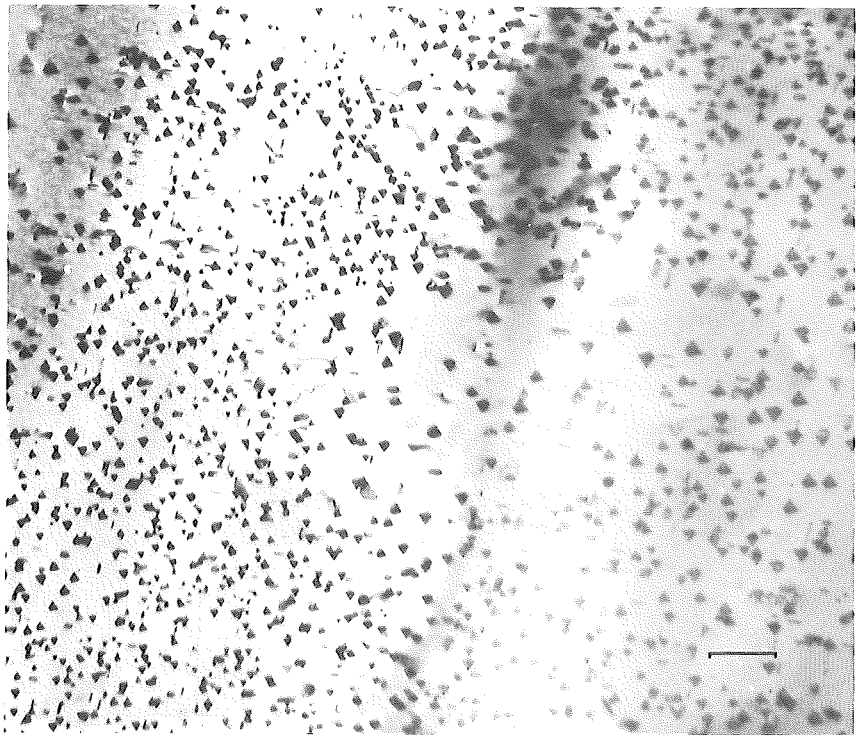

6b)

Fig.6.- a) Stacking fault tetrahedra and faulted loops in Au+1 at.%Pt quenched from 940°C to -5°C and aged 1h at 200°C. $C_T \simeq 2 \cdot 10^{15}/cm^3$. The beam direction is close to [100] and the marking indicates 2500 Å.
b) same as a) but for 99.999 Au. $C_T \simeq 2 \cdot 10^{15}/cm^3$. The beam direction is close to [100].

In Fig.7 there are large faulted and unfaulted loops observed in a zone of a Au+1 at.%Pt specimen, aged at 200°C for 1 hour.

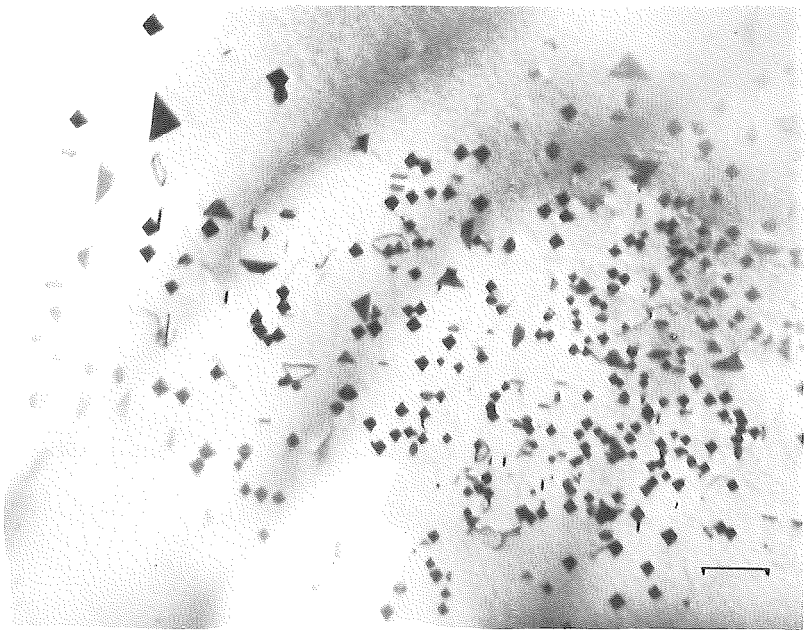

Fig.7. - Stacking-fault tetrahedra, large faulted and unfaulted loops in Au+1 at.%Pt quenched from 940°C to -5°C and aged 1h at 200°C. The beam direction is close to [100] and the marking indicates 2500 Å.

The results are summarized in the Table 1.

Table 1

Specimen type	Aging temperat.	Max.density of SFT/cm^3	Aver.dens of SFT/cm^3	Aver.% fault	Max.% faulted
99.999 Au	100°C	$4 \cdot 10^{15}$	10^{15}	0.5	2
Au+1 at.%Pt	100°C	$3 \cdot 10^{15}$	10^{15}	3	26
99.999 Au	200°C	$14 \cdot 10^{15}$	$6 \cdot 10^{14}$	1	2
Au+1 at.%Pt	200°C	$2.4 \cdot 10^{15}$	$4 \cdot 10^{14}$	10	15

It is possible to conclude from these results that the size and density of the tetrahedra in Au+1 at.%Pt are not substantially different with respect to pure gold.

In doped Au, however, it is possible to observe a larger number of faulted loops and a larger "diffusion distance" from grain boundaries (∿2μm) (fig.8) as compared to pure gold (0.5 μm) in the same experimental conditions.

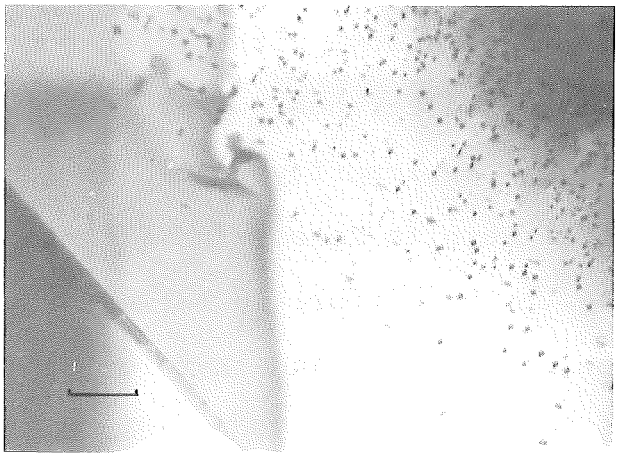

Fig.8.- Large denuded zone in Au+1 at.%Pt quenched from 940°C to -5°C and aged 1 h at 200°C. The marking indicates 0.7 μ.

Discussion

From the above results we may conclude that the interaction between a platinum atom and a vacancy, in gold, is repulsive. In the Lomer approximation[4]) the total vacancy concentration in a dilute alloy at thermal equilibrium is given by

$$C_t = A \exp\left(-\frac{E_V^F}{kT}\right)\left|1-12C_i+12C_i\exp\left(\frac{E_{V_i}^B}{kT}\right)\right| \qquad 1)$$

Where A is the preexponential factor, E_V^F is the activation energy for vacancy formation, C_i is the solute concentration, $E_{V_i}^B$ is the vacancy-impurity binding energy. The previous relation does not give any result for negative $E_{V_i}^B$, because large values of $E_{V_i}^B$ (-0.2, -0.3 eV) change the activation energy by

some thousandths of an eV with respect to that of the pure metal. Shapink[5]) has derived, on the Bragg-Williams approximation the following equation for C_t

$$C_t = A \exp(-\frac{E_V^F}{kT}) \exp(\frac{12E_{V_i}^B C_i}{kT}) \qquad 2)$$

with the same meaning of the symbols of 1). Equation 2)allows for the determination of negative values of $E_{V_i}^B$. The validity of 2) may be determined by measuring the activation energy for vacancy formation (E_V^{Fa}) in alloys with a different impurity concentration, because the difference between E_V^{Fa} and E_V^F should be proportional to the impurity concentration. From 2) and from our experimental results we obtain $E_{V_i}^B$=-1 eV. This value is rather larger compared with the difference between the activation energy for diffusion of Pt in Au and that for self--diffusion in Au, which is of the order of 1 eV, because the change in the activation energy for migration of a vacancy nearest neighbour to an impurity atom contributes to this difference_.

The annealing-out of the quenched-in defects in dilute alloys generally results in a decrease of the recovery rate, and in a recovery stage above that of vacancy migration. The data subsequent dissociation of vacancy-impurity complexes.

For negative vacancy-impurity binding energy the activation energy for escape jump of a vacancy, nearest neighbour of a solute atom with a solvent atom will be less than that in the pure metal[7]). This behaviour has been found in the present work, but we have not attempted to relate it quantitatively to $E_{V_i}^B$, because other investigations are necessary to determine if the vacancy-impurity repulsion will increase the divacance

concentration.

With regard to the electron microscope observations, Van Zuilichen and Burgers[8]) in a 95 Au - 5 Pt alloy observe no essentially different behaviour on quenching, as compared with pure gold. In our experiments the quenching rate and the pre-aging time were selected in such a way to have an high concentration of stacking fault tetrahedra[9,10]). The doping by 1 at.%Pt do not change essentially this density (Table 1), so that it seems to exclude heterogeneous nucleation and therefore an attractive interaction between impurity atom and vacancy.

However, two different effects were observed in Au+1 at.%Pt:
1) The proportion of faulted loops is larger than in pure gold,
2) the diffusion distances from grain boundaries are very high.

It seems to be possible to explain, tentatively, these effects by the following arguments.

The occurrence or non-occurrence of tetrahedra depends on the presence of a sufficient concentration of nuclei[11]), i.e. a sufficiently high concentration of single, di- and trivacancies must be present in thermal equilibrium to assure tetravacancy (in de Jong and Koehler model[11]) or hexavacancy (in Chick model[9]) formation. In both the models the hexavacancy has been assumed to be the smallest vacancy cluster acting as the stable nucleus for the stacking fault tetrahedra.

Now, if the atom impurity-vacancy binding energy is repulsive the vacancy in the neighbourhood of an impurity atom is repelled, consequently the probability to form divacancies increases, since the impurity concentration with respect to vacancies is high and the divacancy binding energy is positive. Thus a condition could be reached during the pre-aging, when $(C_{2V}/C_{3V})_{Au+1\ at.\%Pt} > (C_{2V}/C_{3V})_{99.999Au}$. Under this conditions, the probability to nucleate loops increases in the Au+1 at.%Pt specimens.

The high diffusion distance from grain boundary observed (Fig.8) probably supports this view, since the divacancies are more mobile than single vacancies.

References

1) See for example several papers in "Lattice defects in quenched metals" edited by Cotteril, Doyama, Jackson, Meshii, Academic Press New York (1965).

2) A.J.Mortlock, A.H.Rowe and A.D. Le Claire Phil.Mag. 5 (1960) 803.

3) E.Vogt, Ann.Phys.Lpz. 14 (1932) 23.

4) W.H.Lomer, Vacancies and other point defects in metals and alloys. Institute of Metals. London (1958) p.79.

5) P.W.Schapink, Phil.Mag. 12 (1965) 1055.

6) A.C.Damask, G.J.Dienes, POint defects in Metals, Gordon and Breach 1963 New York.

7) A.D.Le Claire, Phil.Mag. 7 (1962) 141.

8) G.Van Zuilichem, W.G.Burges, Phil Mag. 7 (1962) 981.

9) K.P.Chick, Phys.Stat. Sol. 10 (1965) 659.

10) M.A.Quader, R.A.Dodd, Phil.Mag. 17 (1968) 575.

11) M.de Jong, J.S.Koehler, Phys.Rev. 129 (1963) 40, 49.

THE STUDY OF DEFECTS IN QUENCHED NICKEL

S. SCHERRER, G. LOZES, B. DEVIOT

Laboratoire de Physique du Solide, Ecole des Mines, Nancy
France

Abstract:

Quenched nickel wires are investigated by electrical resistivity measurements and transmission electrons microscopy.

Isochronal annealing curves show 3 stages centered about 60° C, 280° C and 540° C whose activation energies correspond to 0,85 eV, 1,40 eV and 2,2 eV respectively.

A dependence of the recovery of these stages is observed. In less pure nickel the amplitude of the last stage is much larger than the preceding two stages. It seems that in nickel of lower purity clusters form during quench which for higher purity nickel most of them are formed during the anneal that occurs in the preceding two stages. This is consistent with the result of electronic microscopy.

-o-

I - INTRODUCTION.

From cold-work and irradiation techniques (1 to 9) so much information has been already obtained on point defects in nickel. However, the difficulties encountered in quenching pure nickel make this technique much less used.

In this study, results obtained on nickel quenched under conditions where contamination is reduced to the minimum are presented. The experimental conditions are described and an interpretation of the obtained results is proposed.

II - EXPERIMENTAL PROCEDURE.

The starting material is zone melting refined nickel from the "Service de Physique du Solide" of the C.E.N. of Grenoble. They were about 4mm diameter bars which we have rolled and drawn.

We used a quenching method as indicated by DOYAMA and KOEHLER[13]. Two 0.05mm diameter and 4cm separation between potential contacts nickel wires are spot welded on a nickel support connected to the base of a pyrex capsule. The capsule is 12 hours degased at 400° C under a 10^{-6} atmosphere vacuum, then filled with purified helium. Then it is permanently settled in a liquid nitrogen bath.

The sample is then annealed in a temperature range over 1200° C by electrical heating and quenched by switching off. The computed quenching rate was higher than 30,000° C/sec as checked by cathode ray tube tracing.

Sample heating for subsequent anneals was done by D.C. regulated power supply. The mean temperature is controled by Thomson bridge measurements of resistivity.

The resistivity variations of the metal due to the heat treatments are measured at 77° K by a potentiometer method.

The Cambridge type 44.248 potentiometer allows the measurement of tension variation greater than 0.1 μV corresponding to a 10^{-11} $\mu\Omega$-cm resistivity. As far as the electron microscope observations are concerned, 14 μ thick, 1mm wide ribbons were quenched the same way at a rate greater than 20,000° C/sec.

III - EXPERIMENTAL RESULTS.

III.1 - Electrical resistivity measurements.

The samples were annealed at 1000° C during 30 minutes, then at 1300° C for 10 minutes. The resistivity-ratio between room and liquid nitrogen temperature is measured. It is :

$$\eta = \frac{\rho(295) + \rho_i}{\rho(77) + \rho_i}$$

ρ_i, the resistivity difference between the studied metal and the perfect metal depends only upon the lattice defects and impurities.

MERKLEN and DIMITROV[9] checked that the influence of magnetic phenomena are extremely weak at liquid hydrogen temperature for nickel. We then thought, that the ratio η could be chosen as a criterion for bulk purity of our samples. According to pure nickel data $\rho_i = 0$ when $\eta = 14.1$.

We studied series of samples where the ratio η was 13 and 13.8 corresponding respectively to a residual resistivity of $\rho_i = 0.04\,\mu\Omega$-cm and $0.009\,\mu\Omega$-cm.

Figure 1 shows the isochronal graphs of the recovery for these samples between 20° C and 800° C after a quench from 1300° C. The recovery of the quenched-in resistivity occurs in three stages A, B and C.

III.1.1 - Stage A.

For samples whose residual resistivity ρ_i is $0.04\,\mu\Omega$-cm, stage A is centered around 80° C. For purer nickel ($\rho_i = 0.009\,\mu\Omega$cm), stage A lies between 50° C and 100° C with a larger amplitude. Figure 2 shows recovery graphs at 60° C and 70° C.

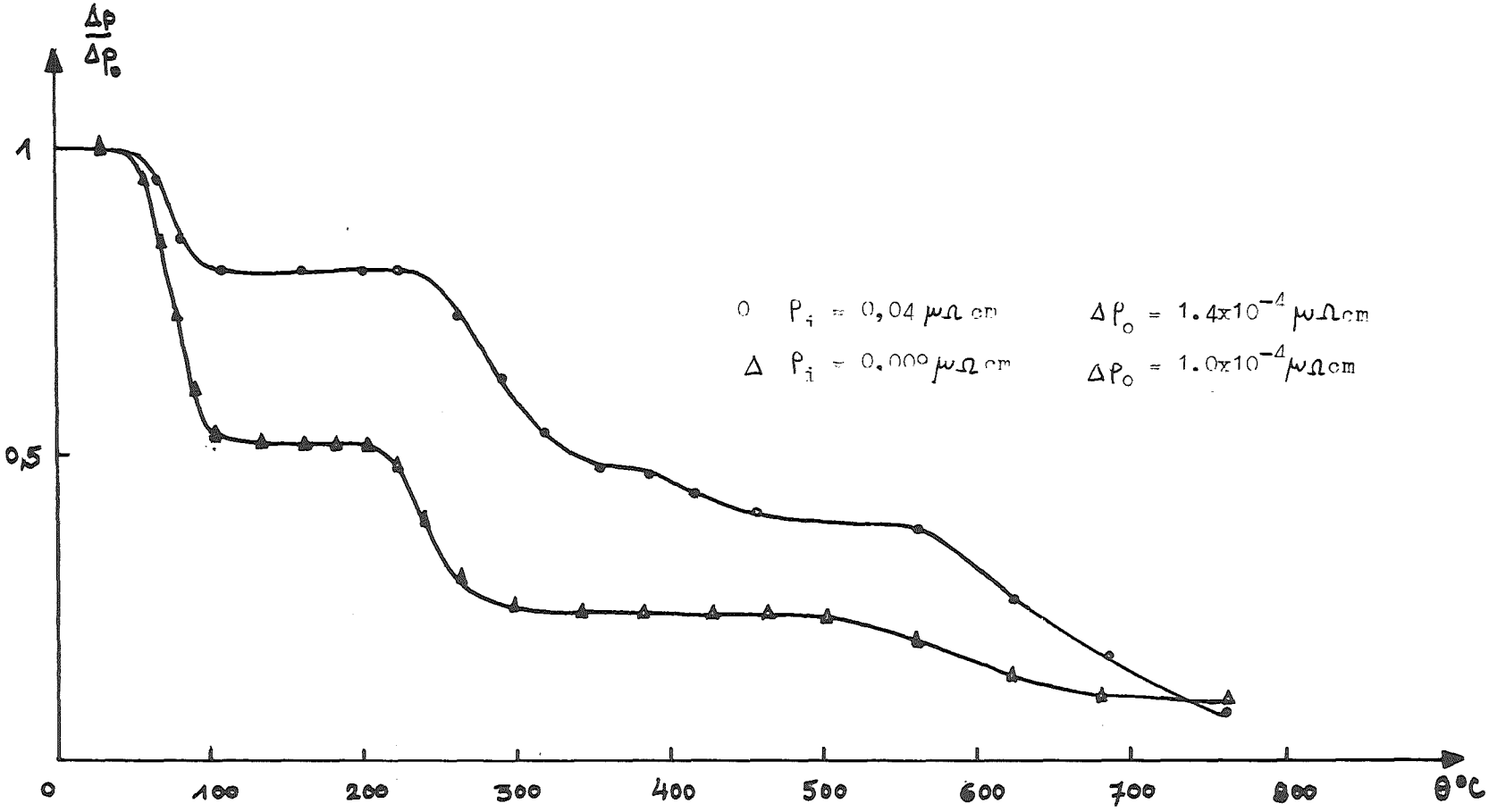

Fig. I - Defect resistivity of isochronal annealing for 5 mn at each of the temperatures. T_q = 1300° C

Stage A follows a first order kinetics (Fig. 3) such as :

$$\Delta\rho(t) = \Delta\rho(0)\ \exp\left(-\frac{t}{\tau_0}\right)$$

The activation energy for the migration of the corresponding defect is equal to :

$$0.85 \pm 0.05 \text{ eV}$$

III.1.2 - Stage B.

It lies usually between 210° C and 320° C. Its amplitude is only weaker than stage A for the purest sample where it spreads over a smaller temperature range.

Its kinetics order lies between 1 and 2 with an activation energy of 1.40 ± 0.02 eV.

III.1.3 - Stage C.

Stage C has usually a larger amplitude which is substantially depleted in the case of the purest metal. It is composed of two substages, the first one between 340° C and 510° C and the second one between 530° C and 730° C. They collapse into one stage beyond 530° C for the purest sample.

III.2 - Electron microscope observations.

Samples whose residual resistivity is $\rho_i = 0.05 \mu\Omega cm$, are quenched from 1350° C and annealed for a hour at 350° C. Franck type dislocation loops (Burgers vector $\frac{1}{3}$ (111)) are observed. (Fig. 4) Loops are not distributed homogeneously throughout the samples. We used those zones where the density was the highest to make some comparisons. The loop density is about 3×10^{-10} loop per site corresponding grossly to 3×10^{-6} vacancies per site, while their mean size is about 500 Å. Figure 5 shows the loop size variation versus sample purity.

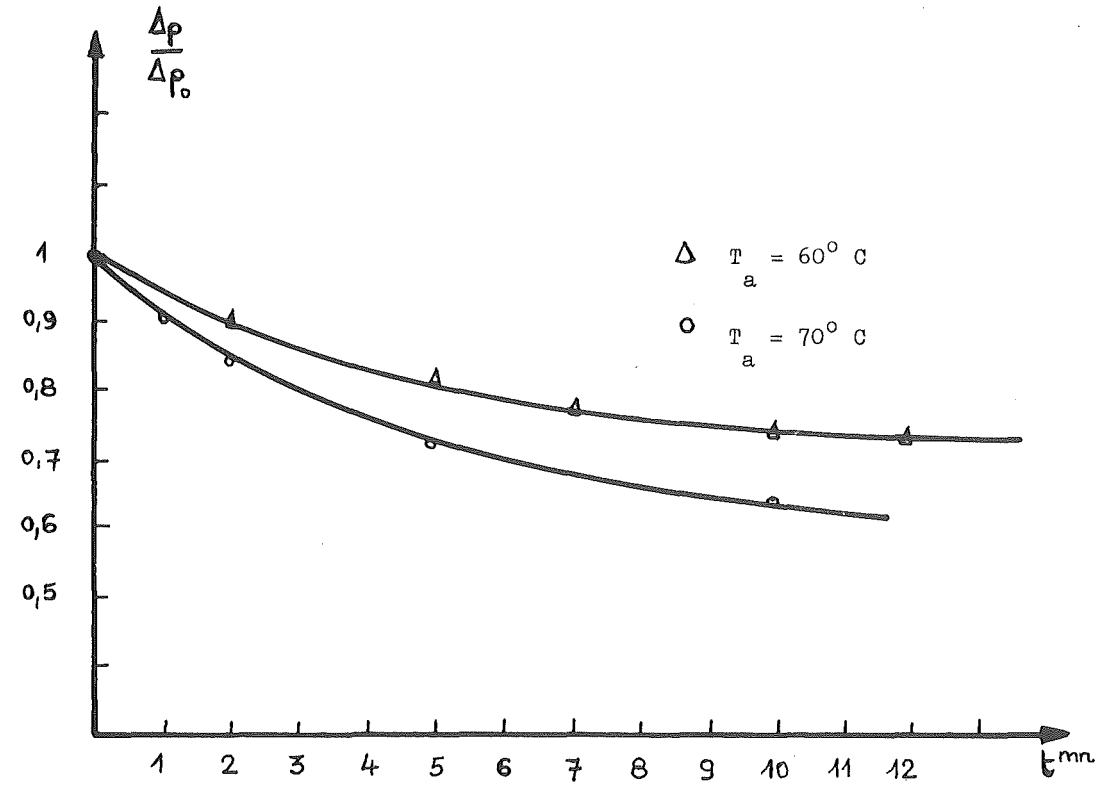

Fig. II - Isothermal recovery in the temperature range of stage A (ρ_i = 0,009 μΩcm).

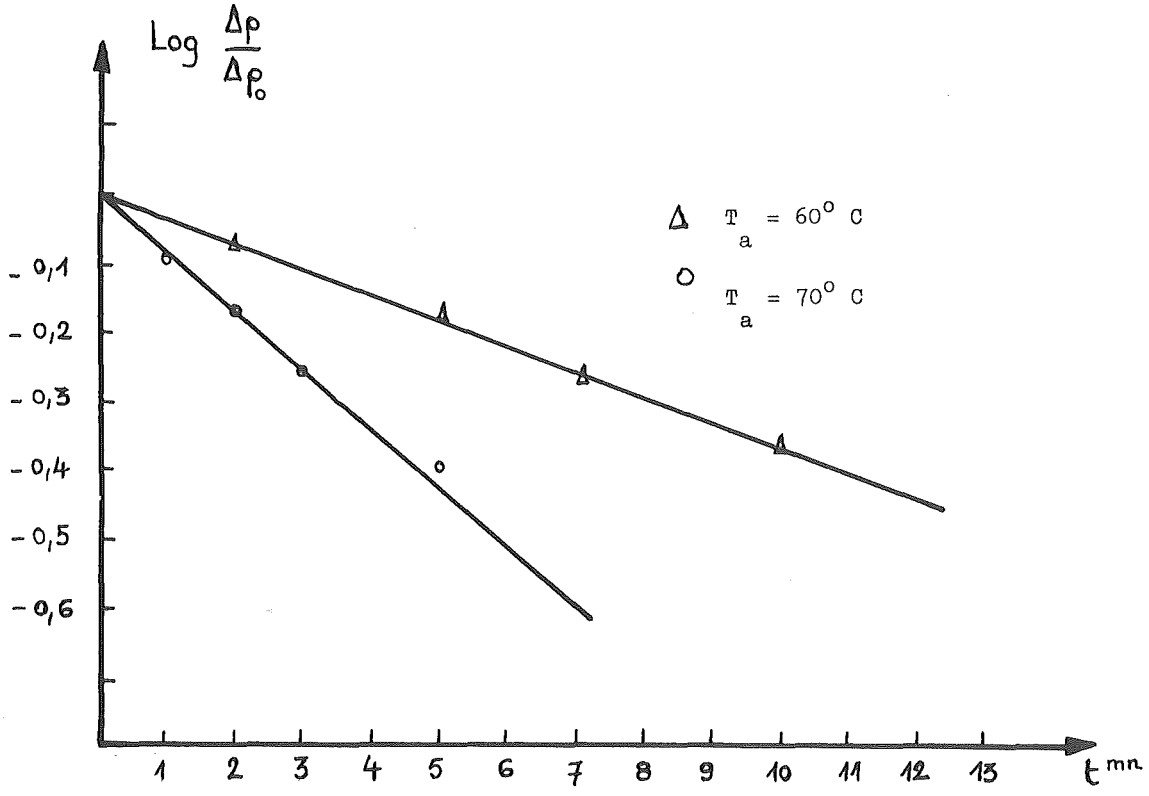

Fig. III - Test of first order kinetics in stage A (ρ_i = 0,009 μΩcm)

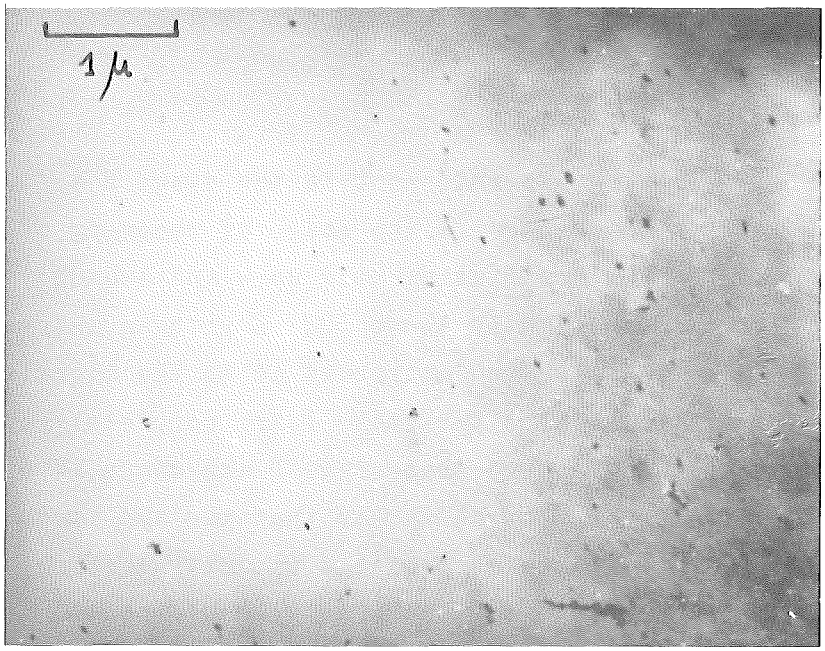

Fig. 4 Electron micrograph of quenched nickel ribbons

T_Q = 1350° C

T_a = 350° C during one hour.

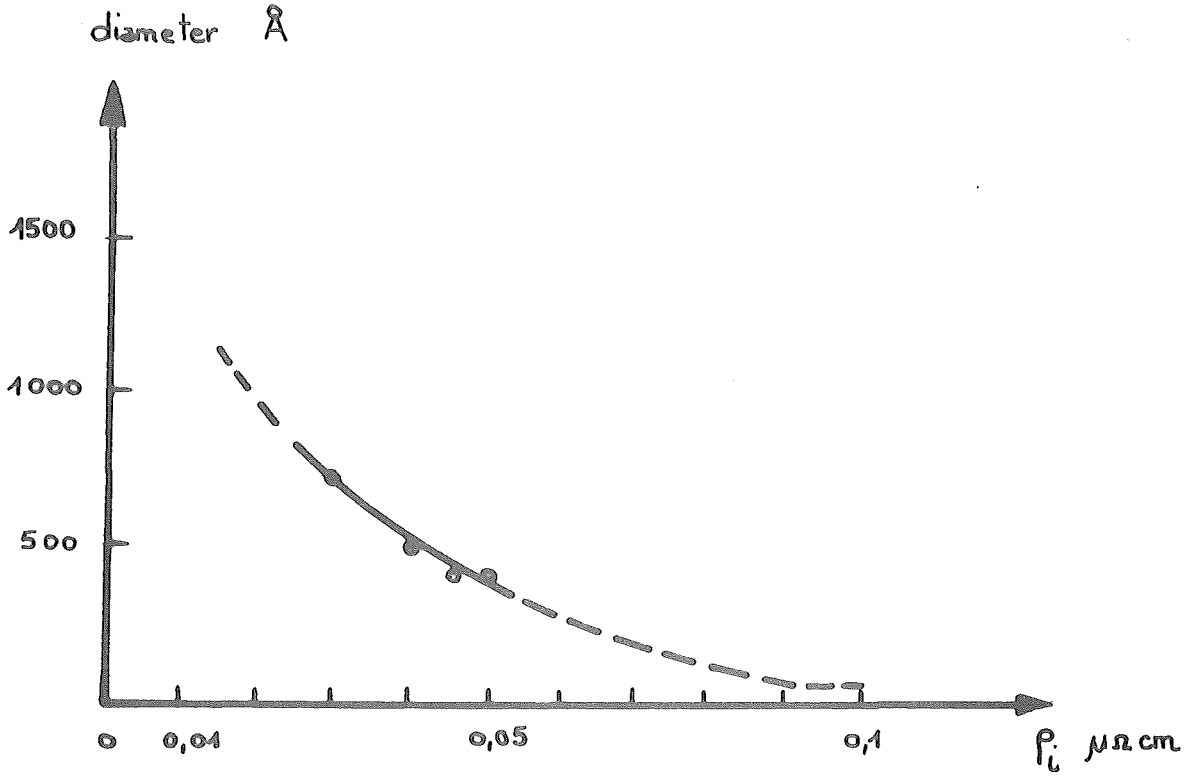

Fig. V - Mean loop size variation versus sample purity.

IV - INTERPRETATION.

The easiest stage to interpret is the stage B of our study. Many authors label as stage IV the stage of recovery of the resistivity in nickel after irradiation cold work and quench[1 to 6, 10, 12]. That stage occurs slightly above 500° K with an activation energy between 1.4 and 1.5 eV. They attribute it to the migration of monovacancies. Our own results for stage B are completely consistent with it so that we do believe that stage B and stage IV of the previous studies are similar. Let us notice that the amplitude of stage B looks practically independent of the impurity content, and occurs in the same temperature range so that we could assume that the migration energy is affected by the impurity-vacancy interaction, only a little.

As far as stage A is concerned, we first note that its recovery corresponds for pure nickel to the half of the quenched-in resistivity. On the other hand, it is drastically reduced by impurities. The temperature range, the activation energy (0.85 eV), the first order kinetics induce us to believe in the trapping of a well specified defect towards fixed sinks. The number of jumps determined experimentally is 10^4. It is smaller than that expected if defects went only to dislocations. The simplest interpretation would be to think of divacancy migration towards small clusters formed during the quench. Impurity content dependence would suggest the difficulty for impurity trepped monovacancies to form divacancies while quenching.

MUGHRABI and SEEGER[12] also found a 0.72 eV activated stage between 50° C and 160° C. Eventhough the details are not similar, they also call on divacancies to explain that stage.

The temperature range of stage C suggest higher order defects which is consistent whith the 2.1 eV activation energy[14].

The amplitude for the less pure sample is too high for being only due to the recovery of clusters which are the combination of the previous defects migrating in stages A and B. We are then induced to believe that clusters were formed during the quench allowing them to grow afterwards.

BIBLIOGRAPHIE -

1) SOSIN, J.A. BRINKMAN - Acta Met., 7 (1960) 478
2) CLAREBROUGH, HARGREAVES, LORETTO, WEST - Acta Met., 8 (1960) 797
3) SCHUMACHER, SCHULE, SEEGER - Z. für Naturforschung, 17a (1962) 328
4) SIMON, SIZMAN - Z. für Naturforschung, 17a (1962) 596
5) MEHRER, KRONMULLER, SEEGER - Phys. Stat. Sol., 10 (1965) 725
6) KRESSEL, SHORT, BROWN - Acta Met., 15 (1967) 525
7) PERETTO - Thèse, Grenoble (1967)
8) BRIDGES, BALL - Phil. Mag., 15 (1967) 1107
9) MERKLEN - Thèse, Paris (1967)
10) SCHERRER, OCTOR, DEVIOT - C.R.A.S., t . 261 (1965) 3571
11) WUTTIG, BIRNBAUM - J. Phys. Chem. Solids, 27 (1966) 225
12) MUGHRABI, SEEGER - Phys. Stat. Sol., 19 (1967) 251
13) DOYAMA, KOEHLER - Phys. Rev., V. 127, N° 1 (1962)
14) DIEHL, AST - Phys. Stat. Sol., 17 (1966) 269

* This paper is a part of a dissertation which will be submitted by S. SCHERRER in fulfillement of the requirements for Thesis in 1969.

VACANCY-IMPURITY INTERACTION DURING AND AFTER QUENCHING OF DILUTE SOLID SOLUTIONS OF COPPER IN NICKEL

B. DEVIOT, H. OCTOR, S. SCHERRER

Laboratoire de Physique du Solide, Ecole des Mines, Nancy
France

Abstract:

A 15,000° C/sec initial quenching rate does not retain vacancies in 0.08 mm diameter high purity nickel wires. Small copper concentration has been introduced to do so.

Plots of isochronal annealing show a copper concentration dependence ; two stages are noticeable :

- stage one (A) ; around 500° K, its amplitude increases with the copper content and follows a first order kinetics with a 1.53 eV activation energy. This stage is interpreted as resulting from vacancy-impurity complexes.
- stage two (B) : between 800 and 1000° K, would be due to the annealing of clusters formed during the quench or stage A.

A 0.25 eV vacancy-impurity binding energy is then deduced.

I N T R O D U C T I O N

Difficulties found during the quench of high purity nickel and the strong influence of low content impurity lead to the systematic study of the role played by a well defined impurity on retaining vacancies during the quench.

Copper was choosen for the following reasons : the copper-nickel solid solution is regular at any concentration allowing a further study at high copper-content ; the diffusion energy of infinitely diluted copper in nickel is smaller than the self diffusion energy of nickel inducing a strong vacancy-impurity interaction ;

the atomic radii of the two elements are very close so that the interaction energy is of a pure electronic nature.

In a first part, experimental conditions are briefly described ; then we discuss the isochronal curve dependence with copper content as to specify the conditions allowing to determine the binding energy E^B_{V-I}.

1 - EXPERIMENTAL CONDITIONS.

The starting material is nickel having been twenty two times zone-refined. Its bulk impurity content is less than 20 p.p.m.

Samples are 0.08mm diameter wires. They are welded on a nickel holder in a carefully degased pyrex capsule. The capsule is filled with helium and permanently placed in a liquid nitrogen bath. The wire is electrically heated and quenched by switching off. All measurements are resistivity measurements using a potentiometer.

Copper is electroplated on the nickel wires. Copper diffusion and homogeneization of the alloy are done within the capsule. Diffusion time is determined from the diffusion constant of copper into nickel. At 1400° K, the local fluctuations of concentration are within one percent the homogeneous concentration obtained after a 10 hour anneal.

The copper content of a sample is extracted from resistivity measurements. To do so, a series of samples has been prepared as previously reported and analysed by spectrocolorimetry[2]. The resistivity increase compared to pure nickel is proportionnal to the atomic ratio of copper, when it goes up to 5.10^{-3} ; at 77° K this increase is $0.98 \pm 05\ \mu\Omega$-cm per atomic percent.

2 - COPPER CONCENTRATION INFLUENCE ON THE QUENCHED IN DEFECTS.

2.1 - Experimental results.

The quenching procedure used has a starting cooling rate of 15,000° C/sec ; it is not sufficient to observe an effect on pure nickel. For quenches from 1000° C, figure 1 gives the "quenched-in resistivity" $\Delta\rho$ versus the copper content C_i. It shows the role of

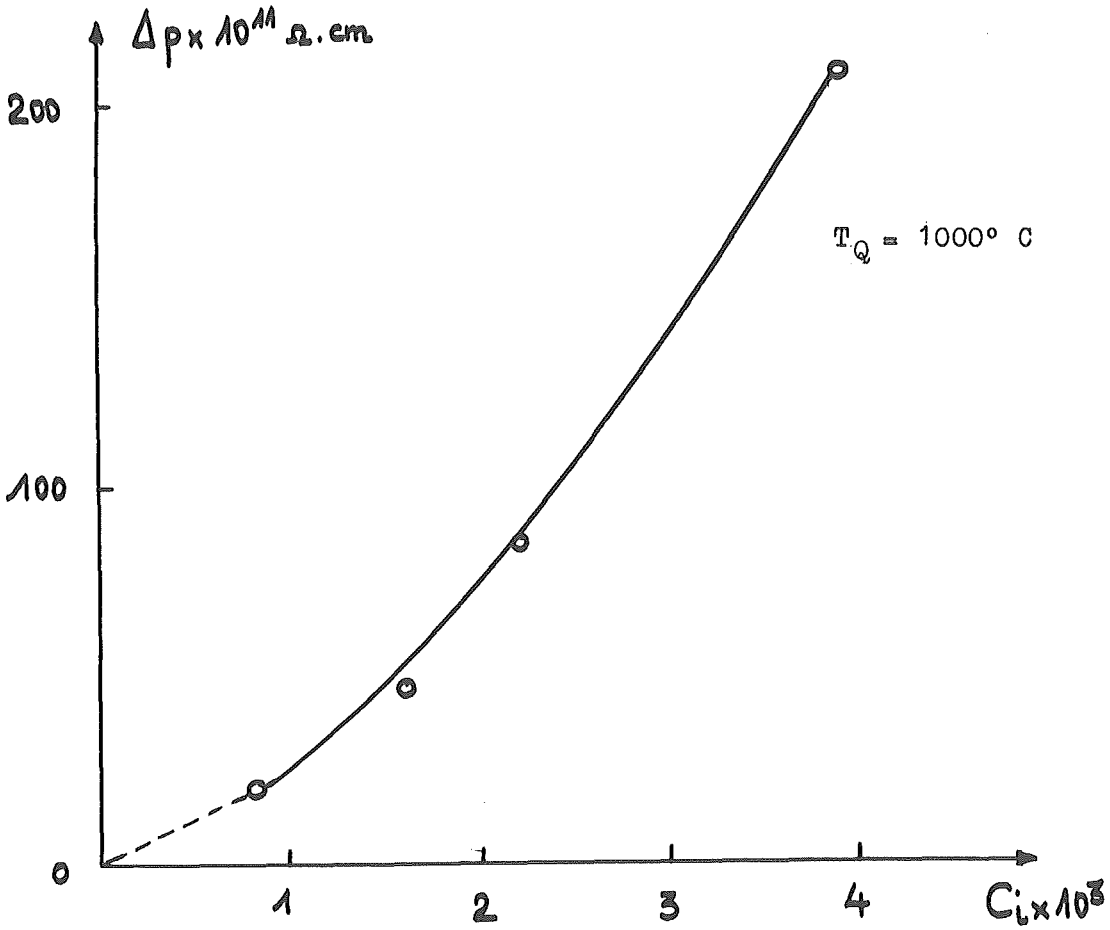

Figure 1 - CHANGE IN RESISTIVITY AFTER QUENCHING FROM 1000° C AS A FUNCTION OF THE ATOMIC CONCENTRATION OF COPPER.

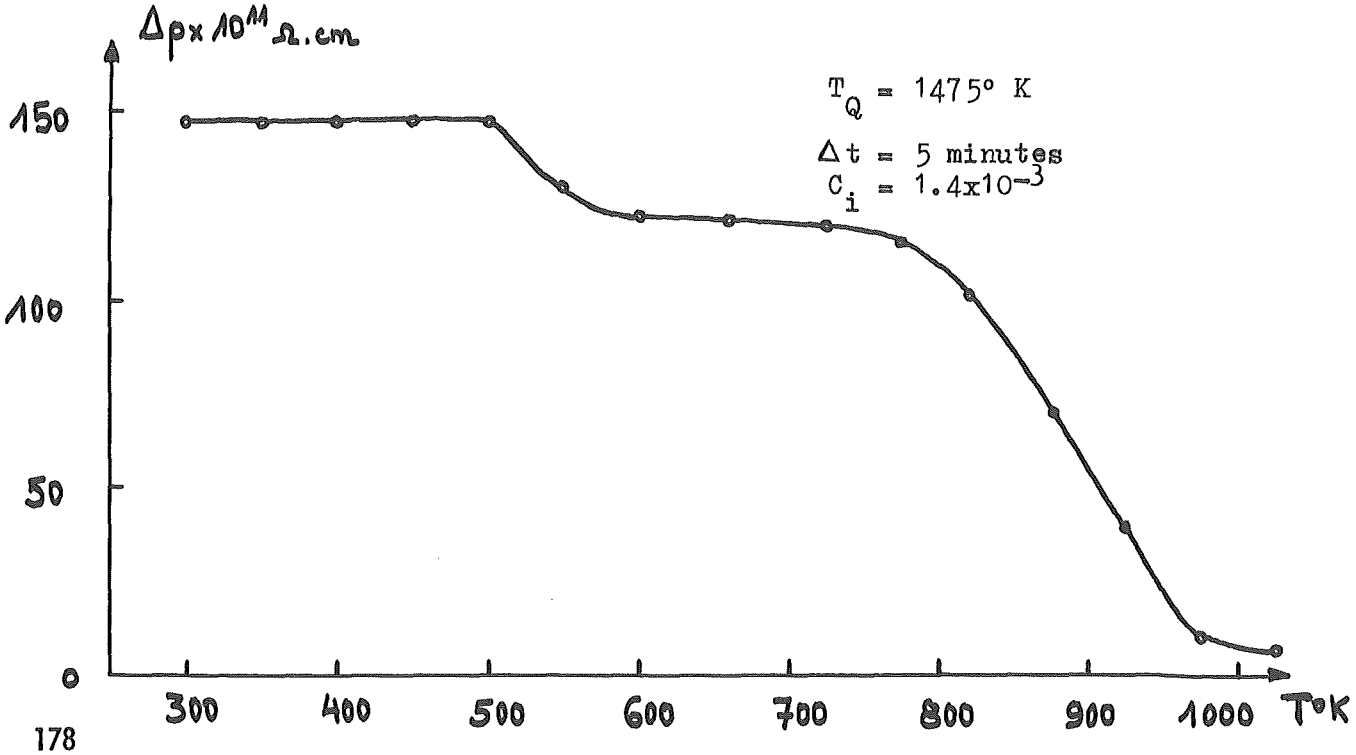

Figure 2 - ISOCHRONAL RECOVERY - CONCENTRATION $C_i = 1.4 \times 10^{-3}$

copper to trap vacancies, predicting a high binding energy between vacancies and impurities.

To deal with this interaction, a study of the annealing of the quenched-in quantity $\Delta\rho$ has been undertaken versus concentration. Different cases have been examined :

a) Copper atomic ratio $C_i = 1.4 \times 10^{-3}$.

A quench from 1200° C induces a resistivity increase of 1.41×10^{-3} $\mu\Omega$-cm ; according to Seeger[3,4], assuming an efficient quench, one should observe a variation of 6.0×10^{-3} $\mu\Omega$-cm for pure nickel.

Figure 2 shows the isochronal curve of the anneal. Two stages are distinguished : the first one, (A), between 500° K and 600° K corresponds to the recovery of 20% of the quenched-in quantity and a second one, (B), consequent beyond 150° K. Above 1100° K, all the resistivity coming from the quench is washed out.

b) Copper atomic ratio $C_i = 3.2 \times 10^{-3}$.

The resistivity $\Delta\rho$ quenched from 1200° C is on the average 2.10×10^{-3} $\mu\Omega$-cm. One finds again two stages (figure 3), but stage A corresponds to an anneal of 55% of the quenched-in resistivity. One has also to note that the annealed quantity is greater than the quenched-in resistivity $\Delta\rho$, so as to say that after annealing, the resistance of the sample is smaller than before quenching.

c) Copper atomic ratio $C_i = 3.9 \times 10^{-3}$.

Figure 4 shows that the trends already noticed in b) are confirmed. Stage A has an amplitude greater than the quenched-in resistivity. This fact has been checked over a large number of isochronal curves and these curves always cut the temperature axis around 600° K. One also notices a decrease of the amplitude of stage B, which is displaced towards lower temperatures by about 100° C.

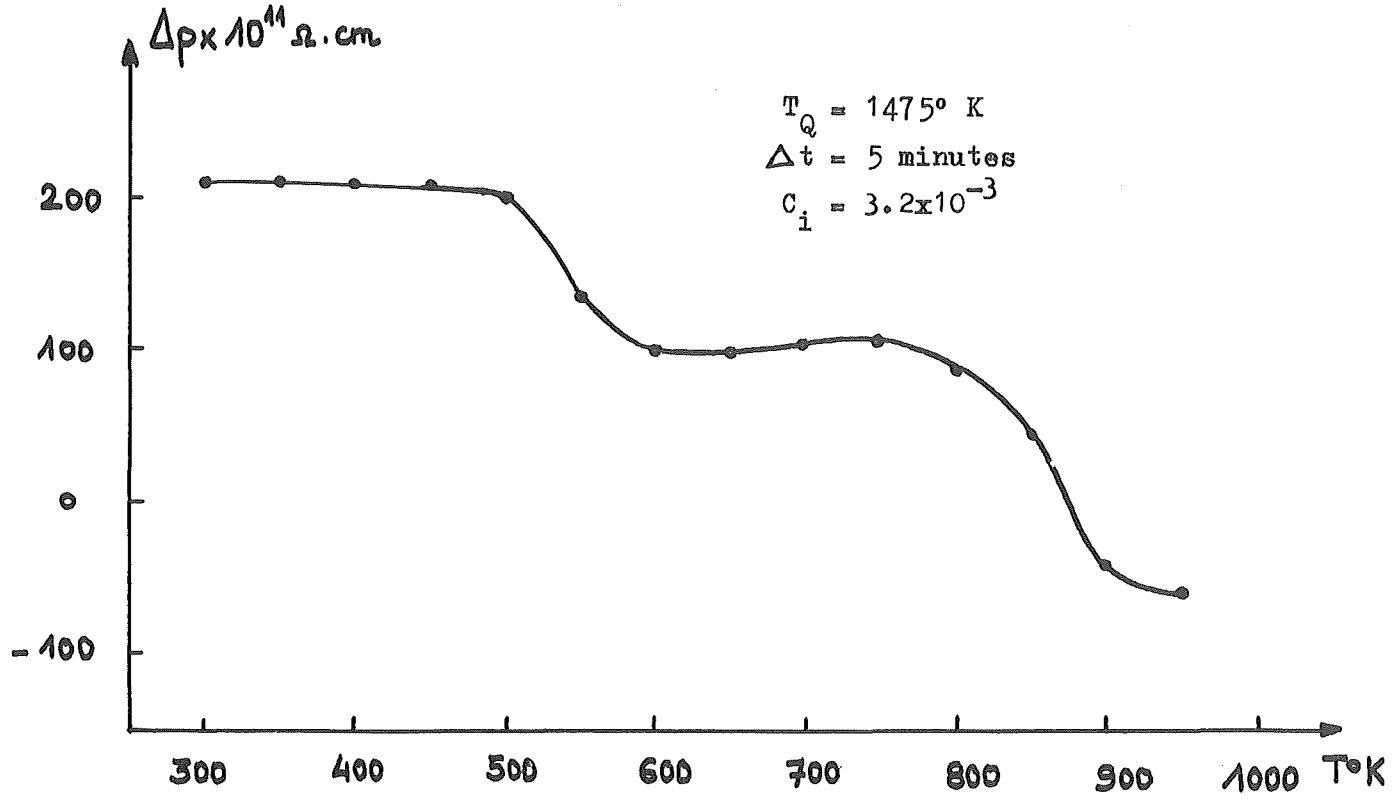

Figure 3 - ISOCHRONAL RECOVERY - CONCENTRATION $C_i = 3.2 \times 10^{-3}$

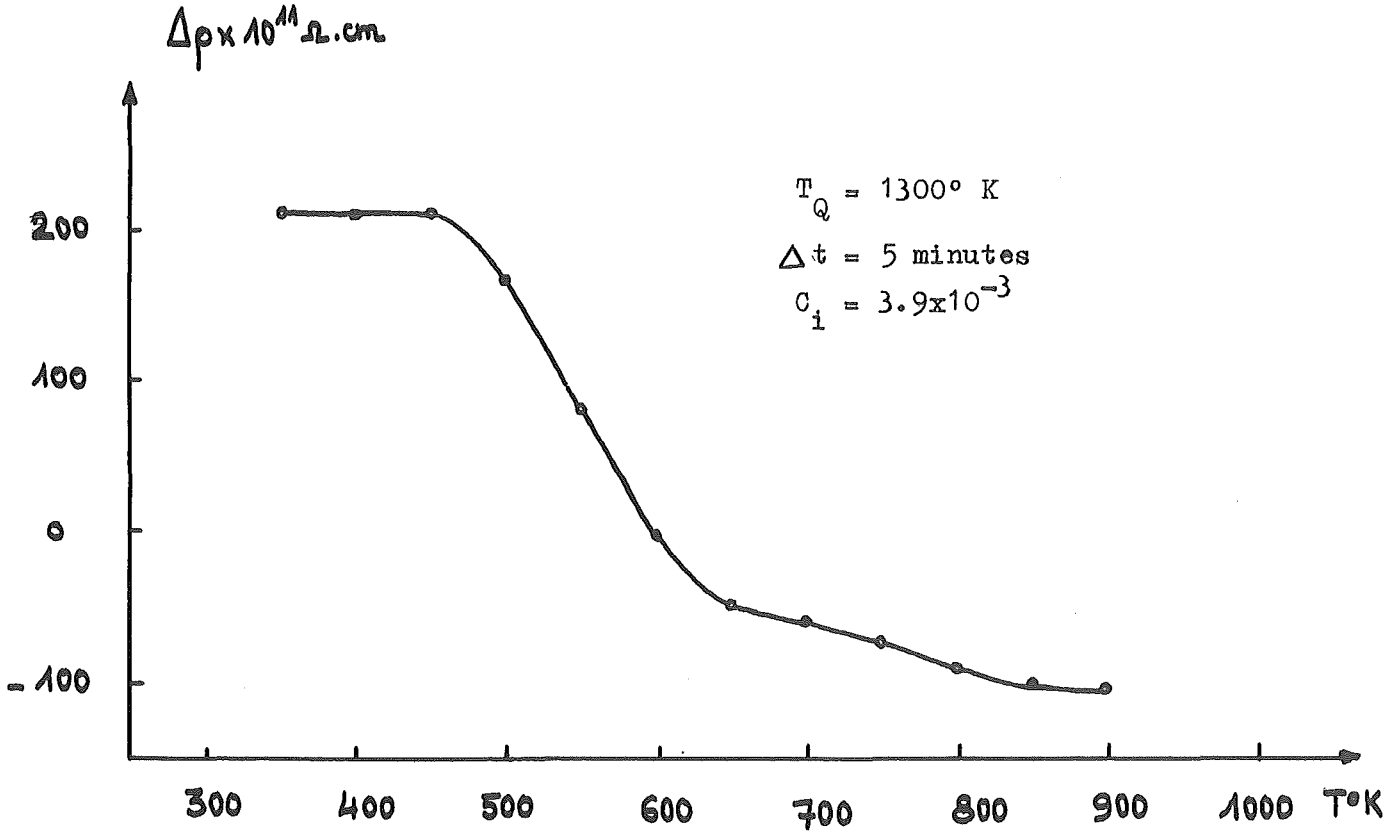

Figure 4 - ISOCHRONAL RECOVERY - CONCENTRATION $C_i = 3.9 \times 10^{-3}$

Moreover, during the successive quenches and annealing periods, the sample is getting purer ; the fact has been checked by quantitative chemical analysis on a sample having undergone fifteen cycles. It leads us to say that during stage A vacancies pull copper atoms in their migration.

The study of stage A shows that its greatest part can be described by a first kinetics. The activation energy determined by the method of Meechan and Brinkman[5] is $1.53 \pm .05$ eV.

The different workers[3,6,7] having dealt with monovacancies in pure nickel define a stage IV whose mean temperature is 500°K and a migration energy of 1.50 eV.

These various facts favor the migration of a vacancy-impurity complex in stage A(according to Quéré[8], the migration energy of such a complex is close to that for a vacancy). For smaller copper concentrations, these complexes, not numerous at the end of the quench, would migrate towards clusters already formed during the quench whose recovery would only intervene during stage B.

For the beginning of stage B, one finds a second order kinetics and an activation energy of 2.60 eV. At 821°K, for a copper concentration $C_i = 1.4 \times 10^{-3}$, the half-period of recovery is about two minutes ; in these conditions, if we were dealing with a defect migration, it would only accomplish ten jumps before recovery. This is only consistent with a local rearrangement which would stabilizes the cluster structure ; let us add that at this temperature, the shape of the isothermal curves depends strongly upon the heat treatment whose aim is to anneal stage A.

Thus, one can think that at the end of the quench no free vacancies exist and that at small concentration the vacancies are essentially trapped into clusters.

On the other hand, the higher the copper content, the higher is the concentration of the vacancy-impurity complexes.

This justifies the choice of $C_i = 3.9 \times 10^{-3}$ to determine the vacancy-copper binding energy E^B_{V-I}. If one assumes that in the case where we deal with complexes having only some constituents, the resistivity of a complex is the sum of the resistivities taken separately, the quenched-in resistivity $\Delta\rho$ corresponds to the part due to vacancies.

3 - THE VACANCY-COPPER BINDING ENERGY IN NICKEL.

It is deduced from the appearent formation energy of vacancies in a dilute solid solution of concentration $C_i = 3.9 \times 10^{-3}$.

Figure 5 shows the classical diagram where the logarithm of the resistivity excess $\Delta\rho$ is plotted with respect to the inverse of the absolute temperature. On the same graph is plotted the line for pure nickel computed from Seeger's data. One can note that between 800 and 1100° K, the quenched-in resistivity $\Delta\rho$ is much more important than in pure nickel ; one determines an appearent formation energy of 1.1 eV. From Lomer[9] relationship and taking into account the formation energy in pure nickel of 1.35 eV[3], a vacancy-impurity binding energy $E^B_1 = 0.34 \pm 0.07$ eV is deduced. However, if one wants to take care of the value of the quenched-in resistivity $\Delta\rho$ at 1000° K for example, by taking $\rho_V = 4\ \mu\Omega$-cm for resistivity, a binding energy $E^B_2 = 0.28 \pm 0.05$ eV would be found.

Although the confidence intervals overlap, we think that the gap is due to Lomer's relationship. As a matter of fact, taking the high value of the binding energy into account, high order complexes can exist besides free vacancies and vacancy-impurity complexes in a thermodynamical equilibrium.

If one admits Dorn and Mitchell's[10] relationship, assuming that the binding energy between a vacancy and two impurity atoms is equal to twice the binding energy E^B, a value of 0.25

$\pm$ 0.05 eV is found for E^B which takes care of both the appearent formation energy and the quenched-in resistivity $\Delta\rho$.

This consistency in the results can justify, a posteriori, the assumptions already given.

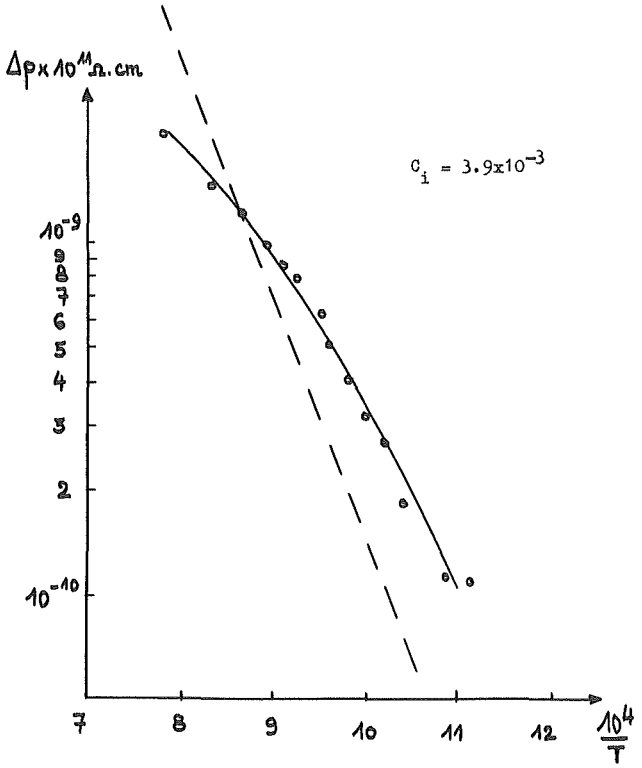

Figure 5 - APPARENT ENERGY OF VACANCY FORMATION.

C O N C L U S I O N

The role of copper as a vacancy-getter during the quench is clearly put into evidence. In particular, it favors the formation of complexes and clusters because of its strong interaction with a vacancy.

A value for E^B was determined by a quasi-chemical model. It leads to a value ten times smaller than for the binding energy.

Finally, one can note that the value of the binding energy E^B_{V-I} measured is fairly consistent with the difference between the diffusion energy of infinitely diluted copper in nickel[11] and the self diffusion of nickel.

B I B L I O G R A P H Y

1) S. SCHERRER, H. OCTOR, B. DEVIOT - C. R. A. S., 261, 3571 (1965)

2) R. CAPELLE - Chimie analytique, 48, 498 (1966)

3) A. SEEGER, SCHOTTKY, SCHUMACHER - Phys. Stat. Sol., 11, 363 (1965)

4) SEEGER - Z. Physik, 146, 217 (1956)

5) MEECHAN, BRINKMAN - Phys. Rev., 103, 1193 (1956)

6) NAKAMURA - J. Phys. Soc. Japan, 16, 2167 (1961)

7) SCHUMACHER, SCHULE, SEEGER - Z. NATURFORSCHUNG, 17a, 228 (1962)

8) QUERE - Défauts ponctuels dans les métaux. Masson, 1967, p. 170

9) LOMER - Vacancies and point defects in metals and alloys. J. Inst. Met. (1958)

10) DORN, MITCHELL - Acta Met., 14, 70 (1966)

11) ADDA, PHILIBERT - La diffusion dans les solides. Presses Univ. de France - Paris (1966)

THE EFFECTS OF INDIUM ON THE RECOVERY OF QUENCHED-IN VACANCIES IN ZONE-REFINED ALUMINIUM

BY

F. C. DUCKWORTH*, T. R. RAMACHANDRAN** AND J. BURKE**

ABSTRACT

The recovery of quenched-in vacancies in a number of aluminium-indium alloys based upon zone-refined aluminium has been studied using resistivity measurements and transmission electron microscopy. Recovery is shown to occur in three stages; (a) solute-vacancy association, (b) the formation of prismatic dislocation loops, and (c) the annealing out of the loops. The kinetics of the first stage are analysed and for low quench temperatures found to be consistent with a modified Damask and Dienes theory. Consideration is given to the possibility of solute-vacancy association occurring during quenching. From loop density measurements the indium-vacancy binding energy is roughly estimated to be 0.27eV.

1. INTRODUCTION

When a dilute solid solution is equilibriated at a temperature T, the total single vacancy concentration C_V is the sum of the concentrations of vacancies associated with solute atoms, C_{Vi}, and of vacancies having only solvent atoms as next nearest neighbours, C_{fV}. Following Lomer[1] these are given by:-

$$C_{fV} = A(1 - 12C_i)\exp(-E_V^F/kT) \quad (1)$$

$$C_{Vi} = A\ 12C_i\exp(-(E_V^F - E_{Vi}^B)/kT \quad (2)$$

---

*Central Electricity Generating Board, Berkeley Nuclear Laboratories, Berkeley, Gloucestershire, U.K.

**Department of Metallurgy, University College, Swansea, Glamorganshire, U.K.

where A is the entropy factor, assumed to be the same for free and associated sites, E_V^F is the energy of formation of a vacancy in the pure solvent, E_{Vi}^B is the solute-vacancy binding energy, C_i is the solute concentration and kT has its usual meaning. It follows from equations (1) and (2) that the ratio C_{Vi}/C_{fV} increases rapidly as T decreases particularly for high values of E_{Vi}^B. Thus unless thermal equilibrium between free and associated vacancies is preserved during cooling, quenching gives rise to an excess of free vacancies at the low temperatures. Recovery then comprises both solute-vacancy association to re-establish the partial equilibrium between the two species characteristic of the annealing temperature and the loss of vacancies to sinks.

Several theoretical treatments of vacancy annealing in dilute alloys have been given[2,3,4,5,6]. Damask and Dienes[2,3] and De Jong[4] showed that association should be very much faster than vacancy loss, contributing a rapid initial transient to the complete recovery process. No experimental study of the association process has been reported.

De Jong[4] showed that the characteristic time of association increases with E_{Vi}^B/kT; thus a high binding energy and low annealing temperature are favourable to such a study. For association to be detectable experimentally requires that some physical property be sensitive to the difference between free and associated vacancies. In a study of the effects of solute additions on the annealing behaviour of quenched zone-refined aluminium it was found that indium produced an additional initial recovery stage not found in either pure aluminium or in the other alloys studied[7], and it seemed probable that this was due to solute-vacancy association, this process causing a substantial decrease in resistivity. Also, in earlier work it had been found that the indium-vacancy binding energy was about 0.4eV[8]. Thus this alloy appeared to be particularly suitable for a study of the solute-vacancy association process, and in this paper we report the results of the investigation.

2. EXPERIMENTAL METHODS

The alloys used contained 46, 60 and 375 atomic p.p.m. indium and were made from zone-refined aluminium and high purity indium. For the electrical resistivity measurements wires of 0.010in. diameter were heated electrically, quenched into calcium chloride solution at -45°C and immediately transferred into liquid nitrogen. Annealing was carried out in alcohol-water baths for sub-zero temperatures and in silicone oil baths for higher temperatures, the temperatures being controlled to $\pm$1°C. Recovery of the quenched-in defects was followed by resistivity measurements at 78°K. The initial quenched-in

resistivity, $\Delta\rho$, after a particular anneal was computed in relation to a reference state obtained by annealing at 240°C for 15 minutes. Further details of the alloy preparation techniques and resistivity measurements were given in a previous paper[8].

Specimens for electron microscopy were quenched in the form of 0.005in. strips, given the appropriate annealing treatments and electropolished in a solution consisting of four parts ethyl alcohol and one part perchloric acid.

3. GENERAL RECOVERY CHARACTERISTICS

A general survey was made of the recovery characteristics of the quenched Al-46 p.p.m. In alloy in order to identify the initial recovery stage with solute-vacancy association. Specimens were quenched from temperatures T_Q in the range 360-570°C and recovery was studied isochronally and isothermally.

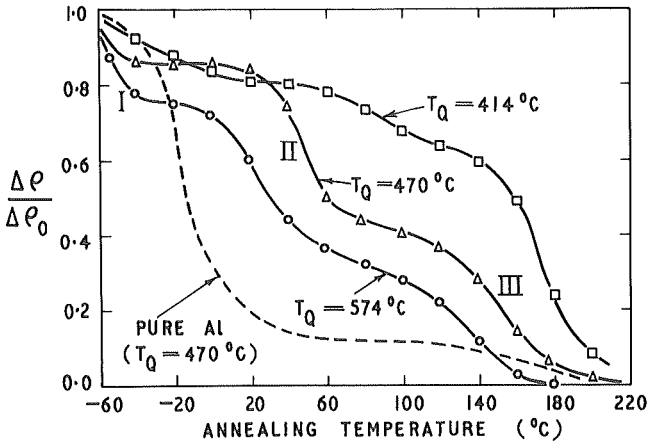

Fig. 1. Isochronal annealing curves (10mins. at each temperature) for recovery of an Al-46 p.p.m. In alloy quenched from T_Q = 574°, 470° and 414°C. The recovery curve for zone-refined aluminium quenched from T_Q = 470°C (broken line) is shown for comparison.

Fig. 1 shows the isochronal annealing curves for T_Q = 574°, 470° and 414°C. Recovery is seen to occur in three stages, subsequently referred to as I, II and III. The corresponding curve for a zone-refined aluminium specimen, quenched from 470°C, is shown for comparison. The outstanding feature of these results is that the alloy has an additional low temperature annealing stage (stage I) which has no counterpart in the pure metal. The first annealing stage in pure aluminium, occurring just below room temperature, is known to be associated with the removal of vacancies by the nucleation and growth of

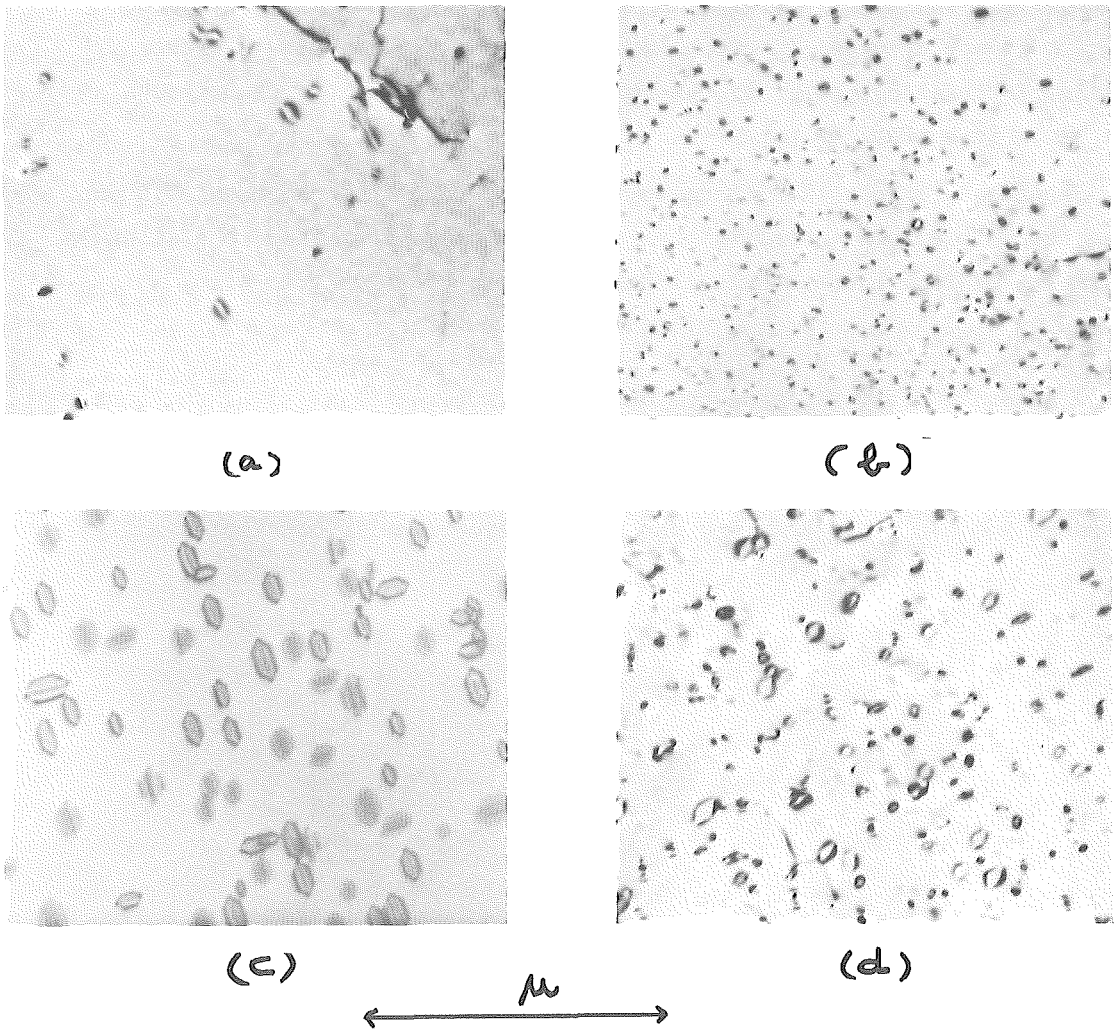

FIG. 2 Dislocation loops in Al and Al-In alloys quenched from 600°C; (001) foil [200] reflection; (a) Al-60 p.p.m. In annealed at 20°C for 5 mins; (b) Al-60 p.p.m. In annealed at 50°C for 1 hour; (c) Pure Al annealed at 50°C for 1 hour; (d) Al-375 p.p.m. In annealed at 100°C for 2 hours.

dislocation loops[9,10] and voids[11]. The presence of a strongly pinning solute should shift this stage to higher temperatures because of the effective decreased mobility of the defects. Thus stage II in the alloy should be due to the formation of dislocation loops.

Thin film electron microscopy was performed to provide confirmatory evidence for this interpretation. A specimen of the 60 p.p.m. indium alloy quenched from 600°C and annealed for 5 minutes at room temperature, i.e. after the completion of stage I (see Fig. 1), showed a low concentration of loops (average diameter 200Å and density 1.1×10^{13} per cm^3 - see Fig. 2(a)) whereas annealing at 50°C, i.e. after stage II, produced a high density of small loops (average diameter 150Å and density 2×10^{14} per cm^3 - see Fig. 2(b)). The loops were much smaller but more numerous in the

alloy compared with a similarly quenched pure aluminium specimen at the end of this recovery stage (shown for comparison in Fig. 2(c)). This would account for the greater residual resistivity in the alloy after this stage than in the pure solvent. It is also noticed from Fig. 2 that in the alloy all the loops are prismatic whereas in the case of pure aluminium about 95% are faulted.

Increasing the indium content raised the requisite ageing temperature for loop formation. This is illustrated in Fig. 2(d) which shows a specimen of the Al-375p.p.m. In alloy annealed at 100°C. The loops had an average diameter of 600Å and a density of 3×10^{13} per cm^3. Ageing this alloy at room temperature produced a very low concentration of loops (1.5×10^{12} per cm^3, average diameter 200Å). After annealing for 60 minutes at 200°C all the loops had disappeared, demonstrating that the final stage of recovery around 200°C (stage III) is due to the annealing of dislocation loops by climb, as in pure aluminium.

It is seen from Fig. 1 that lowering the quench temperature reduces the amount of resistivity recovered in stage II. This is consistent with the behaviour of pure aluminium and is thought to be due to the fact that the vacancy supersaturation becomes inadequate to nucleate loops.

Isothermal annealing at 20°C for different quench temperatures produced the results shown in Fig. 3 illustrating the following main features:-

(1) a rapid resistivity decrease occurred during the first few seconds followed by a long "plateau" for low values of T_Q;

(2) for higher values of T_Q the rapid decrease was followed by a slow resistivity decrease;

(3) the magnitude of the initial decrease increased with T_Q.

The fast initial reaction is readily identified as stage I of the recovery process. The third feature is consistent with the solute-vacancy association mechanism since the number of vacancies available for association increases with T_Q due to an increase in the total defect concentration and a shift of the solute-vacancy equilibrium towards the dissociated state. (This conclusion is not altered if partial association of vacancies and solute atoms occurs during the quench. This possibility will be discussed in some detail later). Moreover, as T_Q increases beyond that at which the solute atom concentration is insufficient to absorb the entire population of quenched-in vacancies (~500°C in this alloy), there should still be some free vacancies after association is complete. These should then be able to anneal out at sinks leading to a steady drop in resistivity following the initial association effect. This mechanism

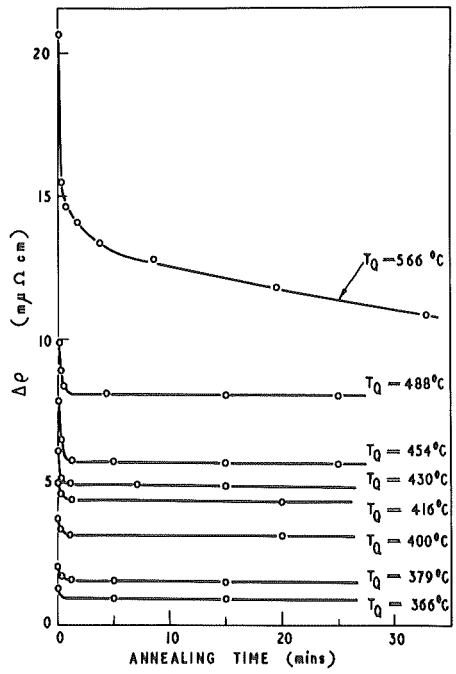

Fig. 3 Isothermal annealing of an Al-46p.p.m.In alloy at 20°C after quenching from various temperatures T_Q°C.

is consistent with feature (2) of the isothermal recovery curves.

On the basis of these results we are led to the conclusion that stage I recovery in the alloy, which occurs at about - 40°C and has no counterpart in the pure solvent, is due to solute-vacancy association.

One further feature of the isothermal recovery behaviour (Fig. 3) which is worthy of comment is that the magnitude of the initial resistivity decrease appears to increase continuously with T_Q, whereas it might be expected to saturate when the quenched-in vacancy concentration becomes equal to the solute concentration. This may be due to the formation of higher order indium-vacancy clusters.

On the basis of the interpretation of stage I recovery in the alloy we shall now examine the kinetics of the process.

4. THE KINETICS OF SOLUTE-VACANCY ASSOCIATION

The isothermal rate of solute-vacancy association is analysed using the approach of Damask and Dienes[2] modified to take account of the resistivity

effects. The basic assumptions, which will be considered in more detail later, are:-

(1) that only single vacancies, single solute atoms and solute-vacancy pairs are involved;

(2) that no loss of vacancies to sinks occurs during association

(3) that the distribution between free and bound vacancies existing at T_Q is retained by the quench.

At any time t of annealing at temperature T let the concentration of free vacancies be C_{fV}, of free solute atoms C_{fi} and of pairs C_{Vi}.

The association process is represented by

$$C_{fV} + C_{fi} \longrightarrow C_{vi} \tag{3}$$

with a rate constant

$$K_1 = 84\nu \exp(-E_V^M/kT) \tag{4}$$

where E_V^M is the activation energy for vacancy migration in pure aluminium and ν is the vibrational frequency.

The dissocation process is

$$C_{Vi} \longrightarrow C_{fV} + C_{fi} \tag{5}$$

the rate constant being

$$K_2 = 7\nu \exp(-(E_V^M + E_{Vi}^B)/kT) \tag{6}$$

Thus the rate equation is

$$\frac{dC_{fV}}{dt} = -K_1 C_{fv} C_{fi} + K_2 C_{Vi} \tag{7}$$

Now $$C_{fi} = C_i - C_{Vi}$$

and $$C_{fV} = C_V - C_{Vi}$$

where C_i and C_V are the total concentrations of solute atoms and retained vacancies respectively.

Hence

$$\frac{dC_{fV}}{dt} = -K_1 C_{fV}^2 + (K_1(C_V - C_i) - K_2)C_{fV} + K_2 C_V \,. \tag{8}$$

Integration gives

$$C_{fV} = \frac{b}{2K_1} + \frac{Y(1 + d\exp(-2YK_1t))}{1 - d\exp(-2YK_1t)} \qquad (9)$$

where

$$b = K_1(C_V - C_i) - K_2$$

$$Y^2 = \frac{b^2}{4K_1^2} + \frac{K_2C_V}{K_1}$$

and d is a constant of integration. This is determined from the boundary condition that at t = 0, $C_{fV} = C^o_{fV}$, the free vacancy concentration characteristic of T_Q and given by equation (1). It will be noted from equation (9) that the decay of vacancy concentration does not have a simple exponential time dependence.

In practice the free vacancy concentration is measured in terms of its resistivity effects. Let the specific resistivities of free vacancies, free solute atoms and solute-vacancy pairs be ρ_{fV}, ρ_{fi} and ρ_{Vi} respectively. The excess resistivity at any instant compared with a reference state in which the defect concentration is zero and all the C_i solute atoms are in solution is

$$\Delta\rho = C_{fV}\rho_{fV} + C_{fi}\rho_{fi} + C_{Vi}\rho_{Vi} - C_i\rho_{fi}$$

$$= C_{fV}(\rho_{fV} + \rho_{fi} - \rho_{Vi}) + C_V(\rho_{Vi} - \rho_{fi})$$

Defining γ as the decrease in specific resistivity due to the association of solute atoms and vacancies

$$\gamma = \rho_{fV} + \rho_{fi} - \rho_{Vi} \qquad (10)$$

gives

$$\Delta\rho = \gamma C_{fV} + (\rho_{fV} - \gamma)C_V \qquad (11)$$

It is usual to express the results in terms of $\Delta\rho/\Delta\rho_o$ with $\Delta\rho_o$, the initial excess resistivity after quenching, computed from equation (11), the appropriate values of C_{fV} and C_V being derived from equations (1) and (2) for the particular quenching temperature.

We have previously estimated the ratio of a bound vacancy to a free vacancy in the alloy to be 0.7[8]; using this value, equation (10) gives $\gamma = 0.3\rho_{fV}$. Taking ρ_{fV} as 2μΩcm./at.% pair concentration, the mean of the

values quoted by Takamura[12], we obtain a value for γ of 0.6μΩcm/at.% pairs. However, this value of γ is dependent on the value of ρ_{fV} which is not very reliable. Since the predicted shape of the annealing curves is sensitive to γ, an independent determination was made using the experimental data given in Fig. 3. Immediately after quenching, equation (11) gives the excess resistivity to be

$$\Delta\rho_o = \gamma C_{fV}^o + (\rho_{fV} - \gamma)C_V$$

After complete association, assuming that the quench temperatures are below that for which $C_V = C_i$, then $C_{fV} = 0$, and the resistivity excess is now

$$\Delta\rho_1 = (\rho_{fV} - \gamma)C_V$$

and the change in $\Delta\rho$ during association is

$$\delta(\Delta\rho) = \gamma C_{fV}^o$$

$$= \gamma A(1 - 12C_i)\exp(-E_V^F/kT_Q) \qquad (12)$$

Thus a graph of $\ln\delta(\Delta\rho)$ against $1/T_Q$ should be linear with gradient $-E_V^F/k$. Values of $\delta(\Delta\rho)$ were obtained from Fig. 3 and gave the results shown in Fig. 4.

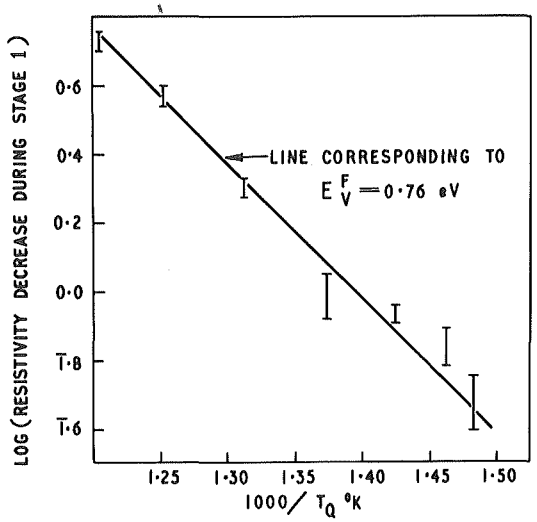

Fig. 4 Plot of logarithm of the decrease in resistivity during stage I annealing versus reciprocal of absolute quench temperature for an Al-46p.p.m. In alloy.

The line drawn corresponds to $E_V^F = 0.76eV$ and is seen to be a reasonable representation of the data. From the intercepts and taking A = 8 gave $\gamma = (0.5 \pm 0.1)\mu\Omega cm./at.\%$ pairs which is in good agreement with the value determined above.

Using the above quoted values of γ, A, ρ_{fV} and E_V^F and taking $E_V^M = 0.65eV$[13] and $E_{Vi}^B = 0.4eV$[8], the shape of the isothermal annealing curves

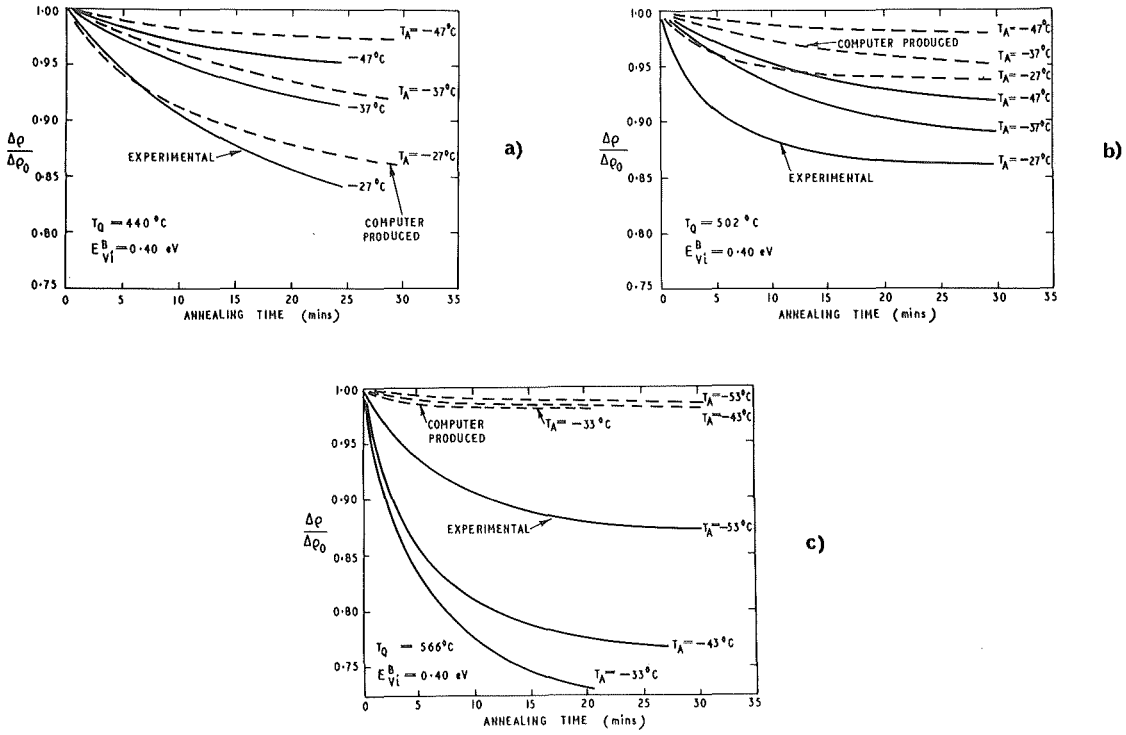

Fig. 5. Comparisons of experimental and theoretical stage I annealing curves for an Al-46p.p.m. In alloy quenched from (a) 440°C, (b) 502°C and (c) 566°C.

within stage I can be predicted for any set of quenching and annealing conditions from equations (9) and (11). To compare the theory with experiment, a resistometric study of isothermal annealing of the Al-46p.p.m. indium alloy was performed after quenching from 440°C, 502°C and 566°C. The theoretical annealing curves for the equivalent conditions were obtained with the aid of a digital computer, and these are shown together with the experimental curves in Fig. 5.

5. DISCUSSION

a). Estimate of E^B_{Vi} from loop density measurements

It is possible to make a crude estimate of the indium-vacancy binding energy from the loop density measurements made before and after stage II recovery.

In pure aluminium loop formation occurs readily at room temperature. In the alloys studied only a low concentration of loops are formed at room temperature, the concentration decreasing with indium content, whereas copious loop formation occurs only after a higher temperature anneal, 50°C for the 60p.p.m. indium alloy and 100°C for the 375p.p.m. indium alloy. It is reasonable to assume that the loops formed at room temperature arise from the unbound vacancies and that higher temperatures are required to free the bound vacancies. On this basis the ratio of vacancies in the form of loops formed before and after stage II annealing is the ratio of C_{fV} to C_{Vi} at 20°C. Using equations (1) and (2) gives E^B_{Vi} = 0.26eV for the alloy containing 60p.p.m. indium and E^B_{Vi} = 0.27eV for that containing 375p.p.m. indium.

These results are of course subject to large error. The loop density count after the room temperature anneal is likely to be a poor estimate of C_{fV} because (a) of the errors in counting low densities, (b) of the loss to permanent sinks, (c) some defects may be too far away from loops to reach them in the time allowed, (d) some loops may be out of contrast or too small to be seen, and (e) the removal of the free vacancies from the system will cause vacancies to be released from the traps.

Errors (b) and (d) also apply to the estimation of C_{Vi} and are partly compensating. In any case the effect of (d) was minimised by using the same diffracting conditions and (b) by deliberately choosing areas remote from dislocations and grain boundaries. Error (e) is likely to be small in view of the high binding energy reported for indium and in view of the experimental observation that higher temperatures are required for substantial loop formation. Moreover, the error from (e) is opposite to those of (a) to (d).

We consider that this result, although admittedly crude, is consistent with the previously reported high vacancy binding energy for indium in aluminium.

b). Kinetics of association

The agreement between the experimental and theoretical annealing curves is reasonable for the lowest quench temperature bearing in mind the uncertainty in the parameters used to compute the theoretical curves.

The tendency for the agreement to be poorer with decreasing temperature

could well be a consequence of the experimental technique. The quenching bath temperature and the lowest annealing temperature were comparable and although transfer into liquid nitrogen was accomplished rapidly the specimens will have had an effective anneal prior to the first measurement so that all given annealing times are in effect smaller than the real times. Such an error accounts for at least part of the disagreement between theory and experiment and we expect best agreement for the highest annealing temperature where this error will be least.

We now consider the agreement for the lowest quench temperature in the light of the assumption used in the theoretical analysis. For low T_Q, $C_v << C_i$ and the value of E^B_{Vi} = 0.4eV exceeds the divacancy binding energy of 0.17eV[13]. Thus a vacancy is more likely to encounter a solute atom before another vacancy and the solute-vacancy pair once formed will be stable relative to the divacancy; thus we expect that divacancies will not be important for the low quench temperature. Similarly it appears unlikely that divacancy-solute clusters will be formed. The importance of solute clustering is more difficult to assess. The solubility of indium is small and precipitation occurs implying that indium clustering will occur. If clusters are inherited from high temperatures this effectively reduces C_i. The annealing curves are not very sensitive to C_i. Solute clustering after quenching should be a slower process than association since association must be a first step in solute diffusion. Also clustering occurs, if at all, during the loss of vacancies to sinks, i.e. in stage II. Thus we conclude that our first assumption, i.e. that only single vacancy - single solute atom association is involved in stage I annealing, is reasonable for low quench temperatures.

The second assumption, i.e. no loss of vacancies to sinks during association, is also reasonable. De Jong[4] showed that the number of jumps a defect makes before association is very much less than that required to reach a sink. Furthermore, the experimental evidence shows that higher temperatures are required for stage II than for stage I.

The most questionable assumption is that of no association during the quench. A theoretical discussion of the reactions occurring during quenching has been given by Doyama[6]. According to this treatment there exists a critical temperature T^* above which vacancy mobility is sufficient to maintain solute-vacancy equilibrium and below which it is not. T^* varies with T_Q, C_i and E^B_{Vi} and the quench rate. The cooling rate was not measured in the present investigation but using reasonable values in conjunction with Doyama's results we estimate T^* to be about 170°C for T_Q = 440°C. The ratio C_{Vi}/C_V after

quenching would thus be about 0.95 which is considerably greater than the figure of 0.28 used in our computations. The significance of this difference may be illustrated by calculating the value of $\Delta\rho/\Delta\rho_o$ after complete association. This is

$$\left(\frac{\Delta\rho}{\Delta\rho_o}\right)' = \frac{(\rho_{fV} - \gamma)C_V}{\gamma C^o_{fV} + (\rho_{fV} - \gamma)C_V} \qquad (13)$$

$C^o_{fV}/C_V = \alpha$, say, is a constant numerical factor which, if no association occurs during quenching, is determined by T_Q only. For $T_Q = 440^oC$, $\alpha = 0.72$. Using this value and that of γ derived from Fig. 4 gives $(\Delta\rho/\Delta\rho_o)' \simeq 0.8$ which is in good agreement with the results in Fig 5(a). (This agreement does not necessarily prove the validity of the assumption of no association during quenching since γ was determined on that basis. It does however demonstrate the internal consistency of the results because different sets of data were used to compute γ and $(\Delta\rho/\Delta\rho_o)'$). If association occurs during the quench, α is determined by T^* being 0.06 for $T^* = 170^oC$. To obtain agreement in this case requires that $\gamma = 1.6\mu\Omega cm/at.\%$ pairs and the ratio of the resistivities of a bound and free vacancy would then be 0.2. This value seems improbably low.

A further prediction of Doyama's theory is that T^* is relatively insensitive to T_Q so that a constant fraction of free vacancies is inherited irrespective of T_Q. Increasing T_Q increases C_V and thus the number of free vacancies and the magnitude of the resistivity decrease during association increases with T_Q. The interpretation of Fig. 3 given previously is not materially affected. This also applies to the derivation of equation (12); the factor $(1-12\ C_i)$ is replaced by a numerical constant related to T^* and this constant when used with the intercept gives the value of γ required to account for the resistivity change $(\Delta\rho/\Delta\rho_o)'$.

The situation for the higher quenching temperature is more complicated; the agreement between theory and experiment becomes worse as T_Q increases. It is interesting to note that some of the effects of any uncertainty in ρ_{fV} can be eliminated by comparing the rate of decay as a function of time. From equations (9) and (11),

$$\frac{d}{dt}(\Delta\rho) = \frac{-4\gamma Y^2 K_1 d \exp(-2YK_1 t)}{(1-d\exp(-2YK_1 t))^2} \qquad (14)$$

whereupon it will be seen that the rate of decay of $\Delta\rho$ is independent on ρ_{fV}.

Fig. 6 shows a comparison of the experimental curves (derived from Fig. 5(b)) and the theoretically predicted curves (from equation (14)) for the variation

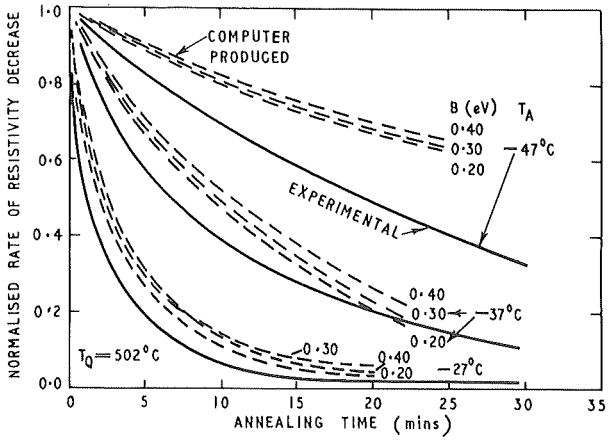

Fig. 6 Comparison of experimental and theoretical differential resistivity decay curves for an Al-46p.p.m. In quenched from 502°C.

of $\frac{d}{dt}\left(\Delta\rho/\Delta\rho_o\right)$ with time at -23°, -37° and -47°C after quenching from 502°C. Note that the agreement is now much improved particularly for the highest annealing temperature. It should also be noted that the predicted association rate is relatively insensitive to E^B_{Vi}. Thus studies of solute-vacancy association kinetics provides no useful information concerning the value of E^B_{Vi}.

Doyama's theory does not apply for the higher T_Q because $C_V > C_i$ and only qualitative considerations are possible. It is known from previous quenching studies on aluminium that divacancy formation becomes increasingly important as T_Q increases. Thus the assumption of single vacancy-single solute atoms interaction is likely to be increasingly in error at high T_Q; this is consistent with the agreement being better for low T_Q. Divacancy migration requires a lower activation energy than a single vacancy, the generally accepted value being $\approx$ 0.50eV[13]. The annealing curves are particularly sensitive to the migration energy of the important defect. If a significant amount of divacancy-solute association occurs a faster rate would result. This is consistent with the fact that the present theory always predicts a slower decay than the actual one and that the divergence increases with T_Q.

6. CONCLUSIONS

1. Vacancy recovery in quenched aluminium containing small additions of indium occurs in three stages, showing (i) solute-vacancy association, (ii) the formation of dislocation loops and (iii) disappearance of the secondary defects.

2. The isothermal rates of stage I annealing for low quenching temperatures are consistent with the Damask and Dienes theory modified to allow for the resistivity of a solute-vacancy pair being less than that of a free vacancy and free solute atom.

3. The present data does not preclude extensive association occurring during the quench as proposed by Doyama[6], but if this is the case an improbably high resistivity change must accompany association.

4. Studies of the solute-vacancy association cannot be used to estimate values of solute-vacancy binding energies.

5. Measurements of loop density after quenching and annealing indicate that the indium-vacancy binding energy in aluminium is high, confirming the results of earlier resistivity studies.

REFERENCES

1. W. M. Lomer, "Vacancies and Other Point Defects in Metals and Alloys" Institute of Metals, 79, (1958).
2. A. C. Damask and G. J. Dienes, Phys. Rev. 120, 99, (1960).
3. A. C. Damask and G. J. Dienes, Acta Met. 12, 797, (1964).
4. M. De Jong, Phil. Mag. 11, 1189, (1965).
5. R. E. Howard and A. B. Lidiard, Phil. Mag. 11, 1179, (1965).
6. M. Doyama, Phys. Rev. 148, 681, (1966).
7. F. C. Duckworth and J. Burke, Brit. J. Appl. Phys. 18, 1071, (1967).
8. F. C. Duckworth and J. Burke, Phil. Mag. 14, 473, (1966).
9. C. Panseri and T. Federighi, Phil. Mag. 3. 1223, (1958).
10. P. B. Hirsch, J. Silcox, R. E. Smallman and K. H. Westmacott, Phil. Mag. 3 897, (1958).
11. M. Kiritani, J. Phys. Soc. Japan 19, 618, (1964).
12. J. Takamura, "Lattice Defects in Quenched Metals" (Academic Press Inc., New York), 521, (1965).
13. M. Doyama and J. S. Koehler, Phys. Rev. 134, A522, (1964).

Fault climb during growth of Frank loops in quenched silver and copper-aluminium alloys.

L.M. CLAREBROUGH and A.J. MORTON

University of Melbourne, Australia

Abstract

The Burgers vectors of the dislocations, bordering steps in the stacking fault in Frank dislocation loops in quenched silver and copper-aluminium alloys, have been identified by comparison of experimental images and images computed using the Head-Humble technique. Similar comparisons show that the edges of Frank dislocation loops in these materials are dissociated. Dissociation of the edges of loops, once aligned along ⟨110⟩, hinders growth of the loops at the edges by simple vacancy addition, and growth continues by climb of the stacking fault. Fault climb is compatible with the observed Burgers vectors and particular configurations of the loops.

I. Introduction

The annihilation of vacancies by climb of dislocations is more difficult for dissociated than undissociated dislocations, since in the former case constriction is necessary for jog formation. However, climb of a dissociated dislocation may occur without constriction if the stacking fault climbs together with the partials (1,2).

Fault climb has been treated theoretically by Escaig (2), but direct experimental evidence for fault climb is lacking. Cotterill (3), using the model of fault climb due to Schapink and de Jong (4), suggested that double loops in quenched aluminium may be an example of fault climb. However, the diffraction contrast associated with these defects indicates that they consist of two overlapping intrinsically faulted Frank dislocation loops (5).

A complex form of Frank loop (referred to here as complex loop) in which one or more steps occur in the stacking fault, has been observed in quenched silver (6), and recent results have shown that defects of this type are common in quenched copper-aluminium alloys, but are not found in aluminium (7). Thus the formation of this type of defect appears to be associated with materials of low stacking-fault energy.

In this paper, the following will be shown from a comparison of experimental and computed electron microscope images:

(a) Frank dislocations in silver and copper-aluminium alloys are dissociated.

(b) Steps in complex loops are usually faulted and bounded by 1/6⟨110⟩ dislocations along step edges.

(c) Occasionally unfaulted steps occur with 1/6⟨112⟩ dislocations along step edges.

(d) Configurations of complex loop occur in which two faulted steps, bounded by 1/6⟨110⟩ dislocations, enclose a triangular region at the edge of the loop.

Complex loops may form either by the union of two edges of neighbouring loops by their dissociation on a common {111} plane,

or by climb of the stacking fault. The union mechanism is compatible with (a) and (b), but incompatible with (c) and (d). However, fault climb is compatible with all four observations.

II. Experimental

Cominco 69 grade silver and two copper-aluminium alloys containing 9.4 and 15.6 at % aluminium were used. Strip specimens 15 cm long, 3 mm wide and 125 μm thick for silver, and 75 μm thick for the copper-aluminium alloys, were heated electrically and quenched into silicone oil at 20°C from an argon atmosphere (silver), and from a carbon monoxide atmosphere (copper-aluminium).

For these quenching conditions, the loops in all materials were generally large (edge lengths of 0.5 μm were common), and were present in low density (maximum density $5 \times 10^{13}/cm^3$) with 25% of the loops complex.

The plane of the loops and the sense of the reflecting vector ($\underline{g}$) were determined in the usual way (8), and simple and complex loops which intersected a foil surface were shown to be intrinsically faulted (9,10).

III. Image Computation

Dislocation images were computed using the Head-Humble technique (11,12), which can treat two dislocations and up to three faulted planes taking account of the true foil normal (FN). The configurations of faults and dislocations involved in the computations are shown in Fig. 1. Fig. 1 (a) and (b) illustrate a section through a foil containing two parallel dislocations (D_1,D_2) bounding three faulted planes (1,2,3); the section plane containing the beam direction ($\underline{B}$) and the line $\underline{B} \wedge \underline{u}$, where $\underline{u}$ is a vector along the dislocation line. The positive sense of the dislocations is out of the paper. Although the same planes are parallel in Fig. 1 (a) and (b), different situations are represented, in that the planes include acute angles in (a) and obtuse angles in (b). These different situations are treated by denoting the normal to plane 2 as downward in (a) and upward in (b). In treating a faulted step in a stacking fault, all planes are faulted and D_1 and D_2 are stairrod dislocations. For an unfaulted step, or two Frank dislocations which are not separated laterally to any great extent, the shear on 2 is taken as zero and D_1 and D_2 are both Shockley or Frank dislocations. A dissociated Frank dislocation is treated by defining the shear on plane 1 (say) to be zero, planes 2 and 3 to be faulted {111} planes and D_1 and D_2 to be Shockley and stair-rod dislocations respectively. To treat overlapping Frank loops, where the overlap is considerable, the programme is modified to treat the situation shown in Fig. 1 (c). Here, plane 2 is always parallel to plane 1, extends over all fields of the computed image, and is no longer bounded by D_1 and D_2. With the shear on plane 3 and the Burgers vector of D_2 put to zero, the geometry reduces to overlapping faults with one fault terminating in the field.

The computed images are made up of 129 profiles, each containing 60 points, with the variation in intensity obtained by the use of different combinations of single and overprinted characters (11). The dislocation runs from left to right, with the top of the foil on the right and the bottom on the left. The programme is such that images can be computed for the whole length of the dislocation from top to bottom of the foil, or for any selected

portion (12). Computation of a selected portion of the dislocation line results in increased magnification in the computed image, and this is frequently needed to obtain adequate resolution of image detail.

In the computations, 7% below and 15% above background intensity have been taken as the visibility limits. That is, respectively darker and lighter characters than those used for background intensity come into operation at these visibility limits. In all computations, the value of 0.1 has been taken for anomalous and real absorption.

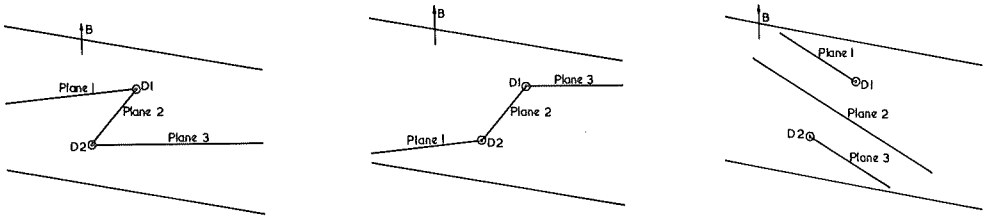

(a) (b) (c)

Fig. 1 Geometrical arrangement of fault planes and dislocations used in image computation

IV. Contrast from Undissociated and Dissociated Frank Dislocations

Computations of theoretical images for undissociated and dissociated Frank dislocations have shown that the contrast from dissociated dislocations differs markedly from that of undissociated dislocations (13), and that the details of the contrast are sensitive to the separation (S) of the Shockley and stair-rod dislocations (14). The main features of the contrast from dissociated Frank dislocations in bright field images, which distinguishes them from undissociated dislocations are as follows:

(a) For 111 reflections, dark contrast occurs when $\underset{\sim}{g}.\underset{\sim}{u} \neq 0$;

(b) For 220 reflections, images are single and continuous, rather than double and dotted, with strong contrast on one side only. The strong contrast does not invert from side to side for $+\underset{\sim}{g}$ and $-\underset{\sim}{g}$;

(c) For 020 reflections, and $\underset{\sim}{g}.\underset{\sim}{u} = 0$, a distinct light band occurs between the edge of the image and the stacking fault fringes, and there is not clear reversal of contrast in $+\underset{\sim}{g}$ and $-\underset{\sim}{g}$. For $\underset{\sim}{g}.\underset{\sim}{u} \neq 0$, reversal of contrast in $+\underset{\sim}{g}$ and $-\underset{\sim}{g}$ depends on the beam direction.

A comparison of experimental and computed images, for edges of Frank dislocation loops in silver and copper-aluminium alloys, shows that the edges of these loops are dissociated. Some of the features of dissociated Frank contrast in copper-aluminium alloys are shown in Figs. 2-4. In each case it can be seen that the computed image for the undissociated Frank dislocation does not match the experimental image. The computed images shown in each case for the dissociated Frank dislocation correspond to a value of S considered to give the best match to the experimental image. These images have been selected from images covering a wide range of separations. Contrast along the edge of a loop for a 111

reflection, and a continuous image with strong contrast on one side for a 220 reflection, are shown in Fig. 2. The fact that the image does not invert from side to side on changing the sense of g for an 022 reflection, and non-reversal of contrast for an 020 reflection are illustrated in Figs. 3 and 4 respectively.

Contrast effects similar to those shown are observed for Frank dislocation loops in silver, and it is concluded that loops in copper-aluminium alloys and in silver are dissociated. Image matching suggests values of S of approximately 60 - 70 Å in silver and in copper 9.4% aluminium alloy, and 140 - 160 Å in the copper 15.6% aluminium alloy. If these values of S are taken as equilibrium separations, the calculated values of Stacking-fault energy are in agreement with node measurements.

V. Complex Loops

Steps in complex loops always lie along ⟨110⟩ directions and can be clearly shown to be steps, for large step heights, by suitable specimen rotation (Fig. 5). However, smaller steps are generally observed only by some change in contrast along a ⟨110⟩ direction within the loop, e.g. fringe displacement and/or a change in intensity. The contrast at steps is, in general, more complex than the dark contrast for 111 reflections and the light contrast for 020 reflections shown by Tunstall and Goodhew (5) to arise from overlapping Frank dislocation loops in aluminium. Fig. 6 is an example of a complex loop in a copper-aluminium alloy showing dark contrast at the step for 020 reflections and light contrast for 111 reflections. Characteristic configurations for complex loops involving a triangular region, or a step symmetrically disposed across the centre of the loop, are shown in Fig. 7 (a) and (b). For complex loops showing triangular regions, one edge of the triangular region was always coincident with one edge of the main loop. This is contrary to the behaviour of double loops in quenched aluminium.

The Burgers vectors of dislocations bordering the steps in complex loops, in silver and the copper 9.4% Al alloy, were determined by comparison of experimental and computed images (7). This involved computation of images for a large number of possible Burgers vectors and a series of step heights, but only a few examples will be given here.*

Generally, it was possible to determine whether a step was acute or obtuse, or whether the dislocations bordering the step were of edge character. However neither of these facts was known for the loop shown in Fig. 7(b). The loop is on (111), with the step AB along $[\bar{1}01]$, and the corners B and A close to the top and bottom surfaces of the foil respectively. The fringe shift across the step suggests a step height of approximately $0.75\,\xi_{111}$ for an acute bend or $0.25\,\xi_{111}$ for an obtuse bend.

All possible Burgers vectors for a faulted or unfaulted obtuse step at a step height of $0.25\,\xi_{111}$ were tested for two reflecting vectors by image computation and in no case was agreement obtained with the experimental images.

---

* All examples given here involve an intrinsic fault in the step, or no fault, but the possibility that the fault in a step is extrinsic has also been tested and found not to fit the experimental images.

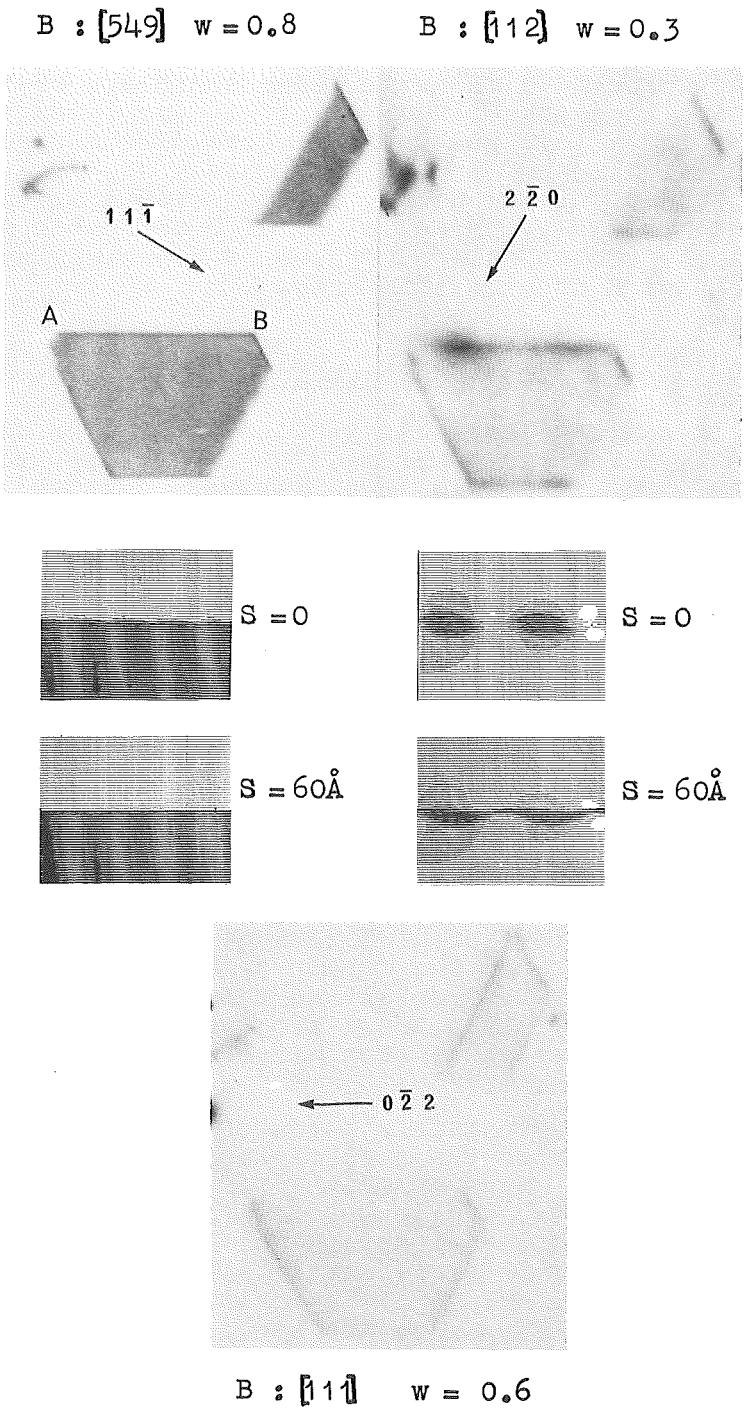

Fig. 2 Comparison of experimental and computed images for the edge AB ($u : [0\bar{1}1]$) of a Frank dislocation loop on (111) in a Cu 9.4% Al alloy. FN is [425] and foil thickness (t) is $7\xi_{111}$. B, w and g are indicated. The experimental images are x120,000, and the line resolution (R) in the computed images is 30 Å.

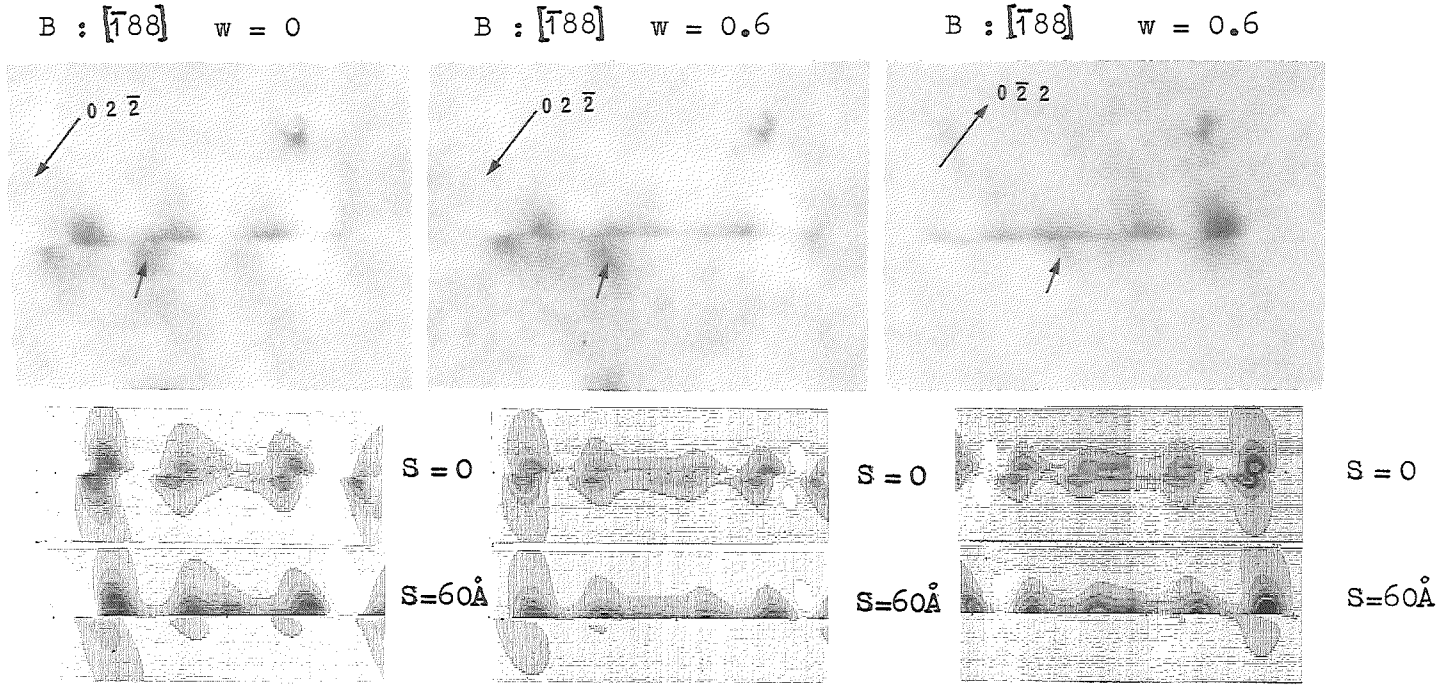

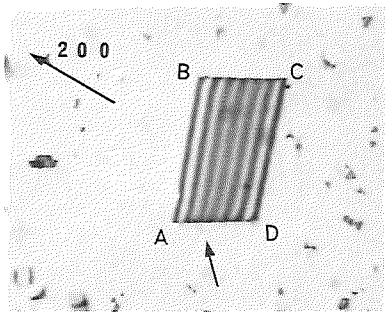

B : [011]

Fig. 3 Comparison of experimental and computed images for the edge AD (u : [1̄01]) of a Frank dislocation loop on (111) in a Cu 9.4% Al alloy. FN is [102] and t is 4ξ022. B, w and g are indicated. The 022 images are x200,000 and the 200 image x60,000. R = 15 Å. An artifact causing contrast in all images is indicated by an arrow.

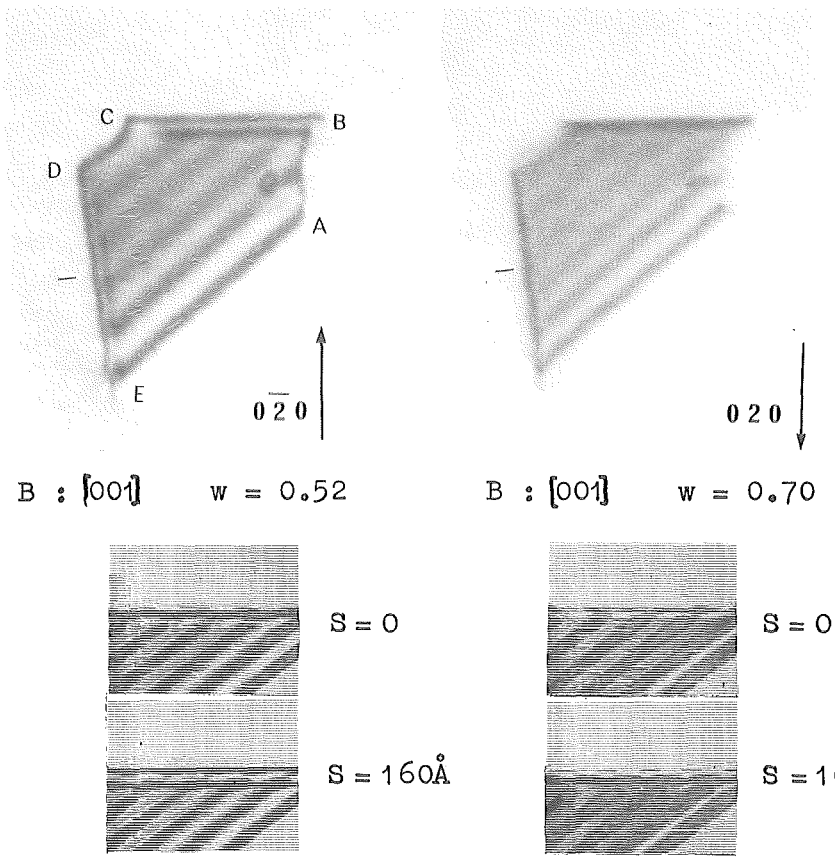

Fig. 4 Comparison of experimental and computed images for the edge CB ($\underline{u}$: [1̄01]) of a Frank dislocation loop on (11̄1) in a Cu 15.6% Al alloy. FN is [207] and t is 6.5 ξ 020. $\underline{B}$, w and $\underline{g}$ are indicated. Micrographs x200,000. R = 20 Å.

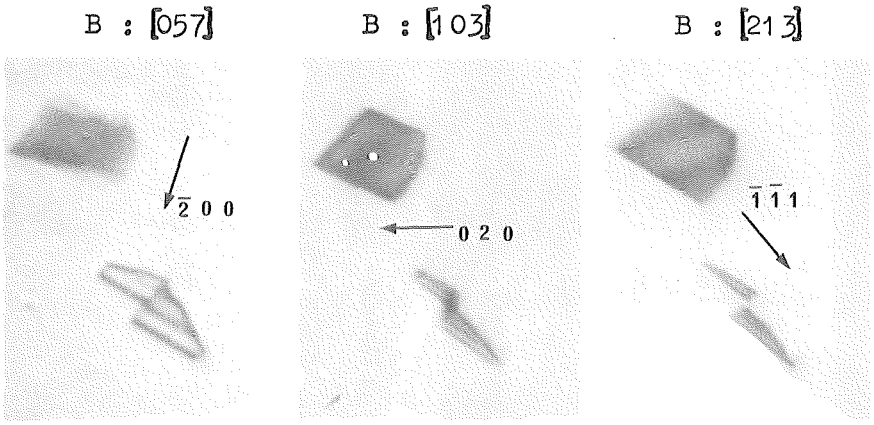

Fig. 5 Large step in a complex loop in a Cu 9.4% Al alloy. x120,000

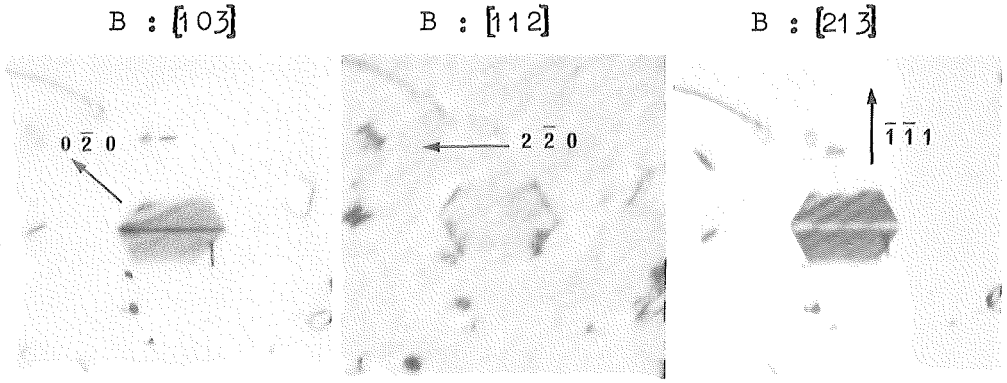

Fig. 6 Contrast at step in a complex loop in a Cu 9.4% Al alloy. x60,000

For an acute bend the possible Burgers vectors of dislocation dipoles bordering the step are 1/6 [101] and 1/3 [101], for a faulted step; 1/6 [12$\bar{1}$], 1/6 [11$\bar{2}$] and 1/6 [$\bar{2}$11] for an unfaulted step; and 1/3 [111] if the defect consists of Frank loops slightly overlapping along AB. All these Burgers vectors were tested by a comparison of experimental and computed images, for a step height of 0.75 ξ_{111}, and eight reflecting vectors. The Burgers vector 1/6 [101] was the only one that gave good matching between the experimental and computed images for all reflecting vectors. In this case, it was possible to show that 1/6 [101] is the correct Burgers vector from fine detail in the $\bar{2}00$ image. Fig. 8 shows the $\bar{2}00$ image of the loop in Fig. 7(b) and the computed images for the above Burgers vectors. The characteristic features of the experimental image at the step AB are the fine dark line, approximately 30 Å wide, in a lighter background in both dark and light fringes, and the shape of the dark fringes at the step. These features occur only in the computed image for the 1/6 [101] Burgers vector. The step in this loop is thus bordered by 1/6 [101] and 1/6 [$\bar{1}$01] stair-rod dislocations at a separation of approximately 180 Å.

Fig. 9 (a) - (d) gives an example where the fringe shift at the surface intersection CDE (Fig. 9(d)) indicates an acute step with a step height of approximately 0.5 ξ_{111}. The loop is on (111) and is intrinsically faulted. The step FD is along [$\bar{1}$10] so that the plane of the step is (11$\bar{1}$). The possible Burgers vectors for the dislocation dipole at the step are 1/6 [110] and 1/3 [110] for a faulted step, 1/6 [2$\bar{1}$1], 1/6 [1$\bar{2}$1] and 1/6 [11$\bar{2}$] for an unfaulted step, and 1/3 [111] if the defect consists of two Frank dislocation loops slightly overlapping along FD. Of these Burgers vectors, only 1/6 [110] fits the experimental images, and the computed images for a step bordered by 1/6 [110] and 1/6 [$\bar{1}\bar{1}$0] dislocations at a separation of 120 Å are compared with the experimental images in Fig. 9. The magnification of the computed image in Fig. 9(b) is not sufficient to resolve the fine detail of the 200 image and this image and a computed image at higher magnification are given in Fig. 9(d).

Fig. 10 is an example of non-edge dislocations bordering a step (cf. 02$\bar{2}$ image in Fig. 10(a)). In this loop, two steps occur along [0$\bar{1}$1]. The loop is on ($\bar{1}$11), is intrinsically faulted and intersects the bottom of the foil along BC. From the fringe shift at the surface, the step HI is obtuse and fringe matching across the step FG indicates that this step is also obtuse. The possible Burgers vectors for the dislocation dipole at the step FG are 1/6 [1$\bar{3}$0], 1/6 [10$\bar{3}$], 1/6 [130] and 1/6 [103] for a faulted step, and 1/6 [12$\bar{1}$] and 1/6 [11$\bar{2}$] for an unfaulted step. The fringe shift at the step suggests a step height of 0.25 ξ_{111}. Image matching indicated that 1/6 [1$\bar{3}$0] and 1/6 [11$\bar{2}$] were the only likely Burgers vectors, and a decision was made between them from a comparison of experimental and computed images for seven reflecting vectors. The most striking difference in the images for these two Burgers vectors was obtained in the 1$\bar{1}$1 image. Experimental and computed images of comparable resolution (Fig. 10(b)) show that 1/6 [11$\bar{2}$] fits all detail of the experimental image. It is concluded that the step along FG is obtuse, unfaulted and bordered by 1/6 [11$\bar{2}$] and 1/6 [$\bar{1}$1$\bar{2}$] dislocations at a separation of approximately 60 Å.

As shown in Fig. 7(a), a characteristic configuration for complex loops is a triangular region within the main loop with one edge of the triangular region along one edge of the main loop. Experimental and computed images for an example of this type in silver are given in Fig. 11.

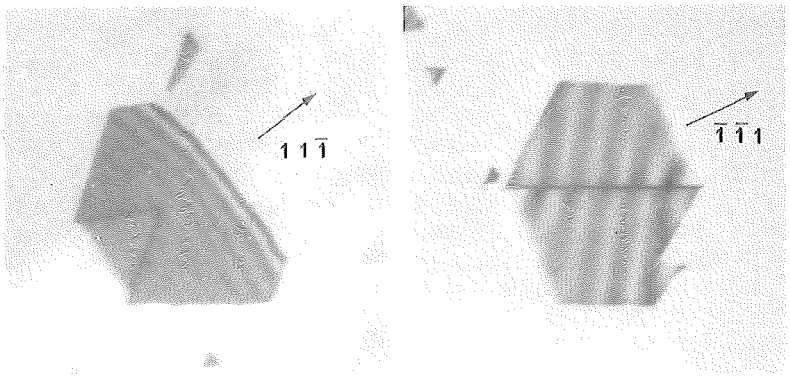

(a) (b)

Fig. 7 Complex loops in (a) silver, (b) Cu 9.4% Al. x 60,000

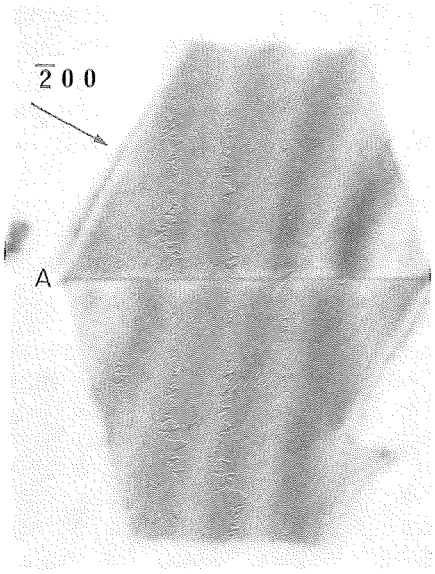

B : [057]

w = 0.46

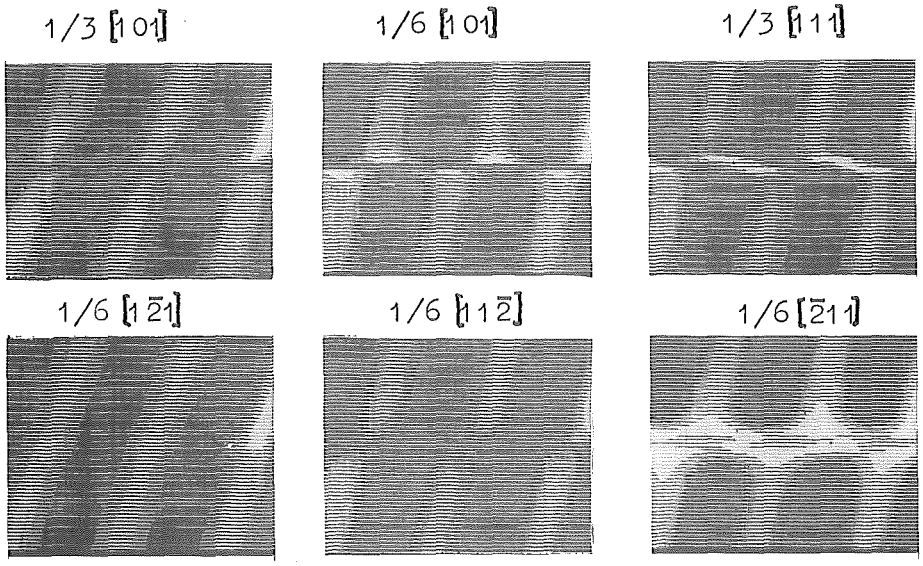

Fig. 8 Comparison of experimental and computed images for the step AB (u : [1̄01]) in a complex loop on (111) in a Cu 9.4% Al alloy. The Burgers vectors corresponding to the various computed images are indicated. FN is [379] and t is 6.5 ξ111. B, w and g are indicated. In all cases the separation of the dislocations at the step is 0.75 ξ111. The micrograph is x200,000 and R = 18 Å.

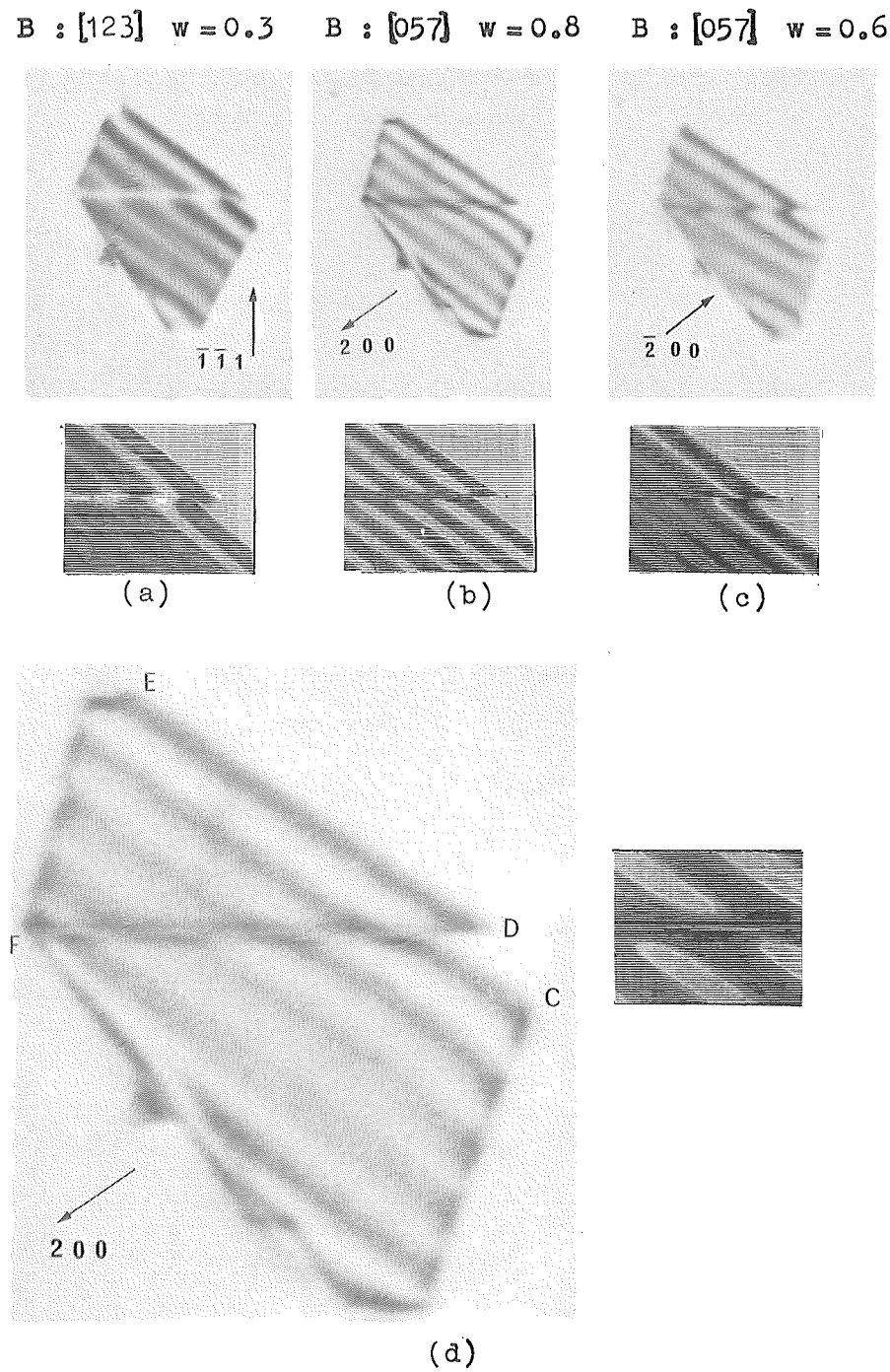

Fig. 9 Comparison of experimental and computed images for the step FD ($u : [\bar{1}10]$) in a complex loop in a Cu 9.4% Al alloy. The loop is on (111) and the step on ($11\bar{1}$). FN is [157] and t is $6\xi_{111}$. B, w and g are indicated. The micrographs in (a), (b) and (c) are x98,000, and in (d) x320,000. All computed images are for 1/6 [110] stair-rod dislocations at a separation of $0.5\,\xi_{111}$. R for (a) - (c) is 30 Å and for (d) is 11 Å.

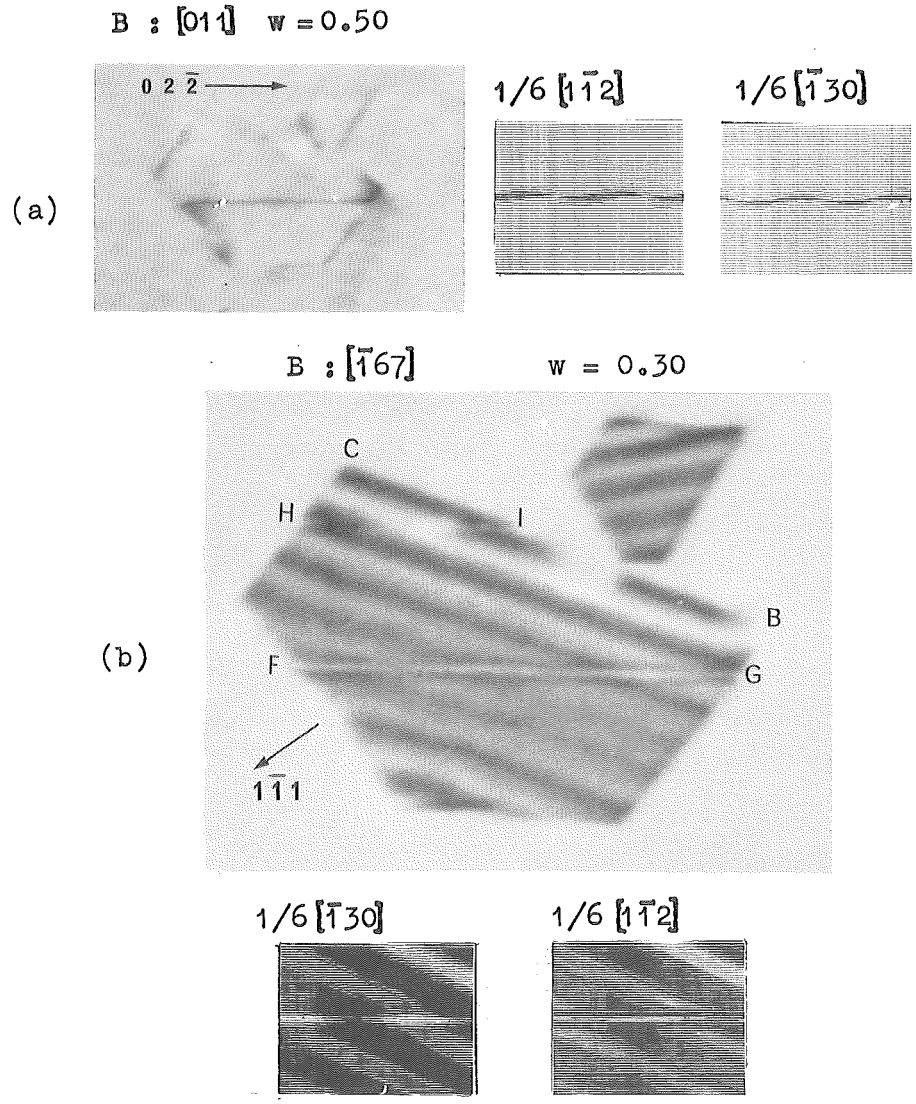

Fig. 10 Comparison of experimental and computed images for the edge FG (u : [01$\bar{1}$]) of a complex loop on ($\bar{1}$11) in Cu 9.4% Al. The Burgers vectors for the computed images are indicated and the separation of the dislocations at the step is 0.25 ξ_{111}. FN is [$\bar{1}$23] and t is 7 ξ_{111}. B, w and g are indicated. The micrograph in (a) is x90,000 and in (b) x200,000. R for (a) is 56 Å and for (b) is 25Å.

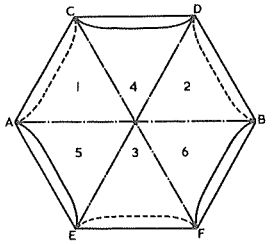

Fig. 12 Schematic illustration of a dissociated Frank loop
_____ above plane, ------ below plane

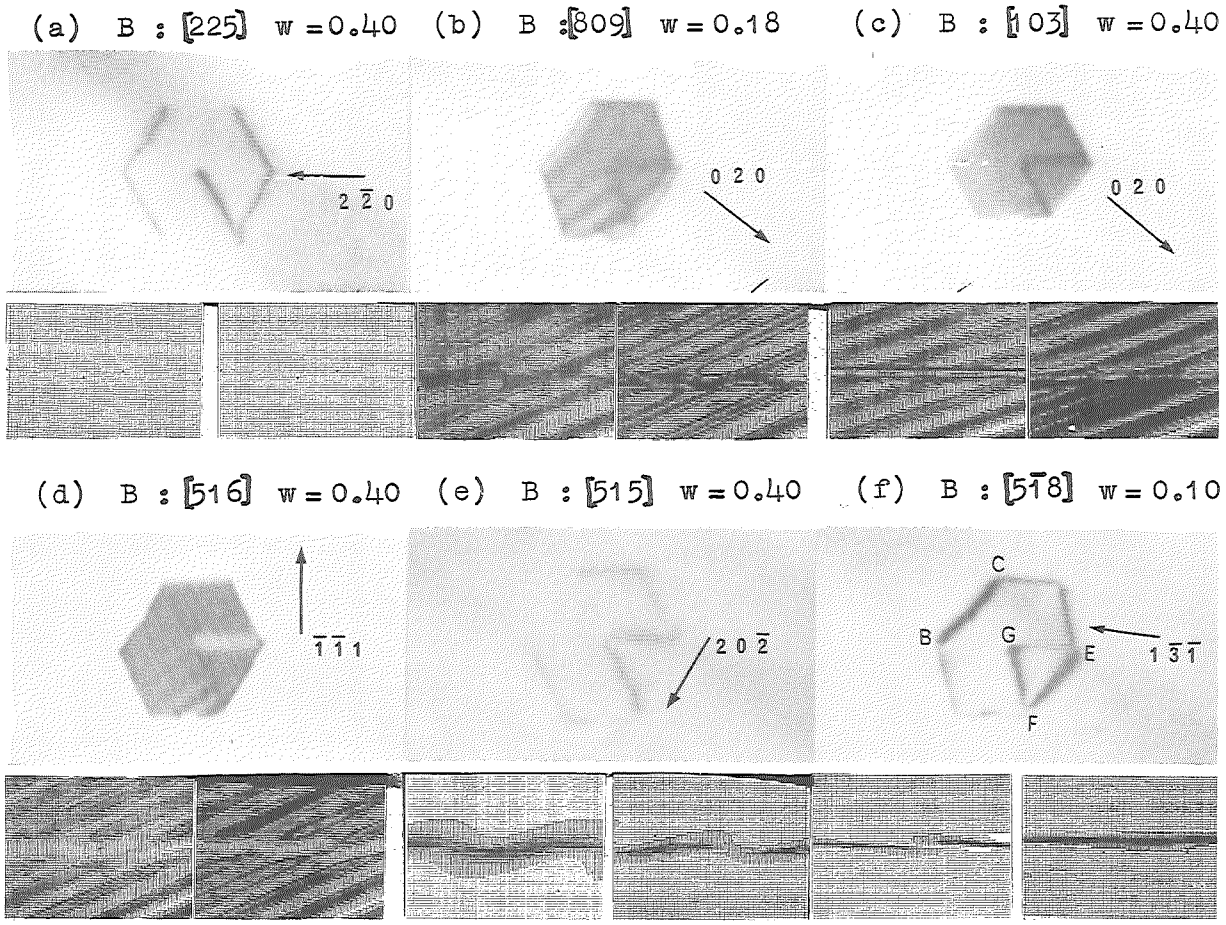

Fig. 11 Comparison of experimental and computed images for the edge GE (u : [1̄10]) of a complex loop on (111) in Ag. The Burgers vector for the computed images on the left is 1/6 [110] and on the right 1/3 [111]. In all computed images the separation of the dislocations along GE is 0.70 ξ_{020}. FN is [418] and t = 9 ξ_{111}. B, w and g are indicated. R is 30 Å for all reflections except 20$\bar{2}$ and 1$\bar{3}$1 where R is 20 Å and 40 Å respectively. All micrographs x100,000.

The loop is on (111) and the $1\bar{3}\bar{1}$ image shows that it does not intersect either surface of the foil. The triangular region EFG is bounded by $[10\bar{1}]$ (EF), $[0\bar{1}1]$ (FG) and $[\bar{1}10]$ (GE). The protrusion outside the main loop of the projection of the triangular region in Fig. 10 (b) and (d) indicates a large separation between the triangular region and the main loop. Further, the geometry of the triangular region and the above protrusion requires that FG and GE, if faulted steps, must be acute. Discussion will be confined here to the edges GE and FE. The dislocations along these edges have edge character (Fig. 11 (a) and (e)). The possibilities for the Burgers vectors of dislocations along GE are 1/6 [110] and 1/3 [110] if GE is a faulted step, 1/6 $[11\bar{2}]$ if GE is an unfaulted step, and 1/3 [111] if the contrast along GE is due to a triangular Frank dislocation loop overlapping a larger hexagonal loop. The contrast along FE is the same as that along BC for all reflecting vectors, so that the defect at FE is unlikely to be two overlapping Frank dislocations and is either an undissociated or dissociated Frank dislocation.

Preliminary computations for the 1/6 [110] and 1/3 [111] Burgers vectors for the edge GE, over a wide range of separations, indicated a separation of the triangular region from the main loop of approximately $0.70\,\xi_{020}$.

Computations have been made for the four possible Burgers vectors along GE, at a separation of 180 Å, for eight reflecting vectors. Obvious discrepancies between the experimental and computed images, e.g. dark instead of light contrast in the $\bar{1}\bar{1}1$ image, dismiss the 1/3 [110] and 1/6 $[11\bar{2}]$ Burgers vectors, leaving the decision to be made between 1/6 [110] and 1/3 [111]. The computed images for these two Burgers vectors are compared with the experimental images in Fig. 11. This comparison indicates a faulted step along GE bordered by 1/6 [110] and 1/6 $[\bar{1}10]$ dislocations at a separation of 180 Å for the following reasons. On rotation from $[80\bar{9}]$ to $[10\bar{3}]$ for the 020 reflection, the contrast along GE changes from an unresolved dark band to resolved dark lines approximately 100 Å apart. This change in contrast is in better agreement with the computed images for 1/6 [110] than for 1/3 [111]. The broad light band in the $\bar{1}\bar{1}1$ image is similar in both computed images, but the width of the band is better matched by 1/6 [110]. The $20\bar{2}$ image is continuous and is thus a better match with 1/6 [110] and the intensity of the $1\bar{3}\bar{1}$ image clearly favours 1/6 [110]. Computed images for the edge FG similarly favour a Burgers vector of 1/6 $[0\bar{1}1]$ for the dislocation dipole along this edge. Computed images for the edge FE indicate that this edge is a dissociated Frank dislocation with a separation of Shockley and stair-rod dislocations of approximately 60 Å.

The complex loop in Fig. 11 thus consists of a triangular region bordered by 1/6 ⟨110⟩ stair-rod dipoles along the steps GE and FG and a dissociated Frank dislocation along FE.

Because of the large amount of computation involved in positively identifying the Burgers vectors of dislocations at steps in complex loops, only a very limited number of cases have been fully treated. Complete computations of all possibilities enabling positive identification of 1/6⟨110⟩ Burgers vectors have been done for seven cases. Complete computations have been done for the two cases found to involve non-edge dislocations and both of these indicate 1/6⟨112⟩ Burgers vectors. Several other cases involving edge dislocations have been partially computed, and these also suggest 1/6⟨110⟩ Burgers vectors. These numbers grossly overestimate the ratio of 1/6⟨112⟩ to 1/6⟨110⟩ Burgers vectors as a deliberate effort was made to find non-edge dislocations at steps.

VI. Discussion

The steps in complex loops are large, varying in height from 60 to 180 Å. Only steps above a certain height would be expected to show detectable diffraction contrast and computations, for 1/6 ⟨112⟩ Burgers vectors at obtuse unfaulted steps and 1/6 ⟨110⟩ Burgers vectors at acute faulted steps, indicate that steps 20 Å high would be difficult to detect experimentally, and that contrast effects in computed images became negligible at step heights less than 10 Å. Thus the observed density of complex loops must be an underestimate.

The presence of complex loops in silver and copper-aluminium alloys, and their absence in aluminium, suggests that their formation is associated with low values of stacking-fault energy. The methods suggested for the formation of these defects both involve the dissociation of Frank dislocations. Dissociation is involved directly in the union of loops, and indirectly for the climb mechanism by making the addition of vacancies difficult at the edge of a growing loop. Diffraction contrast indicates that the edges of Frank dislocation loops in the materials used here are dissociated. In deciding between the two mechanisms, the relatively high incidence of complex loops favours the climb mechanism, since union of two loops requires that the dissociation be co-planar, which should be a relatively rare event, particularly for the low density of loops considered here. Only one example has been observed of a complex loop where the edges formed re-entrant angles consistent with the union of two polygonal loops.

Only 1/6 ⟨110⟩ and 1/6 ⟨112⟩ Burgers vectors have been identified at step edges with the former being the more common. The 1/6 ⟨110⟩ Burgers vector is to be expected for either union or fault climb, but 1/6 ⟨112⟩ is incompatible with union. The 1/6 ⟨112⟩ Burgers vector at unfaulted obtuse steps is compatible with fault climb and will arise if the climbed region departs from a triangular configuration, so that the bounding defects for the climbed nucleus are a combination of 1/3 and 2/3 vacancy jog lines (15). Such steps would remain unfaulted as faulting would involve the formation of high energy stair-rod dislocations or the nucleation of extrinsic fault.

The triangular configuration bounded by low energy stair-rod dislocations along two edges and a dissociated Frank along the third could only form by fault climb. Whilst some complex loops do form by union, it is considered that fault climb is the main mechanism for the formation of these defects.

Fault climb occurs by the nucleation and propagation of jog lines so that the formation of the large steps observed here may seem incompatible with the climb model. However, steps must result if jog lines produce climb up and climb down in different portions of a loop. Combination of regions which have climbed in opposite senses gives steps which increase in height with continued climb, even though climb at all stages involves the movement of jog lines.

The regular forms of complex loop in Fig. 7 were common forms for this defect. Such configurations may result from climb of a dissociated Frank loop. For a dissociated loop, the favoured sense of climb at a particular edge is related to the sense of dissociation. For example, the favoured sense of climb at an edge dissociated below the plane of the loop will be above the plane. Fig. 12 illustrates a hexagonal loop for which alternate edges are dissociated above and below the plane of the loop. Nucleation of climb in regions 1, 2, 5 and 6 will give climb up in 1 and 2 and down in 5 and 6, and further addition of vacancies will unite 1 and

2 and 5 and 6 and give a step along AB where the top half of the loop, which has climbed upwards, combines with the lower half which has climbed downwards. This type of mechanism would produce the configuration of Fig. 7(b). Similarly, the configuration of Fig. 7(a) could arise by climb up in region 1 and down in 4, 5 and 6. It is not necessary for the dissociated Frank dislocation to be constricted at any stage in the climb process (7). Continuation of climb in opposite senses results in changes in shape of the original hexagonal loop.

It is considered that the present results provide evidence for fault climb under conditions of vacancy supersaturation as proposed by Escaig (2). It is likely that, in materials of low stacking-fault energy, nucleation and growth of Frank loops occurs in the same way as in materials of high stacking-fault energy, until the edges of the loops are sufficiently aligned along ⟨110⟩ for dissociation to occur. Once dissociation has occurred, further loop growth takes place by fault climb.

Acknowledgements

We are indebted to Dr. P. Humble for the use of his computer programme, which he developed to treat problems of the type considered here, and to him and Dr. A.K. Head for many helpful discussions. We are grateful to Mr. E.G. Beckhouse for photographic work.

References

1. R.S. Barnes, Acta Metall. 2, 380 (1954).
2. B. Escaig, Acta Metall. 11, 595 (1963).
3. R.M.S. Cotterill, Lattice Defects in Quenched Metals, Academic Press (New York) 1965, (p. 97).
4. F.W. Schapink and M. de Jong, Acta Metall. 12, 755 (1964).
5. W.J. Tunstall and P.J. Goodhew, Phil. Mag. 13, 1259 (1966).
6. L.M. Clarebrough, R.L. Segall and M.H. Loretto, Phil. Mag. 13, 1285 (1966).
7. A.J. Morton and L.M. Clarebrough (to be published).
8. D.J. Mazey, R.S. Barnes and A. Howie, Phil. Mag. 11, 459 (1962).
9. H. Hashimoto, A. Howie and M.J. Whelan, Proc. Roy. Soc. A269, 80 (1962).
10. M.H. Loretto, Phil. Mag. 12, 125 (1965).
11. A.K. Head, Aust. J. Phys. 20, 557 (1967).
12. P. Humble, Aust. J. Phys. 21, 325 (1968).
13. J.M. Silcock and W.J. Tunstall, Phil. Mag. 10, 361 (1964).
14. L.M. Clarebrough and A.J. Morton (to be published).
15. N. Thompson, Proc. Phys. Soc. B66, 481 (1953).

The Annealing Kinetics of Quenched Silver-Gold Alloy Wires*

G. P. Williams, Jr., B. J. Klein**, J. Everett

Wake Forest University, Winston-Salem, N. C., U.S.A.

Abstract

The annealing kinetics of quenched silver-gold wires have been investigated across the entire concentration range of solid solutions. Immediately after the quench an initial increase in resistance which is attributed to the onset of short range order has been observed, followed by a decrease in resistance which is associated with the annihilation of vacancies. The same activation energy is calculated for the ordering and the annihilation processes, and has a minimum at approximately 50 at% gold. The defect is tentatively identified as a single vacancy and the number of vacancy jumps calculated for the completion of the process is consistent with the two mechanisms proposed.

Introduction

In the past decade efforts to describe and explain the behavior of the vacancy in fcc metals have resulted in a concentration of attention to gold and, to a lesser degree, silver, especially in quenching experiments [1]. Although gold is relatively well-behaved, compared to silver, contradictory experiments and controversial theories have resulted and are still unresolved [2].

*This work supported in part by U. S. Atomic Energy Commission.
**Present address: University of North Carolina, Chapel Hill, N. C.

In 1960 Zener relaxation in the AgAu system was first reported [3]. At that time an extensive study of this phenomenon in the AgAu solid solution as a function of concentration was begun in this laboratory [4] in collaboration with experimenters elsewhere performing diffusion experiments in the same system [5]. This solid solution exists over the entire range of concentrations, and reliable thermodynamic and physical data are available for each pure component and various alloy concentrations. The AgAu system is therefore an ideal one for study and not subject to the limitations noted by Childs and LeClaire [6].

The quenching and resistivity studies reported here were initiated to complement these relaxation and diffusion experiments. Very little resistivity data were available for AgAu alloys, and most of that was for dilute concentrations, e.g., less than 1 at% Ag in Au [7]. Only recently have data been reported for more concentrated solid solutions of AgAu [8,9].

Nonetheless, the major ambiguities in the data from pure, as well as from impure specimens, still exist. For example, Meshii [10] observes there is not only a discrepancy in the reported values of the migration energy of a vacancy, but there is also some question as to the identity of the migrating defect, as well as to the configuration of vacancies before and after quench. These problems persist, even in pure gold, as evidenced by a recent study of vacancies and divacancies by Kino and Koehler [11]. The problem is compounded in the alloy because of the possible formation of vacancy-impurity complexes in which the Ag appears to play an active part in inhibiting the motion of the defects, as evidenced by the work of Quéré [12].

The agreement between experiment and theoretical calculations supports the contention that the AgAu system is essentially a regular solid solution at elevated temperatures near the melting point. At lower temperatures there is an indication of ordering in this alloy which affects the degree of regularity of the solution and the vacancy behavior. Fraikor and Hirth [13] associate such an onset of ordering in AgAu with a temperature of approximately 600°C. This investigation shows a maximum short range order destruction at approximately 500°C, which compares favorably with the above value.

The major purpose of this investigation was to determine the concentration dependence of the migration and formation energies of the vacancy and its role in AgAu solid solutions. The results were then to be compared with available diffusion and relaxation data in an attempt to further understand the behavior of the vacancy as well as the mechanism of the processes in which it is involved.

Theory

The methods of analysis of recovery data by which activation energies are abstracted have been concisely summarized by Doyama [14] and will not be repeated here, except to include pertinent equations when useful. It is convenient to define the time required for a specified fractional recovery of some physical property as a relaxation time, τ. This relaxation time obeys an Arrhenius type equation of the form

$$\tau = \tau_o e^{E_m/kT} \qquad (1)$$

where E_m is the effective migration energy of a defect, in practice calculated from the slope of the $\ln \tau$ vs $1/T$ plot. This method is

simple and direct and in general has fewer objections than other techniques.

Similarly, if one assumes the defect is a vacancy and an excess concentration of vacancies is frozen in by rapidly cooling from a higher quench temperature, T_Q, then the fractional concentration of vacancies is

$$C = A_1 e^{-E_F/kT_Q} \qquad (2)$$

Therefore if the resistance is proportional to the vacancy concentration, the slope of a plot of quenched-in resistance vs reciprocal quenching temperature contains the energy of formation E_F.

Unfortunately Eq. (2) is not applicable to the quench behavior observed in the AgAu alloy because the increase in resistance upon quenching is not always proportional to T_Q. In fact, the resistance is frequently lower following the quench, and is not always predictable, nor reproducible. This phenomenon has been previously reported [8,9,15,16] and is assumed to be caused by the thermal destruction of short-range order (SRO) at a quench temperature above some value T', which is the lowest temperature at which such destruction is observed. At an even lower temperature T_c the order extends over longer distances and becomes long-range order. Damask [17] states that AgAu alloys do not exhibit LRO, and Van der Sijde [8] indicates that T_c should be approximately $-50^{\circ}C$. Since annealing temperatures in this investigation are always greater than this value, LRO will not be discussed further.

The effect of SRO on the resistance has been open to speculation. Some authors assume SRO increases the resistance [15], while Damask [18] indicates more experimental evidence is necessary to validate this

assumption. He further states that the sign of the rate of change of resistivity with an ordering parameter may be used to predict the effect of SRO. The analysis of Gibson [19] indicates that AgAu may have a positive value for this ratio. This implies that an increase in SRO will be accompanied by an increase in resistivity. The results of this investigation corroborate this conclusion.

If it is assumed that the vacancies in the alloy even approximate their effect in pure gold, then the change in resistance caused by the annealing of vacancies is 2% of the change caused by SRO for the same anneal time and temperature [15]. Therefore, it is reasonable to separate the processes, and assume that Eq. (2) may be used to define a relaxation time associated with the defect assisted recovery of the destroyed SRO in the initial stage of the isochronal anneal. In the final stage, it defines the relaxation time of the defect annihilation process. The recovery of SRO should therefore be fast and require a smaller number of jumps in a localized region, compared to the defect annihilation process.

The above technique is valid if E_m is not a function of T_a, the annealing temperature. It has been observed experimentally that E_m decreases slightly with increasing T_a. Kino and Koehler [11] have calculated a change in E_m of only 0.1 eV for a change in T_a from $150^{\circ}C$ to $800^{\circ}C$. Since all annealing in this investigation was below $150^{\circ}C$ it is assumed that E_m is temperature independent.

Meechan and Brinkman [20] observe it is possible to determine the order of the recovery kinetics by a detailed analysis of the isothermal

recovery curve and a chemical rate equation of the form

$$\frac{dn}{dt} = -\nu\, n^{i}\, e^{-E_m/kT} \tag{3}$$

where n is the defect concentration, i is the order of the reaction, and ν the jump frequency. This procedure finally yields the time dependence of the property p whose recovery is being monitored, as

$$p^{1-i} = C(t + M) \tag{4}$$

where C is a constant and $M = \frac{p_o^{\,1-i}}{C}$ and t is the time. It is possible to choose a value of M such that a plot of $\ln p$ vs $\ln (t+M)$ yields a straight line. The order of the reaction may be obtained from the slope. However Eq. (4) may be used directly to solve for i. Comparing Eq. (4) for two different time intervals for the same isothermal anneal yields

$$\frac{\left(\frac{p}{p_o}\right)_1^{1-i} - 1}{\left(\frac{p}{p_o}\right)_2^{1-i} - 1} = \frac{t_1}{t_2} . \tag{5}$$

Experimental Procedure

The alloy specimens used in this investigation were obtained from the Sigmund Cohn Corp. and Secon Metals Corp. in the form of 16 mil wires. The components were 99.999% pure prior to alloying. To assure the maximum reproducibility in the data each new specimen was given a 3 hour anneal at a temperature approximately 0.9 of the melting point, followed by a stepwise cooling extending over 12 hours. Following this initial treatment, the procedure was modified by reducing the stepwise cooling to 2 hours between quenches.

The resistance changes were monitored by standard potentiometric techniques at liquid nitrogen temperatures. The specimen was heated by direct current and quenched into distilled water at room temperature at quenching rates of about 3 to 5 x 10^4 C^o per second, as measured from a Polaroid picture of the oscilloscope trace of the decreasing specimen voltage. The transfer to the oil or water annealing baths was as rapid as possible and seldom exceeded five seconds. The bath temperatures were maintained constant to within $\pm$ .05 C^o. The quench temperature was determined from a prior calibration measurement of resistance ratio vs temperature.

The isochronal runs were made to assist in the determination of the proper annealing temperatures to use for each stage of recovery. The time interval at each temperature during the isochronal was four minutes. The isothermal anneals were accomplished by removing the specimen from the constant temperature annealing bath, rinsing it in acetone for quick drying, and then carefully immersing it in liquid nitrogen for the resistance measurement. This was repeated at frequent intervals to obtain a smooth plot of the fractional recovery vs logarithm of time.

Summary of Results

The resistance changes following a quench were monitored in wire alloy specimens of the following atom percentages of Au in Ag : 21.6, 35.5, 53.0, 62.1, 72.8, 81.3, 82.6, and 91.2 Space restrictions limit the data presentation to a few representative plots.

Isochronal curves for several specimens are shown in Fig. 1 below.

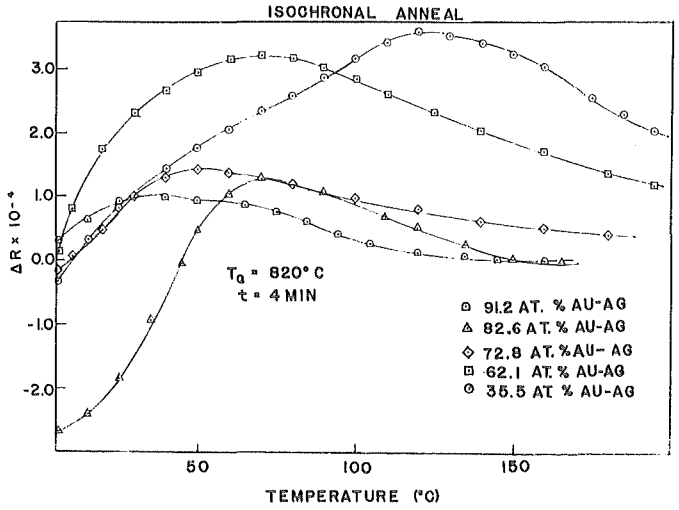

Figure 1. Isochronal annealing curves

Typical isothermal recovery curves are shown in Fig. 2 below.

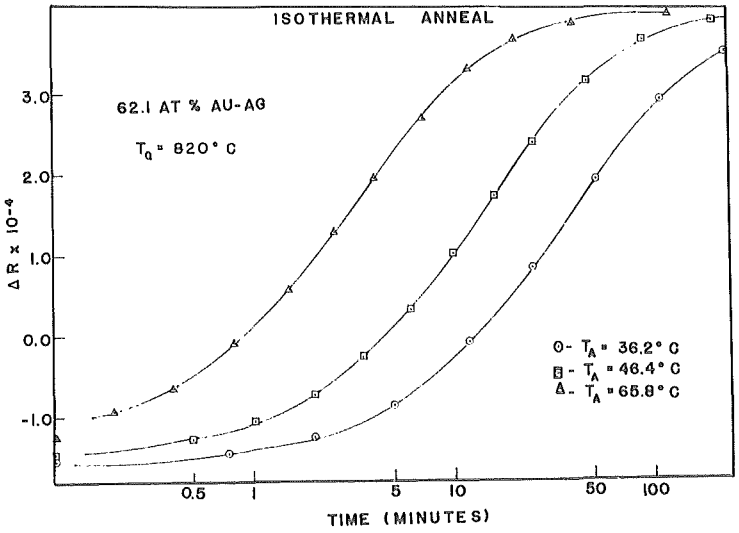

Figure 2. Isothermal recovery curves.

For clarity, only three of the six isothermal annealing runs performed on the 62.1% specimen are included in Fig. 2. The activation energy was calculated from the slope of the line obtained by plotting the ln of the time required for a specified fractional recovery vs the annealing temperature for several isothermal recovery curves. One such typical Arrhenius plot, based on Eq. (1), for the 62.1% specimen is shown in Fig. 3 to the right.

Discussion

A derivative analysis of any of the isochronals in Fig. 1 reveals a complex annealing spectrum. Nevertheless, it is clear that they are all characterized by an initial increase in resistance followed by a subsequent decrease, with a broad, sometimes relatively flat maximum in the mid-temperature range. This type of behavior is in marked contrast to that of pure gold which simply exhibits a resistance decrease as the quenched in vacancies are annihilated at sinks. The seemingly anomalous initial increase in resistance following the quench is attributed to the onset of short range order (SRO), as previously discussed. Apparently the measured resistivity is the result of at least two competing processes, namely, the increase

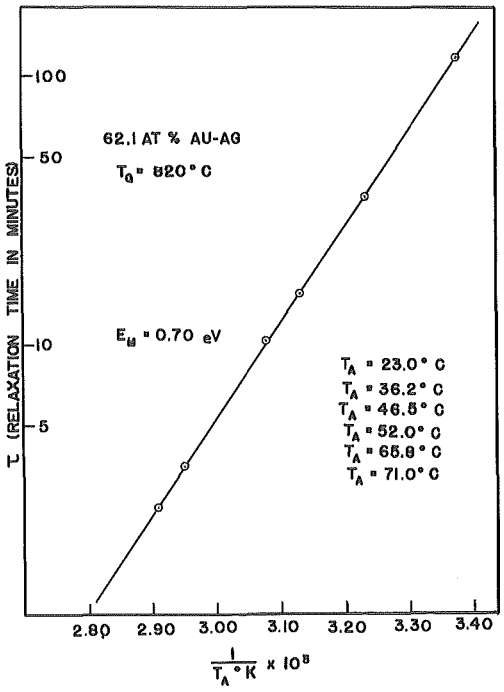

Figure 3. Determination of the migration energy from the isothermals in Fig. 2.

caused by SRO, and the somewhat delayed decrease caused by vacancy annihilation.

Isothermal recovery has been monitored for each of these processes i.e., on the low temperature portion (SRO) as well as on the high temperature side (vacancy annihilation) of the maximum of the isochronal curve.

These two stages of recovery are effectively isolated at different annealing temperatures, and this is illustrated in Fig. 4, below. The comparative rate and the competitive nature of the two processes is evident in the plot.

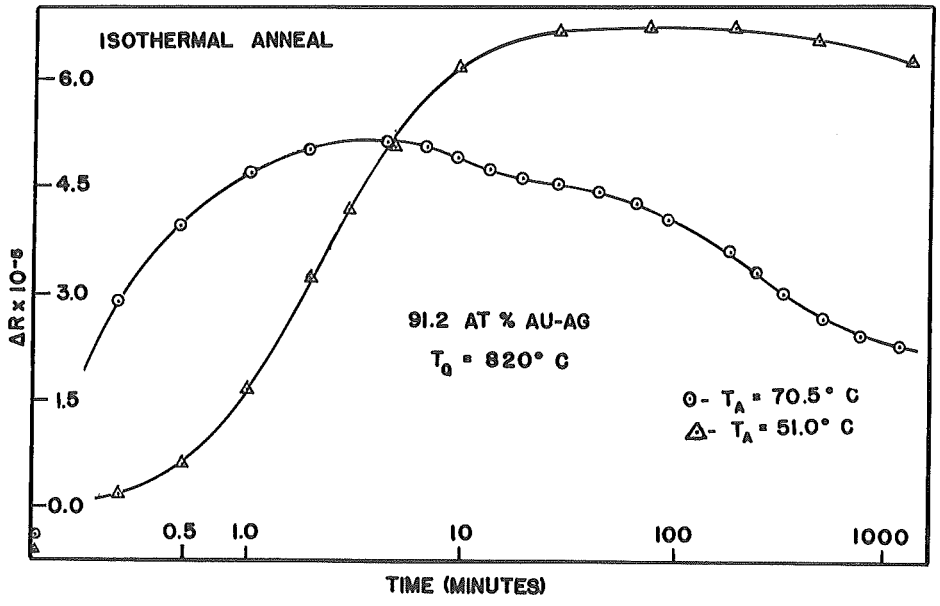

Figure 4. The details of the first stage of recovery are evident in the 51°C anneal; the 70°C anneal primarily reveals the second stage.

The 51°C curve is relatively flat for 30 seconds, but in 10 minutes shows a rapid increase to a maximum. Even after 1000 minutes there is little if any decrease, to signal the beginning of a second stage. In contrast, 70.5°C is hot enough to activate the second process before the

first is complete. Consequently, the maximum is depressed, but is achieved in one-tenth the time required in the 51°C anneal.

Thus from an analysis of the isochronal curves a judicious choice of the temperature for the isothermals enables one to observe the kinetics of one process when the effect of the other is negligible, and vice-versa. Proceeding in this way, activation energies for each process were determined, and found to be the same within experimental error. The energies plotted in Fig. 5 below as a function of concentration therefore represent effective migration energies of the defect responsible for the recovery of both processes and are somewhat larger than those reported by Van der Sijde [8]. Formation energies are calculated by subtracting these migration energies from the activation

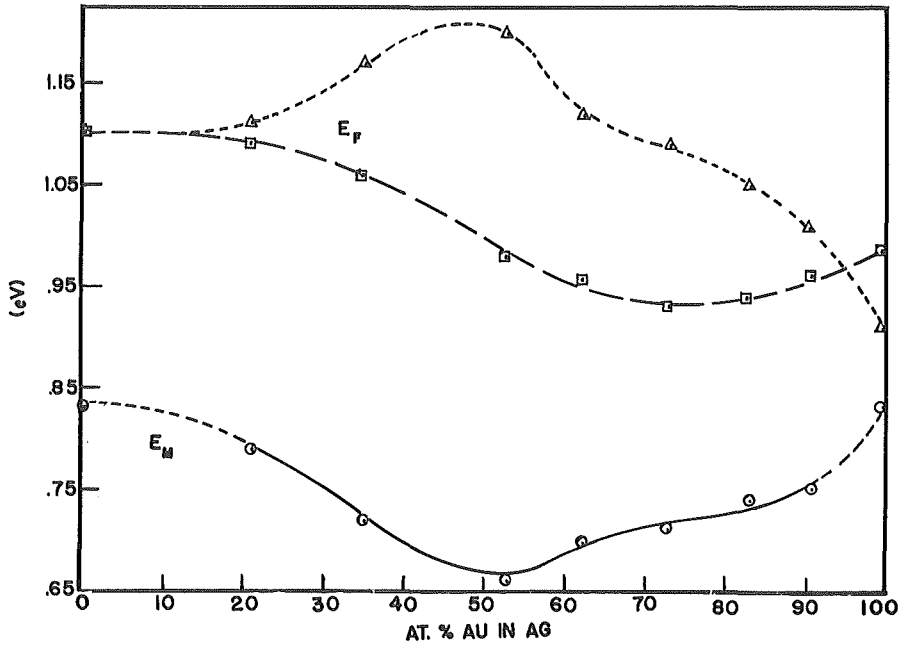

Figure 5. Vacancy Migration and formation energies vs concentration for AgAu alloys. E_m from this study are shown as ⊙'s. The △'s are values of E_F determined by subtraction from diffusion energy of Ag, after Mallard, et al [5]. The ⊡'s are values of E_F calculated after Fraikor & Hirth [21].

energy for diffusion of the Ag tracer from the data of Mallard, et al. [5]. For comparison purposes, formation energies have also been calculated from a theoretical consideration of the concentration of vacancies in binary alloys after Fraikor and Hirth [21], and are also shown in Fig. 5 by the broken line.

Various other experimental features characteristic of the AgAu system are summarized below. The relaxation associated with the SRO process gave τ_o values between 10^{-9} and 10^{-11} seconds, and the number of jumps for the process to go to half-completion was always calculated to lie between 10^3 and 10^5. The corresponding quantities for the annihilation process were 10^{-7} seconds, and 10^7 jumps. These values show order of magnitude consistency with those of similar recovery processes reported elsewhere [1]. Eq. (5) yielded values between 1.0 to 2 for the order of the SRO process. Unfortunately, the data from the annihilation process were insufficient to make this calculation possible.

An examination of the isochronal curves in Fig. 1, shows that the temperature of the "peak" decreases monotonically with increasing Au concentration, with the exception of the 82.6% specimen. This would imply that it is more difficult to destroy the SRO in the Ag-rich alloys. This conclusion is also supported by the fact that higher quench temperatures are necessary to quench out resistance (that is, destroy SRO) in the Ag-rich specimens.

Conclusions

The results of this investigation as discussed above are consistent with the idea that quenching destroys SRO, and the annealing induces

vacancy assisted recovery of the localized regions of order, which apparently become more effective as vacancy traps as the Ag concentration increases. Higher temperature anneals break up the sublattices and eventually lead to the annihilation of vacancies at sinks.

The migration energies shown in Fig. 5 are slightly less than the values for single vacancies cited for the pure components but higher than those generally quoted for divacancies. Since the migration energy might logically be expected to decrease with impurities it is reasonable to assume that the migrating defect in both the SRO and the annihilation processes is the single vacancy.

References

1. R. M. J. Cotteril, et al - "Lattice Defects in Quenched Metals" Academic Press, New York, 1965.
2. J. W. Kauffman, M. Meshii - Reference 1, p. 77.
3. T. J. Turner, G. P. Williams, Jr. - Acta Met 8, 891, 1960.
4. G. P. Williams, Jr., T. J. Turner - To be published.
5. W. C. Mallard, et al - Phys. Rev. 129, 617, 1963.
6. B. G. Childs, A. D. LeClaire - Acta Met 2, 718, 1954.
7. R. Kloske, J. W. Kauffman - Phys. Rev. 126, 123, 1962.
8. B. Van der Sijde - Physica 29, 559, 1963.
9. S. Radelaar - Thesis, Delft (1967); Phys. Stat. Sol. 27, K63, 1968.
10. M. Meshii - Reference 1, p. 387.
11. T. Kino, J. S. Koehler - Phys. Rev. 162, 632, 1967.
12. Y. Quéré - J. Phys. Soc. Jap. - 18, Suppl. III, 91, 1963.
13. F. Fraikor, J. Hirth - J.A.P., 38, 2312, 1967.
14. M. Doyama - Reference 1, p. 167.
15. B. Korevaar - Physica 25, 1021, 1959.
16. R. Asimow - Phil. Mag. 9, 171, 1964.
17. A. Damask - Solid State Physics 1, 1956.
18. A. Damask - J. Phys. Chem. Solids 1, 23, 1956.
19. J. Gibson - J. Phys. Chem. Solids 1, 27, 1956.
20. C. Meechan, J. Brinkman - Phys. Rev. 103, 1193, 1956.
21. F. Fraikor, J. Hirth - Scripta Met. 2, 55, 1968.

QUENCHING PLATINUM AND TUNGSTEN IN SUPERFLUID HELIUM

by

Ronald Gripshover, John Zetts and Jack Bass

Department of Physics

Michigan State University

East Lansing, Michigan, U. S. A.

We are quenching platinum wires into various liquids and in superfluid helium, and tungsten wires in superfluid helium. At high temperatures the resistivities quenched into fine platinum wires cooled in superfluid helium are consistent with those quenched into larger wires plunged into water and kerosene. However there is reason to believe that the platinum and helium interact in a manner which does affect the results obtained. The resistivities quenched into high purity 0.001" and 0.0012" diam tungsten wires ($R_{273^oK} / R_{4.2^oK} > 600$) are comparable to Schultz's published results. However some differences do exist.

Although many properties of vacancies in f.c.c. metals are now known[1], little is known about the properties of vacancies in b.c.c. transition metals. Because these metals strongly absorb gases, to avoid contamination they must be maintained in an ultra-pure environment when heated. The technique of quenching fine wires in superfluid helium developed by Schultz and Rinderer [2][3] represents one means of maintaining ultra-pure atmospheric conditions when heating a wire, while still allowing the rapid quenching necessary for retaining measurable vacancy concentrations. We are planning to use this technique to study the properties of vacancies in some b.c.c. transition metals. To test out our equipment and experimental techniques, and for other reasons

given below, we are now measuring the resistivities quenched into platinum and tungsten wires. In this paper we compare the resistivities retained in platinum wires plunged into water and kerosene with those retained in platinum wires quenched in superfluid helium. We also present preliminary measurements of the resistivities retained in tungsten wires quenched in superfluid helium.

A) Platinum

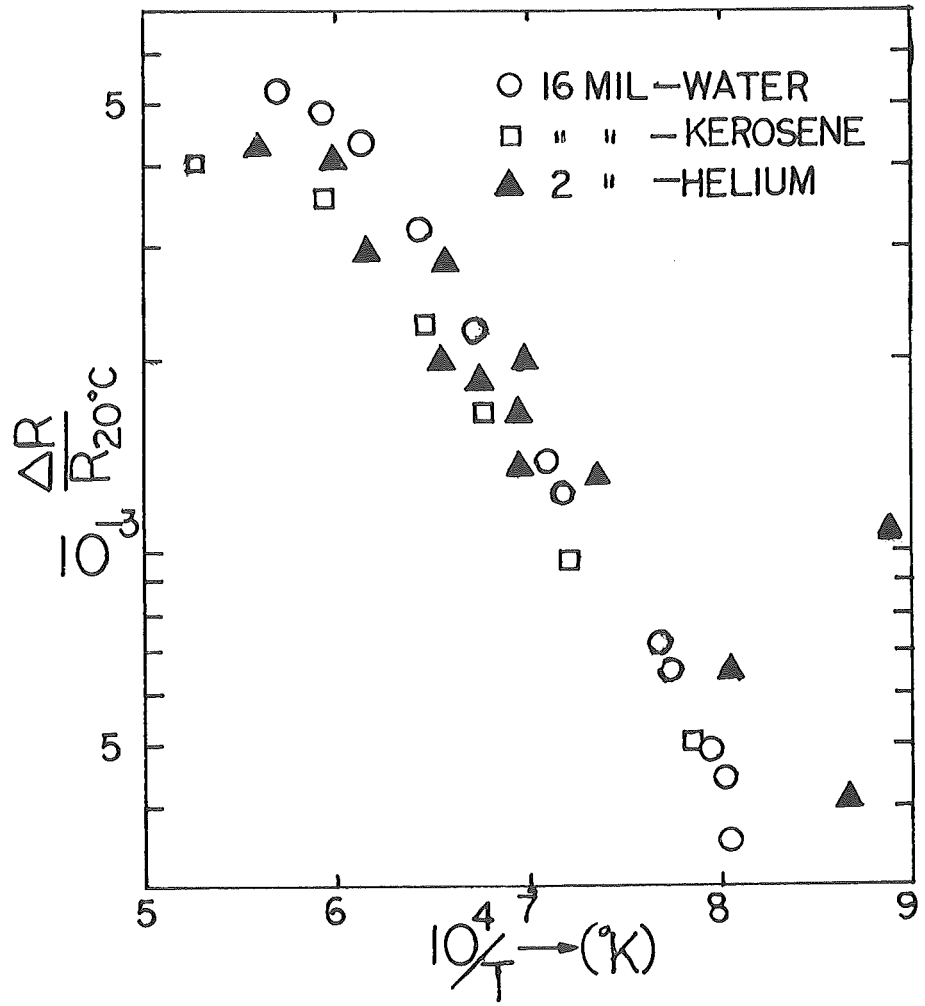

Figure 1: The resistance quenched into platinum wires as a function of quench temperature. To correct for differences in specimen size, the measured resistances are divided by the resistance of the same wire at 293°K.

Figure 1 shows the resistivities retained in 0.016" diam, 99.999 % pure platinum wires quenched into water and kerosene, and the resistivities retained in 0.002" diam, 99.999 % pure platinum wires quenched in superfluid helium. The wires were obtained from the Sigmund Cohn Co., and had resistance ratios ($R_{273^\circ K}$ / $R_{4.2^\circ K}$) of about 1,500 for the 0.002" diam wires and 5,500 for the 0.016" diam wires after annealing in air. The 0.016" diam wires cooled to room temperature in about 0.025 sec when plunged into water, and about 0.18 sec when plunged into kerosene. The 0.002" diam wires cooled at a rate between these two.

At temperatures above 1400°K the resistivities quenched into the 0.002" diam wires fall either on, or between, the resistivities quenched into the 0.016" diam wires. This implies that the helium quench and the liquid quench techniques are measuring the same quantity. However there is substantial scatter in the data, and at temperatures below 1400°K the resistivities quenched into the 0.002" diam wires fall above those for the large wires. These two facts suggest that there is something occurring in the helium quench system which does not occur in the liquid quench system; it appears that there is some interaction between the platinum and the helium. This interaction is most clearly seen through its effect upon the residual resistivity of the fine wires. A 0.002" diam platinum wire having a resistance ratio after air annealing of over 1,500, had this ratio decrease to 1,050 after a short

series of anneals over superfluid helium. Similar increases in residual resistivity occurred in other wires upon annealing in either helium gas at room temperature or above superfluid helium. Subsequent annealing in air caused the residual resistivity to decrease again. We are continuing to investigate this effect.

B) Tungsten

The only previous quenching study of tungsten is that by Schultz[3], who found $E^f_{1v} = 3.3 \pm 0.1$ eV, and a vacancy concentration of 1.1×10^{-4} at the melting point. Kraftmakher and Strelkov[4] obtained $E^f_{1v} = 3.14$ eV from measurements of the specific heat of tungsten, but they obtained a vacancy concentration about two orders of magnitude greater than that found by Schultz. Jeannotte and Galligan[5] estimated the energy of motion for vacancies in tungsten to be $E^m_{1v} = 3.3$ eV from field-ion microscope studies of vacancy motion after irradiation. The sum of these values is $E^f_{1v} + E^m_{1v} = 6.6$ eV, in good agreement with one recent estimate for the activation energy for self-diffusion ($Q = 6.6$ eV[6]), but in disagreement with another ($Q = 5.2$ eV[7]). In order to confirm Schultz's results, and to obtain further information about the motion energy of vacancies in tungsten, we decided to measure the dependence of the resistivity quenched into fine tungsten wires upon quenching speed. Figure 2 shows preliminary results from this study.

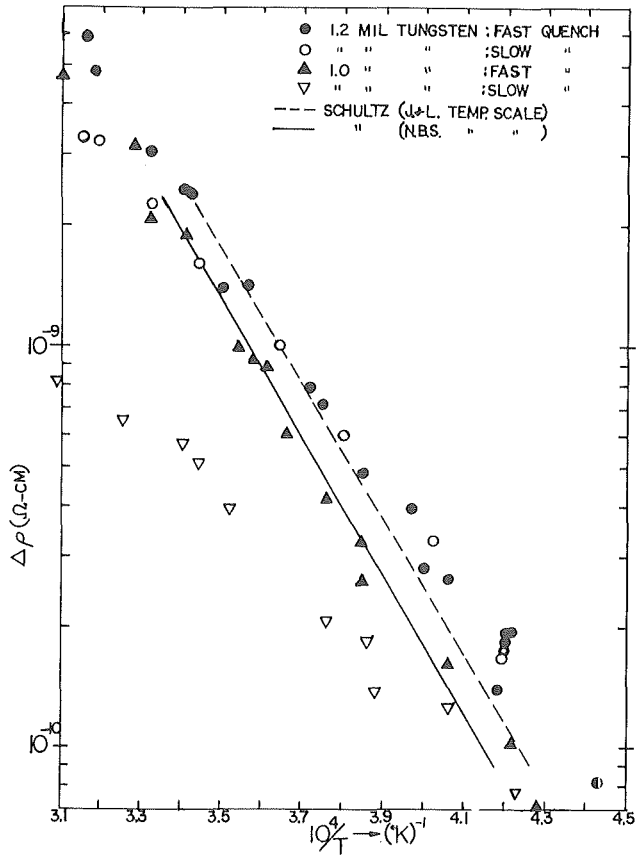

Figure 2: The resistivities quenched into tungsten wires as a function of quench temperature. The circles represent the resistivities quenched into a 1.2 mil diam wire having a resistance ratio $R_{273^\circ K} / R_{4.2^\circ K} = 686$. The triangles represent those quenched into a 1.0 mil diam wire having a resistance ratio $R_{273^\circ K} / R_{4.2^\circ K} = 622$. The filled circles and triangles represent quench speeds varying from about 20,000 °K/sec at 2400°K to 39,000 °K/sec at 3100°K. The open circles represent speeds varying from 17,000°K/sec at 2400°K to 23,000°K/sec at 3100°K. The open triangles represent a speed of 11,000°K/sec, nearly independent of quenching temperature. The dashed line shows Schultz's published results based upon a temperature scale determined using the resistance of tungsten as measured by Jones and Langmuir (J. and L.) (ref. 8). The solid line shows Schultz's data according to the National Bureau of Standards (N.B.S.) scale used in the present study (ref. 9).

As can be seen from fig. 2, when transposed to the N.B.S. temperature scale the resistivities retained in Schultz's 0.0012" diam wires are in excellent agreement with the resistivities retained in our fast quenched 0.001" diam wire, but are smaller than those retained in our fast quenched 0.0012" diam wire. The reasons for the differences between the resistivities retained in our fast quenched 0.001" diam and 0.0012" diam wires are not clear. It is tempting to say that our fast quench 0.0012" diam wire resistivities are close to the resistivities of the equilibrium vacancy concentration, and that the other measurements represent situations in which vacancies are lost to sinks during the quench. The agreement between the fast and slow quench 0.0012" diam wire resistivities at lower temperatures tends to support such an argument. In addition, the large additional vacancy loss produced in the 0.001" diam wire by a change of only a factor of two or three in the quenching speed suggests that the resistivities quenched into this wire do not correspond to the equilibrium vacancy resistivities. On the other hand, this model does not explain why the resistivity retained in the fast quenched 0.001" diam wire stays below that retained in the 0.0012" diam wire at lower temperatures. This is particularly surprising because at high temperatures the resistivities retained in the fast quenched 0.001" diam wire are larger than those retained in the slow quenched 0.0012" diam wire. We

are attempting to investigate these matters further using additional quench speeds and new specimens. For the present we conclude that our results generally confirm Schultz's data, but that some differences remain to be resolved. In particular, our preliminary data suggest that the equilibrium vacancy concentration in tungsten may be a bit larger, and the formation energy a bit smaller, than the values yielded by Schultz's data.

References

1) Lattice Defects in Quenched Metals, edited by R. M. J. Cotterill, et. al., Academic Press, New York, 1965.

2) L. Rinderer and H. Schultz, Physics Lett. 8, 14 (1964).

3) H. Schultz, Lattice Defects in Quenched Metals, edited by R. M. J. Cotterill, et. al., Academic Press, New York, 1965. Page 761.

4) Y. A. Kraftmakher and P. G. Strelkov, Soviet Phys. - Solid State 4, 1662 (1963).

5) D. Jeanotte & J. M. Gulligan, Phys. Rev. Lett. 19, 232 (1967).

6) R. L. Andelin, J. D. Knight, M.Kuhn, Trans. A.I.M.E. (USA) 233, 19 (1965).

7) W. Danneberg, Metall, 15, 977 (1961).

8) H. A. Jones & I. Langmuir, Gen. Elec. Rev. 30, 310 (1927).

9) Temperature, Its Measurement and Control in Science & Industry, Reinhold Publ. Co., New York, 1941, Page 1318.

VACANCIES IN GOLD AND MATTHIESSEN'S RULE

R.R. CONTE , J. DURAL AND Y. QUÉRÉ

Centre d'études nucléaires de Fontenay-aux-Roses,
92, France

Abstract

Deviations to Matthiessen's rule have been observed for vacancies in gold. These deviations are consistent with a decrease of the Debye temperature.

1. Introduction

Matthiessen's rule states that the extra resistivity due to lattice defects $\Delta\rho$ is, in a metal, independant of temperature. It is clear that this rule can be valid only if there is no interaction between these defects and the vibration modes of the metal. Inversely, deviations to this rule may give information about these interactions.

Many such deviations have been observed, specially for irradiation defects in copper [1] , alloying elements in different metals [2] or irradiation defects in α uranium [3] . In this latter case the big observed effect is due to reasons other than changes of vibrational properties.

This paper will describe some measurements of deviation to Matthiessen's rule in the case of lattice vacancies.

2. Experimental procedure

We have used gold wires of diameter : 111 μ . The ratio $\frac{\rho_{300}}{\rho_{4,2}}$ of gold before quenching was of the order of 650. The wires were heated by electrical current, quenched in water, and then, immediately cooled to lower temperatures.

The resistivity, which had been measured with a potentiometer before quenching at 4,2 and 77° K, was measured after quenching at these same temperatures. The extra resistivity due to quenched-in vacancies could thus be determined at 4,2° K ($\Delta\rho_4$) and at 77° K ($\Delta\rho_{77}$). In one case $\Delta\rho_T$ was measured over the range 4,2° K - 300° K in a regulated capsule described elsewhere [4]. Although the quenching temperature was evaluated by measuring the resistance of the wire, we shall rather refer our results to the quenched-in resistivity $\Delta\rho_4$ which will be considered as proportional to the concentration C_V of quenched-in vacancies.

At 4,2° K, where $\frac{d\rho}{dT}$ is negligible, the precision on $\Delta\rho_4$ is as good as is allowed by the precision on the resistivity measurement. At 77° K, where $\frac{d\rho}{dT}$ is $0{,}9.10^{-2}\,\mu\Omega\,cm.°K^{-1}$, the precision on $\Delta\rho_{77}$ depends essentially on the equality of temperature for the measurements before and after the quench. A separate experiment performed on a dummy in the liquid nitrogen bath showed that in a period of 3 hours the resistivity was constant only within $\pm\ 10^{-3}$.

3. Results

We have plotted on figure 1 the difference $\Delta^2\rho_{77} = \Delta\rho_{77} - \Delta\rho_4$ versus the quenched-in resistivity $\Delta\rho_4$. It will be noticed that $\Delta^2\rho_{77}$ is always positive.

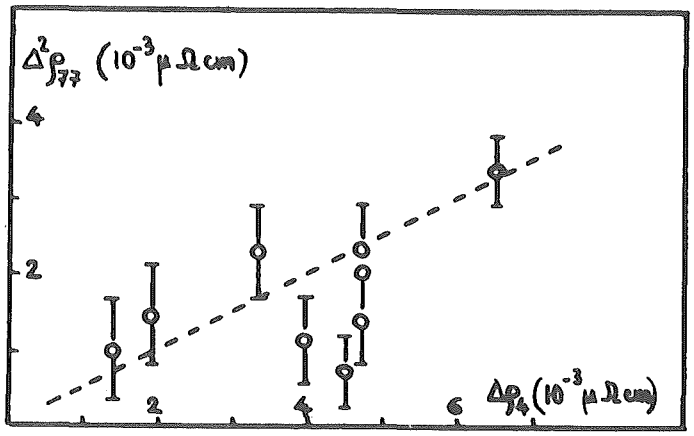

Figure 1

Deviation to Matthiessen's rule $\Delta^2\rho_{77} = \Delta\rho_{77} - \Delta\rho_4$ between 77 and 4,2° K, versus the resistivity $\Delta\rho_4$ of quenched vacancies.

4. Discussion

Let us recall that the thermal part of the resistivity of a metal is given by Gruneisen's equation

$$\rho_T = K \frac{T^5}{\theta^6} \int_0^{\frac{\theta}{T}} \frac{x^5 dx}{(e^x - 1)(1 - e^{-x})}$$

where K is a constant depending on the metal and θ its Debye temperature.

As was noticed by Magnuson and Palmer [1], $\rho_T T$ is a function of $\frac{T}{\theta}$ only, and can be written :

$$\rho_T T = f\left(\frac{T}{\theta}\right) . \qquad (1)$$

If ρ_T is altered ($\rho_T \rightarrow \rho_T + \delta\rho_T$) by a change $\Delta\theta$ of the Debye temperature, one has from (1) :

$$\delta\rho_T = -\frac{\Delta\theta}{\theta^2} f'\left(\frac{T}{\theta}\right)$$

or

$$\delta\rho_T = -\frac{\Delta\theta}{\theta}\left(T\frac{d\rho_T}{dT} + \rho_T\right) . \qquad (2)$$

If one then supposes that the extra resistivity of vacancies $\Delta\rho_T$ is the sum of an intrinsic resistivity independant of temperature and equal to $\Delta\rho_4$ and of a thermal term $\delta\rho_T$, one writes :

$$\delta\rho_T = \Delta\rho_T - \Delta\rho_4$$

$$= \Delta^2\rho_T$$

and in particular

$$\delta\rho_{77} = \Delta^2\rho_{77} \cdot$$

The fact that $\Delta^2\rho_{77}$ was always found positive indicates (from eq. 2) that the change of Debye temperature due to the presence of vacancies is negative as expected from the elasticity theory [5] . Moreover the approximate linearity between $\Delta^2\rho_{77}$ and $\Delta\rho_4$ (see fig. 1), i.e. between $\delta\rho_T$ and C_V , indicates that $|\Delta\theta|$ appears as proportional to C_V.

As for the proportionality constant between $\Delta\theta$ and C_V, no precise value can be deduced at the moment. ρ_T being approximately proportional to T, equation (2) shows that $\delta\rho_T \left(= \Delta^2\rho_T\right)$ should also be proportional to T. This is not the case (see fig. 2 [6]). Consequently the values for $\Delta\theta$ which could be calculated from eq. 2 are not independant of T.

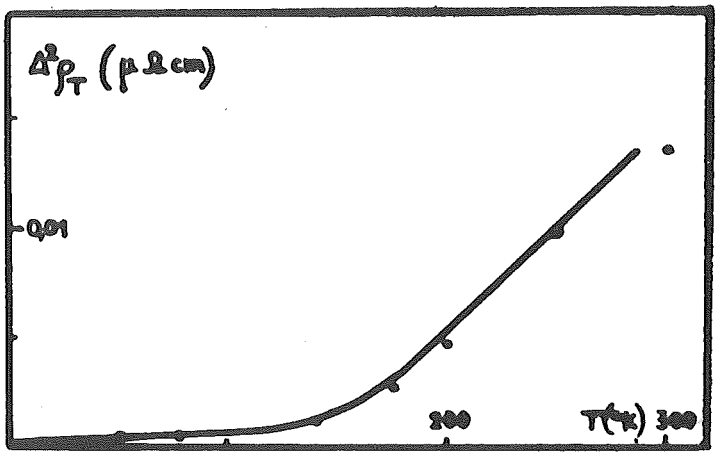

Figure 2

$\Delta^2\rho_T$ (= $\Delta\rho_T - \Delta\rho_4$) plotted versus T for quenched-in vacancies in gold ($\Delta\rho_4 = 4,5.10^{-3}$ $\mu\Omega$ cm)

It is clear that a more thorough study of $\Delta^2\rho_T$ as a function of T is necessary to know whether $\Delta\theta$ is really temperature dependant or whether the hypothesis of a temperature independant intrinsic resistivity of vacancies is wrong.

References

[1] G.D. MAGNUSON and W. PALMER
Phys. Rev. 109, 1990 (1958)

[2] R. REICH
Thesis, Paris University (1965)

[3] J.C. JOUSSET
Phys. Stat. Sol. , in press.

[4] R.R. CONTE and J. DURAL
Rev. Phys. Appl. (March 1968)

[5] Y. QUÉRÉ
Défauts ponctuels dans les métaux, Masson, Paris (1967)

[6] R.R. CONTE and J. DURAL
Physics Lett. , in press.

III. RADIATION DAMAGE IN F.C.C. METALS

PRODUCTION RATES OF FRENKEL DEFECTS DURING LOW TEMPERATURE IRRADIATIONS

H. WOLLENBERGER

Van de Graaff-Labor Aachen der Kerforschungsanlage Jülich

Abstract:

The measurement of Frenkel pair production rates provides a valuable tool for studying:

1. Details of atomic displacement processes (threshold energy, multiple production)
2. Interactions between interstitials and vacancies
3. Interactions between interstitials or vacancies and other lattice defects.

Published and unpublished results regarding these problems will be discussed with respect to conclusive interpretations and open questions. The following subjects will be treated in detail.

Threshold energy determinations depend strongly on the sensitivity of damage rate measurements. The real threshold energies should generally be smaller than the reported values. From measurements of the energy dependence of the production rate in polycristalline specimens the displacement probability function can be obtained, which gives the integral effect of the angular dependence of the threshold energy. The angular dependence itself, however, cannot be evaluated in a unique manner from the displacement probability function. Meaningful measurements in single crystals require specimens with a thickness less than lo/u. Even with such thin crystals the information which can be obtained about the angular dependence of threshold energy is limited in principle. Moreover, the influence of secondary effects on the commonly measured electrical resistivity damage rate is large in very thin specimens. An investigation of both the energy and defect concentration dependence of the production rate at various temperatures, as well as subsequent annealing behaviour provides valuable information for the discussion of details of single and multiple displacement processes.

The interaction between stable interstitials and stable vacancies can be studied by damage rate measurements at low temperatures as a function of the irradiation induced defect concentration. The spontaneous recombination of vacancies and interstitials which originate from different production events reduces the damage rate with increasing defect concentration. The discrepancy between theoretical predictions concerning the spontaneous recombination effect and the experimental damage rates for heavy particle and electron irradiations clearly suggests a remarkable influence of dynamically induced recombinations on the damage rate for heavy particle irradiations. Recent results indicate the significance of such events also for electron irradiations. Moreover, Frenkel pair configurations seem to be altered by the dynamic events occuring during electron irradiation. The influence of the dynamic processes on the damage rates complicates the determination of the spontaneous recombination volume.

The interaction between interstitials and vacancies as well as between these defects and foreign atoms or dislocations strongly affects the production rate at elevated temperatures. Therefore, configuration changes of interstitials and vacancies caused by certain annealing procedures can be studied by such measurements. Furthermore, it is possible to obtain information concerning the binding of interstitials and vacancies by various foreign atom species and dislocations.

THEORETICAL ASPECTS OF PRODUCTION AND INITIAL DISTRIBUTION OF FRENKEL DEFECTS.

G. LEIBFRIED

Technische Hochschule Aachen, Germany

(Abstract not yet received)

Annealing Stages in Irradiated F.C.C. Metals.

W. Schilling

Institut für Festkörper- und Neutronenphysik
Kernforschungsanlage Jülich
Jülich/Germany

Abstract

The annealing behaviour of Frenkel defects will be reviewed using mainly the results of electrical resistivity measurements. Special emphasis will be given to a discussion of the dependence of the observed annealing behaviour on irradiation dose, type of irradiating particles, irradiation temperature, and the effect of vacancy-, radiation- and impurity-doping. The principal points to be reported for the different annealing stages are the following:

Stage I

After electron irradiation of Cu, Al, Ag, Pt and Ni, stage I consists of a number of well defined subpeaks. Stages I_A, I_B, I_C can be interpreted as due to the collapse of close Frenkel pairs, stage I_D and I_E to correlated and uncorrelated recombination of freely migrating interstitials with vacancies. In addition to recombination reactions, the freely migrating interstitials can be immobilized by reactions with other interstitials, impurities, or dislocations. These immobilization reactions lead to the retention of vacancies and interstitials in equal numbers above stage I.

After fast neutron irradiation stage I generally shows less substructure, stage I_E is almost missing and the fraction of interstitials surviving stage I is greatly increased. The same general features are observed after electron and α-particle irradiation to very high doses where saturation effects during defect production have become of importance.

The experimental data available at present indicate that Au shows no annealing stage similar to the stages I_D-I_E that are observed in the other f.c.c. metals.

Stage II

Stage II is more pronounced after low dose heavy particle irradiation than after low dose electron irradiation. Recent high dose electron irradiations have shown stage II recovery similar to that observed for heavy particles. Stage II normally consists of a more or less continuous background annealing. Some substages may be superimposed on this continuum. Impurity doping usually gives rise to additional substages. Stage II occurs also in the recovery of other physical properties e.g. length change, stored energy, and elastic modulus. Possible interpretations which are in accordance with these observations will be outlined.

Stage III

As stage III we define the next (larger) recovery stage observed in irradiated metals above stage I which shifts to lower temperatures with increasing dose. Using this definition, stage III has been clearly identified for Al, Cu, and Au. In Pt preliminary experiments indicate that the final annealing stage (usually called stage IV) shows the above mentioned characteristics.

The activation energies found for stage III after different types of irradiation for Cu, Al and Au are in good general agreement. The kinetics indicate uncorrelated recovery of a freely migrating single defect for electron irradiated metals and correlated plus uncorrelated recovery after neutron irradiation. Impurities and the temperature of irradiation have relatively little effect on stage III recovery. The recovery of irradiated samples containing vacancies from a previous quench show that in Al and Pt the end of stage III overlaps with the recovery peak due to the removal of the quenched in vacancies. In prequenched Au both stages are almost coincident.

Higher stages

Whereas irradiated Al and Pt show complete recovery in stage III, in Cu and Au a resistivity increment remains after neutron and high dose electron irradiation. Electron microscope studies have indicated that interstitial and vacancy clusters persist above stage III. Little information is available on the correlation of the annealing of these defect clusters with resistivity changes.

PHYSICAL PROPERTIES OF POINT DEFECTS IN METALS

H. WENZL
Physik-Department der Technischen Hochschule München, Germany
and K. ISEBECK
Atomic Energy Board, Pretoria, South Africa

Abstract

Structural disorder changes more or less all physical properties of a crystal. We shall discuss mainly the influence of defects induced by irradiation or quenching in the metals aluminium, copper and some others in view of the following remarks.

1. In most cases the properties studied are proportional to the defect numbers or concentrations. In these cases a property change per defect or per unit concentration of defects ("specific property") can be defined. Only then one can speak of the physical property of a point defect. To be able to analyse corresponding measurements it is necessary to use as units not only the vacancy and the interstitials but also different types of multiple defects (e.g. the close Frenkel pairs) etc. The "annealing stage" technique provides a means to distinguish between these different types. Usually the defect numbers are not well known. Then we shall use the ratios of different property changes of this group as a measure for the specific properties of a certain defect (e.g. the ratio of stored energy, lattice parameter change, elastic modulus change, Debye-Waller factor change, neutron scattering cross section etc. and resistivity change). These ratios do not very sensitively depend on the defect type because usually, by passing from one defect to another, the different specific properties change in the same sense, so that accurate measurements are necessary to discriminate between different defect types.

2. Another group of physical properties is independent of the concentration of the "overwhelming" defect type and thus provides specific properties directly (e.g. magnetoresistivity, Hall-coefficient, relative deviation from the Matthiessen rule, partly thermopower etc.). In spite of this advantage only few experiments have been performed until now.

3. In other cases the local distribution of defects in the sample is important (e.g. neutron scattering cross section, pinning force of magnetic flux lines in superconductors etc.). Then correlation functions can be used to describe the influence of the defects on the physical properties.

THE INFLUENCE OF SPONTANEOUS RECOMBINATIONS AND SUB-THRESHOLD EVENTS ON THE DEFECT PRODUCTION AT LOW TEMPERATURE ELECTRON IRRADIATIONS

G. Duesing, H. Hemmerich, W. Sassin, and W. Schilling
Institut für Festkörper- und Neutronenphysik,
Kernforschungsanlage Jülich
Jülich, Germany

Abstract

The resistivity increase per unit irradiation dose in pure aluminum, copper and platinum containing Frenkel defects in different concentrations or quenched-in vacancies (Pt only) is determined. The highest electron doses achieved at 4.2 ^{o}K are $\approx 10^{20}$ electrons/cm^{2}. By means of radiation doping and sub-threshold irradiation (Pt) it is shown that the build-up of defects in these metals is governed by spontaneous recombination processes during defect production as well as by radiation induced recombination of close pairs resulting from nearby sub-threshold energy transfer to the lattice during irradiation. Approximate values for the cross sections of these processes are determined.
Quenching enhances the number of spontaneous recombinations and gives rise to an apparent increase of the damage rate at low defect densities probably due to deviations from Matthiessen's rule.

1. Introduction

A considerable amount of work has been carried out so far in studying the build-up of defects produced in pure metals by electron irradiation. With the exception of one experiment, however, reported by Dworschak et al. /1/ the maximum Frenkel defect concentration introduced by electron irradiation has been small compared to that achieved by neutron irradiation experiments. /2/

We have extended the defect concentrations to a level where radiation annealing processes play an important role in defect production.
The following mechanisms are in principle able to influence the observed resistivity increase per unit dose:

A) Radiation produced defects directly annihilate with adjoining defects which have accumulated during the irradiation or are introduced by doping.

B) Sub-threshold recoil events induce partial annihilation or transformation of the accumulated defects.

C) Athermal long range events like focussed collision chains or channeled high energy atoms are stopped at defects, thereby enhancing the damage production.

D) Deviations from Matthiessen's rule give rise to a non-additivity of the residual resistivities of defects present prior to the irradiation and of defects produced during irradiation.

The theory of radiation annealing given by Dettmann et al. /3/ takes into account mechanism A). The sub-threshold events B) are considered only to the extent as they induce recombination of interstitials and vacancies originating from different displacement events.
In order to regard also the recombination by sub-threshold events of vacancies and interstitials present as close pairs we used a different approach.
If only mechanisms A) and B) are operative we obtain the following equation for the production rate of Frenkel pairs of a certain type k :

$$\frac{dc_k}{d\varphi} = P_k \left[1 - 2 V_a(c) \cdot c \right] + \sum_{l \neq k} P_{l,k} c_l - \sum_{l \neq k} P_{k,l} - P_{k,0} c_k \qquad (1)$$

c_k is taken as the concentration of the type of Frenkel defects that will anneal within a discrete substage of stage I, e.g. stage I_A . P_k is the cross section for the production of type k defects, while c denotes the total concentration of defects of arbitrary types. v_a is the effective volume for spontaneous recombination described by mechanism A). $P_{1,k}$ and $P_{k,1}$ are the

cross sections for the transformation of Frenkel pairs from type 1 to type k and from type k to type 1 respectively due to a nearby sub-threshold event.
Evidence for the existence of such processes will be given in Chap. 3.
Finally, $P_{k,o}$ stands for the cross section for Frenkel pairs of type k to collapse as a result of a sub-threshold recoil event. In these sub-threshold events the energy may be transferred either to neighbor atoms of a Frenkel pair under consideration or directly to its interstitial.

With $c = \sum_k c_k$ and $P = \sum_k P_k$ we obtain

$$\frac{dc}{d\varphi} = P\left[1 - 2 v_a(c) \cdot c\right] - \sum_k P_{k,o} c_k \quad . \tag{2}$$

Thereby the damage rate is expressed as the sum of two terms. If we use the theoretical result derived by Dettmann et al. /3/ for the concentration dependence of v_a, we arrive with $v_a(o) = v_a^o$ at

$$\frac{dc}{d\varphi} = P\left[1 - 2 v_a^o c + (v_a^o c)^2\right] - \sum_k P_{k,o} c_k \quad . \tag{3}$$

We have quantitatively studied the mechanisms described in equation (1) by radiation doping experiments in aluminum, copper and platinum (Chap. 3), by sub-threshold irradiation of platinum (Chap. 4) and by irradiation of previously quenched platinum (Chap. 5).

In addition the mechanisms C) and D) have been investigated by electron irradiation of quenched platinum. The results are discussed and compared with similar investigations by heavy particle irradiation /4-8/ in Chap. 5.

2. Experimental Procedure

The electron irradiations were performed at the low temperature irradiation facility of the Kernforschungsanlage Jülich. This facility will be described elsewhere /9/.
The dimensions of the irradiated area were 5,5 mm x 23 mm. Up to 4 samples could be irradiated simultaneously, the beam intensity profile being homogeneous to about 2 % across the specified area at 10 μ A/cm^2 current density and increasing to 10 % at 90 μ A/cm^2. To prevent excessive heating all samples

were made of thin foils, 10 to 30 μm thick, and vertically mounted inside a duct carrying a stream of liquid helium at a velocity of approximately 10 m/s. 20 μm thick stainless steel windows formed two opposite sides of this duct providing a transmission path for the electron beam.
The duct was a part of the sample chamber, the temperature of which could be regulated between 12 ^{o}K and 300 ^{o}K with an accuracy of $\frac{\Delta T}{T} < 2 \times 10^{-2}$ after the electron beam had been shut off by a beam stopper. Coarse isochronal annealing treatments were performed with temperature steps of 1.5 ^{o}K in the range of recovery stage I and temperature pulse lengths of 10 min duration. Neither the samples, nor the beam position had to be readjusted for the short test irradiations at 4.5 ^{o}K that interrupted the annealing treatment. Resistance measurements were done by standard techniques with an accuracy up to $\pm$ 1 x 10^{-5} . The sensitivity for the determination of resistivity changes depended on the size of individual samples, $\pm$ 1 x $10^{-12}\Omega$cm being a representative figure, however.
All observed resistivity values were corrected for size effects due to surface scattering of conduction electrons using Fuchs' results as reviewed by E.H. Sondheimer /10/. In the case of aluminum, Dworschak et al. /11/ have measured $\varrho_o \cdot l$, the product of the resistivity and the mean free path of the conduction electrons, which determine the influence of the geometry on the observed resistivity and obtained $\varrho_o l/_{Al} = 8.6 \times 10^{-12}\Omega\,cm^2$.
Using their method we deduced from our experiments for copper $\varrho_o l/_{Cu} = 8.2 \times 10^{-12}\Omega\,cm^2$ and for platinum $\varrho_o l/_{Pt} = 5.3 \times 10^{-12}\Omega\,cm^2$.

For the determination of the irradiation dose the electrons were stopped in a Faraday cage after penetration of the sample chamber. Because of the increased divergence of the beam leaving the exit window and due to the emission of secondary electrons no precise absolute calibration of the flux has been obtained as yet. Comparing our initial damage rates for aluminum, copper and platinum with the values known from the literature /19/,/13/ the error in our flux calibration is less than 20 %. Since we used the same irradiation geometry throughout all irradiation runs, the accuracy of all dose values with respect to each other is determined only by variations of the homogeneity of the beam profile. The reproducibility of different runs under identical conditions was

found to be better than 2 %.
Samples were cut from pure rolled material, etched and spot-welded to small alumina frames bearing thin conducting metal layers that had been sintered on to the surface to provide electrical contacts.
The aluminum and copper samples were annealed prior to mounting. The platinum samples were annealed after mounting by resistance heating. Some of the platinum samples were quenched into water to retain an excess concentration of vacancies.
The specifications of the materials used are given in table 1 :

Tab. 1

material	Al	Cu	Pt	
manufacturer	Metals Res.Corp.	Cominco	S. Cohn	Heraeus
nominal purity	5 N	5 N	5 N +	5 N
nominal thickness μm	25	12,7	12,7	10
av.resistance ratio $R_{295°K}/R_{4.5°K}$	1600	2800	3000-9000	3000-9000

3. Defect Production and Radiation Doping in Aluminum, Copper, and Platinum

3.1 Defect Production in the annealed Materials

Radiation annealing has been observed in several metals irradiated with reactor neutrons /2/ and in copper with 3 MeV electrons /1/.
We have measured this effect in aluminum, copper, and platinum irradiated with 3 MeV electrons at 4.5 ^{o}K.
In well annealed high purity samples we found that the increase of the electrical resistivity $\Delta\varrho$ as a function of irradiation dose φ shows a definite approach to saturation.
In this paper, we generally assume that changes in resistivity are proportional to changes in defect concentration and that

$$\Delta\varrho = \varrho_F c_i \qquad (4)$$

where c is the concentration of Frenkel defects and ϱ_F their resistivity per unit concentration. A possible exception to this proportionality is discussed in Chap. 5.
Under this assumption, the defect production rates $dc/d\varrho$ calculated from the observed dose curves decrease with increasing defect concentration, as shown in Figures 1 to 3.

In platinum, extrapolating the observed damage rate to zero, the saturation values are found to be $\Delta\varrho_\infty = 3.75\ \mu\Omega$ cm for the resistivity change and $c_\infty = 0.5$ % for the concentration of Frenkel defects, using $\varrho_F = 7.5 \times 10^{-4}\ \Omega$ cm per unit concentration /13,14/- These values are considerably larger than the $\Delta\varrho_\infty = 2.49\ \mu\Omega$ cm from neutron irradiation /15/, which was obtained after a damage of $\Delta\varrho = 0.55\ \mu\Omega$ cm. The difference shows the great influence of the energy of the primary knock-ons on radiation annealing.
The corresponding values of our electron irradiation of copper (Fig. 2) are $\Delta\varrho_\infty = 0.76\ \mu\Omega$ cm and $c_\infty = 0.3$ %, using $\varrho_F = 2.5 \times 10^{-4}\ \Omega$ cm per unit concentration. A somewhat different value of $\Delta\varrho_\infty = 0.9\ \mu\Omega$ cm has been given by Dworschak et al. /1/ after electron irradiation to $\Delta\varrho = 0.28\ \mu\Omega$ cm. The corresponding neutron irradiation value is $\Delta\varrho_\infty = 0.34\ \mu\Omega$ cm /2/ after $\Delta\varrho = 0.17\ \mu\Omega$ cm.
Because of the nonlinear decrease of the damage rate in aluminum (Fig. 3) a reasonable extrapolation was not possible. After neutron irradiation to $\Delta\varrho = 0.52\ \mu\Omega$ cm a value of $\Delta\varrho_\infty = 0.86\ \mu\Omega$ cm has been observed /2/.

3.2 Doping Experiments

Different samples of aluminum, copper and platinum were irradiated to different dose levels. A coarse isochronal annealing program followed each irradiation. At a limited number of temperatures (approximately 12,21,29,32,60 and 90 °K in the case of aluminum and copper , and 13,17,22,30 and 70 °K for platinum), which were chosen to be situated between annealing peaks already known for the materials used, the normal annealing program was interrupted. A short test irradiation at liquid helium temperature was employed with the same electron beam parameters as in the preceding longtime irradiation, and then the annealing program continued.

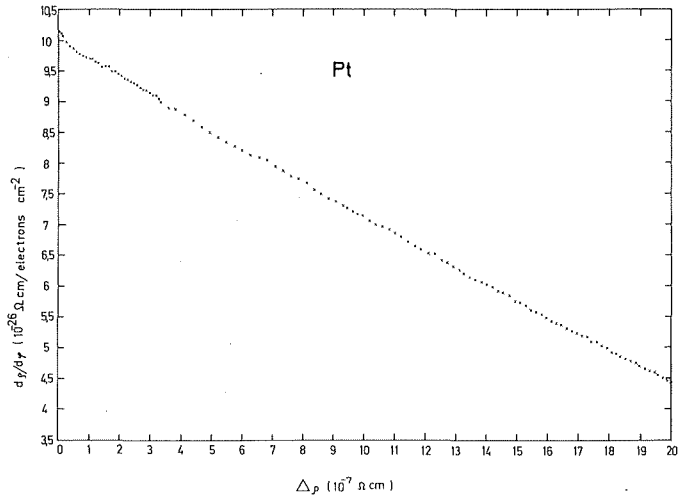

Fig. 1

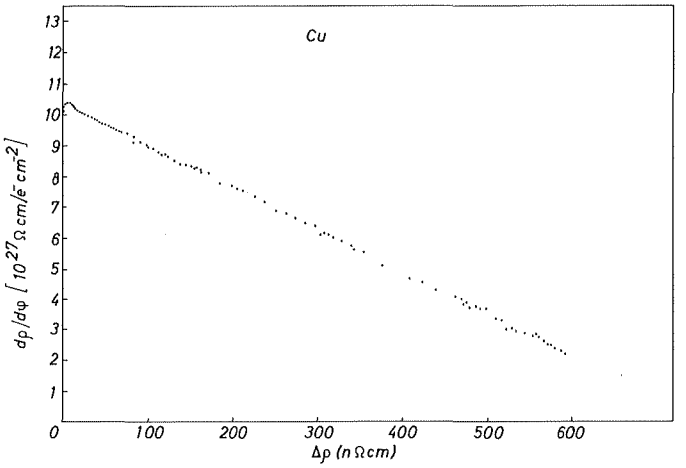

Fig. 2

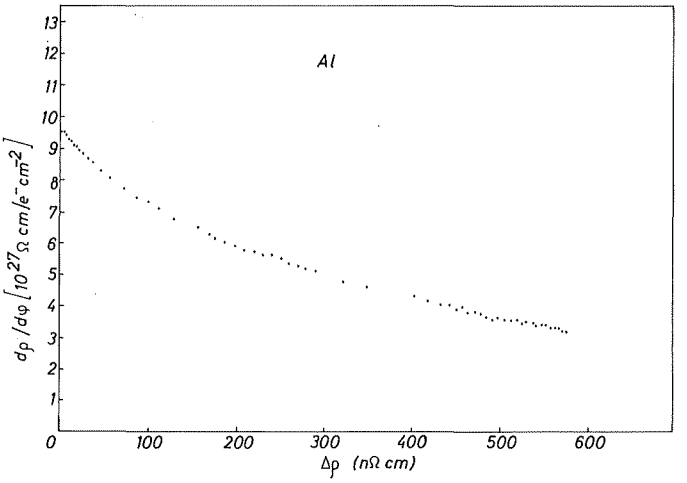

Fig. 3

Figures 1 to 3 Damage rate versus resistivity increase for electron irradiations at annealed platinum (3 MeV), copper (2.8 MeV), and aluminum (2.8 MeV). The electron doses corresponding to the maximum observed resistivity change were $\varphi = 3 \times 10^{19}$ electrons cm^{-2} in platinum and 1.15×10^{20} electrons cm^{-2} in copper and aluminum

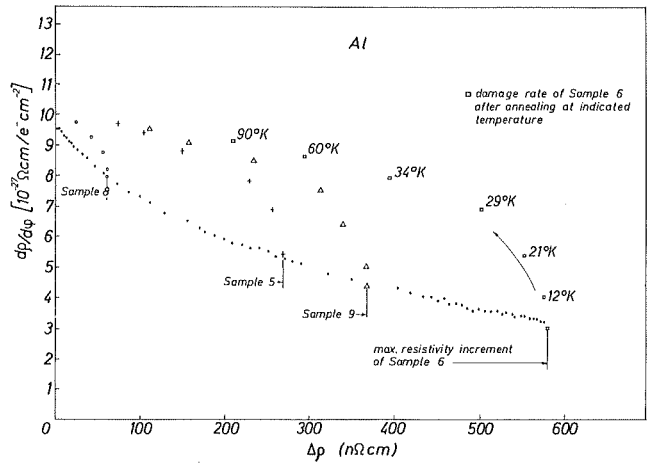

Fig. 4

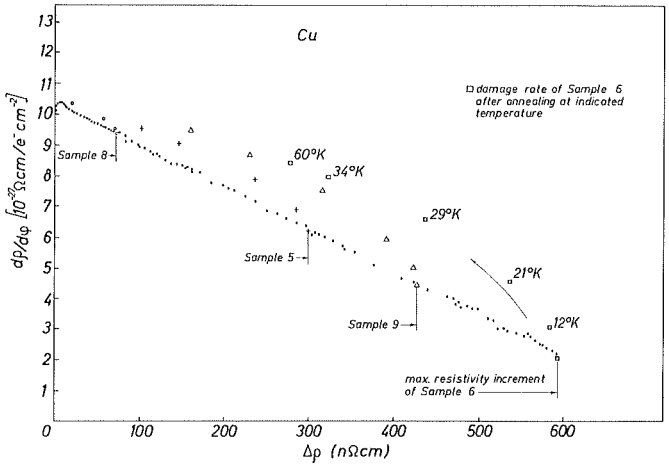

Fig. 5

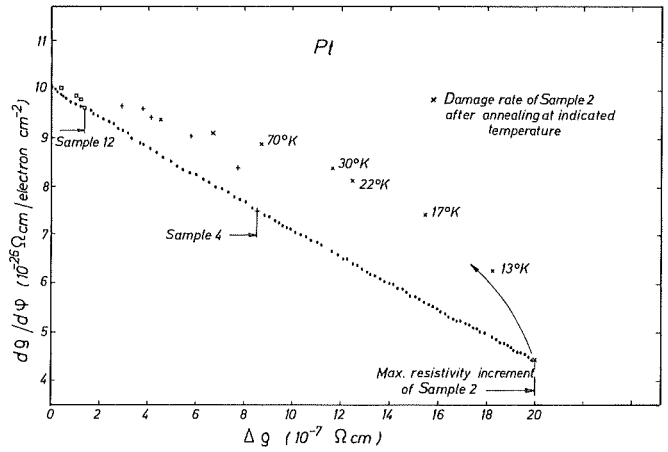

Fig. 6

Fig. 4,5 and 6
Damage rate versus observed resistivity increment in samples which received different electron doses followed by partial thermal annealing treatments at the temperature levels indicated.

The radiation annealing observed during such test irradiations is influenced only by those types of defects that have survived the annealing treatment. Care was taken not to increase the resistivity remaining after the preceding annealing procedure by more than 2 % during any test irradiation.
The results obtained for aluminum, copper and platinum are plotted in Figures 4,5 and 6. It should be noted, that for all samples tested and in the whole range of concentrations covered, the damage rate is increased after any partial annealing treatment. The fastest increase is caused by the annihilation of those defects which possess the lowest activation energies for thermal recombination. Apparently the close Frenkel pairs contribute more strongly to the radiation annealing process than the defects recovering at higher temperatures.

3.3 Isochronal Annealing Experiments

The partial annealing procedure prior to a test irradiation described in the preceding section formed but a small part in a complete isochronal annealing program. Each sample was submitted to such a program, the details of which were given in Chap. 2. The results for copper and aluminum are plotted in Figures 7 and 8.

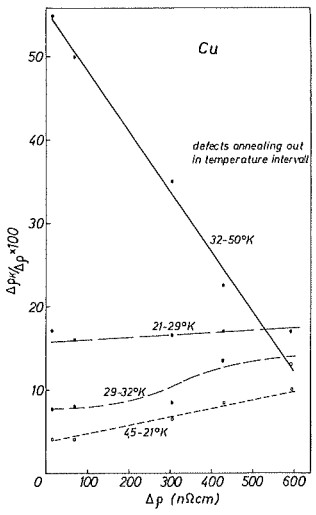

Fig. 7

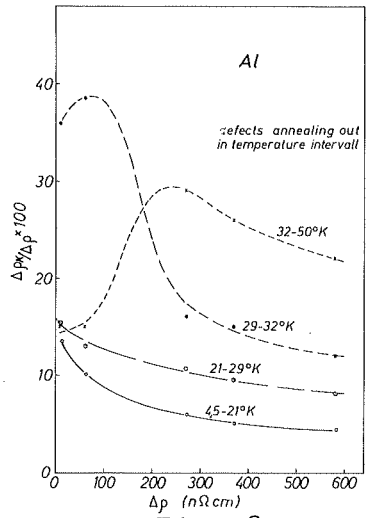

Fig. 8

Fig. 7,8 Fractional resistivity recovery within certain annealing temperature intervals as a function of total resistivity increase resulting from 2.8 MeV electron irradiation

In these figures the amount of fractional recovery found within selected temperature intervals is given as a function of dose as measured by the total initial resistivity increment caused by a 2.8 MeV electron irradiation.
In the case of copper the first two annealing intervals correspond to an annihilation of types of Frenkel defects belonging to the annealing stages I_A and I_B , whereas in the case of aluminum we attribute to these intervals defect types annealing approximately in stages I_B and I_C according to the notation of Chaplin and Simpson /16/.
The observed dose dependence of the fractional annealing in the temperature range between 4,5 and approx. 30 ^{o}K, where close pair collapse predominates, indicates that the build-up of a given type of Frenkel pair during irradiation is to be considered as the net result of transformation processes as well as of production and recombination processes. In particular the increase of the lower substages in copper with total defect concentration gives evidence that Frenkel defects are transformed during irradiation from different configurations into those types which anneal in the substages mentioned above.
To find further evidence for this mechanism we have looked for the annealing behavior of the defects in aluminum, copper and platinum that were introduced during test irradiations as described in section 3.2 Quantitative results will be reported at a later time. However, at the present we can say that for those types of close pairs which were removed prior to a given test irradiation (and thereby built up anew) the absolute amount of recovery was considerably larger than in a virgin sample containing no doping defects, but otherwise having received the same treatment. Since we do not assume that the probability for direct production of these close pairs is increased during the displacement processes of the test irradiation, we have to ascribe the observed increase of the favored types of defects to the transformation of defects that were introduced earlier and survived the annealing treatment prior to the test irradiation in a more stable configuration.

3.4 Interpretation of the Results

3.4.1 Copper

It is possible to describe the dependence of the damage rate on the concentration of defects and the results of the radiation annealing and doping experiments quite satisfactorily with the assumptions that led to equation (3). Using this equation and denoting by c_1 the concentration of those defects which anneal out in the temperature interval from 4.5 - 12 °K, the production rate observed in the first test irradiation (see Fig. 5) is

$$\frac{d\langle c-c_1\rangle}{d\varphi} = P\left[1-2v_a(c-c_1)\cdot\langle c-c_1\rangle\right] - \sum_{k,k>1} P_{k,0}\,c_k \quad . \tag{5}$$

Subtraction of equation (5) from equation (2) gives the difference in the damage rates between test irradiation and the end of the initial irradiation to be

$$\frac{dc}{d\varphi} - \frac{d\langle c-c_1\rangle}{d\varphi} = P\left[2v_a(c-c_1)\cdot\langle c-c_1\rangle - 2v_a(c)\cdot c\right] - P_{1,0}\,c_1 \quad . \tag{6}$$

As a first approximation the dependence of the effective recombination volume v_a on the total defect concentration is neglected and $v_a(c)$ replaced by $v_a(o) = v_a^o$. The amount of type 1 defects which recombine by sub-threshold events is then

$$P_{1,0}\,c_1 = \frac{d\langle c-c_1\rangle}{d\varphi} - \frac{dc}{d\varphi} - 2Pv_a^o c_1 \quad . \tag{7}$$

Multiplying equation (7) by ϱ_F, the first two terms on the right hand side give the resistivity changes per unit dose which were determined experimentally. The recombination volume v_a^o contained in the small correction $2Pv_a^o\Delta\varrho_1$ can be estimated roughly from the test irradiation data after annealing at temperature levels above stage I.

Using equation (7) we have obtained values for $P_{1,o}\Delta\varrho_1$ which are plotted versus $\Delta\varrho_1$ in Fig. 9. Similar derivations yield equations for $P_{2,o}\Delta\varrho_2$ and $P_{3,o}\Delta\varrho_3$ which are included in the same figure. The annealing temperature intervals given for the removal of defects, correspond to 1- below stage I_A, 2- within I_A and 3- within I_B.

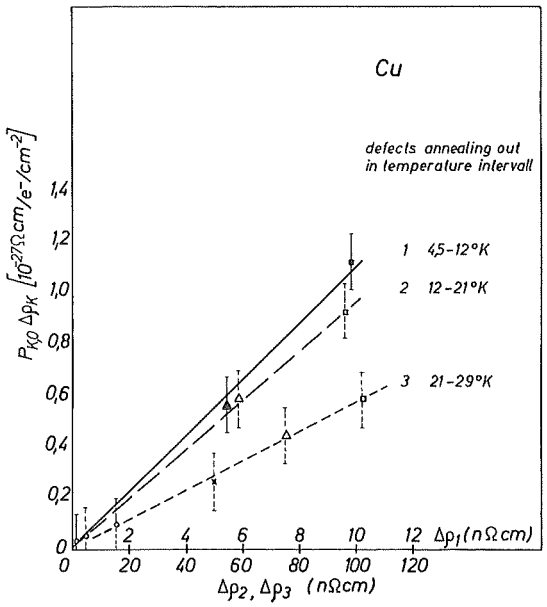

Fig. 9

Resistivity recovery by sub-threshold events per unit dose (2.8 MeV) as a function of type of defect and fractional resistivity contribution present thereof.

Within the accuracy of our experimental data, the relations shown in Fig. 9 are linear, indicating that the cross sections $P_{k,o}$ for radiation induced recombination by sub-threshold events are constants and do not depend on any of the $\Delta\rho_k$. This result holds for a variation of the total Frenkel defect concentration from 6×10^{-5} to 2.5×10^{-3}.

The three cross sections were determined to be approximately $P_{1,o}$ = 110000 barn, $P_{2,o}$ = 9500 barn and $P_{3,o}$ = 5500 barn. Both the fact that the $P_{k,o}$ s are constants and that their magnitude varies strongly with the annealing temperature intervals seem to justify our derivation.

As a check on the consistency of our results we used the data obtained from the test irradiations together with the recovery data and corrected the damage rate $\frac{d\rho}{d\varphi}\big|_{exp.}$ found during the normal build-up (Fig. 2) for sub-threshold recovery events. Doing so we obtain a virtual damage rate given by

$$\frac{d\rho}{d\varphi} = \frac{d\rho}{d\varphi}\Big|_{exp.} + \rho_F \left[P_{1,0}\, c_1(c) + P_{2,0}\, c_2(c) + P_{3,0}\, c_3(c) + \ldots \right] ,$$

which should be in agreement with the predictions of Dettmann et al. /3/ as it contains only spontaneous recombination events. To show the agreement a plot is chosen where, instead of $\frac{d\rho}{d\varphi}$ as a function of $\Delta\rho$, $\frac{\varphi}{\Delta\rho}$ is given as a function of φ . It is easily verified /17/ that

$$\frac{d\rho}{d\varphi} = \rho_F P \left[1 - 2\,\frac{V_a^o}{\rho_F}\Delta\rho + \left(\frac{V_a^o}{\rho_F}\Delta\rho\right)^2 \right] \quad (8) \quad \text{and} \quad \frac{\varphi}{\Delta\rho} = \frac{1}{\rho_F P} + \frac{V_a^o}{\rho_F}\varphi \quad (9)$$

are identical. In this plot one expects a straight line, if the data corrected for sub-threshold events are consistent with the theoretical predictions derived for spontaneous recombination.

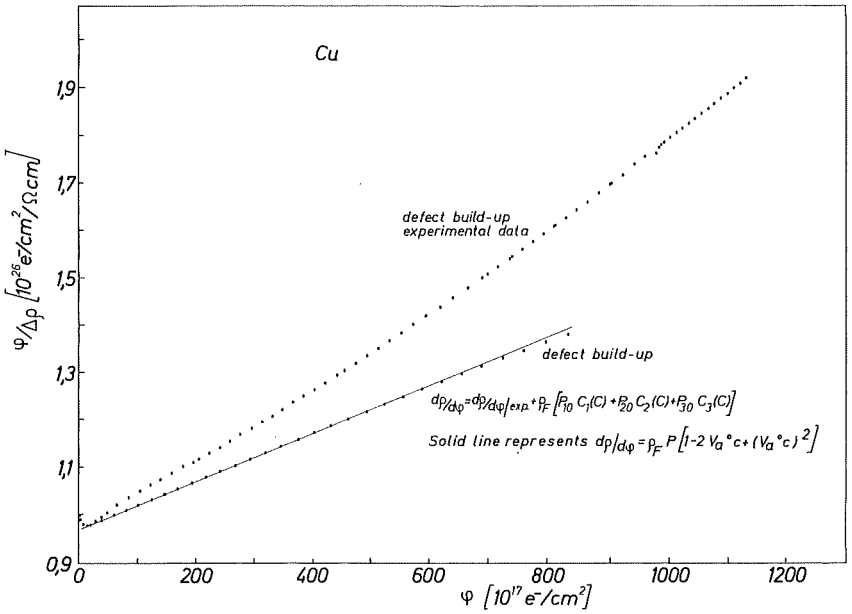

Fig. 10 Defect build-up in Cu before and after correction for radiation induced recovery caused by sub-threshold energy transfers. Solid line represents theoretical predictions /3/. Data are plotted according to equation (9).

The lower curve in Fig. 10 is the result of such a correction. Higher contributions than $P_{3,o}\,\Delta\varrho_3$ were neglected. The deviations from the predicted straight line behavior indicated by the solid line are immaterial.

The uncorrected experimental data are also included in Fig. 10 to demonstrate that the decrease of the damage rate during the defect build-up could not be explained by spontaneous recombination only.

We derive from Fig. 10 a volume for spontaneous recombination of v_a^o = 125 atomic volumes.

3.4.2 Aluminum

The cross sections for recombination of existing Frenkel defects due to sub-threshold recoil events are determined according to the procedure outlined in section 3.4.1. Now $P_{1,o}$, $P_{2,o}$, and $P_{3,o}$ have to be attributed to Frenkel pairs annealing 1- below stage I_B, 2- within I_B and 3- within I_C . $P_{k,o}\,\Delta\varrho_k$ values are plotted

in Fig. 11 as a function of $\Delta\varrho_k$, the resistivity contribution of type k defects to the total resistivity increment

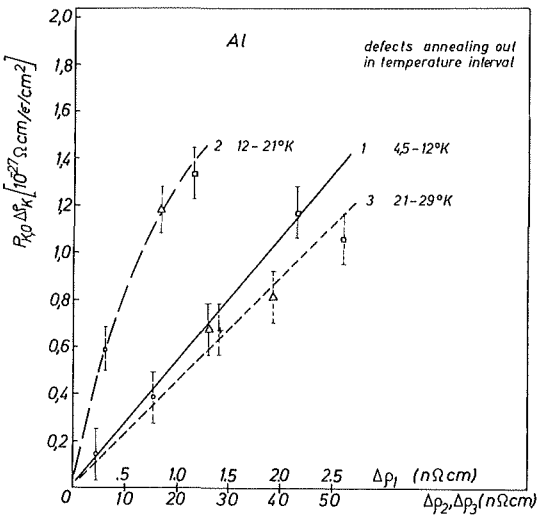

Fig. 11

Resistivity recovery by sub-threshold events per unit dose (2.8 MeV) as a function of type of defect and fractional resistivity contribution present thereof.

We find that the probability for recombination decreases with increasing thermal stability of the Frenkel pairs in agreement with the results found in copper. Contrary to copper, however, the cross section $P_{2,o}$ depends somewhat on the total concentration of defects as is indicated by the curvature of curve 2 in Fig. 11. The cross sections are determined to be approx. $P_{1,o}$ = 520000 barn, $P_{2,o}$ = 70000 barn and $P_{3,o}$ = 22000 barn.
Furhter experiments with a better resolution are needed to clarify, whether this dependence can be explained by physical interaction between different types of defects or not.

Using the same method as in the preceding section, we corrected the damage rate of Fig. 3 for sub-threshold recoil events by means of the data of Fig. 7 and Fig. 11.

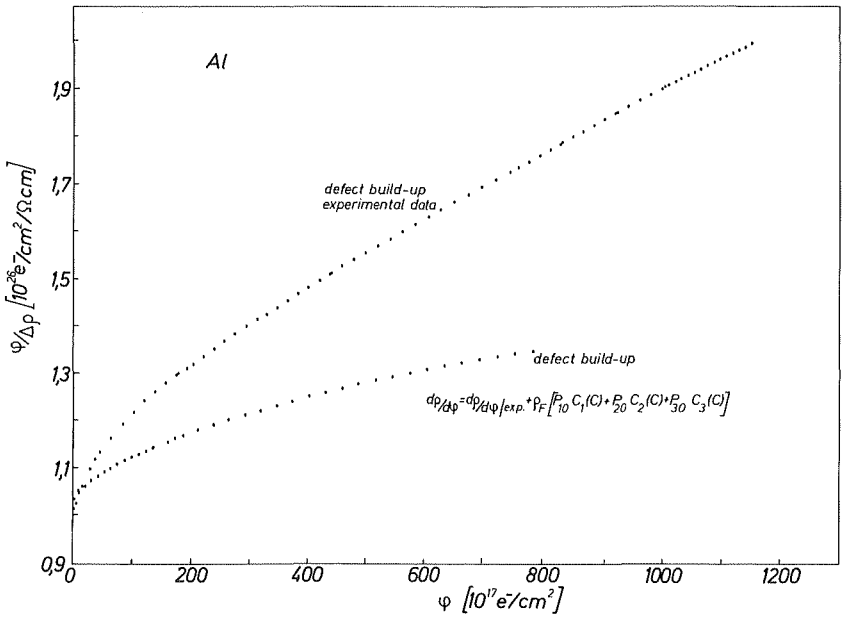

Fig. 12 Defect build-up in Al before and after correction for radiation induced recovery caused by sub-threshold energy transfers. Data are plotted according to equation (9).

The resulting curve in Fig. 12 is not a straight line. Any further corrections would have to account for the influence of defects that anneal out in the temperature range above 29 ^{o}K (stage I_D). We can conclude that such a correction would not be negligible by comparing the data given in Fig. 4 and 7 for aluminum with that in Fig. 5 and 8 for copper . The radiation induced annihilation of defects for the 29-32 ^{o}K annealing range is much stronger in aluminum than in copper, giving rise to a correspondingly larger value for $P_{4,o}\,\Delta\varrho_4$. Unfortunately an exact value for the influence of this type of defect can not be obtained by means of the test irradiations reported here, since thermal clustering of interstitials seems to take place during the annealing in the temperature range of 29 - 32 ^{o}K (stage I_D), thus obscuring the influence of this defect type in its original state. Irradiation doping experiments with smaller electron energies should help to solve this problem since this leads to a more favourable relative occupation of the different substages of stage I /16/.

The results from radiation doping of platinum are discussed in Chap. 4 together with the results obtained from sub-threshold irradiations.

4. Sub-threshold Irradiation and Radiation Doping of Platinum

The fraction of recovery induced by sub-threshold events on radiation annealing has been determined in platinum by two independent types of experiments: Sub-threshold electron irradiations and radiation doping experiments.

4.1 Sub-threshold Irradiations

In platinum, the energy of 1.4 MeV electrons is too small to cause displacements in an undisturbed lattice, i.e., 1.4 MeV electron irradiations are sub-threshold irradiations.
The experimental procedure was the following: Annealed samples were irradiated above threshold with 3 MeV electrons. At various damage levels $\Delta\rho$, the irradiation was interrupted for short 1.4 MeV irradiations. Thereupon the 3 MeV irradiation was continued.
The result of these sub-threshold irradiations is a decrease in the radiation induced change in resistivity. This is plotted in the lower part of Fig. 13 as a negative production rate, $-d\rho/d\varphi$, versus the resistivity increase, $\Delta\rho$, due to the 3 MeV irradiation.

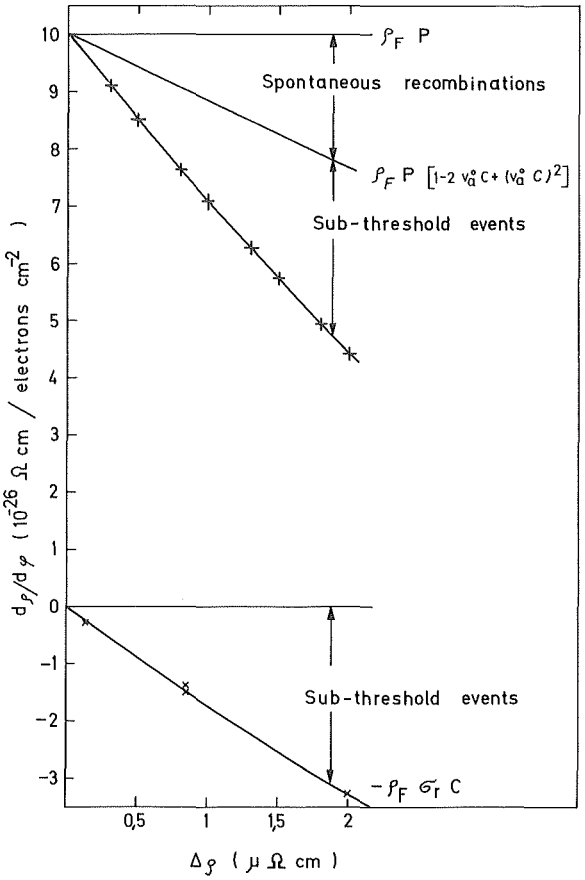

Fig. 13. Production rate for 3 MeV electron irradiation (top) and the recovery rate due to 1.4 MeV electron irradiation (bottom) of platinum as a function of the radiation damage, $\Delta\rho$, due to 3 MeV irradiation. Half the 3 MeV radiation annealing is due to recovery by sub-threshold collisions.

By normalizing this recovery rate with respect to the total damage $\Delta\rho_{3MeV}$ present during the sub-threshold irradiation, a cross section

$$\sigma_r = -\left.\frac{d\rho}{d\varphi}\right|_{1.4\,MeV} \times \frac{1}{\Delta\rho_{3MeV}} \qquad (10)$$

is defined for the total recovery by sub-threshold events. As will be shown below, σ_r slightly depends on $\Delta\rho$ and on the electron energy E. The value for $\Delta\rho_{3MeV} = 2\mu\Omega cm$ is σ_r (E = 1.4 MeV) $\approx$ 16000 barns.

As shown in Chap. 3, mainly close Frenkel pairs are recombined by sub-threshold energy transfers. To check this conclusion independently, radiation doped samples have been annealed stepwise to successively higher temperatures and after each annealing step have been irradiated with 1.4 MeV electrons. The resulting $\sigma_r(T)$ is plotted versus the temperature of annealing immediately prior to a given sub-threshold irradiation in Fig. 14.

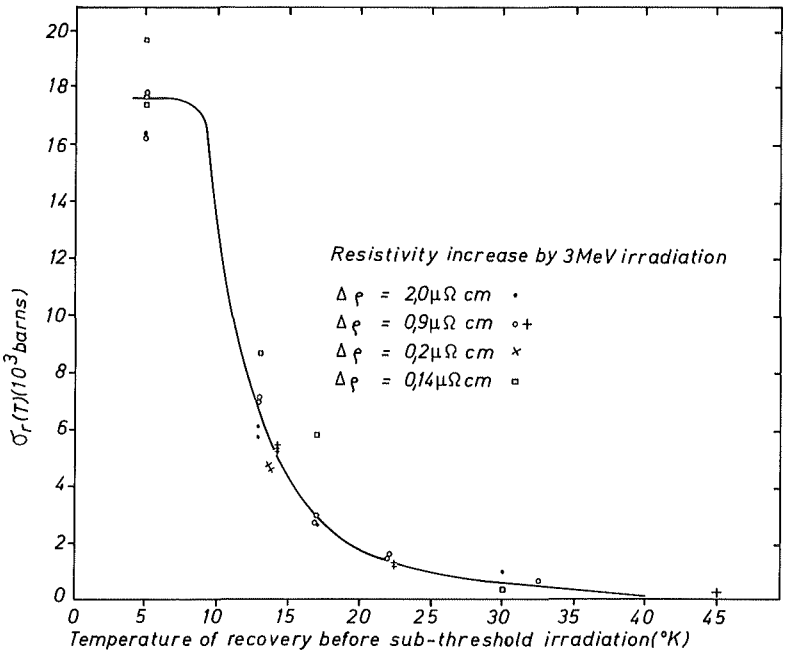

Fig. 14 Cross section for recovery by sub-threshold events in platinum previously irradiated with 3 MeV electrons and annealed at the given temperature.

The solid curve gives the mean temperature dependence of σ_r (T). At low temperatures the curve has been drawn as a constant, taking into account that in platinum almost no recovery takes place up to 9 °K /18/. The figure shows that sub-threshold events mainly

cause annihilation of close Frenkel pairs. However, a small part of the recovery by sub-threshold events remains at the end of stage I (about 22 °K for our damage levels) and even beyond. This small effect may perhaps be interpreted by the release of interstitials trapped in the neighborhood of vacancies or to radiation induced diffusion of insterstitials at 4.5 °K.

A more detailed interpretation has to allow for the different configurations of close Frenkel pairs. According to eq.(2),

$$\left.\frac{d\varrho}{d\varphi}\right|_{1.4\,MeV} = -\varrho_F \sum_k P_{k,0}\, c_k = -\sum_k P_{k,0}\, \frac{c_k(c)}{c}\, \Delta\varrho_{3\,MeV} \qquad (11)$$

where $\Delta\varrho_{3MeV}$ is the total resistivity increase due to the 3 MeV irradiation and

$$\sigma_r = \sum_k P_{k,0}\, \frac{c_k(c)}{c} \,. \qquad (12)$$

Isochronal recovery measurements not presented in this paper show that the fractions c_k/c of close Frenkel pairs decrease with the increasing total concentration, c, of the Frenkel pairs. Using this and eq. (11), the recovery rate due to sub-threshold events should increase less than linearly with $\Delta\varrho$. This is confirmed experimentally (Fig. 13, below).

To check the independence of the $P_{k,o}$, we have plotted $-d\varrho/d\varphi|_{1.4MeV}$ versus the concentration c_{17} of those Frenkel pairs which anneal thermally below 17 °K. The results in Fig. 15 show that the measured $-d\varrho/d\varphi|_{1.4MeV}$ is a linear function of c_{17}.

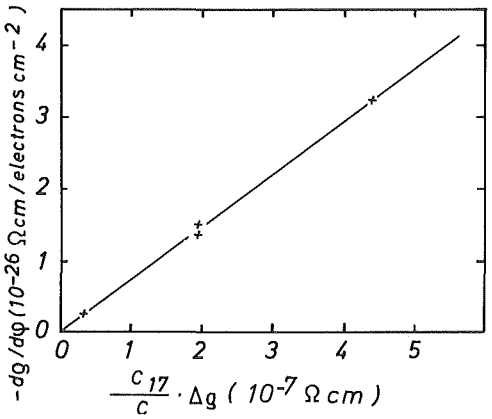

Fig. 15 Recovery rate by 1.4MeV electron irradiation of platinum versus the resistivity of those close Frenkel pairs which are recombined by a 17 °K annealing.

From recovery measurements it is known that most close Frenkel pairs recombine below 17 °K.

Hence c_{17} in Fig. 15 must cover most of the close Frenkel pairs contributing to recombinations by sub-threshold events. Thus,

the conclusion that recovery by sub-threshold processes is proportional to the close pair concentration $c_{c.p.}$:

$$-\left.\frac{d\rho}{d\varphi}\right|_{1.4\ MeV} = P_{c.p.,o}\ c_{c.p.};\ P_{c.p,o} = \text{constant}, \qquad (13)$$

is subject to only a small error since the fraction of close pairs not covered by c_{17} is small and σ_r is changing slowly above this temperature as can be seen in Fig. 14. This result is the same as that found in copper by a different experimental method.

In order to use the sub-threshold irradiations to correct the radiation annealing observed at 3 MeV for the contribution of the sub-threshold events, the energy dependence of σ_r has to be known.

A rigorous theory of σ_r would have to start from the probabilities $g_{ij}(T)$ that by a sub-threshold energy transfer between T and T + dT averaged over all directions on the atom i, the nearby interstitial at position j is recombined with a vacancy at position zero. By averaging the product of $g_{ij}(T)$ times the differential cross sections $K_i(E,T)$ for a single energy transfer, a mean value $\bar{g}(E)$ can be defined:

$$\sigma_r(E) = \bar{g}(E)\ \sigma_s(E)\ .$$

σ_s is the cross section for a single sub-threshold energy transfer and has been calculated in the case of copper by Dworschak et al. /19/, using data by Mott /20/. It was found that σ_s slightly decreases with E increasing from 1 to 3 MeV.

As a first guess we assume that $\bar{g}(E)$ only weakly depends on E and that in platinum σ_s depends on E in the same way as in copper. Then we expect

$$\sigma_r(E = 3\ MeV) \lesssim \sigma_r(E = 1.4\ MeV) \text{ in platinum.}$$

Using this assumption, the 1.4 MeV recovery rate has been subtracted from the 3 MeV damage rate in the upper part of Fig. 13. The figure shows that about 50% of the decrease of the damage rate is due to recombination by radiation induced sub-threshold events.

The remaining part of radiation annealing is caused by spontaneous recombinations and is described by eq. (8).

A plot of $\varphi / \Delta\rho$ versus φ, corresponding to eq. (9) is given in Fig. 16.

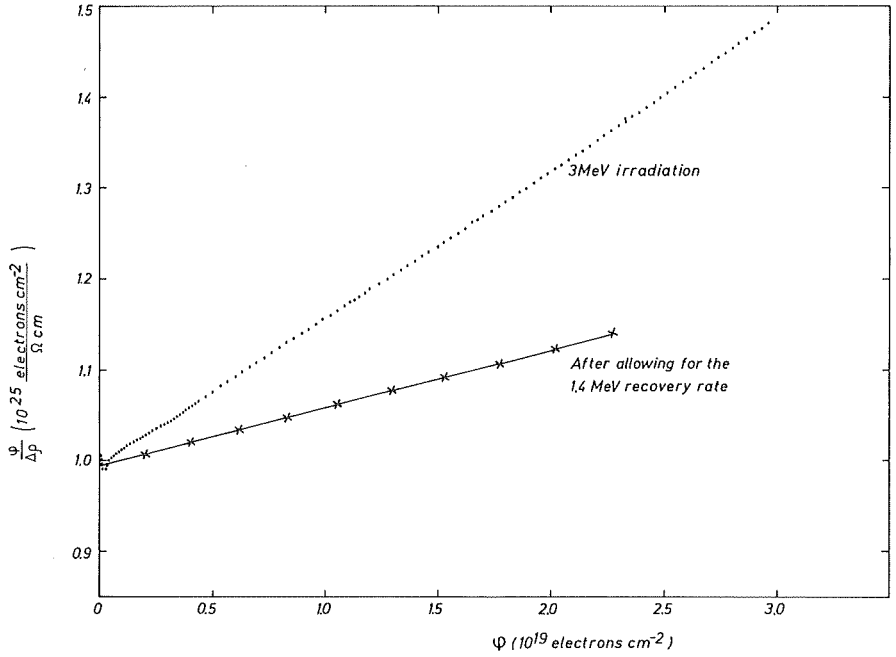

Plot of $\varphi / \Delta\rho$ versus φ for platinum.

Fig. 16 The upper curve is due to spontaneous recombinations and recovery by sub-threshold events, the lower one is due only to spontaneous recombinations. The slope of the lower curve equals v_a^o / ρ_F, the initial value of $\varphi / \Delta\rho$ equals $1/P\rho_F$.

From this figure and from $\rho_F = 7.5 \times 10^{-4} \Omega$cm per unit concentration /13/, the value for the spontaneous recombination volume v_a^o in platinum is found to be

$$v_a^o = 48 \text{ atomic volumes.}$$

4.2 Interpretation of the Radiation Doping Experiments in Platinum

A second method to determine the contribution of recovery by sub-threshold events on radiation annealing is the radiation doping experiment described in Chap. 3.

The results for platinum are shown in Fig. 6. The damage rates are increased by partial thermal recovery of the radiation produced defects. With increasing annealing temperatures, the damage rate values of each sample tend to fall on a line which is common to all samples independent of the damage introduced by previous irradiation. This envelope is constructed in Fig. 17 from the data in Fig. 6. Within the accuracy of our measurements,

the envelope is a straight line.

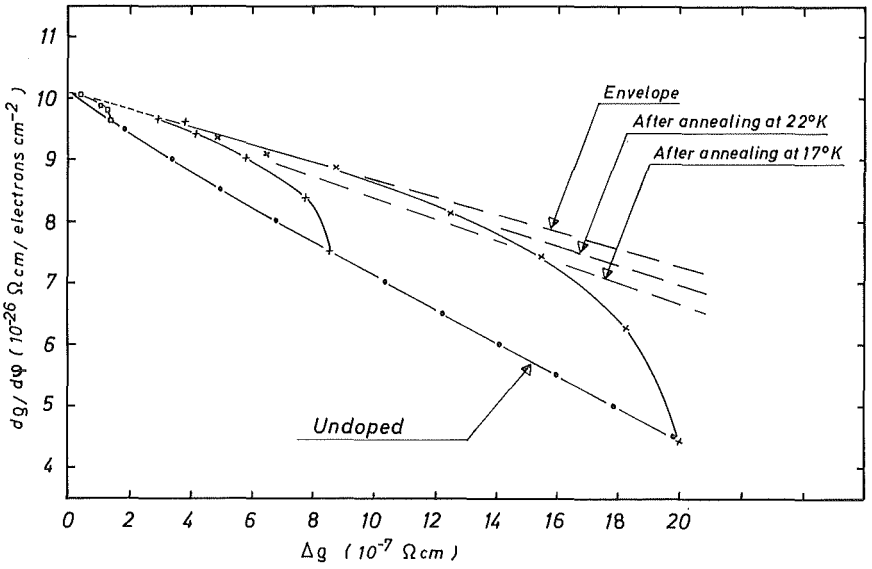

Fig. 17 Radiation doping experiments in platinum. On the envelope, radiation annealing is only due to spontaneous recombinations. On the lower dashed lines, small numbers of sub-threshold events are included. The lowest solid curve is due to the full amount of spontaneous recombinations and recovery by sub-threshold events.

The envelope contains only damage rate values for samples which have previously been annealed at such a high temperature that the σ_r (T) value in Fig. 14 is negligible. This means that all defects which are able to recombine by sub-threshold events are already annihilated. The theoretical expression (8) for the radiation annealing by spontaneous recombination processes describes the observed envelope very satisfactorily yielding a spontaneous recombination volume of v_a^o = 53 atomic volumes and a cross section for recovery by sub-threshold events of

$$\sigma_r \text{ (E = 3 MeV)} = 14100 \text{ barns}$$

for $\Delta\rho = 2\ \mu\Omega$cm.

Within the experimental errors these values are in good agreement with the values we have deduced from sub-threshold irradiations. Allowing for a small decrease of σ_r with energy E would further improve the agreement.

Because of interstitial migration and clustering at the end of stage I, it still may be questioned if the envelope in Fig. 17 yields a good value of the recombination volume v_a^o of free interstitials.

To check this, all damage rates after 22 °K annealing have been approximately connected in Fig. 17 by a straight line and all damage rates after 17 °K likewise. The resulting cross sections σ_{r22} and σ_{r17} for annihilation by sub-threshold events of all defects which are present above and below stage $I_D - I_E$ (approximately 22 °K and 17 °K annealing temperatures, respectively) have been compared with the corresponding data from 1.4 MeV irradiations (Fig. 14). The results are

3 MeV irradiation : $\sigma_{r22} = 0.10\sigma_r$

$\sigma_{r17} = 0.20\sigma_r$

1.4 MeV irradiation : $\sigma_{r22} = 0.08\sigma_r$

$\sigma_{r_{17}} = 0.17\sigma_r$

These data are in a very good agreement and indicate that the influence of interstitial clustering during the end of stage I annealing on our determination of v_a^o is negligible.

5. Defect Production in Quenched Platinum

5.1 High Damage Concentrations

According to the annealing model of Burger et al. /2/, an excess of vacancies injected prior to irradiation provides a constant number of additional recombination volumes and reduces the defect production rate by a constant amount for all values of $\Delta\rho$ (which are not too close to saturation). The larger the quenched-in resistivity, ρ_Q , the larger the constant reduction of the damage rate should be.

This is one of the effects we have found by doping with vacancies (Fig. 18) and it is the dominant one for $\Delta\rho \gtrsim 10^{-7}\,\Omega$cm and $c \gtrsim 1.5 \times 10^{-4}$.

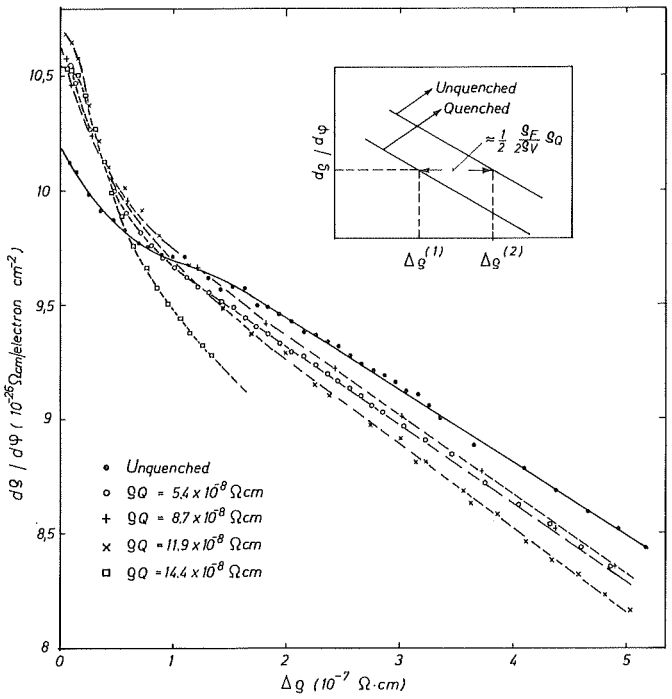

Fig. 18 Damage rate of vacancy doped platinum samples compared with an unquenched sample. ϱ_Q is the quenched-in resistivity. Initially, the damage rate is increased by the vacancy doping. At sufficiently high damage levels, the damage rate is the same in a quenched sample after a damage $\Delta\varrho^{(1)}$ and in an unquenched sample after a damage of $\Delta\varrho^{(2)} = \Delta\varrho^{(1)} + (\varrho_F / 4\varrho_V)\varrho_Q$. This is schematically shown on the inserted figure.

As a first approximation, the probability for spontaneous recombination of a newly produced Frenkel defect is given by the probability, $v_a^o c_v$, that the newly produced interstitial is annihilated by one of the vacancies present in the concentration c_v, plus the probability, $v_a^o c_I$, that the recombination volume of the newly produced vacancy contains one of the interstitials present in the lattice with concentration c_I.
Using $c_I + c_V = 2c + c_V^Q$ with c_V^Q being the concentration of quenched-in vacancies, the total decrease of the damage rate in quenched samples, according to eq. (3), is given by

$$-\frac{d\varrho}{d\varphi} = P\,\varrho_F v_a^o \left(2c + c_V^Q \right) + \sigma_r \varrho_F c. \qquad (14)$$

As shown in Fig. 13, the contribution of recovery by sub-threshold events to the reduction of the damage rate is approximately the same as the contribution of the spontaneous recombinations. Using this, eq. (14) can be transformed into

$$-\frac{d\varrho}{d\varphi} \approx P\, \varrho_F v_a^o \,(\, 4c + c_V^Q \,) \,. \qquad (15)$$

With $\varrho_Q = \varrho_V c_V^Q$, where ϱ_V is the resistivity per unit concentration of vacancies, eq. (15) yields

$$-\frac{d\varrho}{d\varphi} \approx 4\, P\, v_a^o \,(\Delta\varrho + \frac{\varrho_F}{4\,\varrho_V}\,\varrho_Q \,) \,. \qquad (16)$$

As illustrated in Fig. 18 (insert), eq. (16) predicts that the decrease of the damage rate will be the same in a quenched sample after a radiation damage, $\Delta\varrho^{(1)}$, as it is in an unquenched sample after a damage of $\Delta\varrho^{(2)}$, when

$$\Delta\varrho^{(2)} = \Delta\varrho^{(1)} + (\,\varrho_F/4\varrho_V\,)\,\varrho_Q \,. \qquad (17)$$

This theoretically predicted horizontal shift of the damage rate curves by quenching is to be compared with the results given in Fig. 18.

The values of ϱ_V given in the literature /21 to 25,4/ differ appreciably. A good average value is $\varrho_V = 2.6 \times 10^{-4}\,\Omega$cm per unit concentration. Using this value and $\varrho_F = 7.5 \times 10^{-4}\,\Omega$cm per unit concentration /13/, the ratio of the measured horizontal shift of the damage rate curve by quenching (Fig. 17) and the theoretical values of $(\varrho_F/4\varrho_V)\,\varrho_Q$ lays between 0.8 and 1.5. Considering the accuracy of our dose measurement, this is a reasonable result.

5.2 Low Damage Concentrations

For low damage concentrations, the difference between the damage rates of quenched and unquenched samples (Fig. 17) is made up of two effects.

The first is the reduction of the damage rate by pre-quenching as observed at large $\Delta\varrho$.

The second is a damage rate enhancement which is strongest at the beginning of irradiation and fades away at higher damage concentrations, thus causing a faster radiation annealing than is found in annealed samples.

This damage rate enhancement has been previously observed in

Matthiessen's rule as discussed below.

During irradiation of a sample of residual resistivity ρ_0 and quenched-in resistivity ρ_Q, the measured resistivity is

$$\rho = \rho_0 + \rho_Q + \Delta\rho \tag{18}$$

Contrary to eq. (4) which is valid when one type of defects is dominant, the resistivity change $\Delta\rho$ by irradiation is now composed of the resistivity

$$\Delta\rho_F = \rho_F c \tag{19}$$

of irradiation produced defects measured in samples without other defects and a term δ describing the deviation from the additivity of resistivities:

$$\Delta\rho = \Delta\rho_F + \delta. \tag{20}$$

The deviation δ is usually approximated by a Kohler expression. Neglecting the contribution of ρ_0 for high purity samples,

$$\delta = \frac{\alpha\Delta\rho_F \cdot \beta\rho_Q}{\alpha\Delta\rho_F + \beta\rho_Q}. \tag{21}$$

For $\Delta\rho_F \ll \rho_Q$, (22)

$$\delta = \alpha\Delta\rho_F.$$

Using this, the initial value of the rate of resistivity increase is given by

$$\left[\frac{d\rho}{d\varphi}\right]_0 = (1+\alpha)\left[\frac{d\Delta\rho_F}{d\varphi}\right]_0. \tag{23}$$

The value of α gives the relative enhancement of the initial resistivity change per unit dose by the deviation from Matthiessen's rule.

By extrapolating the damage rate curves from high $\Delta\rho$, values of $[d\Delta\rho_F/d\varphi]_0$ have been obtained (Fig. 19).

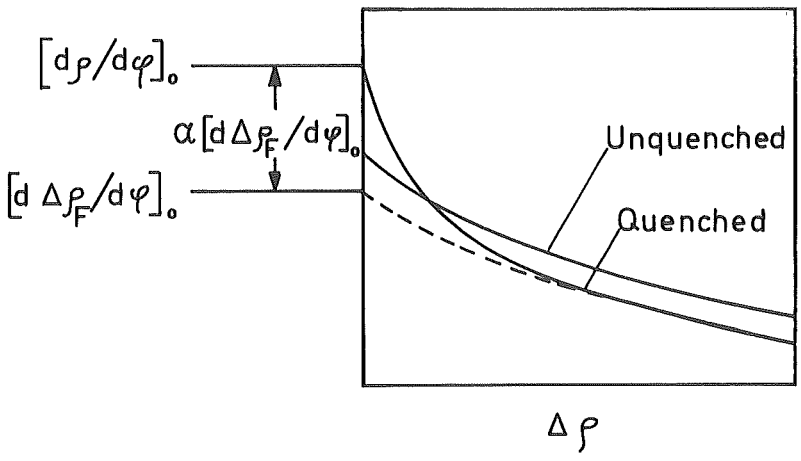

Fig. 19 Evaluation of the relative increment α of the initial damage rate by pre-produced vacancies (schematically). ρ is the measured resistivity, $\Delta\rho_F$ the resistivity of the radiation produced Frenkel defects. The zero index indicates initial values.

From the difference of the extrapolations and the measured values of $[d\rho/d\varphi]_0$ the values of α have been calculated.
Within the accuracy of our dose measurement, α linearly increases with ρ_Q and has values in the range of 6 to 10 %. This result is in good agreement with the vacancy contribution to α which was found by Lengeler /26/ during neutron irradiation of cold-worked copper.

The relative increase of the damage rate (which should be identical with our α) found by Herschbach and Jackson /6,7/ is of the same magnitude, especially when taking into account that in their measurements /6/ the resistivity of one sample with respect to another one is uncertain to 10%.
Swanson's value /8/ of α is twice our value for the same ρ_Q. However, his $\Delta\rho$ is a hundred times smaller than our smallest $\Delta\rho$. Considering our Fig.18 by extension of the measurements to smaller $\Delta\rho$ our values of α might possibly be increased.

6. Summary

Low temperature irradiations have been performed on aluminum, copper and platinum. The defect build-up has been studied in annealed high purity samples and in samples doped by various irradiation and annealing treatments and by quenching.

1. Annealed samples show radiation annealing and irradiations have been made to high enough damage concentrations that saturation values can be estimated. Values of $c_\infty = 0.5$ % in platinum and $c_\infty = 0.3$ % in copper were obtained. In aluminum the decrease of the damage rate is strongly nonlinear and the saturation value cannot be reasonably estimated.
2. The experimental data on radiation annealing can be described by a superposition of recovery by spontaneous recombinations and recovery by sub-threshold events. The spontaneous recombinations can be described by the theoretical results of Dettmann et al. /3/.
3. During sub-threshold irradiation of radiation doped platinum recovery of mainly close pairs takes place.
4. From radiation doping as well as sub-threshold irradiations it has been observed that radiation annealing in platinum is due to approximately equal contributions from spontaneous recombinations and recovery by sub-threshold events.

In platinum, the cross section for recovery by sub-threshold events is σ_r (1.4 MeV)$\approx$ 16000 barns and σ_r (3 MeV)$\approx$14000 barns, the spontaneous recombination volume $v_a^o \approx 50$ atomic volumes. For copper, the corresponding values are $\sigma_r \approx 3900$ barns and v_a^o = 125 atomic values. In aluminum $\sigma_r \approx 7100$ barns.

5. Quenched-in vacancies in platinum reduce the damage rate for all $\Delta\varrho$ due to enhancement of spontaneous recombinations. For small $\Delta\varrho$ only, this decrease in damage rate is masked by an apparent increase in the damage rate which can be explained by deviation from Matthiessen's rule.

Acknowledgments

The authors wish to thank H. Wagner, D. Meißner, and H. Knöll for their helpful cooperation during the experimental set-up and the measurements. The permanent support of the irradiation group and many other members of the institute during the course of the irradiations is very much appreciated as well as helpful discussions with Prof. G. Leibfried who first has proposed the sub-threshold experiments and with Dr. H. Wollenberger. The authors are grateful to Dr. T. Noggle for carefully reading the manuscript.

References

/1/ F. Dworschak, J. Neuhäuser, H. Schuster, J. Wurm, S. Potyka, G.Sokolowski, and H. Wollenberger, Phys. Rev. Letters 16 , 685 (1966)

/2/ G. Burger, H. Meissner, W. Schilling, phys. stat. sol. 4, 281 (1964) phys. stat. sol. 4, 287 (1964)

/3/ K. Dettmann, G. Leibfried, and K. Schroeder, phys. stat. sol. 22 , 423 (1967)

/4/ K. Herschbach, J.J. Jackson, Phys. Rev. 153 , 689 (1967)

/5/ K. Herschbach, J.J. Jackson, Phys. Rev. 153 , 694 (1967)

/6/ J.J. Jackson, K. Herschbach in : Proc. Int. Conf. on Solid State Physics Research with Accelerators, BNL 50083 (1967)

/7/ J.J. Jackson, K. Herschbach, Phys. Rev. 164 , 951 (1967)

/8/ M.L. Swanson, phys. stat. sol. 23 , 649 (1967)

/9/ H. Hemmerich, W. Sassin, to be published

/10/ E.H. Sondheimer, Adv. Phys. 1 , 1 (1952)

/11/ F. Dworschak, H. Schuster, H. Wollenberger , and J. Wurm, phys. stat. sol. 21 , 741 (1967)

/12/ G.W. Iseler, H.I. Dawson, A.S. Mehner, and J.W. Kauffman, Phys. Rev. 146 , 468 (1966)

/13/ E.A. Burke, C.M. Jimenez, L.F. Lowe, Phys. Rev. 141 , 629 (1966)

/14/ A value slightly different from /13/ is given in W. Bauer, W.F. Goeppinger, Phys. Rev. 154 , 584 (1967)

/15/ G. Burger, H. Meissner, W. Schilling (1964) unpublished

/16/ R.L. Chaplin, H.M. Simpson, Phys. Rev. 163 , 587 (1967)

/17/ H. Schuster, Jül. Ber. 541, to be published

/18/ W. Bauer, W.F. Goeppinger, Phys. Rev. 154 , 588 (1967)

/19/ F. Dworschak, Chr. Lehmann, H. Schuster, H. Wollenberger, J. Wurm in : Proc. Int. Conf. on Solid State Physics with Accelerators, BNL 50083 (1967)

/20/ N.F. Mott, Proc. Roy. Soc. A 124 , 426 (1929)
Proc. Roy. Soc. A 135 , 429 (1932)

/21/ B.G. Lazarev, O.N. Ovcharenko, Dokl. Akad. Nauk SSSR 100 , 875 (1955)

/22/ G.L. Bacchella, E. Germagnoli, S. Granata, J. Appl. Phys. 30 , 748 (1959)

/23/ S.D. Gertsriken, N.N. Novikov, Phys. Metals Metallog. (USSR) 9 , 54 (1960)

/24/ G.R. Piercy, Phil. Mag. 5 , 201 (1960)

/25/ J. Polák, phys. stat. sol, 21 , 581 (1967)

/26/ B. Lengeler, private communication

THE STAGE III RECOVERY IN ELECTRON-IRRADIATED ALUMINUM*

W. Bauer

Atomics International
A Division of North American Rockwell Corporation
Canoga Park, California

ABSTRACT

We have studied the irradiation-produced resistivity recovery of 99.9999% pure annealed and prequenched aluminum foils. The prequenched specimen exhibited two distinct recovery peaks, at 245 °K and 320 °K (Stage IV), whereas the unquenched specimen exhibited only one peak at 255 °K (Stage III). The activation energy of the Stage III recovery, analyzed by the Meechan-Brinkman method, was found to be 0.58 eV. The order of reaction kinetics was found to be a function of the recovery. The implications of these results on existing recovery models are discussed.

---

*Based on work sponsored by the Metallurgy Branch, Division of Research, U.S. Atomic Energy Commission, under Contract No. AT(04-3)-701.

INTRODUCTION

Although a relatively large body of experimental results and related analysis of the Stage III recovery of aluminum exists[1-5], a number of problems remain to be solved. Some of these problems are matters of long standing, such as the identity of the migrating defect; others, such as differences in measured activation energies and dependence of activation energies on residual impurities, are of recent origin. In this paper we report the results and analysis of experiments designed to answer some of these questions.

We list here the results of selected previous investigations particularly relevant to this work. Sosin and Rachal[1], using the Meechan-Brinkman[6] method (MB), found the activation energy in Stage III after 80°K electron irradiation to be 0.45 eV. They concluded that their results were consistent with interstitial migration in Stage III. At nearly the same time Federighi and coworkers[2] investigated the Stage III recovery after neutron irradiation. They found an activation energy of 0.61 eV -- a value close to the single vacancy migration energy. Predictably, they concluded that the Stage III recovery was due to the migration of vacancies. Garr and Sosin[3] studied the Stage III recovery of pure and alloyed aluminum after electron irradiation. They made use of both the MB and the second order method for activation energy determinations. They found that the activation energy increased with decreasing purity ranging from 0.46 to 0.63 eV. Since the nature of the recovery depends in a complicated way on residual impurity content, they reasoned that several recovery processes contribute to the stage. Specifically they suggested that interstitial migration, restricted by impurities, takes place in the lower temperature portion and vacancy migration in the higher temperature portion of Stage III. At this time it became apparent that more than just activation energy determinations was necessary to determine the nature of the

recovery processes. Accordingly, Budin and Lucasson[4] investigated the recovery of electron irradiated specimens which were either annealed or quenched prior to irradiation. They found that the Stage III peak was approximately 70°K lower than the Stage IV peak, where the resistivity due to the prequench recovers. Also the Stage III peak of prequenched specimens was shifted to lower temperature and the Stage IV peak to higher temperature upon irradiation (for high temperature quench). They measured the Stage III activation energy to be 0.58 eV and found that the activation energy of the Stage IV peak could be raised by irradiation. They suggested that interstitial migration in Stage III could best account for their results. However, one of the problems that arise from this work was the need to reconcile the activation energy values with the work of Sosin and Rachal. This problem will be discussed later in this paper. Finally we turn to the results of Lwin et al.[5], who also studied the Stage III recovery after electron irradiation. They investigated the activation energy using the slope change and Primak methods, finding a value of 0.62 eV. Using conventional methods they ascertained that the major portion of the recovery obeyed second order. Based mainly on the agreement in activation energy with the single vacancy migration energy, deduced from quenching, they concluded that the Stage III recovery was due to vacancy migration. From their data they found the number of jumps of the migrating defect to be of the order of 10^3 -- a value some two orders of magnitude smaller than what one would expect from a simple model. Lwin et al. hypothesized that the small number of jumps is due to a large capture volume associated with the sinks (presumably interstitial clusters). They also found that the width of the Stage III peak is approximately 30% wider than predicted on the basis of simple second order. They attributed this widening to a natural spread in activation energy.

RESULTS AND DISCUSSION

A. Irradiation-Prequench

In this section we report on experiments designed to evaluate the effect of prequenching on the resistivity recovery after 1 MeV electron irradiation near 10°K. In these experiments one of a pair of specimens is quenched prior to the irradiation, then both specimens are irradiated and annealed together. The quenching procedure consists of heating the sample holder to 0°C, while the sample is resistively heated to an average temperature of 460°C, then the current is shut off, and the sample holder cooled to 4.2°K. While this procedure has the advantage of in situ quenching, irradiation and annealing, it suffers from the fact that quenching temperature is poorly defined due to the relatively short sample and resultant temperature gradient. The relevant experimental resistivity values are summarized in Table I. Here ρ_o is the residual resistivity, $\Delta\rho_R^{4.2°K}$ and $\Delta\rho_R^{200°K}$ the irradiation induced resistivity increase near 10°K and after anneal at 200°K respectively, and $\Delta\rho_q$ the quenched-in resistivity increase.

TABLE I

SUMMARY OF EXPERIMENTAL RESULTS

	Sample A				Sample B			
Run	ρ_o	$\Delta\rho_R^{4.2°K}$	$\Delta\rho_R^{200°K}$	$\Delta\rho_q$	ρ_o	$\Delta\rho_R^{4.2°K}$	$\Delta\rho_R^{200°K}$	$\Delta\rho_q$
	x 10^{-9} ohm-cm				x 10^{-9} ohm-cm			
V	3.56	3.06	0.36	0.77	2.59	4.61	0.53	-
VI	3.55	3.25	0.44	-	2.6	5.5	0.59	0.53

The slope of the isochronal recovery in the Stage III and IV region are shown in Figs. 1 and 2. We note that the unquenched specimen exhibits one

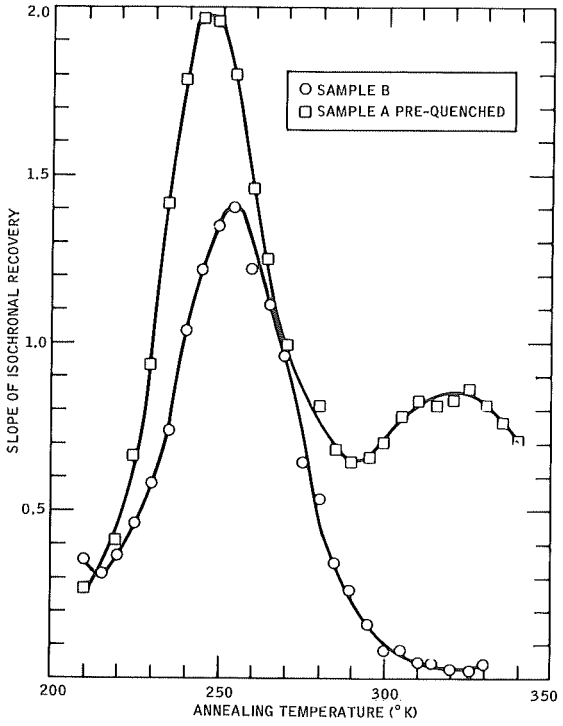

FIGURE 1

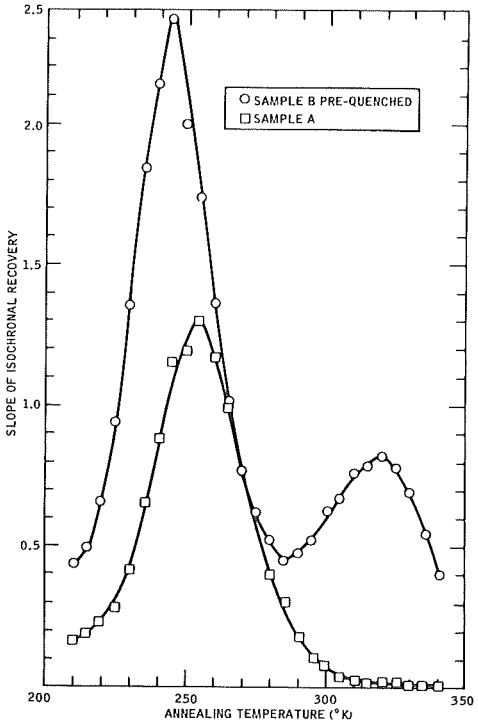

FIGURE 2

FIGURE 1 and 2. Slope of the isochronal recovery as a function of annealing temperature. Either Sample A (Fig. 1) or Sample B (Fig. 2) were prequenched and both samples were irradiated simultaneously.

peak near 255 °K (Stage III) and the prequenched specimen two peaks, at 245 °K and 320 °K (Stage IV). Several observations may be made:

1. The Stage III recovery is enhanced and shifted about 10 °K to lower temperatures when an excess vacancy concentration exists in the lattice.

2. The separation of the centers of Stage III and IV in the prequenched and irradiated sample is about 75 °K, but the stages definitely overlap.

3. These results are qualitatively in good agreement with the work of Budin and Lucasson[4] who irradiated near 100°K. This similarity is significant insofar that in the present work Stage I interstitials were not mobile during irradiation, whereas interstitials are highly mobile in the case of Budin and Lucasson. Thus, the role of interstitial clusters as potential sinks for vacancies is inhibited in their work as compared with this work -- yet the results are very similar.

The results presented thus far can be explained quite simply by interstitial migration in Stage III and vacancy migration in Stage IV. For the purpose of this discussion the origin of the Stage III interstitial may be left unspecified, requiring only the presence of impurities during the migration of the Stage I interstitial. Within this model cognizance has to be taken that vacancies are mobile in the latter half of Stage III (item 2). This provides a natural explanation of the large width noted by Lwin et al.[5]. If the Stage III recovery is to be attributed solely to the migration of vacancies as suggested by Lwin et al., the difference in temperature between Stages III and IV must be due to the different nature of sinks. That is, after quenching the vacancies probably annihilate at grain boundaries or dislocations, whereas after electron irradiation perhaps irradiation produced clusters play a more important role. In light of item 3 above one would have to postulate that the interstitial clusters nucleate at impurities.

B. Activation Energy

We now turn to activation energy measurements. At this point it is perhaps instructive to briefly consider the applicability of the various

activation energy measurement schemes to the Stage III recovery in aluminum in light of the above models. We shall discuss here only the MB, slope-change, Primak and second-order analysis. The first three methods, for a price, can in principle be used to detect non-unique activation energies in a recovery stage, as is to be, perhaps, expected from one of the above models. The last method is of limited utility for a complicated recovery stage as shall be demonstrated later in this paper. The MB method demands that isochronal and isothermal recovery spectra be obtained from samples with the same defect configurations. Normally successive irradiation on the same sample whose recovery is complete are employed. A measure of how successful this approach is in Stage III in aluminum may be noted by the degree of reproducibility of the activation energy in these experiments. The major limitation of the slope change method is experimental. This may be overcome by a large number of experiments. The Primak analysis requires independent knowledge of the frequency factor.

Table II contains a summary of the activation energy determinations of this work using the MB and second order methods, and the temperature range over which the data could be fitted by a straight line. Figures 3 and 4 show the data analyzed by the MB method for the cases which resulted in the highest and lowest values of the activation energy. The reader is referred to Ref. 6 for an explanation of the symbols. An example of the second order method is shown in Fig. 5. It is interesting to note from Table II that a much larger temperature range could be fitted with a straight line with this method. Unfortunately this is deceptive since it merely reflects the insensitivity of the activation energy to the order of kinetics, as will be discussed. It should be noted that Lwin et al. also noted the insensitivity of the Primak analysis to the order of kinetics.

TABLE II

ACTIVATION ENERGY DETERMINATIONS

Experiment Number	Activation Energy	Method	Run(s)	Temperature Range
1	0.65	MB	VI & VII	250 - 280
2	0.67	MB	VI & IX	235 - 275
2	0.45	2nd Ord	VI	220 - 275
4	0.45	2nd Ord	X - A	230 - 285
5	0.495	2nd Ord	X - B	230 - 270
6	0.52	MB	X & XI-A	235 - 270
7	0.54	MB	X & XI-B	235 - 265
8	0.49	2nd Ord	XII - A	240 - 300
9	0.55	2nd Ord	XII - B	240 - 300
10	0.54	MB	XII & XIII-A	240 - 285
11	0.60	MB	XII & XIII-B	240 - 285
12	0.48	2nd Ord	XIV	235 - 290
13	0.46	2nd Ord	XIV - B	235 - 290
14	0.52	MB	XIII - XIV-A	235 - 280

Experiments 1 - 7 First Set of Samples

Experiments 8 - 14 Second Set of Samples

TABLE III

ACTIVATION ENERGY DETERMINATIONS

Figure Reference	Authors and Text Reference	Defect Source
1	Lwin et al.[5]	Electron Irradiation
2a	Budin & Lucasson[4]	Electron Irradiation
2b	Budin & Lucasson[4]	Electron Irradiation
2c	Budin & Lucasson[4]	Quench from 300 °C
3a	Garr & Sosin[3]	Electron Irradiation
3b	Garr & Sosin[3]	Electron Irradiation
4	Sosin & Rachal[1]	Electron Irradiation
5	Federighi et al.[2]	Neutron Irradiation
6a	DeSorbo & Turnbull[7]	Quench from 284 °C
6b	DeSorbo & Turnbull[7]	Quench from 284 - 300 °C
7	Doyama & Koehler[8]	Quench from 301 °C

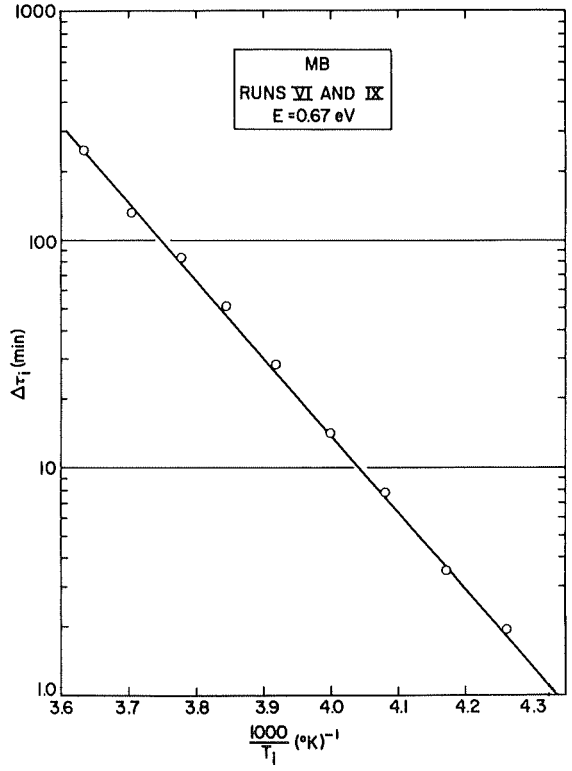

FIGURE 3

FIGURE 3 and 4. Activation energy analysis applied to two sets of runs, chosen to represent the highest and lowest values of the activation energy. The Meechan-Brinkman method and its symbols are explained in Ref. 6.

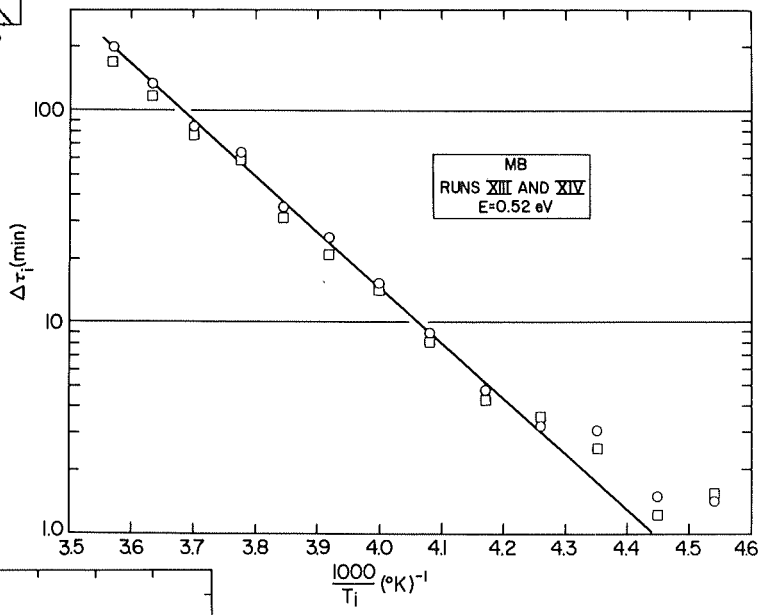

FIGURE 4

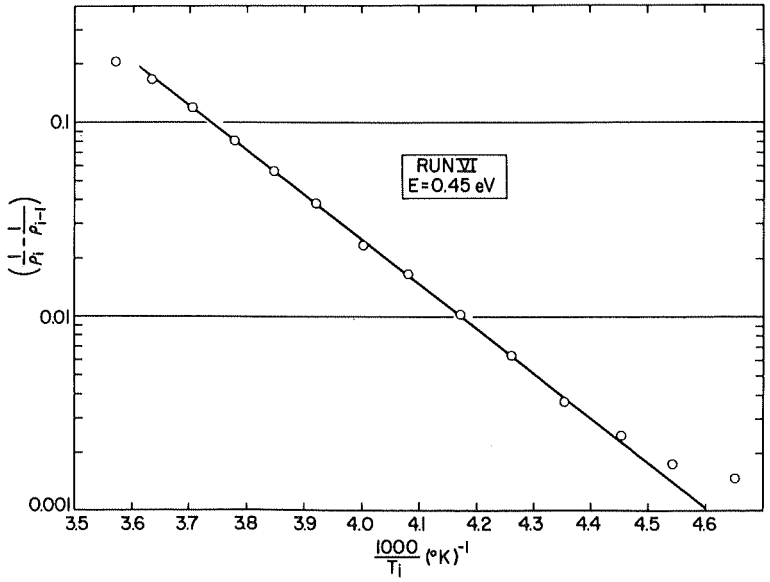

FIGURE 5

FIGURE 5. Activation energy determination by use of the second order method.

The results of Tables II and III are plotted in Fig. 6. In the left hand portion of the figure are the results of the present experiments and the average values of the activation energies as derived by the MB and second order methods. The MB values are to be preferred for reasons which will be discussed in the next section. The spread in the MB values is larger than can be accounted for by experimental error, but the average value of the activation energy is in good agreement with other authors. It is felt that the spread in activation energy values reflects the possible complexity of the Stage III recovery. This was further evidenced by indications of non-unique energy determinations in some of the data.

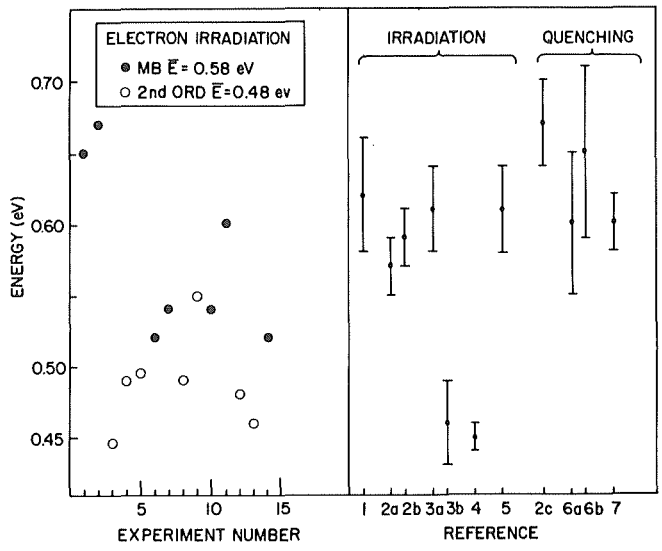

FIGURE 6. Summary of activation energy determinations in this work and from other authors. See Table II for references.

FIGURE 6

Also shown in Fig. 6 are the activation energy measurements in Stages III and IV of other authors. In general there seems to be good agreement among the measurements after irradiation with the exception of Ref. 3b and 4. The discrepancy in the former case will be explained below in connection with

the second order process. The low value of Sosin and Rachal reflects the fact that the activation energy is sensitive to the state of the sample due to the complexity of the recovery process. In fact a close examination of their Fig. 7 reveals evidence for a non-unique energy.

The average activation energy after irradiation (except Refs. 3b and 4) is 0.03 eV less than that of the quench measurements. In light of the uncertainties involved, this difference is clearly not decisive in choosing between the above mentioned models. In connection with this it is important to point out that Budin and Lucasson[4] found that the activation energy in Stage IV was increased slightly by irradiation. They attributed this to a "quench-purefication". That is, the admixture of single and divacancies after the quench was altered toward more single vacancies by the migrating interstitials -- providing further evidence for single vacancy migration in Stage IV.

We now turn to a discussion of the second order method. It can be shown from the kinetic equations that the activation energy can be derived from a plot such as shown in Fig. 5 only if ρ_i refers to that portion of the unrecovered resistivity which is uniquely characterized by that activation energy. Within the model that supposes that vacancies become mobile only near the end of Stage III, the asymptote of the stage or pre-irradiation value of the resistivity is an inappropriate guide to ρ_i. In fact the appropriate value of the asymptote must be at some lower undefined temperature. This procedure has been carried out for Run VI with the result that the apparent activation energy increased from 0.45 to 0.54 eV when the asymptote was moved from the pre-irradiation value to 270°K. The validity of the second order method also depends to what extent the Stage III recovery obeys second order.

C. Order of Kinetics

The data have also been analyzed to determine the order of kinetics. For example the data of Fig. 6 serve as a test of second order. In the data shown in Fig. 7 we have analyzed one of the isothermal runs for the order of kinetics using the MB method[6]. We have also used the $\frac{1}{\rho_i}$ plot with essentially the same result -- second order. This is in agreement with other investigators.

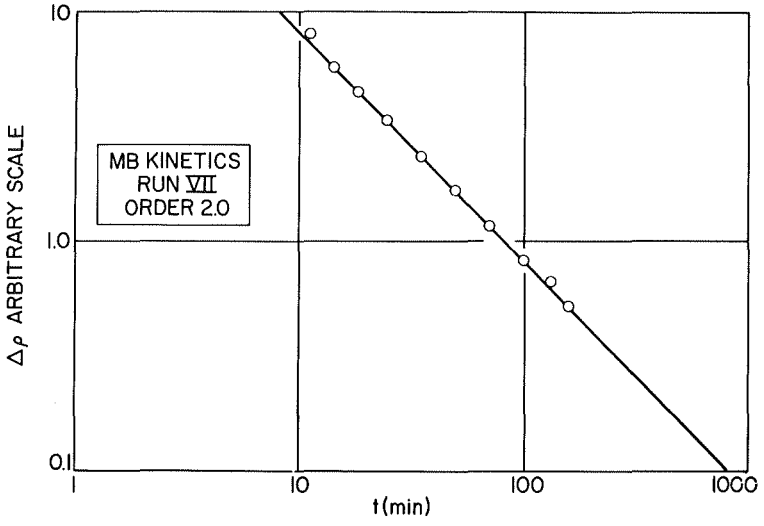

FIGURE 7. The data of an isothermal run analyzed for annealing kinetics by the Meechan-Brinkman method. See Ref. 6 for an explanation of the method and symbols.

FIGURE 7

Nihoul and Stals[9] have pointed out that the above used methods for the determination of the order of kinetics are quite insensitive to changing order and only give some average value of the order. Accordingly we have analyzed the isochronal data of Run VI by the method of Fujita and Damask[10] based on the equation

$$\ell n \left[- \frac{d\Delta\rho}{dT} \exp (E/kT) \right] = \gamma \ell n \Delta\rho + \ell n (K/\mu) . \quad . . . (1)$$

Here γ is the order, $\Delta\rho$ the remaining resistivity, K the frequency factor, and μ the heating rate. Our isochronal annealing schedule can be satisfactorily

approximated by a linear heat up rate as is required by Eq. (1). The result of applying Eq. (1) to the data of Run VI is shown in Fig. 8. The numbers above the arrows indicate the effective order, γ, at that point of the recovery. Clearly the order is above two at the start of the recovery and then decreases to below two as the recovery proceeds. Nihoul and Stals point out that reaction orders larger than two can not be explained within the framework of chemical bimolecular reactions. They show that diffusion limited bimolecular reactions[11] can give rise to orders larger than two. In fact one of their theoretical examples (their Fig. 7) exhibits an order dependence as a function of recovery qualitatively similar to the results shown in Fig. 8. Their theoretical example was for initial concentrations of reactants which differ by 10% and for a relative volume occupied by the capture spheres of 0.1 (see the Waite[11] theory).

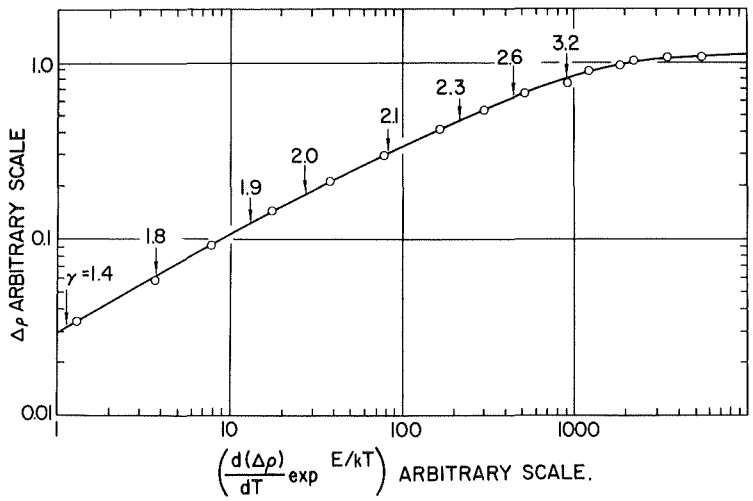

FIGURE 8. The isochronal data of Run VI analyzed for kinetics by the use of Eq. (1). (See Ref. 9 and 10).

FIGURE 8

It seems clear once again (See Stage I in copper[12]) that a diffusion limited bimolecular reaction will serve as an adequate description of a

recovery stage. Considerable work remains to be done, however, before the various parameters within the Waite[11] theory can be evaluated with confidence. This type of analysis may serve as a useful tool in distinguishing between the different recovery models.

SUMMARY

In this paper we have presented new results and reviewed other data which bear on two recovery models for the near room temperature recovery in aluminum. The first model considered (Model i) allows interstitial migration, restricted by impurities, in the lower temperature portion of Stage III and the beginning of vacancy migration in the higher temperature portion of Stage III. The second model (Model v) attributes the Stage III recovery solely to the migration of single vacancies.

The recovery results of the irradiated and prequenched samples presented here are in good qualitative agreement with Model i; whereas, considerably different sink configurations with interstitial clusters nucleating at impurities have to be invoked for Model v. The activation energy measurements in Stages III and IV indicate similar results (necessary for Model v) but there is enough spread not to rule out a small difference. The order of kinetics are shown to be a function of recovery, the dependence being similar to what is expected from a diffusion limited bimolecular reaction. In the case considered the initial concentration of reactants differs by only 10% - further evidence for Model i. More detailed investigations of the reaction kinetics promise to be fruitful, especially in resolving the problem of the temperature difference of Stages III and IV.

REFERENCES

1. A. Sosin and L. H. Rachal, Phys. Rev. 130, 2238 (1963).
2. See for example, T. Federighi, S. Ceresara, and F. Pieragostini, Phil. Mag. 12, 1093 (1965).
3. K. R. Garr and A. Sosin, Phys. Rev. 162, 681 (1967).
4. C. Budin and P. Lucasson in Interaction of Radiation with Solids (Plenum Press, 1967) p 497.
5. Y. N. Lwin, M. Doyama and J. S. Koehler, Phys. Rev. 165, 787 (1968).
6. C. J. Meechan and J. A. Brinkman, Phys. Rev. 103, 1193 (1956).
7. W. DeSorbo and D. Turnbull, Phys. Rev. 115, 560 (1959).
8. M. Doyama and J. S. Koehler, Phys. Rev. 134, A522 (1964).
9. J. Nihoul and L. Stals, Phys. Stat. Sol. 17, 295 (1966).
10. F. E. Fujita and A. C. Damask, Acta Met. 12, 331 (1964).
11. T. R. Waite, Phys. Rev. 107, 463 (1957).
12. J. W. Corbett, R. B. Smith, and R. M. Walker, Phys. Rev. 114, 1460 (1959).

Interaction of point defects with magnesium impurity atoms in neutron-irradiated aluminium

C. DIMITROV-FROIS and O. DIMITROV

Centre d'Etudes de Chimie Métallurgique
15, Rue Georges Urbain, 94-VITRY. France

Abstract

The recovery of electrical resistivity of a series of aluminium-magnesium alloys ($\lesssim 0{,}3.10^{-6}$ to 3200.10^{-6} atomic) has been studied after neutron irradiation at 78°K to doses of a few 10^{17} n/cm^2. The presence of magnesium produces a considerable increase of stage II recovery, up to a constant value which is reached for concentrations higher than 1000.10^{-6}. Stage III increases slowly without reaching a constant value, even for the highest concentration. A small stage III′ appears just above stage III. The results are interpreted in terms of a model of interstitial-trapping by impurities, at 78°K, and detrapping in stage II. On the basis of this model, the following values can be deduced from our experiments :

$E^B_{I\,Mg} = 0{,}29 \pm 0{,}03$ eV

$\rho_{I\,Mg} + \rho_V = 2{,}12$ μΩcm/%

$E^B_{V\,Mg} = 0{,}15 \pm 0{,}09$ eV

I. Introduction

Neutron irradiation at 78°K of an aluminium sample, containing a foreign element, produces an increase of resistivity larger than in the pure metal (1,2). This extra-resistivity is eliminated, according to the nature of the foreign element, mainly in stage II (additions of Mg, Ag, ...) or in stage III (additions of Cu, ...). We have interpreted these results by assuming that interstitial defects, mobile at 78°K, are trapped by impurity atoms during the irradiation, and that the strength of the interaction, supposed to be elastic, depends on the ratio of the effective radius of the foreign element, to that of aluminium (2,3) (The effective radius is calculated from the experimental variation of the lattice parameter of the solid solution, as a function of solute concentration). Foreign atoms whose effective radius is larger than that of aluminium (for instance magnesium), or a little smaller, introduce in the lattice compressive strains or small expansive strains and thus interact weakly with interstitials. The latter are trapped during irradiation, then released at annealing temperatures in the range of stage II. By contrast, foreign atoms whose effective radius is much smaller than that of aluminium introduce expansive strains in the lattice, and trap strongly interstitials, which are no more released at low temperatures.

We have tried to obtain a more precise description by studying the influence of the concentration of one foreign element, namely magnesium, on the recovery behaviour of aluminium after neutron irradiation at 78°K.

II. Experimental procedure

2.1. Samples and irradiation conditions

Two series of dilute aluminium-magnesium alloys, and reference samples of high-purity aluminium, were irradiated at 78°K in the neutron flux of a nuclear reactor, at slightly different doses. The atomic concentration of magnesium and the integrated doses are given in table I.

Table I

Irradiation	Dose n/cm^2 (E > 1 MeV)	Magnesium atomic concentration $x10^6$
M_3	$4.9x10^{17}$	$\leq$ 0.3 - 25 - 65 - 200 - 390
S_3	$3.6x10^{17}$	$\leq$ 0.3 - 390 - 1000 - 1100 - 3200

The aluminium used for the preparation of the alloys and for the reference samples is a metal purified by double-electrolysis and zone-refining. Its total impurity content is smaller than 5.10^{-6} and its magnesium content is smaller than $0.3.10^{-6}$. The techniques for preparing the alloys have been described previously (4). The concentrations of the alloys were determined by complexometry (5) or by atomic absorption spectrometry, except for the alloy containing 25.10^{-6} magnesium, whose concentration was deduced from its low temperature resistivity by reference to the curve of figure 1.

The samples to be irradiated are polycristalline wires, 0.6 mm in diameter, wound on an isolating holder made of oxidized aluminium. Before irradiation, they are annealed at 490°C in a salt-bath, in an argon filled sealed tube. The duration of the annealing is 5 minutes, except for the 3200.10^{-6} alloy which was annealed 30 minutes.

2.2. Electrical resistivity measurements

The introduction and elimination of defects in the samples was followed by measuring the variation of the resistance at 20.3°K, R, relative to a standard, maintained at the same temperature, in liquid hydrogen. The measurements are made with a Diesselhorst type potentiometer, with a sensitivity of 0.01 μV. When the sample

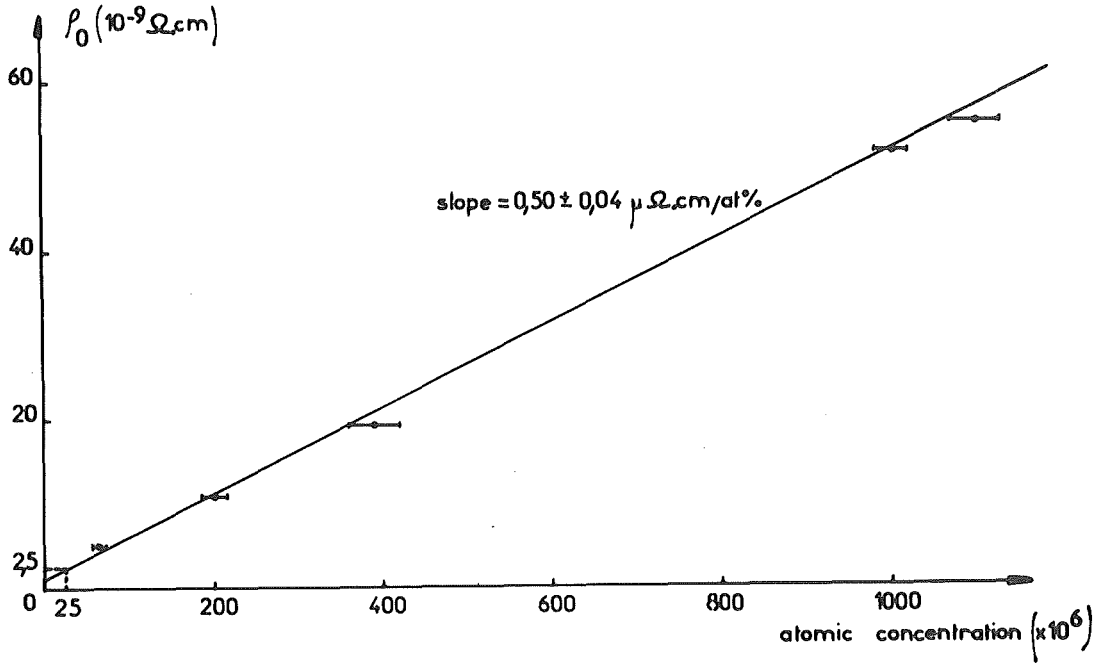

Fig. 1. Influence of magnesium on the electrical resistivity of aluminium at 20.3°K

is completely annealed, one determines the ratio of resistivities at 20.3°K and 294°K (ρ20.3/ ρ294)o and the resistance at 20.3°K, R_o. After an anneal of duration t at temperature T, the resistivity at 20.3°K, $\rho_{T,t}$, is calculated by the relationship :

$$\rho_{T,t} = \frac{R_{T,t}}{R_o} \cdot \left(\frac{\rho_{20.3}}{\rho_{294}^{i}}\right)_o \cdot \rho_{294}^{i}$$

by inserting ρ_{294}^{i} = 2,664 μΩcm (ideal resistivity of aluminium at 294°K (6)) and

$$(\rho_{20.3}/\rho_{294}^{i})_o \simeq \frac{(\rho_{20.3}/\rho_{294})_o}{1 - (\rho_{20.3}/\rho_{294})_o}$$

III. Experimental results

3.L. Influence of concentration on the radiation-induced resistivity increase

For a given dose, the resistivity increment $\Delta\rho$, measured after irradiation, first increases rapidly with the magnesium concentration c, then increases more slowly, for concentrations larger than 400.10^{-6} (fig. 2).

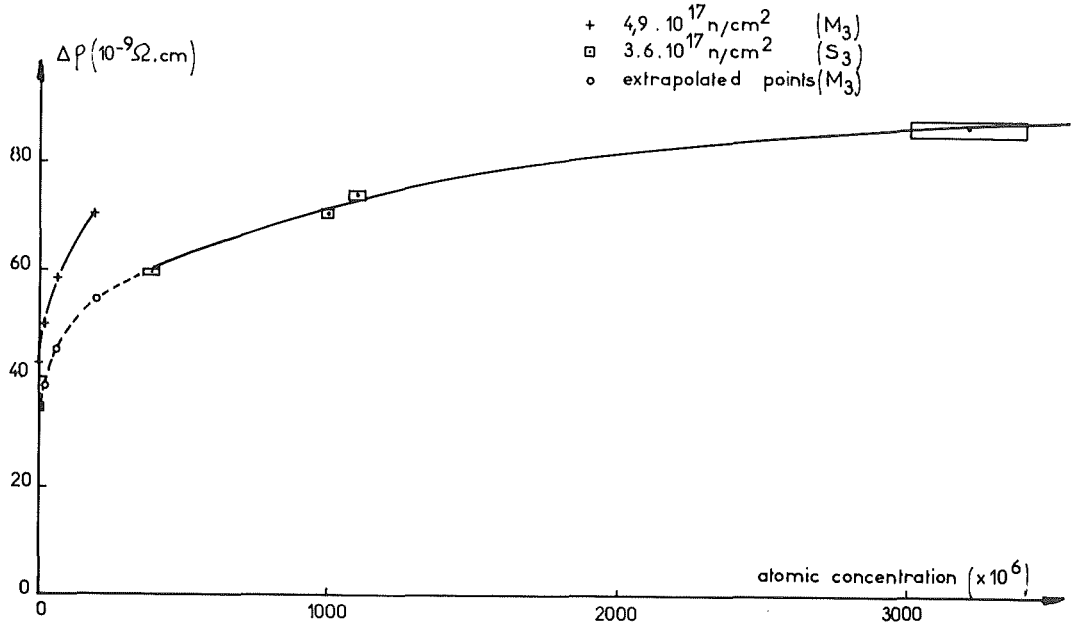

Fig. 2. Variation of the total resistivity created by irradiation as a function of magnesium concentration.

The dashed portion of the curve was established by extrapolating the results for the dilute alloys, which were irradiated at a higher dose. The extrapolation was made by assuming that, for slightly different doses, the curves $\Delta\rho = f(C)$ can be deduced from each other by an orthogonal affinity with respect to the axis of abscissae. The modulus of the affinity was taken equal to the ratio of the excess resistivity measured in the reference samples of high purity aluminium, irradiated at the doses of $4.9.10^{17}$ and $3.6.10^{17}$ n/cm^2.

3.2. Isochronal recovery curves

The recovery of the alloys and of the pure metal was studied by cumulative isochronal anneals of 30 minutes, at intervals of 7.5°K. The following conclusions can be drawn from the recovery curves (fig. 3).

3.2.1. Stage II

This stage, very small in the pure metal, rises strongly for a concentration as low as 25.10^{-6}. It is subdivided in 3 sub-stages, which we have called IIb1, IIb2 and IIb3. By starting from low temperatures, one first observes sub-stage IIb1, which is hardly separated from sub-stage IIb2. The latter is represented in the dilute alloys by a sharp peak, whose position (123°K) changes little with magnesium concentration. A slight shift (4 °K) to lower temperatures is observed for higher concentrations. Sub-stage IIb3 spreads

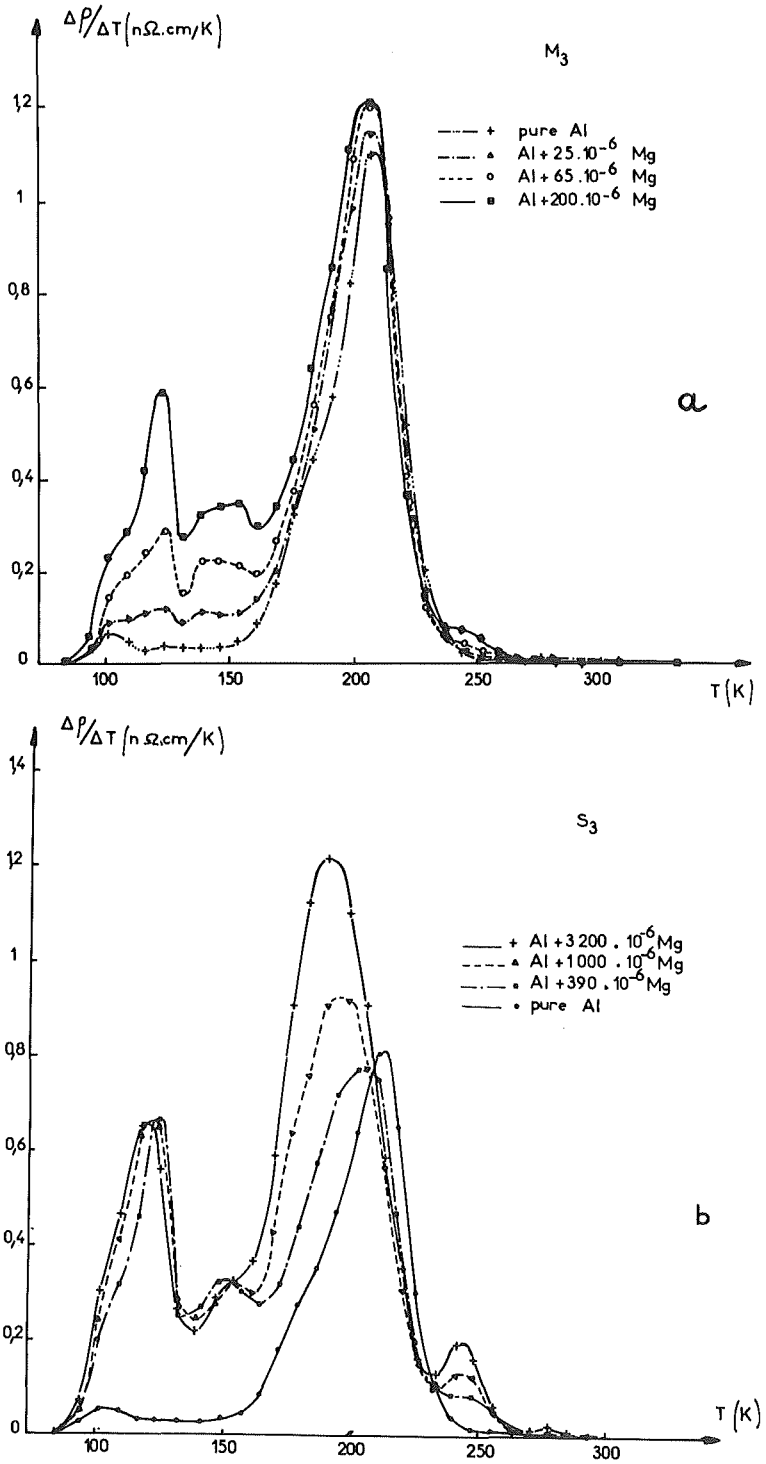

Fig. 3. Differential isochronal recovery curves (7.5°K - 30 min)
a) pure aluminium and alloys of concentration 25.10^{-6} to 200.10^{-6} ($4.9.10^{17}$ n/cm^2)
b) pure aluminium and alloys of concentration 390.10^{-6} to 3200.10^{-6} ($3.6.10^{17}$ n/cm^2)

from 130°K to 165°K and tends to be absorbed, in the most concentrated alloy, by stage III, which increases on its low-temperature side. Figure 4 shows that the resistivity which disappears in substages IIb1 + IIb2 and substage IIb3 increases linearly with magnesium concentration, when this is smaller than 65.10^{-6}, then tends to reach a constant value, above 1000.10^{-6} for sub-stages IIb1 + IIb2, and above 200.10^{-6} for sub-stage IIb3.

3.2.2. Stage III

For small additions of magnesium, the resistivity eliminated in stage III seems to increase rapidly, then to remain nearly constant in the range of concentrations where stage II is increasing (25.10^{-6} - 400.10^{-6}*). (fig. 4a). For larger concentrations, there is a regular increase of stage III, whereas stage II remains constant, with a slowing-down for the highest concentration (fig. 4b)

3.2.3. Stage III'

Between 230°K and 300°K, the development of a new stage is observed. This stage, which we have called III' increases progressively with magnesium concentration (fig. 4).

3.3. Kinetics and activation energies

This study was done with samples of a concentration of 1000.10^{-6}, irradiated to a dose of $5.5.10^{17}$ n/cm^2.

3.3.1. Activation energies

We have evaluated the activation energy for the annealing of the defects, by the simultaneous use of the slope-change method, and by the comparison of an isochronal and an isothermal curve (method of Meechan and Brinkman). It was assumed that the concentration C of a given defect varies as a function of time t, at temperature T, according to a law of the form $dc/dt = -F(C)K_o \exp(-\frac{E}{KT})$,

---

* At the present time, we cannot attribute with certainty this plateau on the curve to a concentration effect. The deviations of the experimental points, from a continuous increase, are largely greater than the differences observed between neighbour samples of the same concentration irradiated simultaneously. However, the variations in the dose received by samples situated in different positions in the irradiation container could give deviations of this order of magnitude, although somewhat smaller.

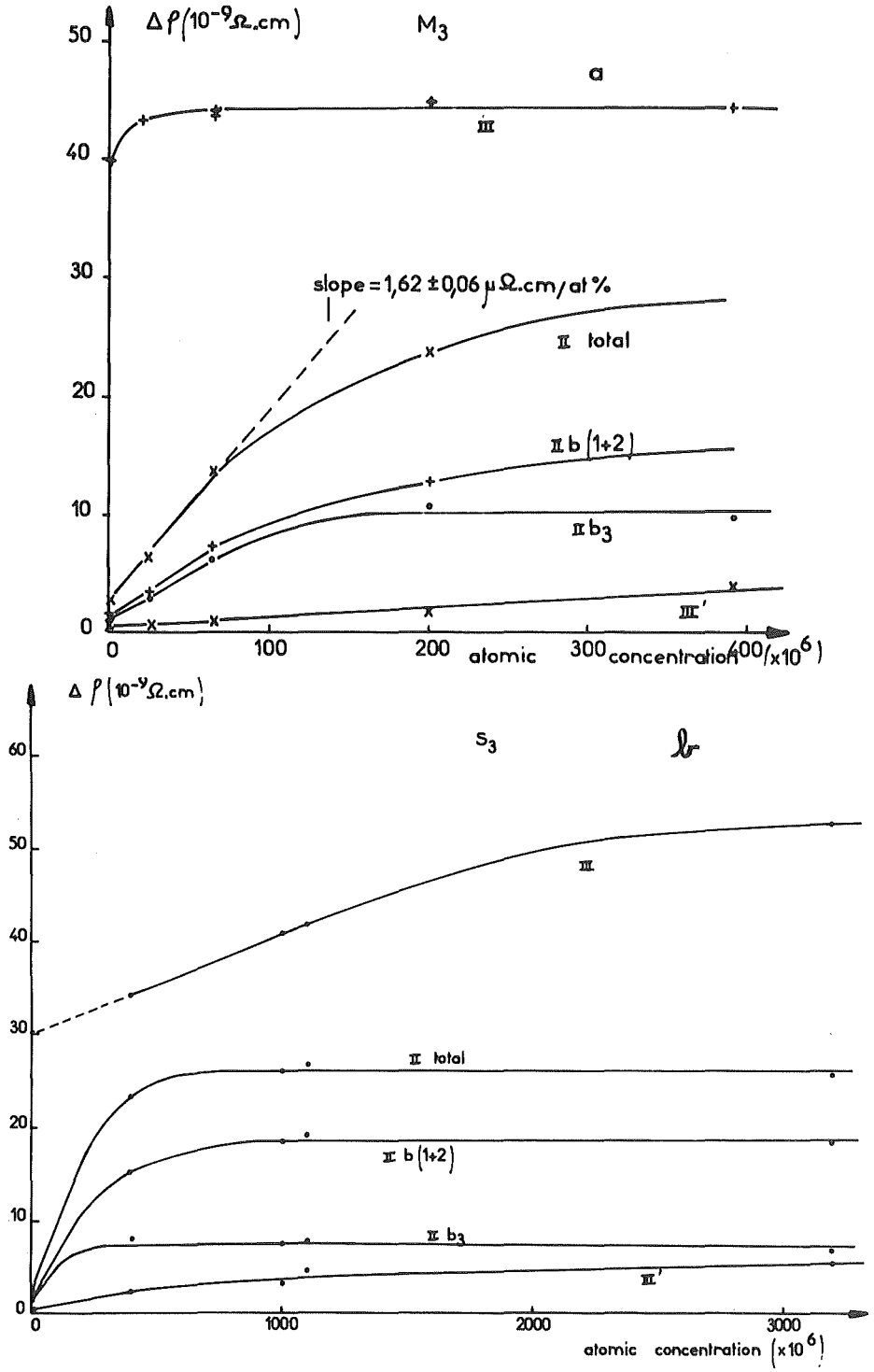

Fig. 4. Variation with concentration of the resistivity eliminated in the different stages of recovery.
a) alloys irradiated to a dose of 4.9×10^{17} n/cm^2
b) alloys irradiated to a dose of 3.6×10^{17} n/cm^2

where E is the activation energy of the thermally activated process.

The experimental values of the activation energy determined by the two methods are given on the differential isochronal curve of fig. 5.

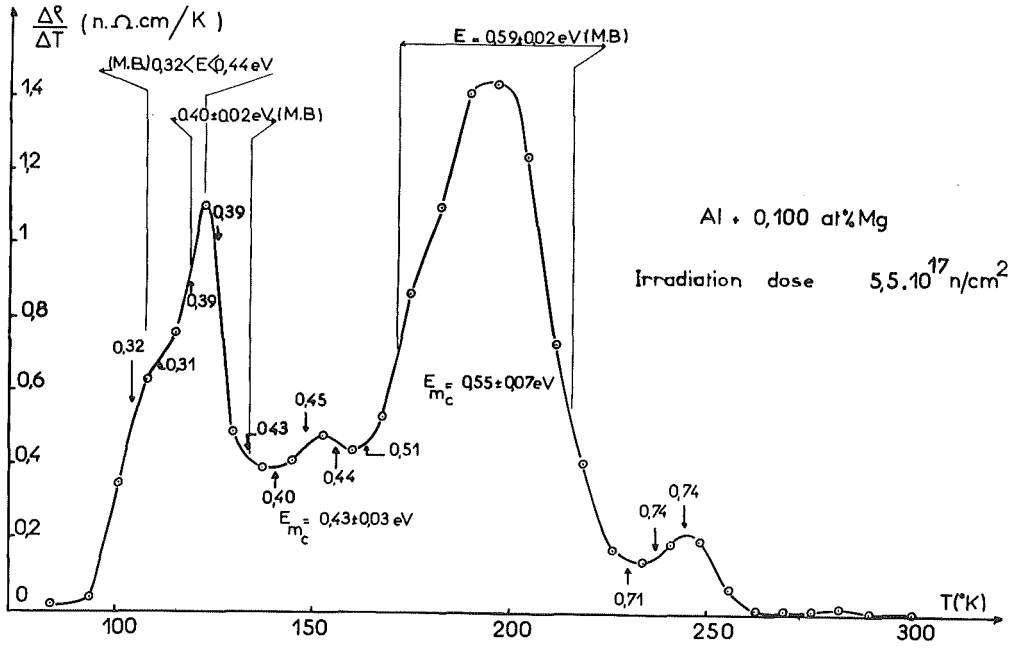

Fig. 5. Activation energy values determined in an alloy with 1000.10^{-6} magnesium - by the method of Meechan and Brinkman (M.B.)
- by the slope-change method (the values are given at the corresponding point of the curve and Emc is the mean value for a stage).

Stage IIb2 is characterized by a constant activation energy of 0.40 ± 0.02 eV. A mean value of 0.43 ± 0.03 eV corresponds to stage IIb3. Fig. 6 shows that an important fraction of stage III anneals out with a constant activation energy of 0.59 ± 0.02 eV.

Within experimental error, the presence of magnesium atoms does not seem to change the value corresponding to the pure metal : 0.58 ± 0.03 eV (slope-change method) and 0.59 ± 0.02 eV (method of Meechan and Brinkman). Finally, a mean value of 0.74 ± 0.07 eV can be associated with stage III'.

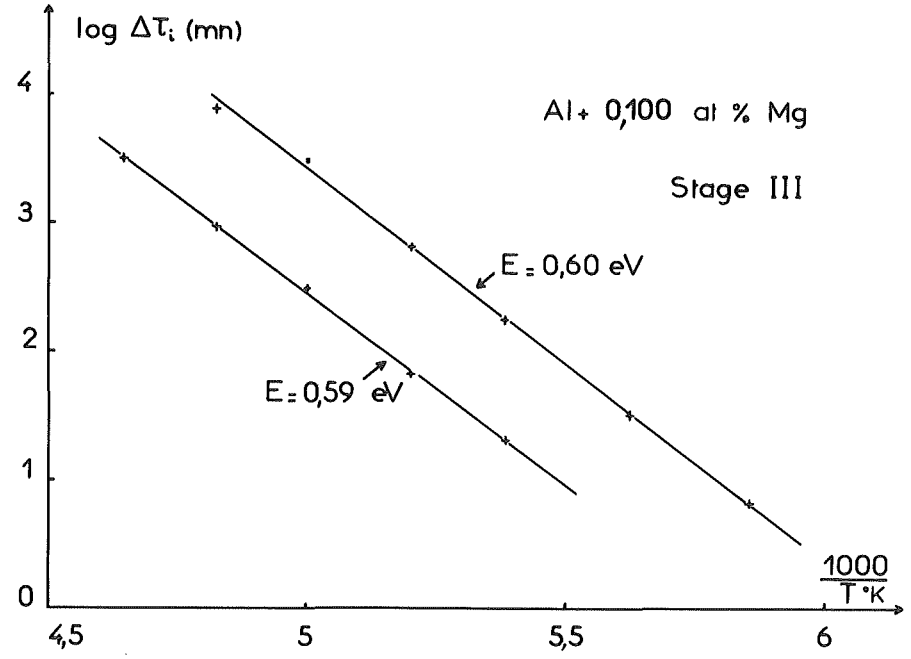

Fig. 6. Determination of the activation energy for stage III in an alloy containing 1000.10^{-6} magnesium (method of Meechan and Brinkman).

3.3.2. Recovery kinetics

We have tried the possibility of representing the kinetics of elimination of the defects during the different stages, by a law analogous to that which governs a chemical reaction of order γ. The curves show that no such law is obeyed for each of the sub-stages of stage II. For stage III, the results are similar to those obtained in pure aluminium, i.e. the recovery partially obeys second order kinetics (for the last 43 % of the stage). The amount of resistivity annealing out with second order kinetics is not substantially larger in the alloy than in the pure metal. It is thus difficult to explain by an amplitude dependence the shifting of this stage to lower temperatures, when the magnesium concentration is increased. It might be that the larger number of foreign atoms results in the appearance of a new sub-stage, which becomes superimposed on the low-temperature side of stage III (fig. 3b). Finally, the last 60 % of stage III' can be represented by a law of order 1.3.

3.3.3. Number of jumps

We have evaluated the number of jumps n corresponding to a 50 % elimination of the defects during stages IIb2, III and III', by using the relation

$$n = Z.\ \nu_o\ .\ \exp\ \frac{S^M}{k}\ .\ \exp - \frac{E^M}{kT}\ \cdot\ t_{1/2}$$

where $t_{1/2}$ is the time required to recover one half of the extra-resistivity corresponding to a given stage during an isothermal anneal at temperature T. The term $Z.\nu_o.\exp\frac{S^M}{k}$ (ν_o : frequency of the atomic vibrations of the lattice, Z : number of saddle-points around

the position of the defect, and S^M : migration entropy of the defect) has been taken equal to $10^{14}\ s^{-1}$. The results are given in table II.

Table II

Stage	II b 2		III b	III'
Activation energy (eV)	0.40 ± 0.02		0.59 ± 0.02	0.74 ± 0.07
Temperature of anneal (°K)	113	123	187.5	245
$\log_{10} t_{1/2}$ (s)	4,78	3,32	4.68	2.44
$\log_{10}$ n	0.97 ± 0.9	0.95 ± 0.8	2.85 ± 0.5	1.25 ± 1.4

N.B. III b is the fraction of stage III which follows second order kinetics.

IV. Discussion of results

The variation, with magnesium concentration, of the total excess of resistivity, in samples irradiated at 78°K, indicates (fig. 2) that, up to a concentration of 3200.10^{-6}, the number of defects obtained after irradiation keeps increasing, that is, the effect of the foreign element is not "saturated". The supplementary resistivity with respect to the pure metal may be assigned to a trapping by the foreign atoms of defects mobile at 78°K, or to the creation, in the presence of impurities, of a larger number of defects. It is not possible, at present, to reject one of these possibilities : it would be necessary to neutron-irradiate simultaneously samples of pure metal and of alloys at a sufficiently large dose ($\sim 10^{17}$ n/cm^2) and at a temperature sufficiently low to avoid free migration of defects (4°K). Such irradiations have been done by Swanson and Piercy (7), but to much smaller doses ($\sim 2.10^{14}$ n/cm^2) and have given the same increase in resistivity for aluminium and for alloys containing magnesium. On the other hand, Snead and Shearin (8), by electron irradiation at 4.2°K, obtained a different increase in pure aluminium and in dilute alloys.

We shall try and explain our results by a trapping mechanism, on the basis of the theoretical models which have been proposed for interpreting the recovery phenomena in irradiated aluminium, and we shall see how a mechanism of increased creation could be taken into account.

4.1. Trapping of defects mobile at irradiation temperature (78°K)

4.1.1. Stage II

We have interpreted (3) the results obtained for stage II, with different alloys, by assuming that an interstitial-type defect, mobile at 78°K, is trapped by the foreign atoms. If stage III is

assigned to the migration of the normal interstitial (model I), the defect trapped at 78°K would be a metastable interstitial ; on the other hand, if a vacancy-type defect is assumed to migrate in stage III (model 2) the trapped defect would be the normal interstitial.

In the case of magnesium additions, the release of this defect takes place in stage II. The hypothesis of a detrapping is consistant with the small number of jumps, corresponding to the recovery in stage II. The constant amplitude reached by stage II for concentrations greater than 1000.10^{-6} implies, for both models, that the number of trapped defects, annihilating after being detrapped, is constant in this range. As a consequence of the importance of the resistivity annealing out in this stage, it must be further concluded, in model 1, that a large fraction of the interstitials created by neutron irradiation are metastable interstitials.

The activation energy of the detrapping process is considered to be equal to the sum of the migration energy of the free defect plus the binding energy defect-impurity atom. In our experiments, we may adopt, as activation energy for detrapping, the activation energy of stage IIb2 (0.40 eV), because this sub-stage represents a large fraction of stage II, and its activation energy is constant and precisely determined. The free defect is assumed to migrate in the high-temperature part of stage I, with an activation energy of 0.11 eV (9). This leads to a value of $E^B_{IMg} = 0.29 \pm 0.03$ eV for the binding energy interstitial-magnesium.

In the range of very small magnesium concentrations, where the number of interstitials is much larger than the number of foreign atoms, it may be assumed that every magnesium atom contributes to the formation of an interstitial-impurity complex. In stage II, the dissociation of the complex leaves a free magnesium atom, and the interstitial annihilates with a vacancy. This results in a decrease in resistivity proportional to magnesium concentration, each foreign atom contributing a resistivity decrement.

$$\Delta\rho_{II} = \rho_{IMg} + \rho_V - \rho_{Mg}$$

The initial slope of the curve (resistivity decrease in stage II as a function of concentration) leads to a value of :

$$\Delta\rho_{II} = 1.62 \pm 0.06 \ \mu.\Omega.cm/at\ \%$$

by taking :

$$\rho_{Mg} = 0.50 \ \mu.\Omega.\ cm/at\ \% \qquad \text{(fig. 1)}$$

it follows :

$$\rho_{IMg} + \rho_V = 2.12 \pm 0.10 \ \mu.\Omega.cm/\%$$

Thus, one has to know the specific resistivity of a vacancy in order to determine that of the complex. The published values for ρ_V range from 1.4 $\mu.\Omega.cm/\%$ to 3 $\mu.\Omega.cm/\%$ (10,11,12). If the value is assumed to be $\rho_V > 2.12$, then the computation has no sense. If $\rho_V \leqslant 2.12$, the published values allow the determination of an upper limit, by using the lowest value of ρ_V :

$$\rho_{IMg} \leq 0.72 \ \mu.\Omega.cm/at\ \%$$

4.1.2. Stage III

The main feature to be explained is the increase of stage III in a range where stage II is constant. Different interpretations may be proposed therefore :

4.1.2.1. Existence of very strongly trapped interstitials, that would disappear in the temperature range of stage III, and whose number would increase with magnesium concentration. This interpretation does not specify the nature of the trapped interstitial and would fit both model 1 and model 2. However it seems more likely that the trend should be the reverse one, that is, the fraction of loosely bound interstitial should increase with magnesium concentration.

4.1.2.2. In model 1, where normal interstitials are assumed to move in stage III, it may be considered that for increasing magnesium concentrations, an increasing fraction of metastable interstitials are converted into normal ones during irradiation or during migration after detrapping in stage III. From the constancy of the amplitude of stage II, one would then have to conclude that the increase in the number of trapped interstitials is just compensated by an equal increase in the number converted to stable interstitials.

4.1.2.3. In model 2, where stage III is assumed to correspond to the disappearance of mobile vacancy-type defects recombining with small immobile interstitial clusters, we may consider, with Federighi (13), that magnesium atoms enhance the nucleation of interstitial clusters, during irradiation or during the dissociation of the interstitial-impurity complexes. The "saturation" of stage II then implies that the number of detrapped interstitials which annihilate in stage II is constant, whereas an increasing fraction of the interstitials contributes to the formation of immobile clusters.

In the last two hypotheses, the constancy of stage II results from the fact that two different physical processes cancel out exactly. Thus, both explanations seem rather artificial.

4.1.3. Stage III'

The recovery of our magnesium alloys has analogies with the aluminium-silicon alloys studied by Federighi (13), but there are marked differences for stage III' : in our case, this takes place at a lower temperature and with a lower activation energy than for silicon. This supplementary stage, whose importance increases with magnesium concentration can be attributed to a detrapping of defects trapped during their migration in stage III : these would be normal interstitials in model 1 or vacancy-type defects in model 2.

The binding energy between these defects and magnesium atoms can then be deduced from the activation energies of stage III' (detrapping) and stage III (free migration). We obtain :

$$E^{B}_{\chi Mg} = 0.74 - 0.59 = 0.15 \pm 0.09 \text{ eV}$$

This value is in good aggreement with the vacancy-magnesium binding energy obtained by other methods (12,14).

4.2. Increased creation of defects in the alloys

A process of increased creation of defects in the presence of foreign atoms can account for a part of the overall resistivity increase in the alloys. However, the same difficulty remains for explaining why, in the range of concentrations higher than 1000.10^{-6}, stage II keeps a constant value whereas stage III is still increasing. There is no apparent reason why the creation of defects annealing out in stage III should be favored at high concentrations.

V. Conclusions

5.1. The presence of magnesium atoms in aluminium samples irradiated at 78°K results in a rapid increase, then in a "saturation" of stage II recovery, in a slow increase of stage III, and in the progressive formation of a stage III'.

5.2. The model, based on the trapping of interstitials during irradiation at 78°K, which we had adopted after the study of various addition elements, is compatible with the present results. If this model is adopted, the following values can be deduced from our experiments :

$$E^{B}_{I\,Mg} = 0.29 \pm 0.03 \text{ eV}$$

$$\rho_{I\,Mg} + \rho_{V} = 2.12 \ \mu.\Omega.\text{cm}/\%$$

$$\rho_{I\,Mg} \leq 0.72 \ \mu.\Omega.\text{cm}/\%$$

$$E^{B}_{V\,Mg} = 0.15 \pm 0.09 \text{ eV}$$

5.3. The present experiments do not bring new fundamental arguments for the choice between the recovery models based on the migration of, respectively, interstitials or vacancy-type defects in stage III.

5.4. One of the important features of the results, namely the existence of a concentration range where stage II is constant and stage III is increasing, is not satisfactorily explained in either of the two models, and implies the consideration of supplementary hypotheses.

References

1. C. FROIS and O. DIMITROV. Comptes Rendus Acad. Sc. Paris 264 C (1967) p. 1923

2. C. DIMITROV-FROIS and O. DIMITROV. Mém. Sc. Rev. Mét. 65 (1968) p. 425

3. C. DIMITROV-FROIS and O. DIMITROV. Comptes Rendus Acad. Sci. Paris 266 C (1968) p. 304

4. C. FROIS and O. DIMITROV. Annales de chimie Paris (1966) 1, p.113

5. R. PŘIBIL. Chem. Commun. Collection. Czechoslov. 19 (1954) p.466

6. C. FROIS. Acta Met. 14 (1966) p. 1325

7. M.L. SWANSON and G.R. PIERCY. Canad. Jl. Phys. 42 (1964) p.1605

8. C.L. SNEAD and P.E. SHEARIN. Phys. Rev. 140 (1965) 5A p.1781

9. K. HERSCHBACH. Phys. Rev. 130 (1963) p.554

10. R.M.J. COTTERILL. Phil. Mag. 8 (1963) p.1937

11. R.O. SIMMONS and R.W. BALLUFI. Phys. Rev. 117 (1960) p.52-62

12. J.I. TAKAMURA in "Lattice defects in quenched metals" (1965) p. 540. Ed. R.M. Cotterill et al. Academic Press. New York and London

13. S.C. ERESARA, T. FEDERIGHI and F. PIERAGOSTINI. Phys. Stat. Sol. 11 (1965) p. 779

14. F.C. DUCKWORTH and J. BURKE. Brit. J. Appl. Phys. 18 (1967) p. 1071

Elimination of point defects in neutron-irradiated aluminium, during deformation at 78°K

O. DIMITROV and C. DIMITROV-FROIS

Centre d'Etudes de Chimie Métallurgique
15, Rue Georges Urbain, 94-Vitry. France

ABSTRACT

Pure aluminium samples, neutron-irradiated at 78°K, have been deformed by compression at the same temperature. Deformation results in a decrease in low-temperature electrical resistivity, which corresponds to the elimination of a fraction of the radiation-induced defects which would recover in the range of stage III. This elimination is produced by the movement of dislocations through the metal. It is shown that the process involved is probably a destruction of interstitial clusters, freeing interstitial defects which disappear rapidly at the deformation temperature.

I. INTRODUCTION

In a series of studies of lattice defects in aluminium, we have tried to examine the interaction between point defects, created by an irradiation at 78°K, and dislocations introduced by a subsequent deformation at the same temperature. We have also determined how the presence of dislocations modifies the recovery of irradiated aluminium. The study is made by electrical resistivity measurements at liquid hydrogen temperature (20.3°K).

II. EXPERIMENTAL TECHNIQUES

2.1. Irradiation conditions

Two series of samples were irradiated at 78°K in pile-neutrons, to doses of 2.7×10^{18} n/cm^2 and 3×10^{18} n/cm^2 (E > 1 MeV). The samples are polycristalline wires of high-purity aluminium, the total impurity content of which is 3 parts per million. Before irradiation they are annealed at 600°C in air for several hours. The values of electrical resistivity measured at 20.3°K before and after irradiation are given in table I for the series S4 (3.10^{18} n/cm^2).

2.2. Compression apparatus

Irradiated samples have been deformed by compression in liquid nitrogen by amounts ranging from 0.3 % to 37 %. The principle of the apparatus for low-temperature compression is given in fig. 1a. The wire is compressed between the plane surfaces of two cylindrical blocks of aluminium alloy, immersed in liquid nitrogen. The lower block has a flat-bottomed groove, 15 mm in width, in which the sample is placed. The groove is machined with precision and gives

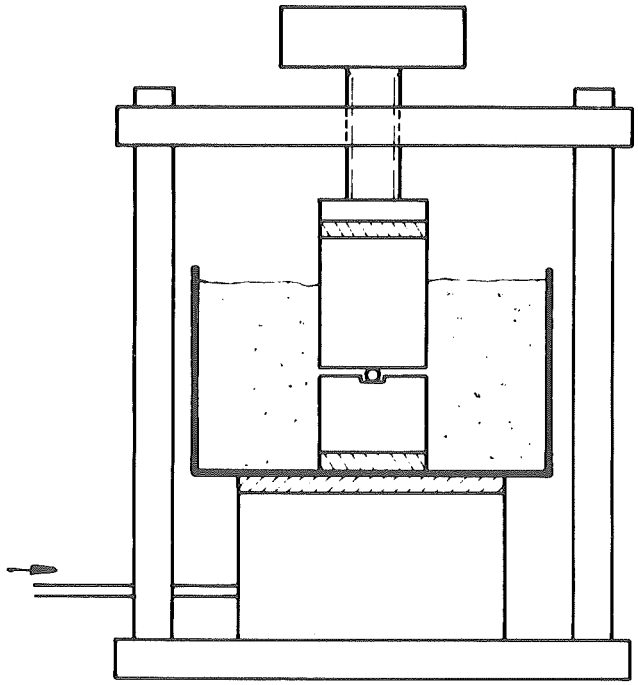

a

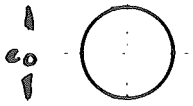

Initial cross-section of the irradiated sample

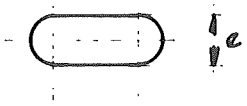

Final cross-section of the sample

b

Fig. 1. a. Principle of the compression apparatus
b. Cross-section of the samples.

a final thickness of the sample, constant within 1/100 of a millimeter. In order to reduce thermal leaks during compression, the cylindrical blocks are thermally insulated by plexiglas discs from the bottom of the liquid-nitrogen container and from the rest-plate of the hydraulic press. After deformation, the samples are fixed in liquid nitrogen on the holders used for measurements and anneals. We have directly checked that during compression the temperature of the samples is not raised by more than 1° above that of liquid nitrogen, and that the whole set of manipulation, except compression, does not produce a significant decrease in specimen resistivity.

2.3. Definition of the amount of compression

For square wires of side e_o, the amount of deformation corresponding to a final thickness e would be $\bar{\varepsilon} = Ln\ e_o/e$. However this formula cannot be used for our wires which have initially a circular cross-section. We have established the relationship :

$$\bar{\varepsilon} = Ln \frac{e_o}{e} - \frac{1}{2} \left[1 - \left(\frac{e}{e_o}\right)^2\right] \qquad [1]$$

by assuming that the cross-section of the compressed wire can be approximated by a rectangle plus two half-circles (fig. 1b).

2.4. Electrical resistivity measurements

The electrical resistivity at 20.3°K of the samples has been determined from the resistance values measured with a Diesselhorst-type potentiometer, with a sensitivity of 0.01 μV. The intensity (1 A) of the sample-current is stabilized, and eventual changes in intensity are checked and corrected by measuring the potential drop across a standard, immersed with the sample in liquid hydrogen.

Resistivity of the compressed samples

The resistivity at 20.3°K of an irradiated and deformed sample, in a given state, ρ_{ID}, is determined by the relationship :

$$\rho_{ID} = \frac{R_{ID}}{R_o} \times \left(\frac{\rho_{20.3}}{\rho^i_{294}}\right)_o \times \rho^i_{294} \qquad [2]$$

where - R_{ID} and R_o are the resistance values at 20.3°K of the irradiated and deformed sample, in the considered state and after complete recovery
- ρ^i_{294} = 2.664 μΩcm is the ideal resistivity of pure aluminium at 294°K (1)

In the completely annealed sample, the measurement of the resistances at 20.3 and 294°K gives the ratio of the resistivities (by neglecting the termal expansion of the sample),

$$\left(\frac{\rho_{20.3}}{\rho_{294}}\right)_o = \left(\frac{R_o}{R_{294}}\right)_o \text{ and allows the determination of :}$$

$$\left(\frac{\rho_{20.3}}{\rho^i_{294}}\right)_o \simeq \frac{\left(\rho_{20.3}/\rho_{294}\right)_o}{1-\left(\rho_{20.3}/\rho_{294}\right)_o}$$

Resistivity of the irradiated samples

As a consequence of the shape-change during compression, it is not possible to use relation 2 in order to determine the resistivity of the irradiated sample before deformation. We have measured the resistance values at 20.3 and 77°K, which give :

$$\frac{\rho_{20.3}}{\rho_{77}} = \frac{R_{20.3}}{R_{77}}$$

From this ratio, we obtain the value $\rho_{20.3}$ by reference to a curve, giving $\rho_{20.3}$ as a function of $\rho_{20.3}/\rho_{77}$, established with a series of irradiated samples, subsequently annealed without deformation.

III. EXPERIMENTAL RESULTS

3.1. Variation of electrical resistivity in the irradiated samples, by deformation at 78°K

A series of samples irradiated at 78°K to a dose of $3.10^{18} n/cm^2$ have been given various amounts of deformation in liquid nitrogen. Table I gives the electrical resistivity measured before and after compression.

Table I

$\rho_O^{20.3}$ (10^{-9} Ωcm) before irradiation	1.11	1.08	1.11	1.07	1.03	1.05	1.02
$\rho_I^{20.3}$ (10^{-9} Ωcm) after irradiation	188.58	186.30	188.98	192.82	191.25	194.38	187.76
$\bar{\varepsilon}$	0	0.003	0.009	0.028	0.126	0.250	0.372
$\rho_{ID}^{20.3}$ (10^{-9} Ωcm) after deformation	188.56	181.22	180.38	181.13	183.47	191.47	187.31
$\Delta\rho$ (10^{-9} Ωcm)	- 0.02	- 5.08	- 8.60	-11.69	- 7.78	- 2.91	- 0.45

Figure 2 gives the relative variation of resistivity measured at 20.3°K, as a function of deformation $\bar{\varepsilon}$. The resistivity variation is defined by the ratio $(\rho_{ID} - \rho_I)/\rho_I$ where ρ_I is the resistivity at 20.3°K of the irradiated sample, and ρ_D the resistivity of the irradiated and deformed sample, measured about 20 minutes after compression. $\bar{\varepsilon}$ is calculated by relationship 1 of section 2.3.

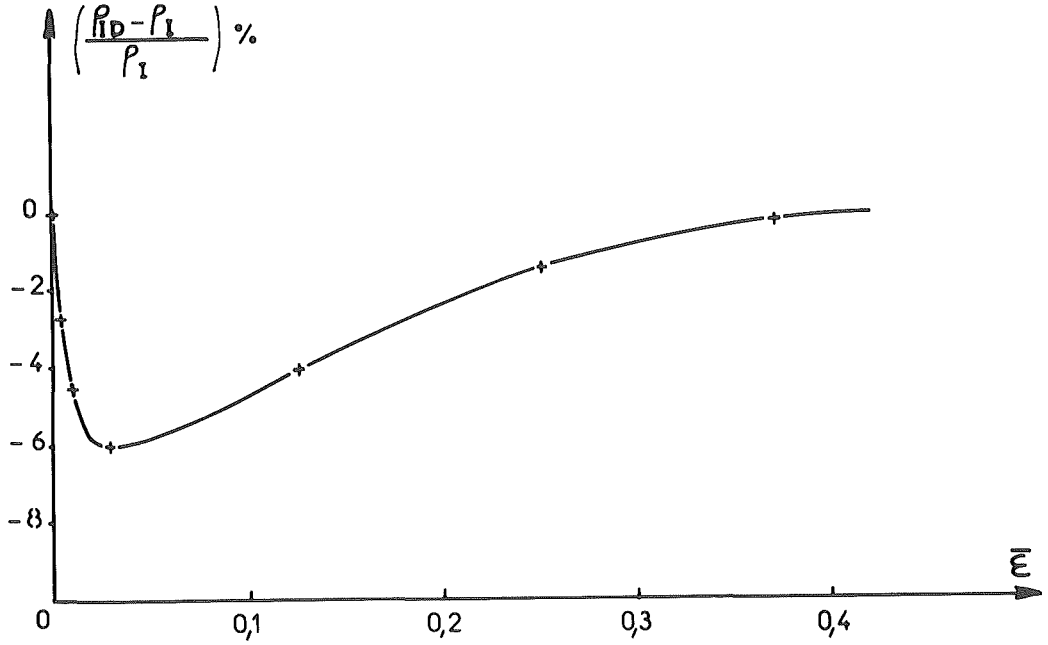

Fig. 2. Resistivity variation of the irradiated samples, by deformation at 78°K

For small amounts of deformation ($\bar{\varepsilon} < 0.03$) a rapid decrease of electrical resistivity is observed. This decrease is largest for $\bar{\varepsilon} = 0.03$: it reaches about 6 % of the resistivity of the as-irradiated sample, ρ_I. For larger amounts of deformation, the decrease in resistivity becomes smaller and smaller, and the initial value of resistivity is reached again for $\bar{\varepsilon}$ about 0.4.

3.2. Recovery of irradiated and deformed samples

3.2.1. Isochronal recovery curves

The study of the isochronal recovery and of the kinetics of elimination of defects has been done simultaneously with samples irradiated at 78°K (2.7×10^{18} n/cm^2) and with samples compressed in liquid nitrogen after irradiation.

The isochronal recovery curves obtained from the variations of electrical resistivity of samples annealed by steps of 60 minutes - 15° (fig. 3 a,b) show the effect of a deformation of $\bar{\varepsilon} = 0.16$, on the recovery of irradiated aluminium. Stages II and III, corresponding to the recovery of radiation induced defects are found with little change. (For the relatively high dose used in our experiments, stage II is very small and does not appear as a well individualized peak on the recovery curves). The amplitude of stage III is somewhat decreased in the irradiated and deformed sample.

Apart from the two preceding stages, we find the stages obtained

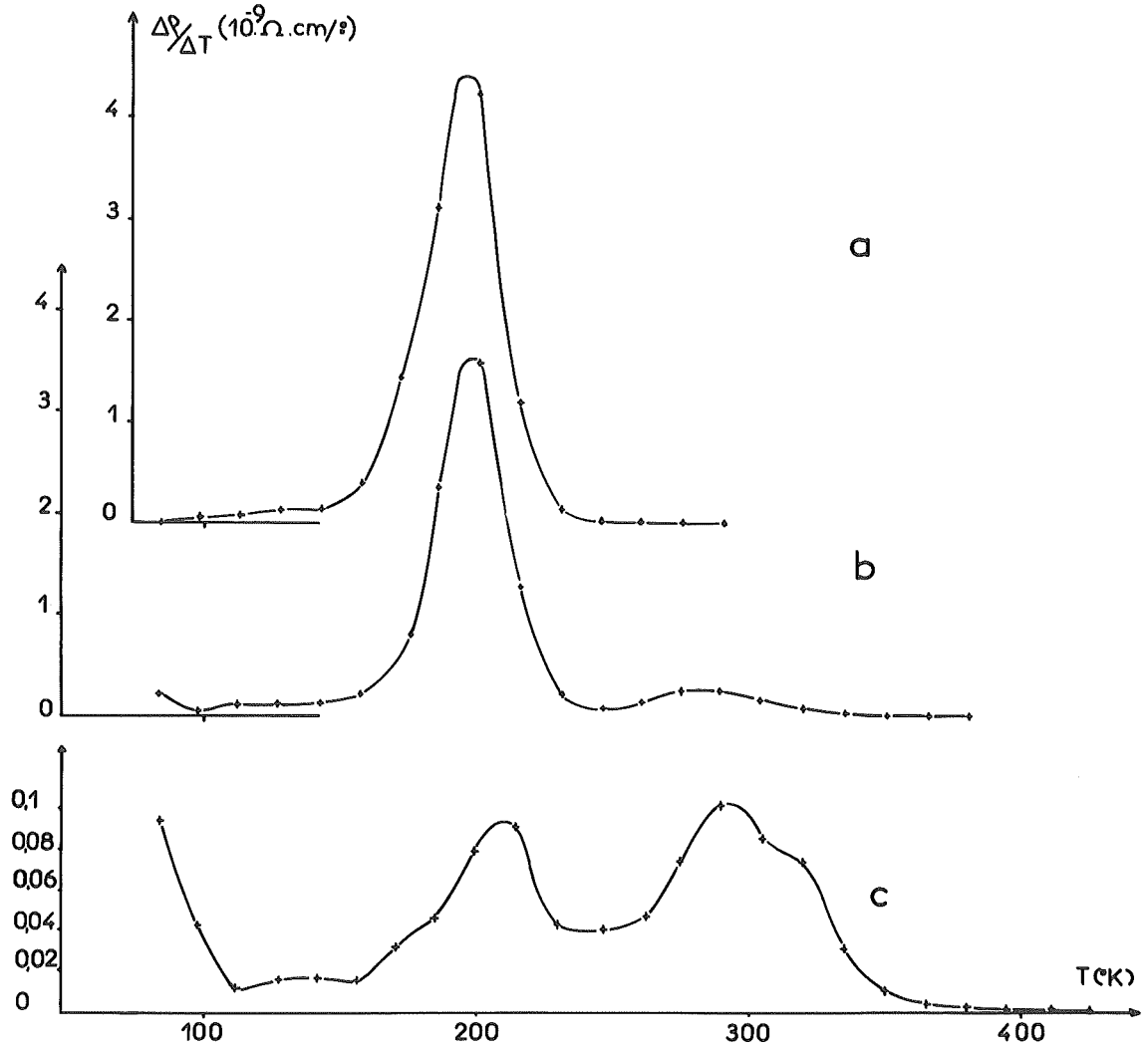

Fig. 3. Differential recovery curves of aluminium samples
a) Irradiated to a dose of 2.7 x 10^{18} n/cm^2
b) Irradiated to the same dose and deformed ($\bar{\varepsilon}$ = 0.16)
c) Unirradiated, deformed ($\bar{\varepsilon}$ = 0.14)

with a deformed unirradiated sample (fig. 3c). At temperatures higher than 250°K, a stage V appears, which is caused by the recrystallization of the metal or, when the amount of deformation is too small to allow recrystallization to take place, by a rearrangement of dislocations. Finally, between deformation temperature and 110°K, we find the stage caused by the elimination of some of the deformation-induced point defects (1).

Table II gives a comparison of the excess resistivity which is eliminated in the different recovery stages for an irradiated, an irradiated and deformed, and a deformed unirradiated sample.

Table II

	Resistivity recovery ($10^{-9}\Omega$.cm)		
	Irradiated	Irradiated and deformed. $\bar{\varepsilon}$ = 0.14	Deformed $\bar{\varepsilon}$ = 0.133
Stage II	6.22	9.26	2.45
Stage III	154.84	129.29	4.89
Stage V	0.78	14.07	6.75
Total	161.84	152.62	14.09

From this table, it can be seen that, for comparable deformation, the presence of radiation-induced defects results in the creation of a larger density of dislocations (increase in stage V).

As for stage III, if we compare the excess resistivity eliminated in the irradiated and in the irradiated-deformed sample, we find that there is no increase, but a large decrease in the amplitude of this stage. Furthermore, measurements made on other irradiated and deformed samples show that for increasing amounts of deformation, there is a pregressive decrease in stage III recovery.

Finally, it can be remarked that the amplitude of stage II in the irradiated and deformed sample is not smaller than the sum of those measured in the irradiated and the deformed samples. Thus the deformation has not resulted in the elimination at 78°K of defects which normally disappear in stage II.

3.2.2. Resistivity decrease corresponding to the elimination of radiation-induced defects, during deformation

The resistivity decrease measured on the samples after deformation (Table I) is only a lower limit for the decrease in resistivity corresponding to the elimination of radiation-induced defects. If we call, in algebrical values,

$\Delta\rho_I$ the variation in resistivity caused by the change in concentration of radiation-induced defects, during deformation

$\Delta\rho_D$ the resistivity of the dislocations introduced by the deformation

$\Delta\rho_{PD}$ the resistivity of the point defects introduced by the deformation

$\Delta\rho$ the total resistivity variation, which is measured experimentally

we can write : $\Delta\rho = \Delta\rho_I + \Delta\rho_D + \Delta\rho_{PD}$

or : $\Delta\rho_I = \Delta\rho - \Delta\rho_D - \Delta\rho_{PD}$

It is not possible to evaluate directly $\Delta\rho_I$, because we do not know $\Delta\rho_{PD}$. On the other hand, $\Delta\rho_D$ can be derived from the recovery curves : it corresponds to the amplitude of stage V, which is the excess-resistivity remaining after the elimination of point defects. Thus, one can obtain a value which is nearer to $\Delta\rho_I$ than the measured decrease $\Delta\rho$, by correcting the latter of the contribution of the dislocations, $\Delta\rho_D$ (table III).

$$\Delta\rho_C = \Delta\rho - \Delta\rho_D$$

Table III

$\bar{\varepsilon}$	0	0.003	0.009	0.028	0.126	0.250	0.372
$\Delta\rho$ ($10^{-9}\Omega$.cm)	-0.02	-5.08	-8.60	-11.69	-7.78	-2.91	-0.45
$\Delta\rho_D$ ($10^{-9}\Omega$.cm)	0	2.52	4.75	6.68	12.69	21.49	31.54
$\Delta\rho_C$ ($10^{-9}\Omega$.cm)	-0.02	-7.60	-13.35	-18.37	-20.47	-24.40	-31.99

Figure 4 shows the variation of $\Delta\rho_C$ as a function of the amount of deformation $\bar{\varepsilon}$.

3.2.3. Recovery kinetics

The lattice-defects introduced by deformation at 78°K do not modify appreciably the kinetics of recovery of the radiation-induced defects in stage III. It is found, as in undeformed irradiated samples, that the end of stage III recovery takes place with second order kinetics. However, the fraction of the recovery corresponding to such kinetics is a little smaller in the irradiated and deformed samples. It represents 49.5 % of the total amplitude of stage III, instead of 52 % in the undeformed samples (fig. 5). Furthermore, isothermal recovery curves obtained at 181.5°K show that the time t 1/2, corresponding to the elimination of the defects of stage III, is larger in the samples deformed after irradiation than in the

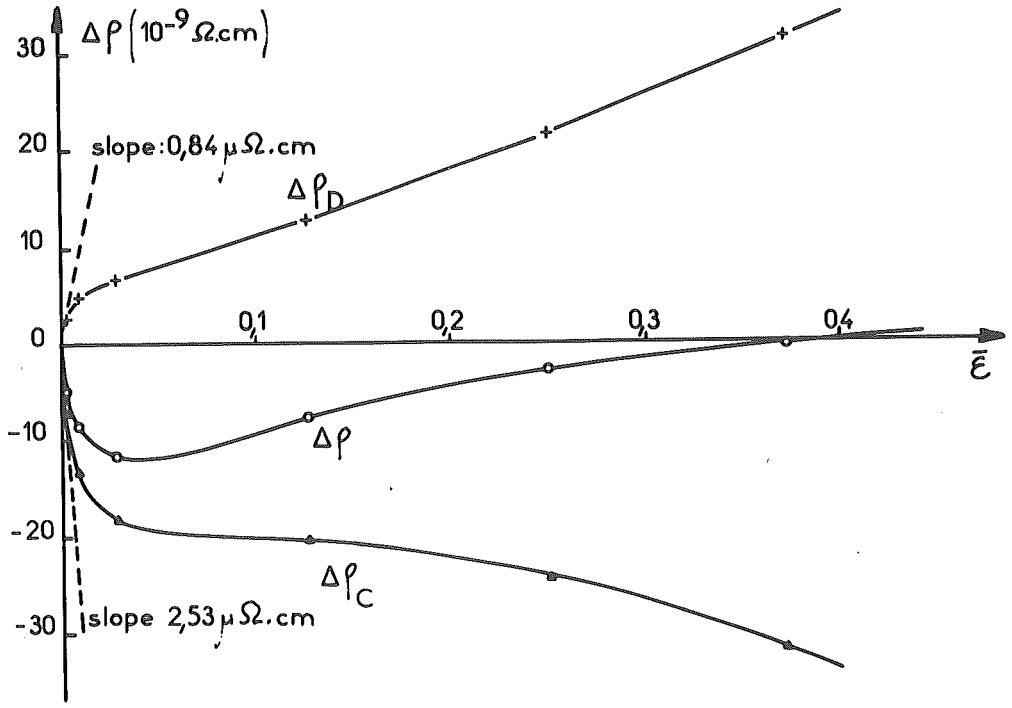

Fig. 4. Variation of the corrected resistivity decrease as a function of deformation amount.

irradiated samples. This is in aggreement with the fact that, in the latter, the concentration of defects eliminated in stage III is larger and that the kinetics are partially of second order.

The activation energies for stage III, determined by the method of Meechan and Brinkman are identical in both types of samples : 0.61 ± 0.02 eV.

IV. INTERPRETATION

4.1. General shape of the resistivity-deformation curve

The increasing part of the curve representing the variation of resistivity as a function of the amount of deformation, for irradiated samples (fig. 2), is easily explained by the creation of dislocations and point defects during deformation : the increase in the number of lattice-defects created results in a resistivity increasing with the deformation. On the other hand, the decrease in resistivity observed for small deformations implies the disappearance of a certain fraction of the defects already present in the metal, that is, radiation-induced defects. Thus, the global phenomenon results from the superposition of the two effects. For small deformations, the elimination of irradiation defects is preponderating and for large deformations, the introduction of deformation-induced defects is the main effect.

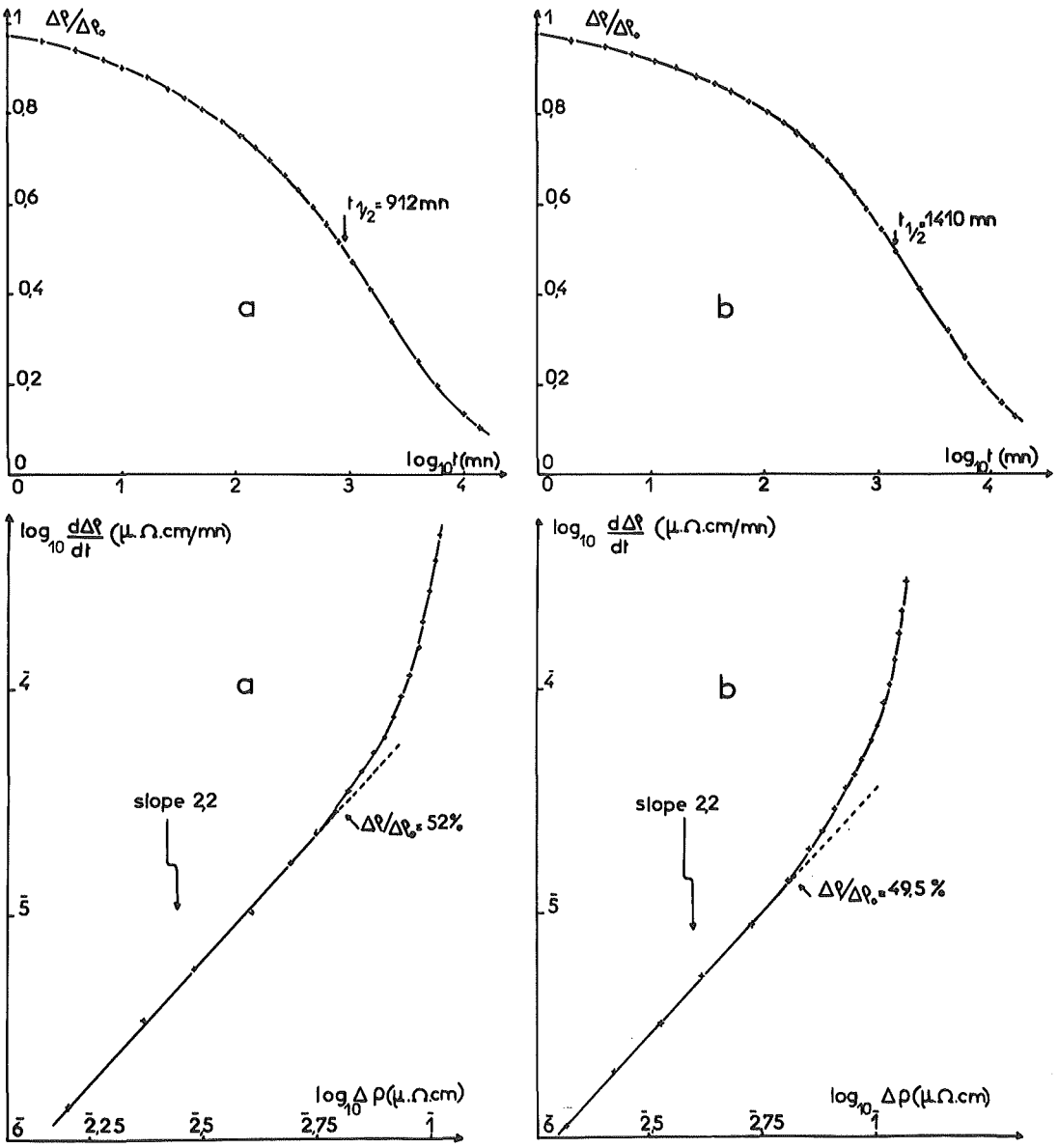

Fig. 5. Isothermal recovery curves at 181.5°K and determination of kinetics in stage III
a) irradiated, undeformed sample
b) irradiated and deformed sample ($\bar{\varepsilon}$ = 0.14)

4.2. Mechanisms for the elimination of irradiation defects

We have considered two types of mechanisms for explaining the phenomenon found in the present experiments, namely the elimination of irradiation defects during deformation at 78°K. These are : mutual annihilation of point defects created by irradiation and point defects created by deformation, or elimination of irradiation-defects by the movement of dislocations in the lattice of the metal, during deformation.

4.2.1. Annihilation with point defects created by deformation

Low-temperature deformation of aluminium creates point defects, a fraction of which are eliminated between 50°K and 100°K (1). Such defects, being mobile at 78°K could annihilate some of the radiation induced defects. In order to check the validity of this hypothesis, we have evaluated the variations of resistivity involved in the deformation, in the simpler case of small deformations. Table IV gives the initial slopes of a number of variations of resistivity, as a function of deformation.

Table IV

Irradiated and deformed samples			
	Dislocations	Point defects	Point defects moving between 50 and 100°K
$(\frac{d\rho}{d\varepsilon})_o^C$ (μΩcm)	$(\frac{d\rho}{d\varepsilon})_o^D$ (μΩcm)	$(\frac{d\rho}{d\varepsilon})_o^{PD}$ (μΩcm)	$(\frac{d\rho}{d\varepsilon})_o^m$ (μΩcm)
- 2.53	0.84	0.50	0.12

$(\frac{d\rho}{d\varepsilon})_o^C$ represents a lower limit for the decrease in resistivity produced by the deformation of irradiated sample (fig. 4)

$(\frac{d\rho}{d\varepsilon})_o^D$ is the increase in resistivity due to the dislocations introduced by deforming an irradiated sample (fig. 4)

$(\frac{d\rho}{d\varepsilon})_o^{PD}$ is the resistivity of the point defects introduced by deformation. From experiments on deformed unirradiated samples, this represents 60 % of the resistivity of dislocations

$(\frac{d\rho}{d\varepsilon})_o^m$ is the resistivity of the deformation-induced point defects which are eliminated between 50 and 100°K. It has been assumed that, as in the case of aluminium strongly deformed at 20°K (1), these defects represent about 24 % of the point defects moving at higher temperatures.

It can be seen that the decrease in resistivity of the irradiated samples is about 20 times as large as the resistivity of the deformation-induced point defects which are able to migrate at 78°K. This excludes the possibility of this decrease being due to a mutual annihilation of deformation defects and irradiation defects. If these two types of defects have a comparable influence on resistivity one would have to admit that one deformation-induced defect is able to eliminate 20 irradiation defects or, conversely, if recombination takes place in the proportion 1 to 1, one must then conclude that radiation-induced defects have a specific resistivity 20 times as large as that of the antagonist deformation-induced defects. Both hypotheses are very unlikely.

4.2.2. Elimination of point defects by the movement of dislocations through the lattice

The movement of dislocations during deformation could result in the disappearance of radiation-induced defects by :

- the recombination of close pairs under the action of the strains existing in the proximity of dislocations
- the absorption of individual defects on the jogs of dislocation lines
- the destruction of defect clusters, freeing individual defects, which then migrate and disappear.

4.2.2.1. Close pairs

For this hypothesis, one has to suppose that close pairs exist in aluminium irradiated at 78°K. If this is the case, their recombination must take place in stage II (3). The results of our measurements show that the hypothesis of a recombination of close pair during deformation has to be rejected :

- The decrease of resistivity directly measured after a deformation of $\bar{\varepsilon} = 0.028$ (11.69×10^{-9} Ωcm) and, a fortiori, the corrected resistivity decrease (18.37×10^{-9} Ωcm) are larger than the excess resistivity which disappears in stage II in the irradiated samples (6.3×10^{-9} Ωcm).
- The study of the recovery of irradiated and deformed samples shows that deformation does not result in the elimination at 78°K of defects which anneal normally in stage II (see section 3.2.1)

4.2.2.2. Individual defects

During their movement, dislocations could sweep the defects encountered and the latter could disappear by absorption on the jogs. Thus, one would observe the disappearance of a certain proportion of the defects moving in stage III, that is, according to the recovery model adopted, vacancies (4) or interstitials (5,6). In the case of vacancies, experiments of deformation after quenching show that this is not a very effective process. Thus, Wintenberger (2) finds that deformation at 20°C of a quenched aluminium sample, therefore containing vacancies, gives an increase in resistivity comparable with that produced in a non-quenched sample. The passing of dislocations through the metal does not result in an important elimination of individual vacancies. By analogy, one may think that this is also the case for individual interstitials.

4.2.2.3. Defect clusters

Finally, one can suppose that the passing of dislocations destroys defect clusters present in the irradiated metal. In such a case, a decrease in resistivity will take place if the cluster can be absorbed by the dislocation or if the resulting defects are mobile at the deformation temperature and disappear at sinks. Thus the deformation of a quenched and aged aluminium sample, therefore containing vacancy clusters, produces a decrease in resistivity (2).

In our experiments, made at 78°K, vacancies are immobile. This makes unlikely that the destroyed clusters are vacancy aggregates, for instance depleted zones (7). One is then led to the conclusion that they are clusters of interstitial defects. This interpretation of our experiments results in the consequence that, in aluminium, interstitial defects are mobile at 78°K and are able to form clusters during irradiation. Thus, this could hardly be an interstitial compelled to move on a straight line, such as a crowdion.

It would be interesting to deform samples, irradiated at 78°K, at a temperature sufficiently low in order to have no long range migration of defects (for instance at 20°K). One would obtain more direct arguments for one of the interpretations given in sections 4.2.2.2. and 4.2.2.3.

V. CONCLUSIONS

5.1. The results of our experiments show that deformation at 78°K of aluminium samples, irradiated at the same temperature, produces a decrease in electrical resistivity.

5.2. This decrease in resistivity is the consequence of an elimination of radiation-induced defects by the movement of dislocations through the metal.

5.3. Consideration of various possible mechanisms leads to interpret the observed phenomena by the destruction of interstitial clusters present in the irradiated metal.

5.4. It follows from this interpretation that, in aluminium, interstitials are mobile at 78°K and are able to form clusters.

References

1. C. FROIS. Acta Met. (1966) 14 p. 1325

2. M. WINTENBERGER. Acta Met. (1959) 7 p. 549

3. R. VON JAN. Phys. Stat. Sol. (1966) 17 p. 361

4. T. FEDERIGHI, S. CERESARA and F. PIERAGOSTINI. Phil. Mag. (1965) 12 p. 1093

5. G. BURGER, H. MEISSNER and W. SCHILLING. Phys. Stat. Sol. (1964) 4 p. 267

6. A. SOSIN and L.H. RACHAL. Phys. Rev. (1963) 130 p. 2238

7. A. SEEGER in Radiation damage in solids, I, p. 101. International Atomic Energy Agency, Vienna 1962

Effect of Deformation on the Recovery of Neutron Irradiated Metals.

S. Okuda, S. Takamura and H. Maeta
Japan Atomic Energy Research Institute
Tokai-mura, Ibaraki, Japan

Abstract

The recovery of point defects in F.C.C. metals after fast neutron irradiation at $15^{o}K$ was studied by measurements of residual resistivity. Especially, the effect of cold work before and after low temperature irradiation on the recovery spectrum was studied. The results seem to show the annealing of interstitial clusters in stage II in cold worked Cu.

1. Introduction

There are various interactions through which the recovery process of point defects may be modified by dislocations; modification of activation energies for migration of the point defects due to the strain field of dislocations, migration and agglomeration along dislocation lines or absorption into dislocation nodes or jogs, and trapping or also conversion of one kind of defects to another by dislocations. These interactions were studied by comparing the recovery after irradiation of annealed specimens and cold worked ones[1~6].

The recovery spectrum of cold worked metals at low temperature are known to be different from those of the irradiated at low temperature[2]. The difference in the defect structure would be the main cause of this difference, but the interaction of the defects with dislocations, especially with fresh pile-up dislocations might also play a role. The latter effect can be studied by measurements of recovery of specimens cold worked after low temperature irradiation. This type of measurements would also help to understand the defect structure after cold work.

In the present experiments, the recovery spectra of the residual resistivity after neutron irradiation of the previously cold worked specimen and after cold work of the neutron irradiated specimen at low temperature were measured and compared with those after neutron irradiation of annealed specimens.

2. Experimental procedures

The specimens used were 99.999 % pure Cu and Au wires of 0.2 ~ 0.4 mm dia. Cu specimens were annealed at 900°C in vacuum, then following treatments were given: Treatment 1, an annealed specimen was irradiated; Treatment 2, an annealed specimen was cold worked at room temperature and aged at 50°C, then irradiated; Treatment 3, an annealed specimen was first irradiated, then deformed by twisting (5 % surface shear strain) at 4.2°K without intermediate warm-up. In order to attain an accurate comparison, the specimens of Treatment 1 were simultaneously irradiated and isochronally annealed with the specimens of Treatments 2 and 3, respectively. Au specimens were annealed at 980°C in air and given Treatments 1 and 2. In Treatment 2, ageing was done at 100°C for Au.

The irradiation was performed by the low temperature irradiation facility (LHTL)[6, 7] set in the horizontal experimental hole of JRR-3 Reactor at the Japan Atomic Energy Research Institute. In this facility which is equipped with a fast converter, the fast neutron flux (> 0.1 MeV) at the specimens was 5×10^{11} n/cm^2 sec and the thermal neutron flux was expected to be about 10^5 times less than that. Therefore, the specimens were irradiated by neutrons with fission spectrum. After irradiation at ~15°K, the specimens were transferred to the double glass Dewar with precautions against warming. The deformation in Treatment 3 was done in this Dewar. The electrical resistivity was measured in liquid He by standard potentiometric method and the isochronal

annealing was performed with 6 minutes pulses at each annealing temperatures.

3. Results and discussions

As it is shown elsewhere[8], the damage rate in Cu was increased by cold work before irradiation in accordance with the previous results[3]. Differential isochronal recovery curves of Cu after 10 hrs. irradiation for Treatments 1 and 2 are shown in Fig. 1. The curve for Treatment 2 in the figure is for the specimen cold worked 106 % (surface shear strain) before irradiation, but no significant difference was observed for the specimen cold worked 53 % before irradiation[8]. The recovery was slightly retarded in stage I and enhanced above $\sim 150^{\circ}K$.

In Fig. 2, isochronal recovery curves of Cu after 29 hrs. irradiation for Treatments 1 and 3 are shown. Their differential isochronal recovery curves and difference ($\Delta\rho_{deform} - \Delta\rho_{anneal}$) are shown in Figs. 3 and 4, respectively. In the specimen of Treatment 3, the resistivity increase due to the deformation was more than 15 % of that due to irradiation. Whereas there was considered to be a slight error in determining the form factor of the specimens of Treatments 1 and 3, no appreciable change in the general form of the curves in Figs. 2~4 should occur. It is seen that in Treatment 3, recovery was retarded from above $30^{\circ}K$ and the amount of recovery in stage I was reduced by about 20 % (Fig. 4). (A corresponding reduction in stage I for Treatment 2 was only about 3 %.) Furthermore, in Treatment 3, a recovery

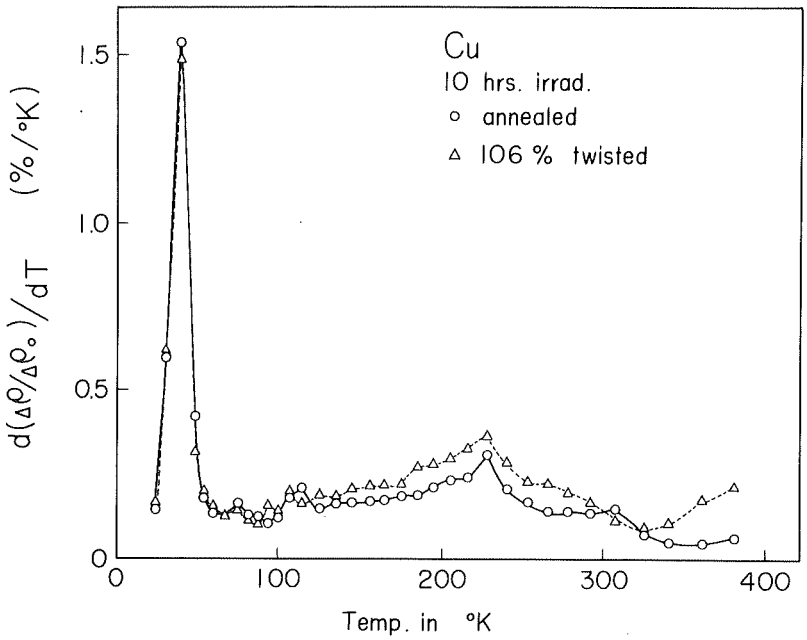

Fig. 1 Differential isochronal recovery curves of fast neutron irradiated copper. O: the specimen annealed before irradiation (Treatment 1), Δ: cold worked and aged at 50°C before irradiation (Treatment 2).

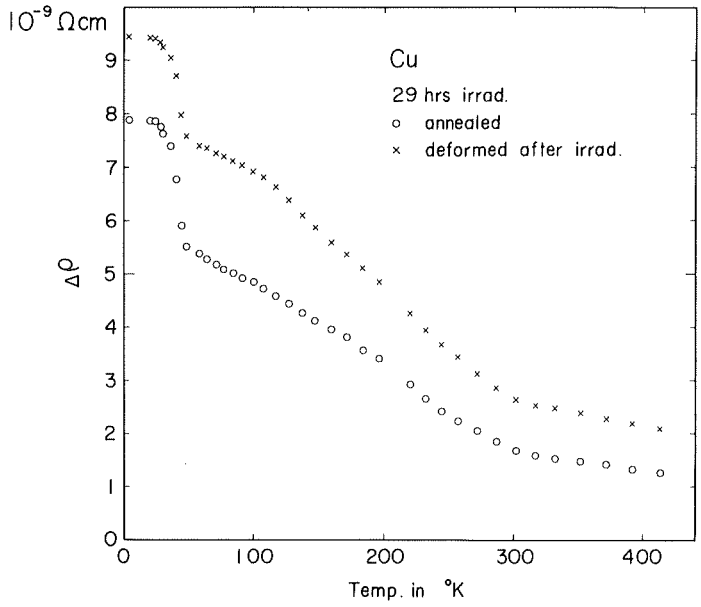

Fig. 2 Isochronal recovery curves of fast neutron irradiated copper. O: the specimen annealed before irradiation (Treatment 1), x: cold worked by torsion (5 % surface shear strain) at 4.2°K after irradiation without intermediate warm-up (Treatment 3).

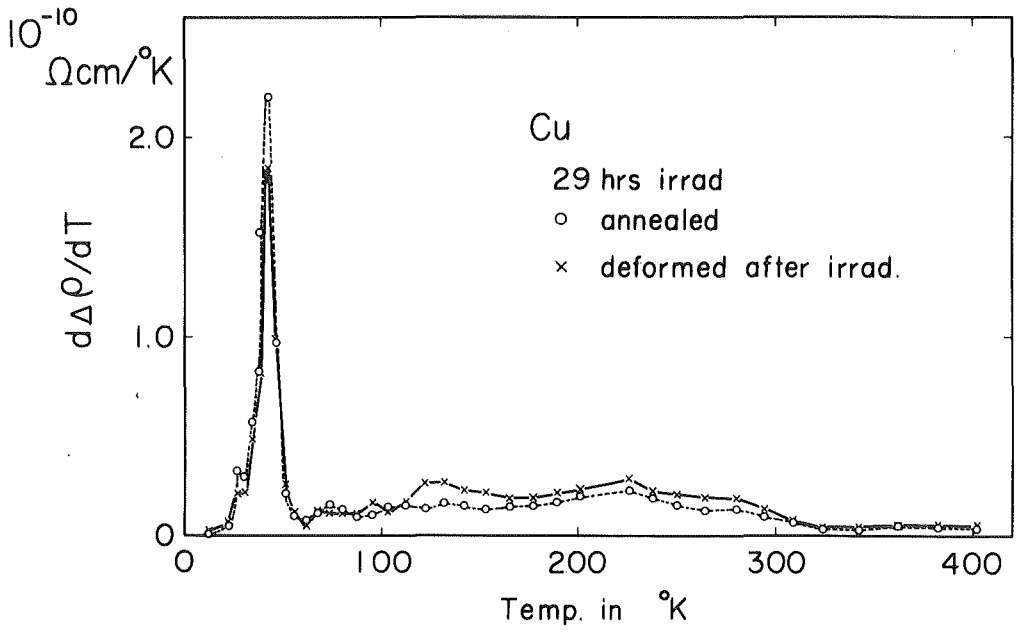

Fig. 3 Differential isochronal recovery curves calculated from Fig. 2.

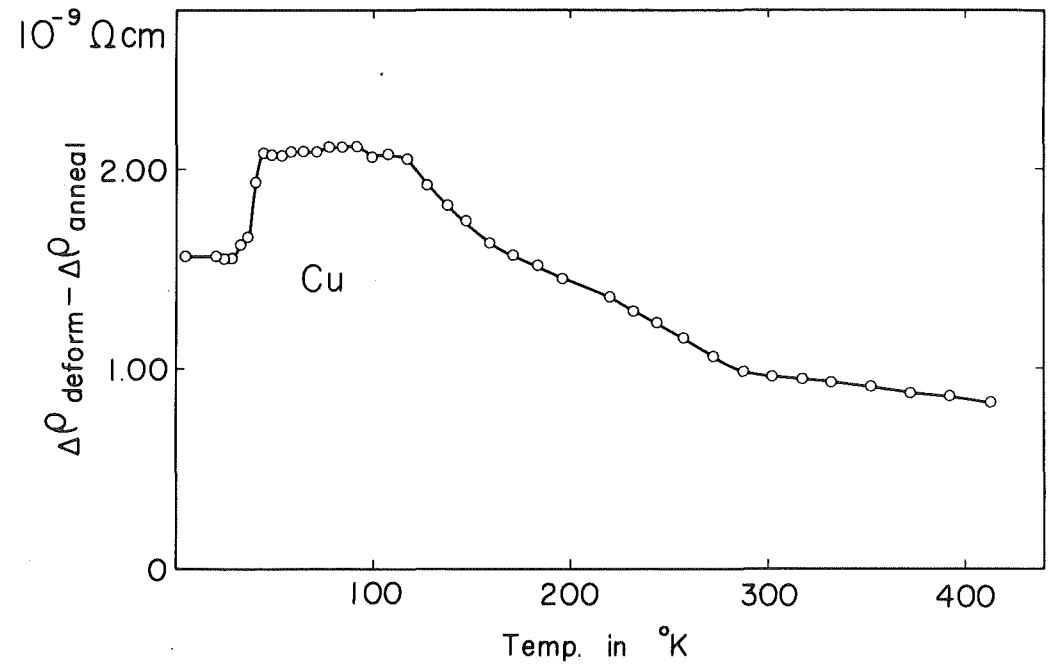

Fig. 4 Difference in resistivity retained at each annealing temperature of Treatments 1 and 3.

peak at 130°K was observed which was not seen in Treatments 1 and 2 (Fig. 3). Enhancement in recovery above ~150°K was similar in Treatments 2 and 3.

The present results apparently show that considerable amount of the close Frenkel pairs were destroyed or transformed into more stable defects by moving dislocations. Because the deformation was performed at 4.2°K, no thermal migration of the defects was expected during the deformation. Further, the dislocation density was expected to be much smaller in Treatment 3 than in Treatment 2, indirect interaction through elastic field of dislocations would not have played an important role. Possibly, the direct cutting of close pairs by moving dislocations would be important in this case.

As for the recovery peak at 130°K, since this peak was also observed in the specimen only cold worked at 4.2°K without irradiation, this peak is considered to be associated with the characteristic defects induced by cold work. It should also be mentioned that the retained resistivity after stage I in Treatments 1 and 2 was much larger than the resistivity increase due to the present cold work in Treatment 3. From the previous experiments, on the recovery after cold work[9], this peak was known not to shift in temperature for different degree of cold work, but seemed to be impurity sensitive. Therefore, this peak is possibly associated with an annihilation of di-interstitials or interstitial clusters produced by cold work. Since the dynamic modulus measurements during recovery after cold work showed dislocation pinning in a similar temperature range[10], some of

these interstitial clusters would move to dislocations and form pinning points in this stage.

The present results seem to show that fresh pile-up dislocations do not have a large influence on the recovery process of point defects at least when measured by residual resistivity.

For Au, differential isochronal recovery curves after 10 hrs. irradiation for Treatments 1 and 2 are shown in Fig. 5. In the figure, the curve for Treatment 2 is for the specimen drawn 90 % (reduction in area) before irradiation, but no significant difference was observed for the specimen drawn 38 % before irradiation[8]. Experiments for Treatment 3 have not been done for Au as yet.

Besides a similar effect of previous cold work on the recovery after irradiation as in Cu, a pronounced effect of previous cold work was observed for the recovery peak at 320°K in Au. As is seen in Fig. 5, by cold work, the 320°K peak shifted in temperature to 290°K, but a peak at ~235°K did not show such a large shift. Burger et al.[11] observed the recovery peaks at 230°K and 330°K in Cu after neutron irradiation which they named as stage III_1 and III_2, respectively. The peaks at 235°K and 320°K in the present results seem to correspond with these stages III_1 and III_2, respectively. According to their interpretation[11], stage III_1 and III_2 are associated with the annihilation of interstitials moving inside depleted zones[12] and outside depleted zones to vacancies, respectively. Because of the difference in the range of migration, dislocation density would have rather

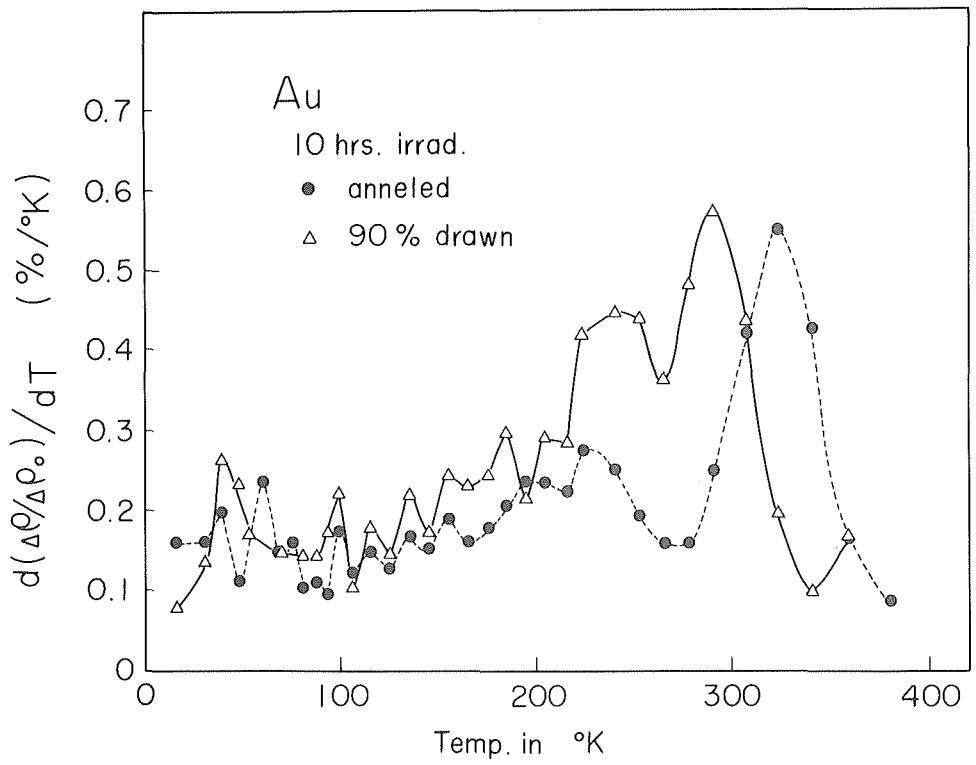

Fig. 5 Differential isochronal recovery curves of fast neutron irradiated gold , ●: the specimen annealed before irradiation (Treatment 1), △: cold worked and aged at 100°C before irradiation (Treatment 2).

large influence on stage III_2, but not on stage III_1. The present results where only stage III_2 shifted to lower temperature by cold work, is in good agreement with this model. A similar but less pronounced effect of cold work was also seen in Cu (Fig. 1). In Cu, the recovery peaks in stages III_1 and III_2 were observed at 230°K and 300°K, respectively.

Invaluable helps given by the members of LHTL group and JRR-3 in performing the present experiments are gratefully acknowledged.

References

1) C.J. Meechan, A. Sosin and J.A. Brinkman, Phys. Rev. 120(1960)411.

2) D.K. Holmes; The interaction of Radiation with solids, ed. R. Strumane et al. (North-Holland, Amsterdam, 1964) p.147.

3) M.L. Swanson and G.R. Piercy, Can. J. Phys. 42(1964)1605.

4) K. Herschbach and J.J. Jackson, Phys. Rev. 153(1967)689.

5) J.J. Jackson and K. Herschbach, Phys. Rev. 170(1968)618.

6) S. Okuda, H. Suzuki, H. Kumamoto, K. Akashi and S. Hagihara, International Cryogenic Engineering Conf. (Tokyo 1967), to be published.

7) S. Okuda, T. Nakanii, S. Takamura,and H. Maeta, Proc. Int. Conf. on the Strength of Metals and Alloys (Tokyo, 1967) to be published.

8) S. Takamura, H. Maeta and S. Okuda, J. Phys. Soc. Japan, to be published.

9) S. Takamura, S. Okuda, J. Phys. Soc. Japan, to be published.

10) S. Okuda, J. Phys. Soc. Japan, 18 Suppl. I (1963) 187.
L.J. Bruner and B.M. Mecs, Phys. Rev. 129(1963)1525.
J. Völkl and W. Schilling, Phys. Kondens, Mat, 1(1963)296.

11) G. Burger, K. Isebeck, J. Völkl, W. Schilling and H. Wenzl, Z. angew. Phys., 22(1967)452.

12) A. Seeger, Int. Conf. Peacefull Uses of Atomic Energy, Geneva (1958) Vol.6, p.250.

STUDY OF STAGE I IN IRRADIATED NICKEL

G. de KEATING-HART, R. COPE, C. MINIER and P. MOSER

Centre d'Etudes Nucléaires Grenoble, France

I - Introduction

For progress to be made in the understanding of irradiation phenomena, it is necessary to devise appreciable improvements in present measurement techniques or to perfect techniques as yet unapplied because of experimental difficulties or of the high cost involved. The experiments described here mark the beginning of efforts made with this attitude at our laboratory at Grenoble.

II - Resistivity Experiments

a) Fine Stucture of Stage I

We have aimed at seeing if the fine structure in the region of stage I, which has been reported recently by different laboratories [1] [2] [3], is partially due to distorsion arising during isochronal thermal treatments in which the temperature changes are very sudden. To this end we have devised a different recovery procedure : We measure, to very high accuracy, the resistivity of a standard sample and of the irradiated sample during a strictly linear increase in temperature. This is not a new idea [4] but up to now, it has not been developped to any extent, no doubt because of the delicate nature of the operation and theoretical reasons such as fears of deviation from Mathiessen's rule. This last important argument has lead us to always carry out both linear temperature increases and isochronal treatments and to compare the results.

Figure 1 shows the results obtained during the recovery of an electron irradiated, monocrystalline nickel sample of high purity. It should be noted that the fine structure is defined by a large number of experimental points ; this is because the curve was obtained directly as the difference between two continous recordings.

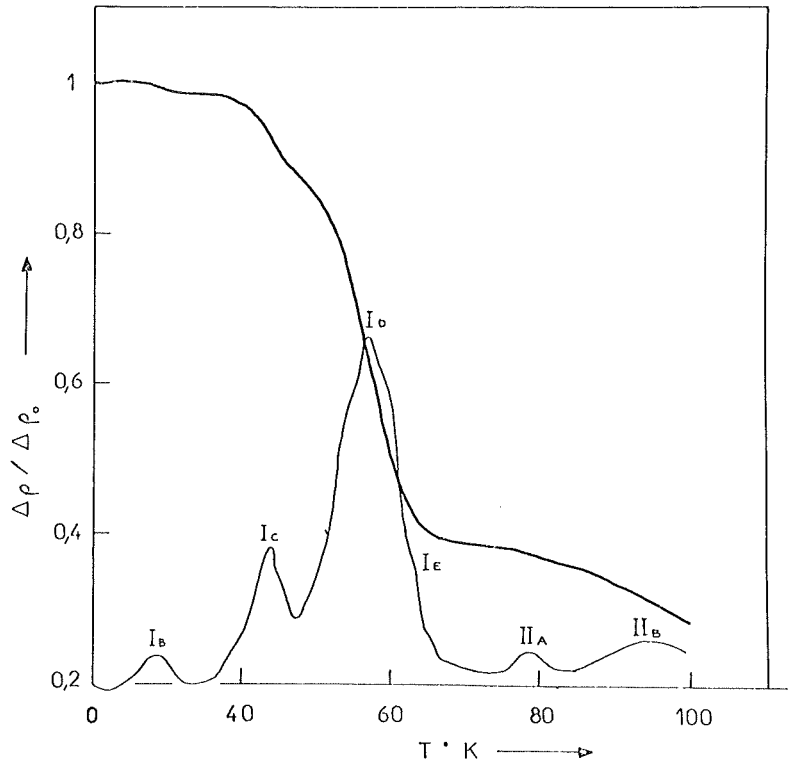

Fig. 1 Recovery of the resistivity of an electron irradiated nickel sample during a linear temperature increase.

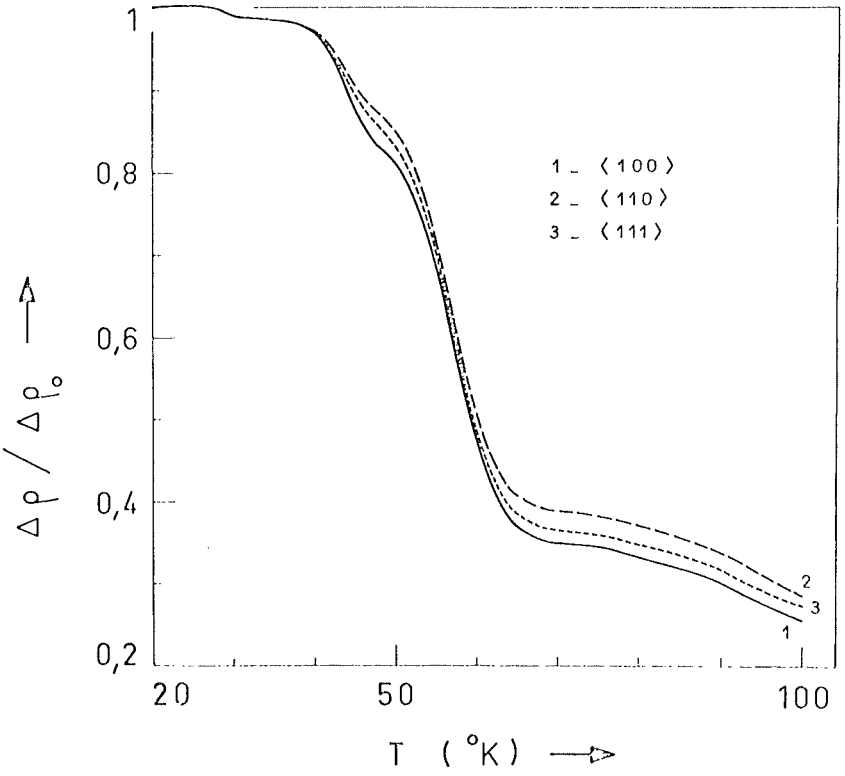

Fig. 2 Recovery of the resistivity of three electron-irradiated single crystals of nickel.

This curve shows a fine structure in two or three sub-stages of stage I_C and in numerous sub-stages of I_D.

b) Influence of Electron Beam Direction on the Recovery of a monocrystal

We have simultaneously irradiated at 20°K three very thin (30 μ) nickel single crystals of high purity. The electron energy was of 3 MeV and the cristallographic directions of the incident beam were $\langle 100 \rangle$, $\langle 110 \rangle$ and $\langle 111 \rangle$.

The experimental details of the preparation of the samples and the technique used for their irradiation has been discussed elsewhere [5]. We mention simply that the mean divergence of the electron beam within the sample was approximatly ten degrees. The resistivity increases were the same for all three samples to within 1 %, this small discrepancy could have resulted simply from a slight inhomogeneity in the beam.

Figure 2 shows the recovery of the resistivity increase of these three single crystals during the same linear temperature rise. It is seen that there is distinct influence of the bombardment direction on the percentage of different stages ; this is also shown in table I

		$\langle 100 \rangle$	$\langle 110 \rangle$	$\langle 111 \rangle$
I_B	23°K - 32°K	I.5	I.5	I.8
I_C	32°K - 48°K	15.5	11.4	12.9
I_D	48°K - 67°K	47.5	47.6	48.3

Another completly independent experiment has confirmed this distinct variation of I_C and the trends in I_B and I_D+I_E. This results will be discussed at the end of the article.

III - Internal Friction Experiments

The study has been undertaken for the following reason : In iron a very important magnetic after-effect band in the region of stage I_E has been reported and attributed to the reorientation of the free interstitial [6]. A corresponding internal friction peak has also been reported [7]. In nickel an equivalent magnetic after-effect has been found [8] and we wish to see if an associated internal friction peak is present.

a) Experimental Techniques

1 - Neutron Irradiations at 28°K

We irradiate six samples at liquid neon temperature (28°K). The retrieval and the mounting into the measuring pendulum is effected without warm-up or deformation of the sample. This very delicate technique is described elsewhere [9] ; one difficulty that had to be overcome was the elimination of parasitic internal friction peaks caused by adsorption of solid air onto the sample.

2 - Electron Irradiations at 20°K

On the contrary, in this kind of experiment the measuring pendulum is fitted into the irradiation cryostat which is evacuated of the liquid hydrogen coolant at the end of the irradiation. This elegant solution is very expensive because it only permits the study of one sample for the irradiation.

b) Results

Results are different depending on whether there is or not a magnetic field applied during the experiments.

1 - Without Magnetic Field

Figure 3 shows the internal friction peaks in polycrystal-

line nickel which has been irradiated at 28°K.

At the very low temperature, three very distinct peaks are revealed which are reproducible from one experiment to another. They are situated at 34°K, 37°K and 44°K and disappear very rapidly. Further, at 54°K there is a characteristic dip and then a plateau which emerges into definite peaks (59°K in particular). In the region of ambient temperature may be seen the peaks previously found by the German group [10].

Figure 4 shows a preliminary result for a nickel single crystal which has been electron irradiated at 20°K. A study of the effect of crystal orientation is presently being made ; this will give information on the symmetry of the associated defects.

2 - With Magnetic Field

In iron it is well known that application of a magnetic field reduces the background noise by diminution of the Bloch walls and this gives a much better resolution of the peaks. We have tried to repeat these experiments on nickel. In figure 5 are shown the results obtained with a longitudinal field of 400 oersted. The background is reduced in modest proportions ; by contrast the system of peaks situated between 30°K and 60°K is strongly attenuated. This very different behaviour of nickel will be analysed further.

IV - Discussions

a) Analogy between Internal Friction and Resistivity

A comparison of figures 1 and 3 allows us to label the internal friction peaks by giving them the names of the stages in the resistivity recovery positions at which they vanish.

Thus the three large internal friction peaks (34°K, 37°K, and 44°K) vanish at the position of stage I_C and we see that the resistivity curves are not incompatible with the superposition of three processes at this position.

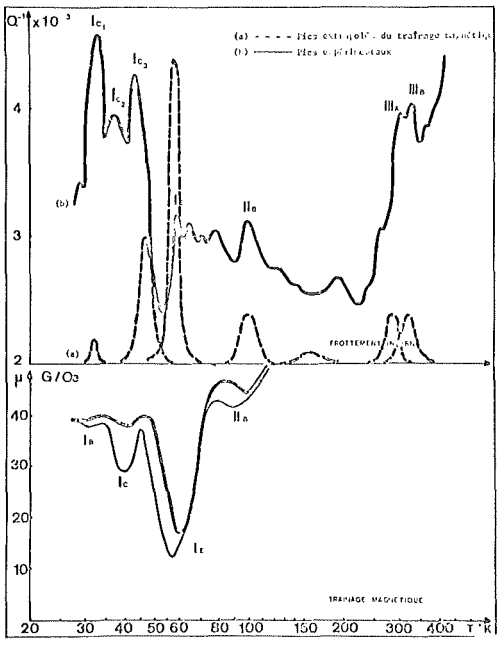

Fig. 3 Pure nickel after irradiation

- upper figure : Internal friction
  a) Peaks calculated from the magnetic after-effect,
  b) Peaks measured after neutron irradiation at 28°K.
- Lower figure : Magnetic after-effect after electron irradiation at 20°K.

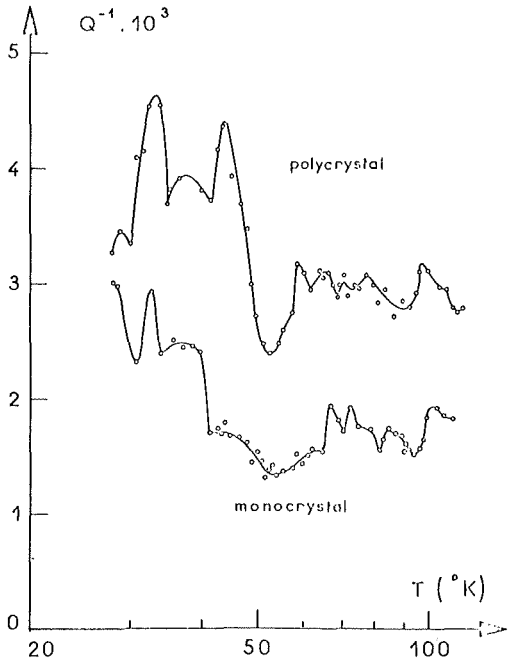

Fig. 4 Internal friction of pure nickel after irradiation

- polycristal : neutron irradiation at 28°K
- monocrystal : electron irradiation at 20°K.

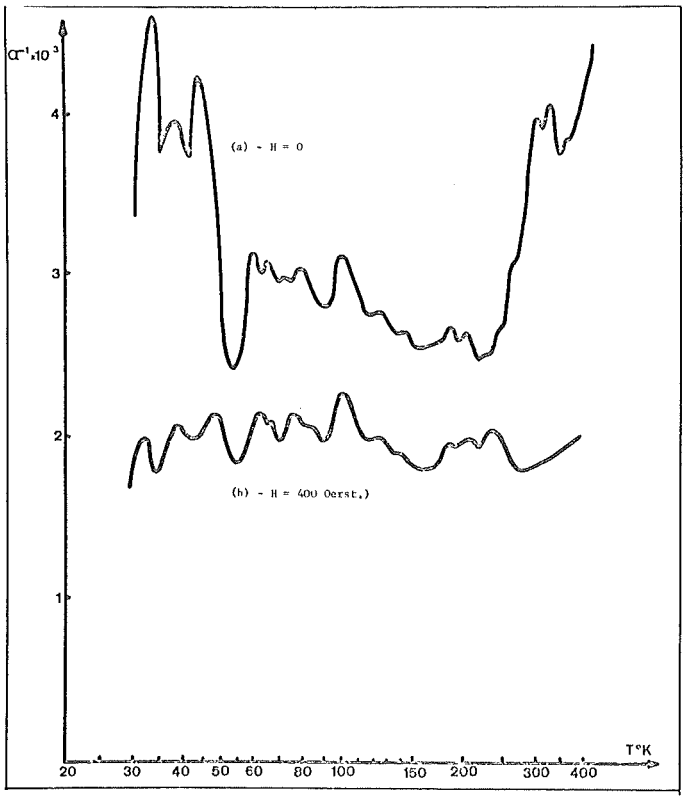

Fig. 5 Effect caused by saturating longitudinal magnetic field (400 oe) on the internal friction of pure, neutron irradiated (28°K) nickel.

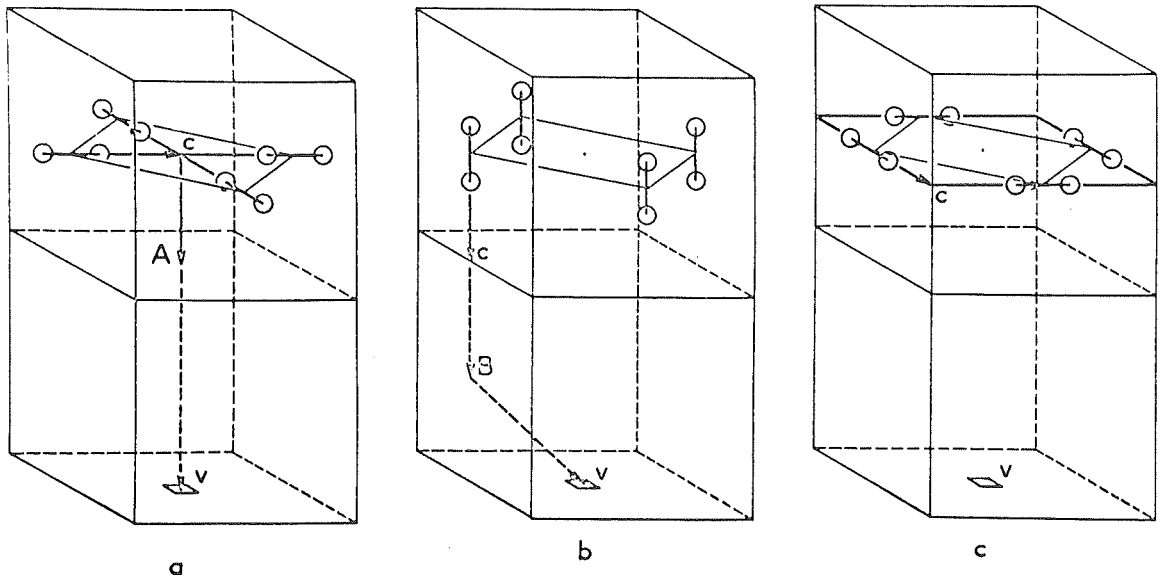

Fig. 6 The three types of close pairs proposed by P. PERETTO for stage I_C

On the other hand it appears that the large complex stage I_D in the recovery of the resistivity is not to be associated with an internal friction peak.

In the viccinity of stage I_E only small phenomena appear : a dip at 54°K and a little peak at 59°K.

b) Analogy between internal friction and magnetic after-effect

The lower part of fig. 3 recalls the magnetic after-effect results of P. PERETTO [8] obtained under analogous experimental conditions with nickel of the same origin.

With the objective of comparing one internal friction peak and one magnetic after effect band cause by a Snoek effect we advance the hypothesis that the defect responsible for each band of after-effect possesses a mechanical anisotropy of the same order as its magnetic anisotropy and then we trace the theoretical internal friction curve which is shown as a dotted line in fig. 3. The following comments arise :

The defects associated with stages I_{C3}, II_B, III_A, and III_B possess comparable magnetic and mechanical anisotropies.

We can say nothing about the defect I_B in the internal friction because at this frequency the peak would appear at a temperature (34°K) at which the stage I_B is already recovered (fig. 1).

It is important to note that the defect associated with stage I_E and which possesses a strong magnetic anisotropy, does not cause any large internal friction peak and is therefore characterised by a very weak mechanical anisotropy.

c) Attempt at identification of the different stages

1 - Stage I_B

Previous work [8] [11] has shown that stage I_B was asso-

ciated with the annealing out of a particular type of close pair. Measurements on single crystals of resistivity as a function of incident beam direction does not yield a difference which is sufficiently clear to be analysed in detail.

2 - Stage I_C

The interpretation proposed earlier by P. PERETTO [8] for this stage was the recovery of a particular type of close pair (Fig. 6.) We must see if our recent experiments confirm this hypothesis.

A) Resistivity experiments on single crystals

We see that stage I_C is clearly favoured by a bombardment in the direction $\langle 100 \rangle$. Let us examine the possibility of interpreting this effect with the proposed close pair model.

Four such close pairs exist around the $\langle 100 \rangle$ direction. They are situated on a cone of half angle $\theta = 18.5°$ as shown in fig. 7 (Note that the split interstitials are represented by their centres of gravity and that the axis of the split does not enter the argument).

Around one $\langle 110 \rangle$ direction there are two such close pairs disposed symmetrically on a cone whose half angle is $\theta = 26.5°$.

Lastly, around the $\langle 111 \rangle$ direction there are 6 close pairs of type I_C situated on a cone of half angle $\theta = 38.5°$.

Thus we see that the probability of creation of a pair of type I_C is significantly greater when the bombardment direction is $\langle 100 \rangle$. It is not surprising that the other two directions have probabilities of a similar order of magnitude because although there is a greater number of pairs possible for the $\langle 111 \rangle$ direction they are clearly more unlikely for this bombardment direction than for $\langle 110 \rangle$

Thus for I_C the resistivity experiments confirm the structure which has been proposed for the close pair.

B - Internal Friction Experiments

The internal friction experiments show that we may associate three relaxation peaks with stage I_C but if the pairs labelled a and c are able to give rise to a relaxation effect, this seems difficult for pair b. More precise experiments on the exact temperature of recovery of the internal friction peaks will permit us to clarify this point.

3 - Stage I_D

The resistivity measurements show that a fine structure exists to this stage. It is of interest to establish that the different types of defect anneal out at this stage without yielding a magnetic after-effect or an internal friction. If the corresponding defect is a close pair then it must be permitted that the interstitial rejoins its original vacancy without involving a process of reorientation on equivalent sites.

In the internal friction curve the very reproducible dip situated at 54°K and coincident with the termination of stage I_D was able to be associated with migration to dislocations thus diminishing the continuous background.

4 - Stage I_E

Previous work [8],[11] has permitted the association of stage I_E with the important band of magnetic after-effect corresponding to the free interstitial which would be in the split configuration in the $\langle 100 \rangle$ direction. The work presented here would indicate that the corresponding mechanical anisotropy would be weak. This experimental result confirms the calculation of HUTTINGTON and JOHNSON [12] which shows that the distorsion of the strain field is small for a $\langle 100 \rangle$ split interstitial in a f.c.c. lattice.

d) Effect of a Magnetic Field on the Internal Friction Peaks

The supression of the internal friction peaks upon the application of an axial field of 400 oersted could be explained by a

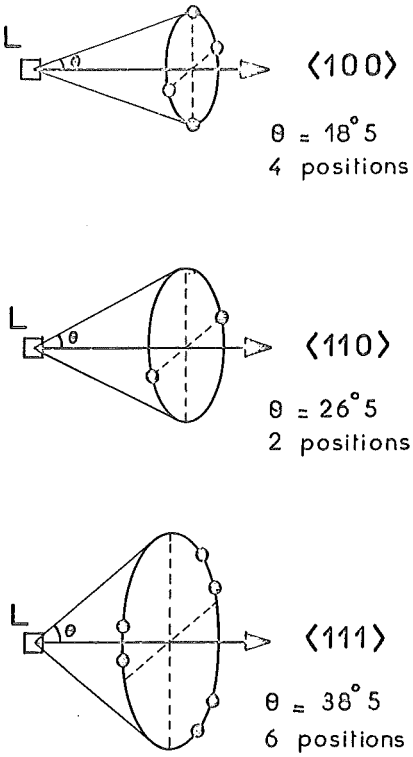

Fig. 7

Disposition of close pairs of type I_C around one bombardment direction.

change in the orientation of the magnetisation I_s . In the absence of a field, I_s lies parallel to the ⟨111⟩ direction and the three equivalent ⟨100⟩ sites are only slightly disturbed by the torsion which promotes the relaxation. When a field is applied I_s is reoriented away from ⟨111⟩ and so strongly favours one site that torsion is not able to promote a relaxation of defects with ⟨100⟩ anisotropy.

Conclusion

These experiments have yielded the most recent results obtained at the "Centre d'Etudes Nucléaires de Grenoble" on irradiation effects in nickel.

An important effect has emerged concerning the direction of the particles incident on a single crystal ; this involves an increase in the numbers of a particular type of close pair.

Also, an internal friction study has revealed the presence of numerous peaks and a model compatible with resistivity and magnetic after-effect is proposed.

REFERENCES

1 G.W. ISELER, H.I. DAWSON, A.S. MEHNER and J.W. KAUFFMAN
Physic Letter 17 - 3, 212 (1965)

2 H.I. DAWSON, G.W. ISELER, A.S. MEHNER and J.W. KAUFFMAN
Physic Letters 18 n°, 247 (1965)

3 F.W. WIFFEN, C.L. SNEAD and J.W. KAUFFMAN
Physic Letters 23 -1, 22 (1966)

4 M. BALARIN and A. ZETZSCHE
Phys. Stat. Sol. 2, 1670 (1962)

5 R. COPE and C. MINIER
to be published

6 P. MOSER, D. DAUTREPPE
J. Phys. Rad. 24, 516 (1963)

7 D. DAUTREPPE, V. HIVERT, P. MOSER, A. SALVI
C.R.A.S. 258, 4539 (1964)

8 P. PERETTO
Thèse 1967 - C.E.N.-G. B.P. 269 - GRENOBLE -

9 G. de KEATING-HART
Thèse 1968 - C.E.N.-G. B.P. 269 - GRENOBLE

10 A. SEEGER and F. WAGNER
Phys. Stat. Sol. 9, 584 (1966)

11 J.L. ODDOU
Thèse 1967 - C.E.N.-G. B.P. 269 - GRENOBLE

12 H.B. HUTTINGTON and R.A. JOHNSON
Acta Met. 10, 281 (1962)

ENERGY RELEASE and RESISTIVITY RECOVERY in COPPER DURING STAGE I RECOVERY*

T. H. Blewitt, A. C. Klank, Terry Scott and M. Lucas**
Metallurgy Division, Argonne National Laboratory, Argonne, Illinois

ABSTRACT

Simultaneous energy release and resistivity recovery during Stage I recovery have been made in copper irradiated in the CP-5 fast flux cryogenic facility as a function of the bombardment temperature. These temperatures have ranged from 20°K through 39°K. The stored energy was measured in situ by an improved Coltman-Blewitt[1] method with the sample being the bulb of a stem compensated gas thermometer. A resistor was cemented on the bulb and the resistivity was measured by the usual IR drop method during the bombardment and during recovery. The data of both properties were recorded automatically with the use of a digital voltmeter. This technique resulted in frequent readings of very short-time duration (of the order of tens of milliseconds).

The results were of considerable significance as the bombardment temperature greatly influenced the annealing kinetics. Bombardments at 20°K and 24.5°K showed a single annealing peak centered at 41°K with a one-to-one correspondence between the resistivity recovery and the energy release. The resistivity recovery following bombardment at 31°K and 33°K was markedly different from the energy release. The energy release curves show two distinct peaks with the first peak centered near 39°K and the second peak centered near

*This work was performed under the auspices of the U.S. Atomic Energy Commission.

**Presently with the University of Sussex, Sussex, England.

Fig. 1a

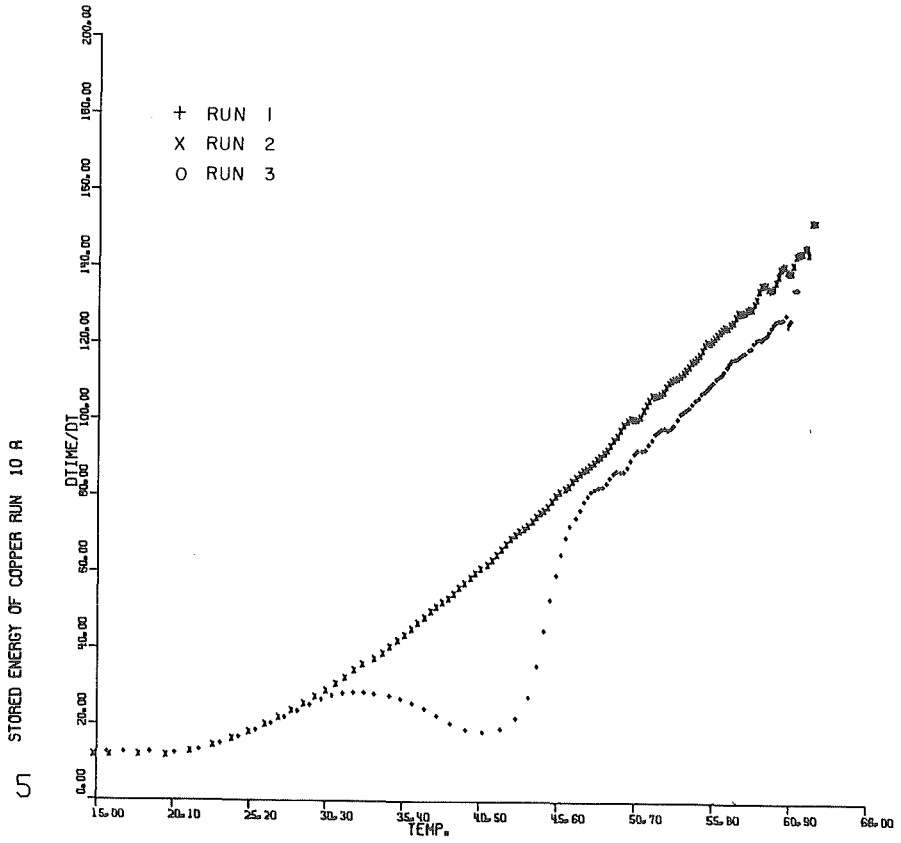

Fig. 1b

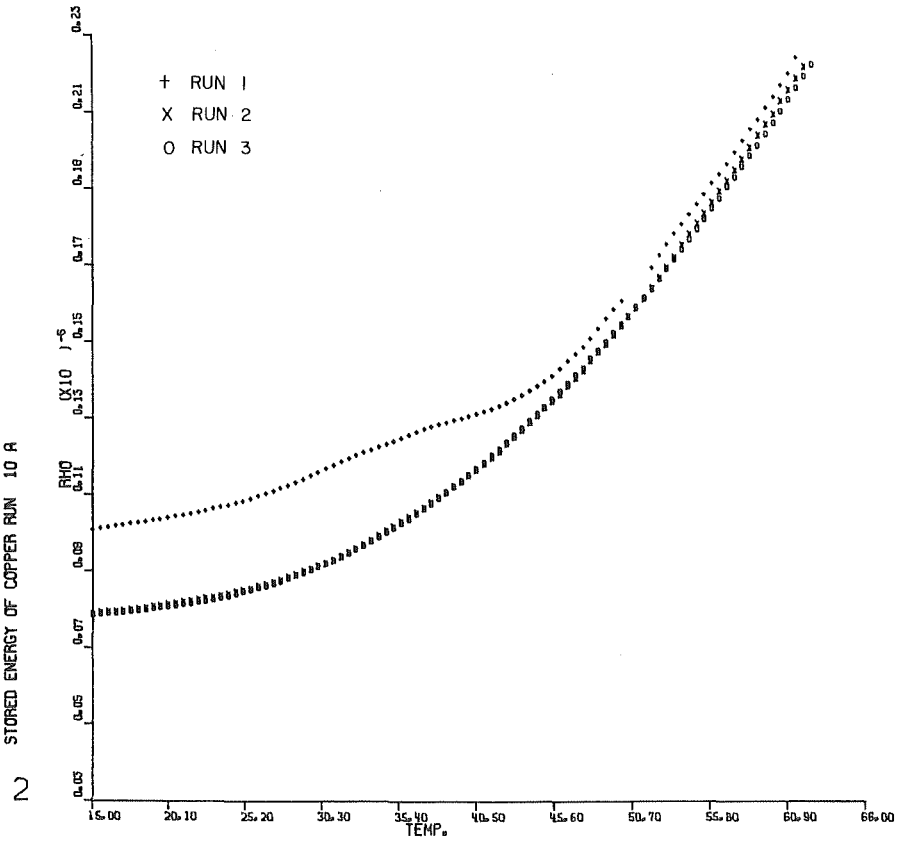

Figs. 1a and 1b. Stored Energy Release and Resistivity Recovery in Copper Bombarded at 24.5°K.

Fig. 2a

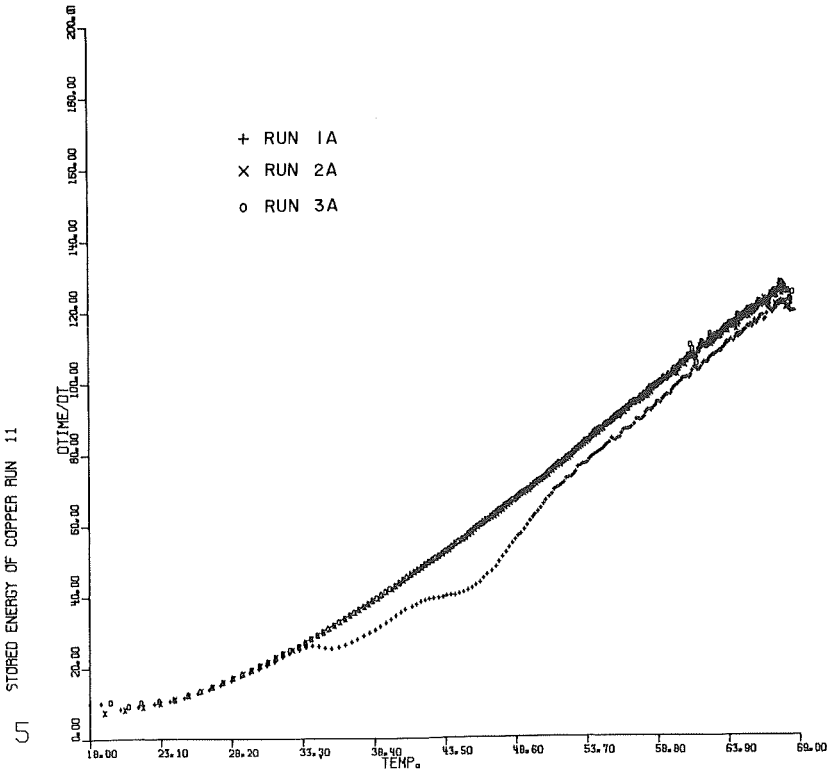

Fig. 2b

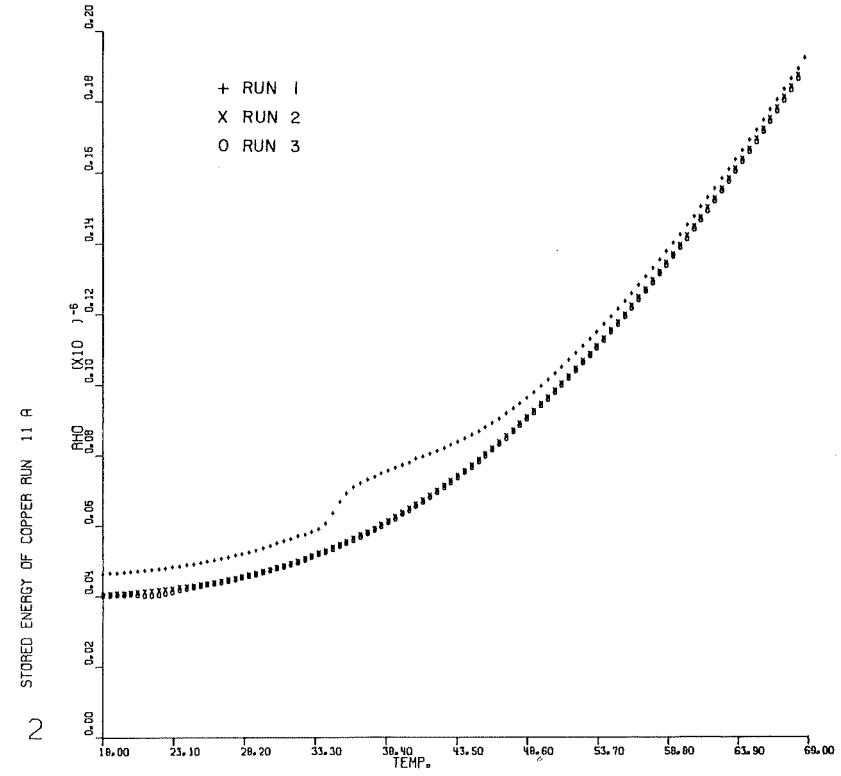

Figs. 2a and 2b. Stored Energy Release and Resistivity Recovery in Copper Bombarded at 33.0°K.

45°K. The resistivity increased by a factor of two during the initial part of the recovery, commencing at the bombardment temperature, continuing for several degrees, and then monatomically decreasing. A 28.5°K bombardment showed the same results as the 31°K and 33°K bombardment but much less markedly so. After a 39°K bombardment, no Stage I recovery was observed.

There can be little doubt the defect structure in a sample bombarded at 24.5°K is vastly different from that in a sample bombarded at 31°K.* Because the absolute temperature at which these effects are observed coincide with the onset of Stage I recovery, it is logical to attribute this difference to defect migration. Something more than simple annhilation is required, and, therefore, long-range migration of a defect, i.e. something greater than a few atomic distances, is suggested to account for the obvious clustering effects that occur. This conclusion would suggest that the two-interstital model of recovery would require a rather extensive revision, if indeed it could be salvaged. Furthermore, it is equally clear the correlated recovery model of Walker and Corbett is not applicable. Please see Figs. 1a, 1b, 2a and 2b.

Perhaps a more serious implication to radiation damage studies that arises from this work is the fundamental discovery that the electrical resistivity does not always reflect the defect concentration. This requires a serious re-evaluation of the conclusions deduced from resistivity measurements, particularly in regard to kinetic analyses.

---

*Studies of dependence of the rate change of resistivity (damage rate) on the neutron dose show an effect of bombardment temperature that supports this conclusion. These will be discussed in a separate communication.

1) Blewitt, T. H., Coltman, R. R. and Klabunde, C. S., J. Phys. Soc. of Japan, 18, Suppl. III (1963).

Effect of Annealing on the Lattice Parameter of Neutron-irradiated Aluminium and Copper

U.Himmler, H. Peisl, A.Sepp and W.Waidelich,
I.Physikalisches Institut der Technischen Hochschule Darmstadt
and W.Wenzl, Physik-Department der Technischen Hochschule München

Pure aluminium and copper crystals were irradiated in the low-temperature irradiation facility of the Munich Research Reactor at 4,6°K. After irradiation and thermal annealing lattice parameter change was measured. In aluminium recovery stages equivalent to that known from electrical resistivity, length and stored energy measurements were observed. The ratio $\Delta V/V \,/\Delta \varrho = 3{,}9 \cdot 10^{3} (\Omega\,\mathrm{cm}^{-1})$. The volume change per Frenkel pair $\Delta V = 1{,}4 \pm 0{,}1$ atomic volumes. In copper four recovery stages were resolved. Additional electrical resistivity and length measurements led to a ratio $\Delta V/V \,/\Delta \varrho = (7{,}6 \pm 0{,}2) \cdot 10^{3}\ (\Omega\mathrm{cm})^{-1}$ in stage I and $(5{,}4 \pm 1{,}0) \cdot 10^{3}\ (\Omega\mathrm{cm})^{-1}$ for all higher stages. Possible explanations for this difference are discussed.

1. Introduction

Defects in neutron-irradiated fcc metals have been investigated many times by measuring various physical properties of irradiated and annealed samples. Most information has been obtained from electrical resistivity measurements. Further insight can be expected by applying another method of investigation. E. g., defects give rise to a distortion of the crystal lattice and to a change of lattice parameter, which can be measured by the X-ray scattering method (1,2) . Comparing lattice parameter and length change one can separate effects due to distortions and due to the change of the number of lattice sites (3). Simultaneously measuring the electrical resistivity change

enables one to compare the data with other measurement and gives furthermore the ratio of volume change to resistivity change, which is a characteristic value for a certain defect, undependant from the property change per defect.
In the following we report about measurements of lattice parameter change in aluminium and copper after neutron-irradiation at 4,6°K and thermal annealing.

2. Experimental

The samples were irradiated in the low-temperature irradiation facility of the Munich Research Reactor at Garching (4,5) . As the X-ray diffraction measurements are not to be performed at the irradiation facility on the reactor bridge, it is necessary to transfer the samples without warming up from the irradiation crystat to the X-ray measuring cryostat. The samples are transfered to a liquid helium container and brought to the X-ray laboratory. There they are transfered to the measuring cryostat. All transfers are made with the aid of a specially constructed transfer and transport cryostat. High accuracy lattice parameter change is obtained from the shift of a high angle X-ray diffraction peak.

21. Samples

Pure aluminium foils (99,999%) of about 5x10x0,5 mm^3 size were used for this investigation. To increase the reflected X-ray intensity they were produced by rolling them to 5% of its original thickness and then glowing above the recrystalisation temperature.
Pure copper single crytals (99,999%) of about 5x10x2 mm^3 size were used for the X-ray investigation and pure polycrystal copper wires (99,999%) for the electrical resistivity measurements.
The samples are fixed to a sample holder allowing their free thermal expansion.

2 2 Irradiation and sample transfer

The samples were irradiated by the fast neutron flux in the reactor(6,7). After irradiation for about 50 to 100 hours and decay of the short-lived isotopes created in the sample and sample holder, the sample can be lifted without warming up into a transport cryostat which is shown in Fig. 1. The inner container can be filled with 0,5 l liquid helium and then the sample, which is fixed at the end of a 10m stainless steel tube, can be lifted from the irradiation cryostat into the transport cryostat and immersed in the liquid helium. The liquid helium filling lasts for half an hour, which is enough time to dismount the transport cryostat from the low temperatur irradiation facility and take it to another place. During transportation evaporating helium blows out trough the opening at the bottom of the cryostat such preventing air to enter into the cryostat. The transport cryostat is now mounted to a liquid helium container and the sample transfered into this container. Here it can be stored and transported to the measuring laboratory. The transport cryostat is again used to bring the sample from the liquid helium container into the measuring cryostat.

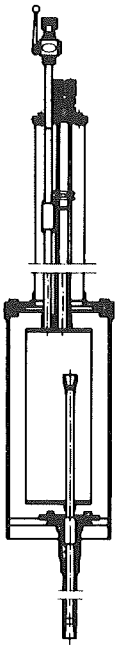

Fig. 1. Transport cryostat

23. Cryostat for the X-ray measurements

As the cryostat and the X-ray setup used for the aluminium measurements has already been described in detail (8) only a short describtion of the improved experimental arrangement used for the copper measurements will be given.
The cryostat used for the X-ray measurements is shown in Fig. 2. The sample holder is brought in a fixed position in the cone 5 inside the sample chamber, which is filled with helium gas as exchange medium. The cone 5 is cooled by a heat exchanger 6 according the evaporation principle (9). Liquid helium is pumped through a thin walled stainless steel tube 7 from a storage container to the cryostat. The enthalpy of the cold helium gas is further used to cool down some irradiation shields 1 and 2. The amount of liquid helium pumped through the heat exchanger is controlled by an arrangement consisting of a thermocouple, potential measuring bridge, a galvanometer, photo resistances and electromagnetic valves. Thus every temperature between $4^{o}K$ and room temperature can be obtained. An additional heating accelerates the heating process during thermal annealing programms.
Two windows of berryllium 3 and 4, each 0,2 mm thick, permit entrance and exit of the X-rays.
The cryostat can be seated on a commercial X-ray diffractometer, the axis of which had been bored through. The supply tube 7 fits in a liquid helium storage container situated under the diffractometer table. A special refilling equipment allows the storage container to be refilled.

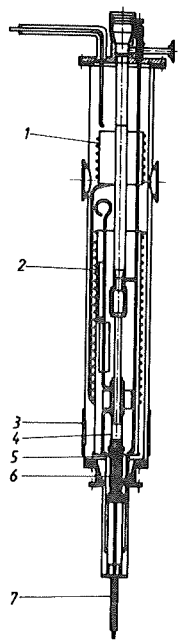

Fig. 2. X-ray measuring cryostat.

24. X-ray measurements

The exact position ϑ of a Bragg X-ray scattering peak was determined by a modified Siemens X-ray diffractometer. The shift $\Delta\vartheta$ of a high angle peak is a sensitive measure for the lattice parameter change $\Delta a/a$

$$\Delta\vartheta = - \Delta a/a \cdot \tan\vartheta \qquad (1)$$

As well for Al as for Cu with characteristic Co K_α X-radiation the highest diffraction angle was obtainable using (420) and (400) planes respectively. The diffraction peaks occured in the back reflection region at about $\vartheta = 80^\circ$, having a half width of about 15'.

25. Annealing programm

For isochronal annealing the crystals were warmed in steps to successively higher temperatures with an isochronal holding time of 10 min. An annealing programm performed with an unirradiated sample showed that the thermal treatment had no effect to the position and intensity of the X-ray according to mechanical deadjustment.

3. Results

Fig. 3. shows isochronal annealing of aluminium, which had been irradiated for 55,6 h at 4,6°K by a total flux of $2 \cdot 10^{18}$ fast neutrons/cm^2. The remaining lattice parameter change after thermal annealing at a given temperature measured at liquid helium temperature is given as a function of annealing temperature. The total annealing lattice parameter change between 4,6 and 300°K is $\Delta a/a = (4{,}4_7 \pm 0{,}4) \cdot 10^{-4}$. The annealing takes place in three distinct annealing stages:

Stage I:	10 - 50	^{o}K,	42% recovery
Stage II:	50 - 120	^{o}K,	25% recovery
Stage III:	120 - 250	^{o}K,	33% recovery

The half width of the diffraction peaks didn't change neither after irradiation nor during annealing.

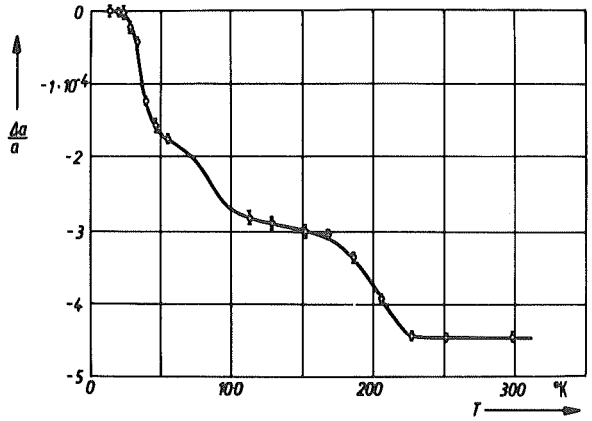

Fig.3. Isochronal annealing of the relative lattice parameter change of aluminium after low-temperature neutron irradiation.

Several measurements were performed in the case of copper. Simultanously with the irradiation of the lattice parameter sample, a sample with the same purity was irradiated for measuring the electrical resistivity change. Fig. 4. shows the change of residual electrical resistivity versus neutron irradiation

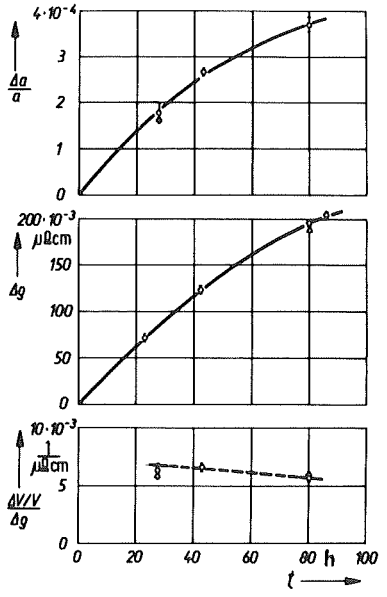

Fig. 4. Change of electrical resistivity and relative lattice parameter after neutron irradiation.

flux in the upper part. In the middle the relative lattice parameter change is given from different samples irradiated for different times in the reactor. The lowest part of Fig. 4 shows the ratio relative volume change $\Delta V/V = 3\,\Delta a/a$ to electrical resistivity change versus irradiation time.

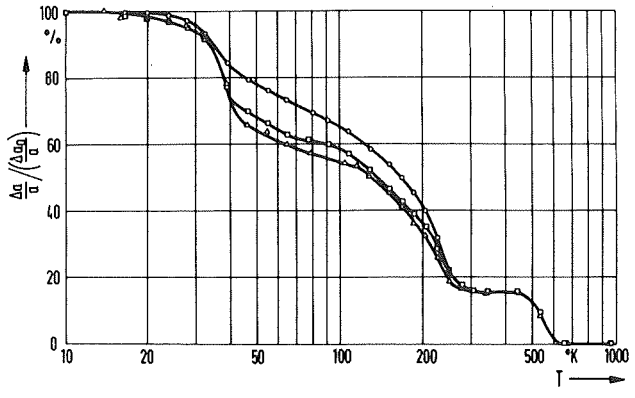

Fig.5. Isochronal annealing of neutron-irradiated copper. Triangles and squares: rel. lattice parameter change, circles: el. resistivity change.

Fig.5 shows annealing of the relative lattice parameter change $\Delta a/a$ measured at liquid helium temperature as a function of annealing temperature for two runs. For normalization the values are divided by the total change $\Delta a_o/a$. The samples were annealed at such high temperatures that one could be sure that all defects had disappeared. Furthermore the lattice parameter of the annealed sample agreed with that of an unirradiated sample.Annealing of the electrical resistivity change after neutron irradiation at the same position in the reactor is shown for comparison in Fig. 5 too. The annealing of neutron irradiated copper takes place in four distinct annealing stages:

StageI:	4	- 60 °K
Stage II-III:	60	- 300°K
Stage V:	300	- 670°K

Although the temperature regions of recovery are the same for lattice parameter and resistivity change, the relative height of the stages is different for the two different properties.

4. Discussion

The volume change caused by defects in a finite crystal has been derived by Eshelby (10) to be

$$(\Delta V/V)_{dist.} = 4\pi\, C\, \gamma\, S / 3\Omega = f \cdot C \qquad (2)$$

$\Delta V/V$ being the relative volume change caused by the distortion of the crystal lattice by a concentration C of defects with a distortion strength S. $\gamma = 3(1-\sigma)/(1+\sigma)$. σ = Poisson ratio. This volume change is determined solely by lattice parameter measurements. Measuring the macroscopic volume change directly gives the sum of volume change according eq. (2) and the volume change by the change of the number of lattice sites. The total volume change is

$$\Delta V/V = C_V - C_V f_V - C_I - C_I f_I \qquad (3)$$

C_V = vacancy concentration, C_I = interstitial concentration, $f_V = f_I$ = volume change per vacancy or interstitial.

For small changes in a cubic crystal $\Delta V/V = 3\Delta L/L$ and $(\Delta V/V)_{dist.} = 3\,\Delta a/a$. Thus eq. (3) becomes

$$3\,(\Delta L/L - \Delta a/a) = C_V - C_I \qquad (4)$$

In the case that pure Frenkel disorder is present in the crystal one expects $\Delta L/L = \Delta a/a$, $C_V = C_I$. If lattice sites are newly created or destroyed, the difference gives directly the concentration of lattice sites.

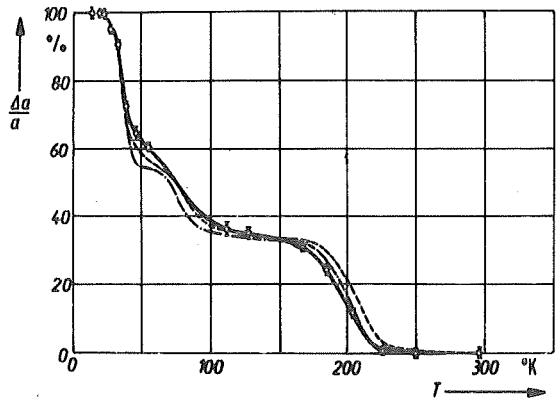

Fig. 6. Annealing of low-temperature neutron-irradiated aluminium.
-.-. Length change and
--- el. resistivity change from (11).

In Fig.6. for comparison the annealing behaviour of the length change and the residual electrical resistivity measured by Wenzl et al. (11) are given together with the lattice parameter data. Within experimental error all magnitudes are equal within the whole annealing run. $\Delta L/L = \Delta a/a$ gives evidence that during irradiation and annealing only Frenkel disorder is present in the crystal. Recovery in each stage must be due tothe recombination of interstitials and vacancies, whatever the initial configuration of these defects might have been.

In Fig.6 also lattice parameter change and electrical resistivity change shows the same behaviour. The annealing volume change divided by the annealing resistivity change $(\Delta V/V)/\Delta\varrho = (3{,}9 \pm 0{,}6)\cdot 10^3\ (\Omega cm)^{-1}$ is the same for all three stages. The ratio $(\Delta V/V)/\Delta\varrho$ is a characteristic magnitude for a certain defect. In all three stages the same defects anneal, which are different in their configuration but not in their specific properties. Taking the value for the resistivily change by 100% defects obtained by Wenzl et al. (11) $\varrho_F = 340\ \mu\Omega cm$, we can determine the volume change by one defect pair:

$$\Delta V_F = 1{,}4 \pm 0{,}1 \text{ atomic volumes.}$$

As the value of $(\Delta V/V)/\Delta\varrho$ is the same in stage I and III this value should not be influenced by some overlapping of the defects' distortion fields in cascades created during neutron irradiation.

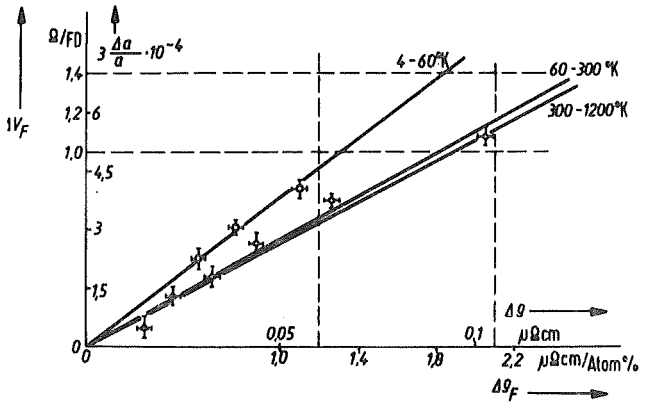

Fig. 7.

Fig. 7. shows the amount of annealing volume change versus annealing resistivity change in the various recovery stages for copper which had been irradiated for different times. Within experimental error three straight lines are obtained. The slopes of the straight lines are:

$$\frac{3\,\Delta a/a}{\Delta \varrho} = \frac{\Delta V/V}{\Delta \varrho} = \begin{cases} 7{,}63 \pm 0{,}22 & (4 - 60\ ^{\circ}K) \\ 5{,}53 \pm 0{,}23\ (m\Omega cm)^{-1} & (60 - 300\ ^{\circ}K) \\ 5{,}34 \pm 0{,}59 & (300 - 1200\ ^{\circ}K) \end{cases}$$

As the points fit straight lines very well the specific defect property annealing in the different recovery stages must be independant on the irradiation dose. The ratio is nearly independant on the irradiation dose during irradiation, as shown in Fig. 4 lower part.
The different slopes of the straight lines show that the defects involved in the different recovery stages are different in their characteristic properties.

As the most simple model for the recovery process one could take the recombination of interstitials with vacancies. These defects exist in different configurations, thus giving rise to the different recovery stages. This model would lead to the following results. In Fig. 7 on the ordinate the volume changes per Frenkel defect pair are marked, according to the calculations for different interstitial configurations of Seeger et al. (12). On the abscissa the resistivity changes per unit concentration of Frenkel defects according measurements of Iseler et al. (13) are marked. Thus for every temperature region a pair of possible values can be determined.
If one assumes that the resistivity change per Frenkel defect does not very much depend on the configuration of the interstitial, wheras the volume change, or lattice parameter change respectively, depends on the configuration, a volume change per defect in the different temperature regions can be evaluated:

4 - 60 °K : ΔV_F = 1,4 atomic volumes
60 - 300 °K : ΔV_F = 1,1 atomic volumes

This explanation is not in agreement with the results obtained by Winkler et al. (14) from magnetorestistance measurements, which is sensitive on anisotropic defects or defect clusters. From this results formation of clusters during annealing must be taken into account. Vacancy clusters in neutron irradiated Cu have also been detected by Rühle (15) above room temperature. The following model would be in agreement with these results too.

During irradiation vacancy clusters are formed in the depleted zones. Recovery in stage I takes place by different processes. The main process is recombination of closed pair Frenkel defects. According to Bauer et al. (16) also a transformation of interstitials to a more stable configuration takes place, probable by the action of a reaction partner. During this transformation the resistivity should be altered only little. The lattice distortion however should be remarkable reduced and so the volume change should be great. In the higher recovery stages interstitials in more stable configurations are annihilated. At the same time the stable interstitials can form clusters, which is observed as an increasing of the magnetoresistance (14). By the free migration of the interstitials also growing of the larger clusters on account of the smaller ones is possible.

The created vacancy and interstitials clusters anneal in stage V.

To explain the different ratios $(\Delta V/V) / \Delta\varrho$ in stage I and in the higher stages, the volume change by the stable interstitial Frenkel pairs must be smaller than by the Frenkel pairs which anneal in stage I. Further the formation of clusters from stable interstitials must give a smaller volume change than the transformation of unstable to stable interstitials.

Acknowledgements

The authors acknowledge the support by Prof. Dr. H. Maier-Leibnitz and Prof. Dr. N. Riehl, and the excellent cooperation with the staff at the Forschungsreaktor Munich.

References

1 R.O. Simmons and R.W. Balluffi; Phys.Rev. 109, 1142 (1958).

2 R.W. Balluffi and R.O. Simmons; J.Appl.Phys. 31, 2284 (1960).

3 R.O. Simmons, in Radiation Damage in Solids, New York, Academic Press 1962.

4 R.Doll, H.Meissner, N.Riehl, W. Schilling, and F. Schmeissner; Z.angew.Phys. 17, 321 (1964).

5 H. Meissner, W. Schilling, and H. Wenzl; Euro Nuclear 2,277 (1965

6 W. Köhler; FRM Bericht Nr. 52 (1963).

7 W. Köhler, and K. Knopf; FRM Bericht Nr. 82 (1966).

8 U. Himmler, H. Peisl, A. Sepp, W. Waidelich, and H. Wenzl; Z. angew. Phys. 23, 8 (1967).

9 see e.g. G. Klipping; Kältetechnik 13, 250 (1961).

10 J.D. Eshelby; Solid State Physics 3, 79 (1956).

11 K. Isebeck, F. Rau, W. Schilling, K. Sonnenberger, P. Tischer, and H. Wenzl; phys.stat.sol. 17, 259 (1966).

12 A. Seeger, E. Mann, and R.v. Jan; J.Phys.Chem.Solids 23, 639 (1962).

13 G.W. Iseler, H.I. Dawson, A.S. Mehner, and I.W. Kaufmann; Phys.Rev. 146, 468 (1966).

14 S. Winkler; Dissertation TH München (1967).

15 M. Rühle; phys.stat.sol. 19, 263 (1967).

16 W. Bauer, A. Seeger, and A. Sosin; Phys. Letters 24A, 195 (1967).

Dilatometric Studies of Radiation Damage in Metals

S. N. Buckley

Metallurgy Division, A.E.R.E., Harwell, England.

1. Introduction.

Inability to resolve individual point defects in bulk metal has forced experimentalists to resort to various subterfuges for their identification and measurement of concentration, mobility and interaction. Some of these indirect techniques yield more clearly interpretable results than others, but it is always difficult to untangle the complications which arise from their interplay with co-existing defects. The less equivocal techniques such as dilatometry unfortunately also tend to be relatively insensitive.

Although dilatometry offers the distinct advantage of discriminating between vacancies and interstitials, it has not hitherto been regarded as an attractive method for studying defect migration because specimens thin enough to be transparent to charged particles of a few MeV energy are too delicate to actuate conventional mechanical or electrical sensors. Vook and Wert[1] resorted to direct optical metrology, but resolution is inexorably limited to about a wavelength so total defect concentrations in annealing studies need to be at least 10^{-3} (compared with 10^{-5} for resistivity[2]), which can only be realised by rather protracted irradiations.

The present paper describes how this inherent insensitivity was mitigated by measuring the inhomogeneity of defect concentration instead of the average concentration. These concentration gradients were deduced by measuring the flexures induced in thin crystal foils during irradiation by a $2\frac{1}{2}$ MeV proton beam from a Van de Graaff accelerator. Foil thicknesses were adjusted so that the beam energy was attenuated by a $\frac{1}{2}$ MeV in passing through; the E^{-1} dependence of Rutherford scattering them resulted in an approximately linear 20% gradient in Frenkel pair generation rate across the foil thickness, and strains associated with the ensuing accumulation of defects flexed the foil.

2. Experimental Techniques.

The experimental arrangement, which is illustrated in Figure 1 consisted of a sample holder horizontally coupled to the Van de Graaff flight tube and a sensitive optical lever system, and vertically coupled to cryogenic and heating equipment and vacuum diffusion pumps.

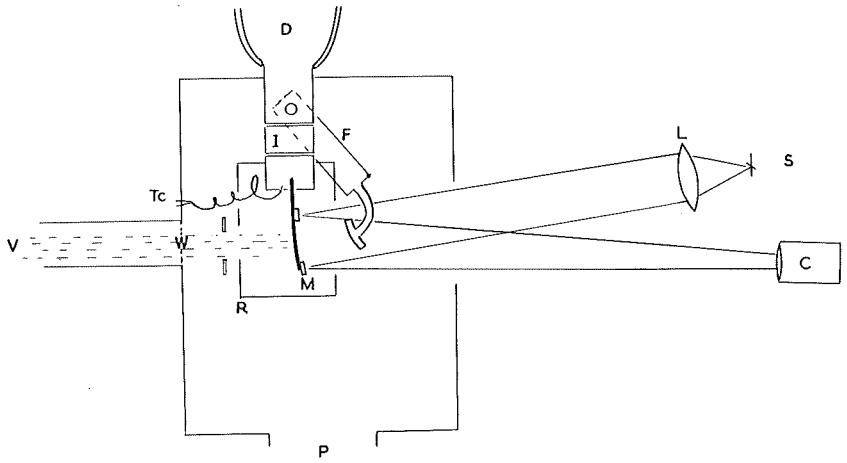

Fig. 1. Schematic diagram of the apparatus.
V, Van de Graff flight tube with optional window W used during gas cooling; I insulator; D base of helium dewar; F pivated cold finger; M mirror; S light source illuminating fiducal line; L lense; C image viewing camera; P diffusion pump; Tc thermocouple; R radiation shield.

The accelerator delivered a monoenergetic proton beam having a 4 x 2 mm eliptical profile. Energies of the incident and exit beams were deduced from the residual range in air. Specimens were 2 x 12 mm 5 to 8μm thick strips of foil partly severed down the length to create a 'U' shaped circuit whose resistance could be measured to indicate the local temperature. Monocrystal foils were made by mounting 100μm thick slices spark machined from 1 cm diameter crystal ingots on wax covered glass plates and then grinding them down to a uniform 30μm with diamond abraisive. After demounting and a preliminary electropolish to about 15μm the foils were etched while being held in a PTFE mask shaped to generate the required 'U' profile, then electropolished down to the required thickness, and finally annealed for 1 hour at 400°C while sandwiched between flat sapphire plates in a vacuum of 10^{-6} torr. Thicknesses were measured prior to annealing using a mechanical comparator reading to $\pm$ 2 x 10^{-6} cm.

Some excessive thinning was evident near foil edges but this and other local inhomogeneities should not be prejudicial to the interpretation. The optical system system consisted of an illuminated fiducal line, a high grade 30 cm focus lense, a pair of 2 mm square aluminised fragments of glass microscope cover slide cemented to opposite extremities of the specimen, and a television camera coupled to a remote receiver. Sensitivity was such that 10^{-7} strain across the specimen thickness produced about 1 mm relative displacement of the final images. A stream of air issuing from an orifice very precisely aligned to be parallel to the plane of the foil cooled the specimen during the ambient temperature irradiations. Exchange gases quickly impaired the reflectivity of mirrors at low temperatures so,as previous experience had demonstrated that cold foils could be slightly flexed without incurring significant irradiation creep, cooling during the irradiations prior to annealing studies was improved by direct thermal contact with a 5 cm radius cylinder pivoted to the base of the helium dewar. This and a short circuiting conductor between the cold finger and the specimen block and radiation shields had to be disconnected before commencing the isochronal annealing studies. Specimen temperatures were controlled by a small electrical heater incorporated in the block and measured with a fine copper constantan thermocouple secured against the clamped end of the foil. Measurement of strain gradients avoids the usual necessity for re-cooling between annealing pulses, so temperatures were raised progressively by $4^{o}K$ increments each held for 20 minutes duration. No attempt has been made to assign activation energies to the recovery kinetics because preliminary experiments, in which the thermocouple temperatures were compared with changes in electrical resistivity of the specimen, indicated the possibility of discrepancies of up to $7^{o}K$. Attention to radiation shielding should mitigate this error in future work.

3. Experimental Results.

The character of dilations manifest during proton irradiations at or above ambient temperatures was very sensitive to the metallurgical condition of the specimen. Annealed foils initially developed a convex surface

to the incident beam, whereas cold rolled metal became concave. Figure 2 illustrates these differences in nominally 5N purity gold.

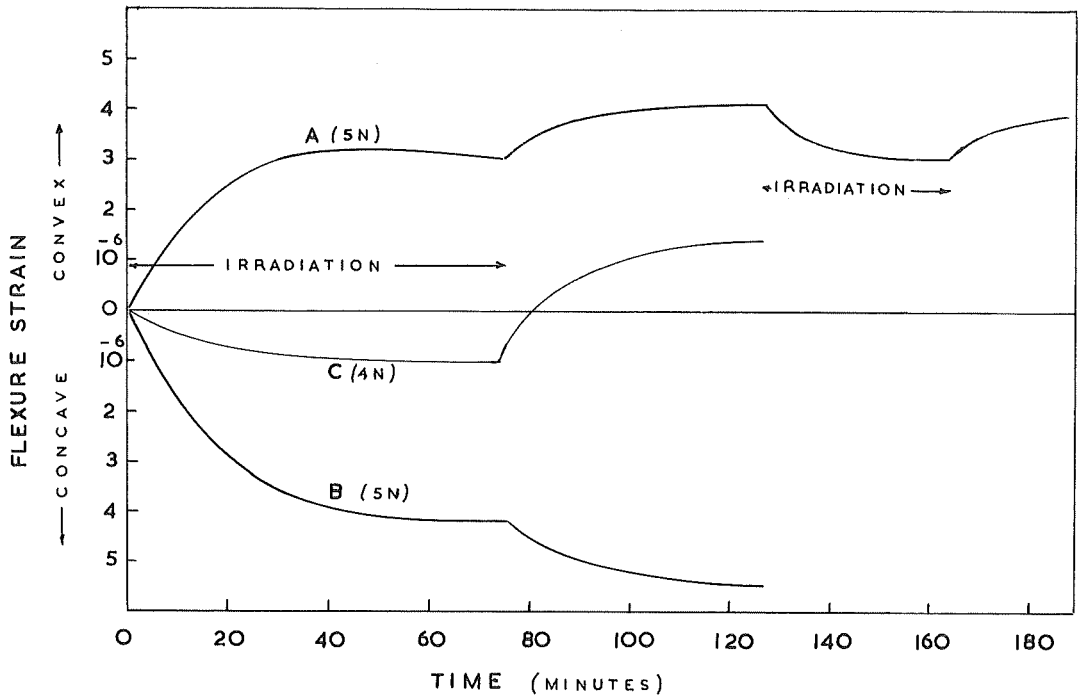

Fig. 2. Flexures of 5N and 4N purity gold during and after irradiation by 3.2×10^{12} $2\frac{1}{2}$ MeV protons cm^{-2} sec^{-1} at $300^{\circ} \pm 10^{\circ}K$, A annealed crystal; B cold rolled metal.

The progressive flexure of the annealed crystal, curve 'A' gradually attenuated during irradiation, and, after approaching a maximum strain about 3×10^{-6} at 10^{16} protons cm^{-2}, slowly reversed to annul the initial deflection. After 75 minutes irradiation the beam was switched off and the crystal immediately began an additional transient flexure of magnitude 1×10^{-6} over a period of 35 minutes. Re-irradiation reversed the latter transient and this cyclic behaviour, could be reproduced repeatedly. Cold worked metal, curve 'B', exhibited a similar trend of attenuation, saturation and post irradiation transients in the concave flexure. The magnitude of the transients tended to increase with decreasing metal purity. γ uranium for example (figure 3), which contained 10 a/o molybdenum and between 10^{-4} and 10^{-3} concentration of interstitial impurities, saturated after almost 10^{-4} strain and post irradiation transients were about 4×10^{-6}.

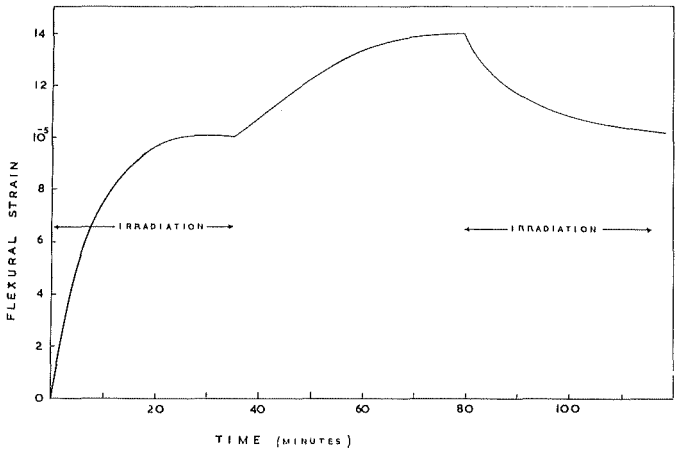

Fig. 3. Flexures of γ uranium during and after irradiation by 5×10^{12} $2\frac{1}{2}$ MeV protons cm^{-2} sec^{-1} at $300^{\circ} \pm 10^{\circ}K$.

All specimens, irrespective of purity or metallurgical condition developed concave curvature during low temperature irradiations, but the kinetics of recovery of flexure of cold worked metal were significantly different from that of annealed metal. Comparative isochronal annealing results on 5N purity copper are shown in figures 4 and 5.

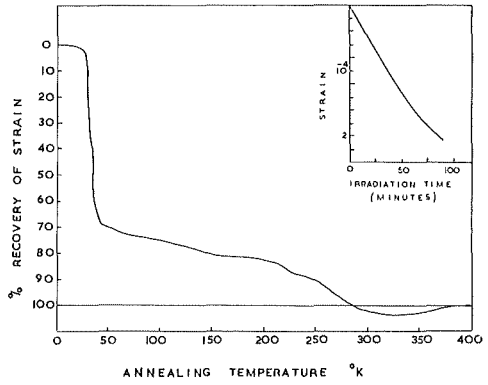

Fig. 4. Flexure of a 5N purity copper crystal during irradiation by 6×10^{12} $2\frac{1}{2}$ MeV protons cm^{-2} sec^{-1} at $12^{\circ} \pm 8^{\circ}K$ (in set) and recovery during subsequent isochronal annealing.

Both annealed and cold rolled specimens developed flexural strains of the order 1.5×10^{-4} after 1.5×10^{16} protons cm^{-2} dose at $12^{\circ}K$. About 70% of this strain had annealed out of the former by $50^{\circ}K$, another 10% gradually

recovered between 50° and 230°K and flexure was back to zero at 280°K. Recovery was however still incomplete because further warming reversed the direction of flexure leaving a 3×10^{-6} convex strain which did not disappear until temperatures approached 400°K. Strain recovery of copper which had been cold rolled prior to irradiation was similar to that of the annealed metal in so far as the principal stages were centred on about 40° and 250°K, but differed in that there was a 15% reversal of recovery between 50 and 60°K, a further 5% reversal between 200° and 260°K and no convex strain above 300°K.

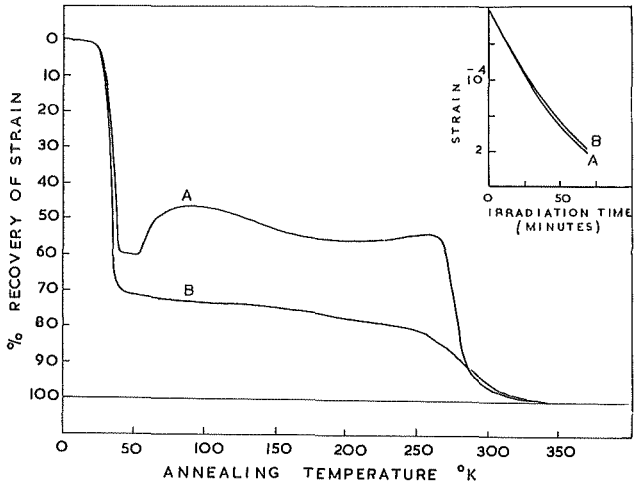

Fig. 5. Flexure of cold rolled 5N purity copper during irradiation by 5×10^{12} $2\frac{1}{2}$ MeV protons cm^{-2} sec^{-1} at 12° ± 8°K (in set) and recovery during subsequent isochronal annealing, A rolling direction parallel to flexure; B rolling direction transverse to flexure.

4. Discussion.

The flexural strains summarised in the preceeding section must be explicable in terms of strain gradients induced by the irradiations and by subsequent annealing treatments. Conceivable dilation centres are trapped protons, i.e. interstitial hydrogen and single or multiple vacancies and self interstitials. Concentration gradients will arise (a) because the frequency of Frenkel pair generation increases as protons slow down in penetrating the specimen (b) if the point defect sink distribution is asymmetrical (c) because of the tendency for displacement and irradiation stimulated diffusion to be preferentially in the forward direction. Contributions 'b' and 'c' are hard to evaluate precisely but as they will be trivial relative to 'a' we shall omit them from

further discussion.

Effect 'a' arises because the displacement cross section $\delta_d = 4\pi \frac{M_1}{M_2} Z_1^2 Z_2^2 \frac{E_R^2}{E_d} \frac{1}{E}$ varies inversely with proton energy E whereas the mean energy $\bar{E} = E_d \ln\left\{\wedge \frac{E}{E_d}\right\}^{(3)}$ of the recoiling nucleus is relatively insensitive to proton energy. The density of defect production therefore increases approximately linearly as the proton decelerates. δ_d for $2\frac{1}{2}$ MeV protons is about 10^{-20} cm^2. A 1μ ampere cm^{-2} beam losing $\frac{1}{2}$ MeV during penetration will consequently generate some 1.3×10^{-2} concentration of Frenkel pairs per hour with an approximately 20% gradient of concentration between entry and exit surfaces. If each Frenkel pair produced $3/2$ atom volumes dilation, specific differential linear strains would be 6×10^{-20} per proton per cm^{-2} or 1.3×10^{-3} per hour. Experimental strains at 12°K (figures 4 and 5) were only about 1×10^{-20} per proton per cm^{-2} but this discrepancy does not seem unreasonable because some spontaneous recombination is inevitable. The smaller convex flexures manifest during ambient temperature irradiations (figures 2 and 3) are similarly explained by postulating that some of the now rapidly migrating interstitials escape to the foil surfaces leaving a residual concentration gradient of excess individual and multiple vacancies. The curious transients evident after cessation of irradiation must be associated with the gradual elimination of strain centres. There are three possibilities. 1. Escape of interstitial hydrogen to the surface. 2. Escape of self interstitials 3. Annihilation of vacancies at dislocation lines, but not at foil surfaces. The first explanation seems unlikely because for foils whose thicknesses were only $1/5$ of the mean proton range the probability of non penetration by an initially monochromatic proton beam is $<10^{-3}$. Linear strains due to retention in interstitial lattice sites would therefore be expected to be $<10^{-24}$ per proton cm^{-2} which is small compared with the experimental 2×10^{-22} strain per proton cm^{-2}. Possibility 3. is untenable because in cold worked metal, where dislocation lines replace foil surfaces as the principal sinks, the direction of the ambient temperature transient reverses to become concave, which signifies dilation. Only self interstitials are consistent with all the evidence.

We expect annealed metal to shrink as interstitials are lost to the foil surfaces, but cold rolled metal can expand unidirectionally as interstitials drain into edge dislocations, because the 'isotropic' dilation of a free interstitial becomes concentrated in the Burgers vector direction of the climbing dislocation. Rolled metal foils have a preferred Burgers vector orientation parallel to the rolling direction which was the direction of flexure.

The close similarity between the isochromal annealing kinetics of strain recovery in low dislocation content copper (figure 4) and numerous previous studies of radiation damage recovery using other techniques, principally electrical resistivity[2][4], is re-assuring and consistent with the expectation that the majority of defects are destroyed by Frenkel pair recombinations. Remembering that only interstitials can contribute to the irradiation produced dilation we see that although about 70% are lost in stage 1 nearly 10% i.e. 10^{-4} concentration survive to 250°K. The latter greatly exceeds the total impurity content ($<10^{-5}$) so if interstitials can migrate at 60°K their retention to 250°K must involve either a second less mobile configuration[5] or the formation of interstitial pairs or larger groups[6][7]. We are able to partly discriminate between these two possibilities because diffusion of interstitials to orientated dislocations in cold rolled metal should be manifest as a unidirectional expansion. Such an expansion was in fact evident between 50° and 60°K in longitudinal sections and absent in transverse sections (figure 5) so, despite the absence of efficient dislocation pinning in internal friction experiments at these temperatures, we surmise that an appreciable fraction of the interstitials created by irradiation are able to diffuse to dislocations. This does not of course preclude the first possibility or trapping of some interstitials by impurity. The sensitivity of the ambient temperature effects in figure 2 in fact supports the contention that impurity catalyses interstitial aggregation and that part of stage III recovery between 280° and 330°K is associated with the release of interstitials from these traps.

Acknowledgements

I am indebted to the Nuclear Physics Division for making the Van de Graaff accelerator and facilities available.

References

1. Vook, R. and Wert, C., 1958, Phys. Rev. 109, 5, 1529.

2. Corbett, J. W., 1966. "Electron Radiation Damage in Semiconductors and Metals" Solid State Physics Supplement 7, Academic Press, London.

3. Kinchin, G. H. and Pease, R. S. "The Displacement of Atoms in Solids by Radiation" Reports on Progress in Physics, 18, 1, 1955.

4. Damask, A. C. and Dienes, G. J. 1963, "Point Defects in Metals", Gordon and Breach, London.

5. Meechan, C. J., Sosin, A. and Brinkman, J. A., 1960, Phys. Rev. 120, 411.

6. Corbett, J. W., Smith, R. B. and Walker, R. M. 1959, Phys. Rev. 114, 1460.

7. Sneed, C. L. Wiffen, F. W. and Kauffman, J. W., 1967, Phys. Rev. 164, 3, 900.

Combined Measurements of Electrical Resistivity and Young's Modulus in Electron Irradiated Copper

G. Roth[1] and V. Naundorf[2]

Abstract

Pairs of copper samples - one for electrical resistivity, the other for Young's modulus measurements - were irradiated simultaniously at 12o°K with 3MeV electrons up to an integrated dose of 2×10^{20} el/cm^2.

The effect of dislocation pinning and the bulk effect of point defects on Young's modulus E could clearly be separated. The following relation between the bulk effect $\Delta E/E$ and the Frenkel defect concentration c_F was found: $\Delta E/E = -75\ c_F$.

Besides strong annealing in stages II and III (18o-3oo°K) and some annealing between 3oo-5oo°K, stage V annealing (5oo-6oo°K) also was observed. In stage III the resistivity annealed more than Young's modulus, whereas the converse occured in stage V.

These measurements are discussed in connection with the electron microscopical observation of point defect clusters after electron irradiation at 12o°K and heating to room temperature.

Introduction

Young's modulus can be changed during irradiation by at least two different mechanisms: Point defects can pin dislocations and thus enlarge the modulus. In addition they can influence the modulus directly, by the residual stress they produce in the lattice (bulk effect) /1/.

The bulk effect was observed by Dieckamp and Sosin /2/ during electron irradiations, by König, Völkl and Schilling /3/ during

[1] Van de Graaff-Labor Aachen der Kernforschungsanlage Jülich

[2] Institut für Allgemeine Metallkunde und Metallphysik der Technischen Hochschule Aachen

α -irradiations of copper. In both experiments the concentration of point defects was not directly measured but only estimated from similar irradiations.

By simultaneous irradiation of a Young's modulus sample and an electrical resistivity sample we intended to reduce the uncertainty in the determination of the modulus change per unit defect concentration. Furthermore the simultaneous measurement of the recovery of the electrical resistivity and the bulk effect of Young's modulus during annealing treatments following the irradiations should provide a sensitive means to detect differences in the recovery behaviour of these two properties.

For clear separation of the influences of dislocation pinning and the bulk contribution to Young's modulus, the Frenkel defect concentration should be as large as possible. Since a liquid nitrogen cryostat was used, the irradiation temperature was above that of stage I and a much smaller damage production rate than in liquid helium irradiations resulted. Nevertheless, for producing point defect concentrations of about $1o^{-4}$ in reasonable irradiation times, unusual high flux densities of $3x1o^{15}$ el/cm^2.sec (that are 5oo μA/cm^2) were utilized.

Experimental Procedure

The sample material was prepared from 99,999% copper (ASARCO), which was rolled to o.o25mm thick foils. A Young's modulus sample (c)and an electrical resistivity sample (a) with shapes as illustrated in Fig. 1 were mounted in a copper frame so that both were situated within the cross section of the electron beam of 3 x 2mm. The Young's modulus sample was eletrostatically excited (electrode d) to flexural vibrations at 2.5 Kc and strain amplitudes of $\varepsilon = 2x1o^{-6}$. Resis-

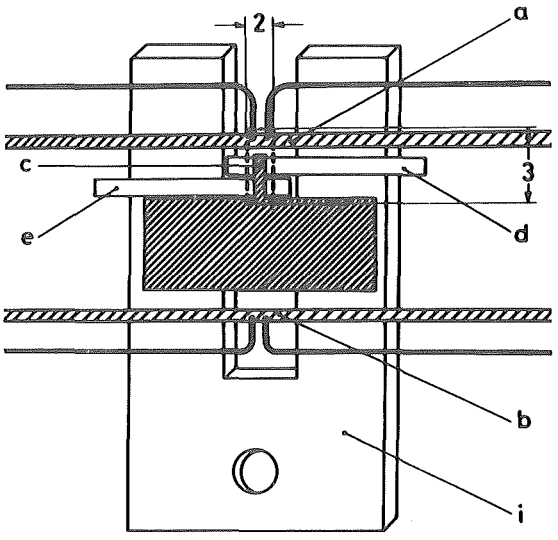

Fig.1:Arrangements of the resistivity sample (a) together with the dummy sample (b) and the Young's modulus sample(c) on a mounting frame (i). The irradiated area of 2x3mm is denoted by dashed lines.

tivity was measured by a Kelvin bridge which yielded the ratio R_x/R_N of the resistance R_x of the irradiated sample (a) and the resistance R_N of a dummy sample (b) (measuring temperature 78°K).

The irradiations were performed with the 3MeV Van de Graaff-accelerator located in Aachen. In this irradiations current densities of 500 /uA/cm^2 with a homogenity of about ±20% within the irradiated area of 3 x 2mm were achieved by using the direct beam of the accelerator. Under these conditions the irradiation temperature was about 120°K.

Before irradiation the samples were annealed in situ for half an hour at 900°K.

Experimental Results

Fig. 2 shows the electrical resistivity and Young's modulus behaviour with increasing electron dose (irradiation temperature about 120°K, measuring temperature 78°K). The Young's modulus increases rapidly in an early stage of irradiation, reaches a maximum at a dose of about $1x10^{18}$ el/cm^2 and decreases at still higher doses. Isochronal anneals also were performed (cf. Fig. 3). Recovery stages both of resistivity and Young's modulus were found between 180-270°K (stage II and III) and between 500-600°K (stage V). Recovery between 300-500°K was continuous without a clearly demonstrated stage IV. In the following, the total temperature range 300-500°K will therefore be called stage IV.

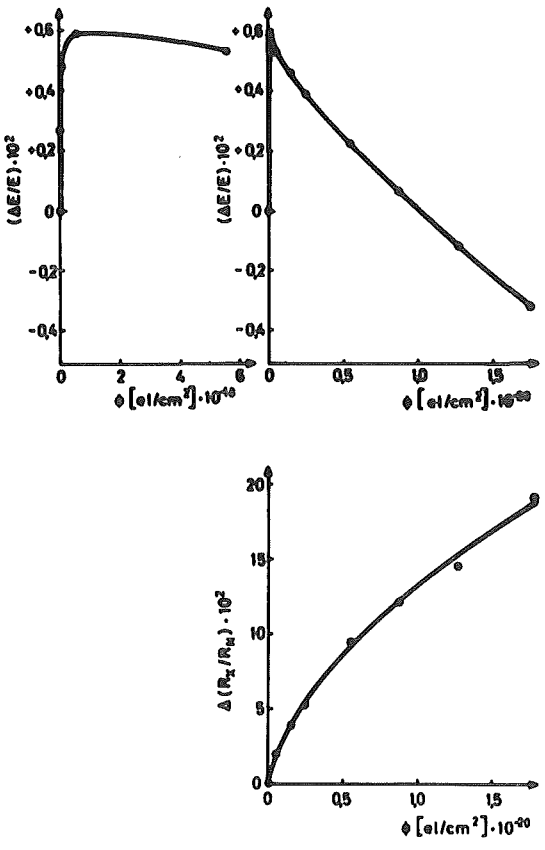

Fig 2: Young's modulus and resistivity behaviour during irradiation with 3MeV electrons at about 120°K (measuring temperature 78°K).

The resistivity was completelyannealed at 600°K. At the same temperature Young's modulus had reached again its maximum value (b) of the early stage of irradiation. During further annealing up to 780°K the resistivity remained constant, whereas Young's modulus decreased to its pre-irradiation value (a).

Discussion

a) Bulk effect

The rapid increase of Young's modulus during the early stages of irradiation is typical for a dislocation pinning process /4/. According to Fig. 2 this process is completed at a dose of about 1×10^{18} el/cm^2. Conversely, the decrease of Young's modulus above 600°K can be attributed to dislocation depinning /5/. So it can be stated that in our experiments with doses of about 10^{20} el/cm^2 the dislocations are pinned during the first percent of the total dose and have no further influence to Young's modulus thereafter untill the annealing treatment above 600°K.

The further Young's modulus changes measured during irradiation above 1×10^{18} el/cm^2 and their subsequent annealing between 78-600°K (cf. Fig. 3) are attributed to the direct influence of irradiation-induced point defects on Young's modulus (bulk effect). This is confirmed by a plot of $\Delta E/E$ versus resistivity increase (cf. Fig. 4), which confirmes that the decrease of Young's modulus measured above 1×10^{18} el/cm^2 is proportional to the point defect concentration, as is expected for a bulk effect.

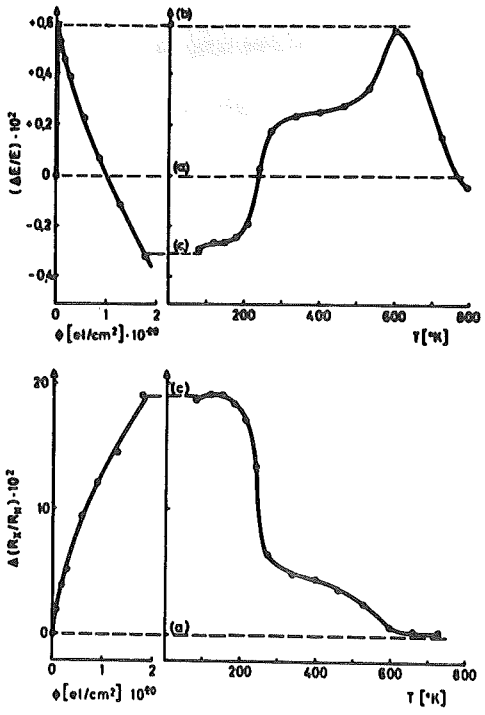

Fig. 3: Isochronal annealing (15 min-pulses, measuring temperature 78°K) of Young's modulus and the electrical resistivity together with their irradiation behaviour. (a)pre-irradiation values, (b)condition of completed dislocation pinning,(c) completed irradiation.

The average slope $(\Delta E/E)/\Delta\rho = -(25 \pm 5) \times 10^{4} [\Omega cm]^{-1}$ was obtained from four irradiations. With $\rho_F = 3 \times 10^{-6} [\Omega cm/at\%$ Frenkel defects] this results in a ratio $(\Delta E/E)/c_F = (-75 \pm 20\%)$. (The usual value of $\rho_F = 2.5 \times 10^{-6}$ was increased by 20% to account for the deviations from Matthiessens's rule expected at the measuring temperatur of $78^{\circ}K$).

For comparison the corresponding value of $(\Delta E/E)/c_F$ found by König et al. /3/ after α-irradiations of copper at $20^{\circ}K$, was -130, and the value found by Sosin and Dieckamp /2/ after electron irradiation (in a revised form /6/) was $-(140 \pm 60\%)$. The value, as calculated by Dienes /1/ was +5. So our result confirms the statement of König et al. /3/, that the measured bulk effect of Young's modulus is more than one order of magnitude larger and of opposite sign as the calculated value.

König et al. /3/ concluded that this large bulk effect is predominantely caused by interstitials. On the other hand, the contribution to the electrical resistivity for interstitials and for vacancies seems to be of the same order of magnitude /11/. The following discussion of the annealing behaviour will make use of these above mentioned contributions to Young's modulus and electrical resistivity.

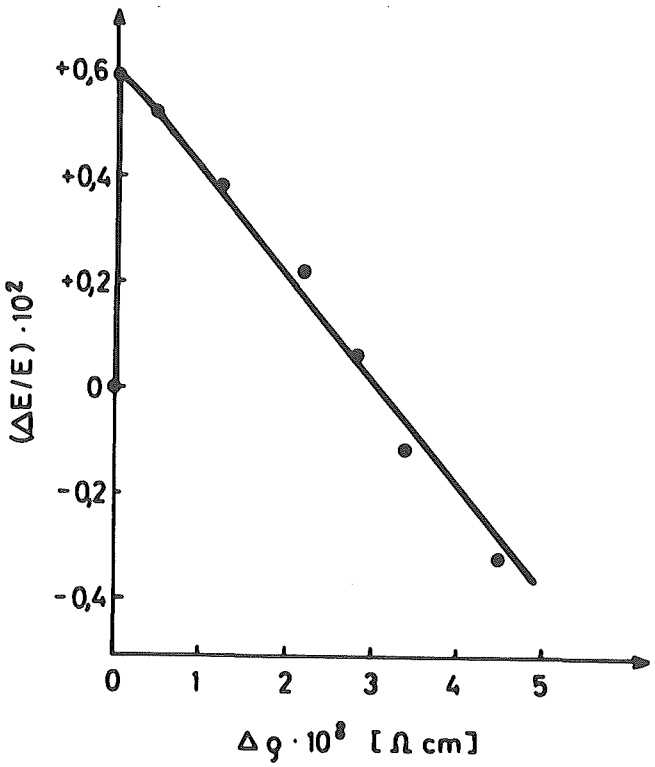

Fig. 4: The measured change of Young's modulus during irradiation at $120^{\circ}K$, plotted versus the measured change of electrical resistivity (measuring temperature $78^{\circ}K$).

b) Annealing behaviour

Annealing of the resitivity and the bulk effect of the Young's modulus is shown in Fig. 5a, the latter being determined relative to the Young's modulus value of the pinned sample (value (b) of Fig.3). From this figure it can be noticed that in spite of the qualitative agreement between the annealing of these two properties, quantitative differences in the magnitude of the annealing stages exist: In stage II+III the resistivity anneals more strongly than Young's modulus, whereas the opposite is true in stage V.

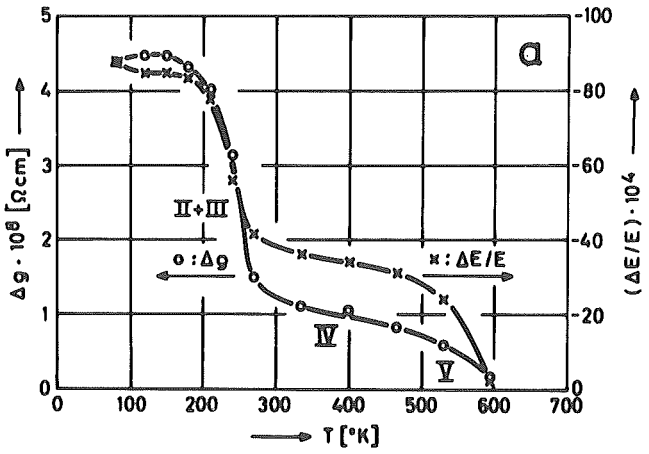

In Fig. 5b the annealing of Young's modulus and resistivity are plotted together according to the data displayed in fig. 5a. In this plot the differences between the annealing of Young's modulus and resistivity are very significant, resulting in deviations of $(\Delta E/E)/\Delta\varrho$ from its average value. The annealing

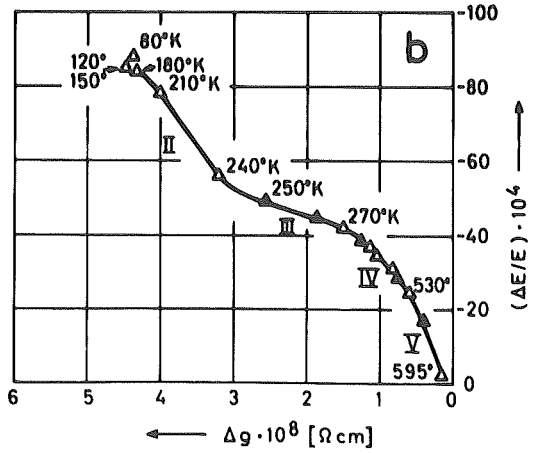

Fig. 5: Comparison of the isochronal annealing of resistivity and the bulk effect of Young's modulus.
5a) The two properties plotted versus annealing temperature.
5b) The two properties plotted versus each other. This curve is constructed by combining the two functions shown in fig. 5a, at which the open triangles represent the measuring points and the filled triangles belong to further values, taken directly from the curves.

between 180-270°K is clearly divided into two stages, which are not detectible in the curves of fig. 5a because of the relative large separation between measurements. In spite of the lack of kinetic measurements in this work, the designation of the annealing between 180-240°K as stage II and between 240-270°K as stage III seems sure according to the results of a dislocation pinning experiment performed with the same material/7/. In Tab. 1 are listed the slopes of $(\Delta E/E)/\Delta\varrho$, measured in two annealing experiments which were performed on the same sample after irradiations with nearly the same doses (run I: $1{,}8 \cdot 10^{20}$ el/cm^2, run II: $2{,}0 \cdot 10^{20}$ el/cm^2). The corrected annealing values are obtained by multiplying the measured annealing values by the ratio of the average irradiation value, obtained from all four irradiations ($25.10^4\,\Omega^{-1}\mathrm{cm}^{-1}$), to the measured irradiation value.

In the following these annealing values will be discussed with regard to the 1-interstitial model with vacancies migrating in stage III and the 2-interstitial model (for description of the two models see for instance /8/). The main difference of the two annealing models exists in the interpretation of stage III, while stage II generally is attributed to the release of trapped interstitials.

First we will consider the 2-interstitial model, where stage III is attributed to the migration of a second interstitial configuration (interstitial-2).
According to Tab. 1 the value of $(\Delta E/E)/\Delta\varrho$ measured in stage III is very small, being only about 30% of that of stage II. So that for a first interpretation within the framework of the 2-interstitial model, it can be stated that this interstitial-2 posseses a much smaller ratio $(\Delta E/E)/\Delta\varrho$ than the interstitial-1.

The radiation damage, still observed at the end of stage III, is caused in this model by immobile vacancies and an equal number of interstitials-1 or -2, which are deeply trapped, for instance by clustering. So the clusters found at room temperature /9/ ought to be of interstitial type (one cluster was observed on 400 produced Frenkel defects. The mean diameter of the clusters was about 30 Å.

Table I

	measured values		corrected values		average of the corrected values
	run I	run II	run I	run II	
Irradiation value	2o.o 10^4	27.o 10^4	25.o 10^4	25.o 10^4	25 10^4
Stage II 18o-24o°K	25.9 10^4	32.1 10^4	32.3 10^4	29.6 10^4	31 10^4
Stage III 24o-27o°K	7.2 10^4	9.8 10^4	9.o 10^4	9.1 10^4	9 10^4
Remaining ratio after stageIII	29.6 10^4	4o.9 10^4	37.o 10^4	37.8 10^4	37 10^4
Stage IV 3oo-5oo°K	2o.o 10^4	25.8 10^4	25.o 10^4	23.9 10^4	24 10^4
Stage V 5oo-6oo°K	52.o 10^4	64.o 10^4	64.9 10^4	59.1 10^4	62 10^4

Ratios $(\Delta E/E)/\Delta\rho$, measured during two irradiations and their following anneals, in $[\Omega cm]^{-1}$. The corrected values are related to the average $25 \cdot 10^4$ $[\Omega cm]^{-1}$ of all four measured irradiation values. The uncertainty of the averaged values (last column) is about $\pm$ 2o%.

So it is concluded that these clusters containe a noticeable amount of all produced defects).

Before further discussion of the annealing above room temperature, it will be asked, if some clue can be found in the measurements for the formation of these clusters. It seems reasonable to ask, if perhaps the very small $(\Delta E/E)/\Delta\varrho$ -value of stage III is even caused by this process: When the low $(\Delta E/E)/\Delta\varrho$ value of stage III is considered to be caused by a clustering process and not to be a characteristic property of the interstitial-2, then vice versa we can assume that the two interstitial configurations do not differ markedly in their $(\Delta E/E)/\Delta\varrho$ -values. So the stage II value would also be adequate for the interstitial-2. In this case recombination during stage III ought to be small because of the small Young's modulus annealing. Therefore the resistivity annealing during stage III, which is about 40% of the total resistivity annealing, would predominantely be caused by clustering. This contribution to the electrical resistivity would be absent for the clustered configuration at the end of stage III and therefore the corresponding ratio $(\Delta E/E)/\Delta\varrho$ ought to be increased at least by a factor of 2. This conclusion however conflicts with the experimental results (cf. Tab. 1), where during stage II a value of $31 \cdot 10^4 [\Omega cm]^{-1}$ was measured and after stage III only a slightly increased value of $37.10^4 [\Omega cm]^{-1}$ was measured. So it seems that for the case of two existing interstitial configurations the small value of $(\Delta E/E)/\Delta\varrho$, measured in stage III, is caused by a real property of the corresponding interstitial and not by clustering.

On the other hand the measurements can be understood well when clustering is assumed to take place below stage III with no drastic change in the value of $(\Delta E/E)/\Delta\varrho$ (which does not mean that the contributions $\Delta E/E$ and $\Delta\varrho$ are unchanged during clustering, but only that these two properties vary in a similar manner). Then the clusters could be formed either during irradiation or during annealing in stage II without strongly influencing the properties of the trapped configuration of the same interstitial-1 and could be observed at the end of stage III together with a corresponding

number of dispersed vacancies. By comparing the $(\Delta E/E)/\Delta\varrho$ values of stage II and at the end of stage III (cf. Tab. 1) it is concluded that during clustering the $(\Delta E/E)/\Delta\varrho$ value has only increased by about 20% (in accordance with the assumption, made above).

When taking into consideration also the annealing above room temperature, it can be stated that during stage IV the resistivity anneals more strongly than the Young's modulus, and causes a value of $(\Delta E/E)/\Delta\varrho$ in stage V, which is almost a factor 2 larger than the corresponding value at the end of stage III (cf. Tab. 1). This can be explained with the assumption that during stage IV clustering of vacancies takes place in addition to recombination. The clustering would cause an additional decrease of resistivity whereas a concomitant decrease of Young's modulus could be neglected because of the small contribution of the vacancies to the bulk effect. The recovery above 500°K (stage V) then is caused by annihilation of clustered vacancies with clustered interstitials.

Now the measurements will be discussed within the framework of the 1-interstitial model with stage III annealing caused by the diffusion of vacancies. The corresponding interstitials are assumed to be immobile because of deep trapping. From the fact that some radiation damage remains in the sample after stage III it can be concluded that a certain portion of the vacancies takes part in reactions other than recombination. Trapping and clustering are such reactions by which vacancies become immobile and thus can survive the stage III annealing. In the case of our high dose irradiations clustering seems favoured, for we have not observed any distinct step during the stage IV annealing as would be expeted for trapped vacanciess /10/. We do observe, however, a stage V as is expected for point defect clusters. Therefore the small ratio $(\Delta E/E)/\Delta\varrho$, which was observed in stage III, can be explained now by the additional decrease of resistivity during clustering of vacancies. The radiation damage which then remains after stage III, in this picture, consists of clustered vacancies and a corresponding number of deeply trapped interstitials. Further it seems reasonable to assume that the state of "deep trapping" is synonimous with the clustering of interstitials.

Therefore the clusters found at room temperature should now be both of vacancy- and of interstitial types.

At this point it will be asked if there is a further clue from the measurements for interstitial clustering: In this connection the existing difference between the irradiation value and the stage II value of $(\Delta E/E)/\Delta\varrho$ (cf. Tab. 1) shall be mentioned. For the 2-interstitial model this difference is clear because the irradiation value reflects the properties of both interstitial configurations whereas the stage II value is only determined by the configuration-1. For the 1-interstitial model, however, the observed difference could suggest that clustering takes place during irradiation. Under these circumstances the clustered interstitials would posses a lower value of $(\Delta E/E)/\Delta\varrho$ than the nonclustered interstitials which anneal in stage II. The consistency of this picture can be proved by considering the ratio $(\Delta E/E)/\Delta\varrho$ which still exists after stage II. In the present interpretation this value would be attributed to the clustered insterstitial configuration together with a corresponding number of still unclustered vacancies. A value of about $18.10^4[\Omega\,cm]^{-1}$ is derived from the $240^\circ K$ annealing data (cf. fig 5), which indeed is appreciably smaller than the stage II value of $31.10^4[\Omega\,cm]^{-1}$ (cf. Tab. 1). So it can be stated that within the framework of the 1-interstitial model the measurements can be interpreted by assuming that interstitial clustering takes place during irradiation, at which these clustered interstitials have only about half the value of $(\Delta E/E)/\Delta\varrho$ as the unclustered ones (together with the corresponding vacancies).

The annealing above room temperature with its smaller slope of $\Delta E/E$ versus $\Delta\varrho$ in stage IV, in comparison with that of stage V, can be explained in this model with the nonuniformity of the size of the observed clusters /9/. Vacancies of the smallest clusters still possess nearly their full contribution to the electrical resistivity. They will recombine at first because of the lower stability of these clusters in comparison with larger ones. So the resistivity decrease per recombining Frenkel

pair will be larger in the early stages of annealing than in the following ones. An additional growth of large vacancy clusters by accretion of smaller ones seems reasonable for the conditions of stage IV postulated above. This reaction would cause a further decrease of resistivity and so also can be cited for explaining the smaller ratio $(\Delta E/E)/\Delta\rho$ measured during stage IV in comparison with stage V.

Summary

An average value $(\Delta E/E)/\Delta\rho = -25 \times 10^4 [\Omega cm]^{-1}$ was measured for Frenkel defects generated during 3 MeV electron irradiation of polycrystalline copper at 120°K. With an assumed $\rho_F = 3 \times 10^{-6}$ [Ωcm/at% Frenkel defects] the following relation between bulk effect of the Young's modulus $\Delta E/E$ and Frenkel defect concentration c_F results: $\Delta E/E = -75 c_F$. Deviations from the average value of $(\Delta E/E)/\Delta\rho$ were observed during various annealing stages. Most striking was the small value in stage III which is only $9 \times 10^4 [\Omega cm]^{-1}$.

The annealing measurements were discussed in connection with the electron microscopical observation of point defect clusters after electron irradiations at 120°K and heating to room temperature.

The interpretations of the measurements suggest clustering of interstitials below stage III. Also clustering of vacancies seems certain. In this case it cannot be decided if this reaction takes place during stage III or during stage IV. Nevertheless some conclusions are given for each of the two possibilities: In the first case the interstitials ought to cluster during the irradiation at 120°K, resulting in a ratio $(\Delta E/E)/\Delta\rho$, which is about half of that of the unclustered interstitials (considered in connection with a corresponding vacancy).

In the second case it cannot be decided if clustering of the interstitials takes place during irradiation or during annealing. But again there are reasons to suggest that clustering occurs below stage III. In thise case the clustered interstitial should

posses a slightly increased ratio $(\Delta E/E)/\Delta\varrho$ when compared with the unclustered one. Additionally a second unclustered interstitial configuration should exist in this case with a much smaller $(\Delta E/E)/\Delta\varrho$ value as the first interstitial configuration.

Literature

/1/ G.J. Dienes, Phys. Rev. 86, 228 (1952) and 87, 666 (1952)

/2/ H. Dieckamp, A. Sosin, J.Appl. Phys. 27, 1416 (1956)

/3/ D. König, J. Völkl, W. Schilling, phys.stat.sol. 7, 591 (1964)

/4/ D. Keefer, J.C.Robinson, A.Sosin, Acta Met. 13, 1135 (1965)

/5/ D. Keefer, A.Sosin, Acta Met. 12, 1041 (1964)

/6/ A. Sosin, D. Keefer in ADVANCES IN MATERIALS RESEARCH, Vol. 2, p. 159, Interscience Publ.

/7/ G. Roth und V. Naundorf to be published

/8/ D.A. Grenning, J.S. Koehler, Phys. Rev. 144, 439 (1966)

/9/ G. Scheidler and G. Roth, to be published

/10/ T.J. Queen, Phil. Mag. 16, 297 (1967)

/11/ A. Seeger, E. Mann, R. v. Jan, J.Phys. and Chem.of Solids 23, 639 (1962)

ELECTRON IRRADIATED PURE NICKEL OBSERVED BY ELECTRON MICROSCOPY

A. BOURRET

C.E.N. GRENOBLE, B.P. 269 - 38 - GRENOBLE - FRANCE

ABSTRACT -

Irradiation of pure nickel foils was carried out between -40°C and +10°C in vacuum (10^{-5} Torr) with 2 or 3 MeV electrons. Subsequentley observed "black dots" are interstitial Frank dislocation loops. There is a well defined critical dose above which agglomerates are visible. The existence of a critical dose gives valuable information about the agglomeration process.

These results prove that an interstitial defect is mobile below stage III. In the stage III temperature range there is a visible agglomeration of interstitials which is interpreted either as a diffusion of loops by pipe diffusion or by diffusion of another interstitial-type defect.

I - INTRODUCTION -

Only very few metals have been studied by electron microscopy. Irradiated copper has been recentley observed by SIGMUND et al. (1) who concluded that agglomeration is possible by homogeneous nucleation and accumulation of defects which it produces; electron irradiation is a good means to investigate directly some obscurities in the irradiation damage process, especially the nature of interstitial migration. Stage III occurs between 80°C and 100°C in nickel ; so it is possible to study the agglomeration before stage III. Subsequent annealing after stage III gives information about migration of defects in this temperature range.

II - EXPERIMENTAL DETAILS -

Zone refined nickel (total impurities content : 40 ppm) was rolled to a thickness of 70 μ. From this foil, specimens were cut and annealed at 800°C for 20 hours in a purified helium atmosphere followed by slow cooling to permit outgassing. These specimens were then electron irradiated with 2 or 3 MeV electrons between -40°C and +10°C in vacuum. An isolated aperture in front of the specimen delimited the exact irradiated area for reproducible dose measurement. The annealing treatements were carried out on the bulk specimens in silicon oil at +100°C. All specimens were electropolished in a mixture of 10 % perchloric acid in butylcellosolve at -10°C. Foils were then examined in an EM 200 Philips microscope fitted with a special goniometer stage.

III - INTERPRETATION OF EXPERIMENTS -

It was possible to determine the size distribution the nature and the type (interstitial or vacancy) of the defects from the photographic enlargements.

The size distribution results were obtained by counting the number of defects with diameters within 10 or 20 Å ranges. Corrections were made for the loss of loops near the foil surface (the stereo-method shows that there is a nearly denuded surface layer of ∿ 100 Å) and also the invisibility of certain loop orientations at a given diffraction condition. Measurement were always carried out using $\vec{g}$ = (200) and at a foil thickness of 650 Å.

The nature of defects was studied by the analysis of the black and white (B.W.) dynamical contrast. The principle first developed by RÜHLE (2) is based on the following effect : the direction $\vec{I}$ going from the black to the white part of the image is the projection in a plane perpendicular to the beam of the burgers vector of a planar defect. Thus this direction $\vec{I}$ is an intrinsic characteristic of the defect and is not dependant on the diffraction vector.

The defect type (vacancy or interstitial) is determined by the stereo-technique (3). This technique is subject to numerous errors, so the validity of results were tested using 50 Å Co precipitates in copper. These precipitates were found to exhibit a vacancy character as is to be expected (4).

IV - EXPERIMENTAL RESULTS -

IV-1 - Defect analysis -

Analysis of the visible black dots shows them to be small Frank dislocation loops as illustrated on fig. 1.

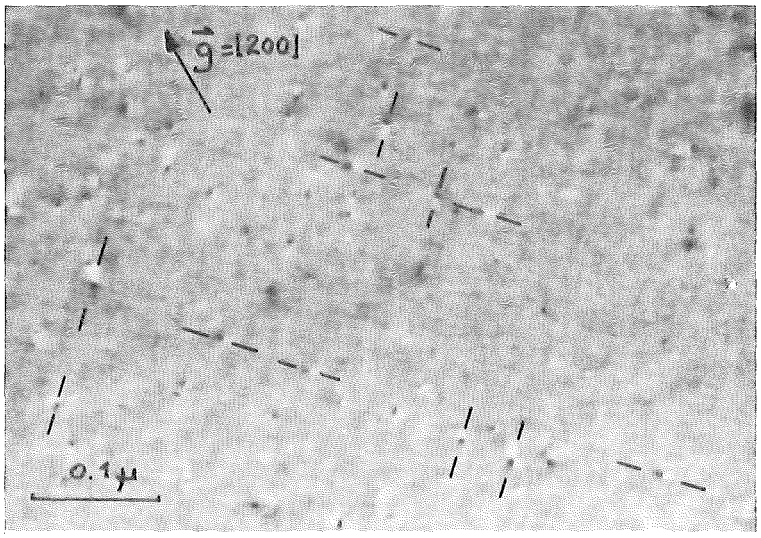

Fig.1 - Electron irradiated nickel ($4{,}6\ 10^{19}$ el/cm^2) showing the B.W. contrast on a (001) foil. The $\vec{I}$ vector is projected on (110) and (1$\bar{1}$0) directions, therefore the black dots are Frank loop dislocations. Bright field. G =

Stereoanalysis shows these loops to be of the interstitial type over the entire diameter range (40-120 Å). There are no detectable vacancy agglomerates.

IV-2 - Dose and energy dependance -

Three parameters are studied for different electron doses :

M_I : total number of visible loops.

$\bar{D}$: mean diameter loops defined by

$$\bar{D} = \frac{\int_o^{\infty} \phi(D)\, D\, d\, D}{\int_o^{\infty} \phi(D)\, d\, D}$$

where $\phi(D)$ is the diameter distribution function of the loops.

N_I : the total number of interstitial agglomerated in a visible form. It is deduced from $\phi(D)$ by

$$N_I = \frac{\pi}{4B^2} \int_o^{\infty} \phi(D)\, D^2\, d\, D$$

where B is the effective surface of a defect. It is assumed that $B = 2.32$ Å for Frank dislocation loop.

All results are summarized in Table 1 for 3 MeV electron irradiation and Table II for 2 MeV electrons, at 10°C followed by annealing at room temperature.

Table I (3 MeV)

Dose el/cm^2	M_1 cm^{-3}	N_1 cm^{-3}	$\bar{D}$ Å
$1.0\ 10^{19}$		i n v i s i b l e	
$2.1\ 10^{19}$	$1.3\ 10^{15}$	$0.1\ 10^{18}$	27
$2.3\ 10^{19}$	$6.1\ 10^{15}$	$1.3\ 10^{18}$	37
$4.6\ 10^{19}$	$5.8\ 10^{15}$	$2.0\ 10^{18}$	45

Table II (2 MeV)

Dose el/cm^2	M_1 cm^{-3}	N_1 cm^{-3}	$\bar{D}$ Å
$1.0\ 10^{19}$		i n v i s i b l e	
$2.4\ 10^{19}$	$2.1\ 10^{15}$	$0.4\ 10^{18}$	35
$5.3\ 10^{19}$	$9.8\ 10^{15}$	$1.7\ 10^{18}$	35

Fig. 2 gives more details on the distribution function corresponding to results of Table I. Since the resolution limit is about 20 Å the results are subject to large errors in the 20-30 Å diameter range. Therefore as the mean diameter is small after electron irradiation counting results are only defined to $\pm$ 30 %.

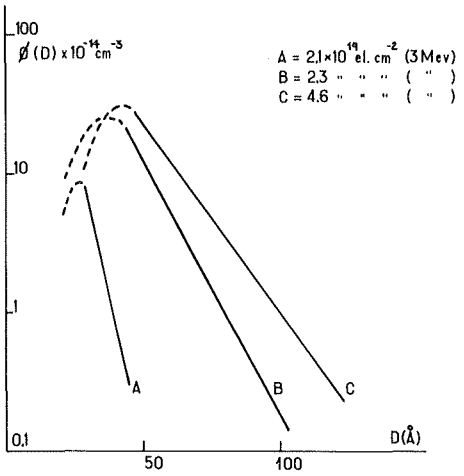

Fig. 2 - Diameter distribution function of loops created by electron irradiation at 3 MeV. There is a marked difference between A and B suggesting the existence of a critical dose.

The following remarks can be made concerning Tables I and II :

1) There is a well defined critical dose below which black dots are invisible : this limit is found very clearly at 3 MeV between 2.0 and 2.3 10^{19} el/cm^2. After irradiation at 2 MeV this limit is in the same dose range $\sim$ 2.10^{19} el/cm^2. This critical dose cannot be explained by the resolution limit (see appendix).

2) The mean diameter of loops increases as the dose increases.

3) There is a ratio of 1.6 between the total number of interstitials agglomerated in a visible form after irradiation at 3 MeV and 2 MeV.

4) The distribution function Ø (D) has an exponential form except for very small diameters : this is due only to the resolution limit of the apparatus.

IV-3 - Reirradiation experiments -

Samples containing vacancy loops whose distribution function Ø (D) was previously measured were electron irradiated at -30°C with a dose of 8.7 10^{19} el/cm^2, in order to test if interstitials are mobile or not at this temperature. It appears clearly (fig. 3) that the number of loops increases in the small diameter range (D = 40 Å) but decreases for larger diameters (D = 90 Å). This fact is easily

understood since free interstitials can give new small interstitial loops (D ≈ 40 Å) but also can be annihilated in vacancy sinks decreasing the number of vacancy loops (larger diameter). Therefore free interstitials are mobile at temperatures lower than -30°C, ie. definitely below stage III.

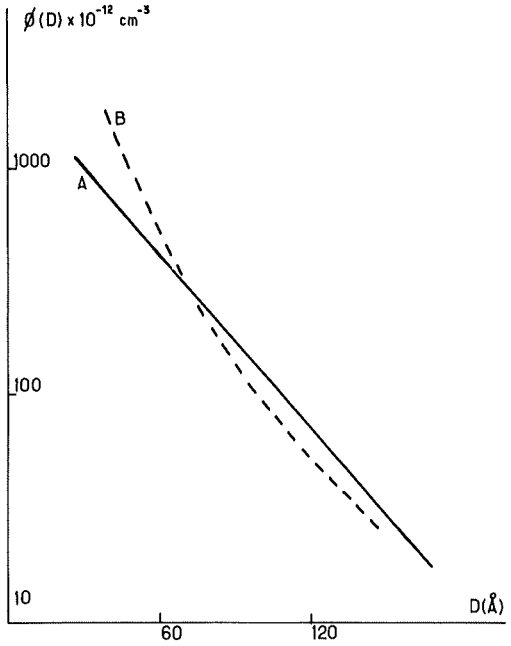

Fig. 3 - Distribution functions of loop diameter.
A) Prior to electron irradiation : big vacancy loops only
B) After electron irradiation, 8,7 10^{19} el/cm^2, 2 MeV at -30°C.

IV.4 - Annealing experiments -

As previously observed (6) there is a visible agglomeration between 20°C and 100°C. This fact is illustrated in fig. 4. Table III presents a summary of additionnal results.

Table III

Electron energy	Dose el/cm^2	N_I cm^{-3} (annealed at room temp.)	N_I cm^{-3} (annealed I hour at 100°C)
3 MeV	$2.1\ 10^{19}$	$0.1\ 10^{18}$	$0.6\ 10^{18}$
3 MeV	$2.3\ 10^{19}$	$1.3\ 10^{18}$	$2.0\ 10^{18}$
2 MeV	$2.4\ 10^{19}$	$0.4\ 10^{18}$	$1.0\ 10^{18}$

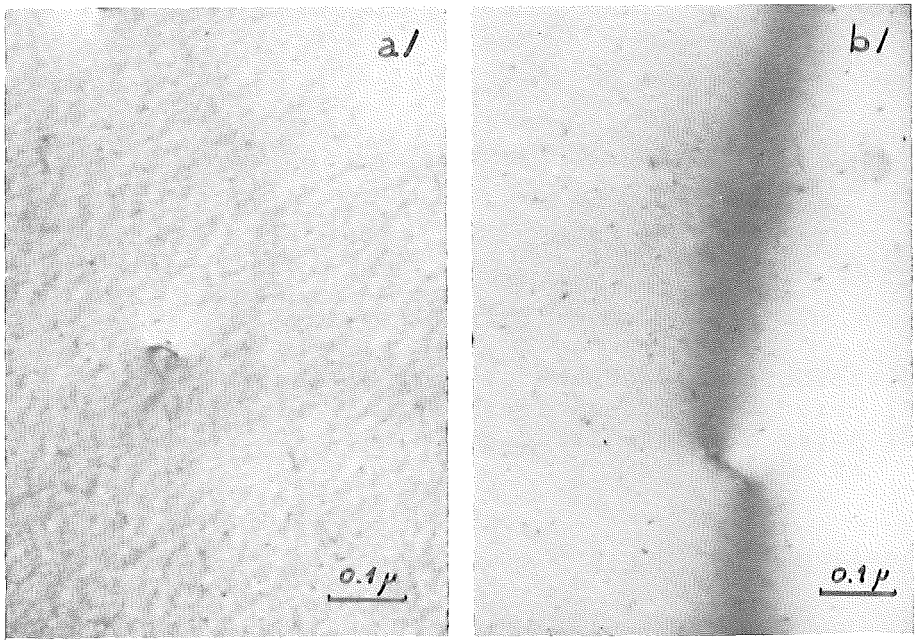

Fig. 4 - Electron irradiated nickel, 2.3 10^{19} el/cm^2, 3 MeV
a) annealed at room temperature
b) annealed I hour at 100°C : the number of loops has markedly increased
Bright field. G = Foil thickness : 650 Å

Therefore the agglomeration in the stage III temperature range is confirmed and is more pronounced for low interstitial concentrations.

IV-5 - Comparison with neutron irradiation (6) -

It is interesting to compare these results with those using neutron irradiation. Three main differences have to be pointed out :

1) After neutron irradiation two types of defect are visible : interstitial Frank dislocation loops and small tetrahedral voids which are vacancy agglomerates.

2) There is no critical dose after neutron irradiation. The total number of interstitials agglomerated increases linearly for small doses (there is a saturation effect for high doses).

3) The efficiency for visible agglomerate production is much lower for electron irradiation than for neutron irradiation. Therefore 12 % of initial interstitials are agglomerated into visible loops after neutron irradiation compared with a mere 0.3 % after electron irradiation.

V - INTERPRETATION OF RESULTS -

V.1 - Interstitial migration below stage III -

All the experimental results are coherent with a free interstitial migration below -30°C, ie. at stage I. This fact is proved either by stereo-microscopy since agglomerates formed by diffusion are of interstitial type, or by the reirradiation experiments where it is proved that an interstitial type defect is migrating below stage III.

V.2 - Agglomeration process -

Only interstitial agglomeration will be considered because vacancies do not form visible agglomerates after electron irradiation. Vacancies are supposed immobile below 100°C so they act only as fixed sinks during agglomeration. Three processes can be invoked for agglomeration :

- a purely random process.
- a coalescence process.
- a process of elastic interaction between clusters ie. loops.

These processes are discussed taking the experimental results into account.

V-2-1 - Purely random process -

It is difficult to explain the existence of big agglomerates by a purely random process. The nucleation conditions are very homogeneous after electron irradiation, so only very small aggregates are expected. If for exemple I_3 (tri-interstitial) is the first agglomerate not mobile at room temperature, C_{I_3} will be high then C_{I_4}, C_{I_5} will decrease very rapidly (C_I is the interstitial concentration). In this case a critical dose cannot be understood, because the number of each kind of agglomerate I_n will increase uniformly with the dose.

V-2-2 - Coalescence process -

A coalescence process similar to coalescence of vacancy loops under supersaturation conditions can be proposed. KOSEVICH et al. (7) has analysed this process for interstitials. Large loops grow at the expense of smaller ones, but this implies that small loops shrink by emitting interstitials. If this process is plausible for vacancies it cannot be imagined to be valid for interstitials since the binding energy of an interstitial to a loop is $\sim$ 3 ev. as soon as the loop contains 10 interstitials (6).

V-2-3 - Influence of elastic interaction -

VARLEY (9) has studied the influence of the elastic interaction. He proposed that a monointerstitial is attracted by a growing loop if it lies at a distance smaller than a radius r ; this radius was supposed fixed whatever the size of the agglomerates and equal to 450 Å. This is unreasonable for the smallest loops but is acceptable for larger ones. The general results of VARLEY, an exponential form of $\emptyset$ (D) for large D, an increase of the mean diameter with the dose are valid and are observed experimentally. But the initial growth of the loops remains to be explained.

Therefore it is necessary not only to introduce an elastic interaction between point defects and a growing loop, but also an elastic interaction between loops. This interaction produces the displacement of entire loops either by glide motion or by conservative climb. At low temperature only glide has to be considered. This process was analysed in details in reference (6). It can be shown that as soon as N_I is higher than a critical number $N_{I,C}$ (ie. a critical dose) the agglomeration process can occur by mutual attraction of different loops. This process is only stopped by the annihilation of interstitials at vacancy sinks during agglomeration. Evaluation of $N_{I,C}$ is difficult because little is known about the PEIRLS NABARRO force in nickel, and the force necessary to remove the stacking fault. A very crude estimation of $N_{I,C}$ based on the elastic limit gives 4.6 to 20.10^{19} interstitials/cm^3. This is to be compared with the $2\ 10^{19}$ el/cm^2 critical dose which gives approximately $2.2\ 10^{19}$ free interstitials/cm^3 able to agglomerate. Only very few regions in the specimen hold this density because most of the interstitials are annihilated at vacancies. This fact explains the small number of interstitials agglomerated in a visible form.

In the temperature range 20-100°C conservative climb is important and can explain the observed agglomeration. It would give a pipe diffusion activation energy of 0.8 ev. which is not unreasonable for nickel. But it is also possible that another type of interstitial defect is mobile in the stage III temperature range. Actually it is impossible to make a choice between these two possibilities ; it is also possible that both processes occur simultaneously but electron microscopy cannot yield more precise information.

VI - CONCLUSION -

After the electron irradiation of nickel foils only interstitial loops are visible, while vacancies remain in a small invisible form. These interstitial loops are formed by the diffusion of free interstitials during a low temperature stage where long range elastic interaction between loops is essential to explain the formation of big clusters. This process explains the existence of a critical dose because the formation of these loops requires a local density of defects higher than 10^{19} to 10^{20} interstitials/cm^3.

In the stage III temperature range there is a visible agglomeration of interstitials which is interpreted either as a diffusion of loops by pipe diffusion, or by the diffusion of an invisible interstitial-type defect.

Acknowledgements

The author would like to express his thanks to Dr. P. PERETTO and Dr. P. MOSER for fruitful discussions and to A. RENAULT, M. PENISSON and P. GARREL for valuable aid in the image counting.

APPENDIX

The influence of a resolution limit of 20 Å on counting results is discussed. The total number of interstitial N_I measured is too small because loops of diameter 0-20 Å are invisible. Evaluation of the correction is made as follows. The distribution function $\emptyset$ (D) is supposed to be exponential as currently observed.

$$dD\,\emptyset\,(D) = a \exp-\frac{D}{D_m}\,dD \qquad D_m : \text{mean diameter of loops}$$

Therefore $N_{I,0}$ the true interstitial concentration is :

$$N_{I,0} = \frac{\pi a}{4B^2} \int_0^\infty D^2 \exp-\frac{D}{D_m}\,dD = \frac{\pi a}{2B^2} D_m^3$$

As $N_{I,0}$ is proportional to the dose ϕ : $N_{I,0} = A\phi$

$$D_m = u\,\phi^{1/3}$$

with $u = \left(\frac{AB^2}{\pi a}\right)^{1/3}$

If the resolution limit is D_r only part of $N_{I,0}$ will be visible. This part is N_I :

$$N_I = \frac{\pi a}{4B^2} \int_{D_r}^\infty D^2 \exp - \frac{D}{D_m}\,dD$$

$$N_I = \frac{A\phi}{2}\left(2 + \frac{2\,D_r}{u\,\phi^{1/3}} + \frac{D_r^2}{u^2\,\phi^{2/3}}\right) \exp-\frac{D_r}{u\phi^{1/3}}$$

N_I versus dose ϕ is plotted on fig. 5 and compared with the true interstitial concentration $N_{I,0}$ for D = 45 Å. As can be seen the resolution limit does not affect the results and the error does not exceed 8 % for $\frac{D_r}{D_m} < 1$.

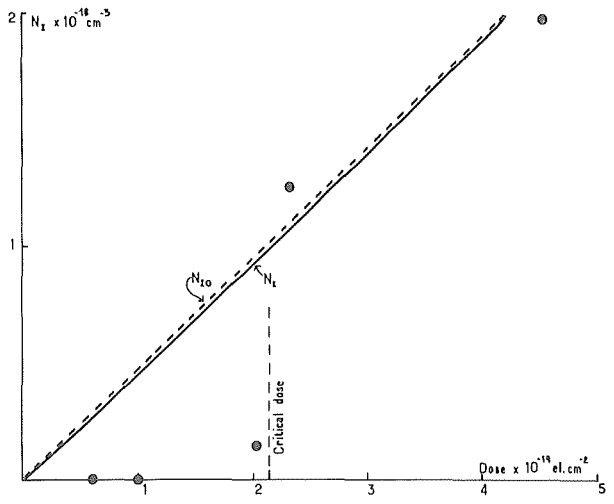

Fig. 5 - Theoretical total number of interstitials N_{Io} and N_I versus electron dose if loops of diameter smaller than 20 Å are invisible. This curve has been adjusted to fit the experimental results marked by crosses. It is clear that above 2.1 10^{19} el/cm^2 the experimental results cannot be interpreted without the concept of a critical dose.

REFERENCES

(1) - P. SIGMUND, G.P. SCHEIDLER, G. ROTH - Upton 1967 Conference on "Solid State Research with Accelerators"

(2) - M. RÜHLE - Phys. Stat. Sol. 19, 263 (1967)

(3) - H. DIEPERS, J. DIEHL - Phys. Stat. Sol. K 16, 109 (1966)

(4) - A. BOURRET, D. DAUTREPPE - Phys. Stat. Sol. K 173, 24 (1967)

(5) - J.L. ODDOU - These - GRENOBLE (1967)

(6) - A. BOURRET, D. DAUTREPPE - Phys. Stat. Sol. (to be published)

(7) - A.M. KOSEVICH, Z.K. SARALIDZE, V.V. SLEVOV Sov. Phys. Sol. St. 6, 2707 (1965)

(8) - R.A. JOHNSON - Phys. Rev. 152, 629 (1966)

(9) - J.H.O. VARLEY - Phil. Mag. 7, 301 (1962)

Electron microscope studies of point defect clusters in electron irradiated copper

G.P. Scheidler[1] and G. Roth[2]

Abstract

Transmission electron microscopy has been used to measure the density and size distribution of visible defect clusters at 20° C in electron irradiated copper as a function of electron dose, irradiation temperature and impurity content. Preliminary observations of defect clusters due to electron irradiation are reported for gold, niobium and platinum.

At a irradiation temperature of 120° K, the cluster density is nearly proportional to the Frenkel-pair concentration introduced by the irradiation. The cluster density decreases more rapidly with increasing irradiation temperature upto 230° K than it does above this temperature. This abrupt change in the temperature dependence occures at the high temperature end of stage II. A comparison of pure (99.999) and impure (99.99) copper at 120° K gave the same cluster densities and size distributions wheras at 230° K the impure material showed a much higher density but with smaller average size of clusters than the purer material. Comparison of neutron irradiated copper with electron irradiated copper indicates that in the former, displacement cascades are an important mechanism leading to cluster formation.

1) Institut für Reaktorwerkstoffe der Kernforschungsanlage Jülich

2) Institut für Festkörper- und Neutronenphysik der Kernforschungsanlage Jülich, Van de Graaff-Labor in Aachen

Introduction

Transmission electron microscope observations have been carried out at room temperature on copper irradiated with 3 MeV-electrons at a temperature of 12o° K[2.]. The specimens contained "black spots" similar to those observed in neutron irradiated copper. A typical photograph of electron damage in copper is shown in fig. 1. It was established that the black spots are caused by electron damage from measurements of the total number of clusters as a function of electron dose[2.] as shown in fig. 2, however, the mechanism of clustering of the generated point defects is not yet known. Interpretation of the results of damage rates[3.) 4.) 5.] leads to the conclusion that the generated interstitials migrate freely at temperatures of 1oo° K. The free migrating interstitials can either recombine with vacancies, can be trapped, or can be converted into the second-interstitial-configuration[6.]. Recent studies of the recovery spectra of copper irradiated at 12o° K and annealed in the rage of 12o° - 6oo° K show differences in the recovery of the Bulk Modulus and electrical resistity which can be accounted for by the formation of interstitial clusters below stage III [7.].

In this investigation an attempt has been made to show the influence of various experimental variables such as dose, irradiation temperature and impurities on the formation of clusters in copper.

Experimental Datails

Copper foils 5o/u thick were rolled from copper rods (99.99 % or 99.999 %) obtained from Johnson Matthey (99.999 %). Two strips 3 mm wide were joined together. A thermocouple was spot-welded near the irradiated area. Before irradiation the foils were annealed in vacuum ($1o^{-4}$ Torr) at 6oo° C for 2 hours followed by slow cooling. The foils contained mainly (001) oriented grains following this treatment.

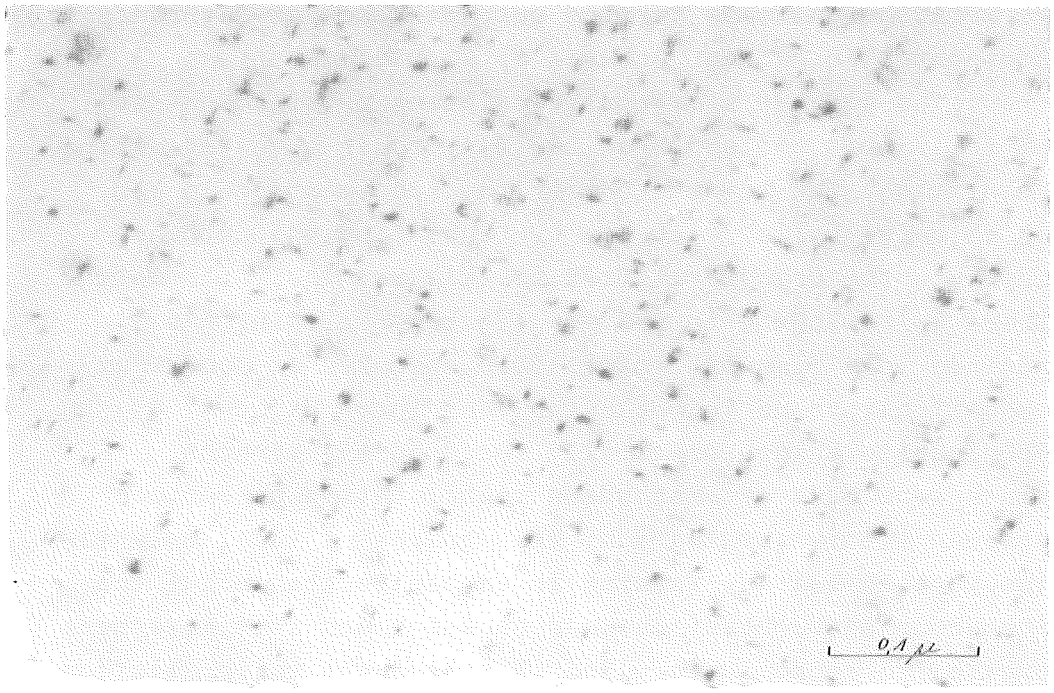

Fig. 1 Electron Irradiated Copper
Dose 10^{20} e/cm^2 3MeV
Irradiation Temperature 120 °K
Observation at 293 °K
Foil Orientation [100]

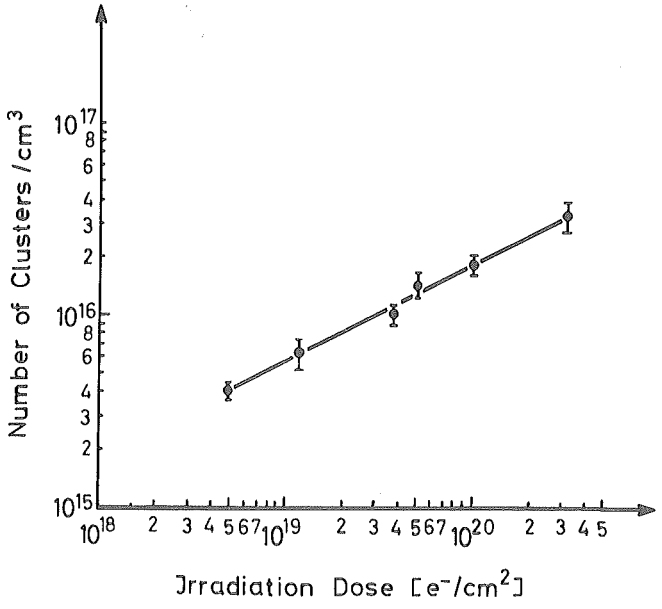

Figure 2 Change in cluster density with dose for copper irradiated with 3 MeV electrons at 120° K. Cluster densities determined at 293° K. The straight line drawn through the experimental points has a slope of 1/2.

The irradiations were carried out with the Van de Graaff accelerator at Aachen. An area of 2 mm diameter was irradiated with an electron beam intensity of 500 $\mu A/cm^2$. The foils were cooled in a liquid nitrogen cryostat during irradiation. The temperature of the specimens could be varied between 120° - 350° K by regulating the nitrogen supply to the cryostat. After irradiation the foils were warmed up to 20° C, thinned by electro-polishing and examined in a Siemens I microscope operated at 100 kV at a magnification of 80.000 using the "through focus" technique to ensure critically focussed micrographs. Prints were made at a standard magnification of 200.000 for quantitative evaluation. Only grains of (001) orientation were evaluated. We wish to emphasize that all of the microscope oberservations were made on specimens that have been annealed to approximately 300° K subsequent to irradiation at a different temperature.

Results

a) The dependence of the cluster density on the irradiation induced Frenkel defects.

Fig. 2 shows that the total number of visible clusters per cm^3 is proportional to the square root of the irradiation dose. Measurements of the electrical resistivity under the same irradiation conditions[7.] but without warming to room temperature show that the change in electrical resistivity is also proportional to the square root of irradiation dose. Hence the cluster concentration is nearly proportional to the Frenkel-pair concentration introduced at 120° K as shown in fig. 3. This comparison indicates that for each visible cluster, on the average, 400 Frenkel defects have been introduced at 120° K.

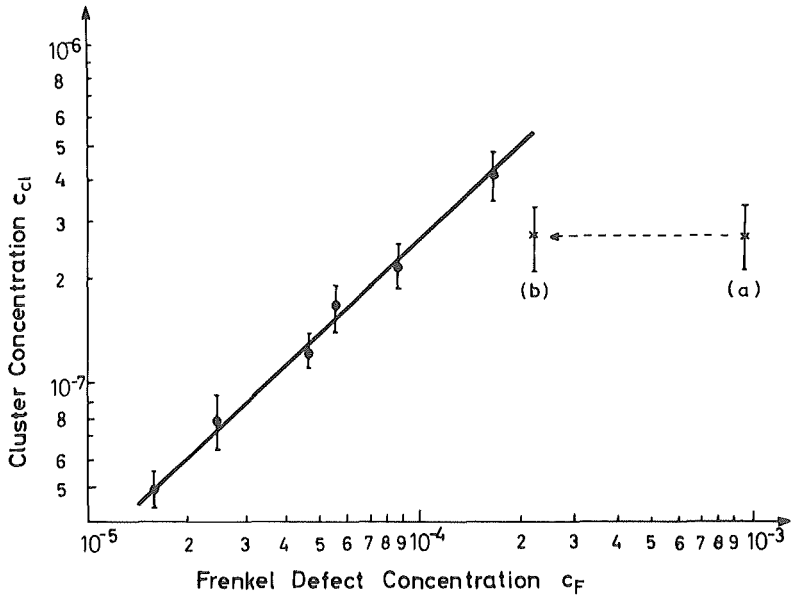

Figure 3 Comparison of cluster concentration determined from resistivity measurements for copper irradiated with 3 MeV electrons at 12o° K. The slope of the straight line drawn through the experimental points is slightly less than one. Points (a) and (b) are from a specimen irradiated at 15° K. The observed cluster concentration is plotted against (a) Frenkel defect concentration for the 15° K irradiation, and (b) Frenkel defect concentration remaining after 78° K anneal.

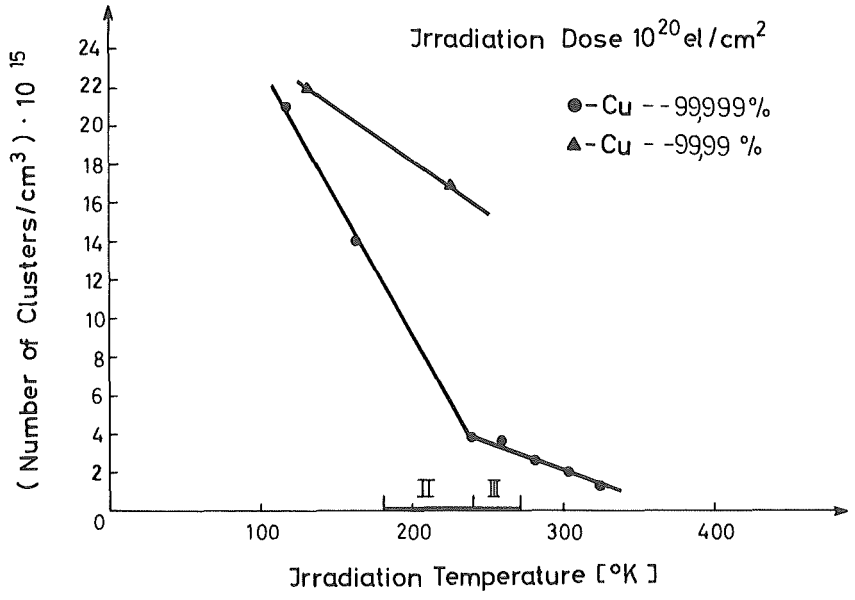

Figure 4 Cluster density versus irradiation temperature for 99.999 % and 99.99 % copper irradiated with 3 MeV electrons to a constant dose of 1o^{2o} e/cm^2.

The result of a 15^{o} K irradiation of copper is also plotted in fig. 3. This foil was irradiated to a dose of $2,9 \times 1o^{19}$ e/cm^2. The change in resistivity due to irradiation was $\Delta\varrho = 24,0 \times 1o^{-8}\Omega$cm, and after raising the temperature to 78^{o} K gave $\Delta\varrho = 5,6 \times 1o^{-8}\Omega$cm. (resistivity measured at 4^{o} K). These $\Delta\varrho$ values correspond to Frenkel-pair concentrations of $2,2 \times 1o^{-4}$ and $9,6 \times 1o^{-4}$ respectively. The observed cluster concentration in this specimen was $2,7 \times 1o^{-7}$. The substantial departures of the points a. (as irradiated) and b. (after stage I annealing) in fig. 3 from the linear relationship found for the $12o^{o}$ irradiations indicate that the cluster concentration is not simply a function of Frenkel-pairs introduced by the irradiation, nor that present after stage I annealing (in which close-pair annealing would be expected to eliminate Frenkel defects that do not contribute to cluster formation). On the other hand, this result indicates that cluster concentration for a given dose is a strong function of the irradiation temperature. For an irradiation at $12o^{o}$ K, it would have required a dose about 2 1/2 times that employed at 15^{o} K to arrive at the cluster concentration observed.

b) The dependence of cluster density on irradiation temperature.

A number of irradiations to a constant dose of $1o^{2o}$ e/cm^2 were carried out at different temperatures. The visible cluster density decreases with increasing irradiation temperature as shown in fig. 4. Two stages are clearly distinguished. Between $12o^{o}$ and $23o^{o}$ K a rapid linear reduction of cluster formation of nearly a factor of 1o is observed. In the stage between $23o^{o}$ and 325^{o} K there is again a linear reduction in cluster formation; but the change is only about one-fifth that observed at the lower temperature.

It is remarkable that the change of cluster formation from a stronger to a weaker temperature dependence coincides with the end of annealing stage II. Since stage II annealing is thought to be due to the release of interstitials from impurity

traps, the strong temperature dependence of the cluster density for irradiation in the temperature interval of $12o^{o}$ K to $23o^{o}$ K suggests that impurity trapping of iterstitials plays an important role in the cluster formation. The abrupt change in the temperature dependence at $23o^{o}$ K must be due to a different mechanism of cluster nucleation. It is suggested that vacancy clustering during the irradiations above $23o^{o}$ K is the mechanism which causes the change in the temperature dependence of the cluster density. Clustering of vacancies during the irradiation would give a reduced capture cross-section for annihilation of migrating interstitials, leading to increased retention of both vacancies and interstitials than would otherwise occur. This in turn would be expected to increase the number and/or average size of the clusters relative to that due to impurity trapping of interstitials alone.

Both vacancy and interstitial clusters have been observed in the copper foils electron irradiated at $12o^{o}$ K[+], however, studies of the relative numbers of the two types of clusters as well as size distributions as a function of temperature have not yet been made to determine possible differences resulting from irradiations above and below $23o^{o}$ K.

c) The dependence of the visible cluster concentration on impurity content of the specimens.

Up to now all experiments were carried out with copper of purity grade of 99.999 %. Copper of another purity grade (99.99 %) was also investigated because impurities act as nucleation traps. Two specimens of 99.99-purity were irradiated with dose $1o^{2o}$ e/cm^2 one at $13o^{o}$ K and the other at 225^{o} K. The results are plotted in fig. 5.

[+]) M. Rühle (MPI-Stuttgart private communication) investigated these foils and found the nature of the clusters to be interstitial and vacancy clusters.

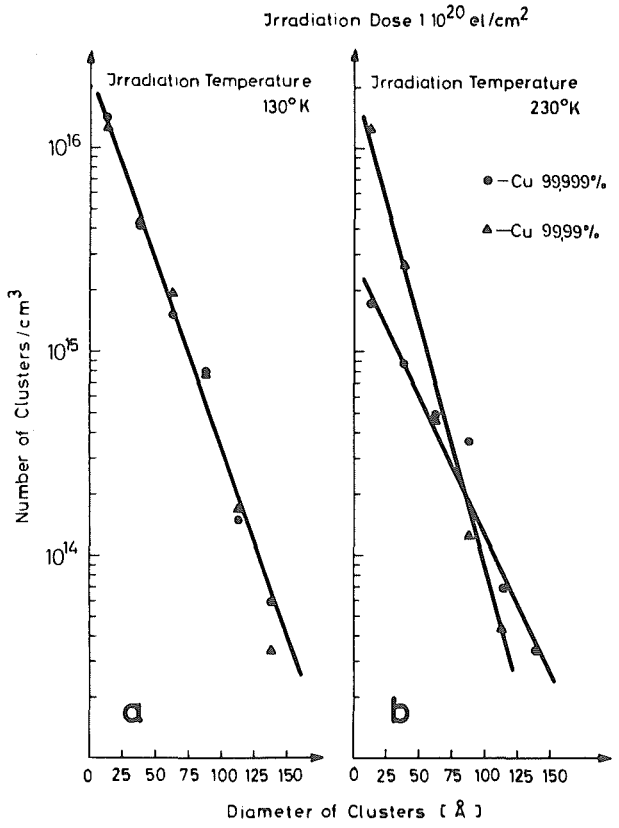

Figure 5 Size distribution of clusters in 99.999 % and 99.99 % copper irradiated with 3 MeV electrons to a dose of $1o^{2o}$ e/cm^2 at $13o^{o}$ K and $23o^{o}$ K.

It is remarkable that the density and size distribution of the clusters is the same for specimens of different purity grade irradiated at $13o^{o}$ K. This is particularly surprising since electrical resistance indicates that the number of defects introduced by irradiation is higher in the impure materials [3.]. At the present time, we have no explanation for this result, and believe further studies on this are necessary.

On irradiating both kinds of copper at $23o^{o}$ K, noticable differences are observed in the number and size distribution of clusters. The number of clusters in the impure material is approximately 5 times larger but the average diameter is smaller than in the case of the pure material.

If one assumes that the visible clusters are dislocation loops as in the case of neutron irradiated copper[8.] one finds in both cases nearly the same number of point defects in clusters in both materials. The higher total density of clusters in the impure material indicates that nucleation conditions are more favorable.

d) Comparison of cluster formation of electron and neutron irradiated copper.

On comparing the ratio of cluster concentration to the irradiation induced defect concentration of a neutron irradiated copper at 4° K and an electron irradiated copper at 15° K, as in table I, one finds that in neutron irradiated copper the ratio is larger by a factor of 7. Comparison of neutron irradiations of the same dose indicates that room temperature irradiation gives a cluster density about 5o % of that resulting from a 4° K irradiation. For electron irradiation, the cluster density due to room temperature irradiation is less than 5 % of that resulting from a 15° K irradiation.

This large difference in the efficiency of cluster formation for neutron irradiations at room temperature as compared to electron irradiations must be associated with the formation of clusters more or less directly from the displacement cascades present in the neutron irradiation. It would be expected that a mechanism for the nucleation and/or formation of clusters from displacement cascades would be much less sensitive to the irradiation temperature than the nucleation process believed to be operative in the electron irradiation case. It is probable that in the neutron irradiations, clusters are also nucleated in part in the same manner as occurs with electron irradiations. The relative importance of this impurity nucleation of clusters should be greater for low temperature irradiation than for room temperature.

Acknowledgments.

We wish to thank Dr. H. Wollenberger and his Radiation Group at Aachen for help in planning the elctron irradiation and making th 15° K irradiation. We also wish to thank Dr. W. Schilling and Dr. T.S. Noggle for helpful discussions on this work.

Table I

Comparison of Cluster Formation in Copper for Neutron and Electron Irradiations.

Type of Irradiation	Irradiation Temperature	Dose	Concentration of Frenkel-Pairs				
			After Irradiation below stage C ($4^{o}K$)	Remaining after annealing above Stage I C ($78^{o}K$)	Cluster Concentration C_{Cl}	$C_{Cl}/C(4^{o}K)$	$C_{Cl}/C(78^{o}K)$
n	$4^{o}K$	$7x10^{17}$ n/cm^2	$1,8x10^{-4}$	$1,2x10^{-4}$	$4,1x10^{-7}$	$2,1x10^{-3}$	$3,1x10^{-3}$
n	$300^{o}K$	$7x10^{17}$ n/cm^2			$2,1x10^{-7}$		
e	$15^{o}K$	$2,9x10^{19}$ el/cm^2	$9,6x10^{-4}$	$2,2x10^{-4}$	$2,7x10^{-7}$	$0,3x10^{-3}$	$1,2x10^{-3}$

Appendix

Gold Stacking fault tetrahedra in foils of Gold electron irradiated at 18o°K and warmed up to room temperature have been observed - as shown in fig. 6. The square shape of many of the clusters is the characteristic appearence of stacking - fault tetrahedra in (001) oriented foils.
The dose dependence of tetrahedra density is shown in fig. 7 and size distribution in fig. 8. The form of the curve is like that observed by K.P. Chik after quenching of Gold. On the other hand one finds a lot of defect clusters where the form is not known specially in the range of o - 5o Å, they are also plotted in fig. 7.

Niobium Defect clusters are also produced in Niobium irradiated at 5o°C with electrons; most of them are clearly resolved loops and are very stable.xx) After annealing treatments (i.e. 3 hours at 8oo°C) the number of loops is only slightly reduced and bigger ones appear.
Before irradiation the foils had been annealed for 1 hour at 15oo°C (vacuum $1o^{-1o}$ mm Hg).

Platinum x) Fig. 10 shows a photograph of electron damage in Platinum irradiated at 9o°K with 3 MeV electrons.

All these investigations are still in progress.

---

x) The irradiation of Platinum has been done at the electron irradiation facility at Jülich.

xx) See fig. 9

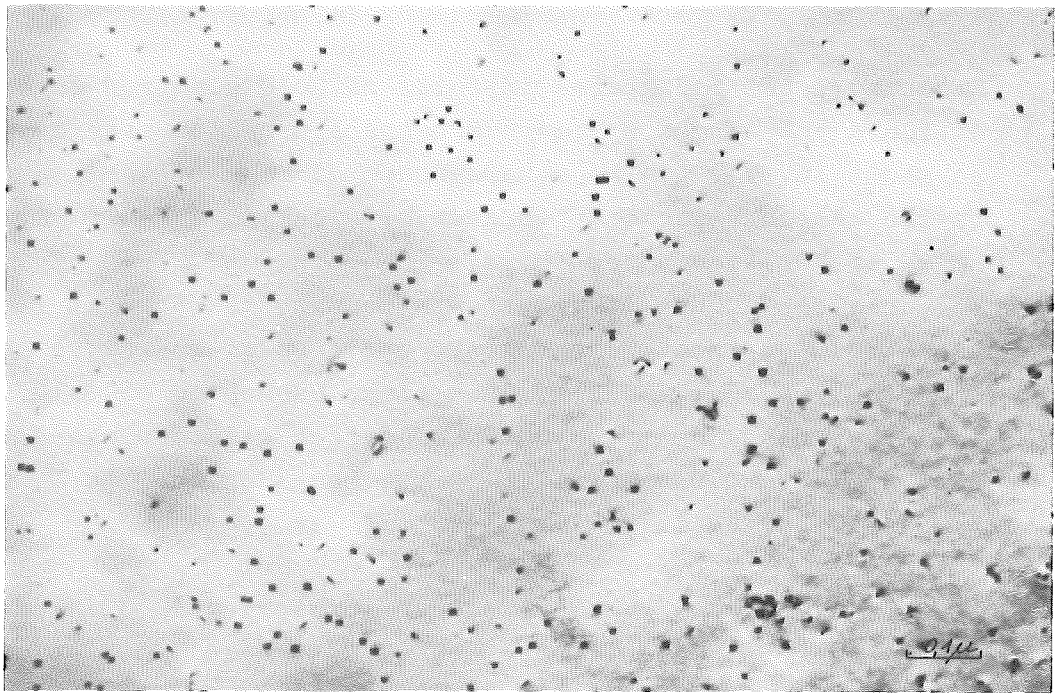

Fig. 6 Electron Irradiated Gold
Dose $1{,}8.10^{20}$ e/cm^2 3MeV
Irradiation Temperature 180 ^{o}K
Observation at 293 ^{o}K
Foil Orientation [100]
Square shape of many clusters is characteristic appearance of Stacking fault tetrahedra in (001) foils.

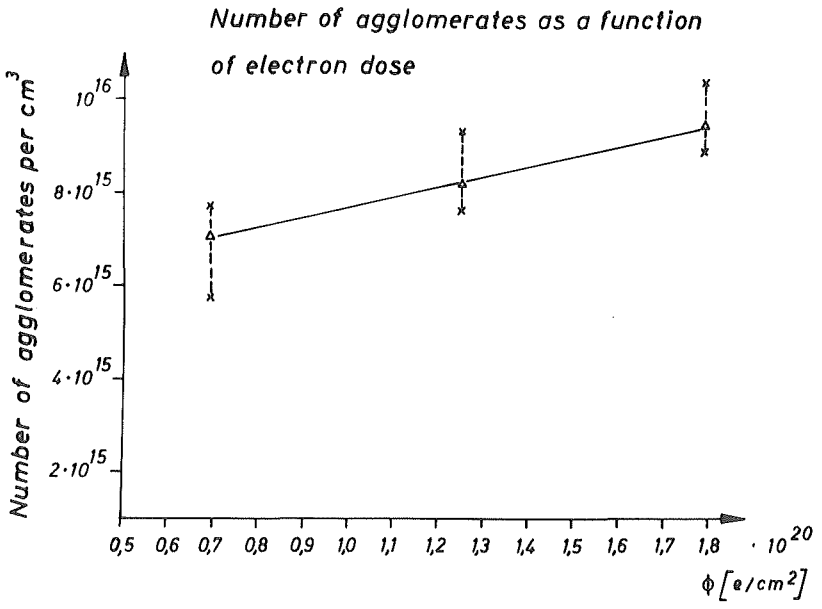

Figure 7 Dose dependence of cluster density in gold irradiated with 3 MeV electrons at 18o^{o} K. Triangles give the tetrahedra density.

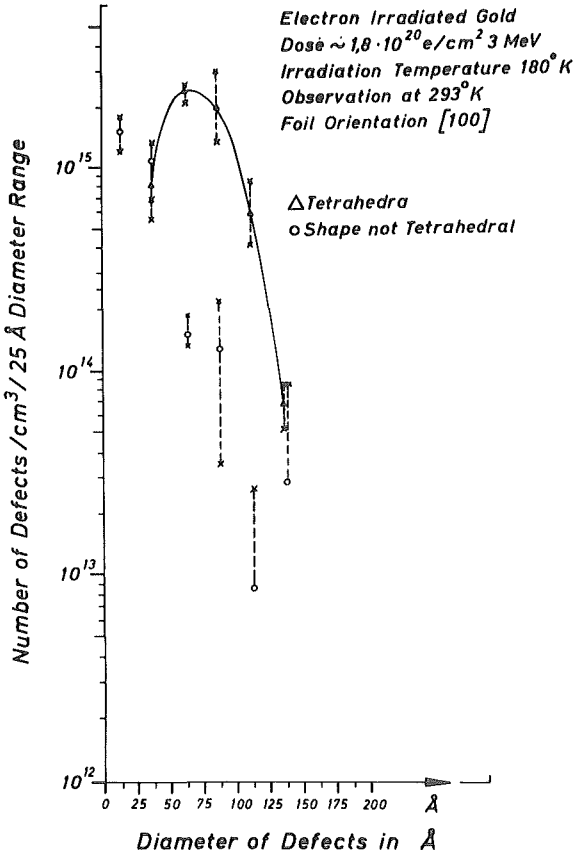

Figure 8
Size distribution of clusters observed in gold irradiated to a dose $\sim$ 1,8 x 10^{20} e/cm^2 with 3 MeV electrons at 180° K. Triangles give the density of tetrahedra, while circles give the density of clusters which do not show the characteristic shape of tetrahedra.

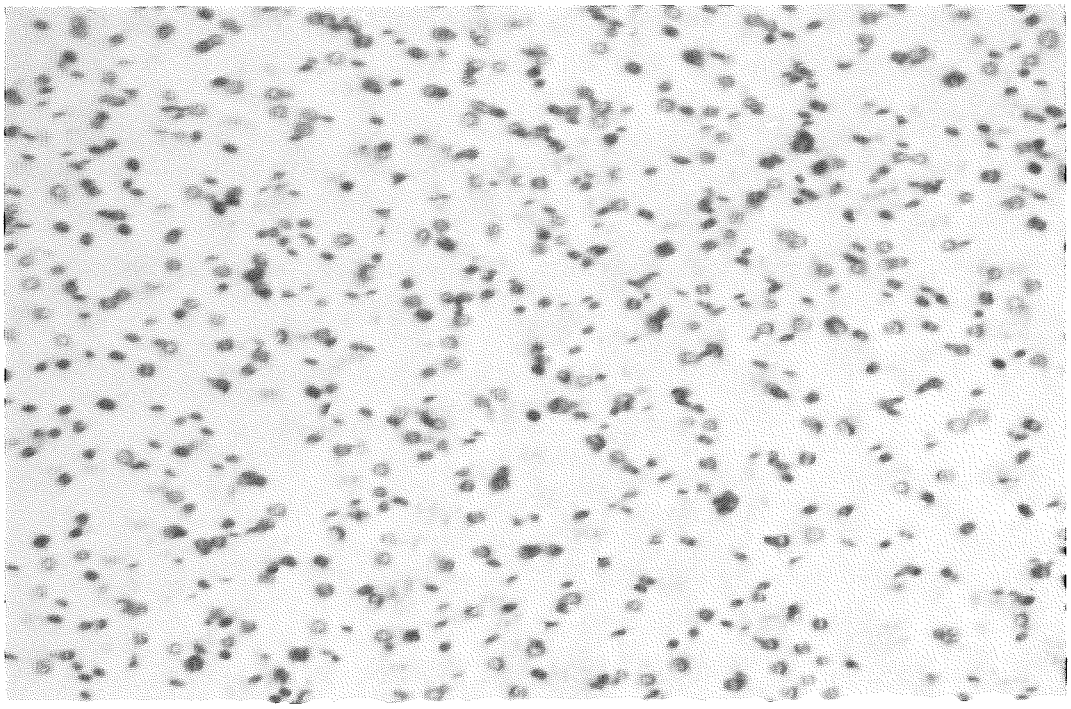

Fig. 9 Electron Irradiated Niobium
Dose 1.10^{20} e/cm^2 3MeV
Irradiation Temperature 50°C
Foil Orientation [111]

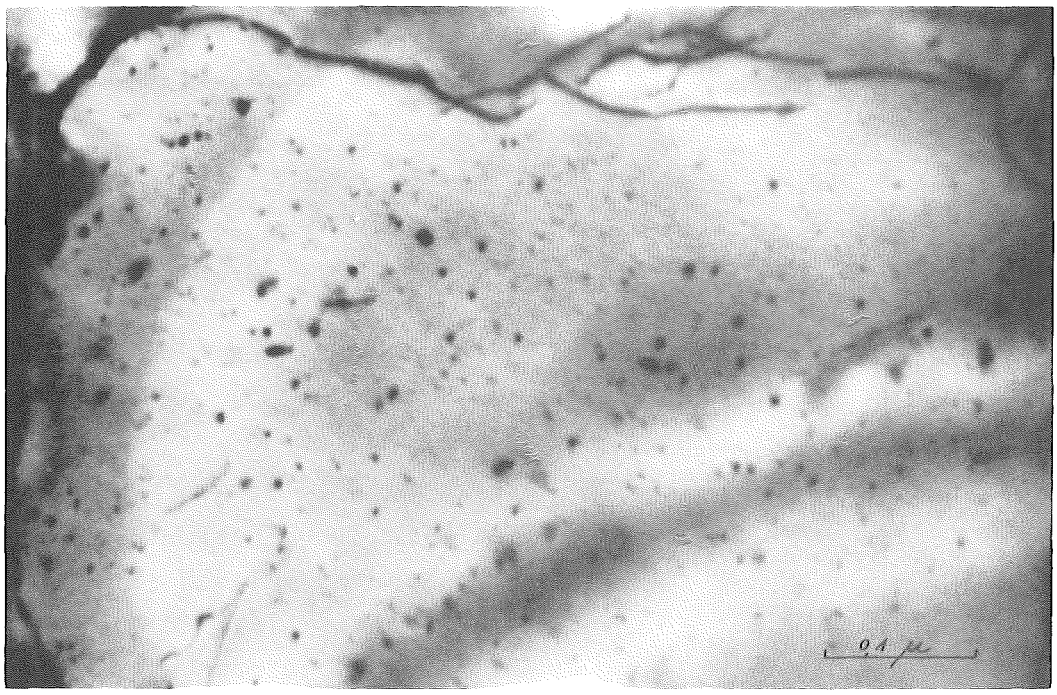

Fig. 10 Electron Irradiated Platinum
Dose $\sim 10^{19}$ e/cm^2
Irradiation Temperature 90°K
Foil Orientation [211]

References

1. G.P. Scheidler, M.J. Makin, F.J. Minter, W.F. Schilling, Proc. Symp. on The Nature of Small Defect Clusters, Harwell 1966, AERE-R 5269, 4o5

2. P. Sigmund, G.P. Scheidler, G. Roth, Proceedings of the International Conference on Solid State Physics Research with Accelerators, Brookhaven 1967 BNL 5oo83, 374

3. R.M. Walker, Radiation Damage in Solids, ed. by D.S. Billington, Academic Press 1962, 594

4. G. Duesing, H. Hemmerich, D. Meissner, W. Schilling, phys. stat. sol. 23, 481 (1967)

5. F. Dworschak, H. Schuster, H. Wollenberger, J. Wurm, phys. stat. sol. im Druck

6. W. Bauer, A. Seeger, A. Sosin, Phys. Letters 24 A, 195 (1967)

7. G. Roth, V. Naundorf, G. P. Scheidler, diese Tagung

8. M. Rühle, F. Häussermann, P. Huber, M. Wilkens, Intern. Elektronenmikroskopische Tagung in Rom, 1968

9. K.-P. Chik, phys. stat. sol. 1o, 659 (1965)

Influence of Irradiation-Induced Defects in Aluminium and Copper on Halleffect, Magnetoresistance and Deviations from Matthiessen's Rule.

K.Böning, B.Lengeler, J.-M.Welter and H. Wenzl

Physik-Department der Technischen Hochschule München and Institut für Festkörper- und Neutronenphysik der Kernforschungsanlage Jülich.

Abstract.

The Hall effect R, magnetoresistance m and deviations d from Matthiessen's rule were measured in pure Aluminium and Copper after neutron irradiation at 4.6°K and during annealing. Since the values of R, m and d sensitively depend on the defect type and are nearly independent of the defect concentration, they could be used to investigate changes of defect configurations during irradiation and annealing which do not show up in the residual electrical resistivity.

1. Introduction.

The electrical transport properties of metals depend on the shape of the Fermi surface and on the scattering potentials for the conduction electrons /1,2,3,4/.

The simplest electron transport property, the residual electrical resistivity, is given primarily by the product of the specific defect property (resistivity per unit concentration) and the defect concentration. Electrical properties as magnetoresistance, Halleffect and deviations from Matthiessen's rule provide a means to measure specifical defect properties independent of the defect concentration; additionally they are sensitive to the strength and anisotropy of the scattering potentials.

We studied the influence of neutron irradiation induced point defects in copper and aluminium on the transport properties. The aim was to investigate specific scattering properties of the defects and to detect possible configuration changes during annealing which usually cannot be seen by simple resistivity measurements.

Low temperature neutron irradiation allows to induce scattering centers of different types in the sample in a reproducible way. However this mixture of different defect types complicates the interpretation of the measurements and the evaluation of specific property changes, even if one uses the "annealing stage" technique, because we are dealing with property changes which may sensitively depend on all the defects remaining in the sample after an annealing step and not only on those which are recovering (whereas activation enthalpy evaluations by resistivity measurements are to a first order of approximation independent of remaining stable defects /5/).

Specific property changes can be uniquely defined for the defects of the last annealing stage, whereas for the other ones only qualitativ statements are possible at the moment.

This report intends to show the possibilities of the methods used and presents only a rough discussion of the results.

2. Experimental Details.

All our samples were of polycristalline material. Some data are presented in Table 1.

	aluminium	copper
form and dimension of the sample	foil $8 \cdot 2 \cdot 0.054$ mm	wire $310 \cdot 0.2^{\phi}$ mm
nominal purity provenance	99.999 % Degussa	99.999 % Asarco
initial resistivity ratio $\rho_{300\,°K} / \rho_{4.6\,°K}$	1400 (size-effect corr. = 2160)	950
transport property studied	transverse magnetoresist. Hall effect	longitudinal magnetoresist. Matthiessen's rule
measurement accuracy	$\pm$ 0.005 μV	$\pm$ 0.1 μV
irradiation dose at 4.6 °K Φt $[n/cm^2]_{E>0.1\,MeV}$	$1.05 \cdot 10^{18}$	$0.60 \cdot 10^{18}$ $2.52 \cdot 10^{18}$

Table 1

The samples were irradiated at liquid helium temperature in the core of the Munich Research Reactor FRM (thermal flux 10^{13} n/cm^{2}s, fast flux $\approx 10^{13}$ n/cm^{2}s for E > 0.1 MeV) /6/.

The resistivity and Halleffect measurements were performed at 4,6°K with the conventional potentiometric method in a cryostat containing a superconducting solenoid for producing variable magnetic fields from o to 3o kG. Further details are reported elsewhere /7/.

No size effect corrections where performed for the Kohler plots according to a procedure suggested by Olsen /8/. They are significant only for the measuring points with $\rho_o / \rho_{o\,max} < 5\%$ (size effect correction > 3%) of aluminium.

3. Copper: Longitudinal magnetoresistance.

For a metal containing one type of scattering centers the relative increase of resistance

$$\frac{\Delta\rho_o(B)}{\rho_o(0)} \equiv \frac{\rho_o(B) - \rho_o(0)}{\rho_o(0)}$$

in a magnetic field B depends according to Kohler's rule /9/ on $B/\rho_o(0)$. Furthermore the value

$$m\left(\frac{B}{\rho_o(0)}\right) \equiv \frac{\Delta\rho_o(B)}{\rho_o(0)} \Bigg|_{\frac{B}{\rho_o(0)}}$$

for a fixed value of $B/\varrho_o(o)$ is specific for the scattering configuration, independently of the concentration of scattering centers. The measured values of $\Delta\varrho_o(B)/\varrho_o(o)$ versus $B/\varrho_o(o)$ are plotted in Fig.1 for different irradiation and annealing conditions characterized by the zero-field residual resistivity $\varrho_o(0)$. The differences between the curves indicate different scattering properties of the corresponding defects, which appears more clearly in Fig.2, where

$$m\left(\frac{B}{\varrho_o(0)} = 3\cdot 10^8 \frac{kG}{\Omega\cdot cm}\right)$$

is plotted versus $\varrho_o(o)$.

Correct numerical calculations were done for isotropic point defects /10/. These results do not - until now - provide a basis for the interpretation of our experimental results and do not give us even qualitative understanding of the behaviour of more complicated - but realistic - defect structures in the samples.

For the discussion of the results we use the relaxation time concept though it is not completely reliable /4/. The basic idea is that the increase of resistivity in a magnetic field is due to an orientation dependent (anisotropic) distribution of the free path of the electrons $\ell_k = v_k \tau_k$ over the Fermi surface, where the variance of the velocity v_k of the electrons is a measure of the deviations of the Fermi surface from spherical shape and the variance of the local relaxation time τ_k is a measure of the anisotropy (orientation-dependence) of the scattering process.

For a given value of $B/\varrho_o(o)$, where $1/\varrho_o(o)$ is proportional to the mean value of the free path $\langle\ell\rangle$, m will increase with increasing variance of the free path and vice versa /11/. Accordingly m is a specific defect property, depending on the scattering potential. If we deal with a mixture of different scattering types, a clear statement about the behaviour of m is difficult to make, unless one type is overwhelming, either because the corresponding defect concentration is quite high or because it has outstanding scattering properties.

What does the experimental value of m tell about ℓ in the case of copper? We distinguish between two regions of the Fermi surface: belly and neck /12/. The Fermi velocity is probably much smaller on the necks than on the bellies /13/.

Before irradiation the overwhelming scattering centers contained in the sample are impurity atoms for which we guess that τ_k is almost independent of the k-direction. In this case m reflects the situation $\ell_N < \ell_B$ which is given by the anisotropy of v_k on the Fermi surface.

During irradiation m increases: the anisotropy of ℓ is increasing. So not only the concentration of the defects increases, but the type changes too, e.g. due to the overlap of cascades with defect nests. After the high dose irradiation (20% of the nests are affected by the overlap) m furthermore increases during annealing in stage II/III. This indicates that now a type of defect with a very large anisotropy predominates.

Without detailed calculations it will not be possible to correlate the measured m values with geometrical configurations of the scattering centers on account of the fact that we are dealing with an effective defect configuration, which is an average over different allowed orientations. If the defects

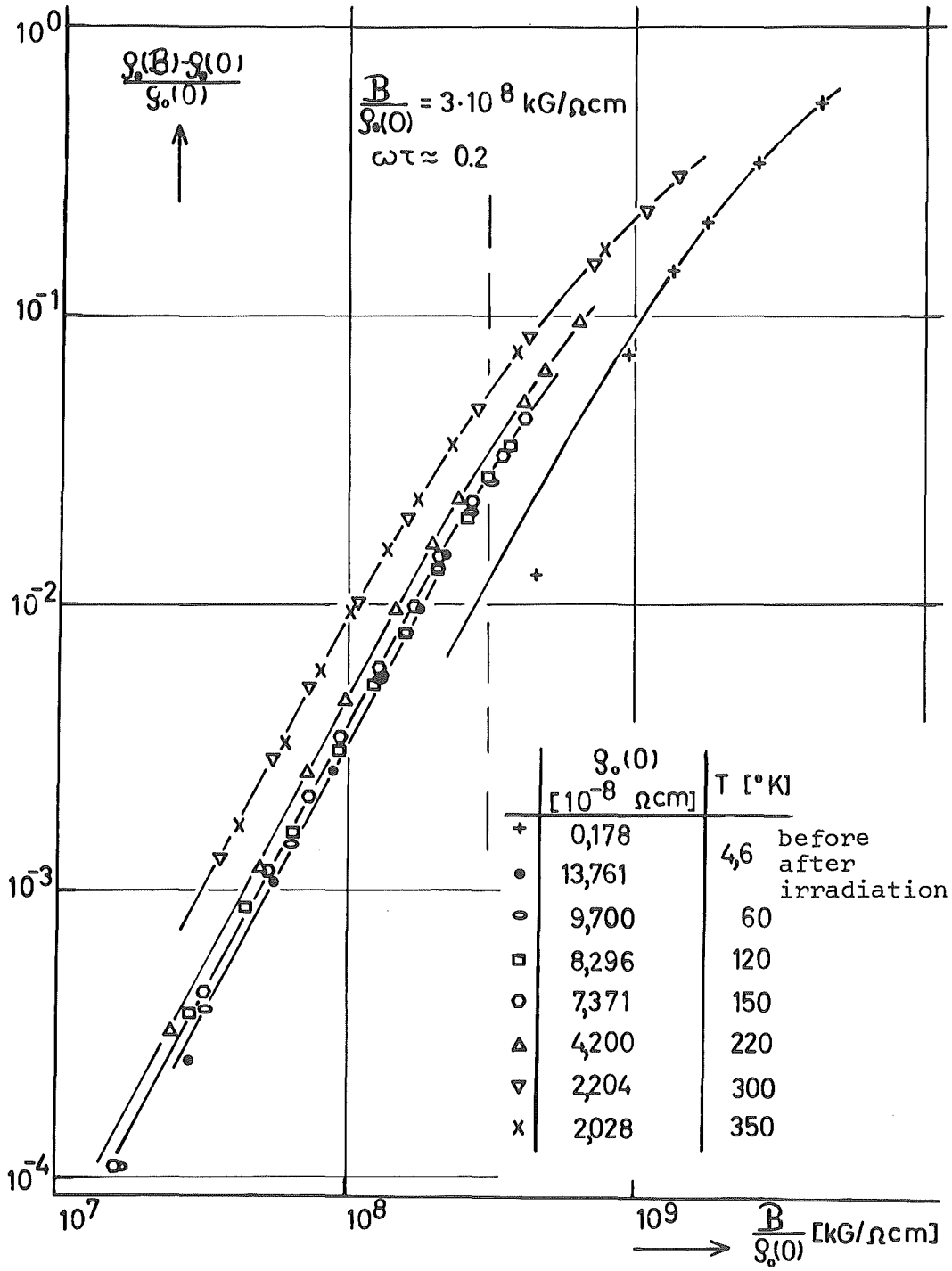

Fig. 1 Longitudinal magnetoresistance of neutron irradiated polycrystalline copper for different values of $\varrho_0(0)$ characterising different irradiation doses and annealing steps.

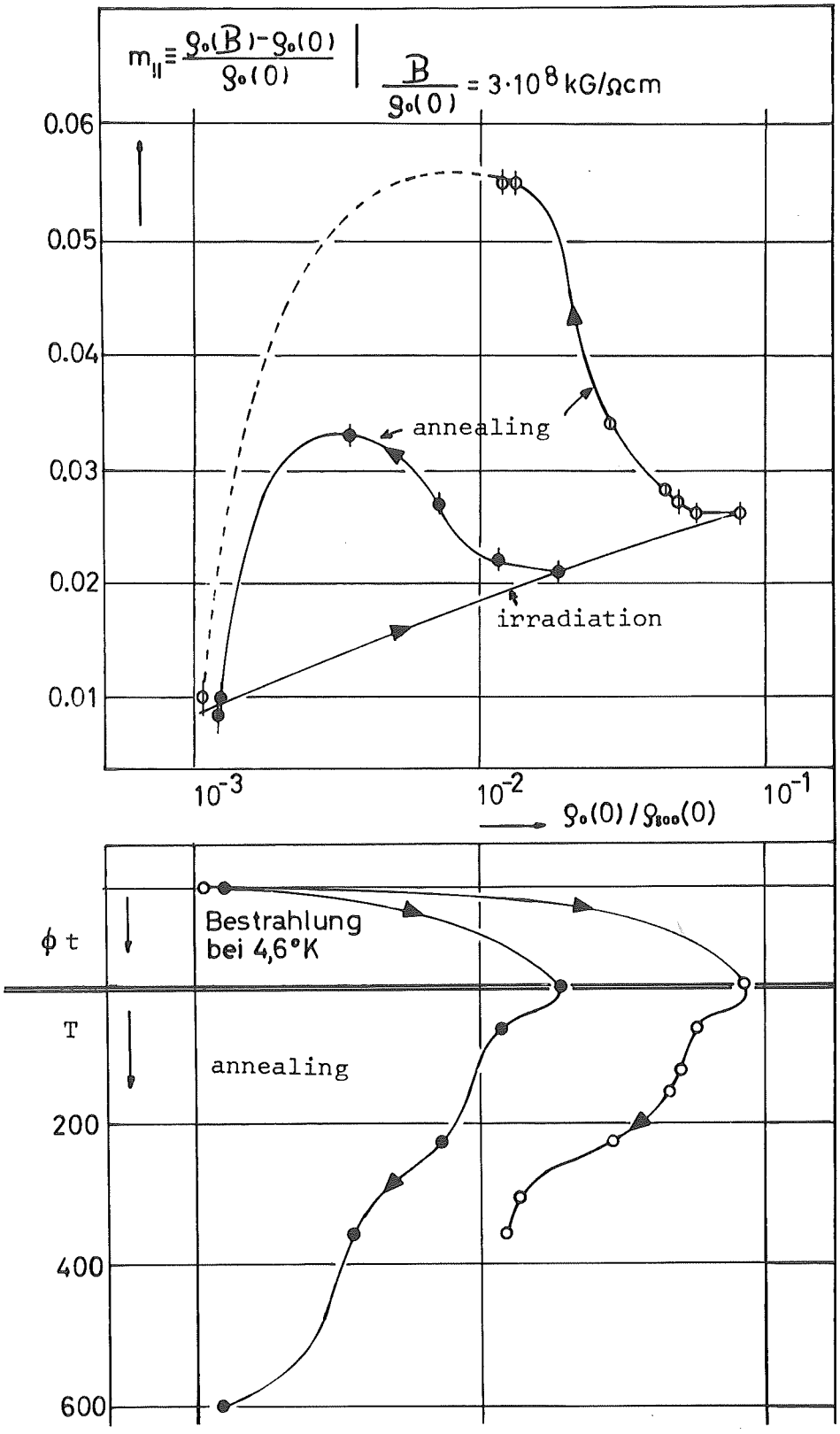

Fig. 2 Longitudinal magnetoresistance of polycrystalline copper during neutron-irradiation and subsequent annealing taken at $B/\varrho_0(0) = 3\cdot10^8$ kG/Ω cm from figure 1.

are distributed at random and the conduction electrons are scattered at random, too, this effective potential has cubic symmetry, even if the individual defects do not have it.

The defects remaining before stage V are vacancy /14/ and probably interstitial aggregates in (111) and equivalent lattice plains. Their effective potential seems to have a quite high scattering cross section in (111) and equivalent directions and thus reduces the relaxation time on the necks, resulting in an increased variance of ℓ ($\ell_N \ll \ell_B$) and increased m.

4. Copper: Deviations from Matthiessen's rule.

Simultaneously with the magnetoresistance we investigated the deviation from Matthiessen's rule at the same experimental conditions.

Matthiessen's rule assumes the simple additivity of partial resistivities due to different types of scattering centers. This is only true if the scattering properties of the different defect types are quite identical /15/. In general we have to add a deviation term Δ to the sum:

$$\varrho(T) = \varrho_0 + \Delta\varrho_0 + \varrho_T + \Delta(\Delta\varrho_0, \varrho_T)$$

$\Delta\varrho_0$ = increase of resistivity with irradiation.

where ϱ_0 is the residual resistivity before irradiation, ϱ_T the resistivity due to phonon scattering. The phonon spectrum is only slightly influenced by the irradiation; we assume that ϱ_T is not changed.

Figure 3 reports the measured $\Delta/\Delta\varrho_0$ as a function of ϱ_T for different annealing stages. For $\varrho_T > \Delta\varrho_0$ (above 50°K) $\Delta/\Delta\varrho_0$ reaches a certain saturation value $(\Delta/\Delta\varrho_0)_{max}$. The value of $d \equiv (\Delta/\Delta\varrho_0)_{max}$ is a specific property of the combined defect-phonon scattering: it is a measure for the difference of scattering anisotropies of defects and phonons /16,17/. Figure 4 indicates the behaviour of d for different irradiation and annealing conditions which is comparable to the behaviour of m (see Fig.2).

5. Aluminium: Hall effect and transverse magnetoresistance.

5.1 Preliminary remarks.

We can apply the same general ideas (Kohler's rule, plotting of the results, anisotropy of the free length, etc.) to the transverse magnetoresistance in Al as to the longitudinal one in Cu (chapter 3). For the Hall-effect we work with the following assumptions:

The Hall-parameter R is plotted against $B/\varrho_0(o)$, corresponding to the Kohler diagram. In the low - ($B/\varrho_0(o) \sim \omega\tau \ll 1$) and high - ($B/\varrho_0(o) \sim \omega\tau \gg 1$) field region (ω = cyclotron frequency) the Hall-coefficient R is insensitive to small variations of $B/\varrho_0(o)$, so that we do not need to fix a well defined value of $B/\varrho_0(o)$ to determine R_0 ($\omega\tau \ll 1$) and R_∞ ($\omega\tau \gg 1$) as it was neccessary for the magnetoresistance coefficient m. Therefore changes in R_0 and R_∞ can be defined much more unambiguously.

Only the high field Hall-coefficient $R_\infty = 1/e(n_- - n_+)$ is an unequivocal measure of the concentration of conduction electrons (electron-like regions of the Fermi-surface: en_+, hole-like regions: en_-; here $n_- - n_+ = -1 \cdot n_0$; n_0 = number of atoms per unit-volume; $e < 0$./18,19/).

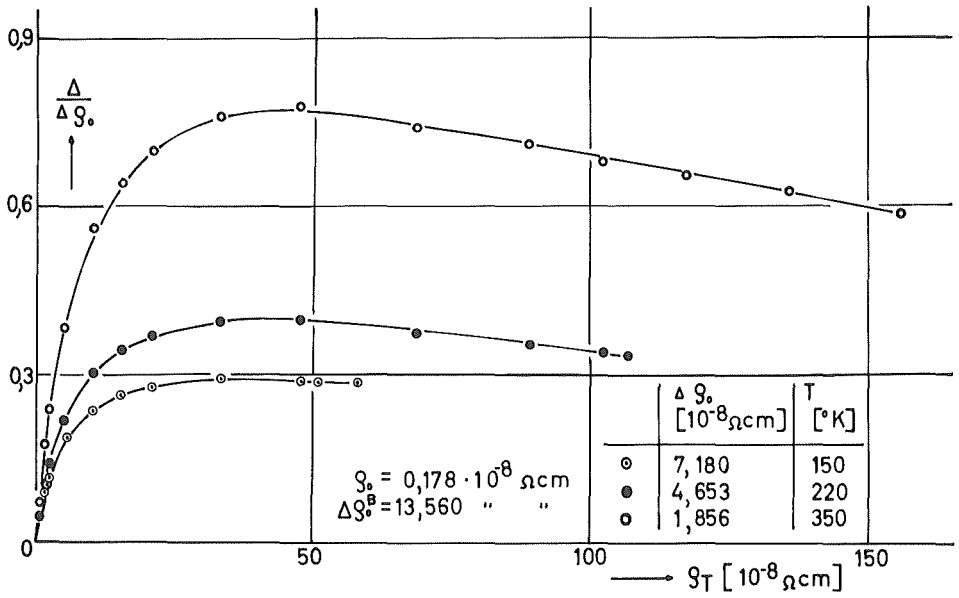

Fig. 3 Deviations from Matthiessen's rule of neutron-irradiated copper after three annealing stages plotted as a function of the resistivity due to phonons.

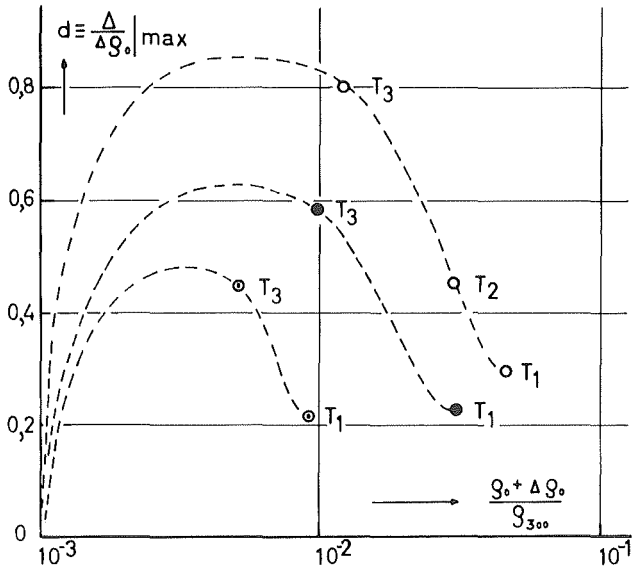

Annealing temperatures:

T_1 = 150°K
T_2 = 220°K
T_3 = 350°K

Fig. 4 Maximum values of the deviations from Matthiessen's rule in copper as a function of the residual resistivity at different annealing stages and for three different irradiation doses.

In the low field Hall-coefficient $R_o = r/ne$ /20/ (ne: true density of conducting electrons times electronic charge; here $n = 3 \cdot n_{oi}$ $e<0$), r depends on the shape of the Fermi-surface and on the scattering potentials /21/ and is thus another specific defect property besides m.

The Fermi-surface of aluminium can be divided into three regions /22,23/: a) the electron-like part in the third zone which is a monster of 36 tubular arms, b) the part in the second zone consisting of a " polyhedra" of 14 electronlike faces, and c) the 36 edges which behave hole-like for the Hall-coefficient. We assume that the velocity on the faces is greater than the one near the edges: $v_E < v_F$.

Increasing scattering anisotropy may lead to a reduction of r and even to a change of sign, if the electrons in the "hole-like" regions of the Fermi-surface are scattered more weakly than those on the other parts.

5.2 Results and discussion.

Figure 5 and 6 show the dosis and annealing curves for magnetoresistance $m = \Delta\varrho_o(B)/\varrho_o(o)$, figure 7 and 8 the same for the Hall-effect R. The behaviour of a certain low-field value $m_o(B/\varrho_o(o) = 4 \cdot 10^{-4}\,kG/\Omega cm)$ and of the low-field Hall-coefficient $R_o(B/\varrho_o(o) = 4 \cdot 10^{-4}\,kG/\Omega cm)$ is summarized in figures 9 and 10.

During irradiation m_o decreases slightly whereas R_o increases and even changes its sign. When the resistivity is about 10 times the initial value, both coefficients saturate. This indicates that in this dose range only the concentration, not the scattering properties of the defects is changed.

During annealing these coefficients do not change until the end of stage I where they decrease sharply and remain almost constant after stage II. Then m_o increases and R_o decreases to their original value.

At the end of stage I the residual resistivity $\varrho_o(o)$ decreases comparatively little. But measurements of internal friction /24/ show that a large number of defects changes its configuration to a new type which determines the annealing at higher temperatures.

The high-field Hall-coefficient R_∞ does not change within the accuracy though a reliable measurement would only be possible for 100 times larger magnetic fields than available to us (30 kG). For a concentration of up to 10^{-5} frenkel-defects/atom there is $\Delta R_\infty/R_\infty < 10^{-3}$, so that the number of conduction electrons seems to remain fairly constant during irradiation.

We want now to discuss the behaviour of m_o and R_o in a very simple model. Assumptions: relaxation time model (see remarks in chapter 3); Fermi surface not altered by the irradiation; separate relaxation times τ for each of the three regions of the Fermi surface ($\tau_{2F} \triangleq$ faces of the 2nd zone; $\tau_{2E} \triangleq$ edges of the 2nd zone; $\tau_3 \triangleq$ third zone monster); $v_{2E} < v_{2F}$ and $\tau_{2E} \approx \tau_{2F}$ for impurity atoms; before irradiation the free paths $\ell_{2E} < \ell_{2F}$ and correspondingly electron like behaviour ($r>0$) /20/ and a certain value of m. The experimental changes of the two coefficients m_o and R_o cannot be explained consistently by taking into account the 2nd zone only ; the "monster" must be included. The variance of ℓ_3 is probably very small, so that we neglect the influence of the monster electrons on m_o and regard only their influence on R_o .

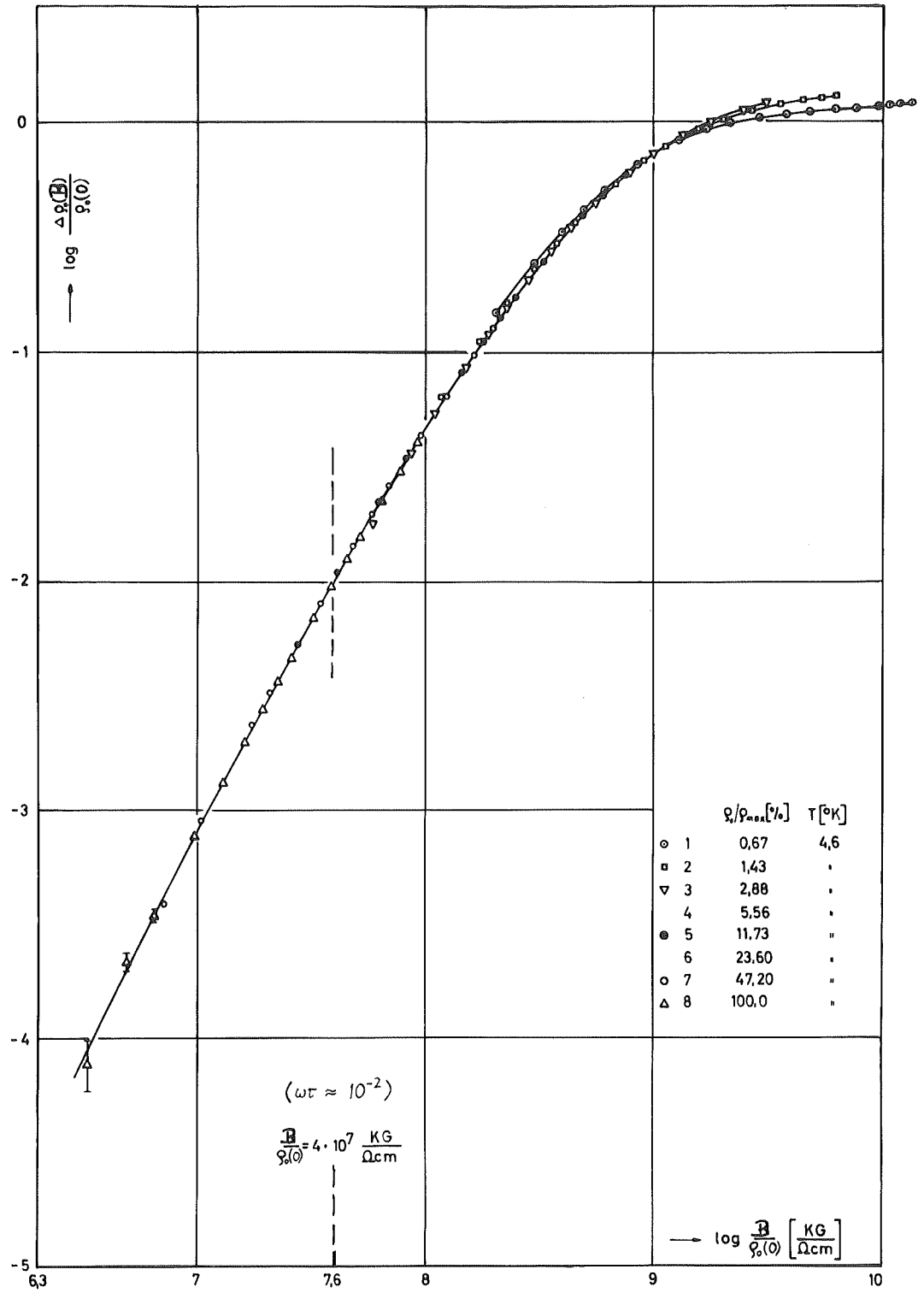

Fig. 5 Transverse magnetoresistance during neutron-irradiation at 4.6°K in Aluminium. The data are taken by successive measurements of log $(\Delta\rho_0(B)/\rho_0(0))$ as a function of log $B/\rho_0(0)$ at different dose levels (1 till 8). The resistivity at each dose level can be found by multiplication of $\rho_{0\,max} = 3.1\ 10^{-7}\ \Omega$ cm with the fraction $\rho_0/\rho_{0\,max}$ listed in the figure.

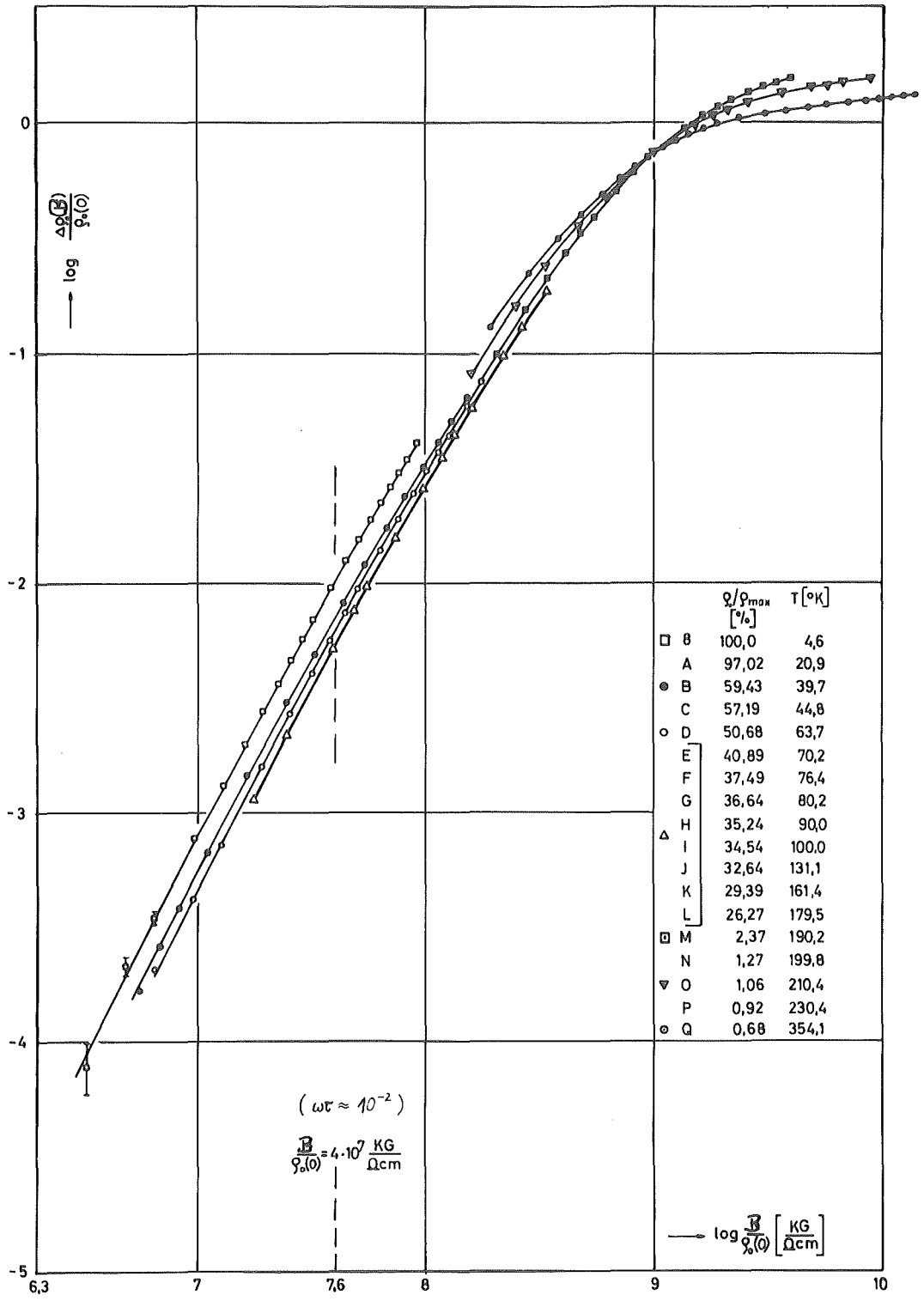

Fig. 6 Transverse magnetoresistance during annealing after neutron-irradiation at 4.6°K in Aluminium. The data are taken by successive measurements of log ($\Delta\rho_0(B)/\rho_0(0)$) as a function of log $B/\rho_0(0)$ after different annealing steps T listed in the figure. The resistivity at each annealing step can be found by multiplication of $\rho_{i,max} = 3.1\ 10^{-7}\ \Omega$ cm with the fraction ρ_0/ρ_{max} listed in the figure.

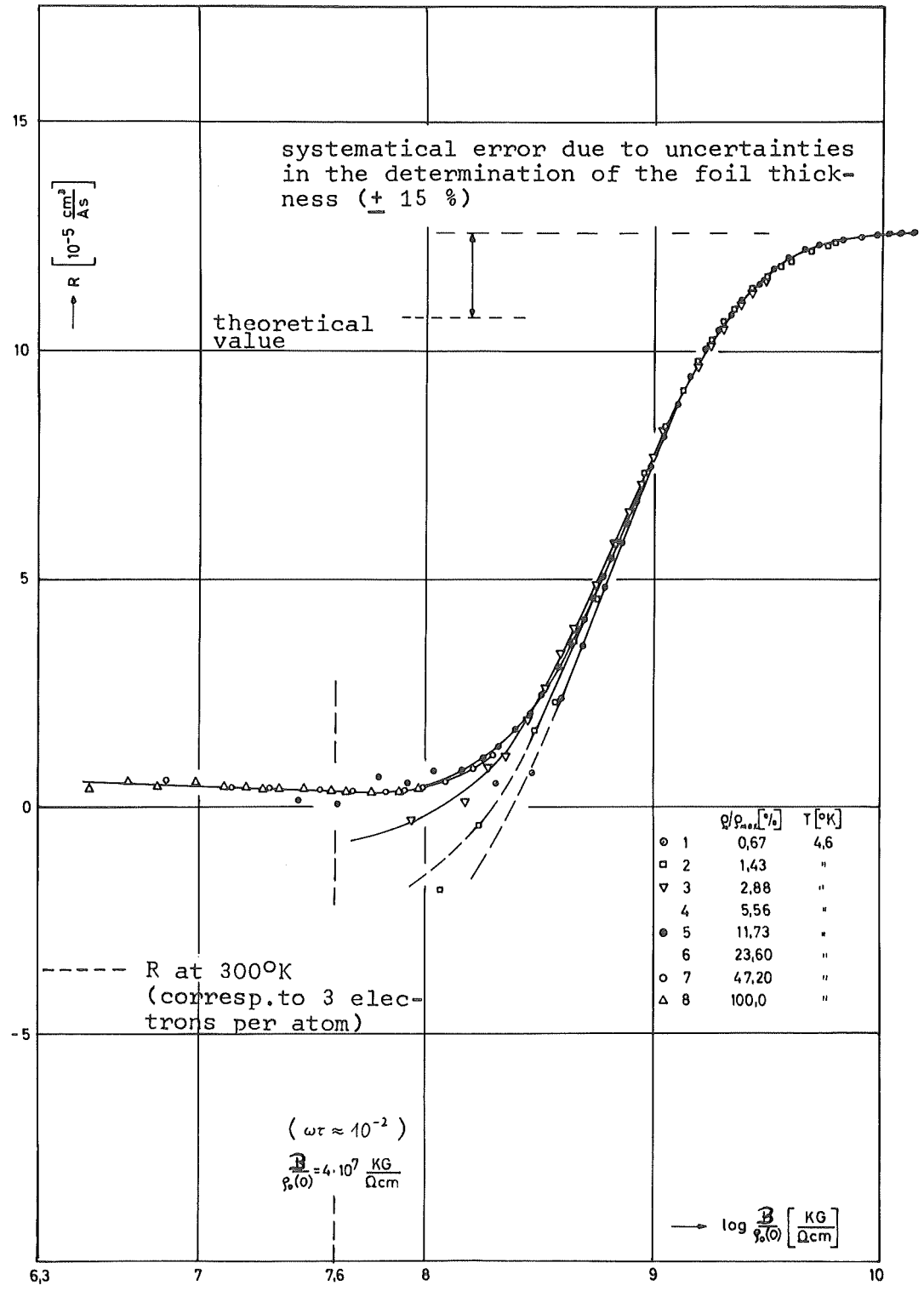

Fig. 7 Hall parameter R plotted as a function of log $B/\rho_0(0)$ for Aluminium during neutron irradiation at 4.6°K. The data are taken by successive measurements of R as a function of log $B/\rho_0(0)$ at different dose levels (1 till 8). The resistivity at each dose level can be found by multiplication of ρ_{max} = 3.1 10^{-7} Ω cm with the fraction ρ_0/ρ_{max} listed in the figure.

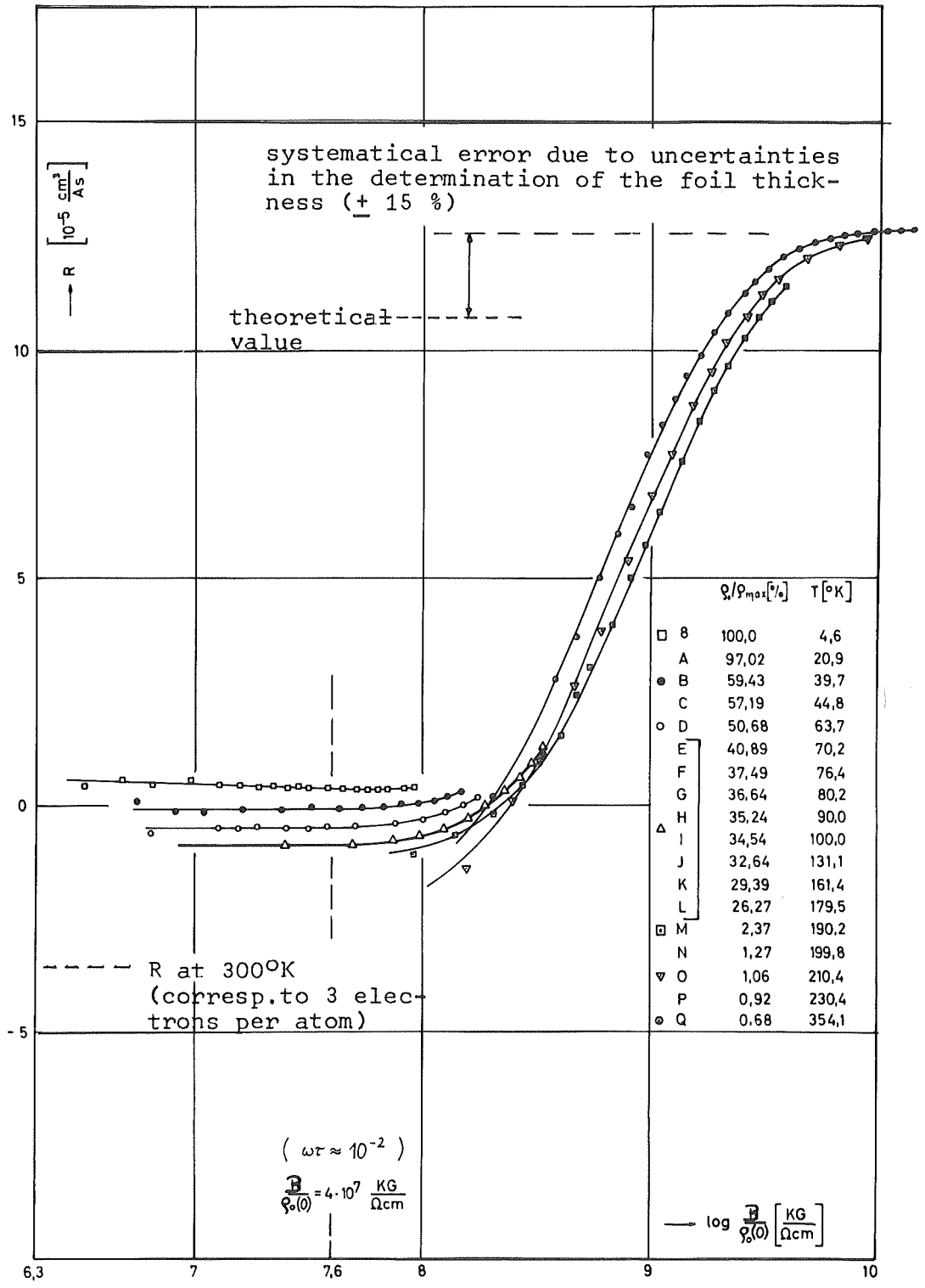

Fig. 8 Hall parameter R plotted as a function of log $B/\rho_0(0)$ for Aluminium during annealing after neutron irradiation at 4.6°K. The data are taken by successive measurements of Hall parameter R as a function of log $B/\rho_0(0)$ after different annealing steps T listed in the figure. The resistivity at each annealing step can be found by multiplication of $\rho_{max} = 3.1\ 10^{-7}\ \Omega$ cm with the fraction ρ_0/ρ_{max} listed in the figure.

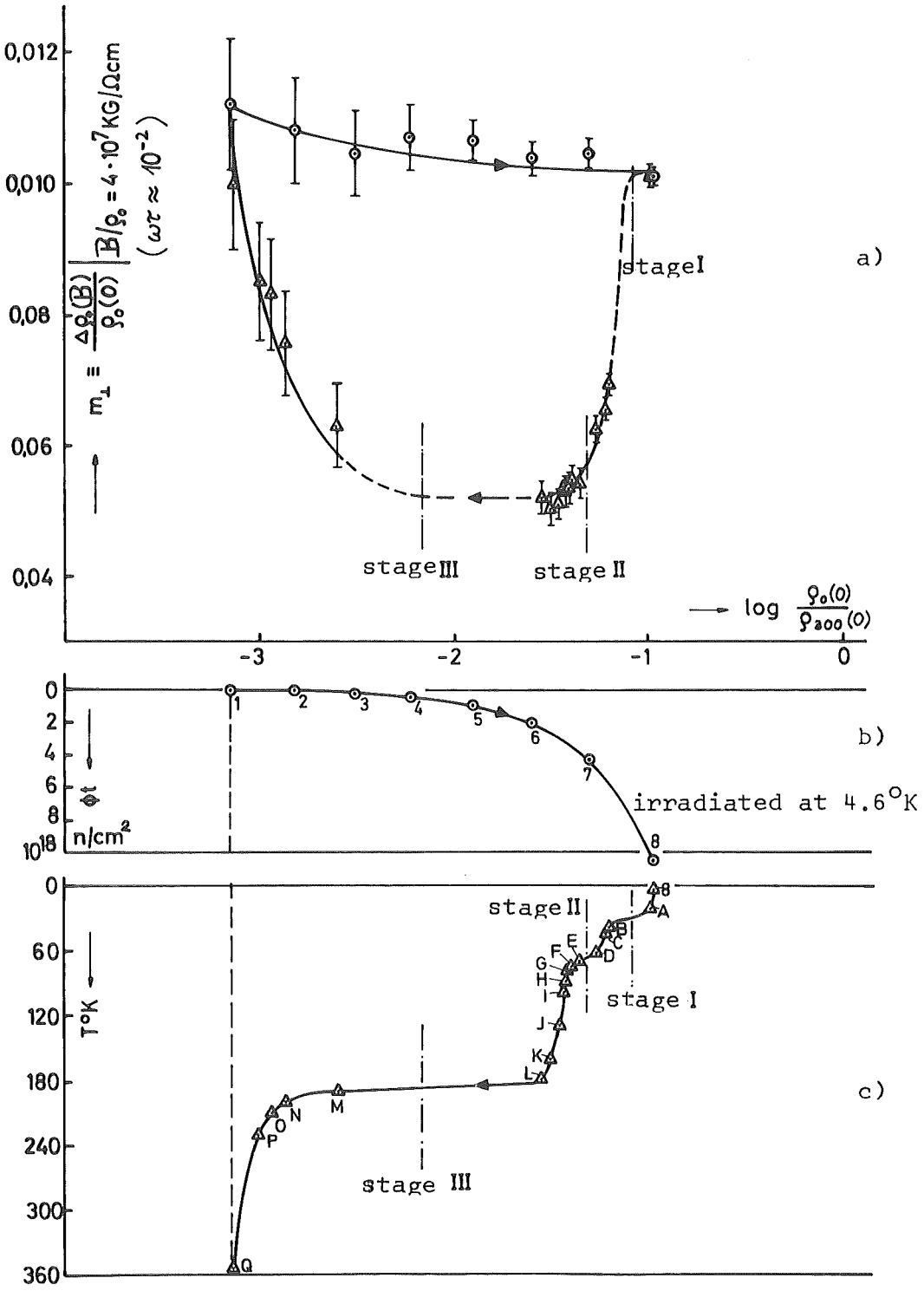

Fig. 9 a) Low-field magnetoresistance during neutron irradiation (O) and annealing (Δ) of Aluminium. The values $\Delta\rho_0(B)/\rho_0(0)$ are taken at $B/\rho_0 = 4 \cdot 10^{-7}$ kG/Ω cm from figures 5 and 6.
b+c) Dose and annealing curve of the electrical resistivity for Aluminium.

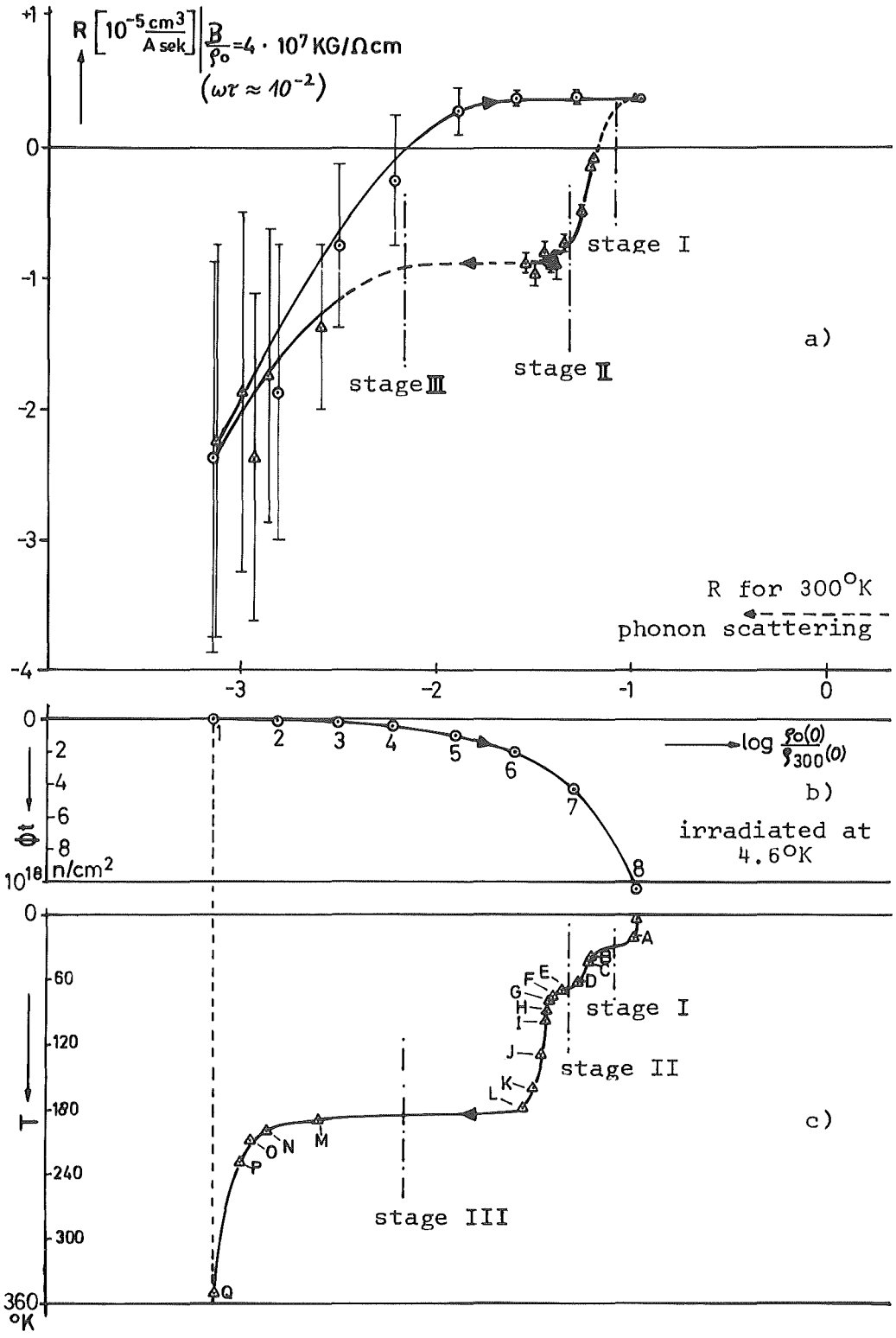

Fig. 10 a) Low-field Hall parameter R during neutron irradiation (O) and annealing of Aluminium. The values R are taken at $B/\varrho_0 = 4 \cdot 10^7 kG/\Omega\,cm$ from figures 7 and 8.
b+c) Dose and annealing curve of the electrical resistivity for Aluminium.

Possible and consistent changes of the free paths with m and R are indicated in Table 2.

Table 2

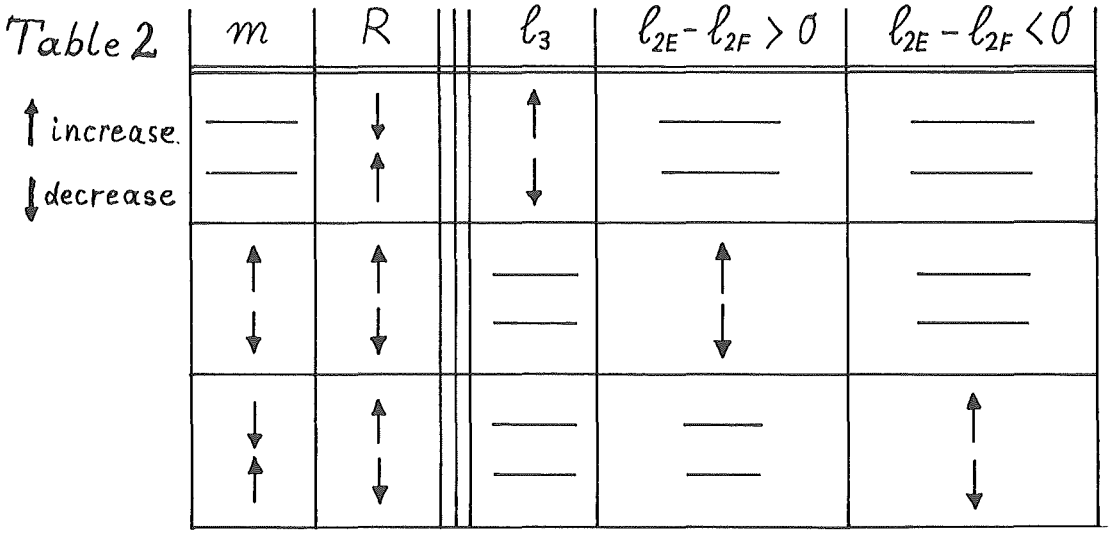

6. Conclusion.

It was demonstrated that the magnetoresistance m, the Hall effect R and the deviations from Matthiessen's rule d are indicating changes of the defect types and can be considered as specific defect properties. They are a measure of the scattering potential for the conduction electrons.

The next work to be done is on the one side to perform experiments on single crystals and on the other side to improve the theoretical basis of the discussion.

References.

/1/ A.Sommerfeld,H.Bethe in "Geiger, Scheel; Handbuch der Physik", Vol.24/2.

/2/ A.B.Pippard: "Documents on Modern Physics - The Dynamics of Conduction Electrons", New York, London, Paris 1965.

/3/ A.Seeger; phys. lett. 2o,6o8 (1966).
/4/ H.Bross in "Festkörperprobleme", Vol.5, Braunschweig 1967.
/5/ F.Bell; this conference.
/6/ H.Meissner,W.Schilling,H.Wenzl; euronuclear 2,277 (1965).
/7/ S.Winkler; Dissertation TH München (1967).
/8/ J.L.Olsen; helv. phys. acta 31,713 (1958).
/9/ M.Kohler; Ann. Physik (5) 32,211 (1938).
/1o/ A.Seeger, E.Mann, K.Clausecker; phys. stat. sol. 24,721 (1967)
/11/ see /1/.
/12/ J.M.Ziman; adv. phys. 1o,1 (1961).
/13/ J.S.Dugdale, L.Firth; September-Conference Zürich 1968.
/14/ M.Rühle, M.Wilkens; phys. stat. sol. 16,K1o5 (1966).
/15/ D.K.C.MacDonald in "Handbuch der Physik", Vol.5, Berlin, Göttingen, Heidelberg 1956.
/16/ H.Bross; Zeitschrift für Naturforschung 14a, 56o (1959).
/17/ see /9/.
/18/ I.M.Lifshitz, M.I.Azbel, M.I.Kaganov; Sov. Phys. JETP 4, 41 (1957).
/19/ E.Fawcett; adv. phys. 13,139 (1964).
/2o/ R.S.Allgaier; phys. rev. 165,775 (1968).
/21/ see /2o/.
/22/ J.N.Cooper, P.Cotti, F.B.Rasmussen; phys. lett. 19,56o (1965).
/23/ W.Harrison; phys. rev. 118,1182 (196o).
/24/ F.Kerscher; Dissertation TH München (1968).

RADIATION DAMAGE IN THIN FILMS CAUSED DURING THEIR VACUUM DEPOSITION BY IRRADIATING WITH IONS OF THE EVAPORATION MATERIAL

E. F. Krimmel

Institut für Angewandte Physik
Universität Tübingen
Tübingen, Germany

Radiation damage is caused in thin films during their vacuum deposition by fast and monoenergetic ions of the evaporation material. The films with uniform thickness over an area of more than 10 cm^2 contain a high and nearly constant damage rate throughout the total volume. Films of Cu, Au, Pt, Ni, Cr, Nb, Pt-Ir, Au-Cr and Fe-Cr deposited at room temperature and exceeding a critical thickness show radiation hardening. Depending on the thickness of the film, sharp and pronounced annealing peaks of the electric resistivity were observed with Au, Pt, Cr and Ni whereby Au and Pt films became soft but Cr and Ni films did not change their mechanical hardness. The surface of the films acts as a sink for the lattice defects. No radiation hardening was observed with Al and Ag.

In an earlier paper describing a universal ion source for producing ions from solids[1] it was proposed to perform radiation damage experiments irradiating a specimen by its own ions to avoid that the irradiating beam itself causes impurities. In this paper method and some first results shall be reported.

Method

To obtain well defined results one needs for these radiation damage experiments an intensive and monochromatic beam of high energetic ions. The ion source has to be universal and simple in its operation[1]. An elektron beam of electrons with energies up to 70 keV and currents in the range of 10 mA is focused on to a solid T (Fig. 1) from which one intends to obtain ions. A plasma channel P is build up covered by a thin film of molten target material[2] as a result of the energy transfer from the electrons to the solid T (Fig. 2). The surface of this film emits a high current of neutral and mainly single ionized atoms. Probably a big fraction of ions

originate in the plasma channel P. All positive ions are accelerated to a collecting specimen plate S which is negatively charged with regard to the solid T and the housing H, whereas the neutral atoms are emitted almost uniformly in all directions of the upper hemisphere. Hence there is no

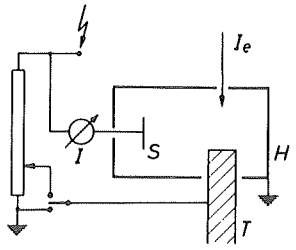

Fig. 1

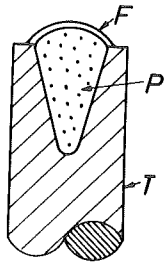

Fig. 2

problem to separate the ions from the neutral atoms or to mix the beams of ions and neutral atoms to any wanted proportion. The energy spread of the ions was measured to be only a few electron volts. Thus for accelerating potentials in the range of 30 kV to 50 kV the ion beam can be considered to be monochromatic. Ion currents were measured up to 26 mA.

On the housing H films are deposited by neutral atoms only. These films show completely different properties if compared with films which are condensed at the specimen plate S by [3] neutral atoms under simultaneous ion irradiation. The polycristalline films condensed in this way on the specimen plate S have always increased adhesive strength and hardness, positive electrochemical potential, higher optical reflection and smaller electrical resistivity than films of the same thickness but deposited on the walls of the housing H. It is immediatly clear that these effects are a result of the irradiation by ions. Hence a part of the proposed experiments can be performed in a simple way using the films condensed on the specimen plate S as samples which have suffered radiation damage due to ion impacts.

The films have a uniform thickness over an area of more than 10 cm^2. Due to the preparation technic the film contain a high and almost constant damage rate throughout the total volume. The film thickness can be chosen in any wanted range. Thinner films are also accesible to electronoptical investigations. By annealing measurements of the electric resistivity the resistance of the films can be chosen in a range convenient for the instrumentation so that other effects like thermoelectric potentials are kept small compared to the effect to be measured and therefore can be neglected. Parts of the solid S and films obtained by simultaneous deposition by neutral atoms on a glass substrate mounted on the wall of the housing H and kept on the potential of the wall were used for comparison.

Al, Ag, Au, Ni, Pt, Nb, Fe and Cr films were condensed at room temperature and at a vacuum of $3 \cdot 10^{-6}$ torr. Under the experimental conditions Al showed no hardening effect due to ion irradiation, a very small effect was observed with Ag and in ascending order a very large one with Cr. Au, Ni, Pt and Cr films were annealed in an oil bath to ensure a reliable temperature measurement. Cu could not be treated in this way because of chemical reactions. Au and Pt films were also annealed in air with no difference in the results. Electrical resistivity annealing was measured over long periods of time at constant room temperature or during heating up the specimen and following cooling down. The adhesive strength of the films and their hardness was tested in a rough way by scratching the film with a steel needle loaded with different weights. By all experiments the ion current was kept at the same amount to obtain comparable results.

Results

1) Dependence on the ion energy: The energy of the ions was changed over a range beginning with 1 keV up to 70 keV. Under the experimental conditions no hardening effect could be observed by ion energies lower than approximatly 5 keV, in-

dependently which material was used. It was concluded that the main observed radiation damage was produced by ions stopped from energies higher than 5 keV, whereas slower ions did not have any significant influence. Therefore experiments using slow ions were not carried out. For our experiments the ion energies were always chosen larger than 30 keV.

2) Active range of the ions: To test the penetration depth of the ions this means the traveling distance along which an ion is active to produce the observed defects a film of the material to be investigated was precondensed on the specimen plate S by conventional methods. After this preparation the experiments were performed as described before. It turned out that the increase of adhesive strength could be observed only by predeposited films thinner than 600 Å. If the predeposited film exceed 600 Å thickness no mechanical effect of ion irradiation with ions in the energy range between 30 keV and 70 keV was observable.

3) Electric resistivity annealing: Films produced under ion bombardement show generally an initial electric resistivity up to 30% less than corresponding films of the same thickness but condensed by neutral atoms only. Most of the samples were annealed immediately after their production, thereby the dependence of the electric resistivity on the film thickness was investigated. For convenience the resistivity annealing was carried out in the range between 25°C and 150°C using a constant temperature gradient of $dT/dt = 2{,}5\,^{\circ}C/min$. After the run the mechanical properties were retested.

Films thinner than a characteristic thickness of somewhat less than 100 Å did not show any hardening due to ion irradiation. It is concluded that the defects responsible mainly for the hardening must have an active sphere about in this range. If the film is too thin, the defects anneal immediately or generally cannot be produced. Comparing with the result of minimum ion energy (section 1) the type of produced defects seems to agree with the model of SEEGERs depleted zones.

a) Chromium: The films were produced by a vacuum of $3 \cdot 10^{-6}$ torr and pressure connected by gold plateletts to the cables leading to the instruments. After this preparation the films were heated up. Fig. 3 shows annealing diagrams of three samples 270 Å, 550 Å and 700 Å thick. A very pronounced annealing peak of the electric resistivity is observed with a temperature position depending on the thickness of the film. The peak is shifted to higher temperatures by increasing the film thickness. Hence in agreement with the observation of a critical minimum film thickness the surface of the film must act as the main sink for the defects to be annealed. Also from this point of view it is not surprising that one does not observe strong effects by irradiating specimens with low energetic ions.

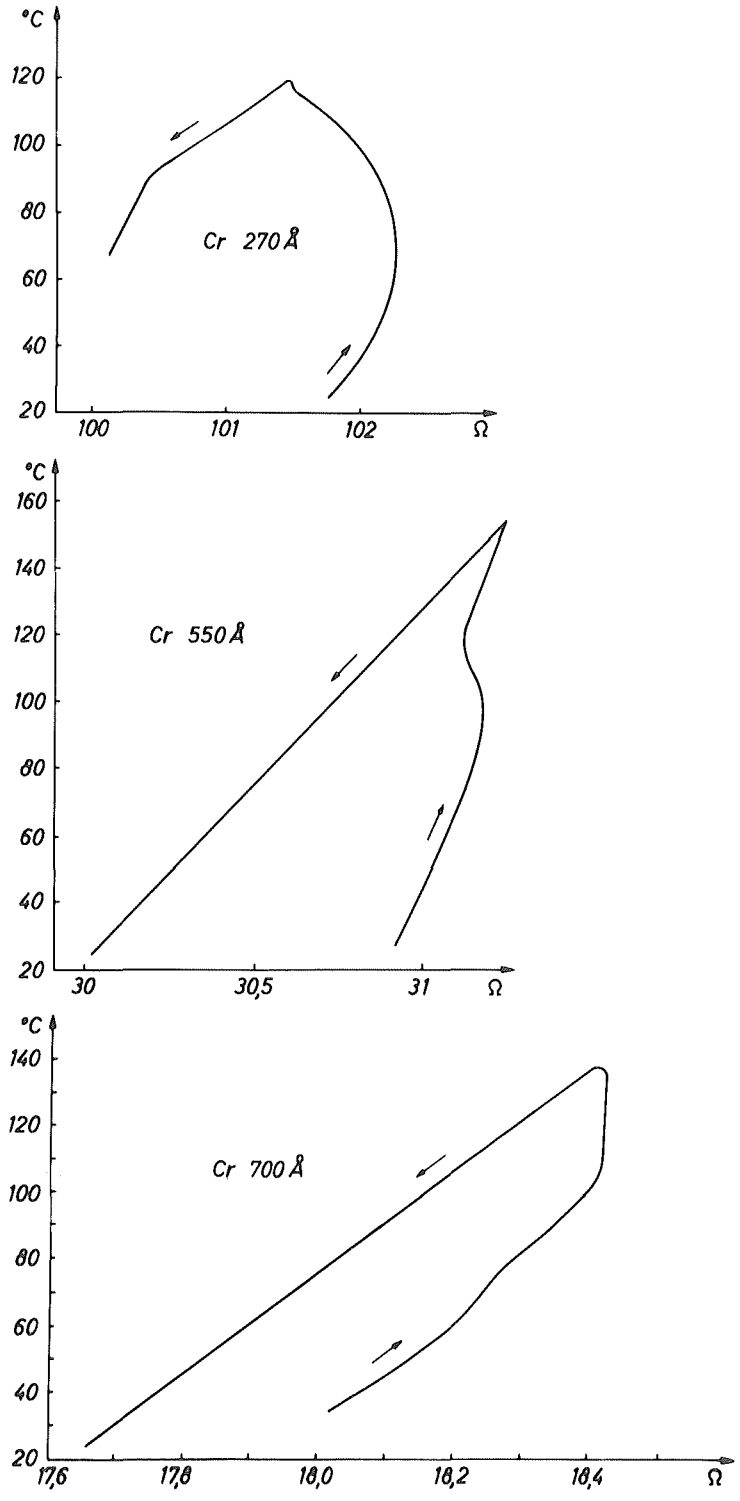

Fig. 3

Cooling the specimen back to room temperature the slope is an almost straight line starting from the tur-

ning point. This means that the main part of the defects is annealed and the straight line gives the temperature coefficient of the electric resistivity of the film annealed up to the highest reached point of the annealing temperature. The large change of the resistivity indicates that the initial defect concentration must be extremely high. Annealing of the Cr films in this temperature range did not change their hardness. Films deposited by neutral Cr atoms without ion irradiation show completely different annealing slopes.

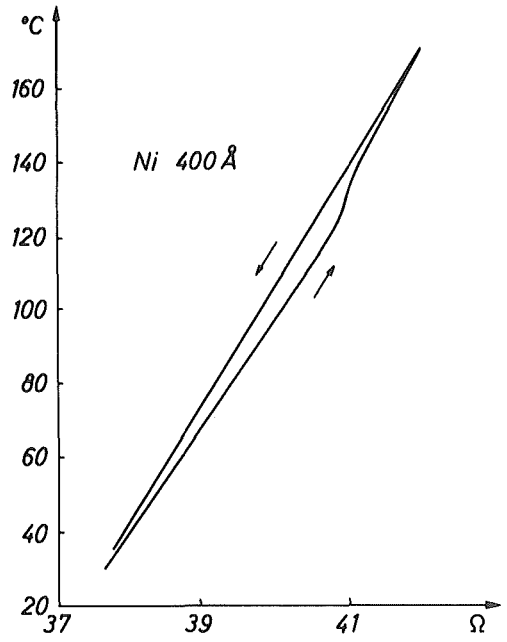

Fig. 4

Results by films of Cu, Ni, Au, Pt investigated less intensively shall be reported shortly.

b) Nickel: Essentially the same type of slope (Fig. 4) as by Cr is observed with a 400 Å thick film. The peak, much less pronounced, occurs at approximately 130°C. Decreasing of the hardness could not be observed.

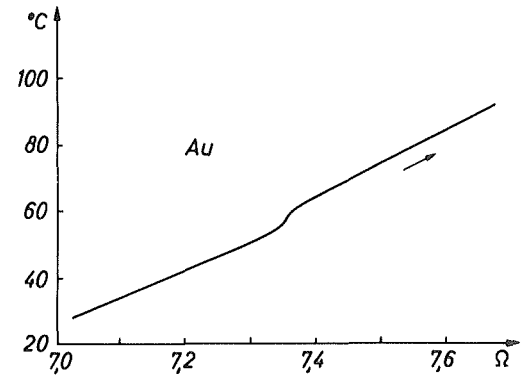

Fig. 5

c) Au, Pt, and Cu: Annealing peaks of Au films were observed by 55°C (Fig. 5) and by thicker layers at 70°C respectively 100°C. The accurate thickness of the films was not measured but was in the range between 100 Å and 300 Å All layers became soft after annealing as were layers deposited by using neutral atoms only. Pt films annealed also on air showed annealing peaks at 200°C where the films became soft and a very strong annealing of the electric resistivi-

ty was observed. No peak was observed by copper but softening was obtained before reaching 100°C.

Reviewing the results: Au, Pt and Cu show similar behavior almost coinciding with annealing stages observed by other experiments[4]. However, they became soft at annealing temperatures considerably lower than reported by other researchers. Ni and Cr did not become soft as it should be expected at least for Ni but in agreement with radiation hardening experiments observed by other work.

Gold showed annealing peaks for thin layers at 55°C. Hence the temperature rise of all specimens during their deposition was much less than up to 55°C performing all experiments under the same conditions. Going back after this statement to the results obtained with Cr: The deposition conditions by all Cr films were the same. Hence either depending on the film thickness there are produced in each case mainly one of different types of defects which anneal at different but closed temperatures or there are produced one or more types of defects but independend from the film thickness, thereupon the shift of the peaks is a result of the different average distance of the surface to the defects, the surface acting as the main sink for migrating defects. But then of course one has to modify the usually applied reaction equation to calculate the activation energy. The relaxation of the lattice in the neighborhood of the surface should not have such an influence on the activation energy by films thicker than 200 Å that the activation energy could be changed in a remarkable way. At the present it is assumed that the shift of the peaks is an annealing property and the dominant migrating defects are interstitials by Cr and Ni but vacancies by Cu, Au and Pt.

1) Krimmel, E.F.; Rev. Sc. Instr. 37, 678 (1966); Nucl.Instr. 60, 231 (1968); French Pat. 1531102.

2) Schwarz, H.; J. appl. Phys. 35, 2020 (1964);

3) Krimmel, E.F. and A.Gordon; Z. angew. Physik 22, 1, (1966) Krimmel, E.F.;Naturwiss. in press

4) Review article: Diehl, J. in: Moderne Probleme der Metallphysik, Springer (1965), 227 ff, I.
Dworschak, F. and J. Koehler; Phys. Rev. 140, A941 (1965)
Grenning, D.A.and J.S.Koehler;Phys.Rev. 144, 439 (1966)
Bauer,W.,A.Seeger and A.Sosin;Phys.Letters 24A,195 (1967)
Attardo,M.J.and J.M.Galligan; Phys.Rev. 161,558 (1967)

IV. POINT DEFECTS IN COLD-WORKED F.C.C. METALS

Point defects in cold worked f.c.c. metals

by
A. van den Beukel
Laboratorium voor Metaalkunde
Technische Hogeschool, Delft,
The Netherlands

Summary

The changes of the physical properties, observed during annealing of cold worked f.c.c. metals prior to recrystallisation, are usually attributed to the annealing out of point defects. Many models have been proposed which account for the production of point defects by moving dislocation mechanisms. One of them, Saada's model, is briefly discussed, because its quantitave prediction of the point defect concentration produced seems to be in agreement with many experimental results.

The recovery spectra of the f.c.c. metals discussed, Al, Cu, Ag, Au, Pt, Pd, Rh and Ni are shown to consist of two main ranges, which are, however, in many cases not due to one single activated process. The two ranges are usually called stage II and III resp.; for Pt, Pd and Rh they are often called III and IV resp. It is proposed to describe the corresponding phenomenological shape of the recovery spectra by a corresponding nomenclature: II and III resp. for the main stages.

It is argued that stage II, at least in heavily cold worked metals, is not due to point defect-impurity interactions, but to intrinsic defects. Several interpretations of this stage (single interstitials, divacancies, close pair recombinations, dislocation rearrangements) can be ruled out almost with certainty. It is suggested that stage II involves the disappearance of interstitial agglomerates. Some experimental evidence is available supporting this suggestion.

The stage III annealing data are compared with the results of quenching and irradiation experiments. Comparison is made difficult by the fact that activation energies observed during these experiments are essentially effective values so that their physical significance is somewhat obscure as yet. However, a cautious comparison between the cold work and quenching data points to the conclusion that vacancy type annealing plays a part in stage III recovery. This conclusion is corroborated by the fact that in dilute alloys of the f.c.c. metals considered often ordering or clustering phenomena are observed in the stage III range. The result of a comparison of the cold work and irradiation data is not incompatible with a vacancy interpretation of stage III for Al, Au and Pt, but introduces the so called stage III dilemma into the interpretation of cold worked Cu and Ni. Moreover, internal friction data for deformed Ni suggest that stage III recovery at least contains a part which is not due to vacancy type defects.

Stage IV as a separate recovery stage is only present in impure Ni and, less clearly, in Cu. It is concluded that the assignment of this stage to single vacancy migration is not yet definitely established.

Finally, three types of experiments are discussed which probably reflect point defect-dislocation interactions: the Hasiguti internal friction peaks and the increases of the flow stress and the elastic constants during annealing of some cold worked metals. These results can be commonly interpreted in terms of the arrival of point defects on the dislocations and their subsequent annihilation.

RECOVERY STAGES IN DEFORMED PLATINUM

Sei MIURA*, Jin-ichi TAKAMURA
and Nobuo OGASA**

Department of Metal Science and Technology
Kyoto University, Kyoto, Japan

Recovery stages, and in particular stages III and IV are studied by resistivity measurements on platinum polycrystals deformed at -195°C. Two sub-stages have been found in stage III, on 10 min/20°C isochronal annealing, in the ranges of temperatures from -20°C to 80°C and from 100°C to 160°C. The former pronounced sub-stage with the activation energy of about 0.7 eV is ascribed to the annihilation of normal interstitials to vacancies as well as the annihilation to dislocations, while the latter weak sub-stage with the energy of about 1.1 eV is due to the annihilation of divacancies to dislocations. It is also shown that single vacancies are annihilated to dislocations at stage IV with the energy of about 1.4 eV. From both experimental data and machine calculations, the following values are suggested :

$E_{1V}^{M} + E_{2V}^{B} - E_{2V}^{M} = 0.54 \pm 0.03$ eV, $E_{1V}^{M} + E_{2V}^{B} = 1.54 \pm 0.03$ eV

$E_{1V}^{M} = 1.41 \pm 0.03$ eV, $E_{2V}^{B} = 0.13 \pm 0.03$ eV, $E_{2V}^{M} = 1.00 \pm 0.03$ eV

$E_{1I}^{M} = 0.75 \pm 0.05$ eV, $E_{2I}^{B} = 0.40 \pm 0.05$ eV, $E_{2I}^{M} = 0.90 \pm 0.05$ eV

INTRODUCTION

For deformed or irradiated fcc metals there have been much arguments on recovery stages, and in particular on stage III which is observed in the range of temperatures between 0.1 and 0.25 of the absolute melting temperature [1]. Corbett et al. [2, 3] and recently Federighi et al. [4] have suggested that vacancies move in stage III, while Li and Nowick [5] and Suzuki [6] have ascribed divacancy migration to stage III.

---

* Now at Dept. of Mechanical Engineering, Doshisha Univ., Kyoto
** Now at Sumitomo Electric Industries, Ltd., Osaka

The other model due to Huntington [7] claims that interstitials move in stage I and di-interstitials in stage III ; the latter suggestion was later supported by Jackson [8] and Dworschak and Koehler [9]. Sosin et al. [10, 11] and also Seeger [12] have insisted, from the second-order reaction characteristic of stage III, that normal interstitials migrate to annihilate with vacancies. This view was not only supported by Simson and Sizmann [13] for deformed high purity nickel, but also confirmed by Seeger et al. [14] from mechanical and magnetic relaxation experiments. On the other hand, Dawson [15] and independently Suzuki [16] have shown that the apparent second-order reaction determined by usual analysis can not be the conclusive evidence for the mutual annihilation of interstitials and vacancies, but could be the process which involves the simultaneous migration of different types of point defects. However, in most fcc metals such as gold, copper and silver stages III and IV are not easy to differentiate one another because of the overlapping of their recovery stages.

In order to clarify the situation stated above, recovery experiments on platinum moderately deformed were carried out to differentiate the recovery stage, if any, into separate stages, bearing in mind that platinum has a high melting point and the large contribution to resistivity of point defects.

EXPERIMENTAL PROCEDURE

Specimens were polycrystalline platinum wires (99.999 % purity) 0.4 mm in diameter annealed in air for 30 minutes at 900°C at which no measurable resistivity change of specimen was observed. For annealing above 900°C in air, however, the increase in the resistivity of specimen was observed, presumably because of the oxidation [17]. Tensile tests were carried out by the Instron-type machine with a strain rate of 0.01/min. Potential leads 0.2 mm in diameter were spot-welded on the specimen. If necessary, the quench was made by plunging the specimen into water just after cutting-off the electric heating current ; the temperature in the gauge length, i. e., the central 9 cm of a 40 cm length was measured from its resistance, and the quenching rate was about 50,000°C/sec.

All resistivity measurements were carried out in liquid nitrogen and its temperature variation was corrected by a dummy specimen. The smallest detectable change in resistivity was about 2×10^{-11} ohm cm. The determination of the shape factor for resistivity of a speci-

men subjected to deformation was made by assuming that the specific resistivity of the specimen fully-annealed after deformation is equal to that before straining. In this way only, satisfactory reproducibility was achieved for resistivity measurements. After deformation or quenching, specimens were isochronally annealed for 10 minutes unless otherwise noted. As the bath for isochronal annealing, iso-pentan (-165°~ 0°C), distilled water (20°~ 80°C), silicon oil (100°~300°C) and salt bath (320°~ 440°C) were used, and at temperatures above 440°C specimens were annealed in air. When silicon oil or salt bath were used, special care was taken to wash and clean the surface of specimen.

RESULTS

1. Isochronal Annealing

(1) Deformation of Annealed Specimens

Changes in electrical resistivity on 10 min/20°C isochronal annealing are shown in Fig. 1 for specimens deformed in tension by 3%, 6% and 10% at -195°C. Six recovery stages *a*, *b*, *c*, *d*, *e* and *f* are found in each specimen, and the resistivity change in each stage increases with strain (Fig. 2). As a whole the recovery process is similar to that observed by Piercy [18] and Jackson [8], but stage *c* found in the present experiment has not been reported.

(2) Deformation of Quenched Specimens

To know the stage at which single vacancies are annihilated, quenched specimens were deformed and isochronally annealed. The quench was made from temperatures below 1400°C so as to freeze-in mostly single vacancies [8, 18, 19, 20]. The time of holding the specimen at the quench temperature was about 20 seconds and the time required for heating-up was about 2 minutes.

The results are shown in Fig. 3. The top curve indicates the recovery stages in a specimen quenched from 1310°C and subsequently deformed in tension by 6% at -195°C. The bottom is the reference curve of a specimen similarly deformed without the prior quench. In a quenched and deformed specimen, as understood from Fig. 3 and also from Table 1, a large increase in resistivity change is observed at stage *d*, while only a slight increase at stage *b* and little change at stage *c* are detected. It is also noticed that stage *b* split into two sub-stages b_1 and b_2 in a quenched specimen when

deformed by more than 6 %.

2. Activation Energies for Recovery and the Annealing Kinetics

The determination of activation energies for stages *b*, *c* and *d* was made by the slope-change method for specimens deformed by 10 % at -195°C. The typical results are shown in Fig. 4. The energies thus obtained are not so accurate but enough to know the magnitude with an accuracy of ±0.1 eV ; the values are 0.75±0.1 eV, 1.1±0.1 eV and 1.45±0.1 eV for stages *b*, *c* and *d*, respectively.

To determine the order of kinetics in stage *b*, isothermal annealing was made at 30°C that is the central temperature of stage *b* for a specimen deformed by 6 % at -195°C. As indicated in Fig. 5,

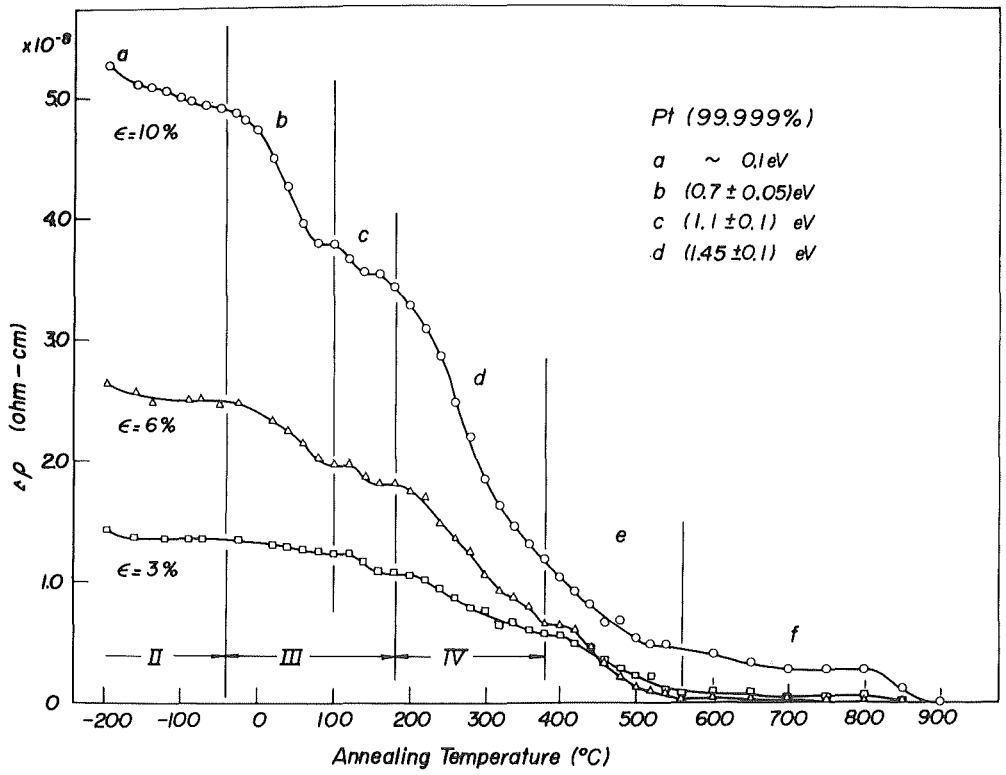

Fig. 1 Isochroanl annealing (10 min/20°C) curves for platinum wires (0.4 mm diam.) stretched by 3 %, 6 % and 10 % at -195°C. Stages *b* and *c* belong to so-called stage III, and stage *d* corresponds to stage IV. Activation energies listed were obtained from the slope-change method (see also Fig. 4).

the linear relation approximately holds when the reciprocal of the recovery fraction is plotted against the annealing time except for the initial stage of annealing. The recovery fraction is given by

$$f = \Delta\rho/\Delta\rho_b = (\rho - \rho_\infty)/(\rho_0 - \rho_\infty) \qquad (1)$$

where ρ is the resistivity after each thermal treatment, and ρ_0 and ρ_∞ are the initial and final reference values for stage b. The value of ρ_0 was taken from a specimen annealed for 10 minutes at -40°C, i.e., the lowest temperature for stage b, while as the value of ρ_∞ was adopted the resistivity of a specimen annealed at 100°C for 10 minutes. It is seen from Fig. 5 that the second order kinetics is operating in stage b, except for the early stage corresponding to the first 30 % decay at which the time law of $t^{2/3}$ does hold.

To know the activation energy in stage d more accurately, isothermal annealing was made at 220°C and 250°C for specimens deformed by 6 % at -195°C. In this case, the resistivity of a specimen annealed for 10 minutes at 180°C was taken as the value of ρ_0 in Eq. (1), while as the value of ρ_∞ was adopted the resistivity after annealing for 2×10^3 minutes at the isothermal temperatures. As seen from Fig. 6, reasonably straight lines are obtained when the

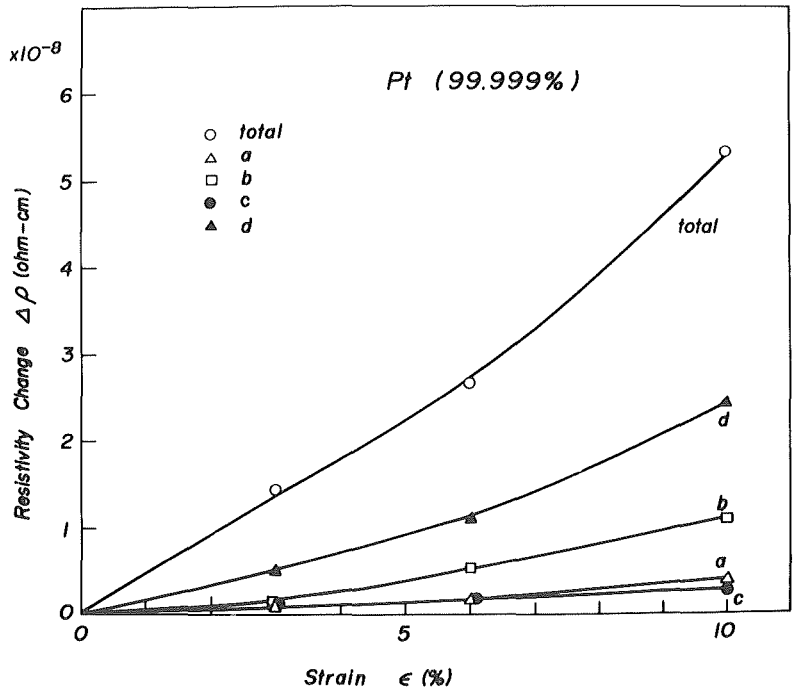

Fig. 2 Resistivity change vs. strain in platinum wires stretched at -195°C

Table 1 Resistivity change $\Delta\rho$ at each stage in specimens deformed in tension by 6 % at -195°C

Specimen	$\Delta\rho$ $\times 10^{-8}$ ohm cm					
	a	*b*	*c*	*d*	*e* + *f*	Total
#17 (quenched from 1310°C)	0.25	0.65	0.15	3.25	0.63	4.93
#5 (annealed)	0.20	0.52	0.16	1.20	0.60	2.68
#11 (annealed)	0.27	0.48	0.15	1.30	0.60	2.80
Difference	<0.05	~0.15	~0	~2.0	~0	~2.2

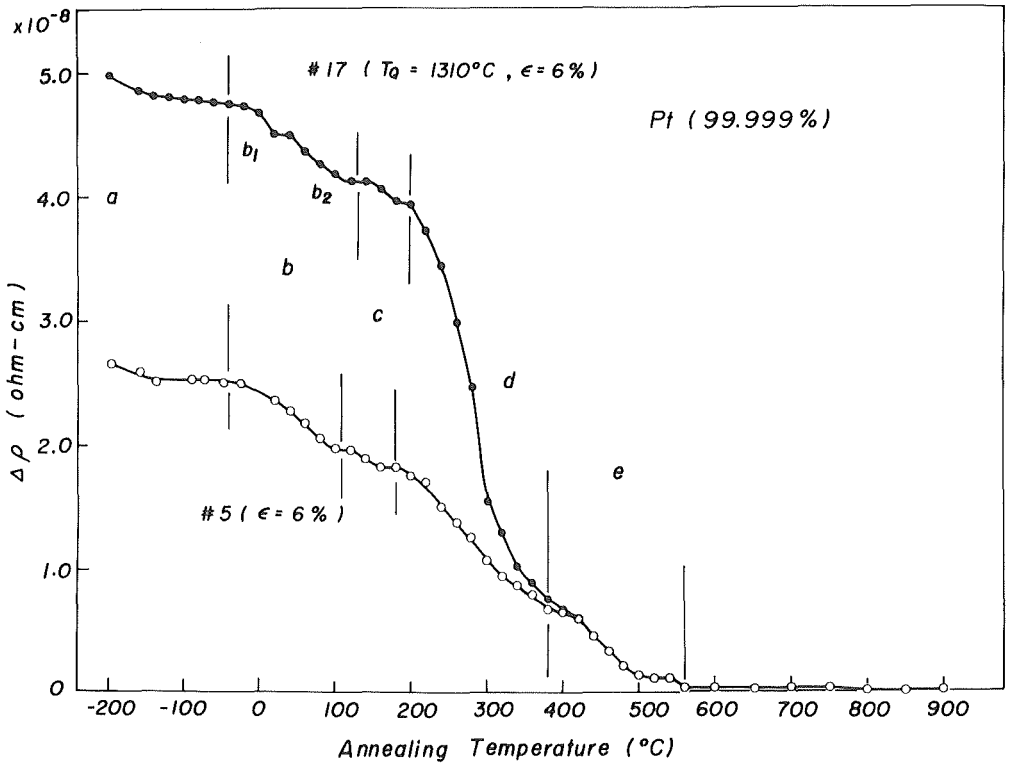

Fig. 3 Isochronal annealing curves for a specimen (bottom) full-annealed and for a specimen (top) quenched from 1310°C, which were deformed by 6 % at -195°C.

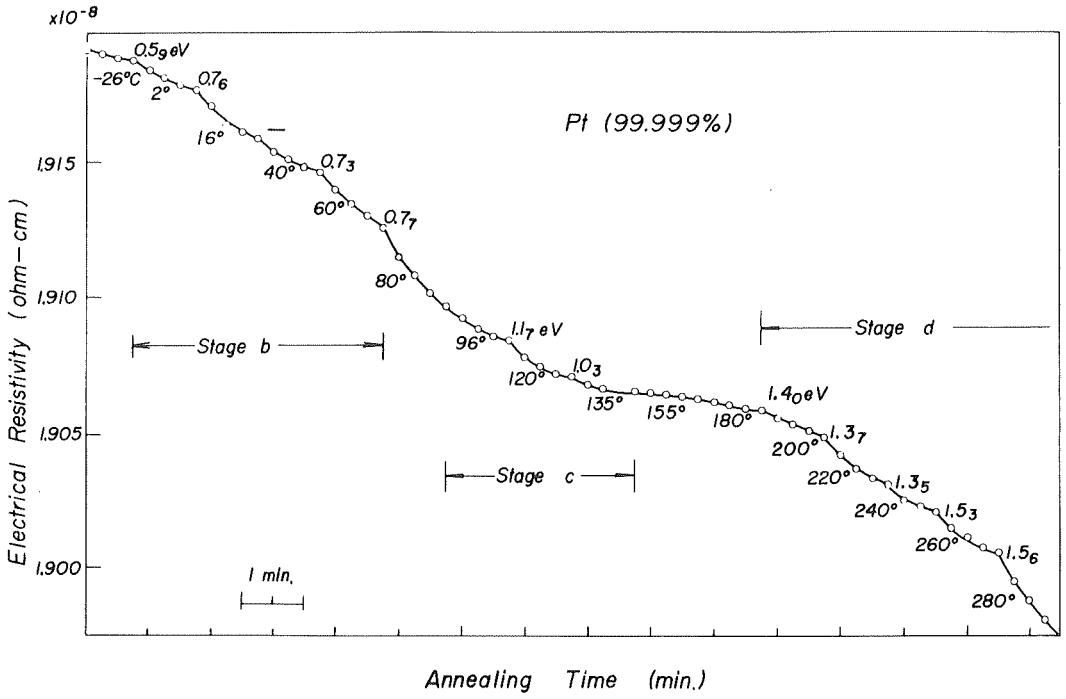

Fig. 4 Determination of the activation energy for each recovery stage in platinum deformed by 10 % at -195°C.

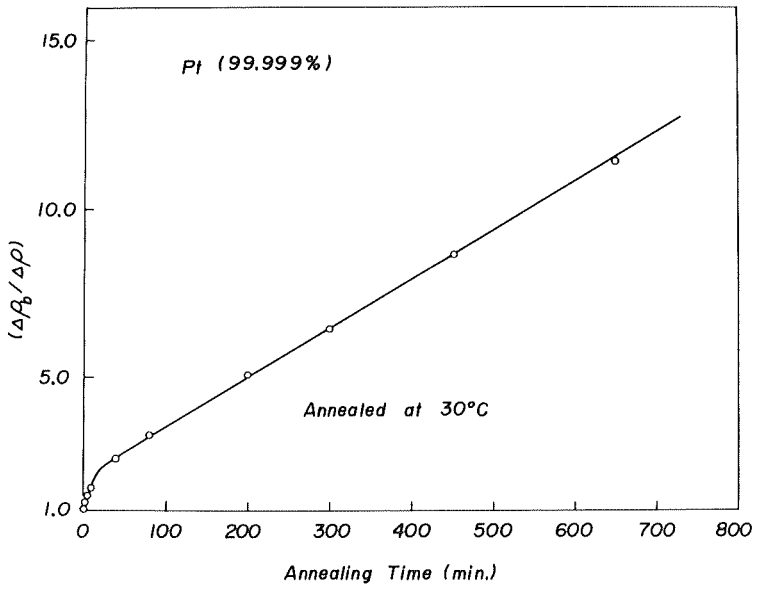

Fig. 5 Reciprocal of recovery fraction vs. annealing time for stage *b* of a specimen deformed 6 % at -195°C.

logarithm of recovery fraction is plotted against $t^{1/2}$. The activation energy determined by a least square method was 1.42 ± 0.04 eV.

DISCUSSION

1. Stage *d* Recovery

Since the temperature of stage *d* ranges from 0.21 T_m to 0.33 T_m, stage *d* is considered to correspond to so-called stage IV [21]. In the following will be described the reasoning that stage *d* is the process at which single vacancies are annihilated to dislocations with migration energy of about 1.4 eV.

First, most quenched-in vacancies are annihilated at stage *d* in a quenched and deformed specimen, as clearly understood from Table 1. The quenching temperature and the cooling rate were about 1300°C and 50,000°C/sec, respectively, and with these conditions the concentration of divacancies to be quenched in a specimen is only at most 1% of the total vacancy concentration since the binding energy of divacancies may be smaller than 0.20 eV [22, 23]. Thus it is said that single vacancies move at stage *d*.

Second, as seen in Fig. 6, the fraction of recovery at stage *d* is very well represented by the time law of $exp(-t^{1/2})$. This time law is generally accepted to show the rate of arrival of vacancies but not interstitials at dislocations, as first pointed out by Coulomb and Friedel [24] and later retreated by Bullough and Newman [25]. Wintenberger [26] and Panseri et al. [27] applied this law to their ex-

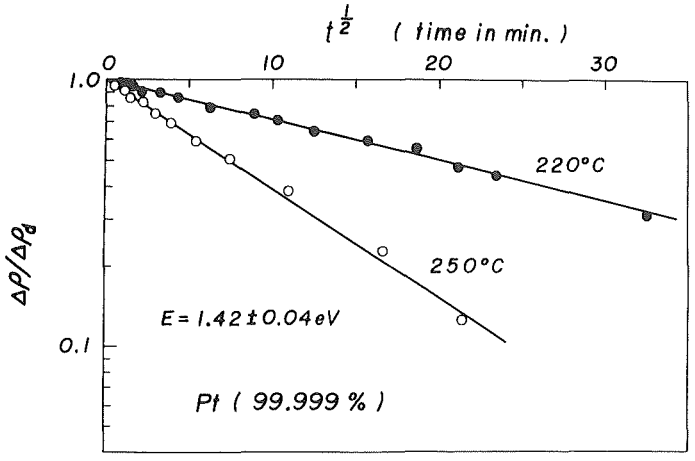

Fig. 6 Semilogarithmic plot of the recovery fraction in a specimen deformed by 6% at -195°C.

periments in the form as

$$C/C_O = exp\,[\,-\pi N\{\,2D\mu b^2 r_O^3 t/kT\}^{1/2}\,]\,, \qquad (2)$$

where C and C_O are the vacancy concentrations at time t and at $t = 0$, respectively, N the dislocation density, D the diffusion coefficient, μ the shear modulus, b the Burgers vector, and r_O the radius of a vacancy ($r_O \simeq b$). If the value of D_1 due to Schumacher et al. [23] is adopted for the time at $\Delta\rho/\Delta\rho_d = 0.5$ in Fig. 6, the density of dislocations from Eq. (2) is found to be $10^{10} \sim 10^{11}/cm^2$. If the value of $E_{1V}^M = 1.42$ eV determined from Fig. 6 is used, the dislocation density obtained from the following equation becomes $5 \times 10^{10}/cm^2$ for a specimen deformed by 6% at -195°C :

$$N = (D_{10} Z \lambda^2 t)^{-1}\, exp(E_{1V}/kT)\,, \qquad (3)$$

where $Z = 12$, and $D_{10} = 3.5 \times 10^{13}$/sec [23].

Third, the activation energy obtained from stage d is about 1.4 eV, which is in the range of values determined as the migration energy of single vacancies by a number of investigators. From quenching experiments, Ascoli et al. [28], Bacchella et al. [29], Jackson [8], Polák [22] and Schumacher et al. [23] have obtained the migration energies of 1.4 ± 0.1 eV in specimens quenched from temperatures below 1400°C, whereas lower values of 1.1 ± 0.1 eV have been reported for specimens quenched from high temperatures above 1600°C [8, 18, 19, 20, 22, 23]. These energies, however, represent only effective energies which are affected by various parameters such as E_{1V}^M, E_{2V}^M, E_{2V}^B E_{3V}^B, C_V, and annealing temperatures. To know the effective energy to be determined from the slope-change method, machine calculations were made at a set of annealing temperatures of 400°C and 420°C for the quench from 1300°C, and a set of 320°C and 340°C for the quench from 1600°C, by varying parameters as $E_{1V}^M = 1.3 \sim 1.5$ eV, $E_{2V}^M = 1.0 \sim 1.2$ eV, $E_{2V}^B = 0.1 \sim 0.3$ eV. The sets of annealing temperatures were chosen to represent the center of the stage from the data of Jackson [8] and Schumacher et al. [23]. In the calculations the following reactions were considered :

$$\left.\begin{array}{l} V_1 + V_1 \rightleftharpoons V_2\,, \quad V_1^* + V_2 \rightleftharpoons V_3\,, \quad V_1 + V_2^* \rightleftharpoons V_3 \\ V_1 \longrightarrow \text{sinks}\,, \quad V_2 \longrightarrow \text{sinks}\,, \end{array}\right\} \qquad (4)$$

where affix * notifies the migrating defect in the corresponding reaction. As a tri-vacancy, for simplicity, only a type with bond angle 60° was considered. The density of line sinks was assumed as $5 \times 10^7/cm^2$, and the cooling rate was 5×10^4 °C/sec.

Effective energies thus obtained were compared with those experimentally determined. If one put a restriction that the difference of effective energies between the quenches from low temperatures and high temperatures is not less than 0.25 eV as actually observed [8, 22, 23], the best fit of computed values to the experimental data was obtained under the following condition :

$$E_{1V}^{M} + E_{2V}^{B} - E_{2V}^{M} = 0.50 \sim 0.55 \text{ eV}. \quad (5)$$

It is also to be noted that the value of about 1.4 eV has been obtained from irradiated specimens by Piercy [18], and Bauer and Sosin [30]. Considering all these situations and in particular the present value of 1.42 eV as well as the well educated value of 1.38 eV due to Schumacher et al. [23], the following value is suggested as a most reasonable value.

$$E_{1V}^{M} = 1.40 \pm 0.03 \text{ eV} \quad (6)$$

2. Stage *b* Recovery

The temperature range of stage *b* and *c* lies between 0.11 T_m and 0.21 T_m, and is thought to correspond to so-called stage III. It will be described below that, in stage *b*, about a half of total interstitials are annihilated to dislocations in the early stage of annealing, and the remaining half to vacancies. It will be also suggested that at least two types of interstitials such as mono- and di-interstitials move in stage *b* with activation energies of about 0.75 eV and 0.90 eV, respectively.

First, as seen from Table 1 and Fig. 3, resistivity change $\Delta\rho$ in stage *b*, in contrast to that in stage *d*, is little increased in a quenched and deformed specimen. This suggests that vacancies do not move at stage *b*. Since monovacancies move at stage *d* as described before, defects migrating at stage *b* must be divacancies or interstitials. However, the value of the energy determined from the slope-change method, i.e., 0.75 ± 0.1 eV is too small as the energy of divacancy migration to explain the effective energies obtained from quenching experiments which were discussed in some detail in the previous section. Thus stage *b* is attributable to the migration of interstitials.

Second, stage *b* obeys the second order reaction except for the initial stage of annealing (Fig. 5). As Seeger [12] suggested, the second order reaction is an evidence for the mutual annihilation of interstitials and vacancies. It is also noticed that the initial stage up to the first 30 % decay obeys the typical strain-aging law of $t^{2/3}$. This indicates that the migrating defects are not vacancies but interstitials, and also

that the annihilation of the interstitials to dislocations is dominant in the early stage of annealing.

Third, when quenched-in vacancies are introduced in a deformed specimen the annihilation rate of interstitials to vacancies is expected to increase in accord with the decrease in the mean jump number for recombination which is expressed by $(\alpha Z C_V)^{-1}$, and this effect was actually observed in platinum by Jackson [8]. As seen from Table 1, the resistivity change at stage *b* in a quenched and deformed specimen (#17) is slightly larger than that in a deformed specimen (#5 or #7). This difference corresponds to the concentration of vacancies eaten by interstitials which should be annihilated to dislocations if quenched-in vacancies have not been introduced. These facts also provide evidence for the mutual annihilation of interstitials and vacancies, since the dislocation density may be little changed in both specimens.

Fourth, the activation energy obtained from stage *b*, 0.75 ± 0.1 eV, is to be compared with the value of 0.72 eV determined from a deformed platinum by Jackson [8], and with 0.7 eV for ion-bombarded platinum by Baker [31]. At present it is difficult to know more accurate value of the migration energy of interstitials, and machine calculations of the recovery stage have been made by adopting suitable models and energies. The details will be described in the last section (Fig. 7), but it is understood that at least two types of interstitials having different migration energies, say about 0.75 eV and 0.90 eV, are involved in stage *b* which could be separated into two stages, depending on the vacancy concentration, as observed in a quenched and deformed specimen. These two types of interstitials may be mono- and di-interstitials, but impurities and in particular oxygen might be necessary to be considered since all specimens were heat-treated in air.

3. Stage *c* Recovery

Stage *c* has the activation energy of 1.1 eV. The reason that this stage has not been observed in platinum may be due to the smallness of the step height and also due to the largeness of the degree of straining of specimens. Dawson [15] has studied the recovery stages in gold, silver and copper weakly deformed, and found that stage III is separated into two sub-stages *b* and *c* when the specimen is strained by $1 \sim 5\,\%$. He attributed stage *c* to di-vacancies, but no conclusion for stage *b* was drawn.

As seen from Table 1, the step height of stage *c* is not changed

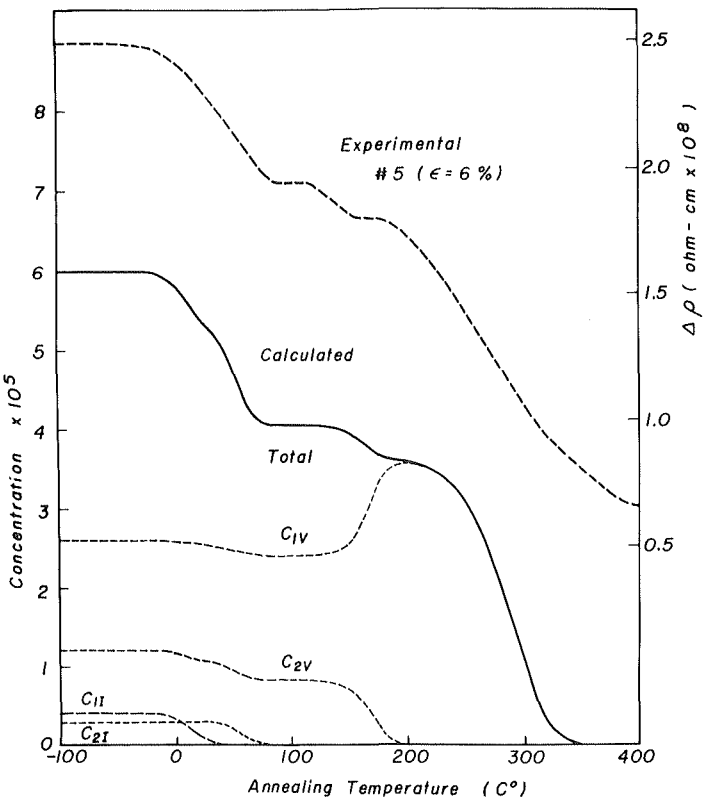

Fig. 7 Computer result for recovery stages on 10 min/20°C isochronal annealing in comparison with the experimental curve for a specimen deformed by 6 % at -195°C. The values adopted in the calculation are :

$E^{M}_{1V} = 1.43$ eV
$E^{M}_{2V} = 1.02$ eV
$E^{B}_{2V} = 0.13$ eV
$E^{M}_{1I} = 0.75$ eV
$E^{M}_{2I} = 0.90$ eV
$E^{B}_{2I} = 0.40$ eV
$N = 5 \times 10^{10}/cm^2$

when quenched. This indicates that stage *c* is not related to vacancies trapped by impurities, otherwise stage *c* should become larger with increasing quenched-in vacancies. Since other stages such as *b* and *d* are assigned to interstitials and monovacancies, respectively, the remaining possibility of assignment for stage *c* is most likely the divacancy migration. The obtained value of 1.1 ± 0.1 eV (Fig. 4) is very close to the migration energy of divacancies determined from quenching experiments described before. From Eqs. (5) and (6) one can obtain the value of E^{M}_{2V} as

$$E^{M}_{2V} = 0.95 \sim 1.1 \text{ eV}, \qquad (7)$$

where $E^{B}_{2V} = 0.1 \sim 0.2$ eV is assumed [22, 23]. For the determination of a more precise value, the results from machine calculations of the recovery stages must be taken into account, which will be described in the next section.

4. Machine Calculations

For the assignment of recovery stages and for the determination of the appropriate value of activation energy for each stage, machine

calculations have been made so that the calculated isochronal annealing curve may fit the experimental data. In the calculations the following reactions were taken into account.

$$\left.\begin{array}{l} I_1 + I_1 \underset{K_2}{\overset{K_1}{\rightleftharpoons}} I_2\,, \quad V_1 + V_1 \underset{K_4}{\overset{K_3}{\rightleftharpoons}} V_2\,, \quad I_1^* + V_1 \xrightarrow{K_5} \text{ann.}\,, \quad I_1^* + V_2 \xrightarrow{K_6} V_1 \\ I_2 + V_1 \xrightarrow{K_7} I_1\,, \quad I_2^* + V_1 \xrightarrow{K_8} I_1\,, \quad I_2^* + V_2 \xrightarrow{K_9} I_1 + V_1\,, \quad I_2^* + V_2 \xrightarrow{K_{10}} I_1 + V_1 \\ I_1 \xrightarrow{K_{11}} \text{sinks}, \quad I_2 \xrightarrow{K_{12}} \text{sinks}, \quad V_1 \xrightarrow{K_{13}} \text{sinks}, \quad V_2 \xrightarrow{K_{14}} \text{sinks} \end{array}\right\} \quad (8)$$

where affix * denotes the migrating defect in the corresponding reaction and K_S are the rate constants which are given as follows.

$$\left.\begin{array}{ll} K_1 = 16\,\nu\, exp\{-E^M_{1I}/kT\}, & K_2 = 32\,\nu\, exp\{-(E^M_{1I} + E^B_{2I})/kT\} \\ K_3 = 84\,\nu\, exp\{-E^M_{1V}/kT\}, & K_4 = 14\,\nu\, exp\{-(E^M_{1V} + E^B_{2V})/kT\} \\ K_5 = 30\,\nu\, exp\{-E^M_{1I}/kT\}, & K_6 = 48\,\nu\, exp\{-E^M_{1I}/kT\} \\ K_7 = 48\,\nu\, exp\{-E^M_{2I}/kT\}, & K_8 = 48\,\nu\, exp\{-E^{M'}_{2I}/kT\} \\ K_9 = 80\,\nu\, exp\{-E^M_{2I}/kT\}, & K_{10} = 16\,\nu\, exp\{-E^{M'}_{2I}/kT\} \\ K_{11} = (2/3)\lambda^2\,\nu\, exp\{-E^M_{1I}/kT\}, & K_{12} = (1/9)\lambda^2\,\nu\, exp\{-E^M_{2I}/kT\} \\ K_{13} = \lambda^2\,\nu\, exp\{-E^M_{1V}/kT\}, & K_{14} = (1/6)\lambda^2\,\nu\, exp\{-E^M_{2V}/kT\} \end{array}\right\} \quad (9)$$

In the above equations, $E^{M'}_{2I} = E^M_{2I} + 0.05$ eV was assumed. A number of sets of energies were examined, and a sample result is shown in Fig. 7 with the experimental curve. The values with which the experimental isochronal annealing curve of a specimen deformed by 6 % at -195°C is well represented are suggested as follows.

$$\left.\begin{array}{l} E^M_{1V} + E^B_{2V} - E^M_{2V} = 0.54 \pm 0.03 \text{ eV}, \quad E^M_{1V} + E^B_{2V} = 1.54 \pm 0.03 \text{ eV} \\ E^M_{1V} = 1.41 \pm 0.03 \text{ eV}, \quad E^M_{2V} = 1.00 \pm 0.03 \text{ eV}, \quad E^B_{2V} = 0.13 \pm 0.03 \text{ eV} \\ E^M_I = 0.75\ \{^{+0.15}_{-0.05}\ \text{eV} \left\{\begin{array}{l} E^M_{1I} = 0.75 \pm 0.05 \text{ eV} \\ E^M_{2I} = 0.90 \pm 0.05 \text{ eV} \end{array}\right. \\ E^B_{2I} = 0.40 \pm 0.05 \text{ eV} \end{array}\right\} \quad (10)$$

with the following defect populations which may be typical in the present specimen deformed by 6 % at -195°C :

$$\left.\begin{array}{ll} C_{1V} = 2.6 \times 10^{-5}, & C_{2V} = 1.2 \times 10^{-5} \\ C_{1I} = 4 \times 10^{-6}, & C_{2I} = 3 \times 10^{-6} \\ N = 5 \times 10^{10}/\text{cm}^2\,. & \end{array}\right\} \quad (11)$$

SUMMARY

Recovery stages, and in particular stages III and IV have been studied by resistivity measurements on platinum deformed at -195°C. In stage III, two sub-stages *b* and *c* have been found. The results obtained are summarized as follows.

(1) In stage *b*, at least two types of normal interstitials such as mono- and di-interstitials move with energies of 0.75 ± 0.05 eV and 0.90 ± 0.05 eV, respectively. In stage *b*, about a half of total interstitials are annihilated to dislocations in the early stage of annealing, and the remaining half to vacancies.

(2) Stage *c* was first found in platinum, and this stage is attributed to the migration of divacancies to dislocations. The migration energy of divacancies is estimated as 1.00 ± 0.03 eV.

(3) Stage *d* corresponds to stage IV at which single vacancies are annihilated to dislocations with the migration energy of 1.41 ± 0.03 eV.

(4) From machine calculations of recovery stages, reasonable energies and typical defect populations are suggested as given in Eqs. (10) and (11), among which the values of $E_{2V}^{B} = 0.13 \pm 0.03$ and $E_{2I}^{B} = 0.40 \pm 0.05$ eV are to be noted.

ACKNOWLEDGEMENTS

The authors wish to express their thanks to Mr. M. Hayase for his assistance in the experiments, to Dr. K. Furukawa, and in particular to Mr. F. Nakamura for their valuable discussions.

REFERENCES

1. See for example, H. G. van Bueren, Imperfections in Crystals, North Holland Pub. Co., Amsterdam 1961.
2. J. W. Corbett and R. M. Walker, Phys. Rev. 110, 767 (1958).
3. J. W. Corbett, R. B. Smith, and R. M. Walker, Phys. Rev. 114, 1452, 1460 (1959).
4. T. Federighi, S. Ceresara, and F. Pieragostini, Phil. Mag. 12, 1093 (1965).

5. C. Y. Li and A. S. Nowick, Phys. Rev. 103, 294 (1956).
6. H. Suzuki, J. Phys. Soc. Japan 18 Suppl. III, 299 (1963).
7. H. B. Huntington, Am. J. Phys. (to be published).
8. J. J. Jackson, Lattice Defects in Quenched Metals, Academic Press, New York and London 1965 (p. 467).
9. F. Dworschak and J. S. Koehler, Phys. Rev. 140, 941 (1965).
10. C. J. Meechan, A. Sosin, and J. A. Brinkman, Phys. Rev. 120, 411 (1960).
11. A. Sosin and L. H. Rachal, Phys. Rev. 130, 2238 (1963).
12. A. Seeger, Radiation Damage in Solids, Intern. Atomic Energy Agency 1, 101 (1962).
13. P. Simson and R. Sizmann, Z. Naturf. 17a, 596 (1962).
14. A. Seeger, and F. J. Wagner, phys. stat. sol. 9, 583 (1965).
15. H. I. Dawson, Acta Met. 13, 453 (1965).
16. H. Suzuki, Preprint, Phys. Soc. Japan, Spring Meeting 2, 29 (1964).
17. G. C. Fryburg, Trans. AIME 233, 1986 (1965).
18. G. R. Piercy, Phil. Mag. 5, 201 (1960).
19. B. G. Lazarev and O. N. Ovčarenko, Dokl. Akad. Nauk. SSSR 100, 875 (1955).
20. F. J. Bradshaw and S. Pearson, Phil. Mag. 1, 812 (1956).
21. See for example, D. Schumacher, Arbeitsbericht, MPI/66/P3 (1966).
22. J. Polák, phys. stat. sol. 21, 581 (1967).
23. D. Schumacher, A. Seeger, and O. Härlin, phys. stat. sol. 25, 359 (1968).
24. P. Coulomb and J. Friedel, Dislocation and Mechanical Properties of Crystals, Wiley, New York 1957 (p. 555).
25. R. Bullough and R. C. Newman, Phil. Mag. 7, 529 (1962).
26. M. Wintenberger, Acta Met. 7, 549 (1959).
27. C. Panseri, S. Ceresara, and T. Federighi, Nuovo Cimento 29, 1223 (1963).
28. A. Ascoli, M. Asdente, E. Germagnoli, and A. Manara, J. Phys. Chem. Solids. 6, 59 (1958).
29. G. L. Bacchlla, E. Germagnoli, and S. Granata, J. Appl. Phys. 30, 748 (1959).
30. W. Bauer and A. Sosin, Phys. Rev. 147, 482 (1966).
31. Baker, see ref. (8), p. 515.

Matthiessen's Rule and the Analysis of Annealing Data from Cold Worked Platinum.

K. Rösch, F. Bell and R. Sizmann

Sektion Physik der Universität München

Abstract

A recovery stage of cold - worked Pt centered about 250°C was analysed from resistivity measuremnet for the evaluation of the activation energy and the reaction order. For this, especially the influence of the measuring temperature of the electrical resistance was investigated. Although there is a remarkable violation of Matthiessen rule the apparent reaction order deduced from the measurements at 4,2°K and 77°K is almost the same. A critical review of the current techniques for the evaluation of the reaction order is made. The consequences are: (i) the activation energy has to be evaluated with the reaction order independent methods, (ii) the formal reaction order should then be analysed from non-isothermal annealing data with the aid of the known activation energy. The recovery stage in Platinum is described by second order process and an activation energy of 1,35 eV.

1. Introduction

The analysis of annealing data represents a means of classifying reaction defect species in terms of activation energy and perhaps reaction order. Experimentally in metals is the measurement of the change in electrical resistance one of the most convenient techniques to determine changes in defect concentrations. The aims of this investigation are (i) to proof that the apparent reaction kinetic is essentially independent of the very temperature where the electrical resistance is measured; (ii) to focus attention on the advantages of non-isothermal evaluation methods of the formal reaction kinetics.

2. Experimental

Platinum wires with a purity of 99,99% were heavily deformed by drawing at room temperature. The logarithmic ratio of the cross-sectional areas of a wire before and after deformation was about 2,2.

The wires were heated by passing a current through them; the temperatures in the isochronal step annealing program were controlled electronically by comparing the wire resistance at the annealing temperature with reference resistances. The temperature steps were 10°C (± 0,15°), the annealing times were 5,00 and 20,00 minutes for two different sets of experiments. The change in electrical resistance after each annealing step was measured at 4,2°K, 77°K, 141° K and 193° K. The accuracy of the measurement of the electrical resistance related to the total change in resistance was ± 0,4‰ at 4,2° K, ± 0,7 ‰ at 77° K, ± 1,5 ‰ at 141° K and ± 2,5 ‰ at 193 ° K.

3. Experimental results

Between room temperature and 450°C only one annealing stage appeared. Fig. 1 shows the normalized resistance change $\frac{R_T - R_E}{R_A - R_E}$ (R_T = resistance after annealing at temperature T, R_A = resistance at the beginning of the annealing stage, R_E = resistance at the end of the stage) for two different specimens, heated with the rates $v_1 = \frac{\Delta T}{\Delta t} = \frac{10°C}{5min}$ and with $v_2 = \frac{\Delta T}{\Delta t} = \frac{10°C}{20min}$. The solid lines represents this set for the measuring temperature of the electrical resistance 4,2°K, the dotted lines for 77° K. The annealing curves for 141° K and 193°K practically coincide with those of 77° K. The non-coincidence of the curves for a fixed heating rate measured at He and N_2 temperatures indicates a violation of Matthiessen 's rule. This means that the change in the residual resistance caused by the defect recovery is not identically with the resistance change measured at an elevated

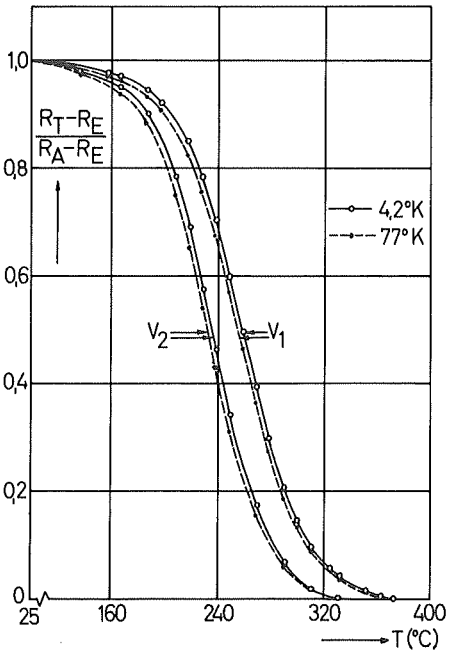

Fig. 1 Isochronal step annealing curves with two different heating rates. Measuring temperatures 4,2° and 77° K.

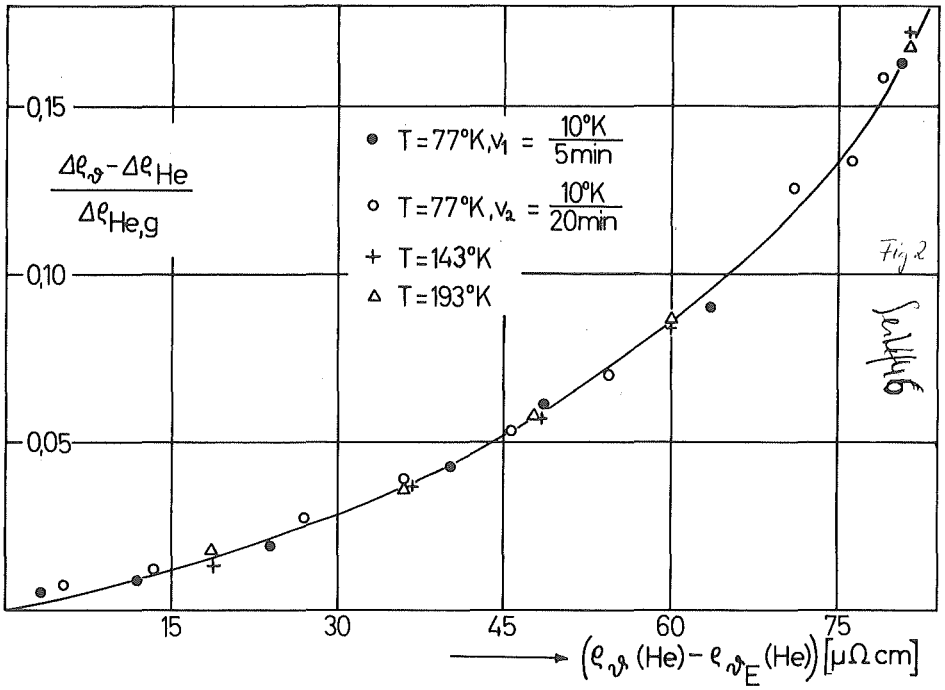

Fig. 2 Deviation from Matthiessen's rule

measuring temperature. Fig.2 reveals this situation more clearly. Here, the difference of the resistance changes $(R_T - R_E)_{\vartheta}$ - $(R_T - R_E)$ He normalized to the total change measured at liquid He -- are plotted against $(R_T - R_E)$ He. The index ϑ represents the measuring temperatures 77°K, 141°K and 193° K. If Matthiessen's rule holds this difference should be zero. Furthermore Fig. 2 indicates that $(R_T - R_E)_{\vartheta}$ is not proportional to $(R_T - R_E)$ He. That is the reason for the non-coincidence of the solid and dotted lines in Fig.1. This fact influences the apparent annealing kinetics.

4. Analysis of the annealing data.

The analysis of annealing data consists of two parts; i) Evaluation of the activation energy, ii) Tests on the formal reaction order. ad i) if the defect concentration C obeys a differential equation of the type

$$-\frac{dc}{dt} = F(c) \exp - E/kT \qquad (1)$$

with the activation energy E and any single valued function F(c).

E can be determined even if F(c) is unknown. This can be done by a) comparing two samples treated with different but arbitrary annealing histories b) heating one sample with a particular annealing program. For case (a) it is necessary that for both samples the initial defect concentrations and their spatial distributions are identical. In general the evaluation of the activation energy for case (a) is much more accurate (finite time or temperature differences) than for (b) (determination of slopes). Nevertheless, even if two samples are available, one should made tests with case (b) to ensure that there is no interferenee from unequal initial states. It should be emphasized that the evaluation of E - current techniques are summarized in /1/ and /2/ - is not only independent of the knowledge of F(c) but even from the proportionality of the defect concentration c to the measured physical property. If the physical property g is connected single valued with c by $g = g(c)$ than it follows from (1)

$$(2) \qquad \frac{dg}{dt} = F'(g) \exp - {}^{E}/_{k\,T}$$

That means that all techniques developed for (1) hold for (2), too. Especially in our case this means that any deviation from Matthiessen's rule does not touch the evaluation of E.

ad ii) The analysis of the reaction kinetics aim at the determination of F(c). The usual way is to try a fit of the experimental data with an integer reaction order model. In contrast to (i) now the connection between c and g (the physical property) must be known. For the electrical resistance usually propertionality is assumed. With other words it is assumed that Matthiessen's rule holds. For the evaluation of the reaction order two kinds of experiments may be performed: Iso - or non - isothermal temperature-time programs. The following plots can be made:

a) differential methods:

i) $\ln\left(-\frac{dc}{dt}\right)$ versus ln c for isothermal treatments.

ii) $\ln\left(-\frac{dc}{dT} \cdot f(T) \exp E/kT\right)$ versus ln c for non -isothermal experiments with heating rates $dT/dt = f(T)$. For this plot, E must be known independently.

Straight line segments will reveal the reaction order n, if simple power law c^n is prevailing.

b) integral methods:

Assuming power laws or polynomials of F(c), integrals of the type $\int \frac{dc}{F(c)}$ can be derived.

i) $\int \frac{dc}{F(c)}$ versus t for isothermal treatments.

ii) Expressions of the kind $\ln \int \frac{dc}{F(c)}$ versus $\ln \int \exp(-E/kT) \cdot f(T)\, dt$. In particular if f(T) is constant or only weakly dependent on T, $\ln \int \exp(-E/kT)\, f(T)\, dt$ is essentially $-(E/k) \cdot (1/T)$; an 1/T plot should result in a straight line. For isochronal annealing with constant temperature steps ΔT integrals can be derived for which exactly straight lines follow in an 1/T- plot if the " right" reaction order is used.

Especially case bii) is of dominating interest. As it can be shown easily the slope of the expected straight lines for an isochronal annealing program is given by - E/k. Now because E is determinable by methods independent of the knowledge of any reaction order , the assumption of a specific annealing model tested by method bii) can be checked by the slope of the resulting straight line. If a straight line results, but in the ln ... versus 1/T-plot the slope is not equal to - E/k the assumed kinetics is proved to be wrong. This is the great advantage of non-isothermal annealing experiments. But in contrast to /3/ we believe it to be hazardous to determine both activation energy and reaction order from these straight line methods. The objections to this technique are the following: (i) the reaction process may not follow a chemical rate equation. If the reaction are diffusion limited, no simple quantities of the kind $\ln \int \frac{dc}{F(c)}$ can be derived, which will give straight lines in a 1/T plot. Therefore the actual data will produce a curved line in a plot of cade bii). But accidentally it may happen, that the experimental data seem to fit a straight line in an 1/T plot with one or other (wrong) reaction order in $\ln \int dc/F(c)$ of case bii). (An example of this situation will be shown later). But the slope of the resulting straight line yields naturally not the right activation energy, thus revealing the deceipt. (ii) In some cases Matthiessen's rule can be violated such that the true kinetics are distorted to give accidentally a straight line in case bii). Again this can be controlled by the activation energy.

According to these objections we believe it to be important to evaluate first the activation energy and then to analyse the kinetics.

4a. Analysis of the activation energy.

According to a technique developed in /1/ the activation energy was determined from the annealing curves of the two specimens isochronically heated with the rates $\Delta T/\Delta t = 10^{\circ}/5$ min and $\Delta T/\Delta t = 10^{\circ}/20$ min.
(The techniques of /1/ were prefered to those given in /3/ because the approximations in /1/ are much better. This results from the unjustified approximation /3/ of a step annealing curve by a linear heating curve, which is displaced by $\Delta T/2$ on the temperature scale. ΔT is the temperature step of the annealing curve).
The results are summarized in table 1.

Table 1

Measuring temperatures ($^{\circ}$K)	Activation energies (eV)	region of annealing
4,2	$1,34 \pm 0,04$	10% -90%
77	$1,35 \pm 0,04$	10% -90%
141	$1,35 \pm 0,05$	10% -90%
193	$1,35 \pm 0,05$	10% -90%

Some remarks should be given to the errors of the activation energy reported in table 1. According to /1/, the activation energy E can be determined for every $(R_T - R_E)/(R_A - R_E)$ - value of both annealing curves. Therefore, in principal one can extract as large a set of activation energies E_i as one likes. This means that in absence of a definite trend of E with annealing state the statistical error of the mean value $\bar{E}$ can be made practically zero. However there may be a systematic error resulting from the uncertainty of drawing the "right" smooth curve through the discretely seperated experimental points obtained by step annealing. This uncertainties can be caused by errors in the resistivity data or the temperature values of the annealing curves; the resistivity errors can be transformed to adequate temperature errors. Thus, the systematic error in the determination of a particular value E_i is given by

$$(3) \qquad (\delta E_i)^2 = \left(\frac{\partial E}{\partial T_1}\right)^2_{T_1 = T_{1i}} (\delta T_{1i})^2 + \left(\frac{\partial E}{\partial T_2}\right)^2_{T_2 = T_{2i}} (\delta T_{2i})^2$$

δT_{1i} and δT_{2i} are the variations in T by drawing different smooth curves through the experimental points determined at the heating rates $\Delta T/\Delta t = 10^{o}/5\text{min}$ and $\Delta T/\Delta t = 10^{o}/20\text{ min}$. From this the weighted mean value

$$\bar{E} = \frac{\sum_i \frac{E_i}{(\delta E_i)^2}}{\sum_i \frac{1}{(\delta E_i)^2}} \qquad (4)$$

of the activation energy is obtained. The systematic error of the mean value is analogous

$$\delta \bar{E}_{sy} = \frac{\sum_i \frac{\delta E_i}{(\delta E_i)^2}}{\sum_i \frac{1}{(\delta E_i)^2}} = \frac{\sum_i \frac{1}{\delta E_i}}{\sum_i \frac{1}{(\delta E_i)^2}} \qquad (5)$$

$\bar{E} \pm \delta \bar{E}_{sy}$ is given in table 1. It is seen that althought the annealing curves measured at He, N_2 or higher temperatures appear to be different the resulting activation energy is identical. This is consistent with the remarks of chapter (4), that the evaluation of the activation energy should be independent of the reliability of Matthiessen's rule.

Fig. 3 shows an example for the determination of the activation energy with only one sample. This can be done according to /1/ at the points where isochronal steps ΔT with increasing temperature are changed to steps ΔT with decreasing temperature. The indicated (much less accurately) energies agree well with those of table 1, an indication that the assumptions made for the technique with two speciments, are essentially correct (see chapter 4). The results show that the activation energy is sufficiently constant over the range from 10 - 90% of the recovery stage.

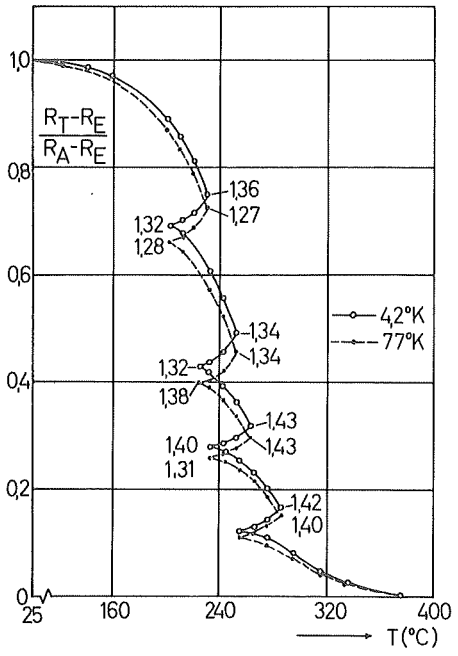

Fig. 3 Evaluation of the activation energy.

4b. Analysis of the kinetics.

First the annealing curves are to be tested on simple chemical rate equations:

$$-\frac{dc}{dt} = k c^{\gamma} \qquad (6)$$

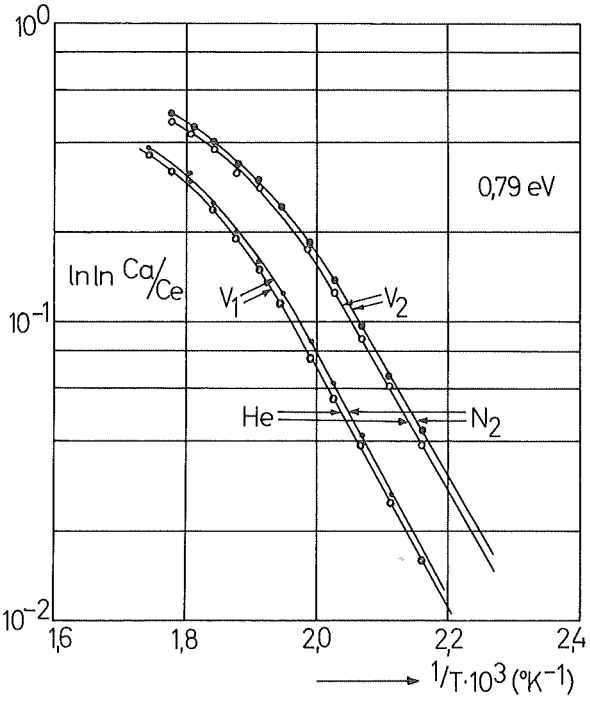

Fig.4 Test on first order kinetics.

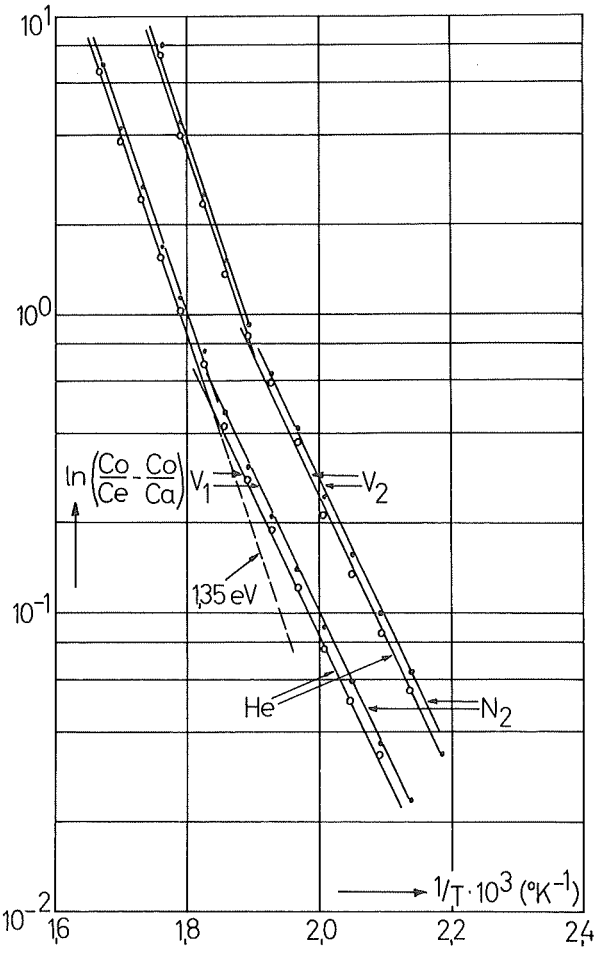

Fig.5 Test on second order kinetics.

For isochronal step annealing the integration of (6) yields for $\gamma = 1$ (first order kinetics)

$$(7) \qquad \ln\ln\frac{c_a}{c_e} = const - \frac{E}{k}\cdot\frac{1}{T}$$

Here $\frac{c_a}{c_e} = \frac{R_T^a - R_E}{R_T^e - R_E}$; R_T^a and R_T^e are the resistances at the beginning and the end of each annealing step. Fig.4 shows the result. Only at the commencement of the recovery stage the curves could be approximated by straight lines, but their slopes are far from $-E/k$ with $E = 1.35$ eV. Therefore simple first order kinetics can be excluded. With $\gamma = 2$ the integration of (6) yields (with equal initial concentrations of the reacting defects)

$$(8) \qquad \ln\left(\frac{c_o}{c_e} - \frac{c_o}{c_a}\right) = const - \frac{E}{k}\cdot\frac{1}{T}$$

Now with the assumption of Matthiessen's rule $\frac{c_a}{c_o} = \frac{R_T^a - R_E}{R_A - R_E}$ is the relative defect concentration at the beginning of each annealing step, $\frac{c_e}{c_o} = \frac{R_T^e - R_E}{R_A - R_E}$ the relative concentration at the end of each step. Again the left hand side of equation (8) is plotted versus $1/T$ in Fig.5 for both heating rates and the measuring temperatures of Ne and N_2. The experimental points coincide with two straight line segments. However, only the left one (>50% of the total recovery) corresponds to the activation energy 1.35 eV, the other straight line corresponds to E = 0.92eV although

the E - analysis has shown that in that region the annealing process is still running with E = 1.35eV. At the beginning of the annealing stage one cannot expect the diffusion limited process to be of simple second order. The trend of the deviation points to a higher order in accord with the theoretical expectation /4/. It may also be seen from Fig.4 and 5 that although there is a violation of the Matthiessen's rule (and even a violation which is not proportional to $(R_T - R_E)_{He}$) this deviation does not sensibly influence the reaction order. The difference between curves measured at He and N_2- temperatures tends to increase the apparent reaction order for the N_2- curve with respect to the He - curve. But this cannot be revealed by the kinetics tests in Fig. 4 and 5, because the maximum difference between N_2 and He curves does not exceed 3% of the total resistance change. This results from (i) the small deviation from linearity of the curve in Fig.2 and (ii) from the normalization of the curves which requires the difference to be zero at the beginning and the end of the recovery stage.

The decisive role of the activation energy as a controlling factor in the determination of the reaction order is demonstrated by the following example. Considering Fig.5 one may assume that the true reaction process may be a modified second order process. Therefore we have recalculated the annealing Process assuming a binary reaction with different initial concentrations of the reacting species. Then the integration of the rate equation yields

$$(9)\quad \ln\ln \frac{\left(\frac{c_e}{c_0}+\frac{1-x}{1+x}\right)\left(\frac{c_a}{c_0}+\frac{1-x}{1+x}\right)}{\left(\frac{c_a}{c_0}-\frac{1-x}{1+x}\right)\left(\frac{c_e}{c_0}+\frac{1-x}{1+x}\right)} \equiv \ln\ln\xi = \text{const} - \frac{E}{k}\cdot\frac{1}{T}$$

Here the relative concentration is given by

$$(10)\quad \frac{c_e}{c_0} = \frac{\frac{R_T^e - R_E}{R_A - R_E} + \frac{1}{2}\cdot\frac{1-x}{x}}{1 + \frac{1}{2}\cdot\frac{1-x}{x}}$$

where $x = C_A^0/C_B^0$ is the ratio of the initial concentrations. C is the total concentration of both defect types ($C = C_A + C_B$). In (10) it is assumed that the specific contribution to the electrical resistance from both types of reactants are equal. Fig. 6 shows the ln ln ξ vs 1/T - plot of the experimental data according to equation (9) with x = 0.9. The straight line spans the region of 5 to 95 % of the entire recovery stage. Hence for only a 10 % difference in the initial concentrations the straight line in the plot seems to give

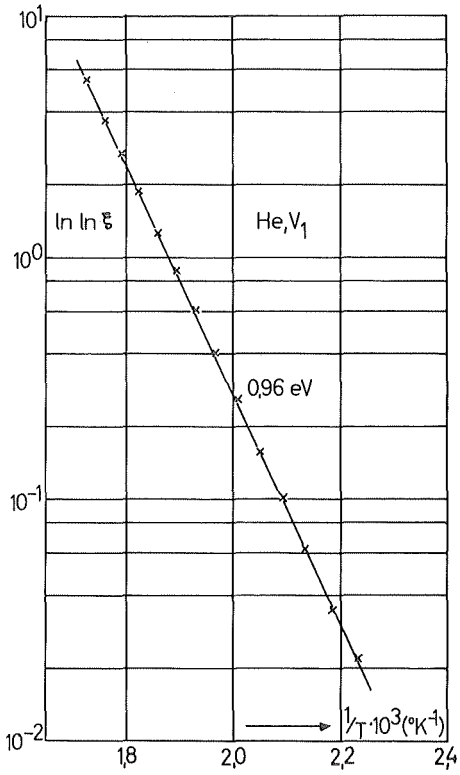

Fig.6 Test on second order kinetics with not equal initial concentrations.

evidence for the"right" kinetical reaction process. However, this interpretation of the defect kinetics must be wrong, since the slope of the straight line does not correspond to the required activation energy of 1.35 eV. (In fact it shows a slope with E = 0.96 eV.) This example dem onstates the hazard of evaluating simultaneously both kinetics and activation energy from annealing data by so called "straight line methods".

5. Deviations from Matthiessen's rule

If Matthiessen's rule holds, the resistivity at a temperature T is given by

$$\rho(T) = \rho_0 + \rho_i(T) \qquad (11)$$

ρ_0 is the residual resistivity at 0°K due only to impurities and physical imperfections. In our case $\rho_0 = \rho_{0D} + \rho_{0V}$, where ρ_{0D} represents the residual resistivity due to defects which anneal between 100° and 450°C, ρ_{0V} is due to all other imperfections and impurities. $\rho_i(T)$ is the ideal part of the resistivity.

According to (11) for two different measuring temperatures T_1 and T_2 the equation

$$\rho_{\vartheta}(T_1) - \rho_{\vartheta_E}(T_1) = \rho_{\vartheta}(T_2) - \rho_{\vartheta_E}(T_2) = \rho_{0D}(\vartheta) \qquad (12)$$

holds. $\rho_{\vartheta}(T)$ is the resistivity measured at T after annealing step at ϑ. ϑ_E means the annealing temperature at the end of the annealing stage ($\rho_{0D}(\vartheta_E) = 0$). Fig. 2 shows that equation (12) does not hold. This deviation may result from two causes:

a) the ideal part of the resistivity may be changed due to defects. Since for high measuring temperatures (N_2 temperature and higher) the ideal resistivity is given by the Grüneisen formula

$$\rho_i(T) \sim \frac{T}{\Theta_R^2} \qquad (13)$$

with Θ_R as the specific Grüneisen temperature (Θ_R represents the phonon spectrum of the material).

If the phonon spectrum is disturbed due to defects, from (13) results

$$\Delta\rho_i(T) \sim \rho_i(T)\,\Delta\Theta_R \qquad (14)$$

Therefore the difference

$$\eta = \left(\rho_{\vartheta}(T) - \rho_{\vartheta_E}(T)\right) - \left(\rho_{\vartheta}(0) - \rho_{\vartheta_E}(0)\right) = \rho_{i\vartheta}(T) - \rho_{i\vartheta_E}(T) \qquad (15)$$

should be proportional to $\rho_i(T)$. Experimentally $\rho_{\vartheta}(0)$ is approximated by

$\rho_{v\ell}$ (liquid He). Fig. 7 shows that this does not represent the experimental situation.

b) Deviations from Matthiessen's rule.

If Matthiessen's rule is violated, (11) can be rewritten

$$\rho(T) = \rho_0 + \rho_i(T) + \Delta(\rho_0, \rho_i) \tag{16}$$

From (16) we obtain

$$\eta = \left(\rho_{v\ell}(T) - \rho_{v\ell_E}(T)\right) - \left(\rho_{v\ell}(0) - \rho_{v\ell_E}(0)\right) = \left(\Delta(\rho_0^{v\ell}, \rho_i(T)) - \Delta(\rho_0^{v\ell_E}, \rho_i(T))\right) - \left(\Delta(\rho_0^{v\ell}, 0) - \Delta(\rho_0^{v\ell_E}, 0)\right) \tag{17}$$

with

$$\rho_0^{v\ell} = \rho_{0v} + \rho_{0D}(v\ell)$$

and

$$\rho_i(0) = 0$$

The left side of equation (17) can be compared with a theoretical expression derived by Kohler /5,6/. The so-called Kohler rule claims

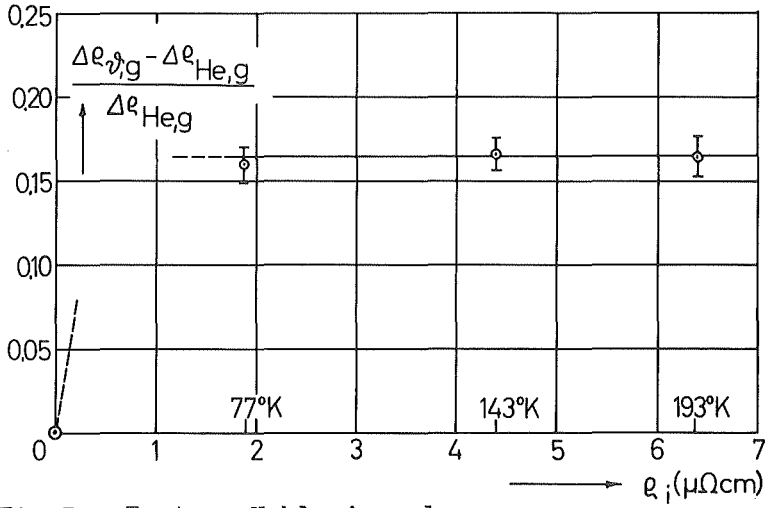

Fig.7. Test on Kohler's rule

$$\Delta(\rho_0, \rho_i(T)) = \alpha\beta \frac{\rho_0 \cdot \rho_i(T)}{\alpha\rho_i(T) + \beta\rho_0} \; ; \quad \alpha, \beta > 0 \tag{18}$$

Therefore, from (17) and (18) follows

$$\eta = \alpha\beta \frac{(\rho_{0v} + \rho_{0D}(v\ell)) \cdot \rho_i(T)}{\alpha\rho_i(T) + \beta(\rho_{0v} + \rho_{0D}(v\ell))} - \alpha\beta \frac{\rho_{0v}\rho_i(T)}{\alpha\rho_i(T) + \beta\rho_{0v}} \tag{19}$$

a) η shall be considered as a function of $\rho_i(T)$

$$\begin{aligned} &\eta \to 0 && \text{for } \rho_i \to 0 \\ &\eta \to \beta\rho_{0D}(v\ell) = \text{const} && \text{for } \rho_i \to \infty \end{aligned} \tag{20}$$

Comparing Fig.7 with (20). it follows that the experimental behaviour

can be described by the equation (20).

b) η shall be considered as a function of $\varrho_{0D}(\nu\ell)$. At high measuring temperatures (e.g. $\alpha\varrho_i \gg \beta\varrho_\sigma$) we obtain from (19)

(21) $$\eta = \beta\,\varrho_{0D}(\nu\ell)$$

As it can be seen from Fig. 7, the temperature of liquid N_2 is high enough in this sense. Since $\varrho_{0D}(\nu\ell) \sim (\varrho_{\nu\ell}(He) - \varrho_{\nu\ell_E}(He))$, Fig.2 may be compared with equation (21). Experimentally, η is not proportional to the resistance difference $R_{\nu\ell} - R_E$ at liquid He. Thus, the defect dependence of the violation of Matthiessen's rule cannot accurately be described by Kohler's rule.

References

/1/ F.Bell and R.Sizmann
phys. stat. sol. 15, 369 (1966)

/2/ R.Sizmann and A.Frank
Chemiker-Ztg./Chem. Apparatur 87, 347 (1963)

/3/ M.Balarin, R.Rattke, and A Zetzsche
phys. sta. sol. 22, 123 (1967)

/4/ T.R.Waite
Phys.Rev. 107, 463 (1957)

/5/ M.Kohler
Z.Physik 126, 495 (1949)

/6/ H.Bross
Z.Naturforschung 14a, 560 (1959)

SEPARATION OF ORIENTABLE POINT DEFECT ANNEALING FROM OTHER RECOVERY EFFECTS, USING ELECTRICAL RESISTIVITY AND MAGNETO-RESISTANCE DATA OBTAINED ON PLASTICALLY DEFORMED NICKEL.

W.Hellenthal and U.Lotter
Physikalisches Institut der Universität, Münster, Germany.

Abstract

Isochronal annealing experiments in the recovery regions III and IV were performed on nickel wires after low (up to 8%) plastic deformation, using measurements of electrical resistivity and magnetoresistance (in an alternating field of small amplitude). The latter method is shown to be very sensitive to recovery processes, thus revealing numerous details. Annealing the samples in different magnetic fields permitted a separation of orientable effects from other recovery contributions occurring simultaneously. The former could be attributed to interstitials (annealing with E^M_{1I} = (1,06 ± 0,05)eV in region III) and vacancies (E^M_{1V} = (1,55 ± 0,10)eV in region IV), stabilizing the magnetization locally by orientation resp. diffusion effects. For some temperature regions investigated, differentiations between recovery with a sequence of real primary substages and variations due to superposition of different types of processes resp. effects are shown to be possible.

1 Introduction

Recovery experiments on nickel have been published by a number of authors, some of them after irradiation or quenching (e.g. [1,3,4,5]) but the majority in connection with plastic deformation [1,2,3,4,6,7,8,9,10]. Structure dependent physical properties used were the average electrical resistivity (e.g. [1,3,6,7,8]), coercitivity [9,10] and the initial susceptibility [2]. In the range of annealing temperatures between 20 and 300 °C two annealing stages (III and IV) were observed with relative variations of the physical property used of only a few percent (for the resistivity this order of magnitude appeared at 77 °K). By an analysis of the recovery and comparison of results from samples with different types of lattice defect production as well as results from theoretical evaluations the stages III and IV have been attributed

to migration of interstitials resp. of vacancies to some adequate sinks.

Other possibilities to obtain information, e.g. combination of observations with different physical properties at the same sample or by investigations of the variation of magnetic anisotropy effects during recovery [11,12], have only occasionally been used for plastically deformed material. As it has recently been pointed out [13,14] only a limited comparison of results from recovery experiments (differring in the amount of prestrain or sample size) might be possible. Resistivity measurements on nickel after low ($\leq 10\%$) plastic deformation [15,16,17] have shown alternating variations noticeably differring from the usual stage type recovery after large prestrain.

The results presented here were obtained during recovery experiments on nickel wires after plastic deformation up to 8%. Besides resistivity measurements of high relative reproducibility ($3 \cdot 10^{-5}$) additionally magnetoresistance data could be obtained each time for the same structural state of the samples. The latter effect has the advantage to provide sufficient sensitivity for samples of small ferromagnetic volume and to show high structural sensitivity (including anisotropy effects) if one compares with other magnetic properties. The aim of these experiments was to use the combination of the above mentioned experimental methods to resolve processes which have not appeared separately in the data published about highly prestrained material. Additionally, different magnetic field treatments during recovery were used to separate simultaneously occurring effects in the recovery spectrum and relate them to some possible mechanisms.

2 Susceptibility and magnetoresistance

The variation δR of the electrical resistivity of ferromagnetic metals is given by

$$\delta R \sim M_s^2 \left(\overline{\cos^2 \varphi} - \overline{\cos^2 \varphi_0} \right) \tag{1}$$

while for the magnetization M the relation

$$M = M_s \, \overline{\cos \vartheta} \tag{2}$$

holds. Here M_s is the saturation magnetization. ϑ is the angle between the direction of the magnetic field H and the local magnetization; φ the angle between the electrical current and the

local magnetization. The subscript o refers each time to the initial situation. In equation (1) and (2) the averaging comprises the whole volume of the sample.

Measuring M(H)-curves with decreasing field amplitudes $\hat{H}$ one finds a disappearance of hysteresis and (in the limit of very small $\hat{H}$) a linear relationship, from which the initial susceptibility χ_A may be evaluated. Simultaneous observation of the variation of magnetoresistance with small $\hat{H}$ show a parabolic relationship (c.f. fig.1). For a given peak value $\hat{H}$ of the field the amplitude

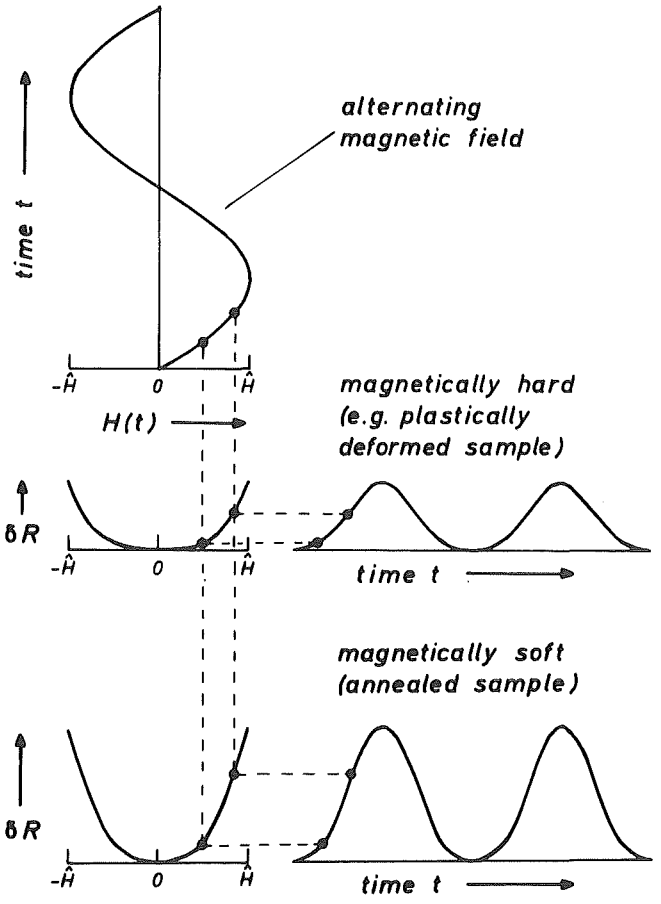

fig.1

Field and time dependent variation of the magnetoresistance effect for structurally different ferromagnetic material (schematically)

of the magnetoresistance variation δR will be used to define a magnetoresistive susceptibility

(3) $$\chi_R = \delta R(\hat{H})/|\hat{H}|$$

At small fields and low temperatures ($|K_1|$ large) the

magnetization reversal is preferentially due to motion of 180° Bloch walls. For field amplitudes $\hat{H}$ near but below the coercivity H_c this mechanism is mostly completed, while now motions of 71° and 109° walls and the onset of domain rotation are found [18].

Due to far-reaching magnetostrictive lattice distortions, which arise with the last mentioned processes, a noticeable sensitivity to lattice defect concentration and configuration may be understood [19,20] . As the magnetoresistance on nickel is a quadratic effect (c.f. eq.(1)) the displacement of 180° walls, which show only small interaction with defects, does not contribute a noticeable resistivity variation [21]. Thus χ_R was expected to be a structure dependent property with larger sensitivity to some types of lattice defects than most of the usual data from magnetization measurements (e.g. χ_R, H_c).

3 Experimental

3.1 Methods of measurement

In an external sinusoidal magnetic field H(t) with frequency f the variation of magnetoresistance $\delta R(t)$ alternates with a basic frequency of 2f due to the quadratic effect (c.f. fig.1). The amplitude of the 2f-signal is related to the magnetoresistive susceptibility χ_R . To use χ_R as a structure dependent quantity a particular set of measurements is done with always the same $\hat{H}$.

The sample is alimented with a constant current (c.f. fig.2). The time-dependent variation of the potential drop then follows $\delta R(t)$. The signal thus obtained is measured by a compensation technique using a 2f-voltage derived from the driving-current for the sinusoidal field H(t) (c.f. fig.2). For a more detailed description of the method see [22].

The average electrical resistivity R of the demagnetized samples was measured with a standard d.c. compensator enabling a relative reproducibility of better than $3 \cdot 10^{-5}$.

3.2 Experimental procedure

The samples for the recovery experiments were taken from nickel wire (99,99% purity, supplied by Johnson, Matthey & Co.,London) with a diameter of 0,25 mm. After annealing near 1000 °C in a vacuum of better than 10^{-5} Torr each specimen was deformed in

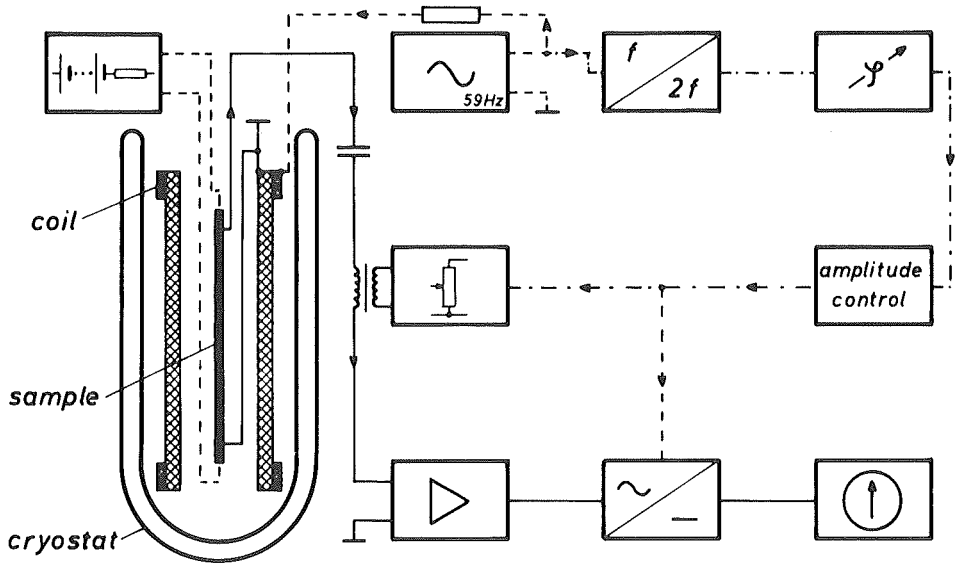

fig.2 Arrangement for the dynamical measurement of the magneto-resistance variation amplitude by compensation (schematically)

liquid nitrogen with a remanent elongation up to 8%. The isochronal annealing treatments with a duration of ten minutes each were carried out in an atmosphere of high purity nitrogen gas. Immediately after attaining a preset value of annealing temperature the samples were each time demagnetized using a coil that surrounded the heating device. With the same solenoid the specimens could be submitted to constant or alternating magnetic fields during the annealing treatments.

The subsequent measurements of the magnetoresistive susceptibility χ_R was done in liquid nitrogen each time in an alternating field with the same amplitudes $\hat{H}$ (below coercivity). The average electrical resistivity was then measured after an additional demagnetizing procedure.

4 Results

Recovery data from nickel wire after low plastic deformation at 77 °K and subsequent isochronal annealing in the range of temperatures between 20 and 300 °C are shown in fig.3. The observed

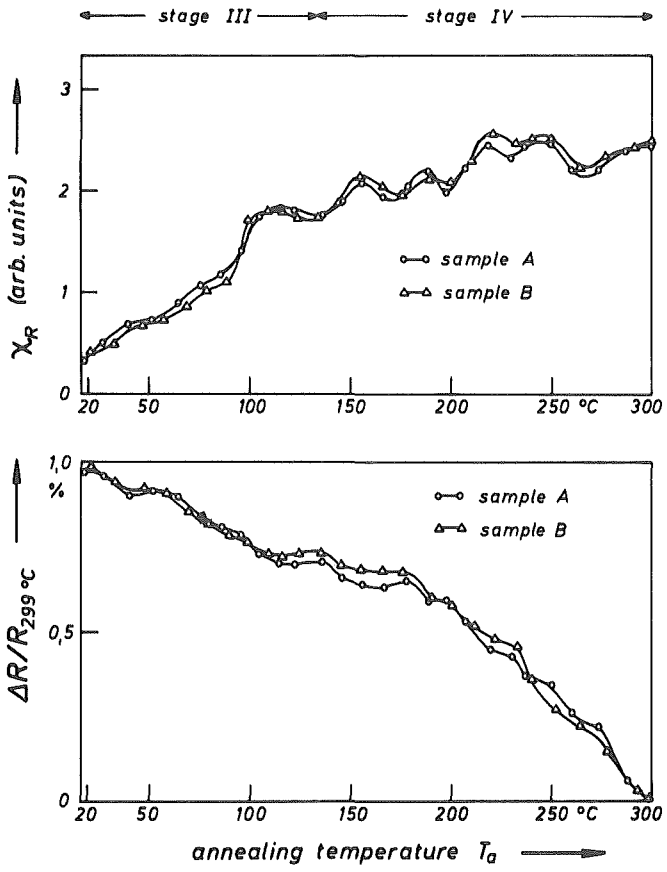

fig.3
Isochronal annealing (10 min for each step) of two nickel wires (0,25 mm diameter) after straining of 8%. Measured are the magnetoresistive susceptibility χ_R and the electrical resistivity at 77 °K (related to the value after annealing at 299 °C)

physical quantities used are the average electrical resistivity R and the magnetoresistive susceptibility χ_R , measured in parallel experiments each time on the same sample. For comparison such results are plotted for two different samples with similar pre-treatment. The individual data were reproducible to better than the point size in the figures. Although the curves have not been adjusted they resemble each other with respect to the amplitude of recovery as well as to the details of the small alternating variations.

A comparison of the results of the two methods of measurement

used, shows the large structure-dependent sensitivity of χ_R varying by about a factor of 10 during recovery over the stages III and IV. The corresponding total decrease of the electrical resistivity amounts only to 1%.

Differring from the recovery behaviour of highly deformed material where only one or two large stages are observed, a number of details has been resolved with the measurements reported here. These include even some small rises of resistivity for consecutive annealing steps. The resistivity and χ_R data vary in opposite direction in most of the conditions investigated.

To obtain additional information due to magnetically influencable

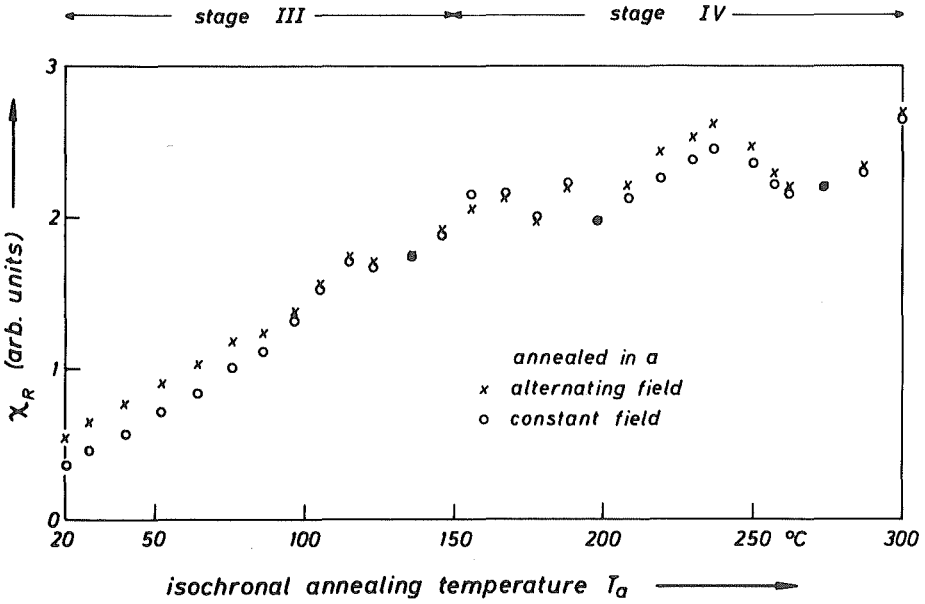

fig.4 Isochronal annealing of nickel wire (after straining of 8%) in an alternating and a constant magnetic field

recovery effects some samples were annealed for each temperature step in two runs of ten minutes each, one with application of an alternating and the other in a constant magnetic field of suitable amplitude. After each of these treatments the samples were cooled down for the measurements of χ_R and R. The annealing behaviour of χ_R thus observed gives two curves (fig.4) with analogously detailed variations but an additional partition in branches of the data between about 20 and 120 °C as well as between 200 and 270 °C.

The corresponding resistivity data did not show such a separation. The amount of splitting up $\Delta\chi_R^{ac,dc}$ has been extracted and plotted in the figs.5 and 6. The orientation effect remains nearly

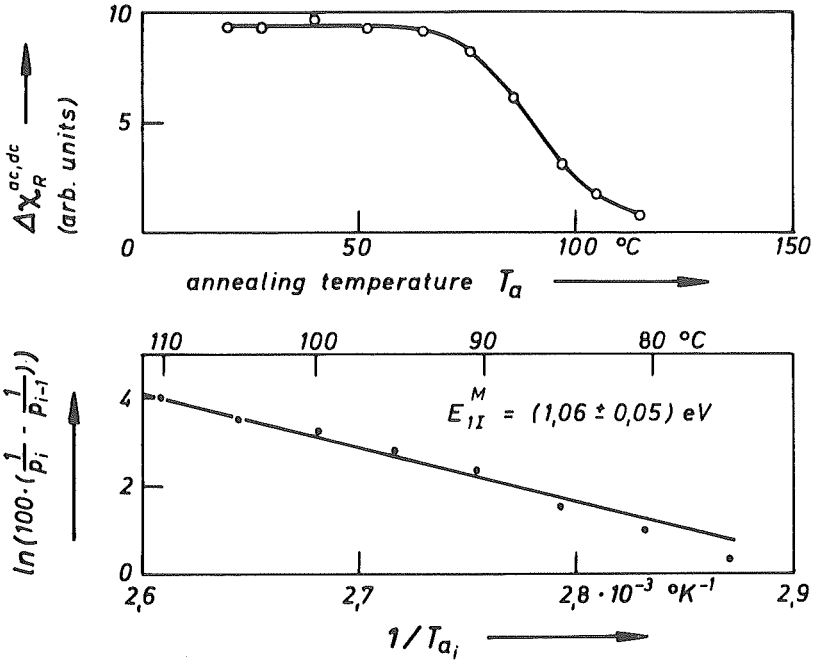

fig.5 Difference $\Delta\chi_R^{ac,dc}$ between corresponding χ_R data measured at 77 °K after isochronal annealing in an alternating or a constant magnetic field at the temperature T_a (upper curve).
Lower diagramm: evaluation of the orientable annealing contribution between 75 and 110 °C following SIMSON and SIZMANN [7] (the points being taken from the interpolation curve)

constant in stage III up to its recovery in a simple stage over a relatively large temperature interval. The orientable effect between 200 and 270 °C rises and decreases in the same temperature interval. The evaluation of both (using figure 5 and 6) by the method of SIMSON and SIZMANN [7] gives for the orientable effect in the lower temperature region an order of reaction $g \approx 2$ and an activation energy for migration of $E = (1,06 \pm 0,05)$eV. For the other process $g \approx 1$ and $E = (1,55 \pm 0,10)$eV was obtained.

fig.6
Evaluation of $\Delta\chi_R^{ac,dc}$ data in analogy to fig.5, now for the temperature interval T_a = 250 to 270 °C

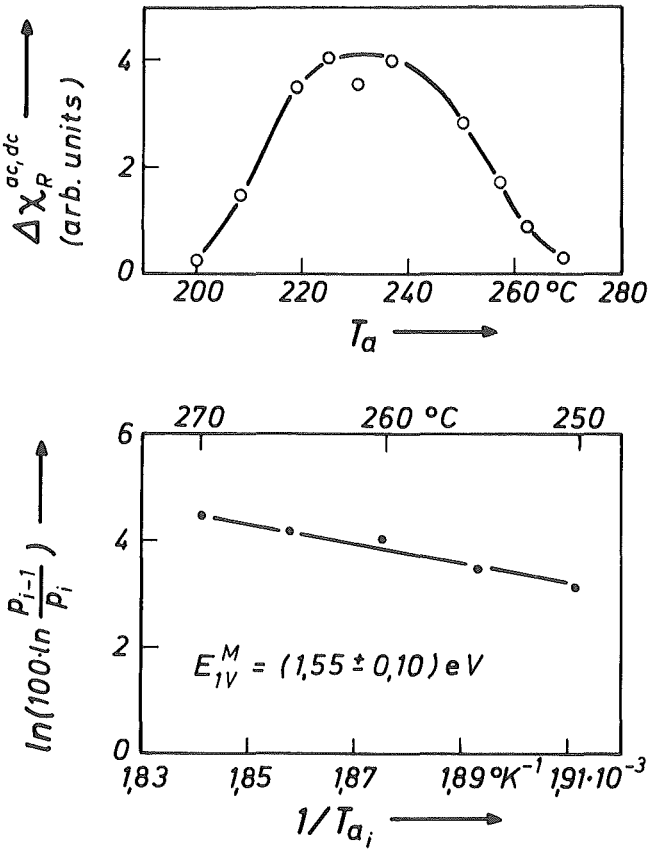

5 Discussion

The preceeding results show the recovery of nickel between 20 and 300 °C after low plastic deformation to be resolved into several well distinguishable processes. On the contrary the same material after high deformation (c.f. e.g. [7,8]) gives only two stages (III and IV) without any noticeable substructure. This differring behaviour may be interpreted as being due to the high defect concentration and different material structure in the latter case. By a varying influence on the local activation energy by interaction between closely sited defects [26,27] the recovery of several defects then may overlap and lead to an apparently unique stage.

The separation of orientable recovery effects during annealing

from other contributions to the recovery spectrum occurring simultaneously (c.f.fig.4) may be interpreted by the assumption that some lattice defects have an influence on the magnetoresistive susceptibility χ_R in a twofold way:

One contribution to the hindrance of magnetization processes may be ascribed to the stress fields of the defects. Another contribution due to the same type of defects can arise by stabilization of the local magnetization through variations in the anisotropy axis distribution of anisotropic defects (orientational stabilization [23,24]) or by diffusion into energetically favorable positions with respect to the magnetoelastic energy (diffusional stabilization [25]). The latter effects can occur if their relaxation times at the temperatures of the annealing experiment are small enough compared with its duration. Magnetization processes which imply local variations of the direction of magnetization would then be hindered.

Defects (e.g. interstitials in dumbell configuration) which cause a pure orientational stabilization [11] generally show a reorientation and recovery at two separated temperature intervals. The occurance of a diffusion stabilization is directly associated with a far-reaching migration and thus with the annihilation of this particular type of defect (e.g.vacancy) [11].

The χ_R data from a sample that has been annealed in an alternating magnetic field may be preferentially due to the first mentioned mechanism. After annealing in a constant external field an additional orientational or diffusional stabilization may grow effective. For this reason differences $\Delta\chi_R^{ac,dc}$ between χ_R data which have been measured after a recovery of a sample at the same temperature, but under two different external field conditions mentioned may be used for the analysis of the annealing processes. The type of stabilizing defect just then contributing to the observed annealing effects in the $\Delta\chi_R^{ac,dc}$ curve may also be assigned to the variations in the R and χ_R recovery.

With the variation of such differences at a sequence of isochronal annealing temperatures stabilizing effects were observed in the temperature region from 20 to 120 °C as well as between 200 and 270 °C (c.f.figs.5 and 6). The preceeding considerations suggest to relate the effect at the lower temperatures to the orientational stabilization with a recovery of the defects

responsible above about 75 °C. Interstitials in dumbell configuration which would be capable to show a relaxation phenomenon above about 0 °C (SEEGER et al. [11]) would be expected to entrain the observed effects. This interpretation is consistent with the order of reaction $g \approx 2$ and the activation energies E^M_{1I} as they were evaluated from the data presented here (c.f.fig.5), being within the limits of error in agreement with results from other authors using various methods for the observations of migration and annihilation of interstitials (e.g. [2,7]).

The appearance of two well separated branches of the recovery of χ_R under different magnetic field treatment during the annealing between 200 and 270 °C (fig.6) may be interpreted by a diffusional stabilization of the local magnetization by vacancies being individually isotropic defects. This interpretation is supported by the order of reaction $g \approx 1$ as well as the activation energy for the migration E^M_{1V} evaluated here, being consistent with results of other authors with different methods [2,3,7,9]. The variation of the field treatment splitting of the recovery curves between 200 and 270 °C (c.f.fig.6) may be interpreted as follows. Just above 200 °C the vacancies diffuse to neighbouring regions in the interior of the material where they can contribute a lowering of the magnetoelastic free energy. Thus metastable sinks arise locally. This effect increases with rising annealing temperature and the number of vacancies becoming mobile. Simultaneously the migration paths grow longer during the temperature interval of the annealing experiments and this leads to a disappearance of the defects by reaction with irreversible sinks. The latter competing effect entrains thus a decay of the magnetic stabilization and therefore of the aforementioned splitting up of the recovery curves. The superposition of both effects is qualitatively consistent with the experimental results (c.f.fig.6) and was used as an argument for the evaluation procedure used for g and E^M_{1V}.

The results of the analysis of the splitting regions may be correlated with corresponding temperature intervals of the R as well as the χ_R recovery (figs.3,4). While the first mentioned annealing contribution proceeds in a single step with only one defect involved each time, the description of the total recovery between 75 °C and 120 °C as well as 200 and 270 °C necessitates a consideration of some additional contributions. These could arise as

a cause of the following possibilities.
a. Simultaneously with the effect influencing the orientable recovery another defect shows migration or rearrangement.
b. During the recovery of one type of defects (e.g.interstitials or vacancies) some transient internal stresses may arise [28] which influence by magnetostriction χ_R as well as the average electrical resistivity R. A detailed discussion of such effects taking into account the distribution of magnetization vectors show a transient decrease in χ_R to be related with a rise in R. The superposition of such an effect on the undisturbed recovery curve may lead to the observed behaviour.

A decision between these two interpretations is not possible from the present experiments. It should be noted that a contribution due to mechanism b. would be consistent with some results from recent recovery experiments on copper [13,17].

According to generally accepted models of point defect production during plastic deformation these defects are sited in rows more or less widely spaced [29]. Such a configuration favors a formation of aggregates of these. For the conditions observed in these experiments divacancies, vacancy tetrahedra and dislocation loops should be taken into consideration. According to results of KRESSEL et al. [8] as well as SEEGER et al. [11] the migration and annihilation of divacancies might be responsible for the stage between about 20 and 50 °C (c.f.fig.3). As their recovery begins even below 0 °C the concentration above 20 °C might expectedly be too small to contribute noticeably to the orientable recovery effects observed here. A formation of vacancy tetrahedra and/or dislocation loops as it has been discussed by SIEGEL et al. [30] could show a preferential probability in a region of temperature where the long-range migration of monovacancies has set in. This would occur in the upper part of the splitting region between about 240 and 270 °C. The decrease of the χ_R curve in this temperature interval (c.f.fig.3) which does not show a significant covariant analogon in the recovery of the electrical resistivity could be ascribed to vacancy agglomeration . These would be expected to increase the hindrance of magnetization processes some more than the spatially distributed individual vacancies would have done [31]. An agglomeration entrains a reduction of the electrical resistivity [32].

References

[1] SOSIN,A. and J.A.BRINKMAN: Acta metallurg. 7,478 (1959)

[2] MEHRER,H., H.KRONMÜLLER u. A.SEEGER: phys.stat.sol. 10,725 (1965)

[3] SCHUMACHER,D., W.SCHÜLE u. A.SEEGER: Z.Naturforschg. 17a, 228 (1962)

[4] JÄGER,H.: Z.Metallkde. 55,17 (1964)

[5] WUTTIG,M. and H.K.BIRNBAUM: J.Phys.Chem.Solids 27,225 (1966)

[6] CLAREBROUGH,L.M., M.E.HARGREAVES, M.H.LORETTO and G.W.WEST: Acta metallurg. 8,797 (1960)

[7] SIMSON,P. u. R.SIZMANN: Z.Naturforschg. 17a,596 (1962)

[8] KRESSEL,H., D.V.SHORT and N.BROWN: Acta metallurg. 15,525 (1967)

[9] KLIMANEK,P., G.REICHEL u. H.SCHARF: phys.stat.sol. 11,723 (1965)

[10] KRAUSE,D. u. G.GRAF: IEEE Trans. Mag-2,483 (1966)

[11] SEEGER,A., H.KRONMÜLLER u. H.RIEGER: Z.angew.Physik 18,377 (1965)

[12] BALTHESSEN,E., K.ISENBECK and H.WENZL : phys.stat.sol. 8,593 (1965)

[13] HELLENTHAL,W., R.LÜCKE, H.OSTHOLT u. J.SIEBENECK: Verhandl. DPG (VI) 3,94 (1968)

[14] HELLENTHAL,W., R.LÜCKE u. H.OSTHOLT: to be published

[15] DAWSON,H.I.: Acta metallurg. 12,113 (1964)

[16] SPARK,I.J.: Acta metallurg. 15,424 (1967)

[17] HELLENTHAL,W. u. J.SIEBENECK: Verhandl. DPG (VI) 2,83 (1967)

[18] KÖSTER,E.: phys.stat.sol. 19,153 (1967)

[19] TRÄUBLE,H. u. A.SEEGER: Z.angew.Physik 21,299 (1966)

[20] TRÄUBLE,H. in "Moderne Probleme der Metallphysik",Band 2 , ed. A.Seeger, Springer, Berlin 1965, p.157

[21] KRONMÜLLER,H. u. O.BUCK: phys.stat.sol. 6,207 (1964)

[22] HELLENTHAL,W. u. U.LOTTER: Z.angew.Physik, in press

[23] NEEL,L.: J.Phys.Radium 13,249 (1952)

[24] KLEIN,M.V. and H.KRONMÜLLER: J.appl.Phys. 33,2191 (1962)

[25] DIETZE,H.-D.: Techn.Mitt.Krupp 17,67 (1959)

[26] OVERHAUSER,A.W.: Phys.Rev. 90,393 (1953)

[27] HUEBENER,R.P. in "Lattice Defects in Quenched Metals", eds. R.M.J.Cotterill, M.Doyama, J.J.Jackson and M.Meshii, Academic Press, New York 1965, p.569

[28] HELLENTHAL,W.: Phys.Letters 27A,251 (1968)

[29] BALLUFFI,R.W.,J.S.KOEHLER and R.O.SIMMONS in "Recovery and Recrystallization of Metals", ed.L.Himmel, Interscience Publishers, New York 1963, p.1

[30] SIEGEL,R.W., R.W.BALLUFFI and L.E.THOMAS: Acta metallurg. 16, 7 (1968)

[31] KRONMÜLLER,H. in "Moderne Probleme der Metallphysik",Band 2 , ed. A.Seeger, Springer, Berlin 1965, p.24

[32] ASDENTE,M. and J.FRIEDEL: J.Phys.Chem.Solids 11,115 (1959)

Author Index